Adaptive analysis-aware defeaturing

Ondine Gabrielle CHANON

*"Le véritable voyage de découverte ne consiste
pas à chercher de nouveaux paysages,
mais à avoir de nouveaux yeux."*

*"The real voyage of discovery consists
not in seeking new landscapes
but in having new eyes."*

— Marcel Proust

À mes parents.

To my parents.

Abstract

Removing geometrical details from a complex domain is a classical operation in computer aided design for simulation and manufacturing. This procedure simplifies the meshing process, and it enables faster simulations with less memory requirements. However, depending on the partial differential equation that one wants to solve in the geometrical model of interest, removing some important geometrical features may greatly impact the solution accuracy. For instance, in solid mechanics simulations, such features can be holes or fillets near stress concentration regions. Unfortunately, the effect of geometrical simplification on the accuracy of the problem solution is often neglected, because its analysis is a time-consuming task that is often performed manually, based on the expertise of engineers. It is therefore important to have a better understanding of the effect of geometrical model simplification, also called defeaturing, to improve our control on the simulation accuracy along the design and analysis phase.

In this thesis, we formalize the process of defeaturing, and we analyze its impact on the accuracy of solutions of some partial differential problems. To achieve this goal, we first precisely define the error between the problem solution defined in the exact geometry, and the one defined in the simplified geometry. Then, we introduce an *a posteriori* estimator of the energy norm of this error. This allows us to reliably and efficiently control the error coming from the addition or the removal of geometrical features. We subsequently consider a finite element approximation of the defeatured problem, and the induced numerical error is integrated to the proposed defeaturing error estimator. In particular, we address the special case of isogeometric analysis based on (truncated) hierarchical B-splines, in possibly trimmed and multipatch geometries. In this framework, we derive a reliable *a posteriori* estimator of the overall error, i.e., of the error between the exact solution defined in the exact geometry, and the numerical solution defined in the defeatured geometry.

We then propose a two-fold adaptive strategy for analysis-aware defeaturing, which starts by considering a coarse mesh on a fully-defeatured computational domain. On the one hand, the algorithm performs classical finite element mesh refinements in a (partially) defeatured geometry. On the other hand, the strategy also allows for geometrical refinement. That is, at each iteration, the algorithm is able to choose which missing

Abstract

geometrical features should be added to the simplified geometrical model, in order to obtain a more accurate solution.

Throughout the thesis, we validate the presented theory, the properties of the aforementioned estimators and the proposed adaptive strategies, thanks to an extensive set of numerical experiments.

Keywords: Defeaturing, geometric simplification; *a posteriori* error estimation, adaptivity; isogeometric analysis, trimming.

Résumé

La suppression de détails géométriques d'un domaine complexe est une opération classique en conception assistée par ordinateur pour la simulation ou la fabrication. Ce processus simplifie l'opération de maillage, et permet des simulations plus rapides et qui nécessitent moins de mémoire. Cependant, en fonction de l'équation aux dérivées partielles que l'on veut résoudre sur le modèle géométrique d'intérêt, la suppression de certains détails géométriques importants peut avoir un impact considérable sur la précision de la solution. Par exemple, pour des simulations en mécanique des solides, ces détails peuvent être des trous ou des congés dans les zones où se concentre la contrainte mécanique. Malheureusement, l'effet de la simplification géométrique sur la précision de la solution du problème est souvent négligée, car son analyse est une tâche fastidieuse qui est souvent faite manuellement et qui est également souvent basée sur la seule expertise des ingénieurs. Il est donc important de mieux comprendre l'effet du *defeaturing*, c'est-à-dire de la simplification de modèles géométriques, pour améliorer notre contrôle sur la précision des simulations tout au long de la phase de conception et d'analyse.

Dans cette thèse, nous formalisons le processus de *defeaturing* et nous analysons son impact sur la précision de la solution de quelques problèmes aux dérivées partielles. Pour atteindre cet objectif, nous définissons d'abord précisément l'erreur entre la solution du problème défini dans la géométrie exacte et celle du problème défini dans la géométrie simplifiée. Ensuite, nous introduisons un estimateur *a posteriori* de cette erreur en norme de l'énergie. Cela nous permet de contrôler de manière fiable et efficace l'erreur provenant de l'ajout ou de la suppression de détails géométriques. Nous considérons ensuite une approximation par éléments finis du problème simplifié, et l'erreur numérique induite est intégrée à l'estimateur d'erreur de *defeaturing* proposé. En particulier, nous abordons le cas de l'analyse isogéométrique basée sur les B-splines hiérarchiques (tronquées), dans des géométries éventuellement trimmées et multipatch. Dans ce cadre-là, nous introduisons un estimateur *a posteriori* fiable de l'erreur globale, c'est-à-dire de l'erreur entre la solution exacte définie dans la géométrie exacte et la solution numérique définie dans la géométrie simplifiée.

Par la suite, nous proposons une double stratégie adaptative pour le *defeaturing*, dont l'initialisation se fait avec un maillage grossier, et sur un domaine de calcul dans lequel tous

les détails géométriques ont été enlevés. D'une part, l'algorithme effectue un raffinement classique du maillage éléments finis, dans une géométrie (partiellement) simplifiée. D'autre part, la stratégie permet également un raffinement géométrique. C'est-à-dire qu'à chaque itération, l'algorithme est capable de choisir quels détails géométriques manquants doivent être ajoutés au modèle géométrique simplifié, afin d'obtenir une solution plus précise.

Tout au long de la thèse, nous validons la théorie présentée, les propriétés des estimateurs susmentionnés et les stratégies adaptatives proposées sur un ensemble étendu de tests numériques.

Mots-clés : *Defeaturing*, simplification de modèles géométriques ; estimation de l'erreur *a posteriori*, adaptativité ; analyse isogéométrique, *trimming*.

Acknowledgements

First and foremost, I wish to thank my supervisor, Prof. Annalisa Buffa, without whom this thesis would never have seen the light of day: I am deeply grateful for your guidance, your support, our scientific and personal discussions, your time and your trust. Thank you for the many things I have learned from you, for providing me the confidence I needed, for creating the best possible work environment, and for showing your enthusiasm by advertising and giving me the opportunity to advertise this work at many conferences.

I would also like to extend my gratitude to Dr. Pablo Antolín, for accepting to take on the role of co-supervisor, for your kindness and your work. Your different point of view on this thesis has allowed me to significantly improve it. I also owe a very special thanks to Dr. Rafael Vázquez: having you join this project has been an important turning point of my PhD journey. Thank you for your seemingly infinite patience and kindness, your very precise proofreading of our works, and the many fruitful discussions we have shared.

I also wish to thank the members of the jury: Prof. Stefan Sauter, Prof. Martin Vohralík and Prof. Nicolas Boumal, for kindly agreeing to review this work as well as for providing useful comments which improved the final version of this dissertation. Many thanks also to Prof. Fabio Nobile, who kindly took on the role of president of the jury.

Additionally, I would like to acknowledge all the past and present members of the continuously growing MNS chair with whom I have exchanged a lot, as well as our precious former and current secretaries, Jocelyne and Pauline. In particular, I would like to thank Espen, for the good laughs and for sharing the office during this last year, Ric, our life master and my reference for finding references, and Ale, for her friendship, her trustworthiness, and for our adventures in the mountains. And most of all, a very special thank you to Luca, *Jjjuca*, for everything we have shared, from the office and coffee breaks to the many hikes and dinners. Thank you for being this incredible friend with whom I feel free to laugh, work as well as cry. I would never trade these roller coaster PhD years to share them with anyone else.

My next acknowledgement goes to the other MATHICSE members, for forming such a friendly and positive group, both at work and out of work. I would like to thank in particular Axel, Cate, *Prof.* Ceci, Davide, Edino, *Prof.* Massei, Maude, Paride, Sam, *Coffee master* Simone, *Sgt.* Statti, Sundar and Yannis. A special thanks goes to Nicolino and Pego who always find the way to make me laugh, to Riccardo whose joyful voice in

Acknowledgements

the next office animated my gray afternoons, and to Eli, who has this incredible capacity to brighten my days. My deepest gratitude also goes to André, for being the kindest and most reliable friend everyone dreams of, and to Ali, not only for sharing our flat, but also our laughs, cries and stress peaks; your unlimited energy has provided me an invaluable motivation. I would also like to sincerely thank Stefano, for the many shared adventures, and for being of unforgettable support during the hardest year of my life.

Additionally, I would like to express my sincere gratitude to my students, who taught me as much as I taught them, to the friends I met during conferences, in particular Davide and Massimo who are the guarantee of great laughter, and to the members of the EPFL first aid team, for introducing me to this world of mutual aid outside of my scientific bubble. Furthermore, I also wish to acknowledge my dear friends Diego, Giorgia, Leo, Luca, and William, for the uncountable evenings we have spent together at SPZ, and the many adventures we have shared. A very special thanks goes to Martino: I particularly cherish the many discussions we have had together, your help has been priceless during hardships and I will never thank you enough. My deepest gratitude is also addressed to the best possible hosts, SPZ: this PhD would definitely not have been as bright without your bonding dinners full of laughs.

I would also like to thank my long lasting friends: thank you Lola, Max and PB, for those many years of friendship and sharing; thank you Gabriella, Julia, Mélanie and Nicky, because your presence always makes me a better person; thank you Cécile, for being my invaluable lifelong friend; thank you Anita, for always being here, your smile always reminds me to look at the bright side; and thank you Carleigh, Jenna and the Sinclair's family, for your support from many (thousands of) kilometers away. Et parce que je ne t'ai jamais assez remercié, merci également à toi, Djo, d'être le plus loyal de tous les amis, à tel point que le mot *ami* n'est qu'un mauvais euphémisme.

A very special thanks goes to Ste and to his wonderful and welcoming family. I will never be able to correctly express how much of this thesis is thanks to you, Ste. Thank you for always believing in me, especially when I was not, thank you for your support, your attention and your craziness, thank you for the many (literal and figurative) kilometers we have walked together: I cannot wait for more.

Last, but clearly not least, I wish to thank my family. En particulier, je suis infiniment reconnaissante envers ma soeur et mon frère, Sabine et Théo : notre trio a été essentiel pour que je trouve un équilibre pendant ces années difficiles pour notre famille. Votre vision du monde m'a poussée à aller de l'avant : bienveillante pour Bibi, passionnée pour Titi, profondément attentionnée pour tous les deux. Pour finir, cette thèse n'aurait certainement pas été possible sans le soutien inconditionnel de mes parents. Papa, Maman, merci de m'avoir donné votre amour, et la force et la confiance nécessaires pour mener à bien mes projets. Il est impossible de mettre des mots sur ce que représente pour moi le fait de terminer cette aventure avec vous deux à mes côtés. Je ne pourrais pas être ici à ce moment précis si ce n'était pas pour vous. Ma dernière pensée va à mes grands-parents qui, je l'espère, seraient fiers du travail contenu dans cette thèse.

Lausanne, September 23rd, 2022   Ondine Chanon

Contents

Contents

Notation

Abbreviations

BVP	Boundary value problem
CAD	Computer-aided design
FEM	Finite element method
HB-spline	Hierarchical B-spline
IGA	Isogeometric analysis
NURBS	Non uniform rational B-spline
PDE	Partial differential equation
THB-spline	Truncated hierarchical B-spline

Sets

$\mathbb{N}$	Set of positive integers
$\mathbb{R}$	Set of real numbers
$\#S$	Cardinality of a discrete set S
$\subset$	Set inclusion allowing for equality
$\hookrightarrow$	Continuous embedding

Differentials

∇	Gradient or Jacobian operator
$\nabla\cdot$	Divergence operator
Δ	Laplacian operator

Inequalities

Let A and B be two expressions depending on a set T of parameters which will be specified and which will change in every chapter of this thesis. We write:

$A \lesssim B$	whenever $A \leq cB$ with a constant $c > 0$ independent of T
$A \simeq B$	whenever $A \lesssim B$ and $B \lesssim A$
$A \ll B$	whenever $A \leq c(T)B$ with a large constant $c > 0$ which may depend on T

Contents

Let $n \in \{2, 3\}$, let $\mathfrak{D} \subset \mathbb{R}^n$, and let Λ be a subset of the boundary of $\mathfrak{D}$.

Vectors and matrices

Let $\mathbf{v}_1, \mathbf{v}_2 \in \mathbb{R}^n$, and let $M_1, M_2 \in \mathbb{R}^{n \times n}$.

$\mathbf{v}_1 \cdot \mathbf{v}_2$	Scalar product
$M_1 : M_2$	Frobenius product
$\| \cdot \|_{\ell^2}$	Discrete ℓ^2-norm, Euclidean vector norm, Frobenius matrix norm

Geometrical domains

$\|\mathfrak{D}\|$	–	n-dimensional Lebesgue measure
–	$\|\Lambda\|$	$(n-1)$-dimensional Hausdorff measure
$\overline{\mathfrak{D}}$	$\overline{\Lambda}$	Closure
$\mathrm{int}(\mathfrak{D})$	$\mathrm{int}(\Lambda)$	Interior
$\partial\mathfrak{D}$	$\partial\Lambda$	Boundary
$\mathrm{conn}(\mathfrak{D})$	$\mathrm{conn}(\Lambda)$	Set of connected components
$\mathrm{hull}(\mathfrak{D})$	$\mathrm{hull}(\Lambda)$	Convex hull
$\mathrm{diam}(\mathfrak{D})$	–	Diameter
–	$\mathrm{diam}(\Lambda)$	Manifold diameter of the convex hull

Functions

Let $v : \mathbb{R}^n \to \mathbb{R}$, $\boldsymbol{v} : \mathbb{R}^n \to \mathbb{R}^n$, $w : \Lambda \to \mathbb{R}$ and $\boldsymbol{w} : \Lambda \to \mathbb{R}^n$.

$v\|_{\mathfrak{D}}$	$\boldsymbol{v}\|_{\mathfrak{D}}$	Restriction to $\mathfrak{D}$
$\overline{v}^{\mathfrak{D}}$	$\overline{\boldsymbol{v}}^{\mathfrak{D}}$	(Component-wise) function average over $\mathfrak{D}$
$\mathrm{supp}\,(v)$	$\mathrm{supp}\,(\boldsymbol{v})$	Support
$\mathrm{tr}_\Lambda(v)$	$\mathrm{tr}_\Lambda(\boldsymbol{v})$	Trace on Λ
$w^\star$	$\boldsymbol{w}^\star$	(Component-wise) extension by 0 to $\partial\mathfrak{D}$

Functional spaces

$C^k(\mathfrak{D})$	$C^k(\Lambda)$	Space of k-times continuously differentiable functions, $k \in \mathbb{N} \cup \{\infty\}$
$L^p(\mathfrak{D})$	$L^p(\Lambda)$	Lebesgue space of exponent $p \in [1, \infty]$
$\boldsymbol{L}^p(\mathfrak{D})$	$\boldsymbol{L}^p(\Lambda)$	Lebesgue space of vector-valued functions, $p \in [1, \infty]$
$\mathbb{L}^p(\mathfrak{D})$	$\mathbb{L}^p(\Lambda)$	Lebesgue space of matrix-valued functions, $p \in [1, \infty]$
$H^s(\mathfrak{D})$	$H^s(\Lambda)$	Sobolev space of order $s \in \mathbb{R}$
$\boldsymbol{H}^s(\mathfrak{D})$	$\boldsymbol{H}^s(\Lambda)$	Sobolev space of vector-valued functions, $s \in \mathbb{R}$
$\mathbb{H}^s(\mathfrak{D})$	$\mathbb{H}^s(\Lambda)$	Sobolev space of matrix-valued functions, $s \in \mathbb{R}$

$H^1_{w,\Lambda}(\mathfrak{D})$	Set of functions $v \in H^1(\mathfrak{D})$ such that $\mathrm{tr}_\Lambda(v) = w$, with $w \in H^{\frac{1}{2}}(\Lambda)$
$\boldsymbol{H}^1_{\boldsymbol{w},\Lambda}(\mathfrak{D})$	Set of functions $\boldsymbol{v} \in \boldsymbol{H}^1(\mathfrak{D})$ such that $\mathrm{tr}_\Lambda(\boldsymbol{v}) = \boldsymbol{w}$, with $\boldsymbol{w} \in \boldsymbol{H}^{\frac{1}{2}}(\Lambda)$
$H^{\frac{1}{2}}_{00}(\Lambda)$	Set of functions $w \in L^2(\Lambda)$ such that $w^\star \in H^{\frac{1}{2}}(\partial\mathfrak{D})$
$\boldsymbol{H}^{\frac{1}{2}}_{00}(\Lambda)$	Set of functions $\boldsymbol{w} \in \boldsymbol{L}^2(\Lambda)$ such that $\boldsymbol{w}^\star \in \boldsymbol{H}^{\frac{1}{2}}(\partial\mathfrak{D})$
$H^{-\frac{1}{2}}_{00}(\Lambda)$	Dual space of $H^{\frac{1}{2}}_{00}(\Lambda)$
$\boldsymbol{H}^{-\frac{1}{2}}_{00}(\Lambda)$	Dual space of $\boldsymbol{H}^{\frac{1}{2}}_{00}(\Lambda)$
$\mathrm{tr}_\Lambda(S)$	Trace space on Λ of the functions in $S \subset H^1(\mathfrak{D})$, i.e., $\{\mathrm{tr}_\Lambda(v) : v \in S\}$
V^*	Dual space of a functional space V

For the next definitions, let $\{\Lambda^k\}_{k=1}^{N_\Lambda}$ be a given partition of Λ such that each Λ^k is a flat element, i.e., it is a straight line if $n = 2$ or a flat square or triangle if $n = 3$.

$\mathbb{Q}_m(\Lambda^k)$	Space of polynomials of degree at most $m \in \mathbb{N}$ on each variable
$\mathbf{Q}_m(\Lambda^k)$	Space of vector-valued polynomials of degree at most m on each variable
$\mathbb{Q}^{\mathrm{pw}}_{m,0}(\Lambda)$	Space of continuous piecewise polynomials $\phi : \Lambda \to \mathbb{R}$ that vanish at the boundary $\partial\Lambda$, i.e. $\phi\|_{\partial\Lambda} \equiv 0$, $\phi\|_{\Lambda^k} \in \mathbb{Q}_m(\Lambda^k)$ for all $k = 1, \ldots, N_\Lambda$
$\mathbf{Q}^{\mathrm{pw}}_{m,\mathbf{0}}(\Lambda)$	Space of continuous piecewise polynomials $\boldsymbol{\phi} : \Lambda \to \mathbb{R}^n$ that vanish at the boundary $\partial\Lambda$, i.e. $\boldsymbol{\phi}\|_{\partial\Lambda} \equiv \mathbf{0}$, $\boldsymbol{\phi}\|_{\Lambda^k} \in \mathbb{Q}_m(\Lambda^k)$ for all $k = 1, \ldots, N_\Lambda$

Norms

$\|\|\cdot\|\|_{\mathfrak{D}}$		Energy norm induced by a bilinear form
$\|\cdot\|_{L^p(\mathfrak{D})}$	$\|\cdot\|_{L^p(\Lambda)}$	L^p-norm, $p \in [1,\infty]$
$\|\cdot\|_{0,\mathfrak{D}}$	$\|\cdot\|_{0,\Lambda}$	L^2-, $\boldsymbol{L}^2$- and $\mathbb{L}^2$-norms
$\|\cdot\|_{s,\mathfrak{D}}$	$\|\cdot\|_{s,\Lambda}$	H^s-, $\boldsymbol{H}^s$- and $\mathbb{H}^s$-norms, $s \in \mathbb{R}$
$\|\cdot\|_{s,\mathfrak{D}}$	$\|\cdot\|_{s,\Lambda}$	H^s-, $\boldsymbol{H}^s$- and $\mathbb{H}^s$-semi-norms, $s \in \mathbb{R}$
$\|\cdot\|_{H^{1/2}_{00}(\Lambda)}$	$\|\cdot\|_{\boldsymbol{H}^{1/2}_{00}(\Lambda)}$	Norm in $H^{\frac{1}{2}}_{00}(\Lambda)$, resp. $\boldsymbol{H}^{\frac{1}{2}}_{00}(\Lambda)$
$\|\cdot\|_{H^{1/2}_{00}(\Lambda)}$	$\|\cdot\|_{\boldsymbol{H}^{1/2}_{00}(\Lambda)}$	Semi-norm in $H^{\frac{1}{2}}_{00}(\Lambda)$, resp. $\boldsymbol{H}^{\frac{1}{2}}_{00}(\Lambda)$
$\|\cdot\|_{H^{-1/2}_{00}(\Lambda)}$	$\|\cdot\|_{\boldsymbol{H}^{-1/2}_{00}(\Lambda)}$	Norm in $H^{-\frac{1}{2}}_{00}(\Lambda)$, resp. $\boldsymbol{H}^{-\frac{1}{2}}_{00}(\Lambda)$

1 Introduction

1.1 Motivation

In a wide range of engineering applications, physics-based simulations are intensively used for the design and manufacturing of complex objects. The following examples are given in [Thakur et al., 2009], to only cite a few:

"Multi-body dynamics simulations are used to determine the sizes of actuators during the design of robots. Finite element simulations are used in structural and thermal analysis of components in the automotive and aerospace industries. Computational fluid dynamics simulation is used in automotive engine cooling system design."

In particular, thanks to the parallel development of computers and of always-faster computing technologies, the finite element method (FEM) has revolutionized every field of engineering since its first steps [Hrennikoff, 1941; Courant, 1943]. The basic idea of FEM is to decompose the considered object, i.e., the computational domain, into a finite number of (mapped) polygonal elements. This process, called meshing, generates an analysis-suitable approximation of the geometry. Then, based on the so-called isoparametric paradigm, the same polynomial functions used to describe the mesh are employed in the analysis to approximate the solution field.

With the advance of engineering knowledge, these simulations are performed on objects of increasing geometric complexity, nowadays mainly described by three-dimensional computer-aided design (CAD) models. These models often contain a large number of geometric details of different scales, also called geometric features. The illustration in Figure 1.1 shows two important components of a car, a combustion engine and a B-pillar, whose designs contain many features of different type. These features are for instance the screw holes in the engine block, the gearwheels' teeth, the rounds at the bottom of the poppet valves, or the longitudinal rounds along the B-pillar. In a design, the presence of features often comes from manufacturing constraints or from mechanical requirements. Fillets and rounds are good examples: they may be added to a design because of the
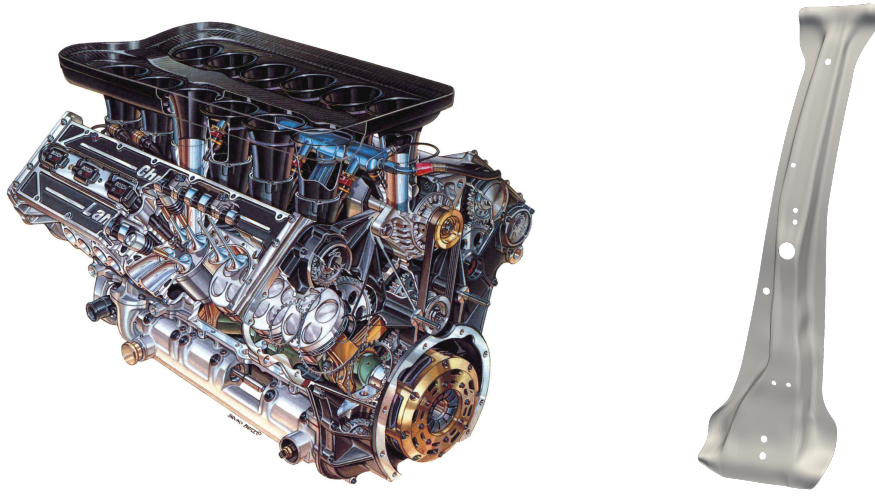
(a) Internal combustion engine of a F1 car.[1]

(b) B-pillar of an individual car.[2]

Figure 1.1 – Two examples of complex geometric designs on which physics-based simulations need to be performed.

need of using round-tipped end mills to manufacture this specific part, or because they are necessary to provide mechanical robustness. This shows the potential complexity of geometrical models on which simulations need to be performed.

Unfortunately, the construction of a finite element mesh on such complex domains may fail, or if it does not, the mesh may require a very large number of elements – or equivalently, degrees of freedom –, therefore leading to simulations which are too costly or even unfeasible. For instance, it has been shown in [White et al., 2003; Lee et al., 2005] that the cost of the underlying simulation may be increased by up to a factor 10 in the presence of a single geometric feature of relatively small size. In addition, in order to meet functionality, manufacturability and aesthetic requirements, the need to adjust geometric parameters requires repeated design changes involving adding or removing geometrical features to the design. This typical process in simulation-based design for manufacturing quickly becomes prohibitive when the geometry is very complicated.

However, depending on the problem at hand, the geometric description of the considered object may unnecessarily increase the complexity of the simulation. That is, the full geometric complexity may not be needed for the underlying analysis. Or in other words, the geometric description of the object may require a high number of degrees of freedom, but not all of them are necessary to perform an accurate analysis, and taking all of them into account is even potentially too costly. For instance, the screw holes away from stress concentration regions add geometric complexity, without having much influence on the

---

[1]Image courtesy to https://www.auto-innovations.com/.
[2]Image courtesy to the authors of [Coradello et al., 2020].

(a) Original geometry with multiple features (fillets, rounds, holes, protrusions).

(b) Defeatured (or simplified) geometry.
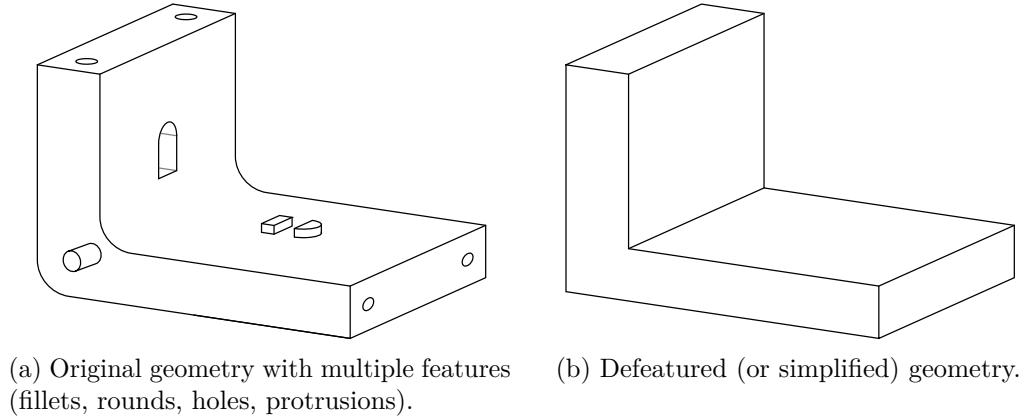
Figure 1.2 – Illustration of defeaturing.

mechanical properties of the combustion engine of Figure 1.1a. At the contrary, the rounds on the poppet valves are essential features for the engine to function properly. To deal with complex geometries and to accelerate the process of analysis-aware geometric design, it is therefore essential to be able to simplify the geometric model, process also called defeaturing, while understanding the effect of this process on the simulation accuracy. The idea of defeaturing is illustrated in Figure 1.2, where a complex geometry is shown together with its simplified version, in which all the features have been removed.

Moreover, the automatic integration of design and analysis tools in a single workflow has been an important topic of research for many years, see [Farouki, 1999; Riesenfeld et al., 2015]. Indeed, the CAD design of an object and its analysis-suitable mesh are *a priori* two distinct geometric descriptions of the same computational domain, and the need to transform the first one into the other is costly, time consuming, and it creates geometric inaccuracies. At the beginning of the century, in the seminal paper [Hughes et al., 2005], a successful methodology has emerged to mitigate this issue. This method is referred to as isogeometric analysis (IGA). The fundamental idea of IGA consists in employing the basis functions used to describe CAD geometries for the numerical analysis of the underlying partial differential equations (PDEs). That is, IGA uses smooth B-splines or variants thereof as basis functions for the solution field. This new paradigm has opened the road to an extensive amount of research; the interested reader is referred to [Cottrell et al., 2009] for a review of the method, and to [Hughes, 2017] for a review of a wide range of real world applications on which the method has shown its potential. The mathematical foundations of IGA have also been developed in [Bazilevs et al., 2006; Beirão da Veiga et al., 2014], and numerous implementations can now be found, see e.g. [Nguyen et al., 2015; Pauletti et al., 2015; Vázquez, 2016].

Different extensions of the original IGA method have been developed in order to deal with geometries of increased complexity: the main developments include for instance multipatch domains [Buffa et al., 2015; Bracco et al., 2020], or geometries obtained by

Boolean operations such as intersections (trimming) [Schmidt et al., 2012; Marussig and Hughes, 2018; Antolín et al., 2019; Wei et al., 2021; Antolín and Hirschler, 2022] or unions [Zuo et al., 2015; Kargaran et al., 2019; Antolín et al., 2021]. Since the tensor-product nature of standard B-splines hinders the possibility of local refinement, the construction of locally refined splines has also been a very active area of research. In this work, we focus on hierarchical B-splines (HB-splines) [Forsey and Bartels, 1988; Kraft, 1997; Vuong et al., 2011] and their truncated counterpart (THB-splines) [Giannelli et al., 2012, 2016; Buffa and Garau, 2017], which are mathematically well-understood, conceptually simple, and easy to implement. Their development and integration in an IGA mesh adaptive framework have been recently reviewed in [Buffa et al., 2021b].

Nevertheless, dealing with very complex geometries remains challenging, and even the most recent and the most efficient methods may come at a prohibitive cost because of the inherent complexity of the designs. This is where analysis-aware defeaturing handily comes into play. More precisely, suppose that one is able to determine which are the geometrical features of a complex geometry that have the least influence on the accuracy of the PDE solution at hand. Then, one can simplify the geometric model by defeaturing, leading to an easier and cheaper analysis. By doing so, the meshing process is also simplified. But it is important to consider the impact of the geometrical changes on the analysis phase, i.e., to control the error introduced by defeaturing, in order to provide an accurate solution of the problem.

1.2 Defeaturing error estimation: literature review

For a long time, defeaturing has been approached using subjective *a priori* criteria, which mostly rely on the engineers' expertise, or which are based on geometrical considerations such as variations in volume or in area of the domain, see [Thakur et al., 2009]. Still based on some *a priori* knowledge of the problem at hand, more objective criteria have then been considered. These indicators are for instance based on the verification of constitutive or conservation laws, see [Fine et al., 2000; Foucault et al., 2004; Rahimi et al., 2018]. However, in order to automatize the simulation-based design process, the interest is to have an *a posteriori* criterion, which assesses the error introduced by defeaturing based on the result of the analysis in the defeatured geometric model. Following this direction, an *a posteriori* criterion is given in [Ferrandes et al., 2009]: it evaluates an approximation of the energy norm between the exact solution of the problem at hand, and the solution on the defeatured geometry. It is intuitively based on the fact that the energy error due to defeaturing is concentrated in the modified boundaries of the geometry, and this boundary error is estimated by solving local problems around each feature. Nevertheless, this approach does not give a demonstrated certification that the proposed criterion is indeed a good estimator of the defeaturing error.

A different approach is based on the concept of feature sensitivity analysis (FSA)

[Gopalakrishnan and Suresh, 2007, 2008; Turevsky et al., 2008, 2009]. This technique relies on topological sensitivity analysis (TSA) [Sokolowski and Zochowski, 1999; Choi and Kim, 2005], which studies the impact of infinitesimal (topological) geometrical changes on the solution of a given PDE. TSA is a method predominantly used in design optimization. The works on FSA study defeaturing in geometries with a single arbitrarily-shaped feature. First order changes of quantities of interest are analyzed when a small internal or boundary hole is removed from the geometry. However, besides the underlying assumption of infinitesimal features, this technique cannot be generalized to more complex features.

An alternative approach, still based on *a posteriori* error estimators, is proposed in [Li et al., 2011] for internal holes. The idea behind this estimator is to reformulate the geometrical defeaturing error as a modeling error. More precisely, the PDE solved in two different geometries, the exact geometry and its defeatured counterpart, is rewritten as two different PDEs on a unique (reference) geometry. The modeling error is then estimated using the dual weighted residual method introduced in [Becker and Rannacher, 2001] and [Oden and Prudhomme, 2002]. This approach follows the lines of [Oden and Vemaganti, 2000; Carstensen and Sauter, 2004; Vemaganti, 2004] that study heterogeneous and perforated materials, [Repin et al., 2003] that studies the error introduced by the approximation of boundary conditions, and [Repin and Sauter, 2020] that more generally studies modeling errors arising in dimension reduction, homogenization and model simplification. These are problems that can be easily related to defeaturing. The developed technique of [Li et al., 2011] has then been generalized in [Li and Gao, 2011; Li et al., 2013a,b; Zhang et al., 2016] to different linear and non-linear problems, and to other types of features. Following similar ideas, another *a posteriori* error estimator is introduced in [Tang et al., 2013], based on the reciprocal theorem which states the conservation of solution flux in the features. However, some heuristic remains in all these contributions, and a precise mathematical study of the estimator with regards to its efficiency and stability is lacking. In particular, it is assumed that the difference between the solutions of the PDE in the exact and defeatured geometries is small, and it relies on the heuristic estimation of constants that depend on the size of the features.

Finally, it is also worth mentioning a very early method for defeaturing which also allows for coarsening, called composite finite elements and developed in [Hackbusch and Sauter, 1997a,b]. In this approach, defeaturing is tightly linked to the underlying finite element mesh, as it is assumed that defeaturing strictly comes from the fact that the mesh cannot resolve the geometrical details of the computational domain. In our approach instead, we want to be able to consider defeaturing independently from any discretization, in order to be able to decouple the errors coming from the defeaturing operation and from the numerical approximation of the problem at hand.

1.3   Objectives and outline

The objective of this work is to deepen and improve the mathematical understanding of defeaturing very complex geometries. After this introductory chapter, the thesis is structured in two main parts.

In Part I, we present a functional framework for analysis-aware defeaturing. That is, we first consider defeaturing in continuous problems, before any numerical approximation is made. This part is organized as follows.

- Chapter 2 first provides some fundamentals of functional analysis, with the basic definitions, the notation and some preliminary functional results used throughout this monograph. Then, we discuss the mathematical foundations for the description of physical phenomena in their differential and variational forms, and we provide fundamental results of existence and uniqueness of the solution of boundary value problems (BVP). Since we are interested in a quantification of the error coming from some approximation of such problems, we also discuss error estimators and the concept of adaptive strategies to reduce this error.

- We then introduce a sound mathematical framework for analysis-aware defeaturing in Chapter 3. To begin with, we consider two- and three-dimensional geometries that contain a single feature, and we work in the context of the Poisson equation for which Neumann boundary conditions are imposed on the feature. A very general feature is considered: it can either be negative (internal or boundary hole), positive (protrusion), or more complex with both positive and negative components. After providing a precise definition of the defeaturing error, we introduce an *a posteriori* estimator of the energy norm of this error. Then, we prove the reliability and efficiency (up to oscillations) of the proposed estimator, whose effectivity index is independent of the size of the feature but not of its shape. This estimator does not only consider geometrical properties of the feature, but it also takes into account the effect of defeaturing on the PDE solution accuracy. Notably, the estimator is very cheap to compute once the PDE solution in the defeatured domain is obtained, as it only requires

  - the solution of a local problem in a simplified feature (as, e.g., its bounding box), only if the feature is not negative;

  - the computation of local integrals on the boundary of the feature.

  Indeed, the proposed estimator is derived from a representation of the defeaturing error that only involves differences between feature boundary terms, as already observed in [Gopalakrishnan and Suresh, 2008; Turevsky et al., 2008] and in [Li and Gao, 2011; Li et al., 2013b,a]. Lastly, we present numerical experiments that both validate the theory presented in the chapter, and show the potential of the

proposed estimator.[3]

- Subsequently, in Chapter 4, we generalize the previous framework and results to computational domains that contain an arbitrary number of geometrical features. We also extend the study to linear elasticity problems and incompressible Stokes equations. In particular, the proposed *a posteriori* estimator of the defeaturing error has an effectivity index independent of the number of features. Based on the theoretical study of the estimator, we propose an adaptive geometric refinement strategy. That is, starting from a fully defeatured geometry, we design an algorithm able to determine at each iteration step which features need to be added to the geometrical model to reduce the defeaturing error. These important features are then added to the (partially) defeatured geometrical model at the next iteration, until the solution attains a prescribed accuracy. Numerical experiments are finally presented in complicated two- and three-dimensional geometries, demonstrating in particular that the proposed adaptive procedure ensures the convergence of the defeaturing error.[4]

Since almost all PDE solutions can only be calculated numerically, then numerical approximation methods need to be integrated to the analysis of defeatured problems. This is the scope of Part II of this thesis, in which we propose a numerical framework for analysis-aware defeaturing. This part, which considers the Poisson equation as driving problem, is structured as follows.

- In Chapter 5, we first present some fundamentals of the numerical approximation of PDEs by the finite element method. This method is then applied to the defeaturing framework, that is, the numerical approximation of the defeatured problem is precisely stated. Subsequently, we present an adaptive finite element analysis-aware defeaturing strategy, which combines the geometric refinement procedure of Chapter 4 with a finite element mesh refinement algorithm. This adaptive strategy is designed to be used with an immersed FEM, in which the mesh is not fitted to the computational domain, nor in particular, to the features that are added along the simulation. The adaptive process is driven by an *a posteriori* estimator of the discrete defeaturing energy error. More precisely, the discrete defeaturing error corresponds to the error between the exact solution defined in the exact fully-featured geometry and the numerical approximation of the solution defined in the defeatured geometry.[5]

---

[3]In accordance with the Wiley publishing agreement, this chapter is adapted from [Buffa et al., 2022b]. The main scientific research as well as the textual elaboration of the publication was performed by the author of this work.

[4]This chapter is adapted from [Antolín and Chanon, 2022]. The main scientific research as well as the textual elaboration of the publication was performed by the author of this work.

[5]Part of this chapter is adapted from [Buffa et al., 2022a]. The main scientific research as well as the textual elaboration of the publication was performed by the author of this work.

- In the remaining part of the thesis, we will concentrate more specifically on IGA as a particular and natural numerical method for the approximation of the defeatured problem. Therefore, in Chapter 6, we give a short introduction to IGA by presenting and reviewing the main properties of B-splines. Then, we review the construction of (T)HB-splines as an extension of B-splines which can be used in an adaptive framework, as they can be locally refined. Lastly, we discuss more advanced spline technologies, in particular multipatch and trimmed B-spline geometries, which allow for a numerical analysis on more complex spline domains.

- Before addressing the numerical analysis of defeaturing complex B-spline geometries, we first develop an adaptive mesh refinement strategy on trimmed geometries, in the context of (T)HB-spline based IGA. This is the content of Chapter 7. This step is needed because in our framework, features are added by immersed quadrature, i.e., without modifying the underlying mesh. And indeed, trimming consists exactly in cutting away parts of a geometric domain without reconstructing a global parametrization, i.e., without re-meshing the domain. It is a widely used operation to create complex designs in CAD, and it generates meshes that are not fitted to the described physical object. In this chapter, we derive an *a posteriori* residual estimator of the energy norm of the numerical approximation error. The estimator is proven to be reliable, independently of the number of hierarchical levels and of the way the trimmed boundaries cut the underlying mesh. Lastly, numerical experiments are presented to validate the presented theory, and to show that the estimator's effectivity index is independent of the size of the active part of the trimmed mesh elements.[6]

- Subsequently, in Chapter 8, we study the combined geometric and mesh refinement strategy of Chapter 5 in the particular case of (T)HB-spline based IGA in (potentially trimmed multipatch) geometries. In this context, we specialize to this setting the proposed *a posteriori* estimator defined in Chapter 5. Secondly, the reliability of the estimator is proven for very general geometric configurations. For the proof, we consider a given fixed iteration of the adaptive process, and a hierarchical mesh which is fitted to the (partially) defeatured geometry at that iteration. Thirdly, we discuss the generalization of the adaptive strategy and of the proof of the estimator's reliability in multipatch and trimmed – therefore unfitted – domains. Finally, numerical experiments are performed to validate the presented theory and to illustrate the proposed adaptive strategy.[7]

To close the dissertation, in Chapter 9, we draw some conclusions on the contributions of this thesis, we highlight some limitations, and we discuss possible future research directions.

---

[6]This chapter is adapted from the submitted paper [Buffa et al., 2021a]. The main scientific research as well as the textual elaboration of the publication was performed by the author of this work.

[7]Part of this chapter is adapted from [Buffa et al., 2022a]. The main scientific research as well as the textual elaboration of the publication was performed by the author of this work.

1.4 Implementation aspects

For the implementation of numerical experiments, several libraries are used in this thesis. They are listed in the following for the sake of completeness.

The methods described in this work, and all the presented numerical experiments except the one of Section 4.6.2, have been implemented on top of *GeoPDEs*[8] [Vázquez, 2016]. *GeoPDEs* is an open-source and free OCTAVE/MATLAB package for the resolution of PDEs. It has been specifically designed for IGA, and it also integrates multipatch and (T)HB-spline techniques.

Moreover, an in-house tool presented in [Antolín et al., 2019, 2022] has been used and linked with *GeoPDEs*. It is used for the geometric description and for the local meshing process required for the integration of trimmed geometries. This tool relies on the open-source geometric modeling environment *IRIT*[9] and on the geometric kernel *OpenCASCADE*[10] [OpenCASCADE, 2018].

Finally, the numerical experiment of Section 4.6.2 has been implemented in *Igatools* [Pauletti et al., 2015]. *Igatools* is a flexible and optimized C++ isogeometric library able to compute fully immersed problems, from which the in-house trimming tool from [Antolín et al., 2019, 2022] has been developed.

---

[8]http://rafavzqz.github.io/geopdes/
[9]https://www.cs.technion.ac.il/~irit/
[10]https://www.opencascade.com/

A functional framework for analysis-aware defeaturing

2 Some fundamentals and preliminaries

In this chapter, we introduce some basic definitions and notations that are used throughout the thesis, while reviewing some fundamentals of functional analysis and of the study of boundary value problems (BVPs). In Sections 2.1 and 2.2, we concentrate on Lebesgue and Sobolev spaces on given domains of $\mathbb{R}^n$, where $n = 2$ or $n = 3$. Trace spaces are of particular importance in the analysis of defeaturing problems that will be developed in the next chapters. Therefore, in Section 2.3, we present already-existing and new results on trace spaces, which will be used in the sequel. Subsequently, in Section 2.4, we lie the mathematical foundations that describe numerous physical phenomena in their differential and variational form. In particular, we address the concept of existence and uniqueness of the solution of the corresponding problem. Finally, we are interested in the analysis of the effect of perturbations or simplifications of the problem, that is, in a quantification of the error when an approximation of the BVP is solved. In Section 2.5, we thus discuss error estimators that control the approximation error, together with adaptive strategies designed to reduce this error.

The notation and derivation used in this chapter follow [Grisvard, 2011; Ern and Guermond, 2021a,b], and the author's contributions are extracted from [Buffa et al., 2022b, 2021a; Antolín and Chanon, 2022]. Moreover, we use the symbol $\lesssim$ to mean any inequality which does not depend on the size of the considered domains, but which can depend on their shape. Note that this symbol will be precisely redefined at the beginning of each chapter in which it is used, and we write $A \simeq B$ whenever $A \lesssim B$ and $B \lesssim A$.

2.1 Domain properties

Let us denote by n the space dimension with $n = 2$ or $n = 3$, and let us define the notion of Lipschitz domain in $\mathbb{R}^n$.

Definition 2.1.1. A *domain* is an open bounded subset of $\mathbb{R}^n$. A domain $\mathfrak{D}$ with boundary $\partial\mathfrak{D}$ is said to be *Lipschitz* if for every $x \in \partial\mathfrak{D}$, there exists a neighborhood $U(x)$ of x such that $U(x) \cap \partial\mathfrak{D}$ is the graph of a Lipschitz function.

Except if otherwise specified, we also assume that domains are connected. Let Λ be a d-dimensional subspace of $\mathbb{R}^n$, $d \in \{n-1, n\}$. If $d = n$, then $|\Lambda|$ denotes the n-dimensional Lebesgue measure of Λ, and if $d = n-1$, then $|\Lambda|$ denotes the $(n-1)$-dimensional Hausdorff measure of Λ. Moreover, we respectively denote $\overline{\Lambda}$ and $\text{int}(\Lambda)$ the closure and the interior of Λ. If Λ is connected and if Λ_* is a non-necessarily connected subset of Λ, we write $\text{hull}(\Lambda_*)$ the convex hull of Λ_*. More precisely, this is the smallest geodesically convex subset of Λ containing Λ_*. That is, given any two points in $\text{hull}(\Lambda_*)$, there is a unique minimizing geodesic contained within $\text{hull}(\Lambda_*)$ that joins those two points. We also denote by $\text{diam}(\Lambda_*)$ the manifold diameter of $\text{hull}(\Lambda_*)$ in Λ, i.e.,

$$\text{diam}(\Lambda_*) := \max\{\rho(x, y) : x, y \in \text{hull}(\Lambda_*)\},$$

where $\rho(x, y)$ is the infimum of lengths of continuous piecewise C^1-paths between x and y in Λ.

In this document, we will need isotropy and regularity assumptions on different pieces of domain boundaries.

Definition 2.1.2. Let Λ be a d-dimensional subset of $\mathbb{R}^n$, $d \in \{n-1, n\}$. We say that Λ is *isotropic* if

$$\text{diam}(\Lambda) \lesssim \max_{\Lambda_c \in \text{conn}(\Lambda)} \left(\text{diam}(\Lambda_c)\right),$$

and each connected component $\Lambda_c \in \text{conn}(\Lambda)$ satisfies $\text{diam}(\Lambda_c)^d \lesssim |\Lambda_c|$.

Note that if Λ is isotropic and if we let $\Lambda_{\max} := \arg\max\limits_{\Lambda_c \in \text{conn}(\Lambda)} \left(\text{diam}(\Lambda_c)\right)$, then

$$\text{diam}(\Lambda)^d \lesssim \text{diam}(\Lambda_{\max})^d \lesssim |\Lambda_{\max}| \leq |\Lambda|.$$

Definition 2.1.3. Let Λ be an $(n-1)$-dimensional subspace of $\mathbb{R}^n$. We say that Λ is *regular* if Λ is piecewise shape regular and composed of flat elements, that is, if there is $N_\Lambda \in \mathbb{N}$ such that for all $k \neq \ell$, $k, \ell = 1, \ldots, N_\Lambda$,

- $\Lambda = \text{int}\left(\bigcup\limits_{k=1}^{N_\Lambda} \overline{\Lambda^k}\right)$,

- $\Lambda^k \cap \Lambda^\ell = \emptyset$,

- $|\Lambda| \lesssim \left|\Lambda^k\right|$,

- Λ^k is flat, i.e. it is a straight line if $n = 2$ or a flat square or triangle if $n = 3$.

Remark 2.1.4. When used, the regularity condition defined in Definition 2.1.3 is taken for the sake of simplicity, but it can be relaxed by considering Λ piecewise smooth and shape regular instead.

2.2 Functional spaces

In this section, all function spaces are considered over the field of real numbers. We introduce in particular the definitions and notations of Lebesgue and Sobolev spaces that will be used throughout the thesis. For a complete presentation, the interested reader is referred to [Yosida, 1974; Brezis, 2011; Grisvard, 2011].

2.2.1 Lebesgue and Sobolev spaces

Let $\mathfrak{D}$ be a domain of $\mathbb{R}^n$. Let $L^p(\mathfrak{D})$ denote the standard Lebesgue spaces of exponent $p \in [1, \infty]$, equipped with the norm $\| \cdot \|_{L^p(\mathfrak{D})}$ defined as follows: for all $v \in L^p(\mathfrak{D})$,

$$\|v\|_{L^p(\mathfrak{D})} := \left(\int_{\mathfrak{D}} |v|^p \, \mathrm{d}x \right)^{\frac{1}{p}} \qquad \text{if } p < \infty,$$

$$\|v\|_{L^\infty(\mathfrak{D})} := \inf\{ C \geq 0 : |v(x)| \leq C \text{ for almost every } x \in \mathfrak{D} \} \qquad \text{if } p = \infty.$$

For every scalar-valued functional space presented in this chapter, the corresponding space of vector-valued functions of dimension n is denoted in bold, and the corresponding space of tensor-valued functions of dimension $n \times n$ is denoted in blackboard bold. That is, for instance, we denote by $\boldsymbol{L}^p(\mathfrak{D}) := [L^p(\mathfrak{D})]^n$ and $\mathbb{L}^p(\mathfrak{D}) := [L^p(\mathfrak{D})]^{n \times n}$ for all $p \in [1, \infty]$, and the corresponding norms are computed component-wise. To simplify the exposition, the notation corresponding to every vector- or tensor-valued functional space and to their corresponding norm is not detailed in the following, but it can be found in the list of notation. Moreover, the results presented in this chapter are given for scalar-valued functions, but the statements and their proofs can be straightforwardly generalized to vector- or tensor-valued functional spaces.

Subsequently, let $H^s(\mathfrak{D})$ denote the standard Sobolev space of order $s \in \mathbb{R}$, $s \geq 0$, equipped with the norm $\| \cdot \|_{s,\mathfrak{D}}$ defined as follows. Let $\boldsymbol{\alpha} := (\alpha_1, \ldots, \alpha_n) \in \mathbb{N}^n$ be a multi-index for which we write $|\boldsymbol{\alpha}| = \sum_{i=1}^n \alpha_i$. If we let $D^{\boldsymbol{\alpha}}$ be the partial derivative operator (in the sense of distributions) defined by

$$D^{\boldsymbol{\alpha}} := \frac{\partial^{|\boldsymbol{\alpha}|}}{\partial x^{\alpha_1} \cdots \partial x^{\alpha_n}},$$

then from [Grisvard, 2011, Definition 1.3.2.1], for all $v \in H^s(\mathfrak{D})$,

$$\|v\|_{s,\mathfrak{D}}^2 := \sum_{|\boldsymbol{\alpha}| \leq s} \|D^{\boldsymbol{\alpha}} v\|_{L^2(\mathfrak{D})}^2, \qquad \qquad \text{if } s \in \mathbb{N},$$

$$\|v\|_{s,\mathfrak{D}}^2 := \|v\|_{\lfloor s \rfloor, \mathfrak{D}}^2 + |v|_{\theta,\mathfrak{D}}^2, \quad |v|_{\theta,\mathfrak{D}}^2 := \int_{\mathfrak{D}} \int_{\mathfrak{D}} \frac{(v(x) - v(y))^2}{|x - y|^{n + 2\theta}} \, \mathrm{d}x \, \mathrm{d}y, \quad \text{if } s = \lfloor s \rfloor + \theta \geq 0.$$
$$(2.1)$$

We note that $L^2(\mathfrak{D}) = H^0(\mathfrak{D})$, so that the norm in $L^2(\mathfrak{D})$ is written $\| \cdot \|_{0,\mathfrak{D}}$. The

corresponding semi-norms $|\cdot|_{s,\mathfrak{D}}$ in $H^s(\mathfrak{D})$ are defined by

$$
|v|_{s,\mathfrak{D}} := \left(\sum_{|\boldsymbol{\alpha}|=s} \|D^{\boldsymbol{\alpha}}v\|_{L^2(\mathfrak{D})}^2 \right)^{\frac{1}{2}}, \qquad \text{if } s \in \mathbb{N},
$$

$$
|v|_{s,\mathfrak{D}} := |v|_{\theta,\mathfrak{D}}, \qquad\qquad\qquad \text{if } s = \lfloor s \rfloor + \theta \geq 0. \qquad (2.2)
$$

Remark that for all $v \in H^1(\mathfrak{D})$ and all $\boldsymbol{v} \in \boldsymbol{H}^1(\mathfrak{D})$, the gradient of v denoted ∇v belongs to $\boldsymbol{L}^2(\mathfrak{D})$, the Jacobian matrix of $\boldsymbol{v}$ denoted $\nabla \boldsymbol{v}$ belongs to $\mathbb{L}^2(\mathfrak{D})$, and

$$
\|\nabla v\|_{0,\mathfrak{D}} = |v|_{1,\mathfrak{D}} \qquad \text{and} \qquad \|\nabla \boldsymbol{v}\|_{0,\mathfrak{D}} = |\boldsymbol{v}|_{1,\mathfrak{D}}.
$$

Moreover, let $H^{-s}(\mathfrak{D})$ denote the dual space of $H^s(\mathfrak{D})$ equipped with the dual norm $\|\cdot\|_{-s,\mathfrak{D}}$ defined as follows: if $\langle \cdot, \cdot \rangle_s$ represents the duality pairing between $H^{-s}(\mathfrak{D})$ and $H^s(\mathfrak{D})$, then for all $v \in H^{-s}(\mathfrak{D})$,

$$
\|v\|_{-s,\mathfrak{D}} := \sup_{\substack{w \in H^s(\mathfrak{D}) \\ w \neq 0}} \frac{\langle v, w \rangle_s}{\|w\|_{s,\mathfrak{D}}}, \qquad (2.3)
$$

The previously introduced definitions of Lebesgue and Sobolev spaces on domains can be extended to manifolds which are (possibly part of) boundaries of Lipschitz domains. The interested reader is referred to [Grisvard, 2011, Section 1.3.3].

2.2.2 Trace spaces

To be able to solve partial differential equation (PDEs), we need to deal with the imposition of boundary conditions, that leads us to the notion of trace. The following theorem is due to Gagliardo [1957].

Theorem 2.2.1 (see e.g., [Ern and Guermond, 2021a, Theorems 3.10 and 3.15]). *Let $\mathfrak{D}$ be a Lipschitz domain of $\mathbb{R}^n$, and let $\Lambda \subset \partial\mathfrak{D}$, $|\Lambda| > 0$. Then*

- *there exists a unique linear continuous map*

$$
\mathrm{tr}_\Lambda : H^1(\mathfrak{D}) \to H^{\frac{1}{2}}(\Lambda)
$$

  called trace operator, such that for all $v \in H^1(\mathfrak{D}) \cap C^0(\overline{\mathfrak{D}})$, $\mathrm{tr}_\Lambda(v) = v|_\Lambda$;

- *there exists a linear continuous map*

$$
R_\Lambda : H^{\frac{1}{2}}(\Lambda) \to H^1(\mathfrak{D})
$$

  called lifting operator, such that $\mathrm{tr}_\Lambda(R_\Lambda(w)) = w$ for all $w \in H^{\frac{1}{2}}(\Lambda)$.

When no confusion is possible, we will write v instead of $\mathrm{tr}_\Lambda(v)$ by abuse of notation. Let us now state in particular the following result on traces, called trace inequality.

Lemma 2.2.2 (see e.g., [Grisvard, 2011, Theorem 1.5.1.10]). *Let $\mathfrak{D} \subset \mathbb{R}^n$ be a Lipschitz domain, and let us denote by $h_{\mathfrak{D}} := \operatorname{diam}(\mathfrak{D})$. Then for all $v \in H^1(\mathfrak{D})$,*

$$\|v\|_{0,\partial\mathfrak{D}} \lesssim h_{\mathfrak{D}}^{-\frac{1}{2}} \|v\|_{0,\mathfrak{D}} + h_{\mathfrak{D}}^{\frac{1}{2}} \|\nabla v\|_{0,\mathfrak{D}}.$$

So let $\mathfrak{D}$ be a Lipschitz domain of $\mathbb{R}^n$, and let $\Lambda \subset \partial\mathfrak{D}$, $|\Lambda| > 0$. If $w \in H^{\frac{1}{2}}(\Lambda)$, then let

$$H^1_{w,\Lambda}(\mathfrak{D}) := \left\{ v \in H^1(\mathfrak{D}) : \operatorname{tr}_\Lambda(v) = w \right\}.$$

Let us also introduce the following trace Sobolev space

$$H^{\frac{1}{2}}_{00}(\Lambda) := \left\{ w \in L^2(\Lambda) : w^\star \in H^{\frac{1}{2}}(\partial\mathfrak{D}) \right\},$$

where $w^\star$ is the extension of w by 0 on $\partial\mathfrak{D}$. Its norm and semi-norm are respectively denoted $\|\cdot\|_{H^{1/2}_{00}(\Lambda)}$ and $|\cdot|_{H^{1/2}_{00}(\Lambda)}$, and they are defined by:

$$\|w\|^2_{H^{1/2}_{00}(\Lambda)} := \|w\|^2_{\frac{1}{2},\Lambda} + |w|^2_{H^{1/2}_{00}(\Lambda)} \quad \text{and} \quad |w|^2_{H^{1/2}_{00}(\Lambda)} := \int_\Lambda \int_{\partial\mathfrak{D}\backslash\Lambda} \frac{w^2(s)}{|s-t|^n} \, \mathrm{d}t \, \mathrm{d}s.$$

We recall from [Grisvard, 2011, Lemma 1.3.2.6], that for all $w \in H^{\frac{1}{2}}_{00}(\Lambda)$,

$$|w|^2_{H^{1/2}_{00}(\Lambda)} \lesssim \int_\Lambda \frac{w^2(s)}{\operatorname{dist}(s,\partial\Lambda)} \, \mathrm{d}s \lesssim |w|^2_{H^{1/2}_{00}(\Lambda)}.$$

Moreover, from [Grisvard, 2011, Equation (1.3.2.7)],

$$\|w\|_{H^{1/2}_{00}(\Lambda)} = \|w^\star\|_{\frac{1}{2},\partial\mathfrak{D}}.$$

In particular, we have

$$|w|^2_{\frac{1}{2},\Lambda} + |w|^2_{H^{1/2}_{00}(\Lambda)} = |w^\star|^2_{\frac{1}{2},\partial\mathfrak{D}}.$$

When Λ is not a connected set, then we define

$$H^{\frac{1}{2}}_{00}(\Lambda) := \left\{ w \in L^2(\Lambda) : w|_{\Lambda_c} \in H^{\frac{1}{2}}_{00}(\Lambda_c), \text{ for all } \Lambda_c \in \operatorname{conn}(\Lambda) \right\},$$

and we equip this space with the norm

$$\|\cdot\|_{H^{1/2}_{00}(\Lambda)} := \left(\sum_{\Lambda_c \in \operatorname{conn}(\Lambda)} \|\cdot\|^2_{H^{1/2}_{00}(\Lambda_c)} \right)^{\frac{1}{2}}.$$

Furthermore, we let $H^{-\frac{1}{2}}_{00}(\Lambda)$ be the dual space of $H^{\frac{1}{2}}_{00}(\Lambda)$, equipped with the dual norm $\|\cdot\|_{H^{-1/2}_{00}(\Lambda)}$ defined as in (2.3).

2.3 Some results on Sobolev and trace spaces

In this section, we state results that are used throughout the thesis. For further details, for more general cases and for the missing proofs, we refer the interested reader to [Lions and Magenes, 1973; Adams, 1975].

2.3.1 Sobolev embeddings

The Sobolev embedding theorem establishes the relationship among Sobolev spaces, Lebesgue spaces, and spaces of continuous functions. It reads as follows.

Theorem 2.3.1 (see e.g., [Ern and Guermond, 2021a, Theorem 2.31]). *Let $\mathfrak{D} \subset \mathbb{R}^n$ be a Lipschitz domain. Then the following continuous embeddings hold:*

- *If $0 \leq s < \dfrac{n}{2}$, then $H^s(\mathfrak{D}) \hookrightarrow L^{p^*}(\mathfrak{D})$ for $p^* = \dfrac{2n}{n - 2s}$.*

- *If $s = \dfrac{n}{2}$, then $H^s(\mathfrak{D}) \hookrightarrow L^q(\mathfrak{D})$ for any $q \in \mathbb{R}$ such that $2 \leq q < \infty$.*

- *If $s > \dfrac{n}{2}$, then $H^s(\mathfrak{D}) \hookrightarrow C^0(\overline{\mathfrak{D}})$.*

These embeddings also hold if we replace $\mathfrak{D}$ by $\partial\mathfrak{D}$, and n by $n - 1$.

In particular, when $s = \dfrac{n}{2}$ in Theorem 2.3.1, then $H^s(\mathfrak{D})$ can be continuously embedded in $L^q(\mathfrak{D})$ for an arbitrarily large q different from infinity. This gives us the intuition that the embedding continuity constant might increase without bound with respect to q. In the following two lemmas, we formalize this result in the reference domain $(0, 2\pi)^n$.

Lemma 2.3.2. *For all $q \in [2, \infty)$ and all $v \in H^{\frac{1}{2}}(0, 2\pi)$,*

$$\|v\|_{L^q(0,2\pi)} \leq c\sqrt{q}\|v\|_{\frac{1}{2},(0,2\pi)},$$

where c is a constant independent of q.

Proof. See [Ben Belgacem et al., 2001, Lemma 5.1]. Note that the proof is very similar to the one given for Lemma 2.3.3 below. $\square$

Lemma 2.3.3. *For all $q \in [2, \infty)$ and all $v \in H^1\big((0, 2\pi)^2\big)$,*

$$\|v\|_{L^q((0,2\pi)^2)} \leq c\sqrt{q}\|v\|_{1,(0,2\pi)^2},$$

where c is a constant independent of q.

Proof. The proof follows [Ben Belgacem et al., 2001, Lemma 5.1], but in the two-dimensional case. In order to use the Fourier decomposition, consider the Hilbert basis of $L^2\big((0,2\pi)^2\big)$ defined by $\varphi_{\mathbf{k}}(x) := \varphi_{k_1}(x_1)\varphi_{k_2}(x_2)$ for all $\mathbf{k} = (k_1, k_2) \in \mathbb{N}^2$, $x = (x_1, x_2) \in (0, 2\pi)^2$, where for $i = 1, 2$, $\varphi_0(x_i) = \frac{1}{\sqrt{2\pi}}$ and $\varphi_k(x_i) = \frac{1}{\sqrt{\pi}}\cos(kx_i)$, $k \in \mathbb{N} \setminus \{0\}$. Let $v \in H^1\big((0,2\pi)^2\big)$ be decomposed as $v = \sum_{\mathbf{k} \in \mathbb{N}^2} v_{\mathbf{k}}\varphi_{\mathbf{k}}$. Then

$$\|v\|_{1,(0,2\pi)^2} = \left[\sum_{\mathbf{k} \in \mathbb{N}^2}(1 + k_1^2 + k_2^2)v_{\mathbf{k}}^2\right]^{\frac{1}{2}}. \tag{2.4}$$

Now, for every $q \in [2, \infty)$, let $q' \in (1, 2]$ such that $\frac{1}{q} + \frac{1}{q'} = 1$. Then by the Hausdorff-Young inequality, there exists a constant C independent of q such that

$$\|v\|_{L^q((0,2\pi)^2)} \leq C\left(\sum_{\mathbf{k} \in \mathbb{N}^2}|v_{\mathbf{k}}|^{q'}\right)^{\frac{1}{q'}}$$

$$= C\left(\sum_{\mathbf{k} \in \mathbb{N}^2}\left(1 + k_1^2 + k_2^2\right)^{-\frac{q'}{2}}\left(1 + k_1^2 + k_2^2\right)^{\frac{q'}{2}}|v_{\mathbf{k}}|^{q'}\right)^{\frac{1}{q'}}.$$

Thus if we let $r \in (2, \infty]$ such that $\frac{1}{r} + \frac{q'}{2} = 1$, by Hölder inequality and using (2.4),

$$\|v\|_{L^q((0,2\pi)^2)} \leq C\left[\sum_{\mathbf{k} \in \mathbb{N}^2}\left(1 + k_1^2 + k_2^2\right)^{-\frac{q'r}{2}}\right]^{\frac{1}{q'r}}\left[\sum_{\mathbf{k} \in \mathbb{N}^2}\left(1 + k_1^2 + k_2^2\right)v_{\mathbf{k}}^2\right]^{\frac{1}{2}}$$

$$= C\left[\sum_{\mathbf{k} \in \mathbb{N}^2}\left(1 + k_1^2 + k_2^2\right)^{-\frac{q}{q-2}}\right]^{\frac{q-2}{2q}}\|v\|_{1,(0,2\pi)^2}.$$

One can conclude the proof by observing that the Riemann serial is bounded by $\sqrt{q}$. $\quad\square$

2.3.2 Poincaré inequalities

In this section, let $\mathfrak{D}$ be a Lipschitz domain, and let $\Lambda \subset \partial\mathfrak{D}$ such that $|\Lambda| > 0$. Let us first concentrate on the standard Poincaré inequality, which requires the trace of the considered function to vanish on a part of the domain boundary.

Lemma 2.3.4 (Poincaré inequality, see e.g. [Ern and Guermond, 2021a, Lemma 3.30])**.** *Let* $h_{\mathfrak{D}} := \mathrm{diam}(\mathfrak{D})$*, and assume that* $|\Lambda|^{\frac{1}{n-1}} \simeq h_{\mathfrak{D}}$*. Then for all* $v \in H^1_{0,\Lambda}(\mathfrak{D})$*,*

$$\|v\|_{0,\mathfrak{D}} \lesssim h_{\mathfrak{D}}\|\nabla v\|_{0,\mathfrak{D}},$$

and thus

$$\|v\|_{1,\mathfrak{D}} = \left(\|\nabla v\|_{0,\mathfrak{D}}^2 + \|v\|_{0,\mathfrak{D}}^2\right)^{\frac{1}{2}} \lesssim \left(1 + h_{\mathfrak{D}}^2\right)^{\frac{1}{2}}\|\nabla v\|_{0,\mathfrak{D}}.$$

In particular, thanks to Poincaré inequality, the semi-norm $|\cdot|_{1,\mathfrak{D}} = \|\nabla\cdot\|_{0,\mathfrak{D}}$ is a norm in $H^1_{0,\Lambda}(\mathfrak{D})$, equivalent to the standard H^1-norm $\|\cdot\|_{1,\mathfrak{D}}$.

Before stating the Poincaré-Friedrichs inequality, let us introduce the following notation. For all function v whose trace is integrable on Λ, we define

$$\overline{v}^{\Lambda} := \frac{1}{|\Lambda|}\int_{\Lambda}\mathrm{tr}_{\Lambda}(v)\,\mathrm{d}s \tag{2.5}$$

as the average of the trace of v on Λ. Similarly, for all integrable function w on $\mathfrak{D}$, $\overline{w}^{\mathfrak{D}}$ denotes the average of w in $\mathfrak{D}$.

Lemma 2.3.5 (Poincaré-Friedrichs inequality, see e.g., [Ern and Guermond, 2021a, Lemma 3.30])**.** *Let $h_{\mathfrak{D}} := \mathrm{diam}(\mathfrak{D})$, and assume that $|\Lambda|^{\frac{1}{n-1}} \simeq h_{\mathfrak{D}}$. Then for all functions $v \in H^1(\mathfrak{D})$,*

$$\left\|v - \overline{v}^{\Lambda}\right\|_{0,\mathfrak{D}} \lesssim h_{\mathfrak{D}}\|\nabla v\|_{0,\mathfrak{D}}.$$

In the following lemmas, we state and prove similar inequalities but on trace spaces and on their dual, beginning from the Poincaré inequality on traces.

Lemma 2.3.6. *Assume that Λ is isotropic according to Definition 2.1.2, and not necessarily connected. Then for all $v \in H^{\frac{1}{2}}_{00}(\Lambda)$,*

$$\|v\|_{0,\Lambda} \lesssim |\Lambda|^{\frac{1}{2(n-1)}}\,\|v\|_{H^{1/2}_{00}(\Lambda)}.$$

Proof. Let $v \in H^{\frac{1}{2}}_{00}(\Lambda)$, and recall that $\Lambda \subset \partial\mathfrak{D}$ for some Lipschitz domain $\mathfrak{D} \subset \mathbb{R}^n$. Without loss of generality, we suppose that $|\partial\mathfrak{D}| = 1$. Then, let us first suppose that Λ is connected. So if we let $v^{\star} \in H^{\frac{1}{2}}(\partial\mathfrak{D})$ be the extension of v by 0, using [Acosta and Borthagaray, 2017, Proposition 2.4] and the isotropy of Λ,

$$\|v\|^2_{0,\Lambda} \lesssim |\Lambda|^{\frac{1}{n-1}}\,|v^{\star}|^2_{\frac{1}{2},\partial\mathfrak{D}} \leq |\Lambda|^{\frac{1}{n-1}}\,\|v\|^2_{H^{1/2}_{00}(\Lambda)}. \tag{2.6}$$

Now, if Λ is not connected, then $\mathrm{dist}(s,\partial\Lambda_c) = \mathrm{dist}(s,\partial\Lambda)$ for all $\Lambda_c \in \mathrm{conn}(\Lambda)$ and for all $s \in \Lambda_c$. Thus

$$\sum_{\Lambda_c\in\mathrm{conn}(\Lambda)}\left\|v|_{\Lambda_c}\right\|^2_{H^{1/2}_{00}(\Lambda_c)} = \sum_{\Lambda_c\in\mathrm{conn}(\Lambda)}\left(\left\|v|_{\Lambda_c}\right\|^2_{\frac{1}{2},\Lambda_c} + \left|v|_{\Lambda_c}\right|^2_{H^{1/2}_{00}(\Lambda_c)}\right)$$

$$\lesssim \|v\|^2_{\frac{1}{2},\Lambda} + \sum_{\Lambda_c\in\mathrm{conn}(\Lambda)}\int_{\Lambda_c}\frac{v^2(s)}{\mathrm{dist}(s,\partial\Lambda_c)}\,\mathrm{d}s$$

$$= \|v\|^2_{\frac{1}{2},\Lambda} + \int_{\Lambda}\frac{v^2(s)}{\mathrm{dist}(s,\partial\Lambda)}\,\mathrm{d}s = \|v\|^2_{H^{1/2}_{00}(\Lambda)}.$$

Therefore, from (2.6),

$$\|v\|^2_{0,\Lambda} = \sum_{\Lambda_c\in\mathrm{conn}(\Lambda)}\|v\|^2_{0,\Lambda_c} \lesssim \sum_{\Lambda_c\in\mathrm{conn}(\Lambda)}|\Lambda_c|^{\frac{1}{n-1}}\,\|v\|^2_{H^{1/2}_{00}(\Lambda_c)} \lesssim |\Lambda|^{\frac{1}{n-1}}\,\|v\|^2_{H^{1/2}_{00}(\Lambda)}. \qquad\square$$

Now, let us state and prove the Poincaré inequality on dual trace spaces.

Lemma 2.3.7. *Assume that Λ is isotropic according to Definition 2.1.2. Then for all $v \in L^2(\Lambda)$,*

$$\|v\|_{H_{00}^{-1/2}(\Lambda)} \lesssim |\Lambda|^{\frac{1}{2(n-1)}} \|v\|_{0,\Lambda}.$$

Proof. Let $\langle \cdot, \cdot \rangle$ denote the duality pairing between $H_{00}^{\frac{1}{2}}(\Lambda)$ and $H_{00}^{-\frac{1}{2}}(\Lambda)$. Then by Lemma 2.3.6, we obtain

$$\|v\|_{H_{00}^{-1/2}(\Lambda)} = \sup_{\substack{z \in H_{00}^{1/2}(\Lambda) \\ z \neq 0}} \frac{\langle v, z \rangle}{\|z\|_{H_{00}^{1/2}(\Lambda)}} \leq \sup_{\substack{z \in H_{00}^{1/2}(\Lambda) \\ z \neq 0}} \frac{\|v\|_{0,\Lambda} \|z\|_{0,\Lambda}}{\|z\|_{H_{00}^{1/2}(\Lambda)}}$$

$$\lesssim \sup_{\substack{z \in H_{00}^{1/2}(\Lambda) \\ z \neq 0}} \frac{\|v\|_{0,\Lambda} |\Lambda|^{\frac{1}{2(n-1)}} \|z\|_{H_{00}^{1/2}(\Lambda)}}{\|z\|_{H_{00}^{1/2}(\Lambda)}} = |\Lambda|^{\frac{1}{2(n-1)}} \|v\|_{0,\Lambda}. \qquad \square$$

Subsequently, let us study the Poincaré-Friedrichs inequality on trace spaces.

Lemma 2.3.8. *Assume that Λ is isotropic according to Definition 2.1.2. Then for all $v \in H^{\frac{1}{2}}(\Lambda)$,*

$$\left\| v - \overline{v}^\Lambda \right\|_{0,\Lambda} \lesssim |\Lambda|^{\frac{1}{2(n-1)}} |v|_{\frac{1}{2},\Lambda}.$$

Proof. Let $v \in H^{\frac{1}{2}}(\Lambda)$. Since Λ is an $(n-1)$-dimensional subspace of $\mathbb{R}^n$, then from (2.1),

$$|v|_{\frac{1}{2},\Lambda}^2 = \int_\Lambda \int_\Lambda \frac{(v(s) - v(t))^2}{|s - t|^n} \, ds \, dt.$$

Moreover, since Λ is isotropic, then $\mathrm{diam}(\Lambda) \lesssim |\Lambda|^{\frac{1}{n-1}}$. Therefore,

$$\left\| v - \overline{v}^\Lambda \right\|_{0,\Lambda}^2 = \int_\Lambda \left(v(s) - \frac{1}{|\Lambda|} \int_\Lambda v(t) \, dt \right)^2 \, ds$$

$$= \frac{1}{|\Lambda|^2} \int_\Lambda \left[\int_\Lambda \left(v(s) - v(t) \right) dt \right]^2 \, ds$$

$$\leq \frac{1}{|\Lambda|^2} \int_\Lambda \left[|\Lambda| \int_\Lambda \left(v(s) - v(t) \right)^2 dt \right] \, ds$$

$$= \frac{1}{|\Lambda|} \int_\Lambda \int_\Lambda \frac{(v(s) - v(t))^2}{|s - t|^n} |s - t|^n \, dt \, ds$$

$$\leq \frac{\mathrm{diam}(\Lambda)^n}{|\Lambda|} \int_\Lambda \int_\Lambda \frac{(v(s) - v(t))^2}{|s - t|^n} \, dt \, ds$$

$$\lesssim |\Lambda|^{\frac{1}{n-1}} |v|_{\frac{1}{2},\Lambda}^2. \qquad \square$$

Finally, the following result also holds true:

Lemma 2.3.9. *Assume that $1 \simeq |\partial\mathfrak{D}| \gg |\Lambda|$. For all $v \in H^{\frac{1}{2}}(\partial\mathfrak{D})$, if we define $\eta \in \mathbb{R}$ as the unique solution of $\eta = -\log(\eta)$,*

$$\|v\|_{0,\Lambda} \lesssim c_\Lambda |\Lambda|^{\frac{1}{2(n-1)}} \|v\|_{\frac{1}{2},\partial\mathfrak{D}}, \quad \text{where} \quad c_\Lambda := \begin{cases} \max\left(-\log\left(|\Lambda|\right),\eta\right)^{\frac{1}{2}} & \text{if } n = 2, \\ 1 & \text{if } n = 3. \end{cases}$$

Proof. Let $v \in H^{\frac{1}{2}}(\partial\mathfrak{D})$. By Sobolev embedding, $H^{\frac{1}{2}}(\partial\mathfrak{D})$ can be continuously embedded in $L^{2p}(\partial\mathfrak{D})$ for every $1 \leq p < \infty$ if $n = 2$, or for every $1 \leq p \leq 2$ if $n = 3$. Therefore, by Hölder inequality,

$$\|v\|_{0,\Lambda}^2 = \sum_{\Lambda_c \in \mathrm{conn}(\Lambda)} \|v\|_{0,\Lambda_c}^2 \leq \sum_{\Lambda_c \in \mathrm{conn}(\Lambda)} |\Lambda_c|^{1-\frac{1}{p}} \|v\|_{L^{2p}(\Lambda_c)}^2 \lesssim |\Lambda|^{1-\frac{1}{p}} \|v\|_{L^{2p}(\partial\mathfrak{D})}^2. \quad (2.7)$$

If $n = 3$, by taking $p = 2$ in (2.7) and by Sobolev embedding,

$$\|v\|_{0,\Lambda}^2 \lesssim |\Lambda|^{\frac{1}{2}} \|v\|_{\frac{1}{2},\partial\mathfrak{D}}^2 = c_\Lambda^2 |\Lambda|^{\frac{1}{n-1}} \|v\|_{\frac{1}{2},\partial\mathfrak{D}}^2.$$

Let us now consider the case $n = 2$. Thanks to Lemma 2.3.2, for all $q \in [2,\infty)$ and all $v \in H^{\frac{1}{2}}(0,2\pi)$,

$$\|v\|_{L^q(0,2\pi)} \leq c\sqrt{q}\|v\|_{\frac{1}{2},(0,2\pi)},$$

where c is a constant independent of q. Then by definition of the L^q-norm and the $H^{\frac{1}{2}}$-norm on a manifold (see [Grisvard, 2011, Sec. 1.3.3]), we obtain $\|v\|_{L^{2p}(\partial\mathfrak{D})} \leq \tilde{c}\sqrt{p}\|v\|_{\frac{1}{2},\partial\mathfrak{D}}$, where $\tilde{c}$ is a constant independent of p. So by taking $p = \max\left(-\log\left(|\Lambda|\right),\eta\right) = c_\Lambda^2$ in (2.7), then $|\Lambda|^{-\frac{1}{p}} \leq e$ and thus

$$\|v\|_{0,\Lambda}^2 \lesssim |\Lambda|^{1-\frac{1}{p}} p \|v\|_{\frac{1}{2},\partial\mathfrak{D}}^2 \lesssim |\Lambda| c_\Lambda^2 \|v\|_{\frac{1}{2},\partial\mathfrak{D}}^2 = c_\Lambda^2 |\Lambda|^{\frac{1}{n-1}} \|v\|_{\frac{1}{2},\partial\mathfrak{D}}^2. \qquad \square$$

2.3.3 Inverse inequalities

Before stating inverse inequalities, let us introduce some polynomial spaces. To do so, suppose that $\{\Lambda^k\}_{k=1}^{N_\Lambda}$ is a partition of Λ such that each Λ^k is a flat element, i.e., a straight line if $n = 2$ or a flat square or triangle if $n = 3$. Then for $m \in \mathbb{N}$, we let $\mathbb{Q}_m(\Lambda)$ be the set of polynomials on Λ of degree at most m, and

$$\mathbb{Q}_{m,0}^{\mathrm{pw}}(\Lambda) := \left\{ \phi : \Lambda \to \mathbb{R} : \phi|_{\partial\Lambda} \equiv 0, \phi|_{\Lambda^k} \in \mathbb{Q}_m(\Lambda^k) \text{ for all } k = 1, \ldots, N_\Lambda \right\}.$$

Let us now state an inverse inequality on trace spaces which will be used in the sequel.

Lemma 2.3.10. *Assume that Λ is isotropic and regular according to Definitions 2.1.2 and 2.1.3, and let $m \in \mathbb{N}$. Then for all $\phi \in \mathbb{Q}_{m,0}^{\mathrm{pw}}(\Lambda)$,*

$$\|\phi\|_{0,\Lambda} \lesssim |\Lambda|^{-\frac{1}{2(n-1)}} \|\phi\|_{H_{00}^{-1/2}(\Lambda)},$$

where the hidden constant increases with m.

Proof. For all $\psi \in \mathbb{Q}_{m,0}^{\mathrm{pw}}(\Lambda) \subset H_0^1(\Lambda)$, the following inverse estimate is well known (see e.g., [Ern and Guermond, 2021a, Lemma 12.1]): with the notation of Definition 2.1.3, for all $k = 1, \ldots, N_\Lambda$,

$$\left|\psi|_{\Lambda^k}\right|_{1,\Lambda^k} \lesssim \left|\Lambda^k\right|^{-\frac{1}{n-1}} \left\|\psi|_{\Lambda^k}\right\|_{0,\Lambda^k},$$

and the hidden constant increases with m. Therefore, since Λ is isotropic and regular, then

$$|\psi|_{1,\Lambda} \lesssim \max_{k=1,\ldots,N_\Lambda} \left(\left|\Lambda^k\right|^{-\frac{1}{n-1}}\right) \|\psi\|_{0,\Lambda} \lesssim |\Lambda|^{-\frac{1}{n-1}} \|\psi\|_{0,\Lambda}.$$

Moreover, from [Lions and Magenes, 1973, Theorem 11.7], we know that the interpolation space

$$\left[H_0^1(\Lambda), L^2(\Lambda)\right]_{\frac{1}{2}} = H_{00}^{\frac{1}{2}}(\Lambda).$$

Therefore, from [Lions and Magenes, 1973, Proposition 2.3], for all $\psi \in \mathbb{Q}_{m,0}^{\mathrm{pw}}(\Lambda)$,

$$\|\psi\|_{H_{00}^{1/2}(\Lambda)} \lesssim |\psi|_{1,\Lambda}^{\frac{1}{2}} \|\psi\|_{0,\Lambda}^{\frac{1}{2}} \lesssim |\Lambda|^{-\frac{1}{2(n-1)}} \|\psi\|_{0,\Lambda}. \tag{2.8}$$

Consequently, for all $\phi \in \mathbb{Q}_{m,0}^{\mathrm{pw}}(\Lambda) \subset H_{00}^{-\frac{1}{2}}(\Lambda)$, since $\mathbb{Q}_{m,0}^{\mathrm{pw}}(\Lambda) \subset H_{00}^{\frac{1}{2}}(\Lambda)$,

$$\|\phi\|_{0,\Lambda} = \frac{\displaystyle\int_\Lambda \phi^2 \,\mathrm{d}s}{\|\phi\|_{0,\Lambda}} \leq \sup_{\substack{\psi \in \mathbb{Q}_{m,0}^{\mathrm{pw}}(\Lambda) \\ \psi \neq 0}} \frac{\displaystyle\int_\Lambda \phi\psi \,\mathrm{d}s}{\|\psi\|_{0,\Lambda}} \lesssim |\Lambda|^{-\frac{1}{2(n-1)}} \sup_{\substack{\psi \in \mathbb{Q}_{m,0}^{\mathrm{pw}}(\Lambda) \\ \psi \neq 0}} \frac{\displaystyle\int_\Lambda \phi\psi \,\mathrm{d}s}{\|\psi\|_{H_{00}^{1/2}(\Lambda)}}$$

$$\leq |\Lambda|^{-\frac{1}{2(n-1)}} \sup_{\substack{v \in H_{00}^{1/2}(\Lambda) \\ v \neq 0}} \frac{\displaystyle\int_\Lambda \phi v \,\mathrm{d}s}{\|v\|_{H_{00}^{1/2}(\Lambda)}} = |\Lambda|^{-\frac{1}{2(n-1)}} \|\phi\|_{H_{00}^{-1/2}(\Lambda)}. \tag{2.9}$$

$\square$

For the following lemmas, let $\mathfrak{D} \subset \mathbb{R}^n$ be a Lipschitz domain, $J \in \mathbb{N}$, and suppose that

$$\partial \mathfrak{D} = \bigcup_{j=1}^{J+1} \overline{\Lambda_j}$$

with $\Lambda_i \cap \Lambda_j = \emptyset$ for all $i, j = 1, \ldots, J+1$, $i \neq j$. Moreover, let

$$\Lambda = \mathrm{int}\left(\bigcup_{j=1}^{J} \overline{\Lambda_j}\right).$$

Then, consider the functional space

$$H := \left\{v \in H_{00}^{\frac{1}{2}}(\Lambda) : v|_{\Lambda_j} \in H_{00}^{\frac{1}{2}}(\Lambda_j), \forall j = 1, \ldots, J\right\} \subset H_{00}^{\frac{1}{2}}(\Lambda)$$

equipped with the broken norm

$$\|\cdot\|_H := \left(\sum_{j=1}^{J} \left\| \cdot \big|_{\Lambda_j} \right\|_{H_{00}^{\frac{1}{2}}(\Lambda_j)}^2 \right)^{\frac{1}{2}}.$$

Finally, let H^* be the dual space of H, equipped with the dual norm $\|\cdot\|_{H^*}$. Before stating and proving an inverse inequality on H, let us first study the relation between the norm on $H_{00}^{\frac{1}{2}}(\Lambda)$ and the norm on H.

Lemma 2.3.11. *For all $v \in H$,*

$$\|v\|_{H_{00}^{1/2}(\Lambda)} \leq \sqrt{J}\|v\|_H,$$

and for all $w \in H_{00}^{-\frac{1}{2}}(\Lambda)$,

$$\|w\|_{H^*} \leq \sqrt{J}\|w\|_{H_{00}^{-1/2}(\Lambda)}.$$

Proof. Let $v \in H \subset H_{00}^{\frac{1}{2}}(\Lambda)$, and let $v|_{\Lambda_j}^\star$ be the extension of $v|_{\Lambda_j}$ by 0 on $\partial \mathfrak{D}$. Then by triangular inequality,

$$\|v\|_{H_{00}^{1/2}(\Lambda)} = \left\| \sum_{j=1}^{J} v|_{\Lambda_j}^\star \right\|_{H_{00}^{1/2}(\Lambda)} \leq \sum_{j=1}^{J} \left\| v|_{\Lambda_j}^\star \right\|_{H_{00}^{1/2}(\Lambda)} = \sum_{j=1}^{J} \left\| v|_{\Lambda_j}^\star \right\|_{\frac{1}{2},\partial\mathfrak{D}}$$

$$= \sum_{j=1}^{J} \left\| v|_{\Lambda_j}^\star \right\|_{H_{00}^{1/2}(\Lambda_j)} \leq \sqrt{J}\|v\|_H. \tag{2.10}$$

Moreover, for all $w \in H_{00}^{-\frac{1}{2}}(\Lambda) \subset H^*$, using (2.10),

$$\|w\|_{H^*} = \sup_{\substack{v \in H \\ v \neq 0}} \frac{\int_\Lambda wv\,\mathrm{d}s}{\|v\|_H} \leq \sqrt{J} \sup_{\substack{v \in H \\ v \neq 0}} \frac{\int_\Lambda wv\,\mathrm{d}s}{\|v\|_{H_{00}^{1/2}(\Lambda)}}$$

$$\leq \sqrt{J} \sup_{\substack{v \in H_{00}^{\frac{1}{2}}(\Lambda) \\ v \neq 0}} \frac{\int_\Lambda wv\,\mathrm{d}s}{\|v\|_{H_{00}^{1/2}(\Lambda)}} = \sqrt{J}\|w\|_{H_{00}^{-1/2}(\Lambda)}. \qquad \square$$

Let us now state and demonstrate an inverse inequality on H.

Lemma 2.3.12. *For all $j = 1, \ldots, J$, assume that $|\Lambda_j| \simeq |\Lambda|$, and suppose that Λ_j is isotropic and regular according to Definitions 2.1.2 and 2.1.3. If we let $m \in \mathbb{N}$, for all piecewise polynomial $\phi \in \mathbb{Q}_m^0$ where*

$$\mathbb{Q}_m^0 := \left\{ \psi \in \mathbb{Q}_{m,0}^{\mathrm{pw}}(\Lambda) : \psi|_{\Lambda_j} \in \mathbb{Q}_{m,0}^{\mathrm{pw}}(\Lambda_j), \forall j = 1, \ldots, J \right\} \subset H,$$

then

$$\|\phi\|_{0,\Lambda} \lesssim |\Lambda|^{-\frac{1}{2(n-1)}} \|\phi\|_{H^*},$$

where the hidden constant increases with m.

Proof. For all $\psi \in \mathbb{Q}_m^0$ and all $j = 1, \dots, J$, $\psi|_{\Lambda_j} \in \mathbb{Q}_{m,0}^{\mathrm{pw}}(\Lambda_j)$, and thus since Λ_j is regular, using (2.8),

$$\left\|\psi|_{\Lambda_j}\right\|_{H_{00}^{1/2}(\Lambda_j)} \lesssim |\Lambda_j|^{-\frac{1}{2(n-1)}} \left\|\psi|_{\Lambda_j}\right\|_{0,\Lambda_j} \lesssim |\Lambda|^{-\frac{1}{2(n-1)}} \left\|\psi|_{\Lambda_j}\right\|_{0,\Lambda_j}.$$

Therefore,

$$\|\psi\|_H = \left(\sum_{j=1}^{J} \left\| \cdot |_{\Lambda_j} \right\|_{H_{00}^{\frac{1}{2}}(\Lambda_j)}^2\right)^{\frac{1}{2}} \lesssim |\Lambda|^{-\frac{1}{2(n-1)}} \|\psi\|_{0,\Lambda}.$$

Consequently, for all $\phi \in \mathbb{Q}_m^0 \subset H$, following the same steps as for (2.9) in the proof of Lemma 2.3.10, replacing $H_{00}^{-\frac{1}{2}}(\Lambda)$ by H^*, $H_{00}^{\frac{1}{2}}(\Lambda)$ by H, and $\mathbb{Q}_{m,0}^{\mathrm{pw}}(\Lambda)$ by $\mathbb{Q}_m^0$, then

$$\|\phi\|_{0,\Lambda} \lesssim |\Lambda|^{-\frac{1}{2(n-1)}} \|\phi\|_{H^*}. \qquad \square$$

2.4 Boundary value problems

In this section, we present the abstract framework that constitutes the mathematical foundations upon which variational numerical methods have been successfully devised to solve PDEs. Then, we summarize some classical results of functional analysis that show the existence and uniqueness of a BVP solution.

Let $\mathfrak{D}$ denote a connected Lipschitz domain of $\mathbb{R}^n$, and consider a BVP of the form

$$\begin{cases} \mathcal{A}u_s = f & \text{in } \mathfrak{D} \\ \mathcal{K}u_s = \kappa & \text{on } \partial\mathfrak{D}, \end{cases} \tag{2.11}$$

where u_s is the unknown solution, f and κ are given functions, $\mathcal{A}$ is a linear differential operator, and $\mathcal{K}$ is a boundary operator corresponding to $\mathcal{A}$.

Let us now consider the variational (or weak) formulation of problem (2.11) that we formally write as follows:

$$\begin{aligned} &\text{find } u_s \in V \text{ such that} \\ &a(u_s, v) = \mathfrak{f}(v), \quad \forall v \in V, \end{aligned} \tag{2.12}$$

where V is a Hilbert space, $a(\cdot, \cdot)$ is a bilinear form on $V \times V$ corresponding to $\mathcal{A}$, and $\mathfrak{f}(\cdot)$ is a linear functional on V that takes into account the right hand side f. Non-

homogeneous boundary conditions contained in $\mathcal{K}$ can either be imposed directly in the definition of V (essential boundary conditions), or implicitly in the definition of $a(\cdot, \cdot)$ and $\mathfrak{f}(\cdot)$ (natural boundary conditions).

Let us now introduce the notion of well-posedness of problem (2.12), originally defined by Hadamard [1932]. To do so, let us first denote V^* the dual space of V, that we equip with the dual norm $\| \cdot \|_{V^*}$.

Definition 2.4.1 (see e.g., [Ern and Guermond, 2021b, Definition 25.1]). Problem (2.12) is *well-posed* if it admits a unique solution for every $\mathfrak{f} \in V^*$, and if there exists a constant $\mathfrak{c} > 0$, uniform with respect to $\mathfrak{f}$, such that the following *a priori* estimate holds true:

$$\|u_s\|_V \leq \mathfrak{c} \|\mathfrak{f}\|_{V^*}. \tag{2.13}$$

Inequality (2.13) states that the solution u_s continuously depends on the problem data, or more precisely on the right hand side $\mathfrak{f}$. Let us now state a fundamental theorem which characterizes the well-posedness of problem (2.12).

Theorem 2.4.2 (Banach-Nečas-Babuška theorem, see e.g., [Ern and Guermond, 2021b, Theorem 25.15]). *Let V be a (real) Hilbert spaces with norm $\| \cdot \|_V$, and let V^* be the dual space of V equipped with the dual norm $\| \cdot \|_{V^*}$. Moreover, assume that the bilinear form $a(\cdot, \cdot) : V \times V \to \mathbb{R}$ is continuous, i.e., there exists a constant $\mathfrak{C} > 0$ such that*

$$|a(w, v)| \leq \mathfrak{C} \|w\|_V \|v\|_V, \qquad \forall w, v \in V. \tag{2.14}$$

If there is a constant $\mathfrak{a} > 0$ such that $a(\cdot, \cdot)$ satisfies

$$\sup_{\substack{w \in V \\ w \neq 0}} a(w, v) > 0, \qquad \forall v \in V, v \neq 0, \tag{2.15}$$

$$\sup_{\substack{v \in V \\ v \neq 0}} \frac{a(w, v)}{\|v\|_V} \geq \mathfrak{a} \|w\|_V, \qquad \forall w \in V, \tag{2.16}$$

then for any linear continuous functional $\mathfrak{f}(\cdot) \in V^*$, there exists a unique solution $u_s \in V$ to (2.12) which satisfies

$$\|u_s\|_V \leq \frac{1}{\mathfrak{a}} \|\mathfrak{f}\|_{V^*}. \tag{2.17}$$

Remark 2.4.3. Condition (2.16) is equivalent to the following condition,

$$\inf_{\substack{w \in V \\ w \neq 0}} \sup_{\substack{v \in V \\ v \neq 0}} \frac{a(w, v)}{\|w\|_V \|v\|_V} =: \mathfrak{a} > 0, \tag{2.18}$$

also known as inf-sup condition.

Let us now discuss two special cases of Banach-Nečas-Babuška Theorem 2.4.2.

- If the bilinear form $a(\cdot, \cdot)$ is continuous and coercive, i.e., if it satisfies (2.14) and

$$\exists \mathfrak{a} > 0 : a(v, v) \geq \mathfrak{a}\|v\|_V^2, \quad \forall v \in V, \tag{2.19}$$

  then conditions (2.15) and (2.16) are satisfied, and problem (2.12) is well-posed. This result is known as Lax-Milgram theorem, see e.g., [Ern and Guermond, 2021b, Lemma 25.2 and Remark 25.6]. In this case, we call energy norm the norm induced by $a(\cdot, \cdot)$, that is, for all $v \in V$, the energy norm of v in $\mathfrak{D}$ is given by

$$\|v\|_{\mathfrak{D}} := \left(a(v, v)\right)^{\frac{1}{2}}. \tag{2.20}$$

  Thanks to the continuity and the coercivity of $a(\cdot, \cdot)$, the energy norm $\|\cdot\|_{\mathfrak{D}}$ is equivalent to the norm $\|\cdot\|_V$ of V.

- Consider now the case in which $\mathcal{A}$ is a saddle point problem. Then the functional space V can be decomposed as $V = \underline{V} \times Q$ where $\underline{V}$ and Q are Hilbert spaces, the unknown u_s and the test functions v can be decomposed as $u_s = (\underline{u}_s, p_s)$ and $v = (\underline{v}, q)$ with $\underline{u}_s, \underline{v} \in \underline{V}$ and $p_s, q \in Q$, and problem (2.12) can be re-expressed as follows:

  find $(\underline{u}_s, p_s) \in \underline{V} \times Q$ such that

$$\begin{cases} \underline{a}(\underline{u}_s, v) + b(\underline{v}, p_s) = \underline{\mathfrak{f}}(\underline{v}), & \forall \underline{v} \in \underline{V}, \\ b(\underline{u}_s, q) = \mathfrak{f}_c(q), & \forall q \in Q, \end{cases} \tag{2.21}$$

  where $\underline{a}(\cdot, \cdot)$ is a bilinear form on $\underline{V} \times \underline{V}$, $b(\cdot, \cdot)$ is a bilinear form on $\underline{V} \times Q$, $\underline{\mathfrak{f}}(\cdot)$ is a linear functional on $\underline{V}$, and $\mathfrak{f}_c(\cdot)$ is a linear functional on Q. To lighten the notation, let us drop the underlines without loss of clarity. Let

$$\mathrm{Ker}_V(b) := \{v \in V : b(v, q) = 0, \forall q \in Q\},$$

  and assume that the bilinear forms $a(\cdot, \cdot)$ and $b(\cdot, \cdot)$ appearing in (2.21) are continuous, i.e., they satisfy (2.14). Then conditions (2.15) and (2.16) of Banach-Nečas-Babuška Theorem 2.4.2 is equivalent to the following conditions:

$$\inf_{\substack{w \in \mathrm{Ker}_V(b) \\ w \neq 0}} \sup_{\substack{v \in \mathrm{Ker}_V(b) \\ v \neq 0}} \frac{a(w, v)}{\|w\|_V \|v\|_V} =: \mathfrak{a} > 0, \tag{2.22}$$

$$\sup_{\substack{w \in \mathrm{Ker}_V(b) \\ w \neq 0}} a(w, v) > 0, \quad \forall v \in \mathrm{Ker}_V(b), v \neq 0, \tag{2.23}$$

$$\inf_{\substack{q \in Q \\ q \neq 0}} \sup_{\substack{v \in V \\ v \neq 0}} \frac{b(v, q)}{\|v\|_V \|q\|_Q} =: \mathfrak{b} > 0. \tag{2.24}$$

This result is known under the name of Ladyzhenskaya-Babuška-Brezzi (LBB)

27

theorem, see e.g., [Ern and Guermond, 2021b, Theorem 49.13]. Note finally that if $a(\cdot, \cdot)$ is coercive on $\mathrm{Ker}_V(b)$, then conditions (2.22) and (2.23) are satisfied. The last condition (2.24) is also often referred to as inf-sup condition, or LBB-condition.

For further details and rigorous proofs, the interested reader is referred to [Ciarlet, 2002; Brenner and Scott, 2008; Quarteroni and Valli, 2008]. Let us finally present the example of Poisson's problem that will be extensively used in this thesis.

Example 2.4.4 (Poisson's problem)**.** Let us consider the Poisson problem defined in a Lipschitz domain $\mathfrak{D} \subset \mathbb{R}^n$ by decomposing $\partial \mathfrak{D} = \overline{\Lambda_D} \cup \overline{\Lambda_N}$ with $\Lambda_D \cap \Lambda_N = \emptyset$, $\Lambda_D \neq \emptyset$. That is, if we let $u_D \in H^{\frac{1}{2}}(\Lambda_D)$, $u_N \in L^2(\Lambda_N)$ and $f \in L^2(\mathfrak{D})$, the considered problem reads:

$$\text{find } u_s : \mathfrak{D} \to \mathbb{R}, \text{ solution of}$$

$$\begin{cases} -\Delta u_s = f & \text{in } \mathfrak{D} \\ u_s = u_D & \text{on } \Lambda_D \\ \dfrac{\partial u_s}{\partial \mathbf{n}} = u_N & \text{on } \Lambda_N. \end{cases} \tag{2.25}$$

Let us formally multiply the first equation of (2.25) by a test function v, and let us integrate the resulting equation by parts, using the boundary conditions given in (2.25). The weak formulation of the Poisson problem then reads:

$$\text{find } u_s \in H^1_{u_D, \Lambda_D}(\mathfrak{D}) \text{ such that}$$
$$a(u_s, v) = \mathfrak{f}(v), \quad \forall v \in H^1_{0, \Lambda_D}(\mathfrak{D}), \tag{2.26}$$

where $a(\cdot, \cdot)$ and $\mathfrak{f}(\cdot)$ are defined for all $w, v \in H^1(\mathfrak{D})$ by

$$a(w, v) := \int_{\mathfrak{D}} \nabla w \cdot \nabla v \, \mathrm{d}x,$$
$$\mathfrak{f}(v) := \int_{\mathfrak{D}} f v \, \mathrm{d}x + \int_{\Lambda_N} u_N v \, \mathrm{d}s.$$

This problem can actually be easily transformed to address the imbalance of the spaces of test and admissible functions, i.e., $H^1_{0, \Lambda_D}(\mathfrak{D})$ and $H^1_{u_D, \Lambda_D}(\mathfrak{D})$ respectively. To do so, let $z_s := R_{\Lambda_D}(u_D)$ be a lifting of the Dirichlet data u_D given by Theorem 2.2.1, and for all test functions $v \in V := H^1_{0, \Lambda_D}(\mathfrak{D})$, let

$$\mathfrak{f}^{z_s}(v) := \int_{\mathfrak{D}} f v \, \mathrm{d}x + \int_{\Lambda_N} u_N v \, \mathrm{d}s - a(z_s, v).$$

Then solving the following problem:

$$\text{find } \mathring{u}_s \in V \text{ such that}$$
$$a(\mathring{u}_s, v) = \mathfrak{f}^{z_s}(v), \quad \forall v \in V \tag{2.27}$$

is equivalent to solving (2.26), since solution u_s of (2.26) can then be obtained as

$$u_s = \mathring{u}_s + z_s.$$

If we equip V with the norm $\|\nabla \cdot \|_{0,\mathfrak{D}}$, it is easy to show that $a(\cdot, \cdot)$ is a continuous and coercive bilinear form on $V \times V$, and $\mathfrak{f}^{z_s}(\cdot)$ is a linear continuous functional. Therefore, thanks to Lax Milgram theorem, problem (2.26) is well-posed, and the following stability estimate is satisfied:

$$\|\nabla u_s\|_{0,\mathfrak{D}} \leq \frac{1}{\mathfrak{a}} \left\| \mathfrak{f}^{z_s} \right\|_{V^*},$$

where $\mathfrak{a}$ is the coercivity constant of $a(\cdot, \cdot)$, i.e. $\mathfrak{a} = 1$ for problem (2.26).

2.5   Error estimation

It is in general very hard to exactly solve a BVP. Therefore, many methods have been developed to solve an approximate problem instead, whose solution gives a controlled approximation of the exact unknown. When a BVP is approximated, may it come from a geometrical or a numerical approximation of the PDE at hand, it is indeed important to be able to control the induced error. To discuss this aspect, let $u_s \in V$ be the exact solution of a PDE expressed in the variational form (2.12), and assume that problem (2.12) is well-posed as it verifies the conditions of Lax-Milgram theorem discussed in the previous section. Then, let U_s be the considered approximation of u_s.

Remark 2.5.1. In the next chapters of Part I of this thesis, U_s will be the solution u_d (or $\boldsymbol{u}_\mathrm{d}$ in the vectorial case) of the defeatured problem precisely defined in Chapter 3 (respectively, Chapter 4) . In the finite element literature, U_s often denotes the numerical approximation u_s^h of u_s; this will be the case in Part II of this thesis, and in particular in Chapter 7. In Chapter 8, U_s will be a combination of both, i.e., it will be the numerical approximation of the defeatured problem solution, denoted u_d^h.

2.5.1   *A priori* estimation

To begin with, one may want to estimate the relative error between u_s and U_s, in order to quantify the magnitude of the approximation error. This is the realm of *a priori* error bounds that are expressed in the form

$$\|| u_s - U_s \|| \leq \hbar \, \mathcal{G}(u_s), \tag{2.28}$$

where $\hbar$ depends on the approximation method parameters, $\mathcal{G}(\cdot)$ is a norm (or more generally a functional) that depends on the smoothness of the exact solution u_s, and $\||\cdot\||$ is the functional norm in which the error is measured.

In the context of numerical approximation, there exist rigorous *a priori* error estimates for the finite element method. The most relevant results for this thesis will be given in Part II, where the numerical approximation of the defeaturing problem is studied. For more details, the interested reader is referred to [Ciarlet, 2002; Brenner and Scott, 2008]. In the context of defeaturing instead, the *a priori* analysis is still an open problem that is beyond the scope of this work.

2.5.2   *A posteriori* estimation

Although *a priori* analysis constitutes the mathematical foundations of many approximation methods such as the finite element method, it cannot be used in practical applications since the exact unknown solution u_s appears on both side of the inequality (2.28). Finding a computable error bound which does not require the knowledge of the exact solution falls into the realm of *a posteriori* error estimation. More precisely, the aim of *a posteriori* estimation is to find a functional $\mathscr{E}(U_s)$ which does not depend on u_s, such that

$$\||u_s - U_s\|| \leq C_{\mathrm{up}}\, \mathscr{E}(U_s) \qquad\qquad \text{(reliability)}, \qquad\qquad (2.29)$$

$$C_{\mathrm{lo}}\, \mathscr{E}(U_s) \leq \||u_s - U_s\|| \qquad\qquad \text{(efficiency)}, \qquad\qquad (2.30)$$

where C_{up} and C_{lo} are non-negative constants independent of u_s and U_s, and of the approximation parameters (e.g., underlying model precision, size of geometrical features, mesh size, etc.). This question is crucial in engineering applications, since for an approximation of the problem at hand, one needs to know the level of accuracy of the corresponding analysis. *A posteriori* bounds of the error are mostly used to steer adaptive strategies that allow for a reliable and efficient fine tuning of the approximation parameters.

In this work, we concentrate on explicit residual-type *a posteriori* error estimators with $\||\cdot\|| := \||\cdot\||_{\mathfrak{D}}$, where $\||\cdot\||_{\mathfrak{D}}$ is the energy norm (2.20) of the problem at hand. The starting point to derive this family of estimators is to find a representation of the error

$$e := u_s - U_s,$$

using the weak formulation (2.12). That is, using (2.12) and by linearity of the bilinear form $a(\cdot, \cdot)$,

$$a(e, v) = a(u_s, v) - a(U_s, v) = \mathfrak{f}(v) - a(U_s, v) =: \mathscr{R}_{U_s}(v), \quad \text{ for all } v \in V, \qquad (2.31)$$

where $\mathscr{R}_{U_s}(\cdot)$ is the residual of U_s in a weak sense. The quantity $\mathscr{R}_{U_s}(\cdot)$ does not explicitly depend on the exact solution u_s; it only depends on u_s through the variational formulation (2.12) of the problem at hand.

By performing some mathematical steps, we first aim at finding an estimate

$$\mathscr{R}_{U_s}(v) \leq C_{\text{up}}\,\mathscr{E}(U_s)\|v\|_{\mathfrak{D}}, \quad \forall v \in V, \tag{2.32}$$

where $\mathscr{E}(U_s)$ only contains computable quantities. Common ingredients for this step are integration by parts and Poincaré inequalities, see Section 2.3.2. Combining (2.31) and (2.32) and choosing $v = e$, we obtain

$$\|e\|_{\mathfrak{D}}^2 = a(e, e) = \mathscr{R}_{U_s}(e) \leq C_{\text{up}}\,\mathscr{E}(U_s)\|e\|_{\mathfrak{D}}. \tag{2.33}$$

Thus after simplifying (2.33) on both sides, the reliability estimate (2.29) can be demonstrated.

Subsequently, to demonstrate the efficiency estimate (2.30), one first needs to find the correct dual space W^* in which lies the residual $\mathscr{R}_{U_s}(\cdot)$, where W is a subset of V that can be continuously embedded in it, i.e., $W \hookrightarrow V$. Then, one needs to derive an estimate

$$\mathscr{E}(U_s) \leq C_1 \|\mathscr{R}_{U_s}\|_{W^*}, \tag{2.34}$$

where $\|\cdot\|_{W^*}$ is the dual norm in W^* and C_1 is a non-negative constant independent of the approximation parameters. Common ingredients for this step are inverse inequalities, see Section 2.3.3. This is sufficient to prove the efficiency estimate (2.30): indeed, using (2.31), using the continuity of $a(\cdot, \cdot)$ from (2.14), and since the energy norm on V is equivalent to the norm $\|\cdot\|_V$, then if $\|\cdot\|_W$ is the considered norm of W,

$$\begin{aligned}
\mathscr{E}(U_s) \leq C_1 \|\mathscr{R}_{U_s}\|_{W^*} = C_1 \sup_{\substack{w \in W \\ w \neq 0}} \frac{\mathscr{R}_{U_s}(w)}{\|w\|_W} &\leq C_1 C_2 \sup_{\substack{w \in W \\ w \neq 0}} \frac{a(e, w)}{\|w\|_V} \\
&\leq C_1 C_2 \sup_{\substack{v \in V \\ v \neq 0}} \frac{a(e, v)}{\|v\|_V} \leq \mathfrak{C} C_1 C_2 \sup_{\substack{v \in V \\ v \neq 0}} \frac{\|e\|_V \|v\|_V}{\|v\|_V} \\
&= \mathfrak{C} C_1 C_2 \|e\|_V \leq C_{\text{lo}}^{-1} \|e\|_{\mathfrak{D}},
\end{aligned}$$

where C_2 is a non-negative constant independent of the approximation parameters, $\mathfrak{C}$ is the continuity constant appearing in (2.14), and C_{lo} is a constant that only depends on $\mathfrak{C}$, C_1, C_2, and on the constant of equivalence between $\|\cdot\|_V$ and $\|\cdot\|_{\mathfrak{D}}$.

Lastly, we introduce the so-called effectivity index

$$\eta_{\text{eff}} := \frac{\mathscr{E}(U_s)}{\|e\|_{\mathfrak{D}}}, \tag{2.35}$$

which measures how well the estimator approximates the true error, where the optimal value of η_{eff} is one.

We remark that (2.29) and (2.30) provide a computable bound on the error, except for

the presence of the constants C_{up} and C_{lo}. In the literature, some effort has been put into finding a way to estimate these constants, we refer for instance to [Johnson and Hansbo, 1992; Destuynder and Métivet, 1999; Vohralík, 2011; Hannukainen et al., 2012]. However, while providing a sharp bound is an important property of an error estimator, we will see in the following chapters that it is not crucial to drive an adaptive strategy for fine tuning the approximation parameters.

For more details on *a posteriori* error estimation in the context of numerical approximation with finite element methods, the interested reader is referred to [Verfürth, 1994, 2013], and to Part II of the thesis. The remaining of Part I is instead dedicated to the *a posteriori* error analysis of the analysis-aware defeaturing problem, which is first introduced in Chapter 3.

Remark 2.5.2. A vast amount of literature is dedicated to the study of error estimators, and only a brief review of what is used in this thesis is presented in this section. For other common types of *a posteriori* error estimators such as implicit or recovery-based error estimators in the finite element context, the interested reader is referred to [Zienkiewicz and Zhu, 1987; Ainsworth and Oden, 1997; Grätsch and Bathe, 2005]. We also highlight that often in engineering applications, one is interested in local quantities rather than global errors such as the energy norm of the error. This is the realm of research of the so-called goal-oriented estimators. For an in-depth discussion on the subject the reader is referred to [Oden and Prudhomme, 2002; Grätsch and Bathe, 2005, 2006] and to the references therein.

2.5.3   Adaptivity

We have previously mentioned that *a posteriori* error estimators are often used to steer adaptive strategies which fine tune the approximation parameters. Let us summarize in this section the main steps composing an adaptive loop. For a review of the fundamental concepts underlying adaptive finite element methods, we refer to [Nochetto et al., 2009; Nochetto and Veeser, 2011] and to the references therein.

Using the notation from [Buffa and Giannelli, 2016], one iteration of an iterative process is composed of the following four main building blocks:

$$\boxed{\text{SOLVE}} \longrightarrow \boxed{\text{ESTIMATE}} \longrightarrow \boxed{\text{MARK}} \longrightarrow \boxed{\text{REFINE}}$$

More precisely, one first SOLVEs the approximation of the PDE at hand to obtain the approximate solution U_s. Then, the approximation error is ESTIMATEd by a suitable *a posteriori* error estimator $\mathscr{E}(U_s)$. If the error estimator is not below a prescribed tolerance, then the approximation parameters need to be updated to obtain a better approximation. In this thesis, the approximation parameters consist of:

1. local geometrical details of smaller scale present in the domain in which the PDE is defined (see Chapter 3),

2. the elements' size of the underlying finite element mesh (see Chapter 5).

When deriving *a posteriori* error estimators, one looks for an expression that can be decomposed as follows:

$$\mathscr{E}(U_s) = \left(\sum_{\tau \in T} \mathscr{E}_\tau(U_s)^2 \right)^{\frac{1}{2}},$$

where T is the set of approximation parameters, and where $\mathscr{E}_\tau(U_s)$ is an estimation of the local error contribution due to parameter $\tau \in T$. In this way, one can determine which parameter most contributes to the error, and thus which parameter should be chosen more carefully. This corresponds to the MARK module of the adaptive loop. Several marking strategies have been proposed in the literature, see for instance [Babuška and Rheinboldt, 1978; Johnson, 1990]. Let $0 < \theta \leq 1$ be a marking parameter, and let $T_{\mathrm{m}} \subset T$ denote the set of marked approximation parameters, then the predominant strategies are the following:

- Maximum strategy: a parameter $\tau_{\mathrm{m}} \in T$ is marked, i.e., $\tau_{\mathrm{m}} \in T_{\mathrm{m}}$, if it satisfies

$$\mathscr{E}_{\tau_{\mathrm{m}}}(U_s) \geq \theta \max_{\tau \in T} \left(\mathscr{E}_\tau(U_s) \right). \tag{2.36}$$

- Dörfler strategy [Dörfler, 1996]: the set of marked parameters $\tau_{\mathrm{m}} \in T_{\mathrm{m}}$ is obtained by sequentially choosing the parameter corresponding to the largest estimator contribution $\mathscr{E}_{\tau_{\mathrm{m}}}(U_s)$, until the following criterion is met:

$$\left(\sum_{\tau_{\mathrm{m}} \in T_{\mathrm{m}}} \mathscr{E}_{\tau_{\mathrm{m}}}(U_s)^2 \right)^{\frac{1}{2}} \geq \theta \mathscr{E}(U_s). \tag{2.37}$$

With this marking strategy, error reduction is guaranteed at each iteration of the adaptive loop.

Finally, the marked parameters in T_{m} are REFINEd, where refinement has a different meaning depending on the type of parameters. In this thesis, using the same numeration as above,

1. the marked geometrical details are added or removed from the geometrical model on which the PDE is solved (see Chapter 3),

2. the marked mesh elements are refined in a classical way, where we refer for instance to [Morin et al., 2002]. The special case of, possibly trimmed, hierarchical isogeometric meshes is discussed in Chapters 6 and 7.

3 *A posteriori* error estimation: single feature geometries

Defeaturing consists in simplifying geometrical models by removing the geometrical details of smaller scale, called features, that are considered not relevant for a given simulation. Feature removal and simplification of CAD models enables faster simulations for engineering analysis problems, and it simplifies the underlying meshing problem that is otherwise often unfeasible. Understanding well the effects of this process is an important step for the automatic integration of design and analysis into a single workflow. The aim of this chapter is to give a solid mathematical framework for analysis-aware defeaturing.

Let us consider a potentially complicated open Lipschitz domain $\Omega \subset \mathbb{R}^n$ on which we want to solve a PDE. More precisely, let us assume that Ω contains geometrical details of smaller scale. As illustrated in Figure 3.1, there exist three kinds of such geometrical features: a feature $F \subset \mathbb{R}^n$ is said to be

- negative if $\left(\overline{F} \cap \overline{\Omega} \right) \subset \partial\Omega$,

- positive if $F \subset \Omega$,

- complex if it is composed of both negative and positive components.

A negative feature corresponds to a part where some material has been removed (e.g., a

(a) Internal negative feature. (b) Negative feature on the boundary. (c) Positive feature. (d) Complex feature.
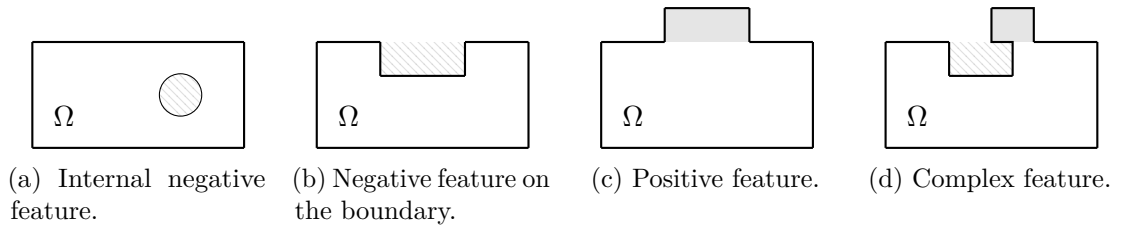
Figure 3.1 – Domains with different types of geometrical features F. In each case, the negative component of F is dashed while its positive component is filled in gray.

hole), a positive feature corresponds to the addition of some material (e.g., a protrusion), and a feature is complex in the most general situation that corresponds to both the addition and the removal of some material. We note than an internal feature (e.g., an internal hole) is a special case of negative feature.

However, we suppose that we cannot solve the given PDE on the given computational domain because of the complexity of Ω coming from the presence of the features. Therefore, we want to solve a similar problem instead, called defeatured (or simplified) problem, in a defeatured domain Ω_0 where features are removed: holes are filled with material, and protrusions are cut out of the computational domain.

In this chapter, we work in the context of the Poisson equation defined in a geometry Ω containing a single feature F. We assume that Neumann boundary conditions are imposed on the boundary of the feature. The multi-feature case is studied in the subsequent Chapter 4. The effects of defeaturing on the analysis are often neglected and, as of today, there are basically very few strategies to quantitatively evaluate such an impact. Therefore, after precisely defining the defeaturing problem, we introduce an *a posteriori* estimator of the energy norm of the defeaturing error which is easy to compute, and which explicitly depends on the size of the feature. We also demonstrate its reliability and efficiency up to oscillations. The estimator is very cheap to compute: after the computation of the solution in the simplified domain Ω_0 and in a simplified positive component of the feature (as, e.g., its bounding box), it only requires the computation of local boundary integrals. Indeed, the proposed estimator is derived from a representation of the defeaturing error that only involves differences between boundary terms on the feature, as already observed in [Gopalakrishnan and Suresh, 2008; Turevsky et al., 2008] and in [Li and Gao, 2011; Li et al., 2013b,a].

To ease the exposition, the defeaturing problem is first precisely defined in Section 3.1 in the simpler setting in which the geometry contains a feature which is either negative or positive. It allows us to introduce the notation that is then used throughout the thesis. Then in Section 3.2, the defeaturing error estimator is derived and analyzed in the case in which the geometry contains a negative feature. Subsequently, in Section 3.3, the defeaturing problem is generalized to a geometry with a complex feature, and the *a posteriori* defeaturing error estimator is generalized and analyzed in this case in Section 3.4. The study of the defeaturing problem when the feature is positive can be deduced from Section 3.4 as a special case. Finally, in Section 3.5, we present a validation of the previously presented results. Our validation is obtained by comparing errors and defeaturing estimators for numerical solutions on very fine meshes. This chapter closely follows [Buffa et al., 2022b].

3.1 Defeaturing problem: geometry with a negative or a positive feature

In this section, we precisely define the analysis-aware defeaturing problem when the exact geometry Ω contains either a negative or a positive feature, using the Poisson equation as model problem. Let us first introduce the considered problem in the exact geometry Ω.

Let $\mathbf{n}$ be the unitary outward normal to Ω, let $\partial\Omega = \overline{\Gamma_D} \cup \overline{\Gamma_N}$ with $\Gamma_D \cap \Gamma_N = \emptyset$, $|\Gamma_D| > 0$, and let $g_D \in H^{\frac{3}{2}}(\Gamma_D)$, $g \in H^{\frac{1}{2}}(\Gamma_N)$ and $f \in L^2(\Omega)$. We are interested in the following Poisson equation defined in the exact geometry Ω:

$$\text{find } u : \Omega \to \mathbb{R}, \text{ solution of}$$

$$\begin{cases} -\Delta u = f & \text{in } \Omega \\ u = g_D & \text{on } \Gamma_D \\ \dfrac{\partial u}{\partial \mathbf{n}} = g & \text{on } \Gamma_N. \end{cases} \tag{3.1}$$

In the framework presented in Section 2.4, let us formally multiply the first equation of (3.1) by a test function v, and let us integrate the resulting equation by parts using the boundary conditions given in (3.1). The weak formulation of the Poisson problem then reads:

$$\text{find } u \in W := H^1_{g_D, \Gamma_D}(\Omega) \text{ such that}$$

$$a_\Omega(u, v) = \mathfrak{f}_\Omega(v), \quad \forall v \in V := H^1_{0, \Gamma_D}(\Omega) \tag{3.2}$$

where $a_\Omega(\cdot, \cdot)$ and $\mathfrak{f}_\Omega(\cdot)$ are defined by

$$a_\Omega(w, v) := \int_\Omega \nabla w \cdot \nabla v \, \mathrm{d}x \qquad \text{for all } w \in W, v \in V,$$

$$\mathfrak{f}_\Omega(v) := \int_\Omega f v \, \mathrm{d}x + \int_{\Gamma_N} g v \, \mathrm{d}s \qquad \text{for all } v \in V.$$

The analysis done in Example 2.4.4 uses Banach-Nečas-Babuška Theorem 2.4.2 to demonstrate that a Poisson problem as (3.2) is well-posed, when V is equipped with the norm $\|\nabla \cdot\|_{0,\Omega}$.

Let us now assume that the exact geometry Ω contains a single open Lipschitz feature F which is either positive or negative, and let us precisely define the considered defeaturing problem in this context. First, we define the defeatured (or simplified) geometry $\Omega_0 \subset \mathbb{R}^n$ as follows:

- if F is negative, $\Omega_0 := \mathrm{int}\left(\overline{\Omega} \cup \overline{F}\right)$,

- if F is positive, $\Omega_0 := \Omega \setminus \overline{F}$,

(a) Domain with a negative feature.

(b) Domain with a positive feature.

(c) Simplified domain corresponding to domains (a) and (b).

(d) Domain with a positive feature, $\Omega := \mathrm{int}\left(\overline{\Omega_0} \cup \overline{F}\right)$.
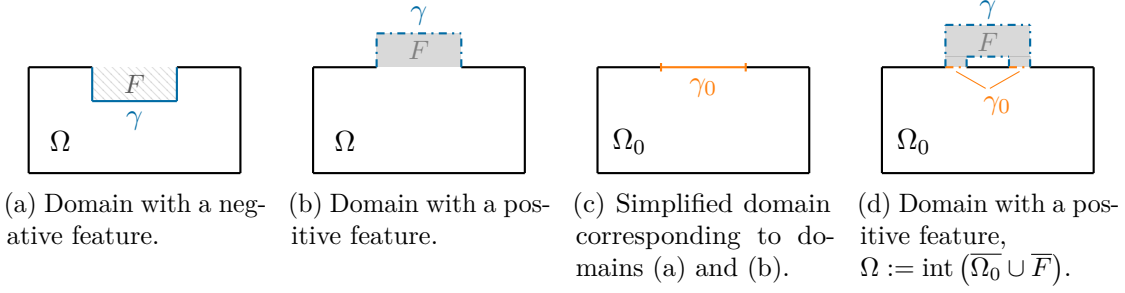
Figure 3.2 – Illustration of the notation in different geometries with a negative or a positive feature.

(a) Exact domain Ω.

(b) Possible simplified domain $\Omega_0 := \mathrm{int}(\overline{\Omega} \cup \overline{F})$ with a negative feature F.

(c) Possible simplified domain $\Omega_0 = \Omega \setminus \overline{F}$ with a positive feature F.
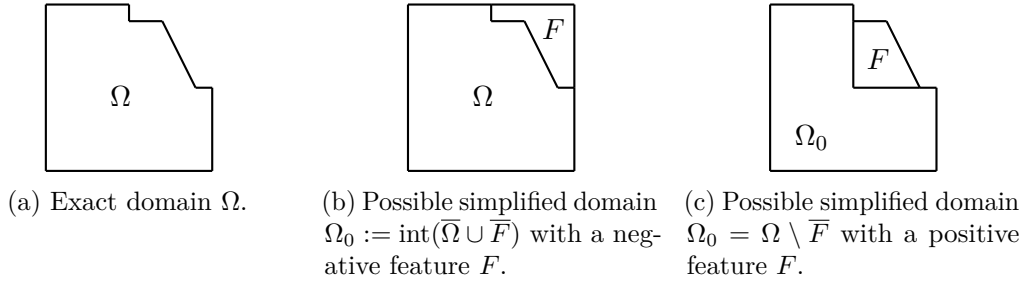
Figure 3.3 – Exact geometry Ω and different possible defeatured geometries Ω_0.

and we assume that Ω_0 is also an open Lipschitz domain. In other words, if the feature F is negative, then the exact domain Ω is embedded in the defeatured domain Ω_0; if F is positive instead, the exact domain Ω is the union of the defeatured domain Ω_0 and the feature F, as illustrated in Figure 3.2.

Remark 3.1.1. Given a complicated geometry Ω without any further information, one cannot always easily tell whether the features it contains are negative or positive, see Figure 3.3. Therefore, this is often a choice that the user needs to make, based on the available geometric information at hand. If one has access to a simplified geometry, for instance thanks to the history of (CAD) operations from which the exact geometry Ω is built, then it is possible to define F from Ω and Ω_0, instead of defining Ω_0 from Ω and F. The individuation of features in a given geometry and the construction of a corresponding simplified geometric model can be complicated tasks, see [Thakur et al., 2009] for a review of possible techniques. However, this goes beyond the scope of this work, which supposes at its roots that the feature information is known.

Now, let $\mathbf{n}_0$ and $\mathbf{n}_F$ be the unitary outward normals to Ω_0 and F respectively. In this work, the analysis is performed under the following assumption:

Assumption 3.1.2. In the exact problem (3.1), a Neumann boundary condition is imposed on the feature's boundary, i.e.,

$$\Gamma_D \cap \partial F = \emptyset.$$

Moreover, let γ be the piece of boundary of Ω that is removed by defeaturing, and let γ_0 be the piece of boundary of Ω_0 replacing it, that is,

$$\gamma_0 := \partial F \setminus \overline{\Gamma_N} \subset \partial\Omega_0 \quad \text{and} \quad \gamma := \partial F \setminus \overline{\gamma_0} \subset \partial\Omega,$$

so that $\partial F = \overline{\gamma} \cup \overline{\gamma_0}$ and $\gamma \cap \gamma_0 = \emptyset$ (see Figure 3.2). In particular, note that an internal feature F is a negative feature for which $\gamma = \partial F$ and $\gamma_0 = \emptyset$. In the following, the defeaturing problem is stated, and the cases in which F is either positive or negative are treated separately.

If feature F is negative, choose any L^2-extension of $f \in L^2(\Omega)$ in F, that we still write $f \in L^2(\Omega_0)$ by abuse of notation. Note that such an extension is not needed for a positive feature. Then, instead of (3.1), the following defeatured (or simplified) problem is solved: after choosing $g_0 \in H^{\frac{1}{2}}(\gamma_0)$, find $u_0 \in H^1(\Omega_0)$, the weak solution of

$$\begin{cases} -\Delta u_0 = f & \text{in } \Omega_0 \\ u_0 = g_D & \text{on } \Gamma_D \\ \dfrac{\partial u_0}{\partial \mathbf{n_0}} = g & \text{on } \Gamma_N \setminus \gamma \\ \dfrac{\partial u_0}{\partial \mathbf{n_0}} = g_0 & \text{on } \gamma_0, \end{cases} \tag{3.3}$$

that is, $u_0 \in H^1_{g_D,\Gamma_D}(\Omega_0)$ satisfies for all $v_0 \in H^1_{0,\Gamma_D}(\Omega_0)$,

$$\int_{\Omega_0} \nabla u_0 \cdot \nabla v_0 \, \mathrm{d}x = \int_{\Omega_0} f v_0 \, \mathrm{d}x + \int_{\Gamma_N \setminus \gamma} g v_0 \, \mathrm{d}s + \int_{\gamma_0} g_0 v_0 \, \mathrm{d}s. \tag{3.4}$$

Thanks to Example 2.4.4, we know that problem (3.4) is well-posed. The choice of defeatured problem data f in F and g_0 on γ_0 will be guided by Remark 3.2.1, and further discussed in Section 3.5.2.3. We only anticipate here that the best possible choices satisfy a conservation assumption of the solution flux in the feature, given by (3.12). We are now interested in controlling the energy norm of the defeaturing error "$u - u_0$" in Ω, that we suitably define in what follows.

Negative feature case: in this setting, the boundary γ will play an important role in the sequel, and the analysis is made under the following assumption.

Assumption 3.1.3. The boundary γ is isotropic according to Definition 2.1.2.

Since $\Omega \subset \Omega_0$ when F is negative, then we consider the restriction of u_0 to Ω to define the defeaturing error. That is, the energy norm of the defeaturing error is defined by

$$\left\Vert\! \left\vert u - u_0|_\Omega \right\vert \!\right\Vert_\Omega := \left(a_\Omega(u - u_0|_\Omega, u - u_0|_\Omega) \right)^{\frac{1}{2}} = \left\Vert \nabla\left(u - u_0|_\Omega\right) \right\Vert_{0,\Omega} = \left\vert u - u_0|_\Omega \right\vert_{1,\Omega}.$$

(a) Domain Ω with a positive feature F.

(b) Simplified domain Ω_0 and positive feature F, $\Omega = \text{int}\left(\overline{\Omega_0} \cup \overline{F}\right)$.

(c) Example of extended feature domain $\tilde{F} \supset F$.
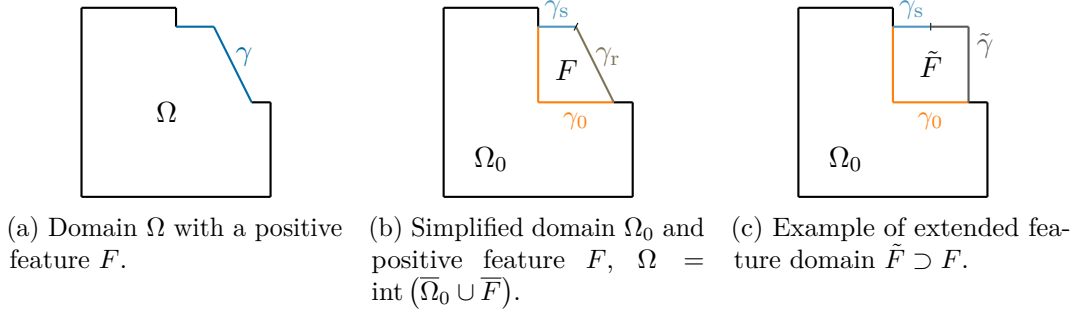
Figure 3.4 – Illustration of the notation in a geometry with a positive feature.

Positive feature case: in this setting, the solution u_0 is only defined in the defeatured geometry Ω_0, but Ω_0 does not contain the feature F since $F \subset \Omega$ but $F \not\subset \Omega_0$. That is, the solution u_0 is not defined everywhere in the exact geometry $\Omega = \text{int}\left(\overline{\Omega_0} \cup \overline{F}\right)$. Therefore, to define the defeaturing error, and since Ω is the union of Ω_0 and F, one needs to solve a problem to extend u_0 to F. The most natural extension would be the solution of

$$\begin{cases} -\Delta \tilde{u}_0 = f & \text{in } F \\ \tilde{u}_0 = u_0 & \text{on } \gamma_0 \\ \dfrac{\partial \tilde{u}_0}{\partial \mathbf{n}_F} = g & \text{on } \gamma. \end{cases} \tag{3.5}$$

However, F may be complex or even non-smooth (see examples of Section 3.5.3), thus finding or computing the solution of (3.5) may be cumbersome. Therefore, instead of solving the extension problem (3.5) in the positive feature F, we can choose to solve an extension problem in a simpler domain $\tilde{F}$ which shares γ_0 as a boundary. More precisely, let $\tilde{F} \subset \mathbb{R}^n$ be a Lipschitz domain that contains F and such that $\gamma_0 \subset \left(\partial \tilde{F} \cap \partial F\right)$, that is, $\tilde{F}$ is a suitable (simple) domain extension of F. It can be for instance the bounding box of F, if the boundary of the latter contains γ_0. Note that it is possible to have $\tilde{F} \cap \Omega_0 \neq \emptyset$, but we also assume that

$$G := \tilde{F} \setminus \overline{F}$$

is Lipschitz. We also remark that one can look at $\tilde{F}$ as the defeatured geometry of the positive feature F, that is, as a geometry simplified from the exact geometry F, for which G is a negative feature.

Let $\tilde{\mathbf{n}}$ be the unitary outward normal to $\tilde{F}$, let $\tilde{\gamma} := \partial \tilde{F} \setminus \partial F$, and let γ be decomposed as $\gamma = \text{int}(\overline{\gamma_s} \cup \overline{\gamma_r})$, where γ_s and γ_r are open, γ_s is the part of γ that is shared with $\partial \tilde{F}$ while γ_r is the remaining part of γ, that is, the part that does not belong to $\partial \tilde{F}$. This notation is illustrated in Figure 3.4. Note that γ_0 and $\tilde{\gamma}$ are "simple" boundaries since they are the boundaries of the chosen simplified geometry Ω_0 and of the chosen extended

feature domain $\tilde{F}$, respectively. As they will play an important role in the *a posteriori* defeaturing error analysis of a geometry with a positive feature, we remark in particular that γ_0 and $\tilde{\gamma}$ can be non-connected sub-manifolds, as illustrated in Figure 3.2d, and we make the following assumption.

Assumption 3.1.4. The boundaries γ_0 and γ_r are isotropic according to Definition 2.1.2.

Therefore, when F is positive, let us choose an L^2-extension of f in G that we still write f by abuse of notation. Then we can solve the following extension of the solution u_0 of (3.3) in $\tilde{F}$ instead of F: after choosing $\tilde{g} \in H^{\frac{1}{2}}(\tilde{\gamma})$, find $\tilde{u}_0 \in H^1\left(\tilde{F}\right)$, the weak solution of

$$
\begin{cases}
-\Delta \tilde{u}_0 = f & \text{in } \tilde{F} \\
\tilde{u}_0 = u_0 & \text{on } \gamma_0 \\
\dfrac{\partial \tilde{u}_0}{\partial \tilde{\mathbf{n}}} = \tilde{g} & \text{on } \tilde{\gamma} \\
\dfrac{\partial \tilde{u}_0}{\partial \tilde{\mathbf{n}}} = g & \text{on } \gamma_s,
\end{cases}
\tag{3.6}
$$

that is, $\tilde{u}_0 \in H^1_{u_0,\gamma_0}\left(\tilde{F}\right)$ satisfies for all $\tilde{v} \in H^1_{0,\gamma_0}\left(\tilde{F}\right)$,

$$
\int_{\tilde{F}} \nabla \tilde{u}_0 \cdot \nabla \tilde{v} \, \mathrm{d}x = \int_{\tilde{F}} f \tilde{v} \, \mathrm{d}x + \int_{\tilde{\gamma}} \tilde{g} \tilde{v} \, \mathrm{d}s + \int_{\gamma_s} g \tilde{v} \, \mathrm{d}s.
\tag{3.7}
$$

Thanks to Example 2.4.4, we know that problem (3.7) is well-posed. The choice of defeatured problem data f in G, g_0 on γ_0 and $\tilde{g}$ on $\tilde{\gamma}$ will be guided by Remark 3.4.2, and further discussed in Section 3.5.2.3. We only anticipate here that the best possible choices satisfy conservation assumptions of the solution flux in the feature, given by (3.31). Then, let us define the extended defeatured solution $u_d \in H^1_{g_D,\Gamma_D}(\Omega)$ as

$$
u_d = u_0 \quad \text{in } \Omega_0 \qquad \text{and} \qquad u_d = \tilde{u}_0|_F \quad \text{in } F.
$$

Finally, the energy norm of the defeaturing error is defined by

$$
\|\!|u - u_d|\!\|_\Omega := \left(a_\Omega(u - u_d, u - u_d)\right)^{\frac{1}{2}} = \left\|\nabla\left(u - u_d\right)\right\|_{0,\Omega} = |u - u_d|_{1,\Omega}.
$$

The *a posteriori* error analysis of the defeaturing problem in this setting can be deduced as a special case of the analysis presented in Section 3.4, in which a geometry containing a general complex feature is considered.

Remark 3.1.5. In the sequel, the defeaturing problem is analyzed in the case in which all domains are Lipschitz, and under the isotropy Assumptions 3.1.3 and 3.1.4. A finer analysis could be performed to take into account more general geometries such as the non-Lipschitz fillet of Section 3.5.3, but this goes beyond the scope of this work.

Whenever F is negative and $\sigma := \gamma$, or F is positive and $\sigma := \gamma_0$ or $\sigma := \gamma_{\mathrm{r}}$, and if σ is regular according to Definition 2.1.3, then for all $m \in \mathbb{N}$, we define

$$\Pi_{m,\sigma} : L^2(\sigma) \to \mathbb{Q}^{\mathrm{pw}}_{m,0}(\sigma) \tag{3.8}$$

as the extension of the Clément operator on σ introduced in [Clément, 1975] and further developed in [Bernardi and Girault, 1998] (see also Chapter 5).

3.2 Defeaturing error estimator: negative feature case

In this section, an optimal *a posteriori* defeaturing error estimator is derived in the simplest setting of a negative feature. We show that the derived estimator is an upper bound and a lower bound (up to oscillations) of the energy norm of the defeaturing error. The key issue in the subsequent analysis is to track the dependence of all constants from the size of the feature. Although it would be possible to present the equivalent analysis for a positive feature, we have decided to omit it and to let the positive feature case be a consequence of the more general case of a complex feature, whose dedicated analysis is presented in Section 3.4.

Let us therefore assume that F is a negative feature of the exact geometry Ω, and recall the definition of solution u_0 solving the defeatured problem (3.4). Moreover, suppose that γ is isotropic according to Definition 2.1.2, and after observing that $\mathbf{n}_F = -\mathbf{n}$ on γ, let

$$d_\gamma := g + \frac{\partial u_0}{\partial \mathbf{n}_F} = g - \frac{\partial u_0}{\partial \mathbf{n}} \tag{3.9}$$

be the error term on the Neumann data defined on γ. Then if we let $\eta \in \mathbb{R}$ be the unique solution of $\eta = -\log(\eta)$, and if we let

$$c_\gamma := \begin{cases} \max\left(|\log(|\gamma|)|, \eta\right)^{\frac{1}{2}} & \text{if } n = 2 \\ 1 & \text{if } n = 3, \end{cases} \tag{3.10}$$

we define the *a posteriori* defeaturing error estimator as

$$\mathscr{E}_D(u_0) := \left(|\gamma|^{\frac{1}{n-1}} \left\|d_\gamma - \overline{d_\gamma}^\gamma\right\|^2_{0,\gamma} + c_\gamma^2 |\gamma|^{\frac{n}{n-1}} \left|\overline{d_\gamma}^\gamma\right|^2\right)^{\frac{1}{2}}, \tag{3.11}$$

where we recall that $\overline{d_\gamma}^\gamma$ denotes the average value of d_γ over γ as defined in (2.5).

We first show that the quantity $\mathscr{E}_D(u_0)$ is a reliable estimator for the defeaturing error, i.e., it is an upper bound for the defeaturing error, see Theorem 3.2.3. Then, assuming that γ is also regular according to Definition 2.1.3, and under mild assumptions for the two-dimensional case, we show that it is also efficient (up to oscillations), i.e., it is a

lower bound for the defeaturing error up to oscillations, see Theorem 3.2.4. This means that the whole information on the error introduced by defeaturing a negative feature, in the energy norm, is encoded on the boundary γ, and can be accounted by suitably evaluating the error made on the normal derivative of the solution.

In this section, the symbol $\lesssim$ is used to mean any inequality which does not depend on the size of F, but which can depend on its shape.

Remark 3.2.1. Consider the simplified problem (3.3) restricted to F with the natural Neumann boundary condition on γ, that is, $u_0|_F \in H^1(F)$ satisfies

$$\begin{cases} -\Delta\left(u_0|_F\right) = f & \text{in } F \\ \dfrac{\partial\left(u_0|_F\right)}{\partial \mathbf{n}_0} = g_0 & \text{on } \gamma_0 \\ \dfrac{\partial\left(u_0|_F\right)}{\partial \mathbf{n}_F} = \dfrac{\partial u_0}{\partial \mathbf{n}_F} & \text{on } \gamma. \end{cases}$$

By abuse of notation, we omit the explicit restriction of u_0 to F. Then, if we multiply the restricted problem by the constant function 1 and integrate by parts, we obtain

$$\int_F f \,\mathrm{d}x + \int_{\gamma_0} g_0 \,\mathrm{d}s + \int_\gamma \frac{\partial u_0}{\partial \mathbf{n}_F} = 0.$$

Consequently,

$$\overline{d_\gamma}^\gamma = \overline{\left(g + \frac{\partial u_0}{\partial \mathbf{n}_F}\right)}^\gamma = \frac{1}{|\gamma|}\left(\int_\gamma g \,\mathrm{d}s - \int_{\gamma_0} g_0 \,\mathrm{d}s - \int_F f \,\mathrm{d}x\right).$$

Therefore, the second term of the estimator $\mathscr{E}_D(u_0)$ in (3.11) only depends on the defeatured problem data, and more precisely on the choice of g_0 that one considers on γ_0, and on the choice of the extension of f that one considers in the feature F. As a consequence, if the second term of the estimator (3.11) dominates, this means that the defeatured problem data should be better chosen. Moreover, under the following reasonable flux conservation assumption

$$\int_\gamma g \,\mathrm{d}s - \int_{\gamma_0} g_0 \,\mathrm{d}s - \int_F f \,\mathrm{d}x = 0, \tag{3.12}$$

the defeaturing error estimator (3.11) rewrites

$$\mathscr{E}_D(u_0) = |\gamma|^{\frac{1}{2(n-1)}} \|d_\gamma\|_{0,\gamma}.$$

Note that condition (3.12) is easily met if the Neumann boundary condition g and the source function f are zero in the vicinity of the feature.

Remark 3.2.2. Since $(4c_\gamma^2 - 1) > 0$ for all γ, then by Cauchy-Schwarz inequality,

$$\mathscr{E}_D(u_0) \lesssim |\gamma|^{\frac{1}{2(n-1)}} \left[\left\| d_\gamma - \overline{d_\gamma}^\gamma \right\|_{0,\gamma}^2 + 4c_\gamma^2 |\gamma| \left(\overline{d_\gamma}^\gamma \right)^2 \right]^{\frac{1}{2}}$$

$$= |\gamma|^{\frac{1}{2(n-1)}} \left[\| d_\gamma \|_{0,\gamma}^2 + \left(4c_\gamma^2 - 1 \right) |\gamma| \left(\overline{d_\gamma}^\gamma \right)^2 \right]^{\frac{1}{2}}$$

$$\lesssim c_\gamma |\gamma|^{\frac{1}{2(n-1)}} \| d_\gamma \|_{0,\gamma} =: \tilde{\mathscr{E}}_D(u_0).$$

One could be tempted to use the simpler indicator $\tilde{\mathscr{E}}_D(u_0)$, but when $n = 2$ and under the flux conservation condition (3.12), $\tilde{\mathscr{E}}_D(u_0)$ is sub-optimal since $\tilde{\mathscr{E}}_D(u_0) = c_\gamma \mathscr{E}_D(u_0)$ in this case. Indeed, no lower bound can be provided for $\tilde{\mathscr{E}}_D(u_0)$.

3.2.1   Reliability

In this section, we state and prove that the error indicator defined in (3.11) is reliable, that is, it is an upper bound for the defeaturing error.

Theorem 3.2.3. *Let u and u_0 be the weak solutions of problems (3.1) and (3.3), respectively. If γ is isotropic according to Definition 2.1.2, then the defeaturing error in the energy norm is bounded in terms of the estimator $\mathscr{E}_D(u_0)$ introduced in (3.11) as follows:*

$$\left| u - u_0|_\Omega \right|_{1,\Omega} \lesssim \mathscr{E}_D(u_0).$$

Proof. Let us first consider the simplified problem (3.3) restricted to Ω with the natural Neumann boundary condition on γ, that is, since $\mathbf{n}_F = -\mathbf{n}$ on γ, the restriction $u_0|_\Omega \in H^1_{g_D, \Gamma_D}(\Omega)$ is the weak solution of

$$\begin{cases} -\Delta \left(u_0|_\Omega \right) = f & \text{in } \Omega \\ u_0|_\Omega = g_D & \text{on } \Gamma_D \\ \dfrac{\partial \left(u_0|_\Omega \right)}{\partial \mathbf{n}} = g & \text{on } \Gamma_N \setminus \gamma \\ \dfrac{\partial \left(u_0|_\Omega \right)}{\partial \mathbf{n}} = -\dfrac{\partial u_0}{\partial \mathbf{n}_F} & \text{on } \gamma. \end{cases} \tag{3.13}$$

By abuse of notation, we omit the explicit restriction of u_0 to Ω. Then, for all test functions $v \in H^1_{0, \Gamma_D}(\Omega)$,

$$\int_\Omega \nabla u_0 \cdot \nabla v \, \mathrm{d}x = \int_\Omega f v \, \mathrm{d}x + \int_{\Gamma_N \setminus \gamma} g v \, \mathrm{d}s - \int_\gamma \frac{\partial u_0}{\partial \mathbf{n}_F} v \, \mathrm{d}s. \tag{3.14}$$

Let $e := u - u_0 \in H^1_{0, \Gamma_D}(\Omega)$. Then from equations (3.2) and (3.14), for all $v \in H^1_{0, \Gamma_D}(\Omega)$,

$$\int_\Omega \nabla e \cdot \nabla v \, \mathrm{d}x = \int_{\Gamma_N} g v \, \mathrm{d}s - \int_{\Gamma_N \setminus \gamma} g v \, \mathrm{d}s + \int_\gamma \frac{\partial u_0}{\partial \mathbf{n}_F} v \, \mathrm{d}s$$

$$= \int_\gamma \left(g + \frac{\partial u_0}{\partial \mathbf{n}_F} \right) v \, \mathrm{d}s = \int_\gamma d_\gamma v \, \mathrm{d}s. \tag{3.15}$$

Now, if we take $v = e \in H^1_{0,\Gamma_D}(\Omega)$ in (3.15), then

$$|e|^2_{1,\Omega} = \int_\gamma d_\gamma e \, \mathrm{d}s = \int_\gamma \left(d_\gamma - \overline{d_\gamma}^\gamma \right) e \, \mathrm{d}s + \overline{d_\gamma}^\gamma \int_\gamma e \, \mathrm{d}s. \qquad (3.16)$$

Let us first estimate the first term of (3.16). Thanks to Poincaré inequality of Lemma 2.3.8 and a trace inequality,

$$\begin{aligned}
\int_\gamma \left(d_\gamma - \overline{d_\gamma}^\gamma \right) e \, \mathrm{d}s = \int_\gamma \left(d_\gamma - \overline{d_\gamma}^\gamma \right)(e - \overline{e}^\gamma) \, \mathrm{d}s &\leq \left\| d_\gamma - \overline{d_\gamma}^\gamma \right\|_{0,\gamma} \| e - \overline{e}^\gamma \|_{0,\gamma} \\
&\lesssim \left\| d_\gamma - \overline{d_\gamma}^\gamma \right\|_{0,\gamma} |\gamma|^{\frac{1}{2(n-1)}} |e|_{\frac{1}{2},\gamma} \leq |\gamma|^{\frac{1}{2(n-1)}} \left\| d_\gamma - \overline{d_\gamma}^\gamma \right\|_{0,\gamma} |e|_{\frac{1}{2},\partial\Omega} \\
&\lesssim |\gamma|^{\frac{1}{2(n-1)}} \left\| d_\gamma - \overline{d_\gamma}^\gamma \right\|_{0,\gamma} |e|_{1,\Omega}. \qquad (3.17)
\end{aligned}$$

Moreover, the second term of (3.16) can be estimated thanks to Lemma 2.3.9 and a trace inequality, that is,

$$\begin{aligned}
\overline{d_\gamma}^\gamma \int_\gamma e \, \mathrm{d}s \leq \left| \overline{d_\gamma}^\gamma \right| |\gamma|^{\frac{1}{2}} \| e \|_{0,\gamma} &\lesssim \left| \overline{d_\gamma}^\gamma \right| c_\gamma |\gamma|^{\frac{1}{2(n-1)} + \frac{1}{2}} \| e \|_{\frac{1}{2},\partial\Omega} \\
&\lesssim c_\gamma |\gamma|^{\frac{n}{2(n-1)}} \left| \overline{d_\gamma}^\gamma \right| |e|_{1,\Omega}. \qquad (3.18)
\end{aligned}$$

Therefore, combining (3.16), (3.17) and (3.18), and simplifying on both sides, we obtain the desired result. $\qquad \square$

3.2.2 Efficiency

In this section, we state and prove that the error indicator defined in (3.11) is efficient, that is, it is a lower bound for the defeaturing error, up to oscillations. In the case $n = 2$, the flux conservation assumption (3.12) is also required.

Theorem 3.2.4. *Let u and u_0 be as in Theorem 3.2.3, and assume that γ is isotropic and regular according to Definitions 2.1.2 and 2.1.3. Suppose that either $n = 3$, or $n = 2$ and the flux conservation condition (3.12) is satisfied. Then the defeaturing error, in the energy norm, bounds up to oscillations the estimator $\mathscr{E}_D(u_0)$ introduced in (3.11), that is*

$$\mathscr{E}_D(u_0) \lesssim \left| u - u_0|_\Omega \right|_{1,\Omega} + \mathrm{osc}(u_0),$$

where

$$\mathrm{osc}(u_0) := |\gamma|^{\frac{1}{2(n-1)}} \| d_\gamma - \Pi_m (d_\gamma) \|_{0,\gamma} \qquad (3.19)$$

for any $m \in \mathbb{N}$, with $\Pi_m := \Pi_{m,\gamma}$ being the extension of the Clément operator defined in (3.8).

Proof. To simplify the notation, we omit to explicitly write the restriction of u_0 to Ω

when it would be necessary, since the context makes it clear. As before, let us define the error $e := u - u_0 \in H^1_{0,\Gamma_D}(\Omega)$. From equation (3.15), for all $v \in H^1_{0,\Gamma_D}(\Omega)$,

$$\int_\gamma d_\gamma v \, \mathrm{d}s = \int_\Omega \nabla e \cdot \nabla v \, \mathrm{d}x \leq |e|_{1,\Omega} |v|_{1,\Omega}. \tag{3.20}$$

Now, for all $w \in H^{\frac{1}{2}}_{00}(\gamma)$, let $u_w \in H^1_{0,\partial\Omega\setminus\gamma}(\Omega) \subset H^1_{0,\Gamma_D}(\Omega)$ be the unique weak solution of

$$\begin{cases} -\Delta u_w = 0 & \text{in } \Omega \\ u_w = w^\star & \text{on } \partial\Omega, \end{cases}$$

where $w^\star$ is the extension of w by 0. Then

$$|u_w|_{1,\Omega} \lesssim \|w^\star\|_{\frac{1}{2},\partial\Omega} = \|w\|_{H^{1/2}_{00}(\gamma)}$$

by continuity of the solution on the data. Therefore, using (3.20),

$$\|d_\gamma\|_{H^{-1/2}_{00}(\gamma)} = \sup_{\substack{w \in H^{1/2}_{00}(\gamma) \\ w \neq 0}} \frac{\displaystyle\int_\gamma d_\gamma w \, \mathrm{d}s}{\|w\|_{H^{1/2}_{00}(\gamma)}} \lesssim \sup_{\substack{w \in H^{1/2}_{00}(\gamma) \\ w \neq 0}} \frac{\displaystyle\int_\gamma d_\gamma u_w \, \mathrm{d}s}{|u_w|_{1,\Omega}}$$

$$\leq \sup_{\substack{v \in H^1_{0,\Gamma_D}(\Omega) \\ v \neq 0}} \frac{\displaystyle\int_\gamma d_\gamma v \, \mathrm{d}s}{|v|_{1,\Omega}} \leq \sup_{\substack{v \in H^1_{0,\Gamma_D}(\Omega) \\ v \neq 0}} \frac{|e|_{1,\Omega} |v|_{1,\Omega}}{|v|_{1,\Omega}} = |e|_{1,\Omega}. \tag{3.21}$$

Moreover, using Remark 3.2.2 if $n = 3$, or Remark 3.2.1 if $n = 2$ and the flux conservation condition (3.12) is satisfied, then

$$\mathscr{E}_D(u_0) \lesssim |\gamma|^{\frac{1}{2(n-1)}} \|d_\gamma\|_{0,\gamma}.$$

Therefore, using the triangle inequality and applying the inverse inequality of Lemma 2.3.10, we get

$$\mathscr{E}_D(u_0) \lesssim |\gamma|^{\frac{1}{2(n-1)}} \left(\|\Pi_m(d_\gamma)\|_{0,\gamma} + \|d_\gamma - \Pi_m(d_\gamma)\|_{0,\gamma} \right)$$
$$\lesssim \|\Pi_m(d_\gamma)\|_{H^{-1/2}_{00}(\gamma)} + |\gamma|^{\frac{1}{2(n-1)}} \|d_\gamma - \Pi_m(d_\gamma)\|_{0,\gamma}. \tag{3.22}$$

Finally, using another time the triangle inequality, Lemma 2.3.7 and (3.21), we obtain

$$\|\Pi_m(d_\gamma)\|_{H^{-1/2}_{00}(\gamma)} \leq \|d_\gamma\|_{H^{-1/2}_{00}(\gamma)} + \|\Pi_m(d_\gamma) - d_\gamma\|_{H^{-1/2}_{00}(\gamma)}$$
$$\lesssim |e|_{1,\Omega} + |\gamma|^{\frac{1}{2(n-1)}} \|d_\gamma - \Pi_m(d_\gamma)\|_{0,\gamma}. \tag{3.23}$$

Consequently, combining (3.22) and (3.23), and recalling definition (3.19) of the oscilla-

tions, then

$$\mathscr{E}_D(u_0) \lesssim |e|_{1,\Omega} + \mathrm{osc}(u_0). \qquad \square$$

Remark 3.2.5. In some sense, the oscillations pollute the lower bound in Theorem 3.2.4. It is therefore important to make sure that the oscillations are asymptotically smaller than the defeaturing error, with respect to the size of the feature. While there is a strong numerical evidence of it (see Section 3.5), an *a priori* error analysis of the defeaturing problem is needed in order to obtain a rigorous proof, but this goes beyond the scope of this work. However, we are expecting the term $\|d_\gamma\|_{0,\gamma}$ to depend on the measure of γ. When the data is regular, so is u_0, and it is then always possible to choose m large enough so that the asymptotic behavior of the oscillations is $\mathcal{O}\left(|\gamma|^{m+\frac{1}{2(n-1)}}\right)$. Therefore, upon a wise choice of m, the oscillations converge faster than the defeaturing error with respect to the measure of γ.

3.3 Defeaturing problem: geometry with a complex feature

Instead of only discussing a defeaturing error estimator for a geometry containing a positive feature, we directly generalize the previous study to a geometry containing a complex feature, that is, a feature containing both negative and positive components. To do so, we first extend in this section the analysis-aware defeaturing problem of Section 3.1 to a geometry Ω which contains a general complex feature.

Let us therefore assume that Poisson problem (3.2) is solved in an exact geometry Ω which contains a complex open Lipschitz feature F, i.e., F is an open Lipschitz domain composed of a negative component F_n and a positive component F_p that can have a non-empty intersection (see Figure 3.5). More precisely, $F = \mathrm{int}\left(\overline{F_\mathrm{n}} \cup \overline{F_\mathrm{p}}\right)$, where F_n and F_p are open Lipschitz domains such that if we let

$$\Omega_\star := \Omega \setminus \overline{F_\mathrm{p}},$$

then $F_\mathrm{p} \subset \Omega$ and $\overline{F_\mathrm{n}} \cap \overline{\Omega_\star} \subset \partial\Omega_\star$, as illustrated in Figures 3.5 and 3.6. In particular, note that if $F_\mathrm{p} = \emptyset$ and $F = F_\mathrm{n}$, then F is negative, while if $F_\mathrm{n} = \emptyset$ and $F = F_\mathrm{p}$, then F is positive, as defined in Section 3.1. In this setting, the defeatured geometry is defined by

$$\Omega_0 := \mathrm{int}\left(\overline{\Omega_\star} \cup \overline{F_\mathrm{n}}\right) \subset \mathbb{R}^n, \qquad (3.24)$$

and as before, we also assume that $\Omega_\star$ and Ω_0 are an open Lipschitz domains. Note that in general $\Omega_\star \subset \Omega \cap \Omega_0$ (see Figure 3.5f), but the set equality holds when F is completely negative or positive.

As in the previous sections, let $\mathbf{n}_0$ be the unitary outward normal to Ω_0, and let $\mathbf{n}_F$ be the unitary outward normal to F_n and to F_p. The vector $\mathbf{n}_F$ may not be uniquely defined if the outward normal to F_n is of opposite sign of the outward normal to F_p, but

(a) Domain with a negative feature.

(b) Domain with a positive feature.

(c) Domain with a general complex feature.

(d) Simplified domain for domains (a)–(c), (e)–(f).

(e) Domain with a general complex feature.

(f) Domain with a general complex feature.

(g) Simplified domain for domains (e), (f).

(h) Domain with a positive feature, $\Omega := \mathrm{int}\left(\overline{\Omega_0} \cup \overline{F}\right)$.
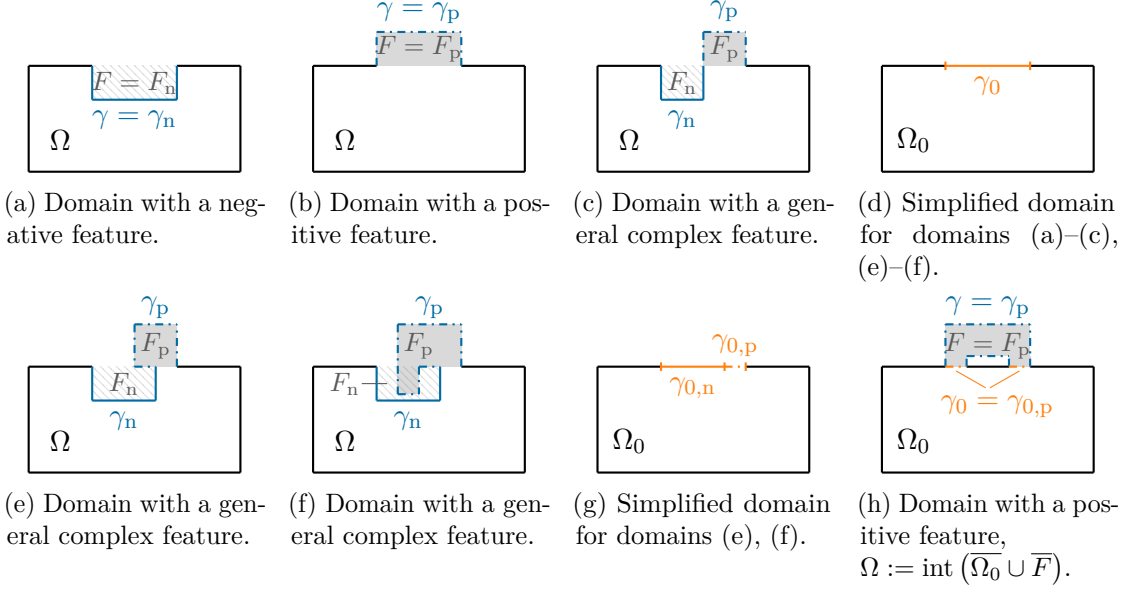
Figure 3.5 – Different geometries with a negative, a positive, or a general complex feature.

we allow this abuse of notation since the context will always make it clear. Similarly to the negative feature case, the analysis is performed under the following assumption:

Assumption 3.3.1. In the exact problem (3.1), a Neumann boundary condition is imposed on the feature's boundary, i.e.,

$$\Gamma_D \cap (\partial F_\mathrm{n} \cup \partial F_\mathrm{p}) = \emptyset,$$

Furthermore, in a similar way to Section 3.1, let γ be the piece of boundary of Ω removed by defeaturing, and let γ_0 be the piece of boundary of Ω_0 replacing it, that is,

$$\gamma_0 := \mathrm{int}\left(\overline{\gamma_{0,\mathrm{n}}} \cup \overline{\gamma_{0,\mathrm{p}}}\right) \subset \partial\Omega_0 \quad \text{with} \quad \gamma_{0,\mathrm{n}} := \partial F_\mathrm{n} \setminus \partial\Omega_\star, \quad \gamma_{0,\mathrm{p}} := \partial F_\mathrm{p} \setminus \partial\Omega,$$
$$\gamma := \mathrm{int}\left(\overline{\gamma_\mathrm{n}} \cup \overline{\gamma_\mathrm{p}}\right) \subset \partial\Omega \quad \text{with} \quad \gamma_\mathrm{n} := \partial F_\mathrm{n} \setminus \overline{\gamma_{0,\mathrm{n}}}, \quad \gamma_\mathrm{p} := \partial F_\mathrm{p} \setminus \overline{\gamma_{0,\mathrm{p}}},$$

so that $\partial F_\mathrm{n} = \overline{\gamma_\mathrm{n}} \cup \overline{\gamma_{0,\mathrm{n}}}$ with $\gamma_\mathrm{n} \cap \gamma_{0,\mathrm{n}} = \emptyset$, and $\partial F_\mathrm{p} = \overline{\gamma_\mathrm{p}} \cup \overline{\gamma_{0,\mathrm{p}}}$ with $\gamma_\mathrm{p} \cap \gamma_{0,\mathrm{p}} = \emptyset$ (see Figures 3.5 and 3.6).

Similarly to the negative feature case, choose any L^2-extension of the restriction $f|_{\Omega_\star}$ in the negative component F_n of F, that we still write $f \in L^2(\Omega_0)$ by abuse of notation. Then instead of (3.1), we solve the defeatured (or simplified) problem (3.3) whose weak formulation is given in (3.4), and we obtain $u_0 \in H^1_{g_D,\Gamma_D}(\Omega_0)$. As previously, we are interested in controlling the energy norm of the defeaturing error "$u - u_0$" in Ω, that we suitably define in what follows.

Similarly to the positive feature case, the solution u_0 of the defeatured problem is not

(a) Domain Ω with a complex feature.

(b) Defeatured domain Ω_0 and simplified positive component $\tilde{F}_{\mathrm{p}}$.

(c) Domains $\Omega_\star$, F_{n}, F_{p} and G_{p}.

(d) Domain $\tilde{\Omega}$.
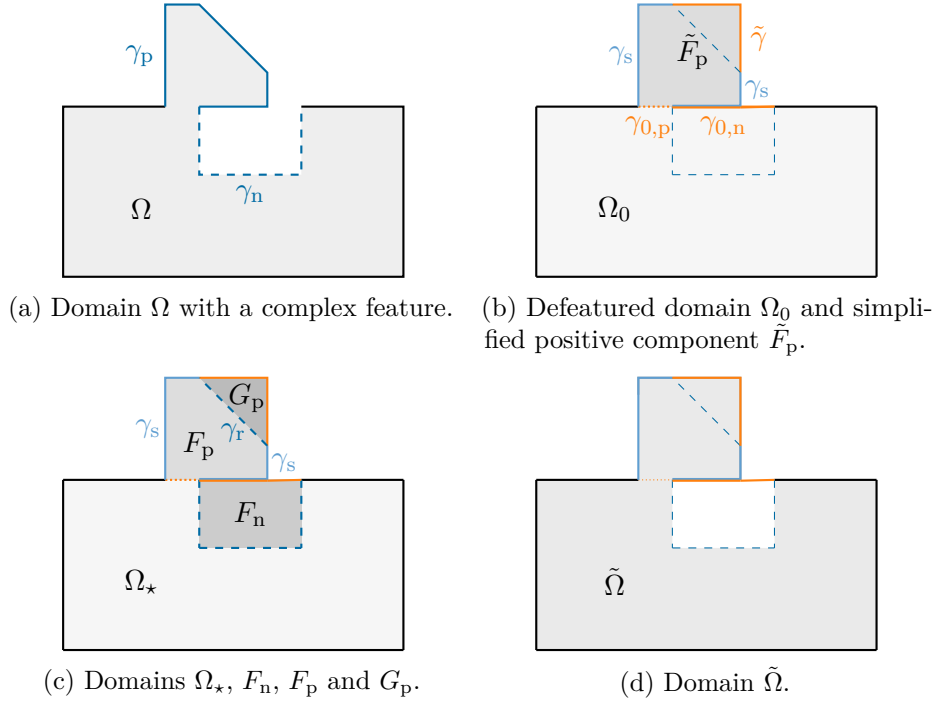
Figure 3.6 – Illustration of the notation for a geometry with a complex feature whose positive and negative components share a part of the boundary.

defined everywhere in Ω since $F_{\mathrm{p}} \not\subset \Omega_0$ but $F_{\mathrm{p}} \subset \Omega$. Therefore, we need to solve an extension problem for u_0 in a domain which contains F_{p}. Following the same rationale for F_{p} as the one exposed in Section 3.1, let $\tilde{F}_{\mathrm{p}} \subset \mathbb{R}^n$ be a Lipschitz domain that contains F_{p} and such that $\gamma_{0,\mathrm{p}} \subset \left(\partial \tilde{F}_{\mathrm{p}} \cap \partial F_{\mathrm{p}}\right)$, that is, $\tilde{F}_{\mathrm{p}}$ is a suitable (simple) domain extension of F_{p}, see Figure 3.6. To simplify the following exposition, let us assume that

$$\tilde{F}_{\mathrm{p}} \cap \Omega_\star = \emptyset,$$

even if this hypothesis could easily be removed. Furthermore, let

$$G_{\mathrm{p}} := \tilde{F}_{\mathrm{p}} \setminus \overline{F_{\mathrm{p}}}, \qquad \tilde{\Omega} := \mathrm{int}\left(\overline{\Omega} \cup \overline{G_{\mathrm{p}}}\right) = \mathrm{int}\left(\overline{\Omega_\star} \cup \overline{\tilde{F}_{\mathrm{p}}}\right), \tag{3.25}$$

and let us also assume that G_{p} is Lipschitz. Now, choose any L^2-extension of f in $\tilde{F}_{\mathrm{p}}$, that we still write f by abuse of notation. Let $\tilde{\mathbf{n}}$ be the unitary outward normal to $\tilde{F}_{\mathrm{p}}$, let $\tilde{\gamma} := \partial \tilde{F}_{\mathrm{p}} \setminus \partial F_{\mathrm{p}}$, and let γ_{p} be decomposed as $\gamma_{\mathrm{p}} = \mathrm{int}(\overline{\gamma_{\mathrm{s}}} \cup \overline{\gamma_{\mathrm{r}}})$, where γ_{s} and γ_{r} are open, γ_{s} is the part of γ_{p} that is shared with $\partial \tilde{F}_{\mathrm{p}}$ while γ_{r} is the remaining part of γ_{p}, that is, the part that does not belong to $\partial \tilde{F}_{\mathrm{p}}$, see Figure 3.6.

Therefore, and as for the positive feature case, we can define the extension

$$\tilde{u}_0 \in H^1_{u_0, \gamma_{0,\mathrm{p}}}\left(\tilde{F}_{\mathrm{p}}\right)$$

of the defeatured solution u_0 as the weak solution of (3.6), where F, $\tilde{F}$ and γ_0 are replaced by F_p, $\tilde{F}_\mathrm{p}$ and $\gamma_{0,\mathrm{p}}$, respectively. Now, we can define the extended defeatured solution $u_\mathrm{d} \in H^1_{g_D,\Gamma_D}(\Omega)$ as

$$u_\mathrm{d} = u_0|_{\Omega_\star} \quad \text{in } \Omega_\star = \Omega \setminus \overline{F_\mathrm{p}} \qquad \text{and} \qquad u_\mathrm{d} = \tilde{u}_0|_{F_\mathrm{p}} \quad \text{in } F_\mathrm{p}. \tag{3.26}$$

Then, the energy error of the defeaturing error is defined by

$$\|\!\|u - u_\mathrm{d}\|\!\|_\Omega = \|\nabla(u - u_\mathrm{d})\|_{0,\Omega} = |u - u_\mathrm{d}|_{1,\Omega}.$$

Remark 3.3.2. Note that if $F_\mathrm{n} \cap F_\mathrm{p} \neq \emptyset$, it may happen that $u_0 \neq \tilde{u}_0$ on $F_\mathrm{n} \cap F_\mathrm{p}$. But in this case, the definition of u_d in (3.26) specifies that $u_\mathrm{d} = \tilde{u}_0$ on $F_\mathrm{n} \cap F_\mathrm{p}$.

To ease the notation in the sequel, let

$$\Gamma^0_N := (\Gamma_N \setminus \gamma) \cup \gamma_0 \quad \text{and} \quad \tilde{\Gamma}_N := \gamma_\mathrm{s} \cup \tilde{\gamma} \tag{3.27}$$

be the Neumann boundaries of Ω_0 and of $\tilde{F}_\mathrm{p}$, respectively, and let

$$\Gamma := \gamma_\mathrm{n} \cup \gamma_\mathrm{r} \cup \gamma_{0,\mathrm{p}} \quad \text{and} \quad \Sigma := \{\gamma_\mathrm{n}, \gamma_{0,\mathrm{p}}, \gamma_\mathrm{r}\}. \tag{3.28}$$

In the following section and chapters, we will see that the boundaries in Σ play an important role in the analysis of the defeaturing problem. The analysis is performed under the following assumption, similar to Assumptions 3.1.3 and 3.1.4.

Assumption 3.3.3. Each boundary $\sigma \in \Sigma$ is isotropic according to Definition 2.1.2.

Note that as already observed in Section 3.1, these boundaries can be non-connected sub-manifolds, see e.g., Figure 3.5h.

3.4 Defeaturing error estimator: complex feature case

In this section, we generalize the previously introduced optimal *a posteriori* defeaturing error estimator to the framework of Section 3.3, in which the exact geometry Ω contains a complex feature. Building upon the study of Section 3.2, we show that the derived estimator is an upper bound and a lower bound (up to oscillations) of the energy norm of the defeaturing error, by accurately tracking the dependence of all constants from the size of the feature.

Recalling the definition of the defeaturing solution u_d from (3.26), let d_Σ be piecewise defined as $d_\Sigma|_\sigma := d_\sigma$ for all $\sigma \in \Sigma$, with

$$d_\sigma := \begin{cases} g - \dfrac{\partial u_\mathrm{d}}{\partial \mathbf{n}} & \text{if } \sigma = \gamma_\mathrm{n} \text{ or } \sigma = \gamma_\mathrm{r} \\ -\left(g_0 + \dfrac{\partial u_\mathrm{d}}{\partial \mathbf{n}_F}\right) & \text{if } \sigma = \gamma_{0,\mathrm{p}}. \end{cases} \tag{3.29}$$

That is, d_σ is the error term on the Neumann data for $\sigma = \gamma_{\mathrm{n}}$ or $\sigma = \gamma_{\mathrm{r}}$, and $d_{\gamma_{0,\mathrm{p}}}$ is the jump in the normal derivative of u_{d} due to the Dirichlet extension of u_{d} in the positive component of the feature. Then, we define the *a posteriori* defeaturing error estimator as

$$
\mathscr{E}_D(u_{\mathrm{d}}) := \left[\sum_{\sigma \in \Sigma} \left(|\sigma|^{\frac{1}{n-1}} \left\| d_\sigma - \overline{d_\sigma}^\sigma \right\|_{0,\sigma}^2 + c_\sigma^2 \, |\sigma|^{\frac{n}{n-1}} \left| \overline{d_\sigma}^\sigma \right|^2 \right) \right]^{\frac{1}{2}}, \tag{3.30}
$$

where c_σ is defined as in (3.10), and where we recall that for all $\sigma \in \Sigma$, $\overline{d_\sigma}^\sigma$ denotes the average value of d_σ over σ as defined in (2.5).

Remark 3.4.1. If F is a negative feature, then $\mathscr{E}_D(u_{\mathrm{d}}) = \mathscr{E}_D(u_0)$ simplifies into the previously introduced expression from (3.11), while if F is a positive feature, then $\mathscr{E}_D(u_{\mathrm{d}}) = \mathscr{E}_D(\tilde{u}_0)$ simplifies into

$$
\begin{aligned}
\mathscr{E}_D(\tilde{u}_0) := \Bigg(& |\gamma_0|^{\frac{1}{n-1}} \left\| \left(g_0 + \frac{\partial \tilde{u}_0}{\partial \mathbf{n}_F} \right) - \overline{\left(g_0 + \frac{\partial \tilde{u}_0}{\partial \mathbf{n}_F} \right)}^{\gamma_0} \right\|_{0,\gamma_0}^2 \\
& + |\gamma_{\mathrm{r}}|^{\frac{1}{n-1}} \left\| \left(g - \frac{\partial \tilde{u}_0}{\partial \mathbf{n}} \right) - \overline{\left(g - \frac{\partial \tilde{u}_0}{\partial \mathbf{n}} \right)}^{\gamma_{\mathrm{r}}} \right\|_{0,\gamma_{\mathrm{r}}}^2 \\
& + c_{\gamma_0}^2 \, |\gamma_0|^{\frac{n}{n-1}} \left| \overline{\left(g_0 + \frac{\partial \tilde{u}_0}{\partial \mathbf{n}_F} \right)}^{\gamma_0} \right|^2 + c_{\gamma_{\mathrm{r}}}^2 \, |\gamma_{\mathrm{r}}|^{\frac{n}{n-1}} \left| \overline{\left(g - \frac{\partial \tilde{u}_0}{\partial \mathbf{n}} \right)}^{\gamma_{\mathrm{r}}} \right|^2 \Bigg)^{\frac{1}{2}}.
\end{aligned}
$$

In this section, we first show that the quantity $\mathscr{E}_D(u_{\mathrm{d}})$ is a reliable estimator for the defeaturing error, i.e., it is an upper bound for the defeaturing error, see Theorem 3.4.4. Then, assuming that γ_{n}, γ_{r} and $\gamma_{0,\mathrm{p}}$ are also regular according to Definition 2.1.3, and under mild assumptions for the two-dimensional case, we show that it is also efficient (up to oscillations), i.e., it is a lower bound for the defeaturing error up to oscillations, see Theorem 3.4.5.

In the remaining part of this chapter, the symbol $\lesssim$ is used to mean any inequality which does not depend on the size of F_{n}, of F_{p}, or of the positive extension $\tilde{F}_{\mathrm{p}}$, but which can depend on their shape.

Remark 3.4.2. Consider the simplified extended problem (3.6) restricted to F_{p} and then to $\tilde{F}_{\mathrm{p}} \setminus F_{\mathrm{p}}$, with the natural Neumann boundary condition on $\gamma_{0,\mathrm{p}}$ and γ_{r} respectively, in a similar way to (3.13). By abuse of notation and as previously, we omit the explicit restriction of $\tilde{u}_0$ to F_{p} or to $\tilde{F}_{\mathrm{p}} \setminus F_{\mathrm{p}}$. Then if we multiply the restricted problems by the constant function 1 and integrate by parts, we obtain

$$
\int_{F_{\mathrm{p}}} f \, \mathrm{d}x + \int_{\gamma_{\mathrm{p}}} g \, \mathrm{d}s + \int_{\gamma_{0,\mathrm{p}}} \frac{\partial \tilde{u}_0}{\partial \mathbf{n}_F} \, \mathrm{d}s = 0,
$$

$$
\text{and} \quad \int_{\tilde{F}_{\mathrm{p}} \setminus F_{\mathrm{p}}} f \, \mathrm{d}x + \int_{\tilde{\gamma}} \tilde{g} \, \mathrm{d}s - \int_{\gamma_{\mathrm{r}}} \frac{\partial \tilde{u}_0}{\partial \mathbf{n}} \, \mathrm{d}s = 0.
$$

Consequently,

$$
\overline{d_{\gamma_{0,\mathrm{p}}}}^{\gamma_{0,\mathrm{p}}} = \overline{\left(g_0 + \frac{\partial \tilde{u}_0}{\partial \mathbf{n}_F}\right)}^{\gamma_{0,\mathrm{p}}} = \frac{1}{|\gamma_{0,\mathrm{p}}|} \left(\int_{\gamma_{0,\mathrm{p}}} g_0 \, \mathrm{d}s - \int_{\gamma_{\mathrm{p}}} g \, \mathrm{d}s - \int_{F_{\mathrm{p}}} f \, \mathrm{d}x\right),
$$

$$
\overline{d_{\gamma_{\mathrm{r}}}}^{\gamma_{\mathrm{r}}} = \overline{\left(g - \frac{\partial \tilde{u}_0}{\partial \mathbf{n}}\right)}^{\gamma_{\mathrm{r}}} = \frac{1}{|\gamma_{\mathrm{r}}|} \left(\int_{\gamma_{\mathrm{r}}} g \, \mathrm{d}s - \int_{\tilde{\gamma}} \tilde{g} \, \mathrm{d}s - \int_{\tilde{F}_{\mathrm{p}} \backslash F_{\mathrm{p}}} f \, \mathrm{d}x\right).
$$

Moreover, as in Remark 3.2.1, it can be seen that

$$
\overline{d_{\gamma_{\mathrm{n}}}}^{\gamma_{\mathrm{n}}} = \frac{1}{|\gamma_{\mathrm{n}}|} \left(\int_{\gamma_{\mathrm{n}}} g \, \mathrm{d}s - \int_{\gamma_{0,\mathrm{n}}} g_0 \, \mathrm{d}s - \int_{F_{\mathrm{n}}} f \, \mathrm{d}x\right).
$$

Therefore, the terms involving the average values of d_σ in the estimator $\mathscr{E}_D(u_{\mathrm{d}})$ defined in (3.30) only depend on the defeatured problem data. More precisely, they only depend on the choice of g_0 and $\tilde{g}$ that one chooses on γ_0 and $\tilde{\gamma}$ respectively, and on the choice of the extension of f that one considers in the extended feature $\tilde{F}_{\mathrm{p}}$. As a consequence, if those terms dominate, this means that the defeatured problem data should be better chosen. Moreover, under the following reasonable flux conservation assumptions

$$
\int_{\gamma_{0,\mathrm{p}}} g_0 \, \mathrm{d}s = \int_{\gamma_{\mathrm{p}}} g \, \mathrm{d}s + \int_{F_{\mathrm{p}}} f \, \mathrm{d}x, \qquad \int_{\tilde{\gamma}} \tilde{g} \, \mathrm{d}s = \int_{\gamma_{\mathrm{r}}} g \, \mathrm{d}s - \int_{\tilde{F}_{\mathrm{p}} \backslash F_{\mathrm{p}}} f \, \mathrm{d}x,
$$

$$
\text{and} \qquad \int_{\gamma_{0,\mathrm{n}}} g_0 \, \mathrm{d}s = \int_{\gamma_{\mathrm{n}}} g \, \mathrm{d}s - \int_{F_{\mathrm{n}}} f \, \mathrm{d}x, \tag{3.31}
$$

the defeaturing error estimator (3.30) rewrites

$$
\mathscr{E}_D(u_{\mathrm{d}}) := \left(\sum_{\sigma \in \Sigma} |\sigma|^{\frac{1}{n-1}} \|d_\sigma\|_{0,\sigma}^2\right)^{\frac{1}{2}}.
$$

Conditions (3.31) are easily met if the Neumann boundary condition g and the source function f are zero in the vicinity of the feature.

Remark 3.4.3. Analogously to the case of a negative feature in Remark 3.2.2, note that

$$
\mathscr{E}_D(u_{\mathrm{d}}) \lesssim \left(\sum_{\sigma \in \Sigma} c_\sigma^2 |\sigma|^{\frac{1}{n-1}} \|d_\sigma\|_{0,\sigma}^2\right)^{\frac{1}{2}} =: \tilde{\mathscr{E}}_D(u_{\mathrm{d}}).
$$

One could be tempted to use the simpler indicator $\tilde{\mathscr{E}}_D(u_{\mathrm{d}})$, but when $n = 2$ and under the flux conservation conditions (3.31), $\tilde{\mathscr{E}}_D(u_{\mathrm{d}})$ is sub-optimal since in this case, $\tilde{\mathscr{E}}_D(u_{\mathrm{d}}) \lesssim \max_{\sigma \in \Sigma} (c_\sigma) \mathscr{E}_D(u_{\mathrm{d}})$. Indeed, no lower bound can be proven for $\tilde{\mathscr{E}}_D(u_{\mathrm{d}})$.

3.4.1 Reliability

In this section, we state and prove that the error indicator defined in (3.30) is reliable, that is, it is an upper bound for the defeaturing error.

Theorem 3.4.4. *Let u be the solution of problem (3.2) defined in the exact domain Ω, and let u_{d} be the defeaturing solution defined in (3.26). If γ_{n}, γ_{r} and $\gamma_{0,\mathrm{p}}$ are isotropic according to Definition 2.1.2, then the defeaturing error in the energy norm is bounded in terms of the estimator $\mathscr{E}_D(u_{\mathrm{d}})$ introduced in (3.30) as follows:*

$$|u - u_{\mathrm{d}}|_{1,\Omega} \lesssim \mathscr{E}_D(u_{\mathrm{d}}).$$

Proof. Using arguments similar to Theorem 3.2.3, let us first consider the original problem (3.1) restricted to $\Omega_\star := \Omega \setminus \overline{F_{\mathrm{p}}}$ with the natural Neumann boundary condition on $\gamma_{0,\mathrm{p}}$, that is, the restriction $u|_{\Omega_\star} \in H^1_{g_D,\Gamma_D}(\Omega_\star)$ is the weak solution of

$$\begin{cases} -\Delta\left(u|_{\Omega_\star}\right) = f & \text{in } \Omega_\star \\ u|_{\Omega_\star} = g_D & \text{on } \Gamma_D \\ \dfrac{\partial\left(u|_{\Omega_\star}\right)}{\partial\mathbf{n}} = g & \text{on } \Gamma_N \setminus \gamma_{\mathrm{p}} \\ \dfrac{\partial\left(u|_{\Omega_\star}\right)}{\partial\mathbf{n}_0} = \dfrac{\partial u}{\partial\mathbf{n}_0} & \text{on } \gamma_{0,\mathrm{p}}. \end{cases} \tag{3.32}$$

By abuse of notation, we omit the explicit restriction of u to $\Omega_\star$. Then for all test functions $v_0 \in H^1_{0,\Gamma_D}(\Omega_\star)$,

$$\int_{\Omega_\star} \nabla u \cdot \nabla v_0 \,\mathrm{d}x = \int_{\Omega_\star} f v_0 \,\mathrm{d}x + \int_{\Gamma_N \setminus \gamma_{\mathrm{p}}} g v_0 \,\mathrm{d}s + \int_{\gamma_{0,\mathrm{p}}} \frac{\partial u}{\partial\mathbf{n}_0} v_0 \,\mathrm{d}s. \tag{3.33}$$

Then, let us consider the simplified problem (3.3) restricted to $\Omega_\star$ with the natural Neumann boundary condition on γ_{n}, in the same way as in (3.13). Since $u_{\mathrm{d}}|_{\Omega_\star} = u_0|_{\Omega_\star}$ by definition, if we omit the explicit restriction of u_{d} to $\Omega_\star$, then for all $v_0 \in H^1_{0,\Gamma_D}(\Omega_\star)$,

$$\int_{\Omega_\star} \nabla u_{\mathrm{d}} \cdot \nabla v_0 \,\mathrm{d}x = \int_{\Omega_\star} f v_0 \,\mathrm{d}x + \int_{\Gamma_N \setminus \gamma} g v_0 \,\mathrm{d}s + \int_{\gamma_{\mathrm{n}}} \frac{\partial u_{\mathrm{d}}}{\partial\mathbf{n}} v_0 \,\mathrm{d}s + \int_{\gamma_{0,\mathrm{p}}} g_0 v_0 \,\mathrm{d}s. \tag{3.34}$$

Let $e := u - u_{\mathrm{d}} \in H^1_{0,\Gamma_D}(\Omega)$. So from (3.33) and (3.34), for all $v_0 \in H^1_{0,\Gamma_D}(\Omega_\star)$, we obtain

$$\int_{\Omega_\star} \nabla e \cdot \nabla v_0 \,\mathrm{d}x = \int_{\gamma_{\mathrm{n}}} \left(g - \frac{\partial u_{\mathrm{d}}}{\partial\mathbf{n}}\right) v_0 \,\mathrm{d}s + \int_{\gamma_{0,\mathrm{p}}} \left(\frac{\partial u}{\partial\mathbf{n}_0} - g_0\right) v_0 \,\mathrm{d}s. \tag{3.35}$$

Now, let us consider the simplified extended problem (3.6) restricted to F_{p} with the natural Neumann boundary condition on γ_{r}, in a similar way to (3.32). Note that $u_{\mathrm{d}}|_{F_{\mathrm{p}}} = \tilde{u}_0|_{F_{\mathrm{p}}}$, and by abuse of notation and as previously, we omit the explicit restriction of u_{d} to F_{p}. That is, $u_{\mathrm{d}} \in H^1\left(F_{\mathrm{p}}\right)$ is one of the infinitely-many solutions (up to a constant) of

$$\int_{F_{\mathrm{p}}} \nabla u_{\mathrm{d}} \cdot \nabla v_{\mathrm{p}} \,\mathrm{d}x = \int_{F_{\mathrm{p}}} f v_{\mathrm{p}} \,\mathrm{d}x + \int_{\gamma_{\mathrm{s}}} g v_{\mathrm{p}} \,\mathrm{d}s + \int_{\gamma_{0,\mathrm{p}} \cup \gamma_{\mathrm{r}}} \frac{\partial u_{\mathrm{d}}}{\partial\mathbf{n}_F} v_{\mathrm{p}} \,\mathrm{d}s, \quad \forall v_{\mathrm{p}} \in H^1\left(F_{\mathrm{p}}\right). \tag{3.36}$$

And let us consider the original problem (3.1) restricted to F_p with the natural Neumann boundary condition on $\gamma_{0,p}$, again in a similar way to (3.32). By abuse of notation and as previously, we omit the explicit restriction of u to F_p. So $u \in H^1\left(F_p\right)$ is one of the infinitely-many solutions (up to a constant) of

$$\int_{F_p} \nabla u \cdot \nabla v_p \, \mathrm{d}x = \int_{F_p} f v_p \, \mathrm{d}x + \int_{\gamma_p} g v_p \, \mathrm{d}x + \int_{\gamma_{0,p}} \frac{\partial u}{\partial \mathbf{n}_F} v_p \, \mathrm{d}s, \quad \forall v_p \in H^1\left(F_p\right). \quad (3.37)$$

Consequently, from (3.36) and (3.37), for all $v_p \in H^1\left(F_p\right)$,

$$\int_{F_p} \nabla e \cdot \nabla v_p \, \mathrm{d}x = \int_{\gamma_{0,p}} \frac{\partial \left(u - u_d\right)}{\partial \mathbf{n}_F} v_p \, \mathrm{d}s + \int_{\gamma_r} \left(g - \frac{\partial u_d}{\partial \mathbf{n}_F}\right) v_p \, \mathrm{d}s. \quad (3.38)$$

Let $v \in H^1_{0,\Gamma_D}(\Omega)$, then $v|_{\Omega_\star} \in H^1_{0,\Gamma_D}(\Omega_\star)$ and $v|_{F_p} \in H^1\left(F_p\right)$. Therefore, from equations (3.35) and (3.38), since $\mathbf{n}_0 = -\mathbf{n}_F$ on $\gamma_{0,p}$, and since $\mathbf{n} = \mathbf{n}_F$ on γ_r, then recalling the definitions of Σ in (3.28) and d_σ in (3.29), we obtain

$$\int_\Omega \nabla e \cdot \nabla v \, \mathrm{d}x = \sum_{\sigma \in \Sigma} \int_\sigma d_\sigma v \, \mathrm{d}s. \quad (3.39)$$

Now, if we take $v = e \in H^1_{0,\Gamma_D}(\Omega)$ in (3.39), then

$$|e|^2_{1,\Omega} = \sum_{\sigma \in \Sigma} \int_\sigma d_\sigma e \, \mathrm{d}s = \sum_{\sigma \in \Sigma} \left[\int_\sigma \left(d_\sigma - \overline{d_\sigma}^\sigma\right)(e - \overline{e}^\sigma) \, \mathrm{d}s + \overline{d_\sigma}^\sigma \int_\sigma e \, \mathrm{d}s \right]. \quad (3.40)$$

For each $\sigma \in \Sigma$, the first terms of (3.40) can be estimated as in (3.17), using Lemma 2.3.8, trace inequalities and the discrete Cauchy-Schwarz inequality. Thus we obtain:

$$\sum_{\sigma \in \Sigma} \int_\sigma \left(d_\sigma - \overline{d_\sigma}^\sigma\right)(e - \overline{e}^\sigma) \, \mathrm{d}s \lesssim \sum_{\sigma \in \Sigma} |\sigma|^{\frac{1}{2(n-1)}} \left\|d_\sigma - \overline{d_\sigma}^\sigma\right\|_{0,\sigma} |e|_{\frac{1}{2},\sigma}$$

$$\lesssim \left(\sum_{\sigma \in \{\gamma_n, \gamma_r\}} |\sigma|^{\frac{1}{2(n-1)}} \left\|d_\sigma - \overline{d_\sigma}^\sigma\right\|_{0,\sigma} \right) \|e\|_{1,\Omega}$$

$$+ |\gamma_{0,p}|^{\frac{1}{2(n-1)}} \left\|d_{\gamma_{0,p}} - \overline{d_{\gamma_{0,p}}}^{\gamma_{0,p}}\right\|_{0,\gamma_{0,p}} \|e\|_{1,\Omega_\star}$$

$$\lesssim \left(\sum_{\sigma \in \Sigma} |\sigma|^{\frac{1}{n-1}} \left\|d_\sigma - \overline{d_\sigma}^\sigma\right\|^2_{0,\sigma} \right)^{\frac{1}{2}} |e|_{1,\Omega}. \quad (3.41)$$

Moreover, for each $\sigma \in \Sigma$, the last terms of (3.40) can be estimated using Lemma 2.3.9, trace inequalities and the discrete Cauchy-Schwarz inequality to obtain

$$\sum_{\sigma \in \Sigma} \overline{d_\sigma}^\sigma \int_\sigma e \, \mathrm{d}s \lesssim \sum_{\sigma \in \Sigma} \left| \overline{d_\sigma}^\sigma \right| |\sigma|^{\frac{1}{2}} \|e\|_{0,\sigma}$$

$$\lesssim \left(\sum_{\sigma \in \{\gamma_\mathrm{n}, \gamma_\mathrm{r}\}} \left| \overline{d_\sigma}^\sigma \right| c_\sigma \, |\sigma|^{\frac{1}{2(n-1)}+\frac{1}{2}} \right) \|e\|_{\frac{1}{2}, \partial\Omega}$$

$$+ \left| \overline{d_{\gamma_{0,\mathrm{p}}}}^{\gamma_{0,\mathrm{p}}} \right| c_{\gamma_{0,\mathrm{p}}} \, |\gamma_{0,\mathrm{p}}|^{\frac{1}{2(n-1)}+\frac{1}{2}} \|e\|_{\frac{1}{2}, \partial\Omega_\star}$$

$$\lesssim \left(\sum_{\sigma \in \Sigma} c_\sigma^2 \, |\gamma_\sigma|^{\frac{n}{n-1}} \left| \overline{d_\sigma}^\sigma \right|^2 \right)^{\frac{1}{2}} |e|_{1,\Omega}. \tag{3.42}$$

Therefore, combining (3.40), (3.41) and (3.42), and simplifying on both sides, we obtain the desired result. $\qquad\square$

3.4.2 Efficiency

In this section, we state and prove that the error indicator defined in (3.30) is efficient, that is, it is a lower bound for the defeaturing error, up to oscillations. In the case $n = 2$, the flux conservation assumptions (3.31) are also required.

Theorem 3.4.5. *Consider the same notation and assumptions as in Theorem 3.4.4, let Σ be defined as in (3.28), and assume that all $\sigma \in \Sigma$ are also regular according to Definition 2.1.3 with $|\gamma_\mathrm{n}| \simeq |\gamma_\mathrm{r}| \simeq |\gamma_{0,\mathrm{p}}|$. Suppose that either $n = 3$, or $n = 2$ and the flux conservation conditions (3.31) are satisfied. Then the defeaturing error, in the energy norm, bounds up to oscillations the estimator $\mathscr{E}_D(u_\mathrm{d})$ introduced in (3.30), that is*

$$\mathscr{E}_D(u_\mathrm{d}) \lesssim |u - u_\mathrm{d}|_{1,\Omega} + \mathrm{osc}(u_\mathrm{d}), \quad \mathrm{osc}(u_\mathrm{d}) := |\Gamma|^{\frac{1}{2(n-1)}} \left(\sum_{\sigma \in \Sigma} \|d_\sigma - \Pi_m(d_\sigma)\|_{0,\sigma}^2 \right)^{\frac{1}{2}} \tag{3.43}$$

for any $m \in \mathbb{N}$, with Γ defined in (3.28), d_σ defined in (3.29), and Π_m such that $\Pi_m|_\sigma \equiv \Pi_{m,\sigma}$ for all $\sigma \in \Sigma$, $\Pi_{m,\sigma}$ being the extension of the Clément operator defined in (3.8).

Proof. As before, let $e := u - u_\mathrm{d} \in H^1_{0,\Gamma_D}(\Omega)$. Then from equation (3.39), for all $v \in H^1_{0,\Gamma_D}(\Omega)$,

$$\sum_{\sigma \in \Sigma} \int_\sigma d_\sigma v \, \mathrm{d}s = \int_\Omega \nabla e \cdot \nabla v \, \mathrm{d}x \leq |e|_{1,\Omega} |v|_{1,\Omega}. \tag{3.44}$$

Now, let $H := \left\{ v \in H^{\frac{1}{2}}_{00}(\Gamma) : v|_\sigma \in H^{\frac{1}{2}}_{00}(\sigma), \text{ for all } \sigma \in \Sigma \right\}$, equipped with the norm

$$\|\cdot\|_H := \left(\sum_{\sigma \in \Sigma} \|\cdot\|^2_{H^{1/2}_{00}(\sigma)} \right)^{\frac{1}{2}},$$

and let H^* be its dual space equipped with the dual norm $\|\cdot\|_{H^*}$. Recall that $\Omega_\star := \Omega \setminus \overline{F_p}$, so that $\Omega = \mathrm{int}\left(\overline{\Omega_\star \cup F_p}\right)$. So for all $w \in H$, let us define piecewise the function $u_w \in H^1_{0,\partial\Omega\setminus(\gamma_n\cup\gamma_r)}(\Omega)$ as the unique solution of

$$\begin{cases} -\Delta\left(u_w|_{F_p}\right) = 0 & \text{in } F_p \\ u_w|_{F_p} = \left(w|_{\gamma_r\cup\gamma_{0,p}}\right)^\star & \text{on } \partial F_p, \end{cases} \qquad \begin{cases} -\Delta\left(u_w|_{\Omega_\star}\right) = 0 & \text{in } \Omega_\star \\ u_w|_{\Omega_\star} = \left(w|_{\gamma_n\cup\gamma_{0,p}}\right)^\star & \text{on } \partial\Omega_\star, \end{cases}$$

where $\left(w|_{\gamma_r\cup\gamma_{0,p}}\right)^\star$ and $\left(w|_{\gamma_n\cup\gamma_{0,p}}\right)^\star$ are the extensions by 0 of $w|_{\gamma_r\cup\gamma_{0,p}}$ on ∂F_p and of $w|_{\gamma_n\cup\gamma_{0,p}}$ on $\partial\Omega_\star$, respectively. Then by continuity of the solution on the data and from Lemma 2.3.11,

$$\begin{aligned} |u_w|_{1,\Omega} &= \left(|u_w|^2_{1,F_p} + |u_w|^2_{1,\Omega_\star}\right)^{\frac{1}{2}} \\ &\lesssim \left(\left\|\left(w|_{\gamma_r\cup\gamma_{0,p}}\right)^\star\right\|^2_{\frac{1}{2},\partial F_p} + \left\|\left(w|_{\gamma_n\cup\gamma_{0,p}}\right)^\star\right\|^2_{\frac{1}{2},\partial\Omega_\star}\right)^{\frac{1}{2}} \\ &= \left(\|w\|^2_{H^{1/2}_{00}(\gamma_r\cup\gamma_{0,p})} + \|w\|^2_{H^{1/2}_{00}(\gamma_n\cup\gamma_{0,p})}\right)^{\frac{1}{2}} \lesssim \|w\|_H. \end{aligned} \tag{3.45}$$

So, recalling that by definition, $d_\Sigma|_\sigma = d_\sigma$ on each $\sigma \in \Sigma$, thanks to (3.44) and (3.45) and since $H^1_{0,\partial\Omega\setminus(\gamma_n\cup\gamma_r)}(\Omega) \subset H^1_{0,\Gamma_D}(\Omega)$, then

$$\|d_\Sigma\|_{H^*} = \sup_{\substack{w\in H \\ w\neq 0}} \frac{\int_\Gamma d_\Sigma w\,\mathrm{d}s}{\|w\|_H} \lesssim \sup_{\substack{w\in H \\ w\neq 0}} \frac{\sum_{\sigma\in\Sigma}\int_\sigma d_\sigma u_w\,\mathrm{d}s}{|u_w|_{1,\Omega}} \leq \sup_{\substack{v\in H^1_{0,\Gamma_D}(\Omega) \\ v\neq 0}} \frac{\sum_{\sigma\in\Sigma}\int_\sigma d_\sigma v\,\mathrm{d}s}{|v|_{1,\Omega}} \leq |e|_{1,\Omega}. \tag{3.46}$$

Moreover, using Remark 3.4.3 if $n = 3$, or Remark 3.4.2 if $n = 2$ and the flux conservation conditions (3.31) are satisfied, then

$$\mathscr{E}_D(u_d) \lesssim \left(\sum_{\sigma\in\Sigma} |\sigma|^{\frac{1}{n-1}} \|d_\sigma\|^2_{0,\sigma}\right)^{\frac{1}{2}}.$$

Therefore, using the triangle inequality, and the fact that $|\gamma_n| \simeq |\gamma_r| \simeq |\gamma_{0,p}| \simeq |\Gamma|$, then

$$\begin{aligned} \mathscr{E}_D(u_d)^2 &\leq \sum_{\sigma\in\Sigma} |\sigma|^{\frac{1}{n-1}} \|\Pi_m(d_\sigma)\|^2_{0,\sigma} + \sum_{\sigma\in\Sigma} |\sigma|^{\frac{1}{n-1}} \|d_\sigma - \Pi_m(d_\sigma)\|^2_{0,\sigma} \\ &\lesssim |\Gamma|^{\frac{1}{n-1}} \|\Pi_m(d_\Sigma)\|^2_{0,\Gamma} + |\Gamma|^{\frac{1}{n-1}} \|d_\Sigma - \Pi_m(d_\Sigma)\|^2_{0,\Gamma}. \end{aligned}$$

Now, we use the definition of the broken norm in H^* to apply the inverse inequality of Lemma 2.3.12. Recalling definition (3.43) of the oscillations, and using again the triangle

inequality, we thus obtain

$$\mathscr{E}_D(u_{\mathrm{d}})^2 \lesssim \|\Pi_m(d_\Sigma)\|_{H^*}^2 + \mathrm{osc}\,(u_{\mathrm{d}})^2$$
$$\lesssim \Big(\|d_\Sigma\|_{H^*} + \|\Pi_m(d_\Sigma) - d_\Sigma\|_{H^*} + \mathrm{osc}\,(u_{\mathrm{d}}) \Big)^2. \qquad (3.47)$$

Furthermore, applying Lemma 2.3.11 and then Lemma 2.3.7, we have

$$\|\Pi_m(d_\Sigma) - d_\Sigma\|_{H^*} \lesssim \|\Pi_m(d_\Sigma) - d_\Sigma\|_{H_{00}^{-1/2}(\Gamma)}$$
$$\lesssim |\Gamma|^{\frac{1}{2(n-1)}} \|\Pi_m(d_\Sigma) - d_\Sigma\|_{0,\Gamma} = \mathrm{osc}\,(u_{\mathrm{d}})\,. \qquad (3.48)$$

To conclude, we plug in (3.46) and (3.48) into equation (3.47), and thus

$$\mathscr{E}_D(u_{\mathrm{d}}) \lesssim |e|_{1,\Omega} + \mathrm{osc}(u_{\mathrm{d}})\,. \qquad \qquad \square$$

Remark 3.4.6. As in Remark 3.2.5, when the data is regular, it is always possible to choose m large enough so that the asymptotic behavior of the oscillations is $\mathcal{O}\left(|\Gamma|^{m+\frac{1}{2(n-1)}} \right)$. Therefore, we can make sure that the oscillations get small with respect to the defeaturing error, when the feature gets small.

3.5 Numerical considerations and experiments

From the definition of the *a posteriori* defeaturing error estimator (3.30) in the most general case of a complex feature, we only need to perform the following steps to estimate the error introduced by defeaturing the problem geometry.

(i) Choose the Neumann data g_0 and the extension of the right hand side f in the negative component F_{n} of feature F, and solve the defeatured problem (3.3).

(ii) For the positive component F_{p} of the feature F, solve the local extension problem (3.5). However, features may be geometrically complex, and the solution of the extension problem an unwanted burden. Therefore, instead of (3.5), one can solve the extension problem (3.6) in a chosen (simple) domain $\tilde{F}_{\mathrm{p}}$ that contains F_{p} and such that $\gamma_{0,\mathrm{p}} \subset \left(\partial \tilde{F}_{\mathrm{p}} \cap \partial F_{\mathrm{p}} \right)$.

(iii) Compute the boundary averages and integrals $\overline{d_\sigma}^\sigma$ and $\left\| d_\sigma - \overline{d_\sigma}^\sigma \right\|_{0,\sigma}$ for each $\sigma \in \Sigma$, as defined in (3.29). That is, we suitably evaluate the error made on the normal derivative of the solution on specific parts of the boundaries of the features.

In the remaining part of this section, we present a few numerical examples to illustrate the properties of the proposed defeaturing error estimator. While validating the theory developed in Sections 3.2 and 3.4, we study in particular:

- the impact of the shape and size of the feature on the defeaturing error and estimator, and how the proposed estimator can distinguish between a very small but important feature and a large feature which has no impact on the defeaturing error;

- the convergence of the defeaturing error and estimator with respect to the size of F when F is a negative, positive or complex two-dimensional feature, and when F is a negative or positive three-dimensional feature;

- the choice of defeaturing data (extension of the right hand side f in a negative feature, and Neumann boundary conditions g_0 and $\tilde{g}$), and how a bad choice can lead to the divergence of the defeaturing error and estimator;

- the choice of feature extension $\tilde{F}$ and its impact on the analysis;

- two examples in which the feature is not a Lipschitz domain.

We use IGA for the numerical approximation of the considered PDEs. This numerical method will be introduced in detail in Chapter 6. In order to neglect the error due to the numerical approximation, a rather fine tensor-product mesh is used. In particular, small elements are required close to the boundaries of the features, and the size of the mesh is chosen such that the rate of convergence of the defeaturing error does not change any more under mesh refinement. For the geometrical description of the features and the local meshing process required, multipatch and trimming techniques have been used, see Chapter 6 and, e.g., [Antolín et al., 2019, 2022; Wei et al., 2021].

3.5.1 Impact of some feature properties on the defeaturing error

In this section, we study the impact of the shape and the size of a feature on the defeaturing error and estimator, and of the choice of the defeatured Neumann data. Moreover, as the estimator depends upon the size of the features and the size of the solution gradients "around" the feature, we will be able to show an example where small features count more than big ones.

3.5.1.1 Feature shape

In this example, we compare the behavior of the error and the estimator on the same Poisson problem in three different geometries: one with a star-shaped feature, another one with a circular feature, and the last one with a squared feature. Let

$$\Omega_0 := \left\{ \boldsymbol{x} \in \mathbb{R}^2 : \|\boldsymbol{x}\|_{\ell^2} < 1 \right\},$$

let $\Omega_t := \Omega_0 \setminus \overline{F_t}$, $\Omega_c := \Omega_0 \setminus \overline{F_c}$ and $\Omega_s := \Omega_0 \setminus \overline{F_s}$, with

(a) Domain with a star-shaped feature.

(b) Domain with a circular feature.

(c) Domain with a square-shaped feature.
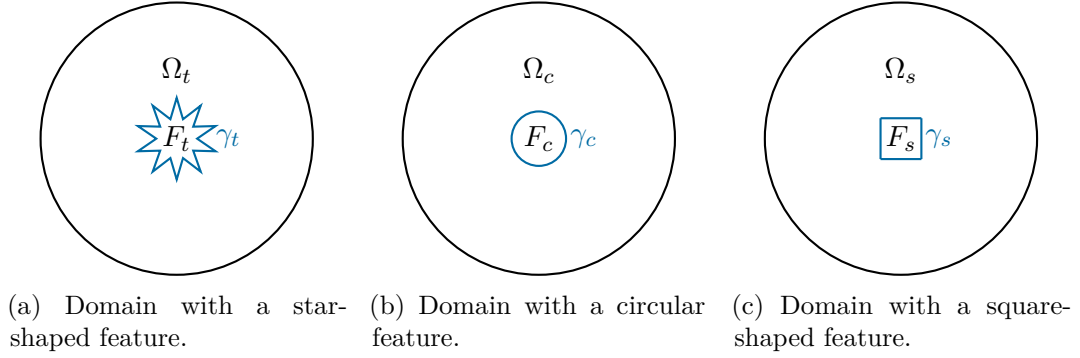
Figure 3.7 – Numerical test 3.5.1.1 – Comparison between feature shapes.

Domain Ω	Perimeter of F	Area of F	$\mathscr{E}_D(u_0)$	$\|u - u_0\|_{1,\Omega}$	$\dfrac{\|u - u_0\|_{1,\Omega}}{\|u\|_{1,\Omega}}$	η_{eff}
$\Omega_t,\ r_t = 1.83 \cdot 10^{-2}$	0.400	$2.07 \cdot 10^{-3}$	$1.98 \cdot 10^{-3}$	$1.56 \cdot 10^{-3}$	$2.49 \cdot 10^{-3}$	1.27
$\Omega_c,\ r_c = 6.37 \cdot 10^{-2}$	0.400	$1.27 \cdot 10^{-2}$	$1.21 \cdot 10^{-2}$	$8.42 \cdot 10^{-3}$	$1.37 \cdot 10^{-2}$	1.45
$\Omega_s,\ r_s = 5.00 \cdot 10^{-2}$	0.400	$1.00 \cdot 10^{-2}$	$9.57 \cdot 10^{-3}$	$6.74 \cdot 10^{-3}$	$1.07 \cdot 10^{-2}$	1.42
$\Omega_c,\ r_c = 5.64 \cdot 10^{-2}$	0.355	$1.00 \cdot 10^{-2}$	$1.01 \cdot 10^{-2}$	$6.76 \cdot 10^{-3}$	$1.08 \cdot 10^{-2}$	1.51
$\Omega_t,\ r_t = 4.02 \cdot 10^{-2}$	0.880	$1.00 \cdot 10^{-2}$	$7.53 \cdot 10^{-3}$	$6.65 \cdot 10^{-3}$	$1.38 \cdot 10^{-2}$	1.13

Table 3.1 – Numerical test 3.5.1.1 – Results of the comparison between feature shapes.

- F_t the 10-branch regular star of inner radius $r_t > 0$, outer radius $2r_t$, and which is centered at $(0,0)^T$,

- F_c the circle of radius $r_c > 0$, centered at $(0,0)^T$,

- F_s the square of side length $2r_s > 0$, centered at $(0,0)^T$,

as illustrated in Figure 3.7. We choose $r_t, r_c, r_s > 0$ such that F_t, F_c and F_s have, first, the same area, and then, the same perimeter. We consider Poisson problem (3.1) solved in Ω_t, Ω_c and in Ω_s, and its defeatured version (3.3). We take $f \equiv 1$ in Ω_0, $g_D \equiv 0$ on $\Gamma_D := \partial\Omega_0$, and $g \equiv 0$ on ∂F_t, on ∂F_c and on ∂F_s. The results are summarized in Table 3.1.

We can see that the larger the area of a feature, the larger the defeaturing error and estimator. Moreover, the effectivity index η_{eff} only changes slightly when considering the same feature but with different measures. Based on the developed theory, η_{eff} is independent of the measure of the considered feature and its boundary. Therefore, the small change in the effectivity index is due to numerical approximation, the solutions not being exact but being obtained on a very fine mesh. Furthermore, the shape of the feature does not impact much the defeaturing estimator: we do not observe any major difference between the smooth feature (the circle), the convex non-smooth Lipschitz feature (the square), and the non-convex non-smooth Lipschitz feature (the star). Our

(a) Exact domain Ω with two features (not at scale).

(b) Exact solution in Ω.
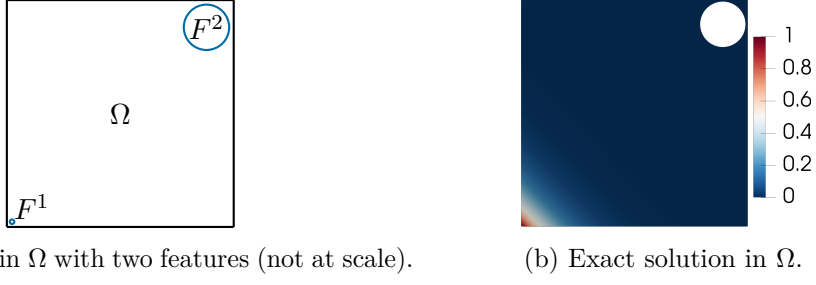
Figure 3.8 – Numerical test 3.5.1.2 – Geometry with two features of different size, and exact solution.

theory indeed treats those different types of geometries in the same way. Finally, even if the estimator is referred to the absolute error, both the relative and the absolute errors are given to be able to quantify the magnitude of the defeaturing effect.

3.5.1.2   Feature size

Removing a small feature where the solution of the PDE has a high gradient can significantly increase the defeaturing error, while the error might almost not be affected when removing a large feature where the solution of the PDE is nearly constant. The following example shows that our estimator is also able to capture this. Let $\Omega_0 := (0,1)^2$ and $\Omega := \Omega_0 \setminus \left(\overline{F^1} \cup \overline{F^2} \right)$, where F^1 and F^2 are circles of two different sizes given by

$$F^1 := \left\{ \boldsymbol{x} \in \mathbb{R}^2 : \left\| \boldsymbol{x} - \boldsymbol{x}^1 \right\|_{\ell^2} < 10^{-3}, \, \boldsymbol{x}^1 = \left(1.1 \cdot 10^{-3}, 1.1 \cdot 10^{-3} \right)^T \right\},$$

$$F^2 := \left\{ \boldsymbol{x} \in \mathbb{R}^2 : \left\| \boldsymbol{x} - \boldsymbol{x}^2 \right\|_{\ell^2} < 10^{-1}, \, \boldsymbol{x}^2 = \left(8.9 \cdot 10^{-1}, 8.9 \cdot 10^{-1} \right)^T \right\}.$$

similarly to Figure 3.8a. We consider Poisson problem (3.1) solved in Ω, and its defeatured version (3.3) in Ω_0. Let $f(x,y) := -128e^{-8(x+y)}$ in Ω_0, $g_D(x,y) := e^{-8(x+y)}$ on

$$\Gamma_D := \left([0,1) \times \{0\} \right) \cup \left(\{0\} \times [0,1) \right),$$

the bottom and left sides, $g(x,y) := -8e^{-8(x+y)}$ on $\partial\Omega_0 \setminus \overline{\Gamma_D}$, and finally $g \equiv 0$ on $\partial F^1 \cup \partial F^2$. Since the geometry contains two features, we call $\mathscr{E}_D^1$ and $\mathscr{E}_D^2$ the defeaturing estimators defined in (3.11) and computed, respectively, on the boundary of F^1 and on the boundary of F^2, and we consider

$$\mathscr{E}_D(u_0) := \left(\mathscr{E}_D^1(u_0)^2 + \mathscr{E}_D^2(u_0)^2 \right)^{\frac{1}{2}} \tag{3.49}$$

as the total defeaturing estimator.

With this choice, the solution to Poisson's problem has a very high gradient near feature

$\mathscr{E}_D^1(u_0)$	$\mathscr{E}_D^2(u_0)$	$\mathscr{E}_D(u_0)$	$|u - u_0|_{1,\Omega}$	$\dfrac{|u - u_0|_{1,\Omega}}{|u|_{1,\Omega}}$	η_{eff}
$5.03 \cdot 10^{-2}$	$7.86 \cdot 10^{-6}$	$5.03 \cdot 10^{-2}$	$1.45 \cdot 10^{-2}$	$2.05 \cdot 10^{-2}$	3.47

Table 3.2 – Numerical test 3.5.1.2 – Results of the comparison between feature sizes.

F^1, and it is almost constantly zero near feature F^2, as we can observe in Figure 3.8b. Therefore, one can expect the presence of F^1 to be more important than F^2 with respect to the solution accuracy, even if F^1 is notably smaller than F^2. The results are presented in Table 3.2, where we can see that this is indeed the case: the estimator on F^2 is four orders of magnitude smaller than the estimator on F^1, even if the radius of F^1 is two orders of magnitude smaller than the one of F^2. This confirms the fact that the proposed estimator as written in (3.30) correctly trades off the measure of the features and their position in the geometrical domain, in order to correctly assess the impact of defeaturing on the solution.

Finally, and as in the previous numerical experiment of Section 3.5.1.1, both the relative error and the absolute error are given to be able to quantify the magnitude of the defeaturing effect. In the following, we will be interested in the convergence of the error and estimator with respect to the size of the feature. Since the relative error is a scaling of the absolute error, the convergence will be the same whether one considers the relative or the absolute error. Moreover, since the magnitude of the error depends on the problem at hand (geometries, size of the feature, and PDE data), and since the derived estimator is referred to the absolute error, we will only look at the absolute defeaturing error in the next experiments.

3.5.2 Error convergence with respect to the feature size

We now analyze the convergence of our estimator with respect to the size of the feature and we compare it with the convergence of the defeaturing error. Moreover, we show an example in which the choice of the defeatured problem data influences drastically the convergence of both the estimator and the defeaturing error.

3.5.2.1 Two-dimensional geometries

We begin with two-dimensional examples of geometries with a negative feature. For $k = 0, 1, \ldots, 6$, let $\varepsilon = \dfrac{10^{-2}}{2^k}$, and let $\Omega_\varepsilon^i := \Omega_0 \setminus \overline{F_\varepsilon^i}$ for $i = 1, 2$ with $\Omega_0 := (0, 1)^2$ and

$$F_\varepsilon^1 := \left\{ \boldsymbol{x} = (x, y)^T \in \mathbb{R}^2 : \left\| \boldsymbol{x} - (0.5, 1)^T \right\|_{\ell^2} < \varepsilon, \ y < 1 \right\},$$
$$F_\varepsilon^2 := (1 - \varepsilon, 1)^2,$$

(a) Geometry with negative feature F_ε^1.

(b) Geometry with negative feature F_ε^2.

(c) Geometry with positive feature F_ε^3.

(d) Geometry with positive feature F_ε^4.
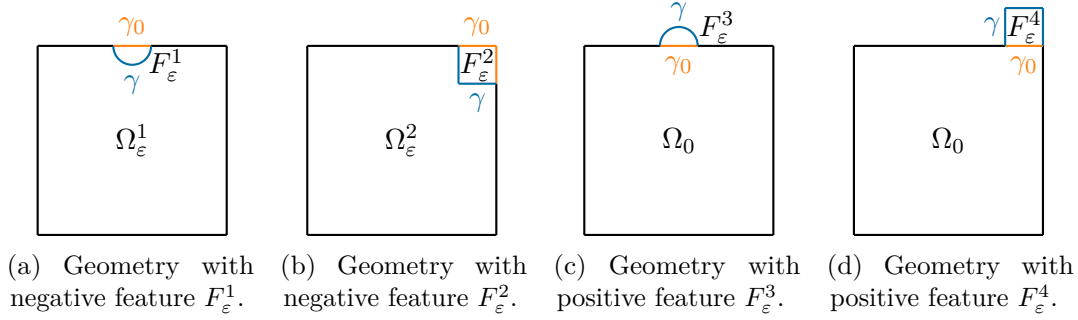
Figure 3.9 – Numerical test 3.5.2.1 – 2D geometries Ω_ε^i, $i = 1, 2, 3, 4$.

as in Figures 3.9a and 3.9b. For $i = 1, 2$, we consider Poisson problem (3.1) solved in Ω_ε^i, and its defeatured version (3.3) in Ω_0. We take $f(x, y) := 10\cos(3\pi x)\sin(5\pi y)$ in Ω_0, $g_D \equiv 0$ on

$$\Gamma_D := (0, 1) \times \{0\},$$

$g \equiv 0$ on $\Gamma_N := \partial\Omega_\varepsilon^i \setminus \overline{\Gamma_D}$, and $g_0 \equiv 0$ on $\partial\Omega_0 \setminus \partial\Omega_\varepsilon^i$. We respectively call $u^{(i)}$ and $u_0^{(i)}$ the exact and defeatured solutions.

The results are presented in Figure 3.10a. Both the error and the estimator converge with respect to the size of the feature as $\varepsilon \propto |\gamma|$ in the first geometry Ω_ε^1, and as $\varepsilon^2 \propto |\gamma|^2$ in the second geometry Ω_ε^2. The difference in asymptotic behavior of the error depends on geometric symmetries and on the Neumann boundary conditions. Indeed, Ω_ε^2 has features with sides parallel to $\partial\Omega_0$. Moreover, the effectivity index is indeed independent of the size of the feature since it remains nearly equal to 1.81 and 1.78, respectively, for all values of ε. That is, as predicted by the theory in Theorems 3.2.3 and 3.2.3, the estimator is both reliable and efficient, here in dimension two, and its effectivity index is independent of the size of the considered negative feature.

Let us now consider two-dimensional examples of geometries with a positive feature. Let Ω_0, Γ_D, f, g_D and g be as before, and let $\Omega_\varepsilon^j := \mathrm{int}\left(\overline{\Omega_0} \cup \overline{F_\varepsilon^j}\right)$ for $j = 3, 4$ with

$$F_\varepsilon^3 := \left\{ \boldsymbol{x} = (x, y)^T \in \mathbb{R}^2 : \left\| \boldsymbol{x} - (0.5, 1)^T \right\|_{\ell^2} < \varepsilon, \ y > 1 \right\},$$
$$F_\varepsilon^4 := (1 - \varepsilon, 1) \times (1, 1 + \varepsilon),$$

as in Figures 3.9c and 3.9d. Let $\Gamma_N := \partial\Omega_\varepsilon^j \setminus \overline{\Gamma_D}$. For each $j = 3, 4$, we consider the same Poisson problem (3.1) as before, but solved in Ω_ε^j. We also solve its defeatured version (3.3) in Ω_0 with $g_0 \equiv 0$ on $\partial\Omega_0 \setminus \partial\Omega_\varepsilon^j$. Then, we extend the defeatured solution to F_ε^j by solving (3.6) with $\tilde{F} := F_\varepsilon^j$. We respectively call $u^{(j)}$ and $u_0^{(j)}$ the exact and defeatured solutions, and $u_\mathrm{d}^{(j)}$ the defeatured solution extended to F_ε^j.

The results are presented in Figure 3.10b. As for the negative feature case, the error in Ω_0 and the estimator converge with respect to the size of the feature as $\varepsilon \propto |\gamma_0|$ in the

(a) Geometries Ω_ε^1, Ω_ε^2 with a negative feature.

(b) Geometries Ω_ε^3, Ω_ε^4 with a positive feature.

(c) Geometry Ω_ε^5 with a complex feature.

(d) Geometry Ω_ε^6 with a complex feature.
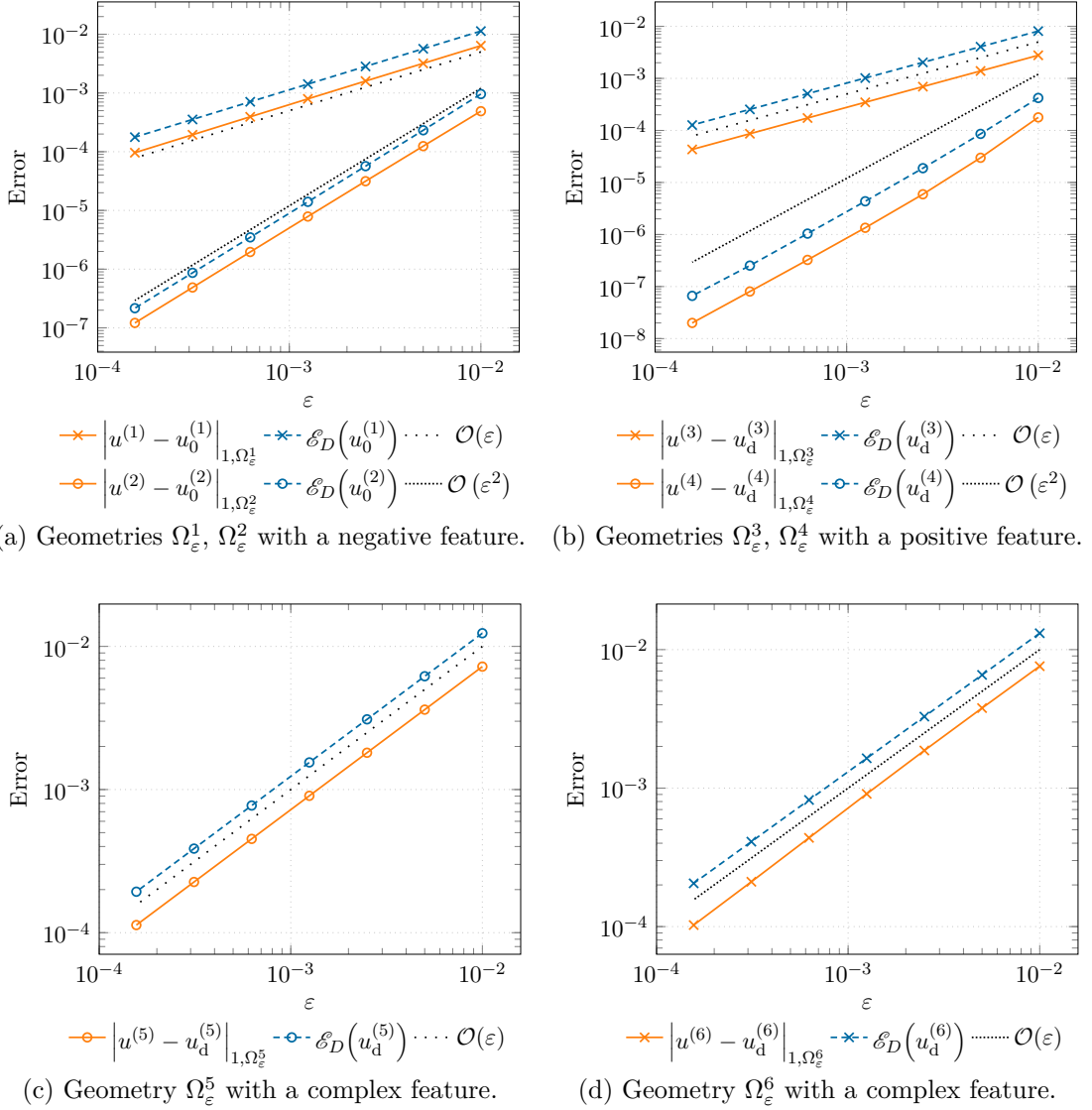
Figure 3.10 – Numerical test 3.5.2.1 – Convergence of the error and estimator in 2D domains with one feature.

first geometry Ω_ε^3, and as $\varepsilon^2 \propto |\gamma|^2$ in the second geometry Ω_ε^4. Again, the difference in asymptotic behavior of the error depends on symmetries and on the Neumann boundary conditions. Indeed, Ω_ε^4 has features with sides parallel to $\partial\Omega_0$. Moreover, the effectivity index is indeed almost independent of the size of the feature since it remains nearly equal to 2.93 and 3.22, respectively, for all values of ε. That is, as predicted by the theory in Theorems 3.4.4 and 3.4.5, the estimator is both reliable and efficient, here in dimension two, and its effectivity index is independent of the size of the considered positive feature. We also remark that the effectivity indices for the positive features are a little bit larger than the ones for the negative features, and this may come from the smoothness of the defeatured solution u_{d}, see Remark 3.5.1.

(a) Exact domain Ω_ε^5.

(b) Zoom on the upper boundary of Ω_0 (up) and Ω_ε^5 (down).

(c) Exact domain Ω_ε^6.

(d) Zoom on the upper boundary of Ω_0 (up) and Ω_ε^6 (down).
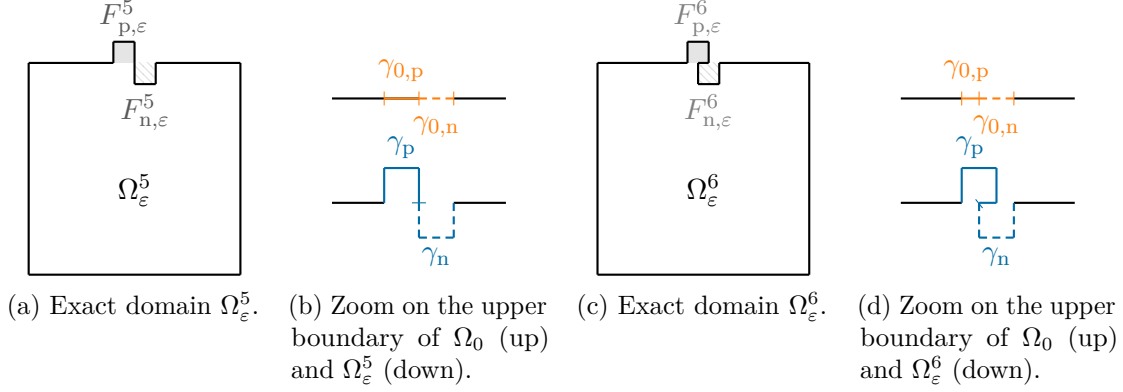
Figure 3.11 – Numerical test 3.5.2.1 – Exact domains Ω_ε^5 and Ω_ε^6.

Let us finally consider two-dimensional examples of geometries with a general complex feature. Let Ω_0, Γ_D, f, g_D and g be again as before, and for $\ell = 5, 6$, let

$$\Omega_\varepsilon^\ell := \text{int}\left(\overline{\Omega_0} \cup \overline{F_{n,\varepsilon}^\ell} \setminus \overline{F_{p,\varepsilon}^\ell}\right)$$

where, as illustrated in Figure 3.11,

$$
\begin{aligned}
F_{p,\varepsilon}^5 &:= (0.5 - \varepsilon, 0.5) \times (1, 1 + \varepsilon), \\
F_{n,\varepsilon}^5 &:= (0.5, 0.5 + \varepsilon) \times (1 - \varepsilon, 1), \\
F_{p,\varepsilon}^6 &:= \left(0.5 - \frac{3\varepsilon}{4}, 0.5 + \frac{\varepsilon}{4}\right) \times (1, 1 + \varepsilon), \\
F_{n,\varepsilon}^6 &:= \left(0.5 - \frac{\varepsilon}{4}, 0.5 + \frac{3\varepsilon}{4}\right) \times (1 - \varepsilon, 1).
\end{aligned}
$$

For each $\ell = 5, 6$, let $\Gamma_N := \partial\Omega_\varepsilon^\ell \setminus \overline{\Gamma_D}$ and we consider the same Poisson problem (3.1) as before, but solved in Ω_ε^ℓ. We also solve its defeatured version (3.3) in Ω_0 with $g_0 \equiv 0$ on γ_0. Note from Figure 3.11 that γ_0 is different whether $\ell = 5$ or $\ell = 6$. Then, we extend the defeatured solution to F_ε^ℓ by solving (3.6) with $\tilde{F} := F_{n,\varepsilon}^\ell$. As before, we respectively call $u^{(\ell)}$ and $u_0^{(\ell)}$ the exact and defeatured solutions, and $u_d^{(\ell)}$ the defeatured solution extended to $F_{n,\varepsilon}^\ell$.

The results are presented in Figures 3.10c and 3.10d. As for the negative and positive feature cases, the error in Ω_0 and the estimator converge with respect to the size of the feature as $\varepsilon \propto |\gamma_n| \simeq |\gamma_{0,p}|$ in both geometries Ω_ε^5 and Ω_ε^6. Moreover, the effectivity index is indeed almost independent of the size of the feature since it remains nearly equal to 1.71 and 1.84, respectively, for all values of ε. That is, as predicted by the theory in Theorems 3.4.4 and 3.4.5, the estimator is both reliable and efficient, here in dimension two, and its effectivity index is independent of the size of the considered complex feature.

(a) Geometry Ω_ε^1 with negative feature F_ε^1. (b) Geometry Ω_ε^2 with negative feature F_ε^2. (c) Geometry Ω_ε^3 with positive feature F_ε^3. (d) Geometry Ω_ε^4 with positive feature F_ε^4.
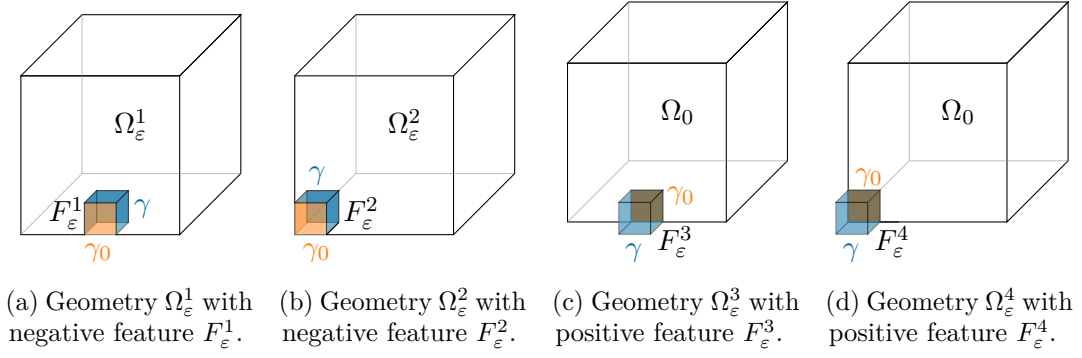
Figure 3.12 – Numerical test 3.5.2.2 – 3D geometries Ω_ε^i, $i = 1, 2, 3, 4$.

3.5.2.2 Three-dimensional geometries

Let us first consider three-dimensional examples of geometries with a negative feature. Let $\varepsilon = \dfrac{10^{-2}}{2^k}$ for $k = 0, 1, \ldots, 6$, and $\Omega_\varepsilon^i := \Omega_0 \setminus \overline{F_\varepsilon^i}$ for $i = 1, 2$ with $\Omega_0 := (0, 1)^3$ and

$$F_\varepsilon^1 := \left(0.5 - \frac{\varepsilon}{2}, 0.5 + \frac{\varepsilon}{2} \right) \times (1 - \varepsilon, 1) \times (0, \varepsilon),$$

$$F_\varepsilon^2 := F_\varepsilon^1 + \left(0.5 - \frac{\varepsilon}{2}, 0, 0 \right)^T,$$

as in Figures 3.12a and 3.12b. For each $i = 1, 2$, we consider Poisson problem (3.1) solved in Ω_ε^i, and its defeatured version (3.3) in Ω_0. We take

$$f(x, y) := 10 \cos(3\pi x) \sin(5\pi y) \sin(7\pi z) \quad \text{in } \Omega,$$

$$g_D \equiv 0 \quad \text{on} \quad \Gamma_D := (0, 1) \times \{0\} \times (0, 1),$$

$g \equiv 0$ on $\Gamma_N := \partial \Omega_\varepsilon^i \setminus \overline{\Gamma_D}$, and $g_0 \equiv 0$ on $\partial \Omega_0 \setminus \partial \Omega_\varepsilon^i$.

The results are presented in Figure 3.13a. Both the error and the estimator converge with respect to the size of the feature as $\varepsilon^{\frac{3}{2}} \propto |\gamma_0|^{\frac{3}{4}}$ in the first geometry Ω_ε^1, and as $\varepsilon^{\frac{5}{2}} \propto |\gamma|^{\frac{5}{4}}$ in the second geometry Ω_ε^2. Moreover, the effectivity index is indeed independent of the size of the feature since it remains nearly equal to 1.87 and 1.92, respectively, for all values of ε. That is, again as predicted by the theory in Theorems 3.2.3 and 3.2.4, the estimator is both reliable and efficient, here in dimension three, and its effectivity index is independent of the size of the considered negative feature.

Let us now consider three-dimensional examples of geometries with a positive feature. Let Ω_0, Γ_D, f, g_D, and g be as before, and let $\Omega_\varepsilon^j := \text{int}\left(\overline{\Omega_0} \cup \overline{F_\varepsilon^j} \right)$ for $j = 3, 4$ with

$$F_\varepsilon^3 := \left(0.5 - \frac{\varepsilon}{2}, 0.5 + \frac{\varepsilon}{2} \right) \times (1, 1 + \varepsilon) \times (0, \varepsilon),$$

$$F_\varepsilon^4 := F_\varepsilon^3 + \left(0.5 - \frac{\varepsilon}{2}, 0, 0 \right)^T,$$

(a) Geometries Ω_ε^1, Ω_ε^2 with a negative feature.   (b) Geometries Ω_ε^3, Ω_ε^4 with a positive feature.
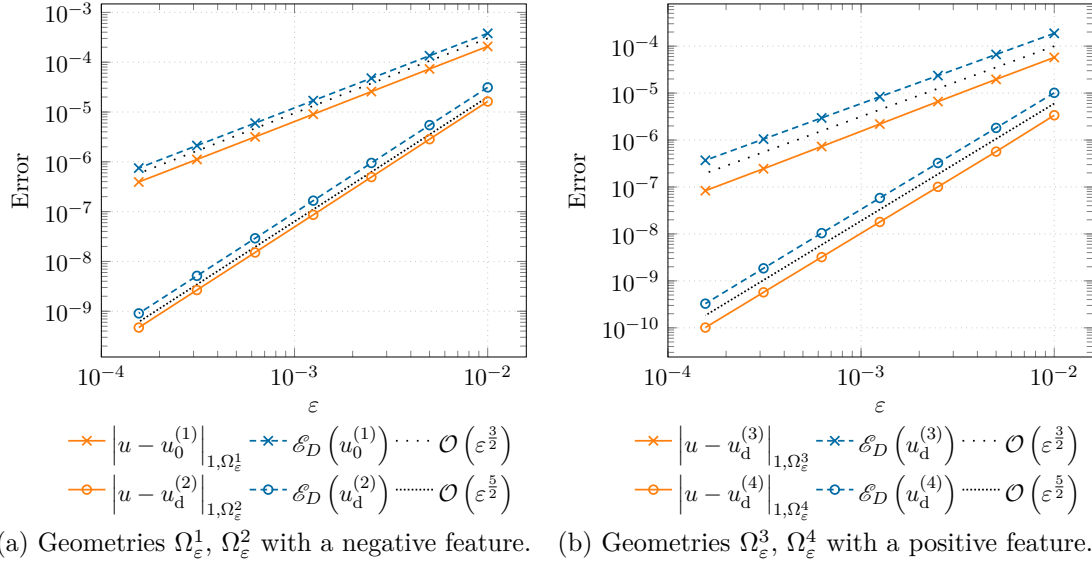
Figure 3.13 – Numerical test 3.5.2.2 – Convergence of the error and of the estimator in 3D domains with one feature.

as in Figures 3.12c and 3.12d. Let $\Gamma_N := \partial\Omega_\varepsilon^j \setminus \overline{\Gamma_D}$. For each $j = 3, 4$, we consider the same Poisson problem (3.1) as before, but solved in this Ω_ε^j. We also solve its defeatured version (3.3) in Ω_0 with $g_0 \equiv 0$ on $\partial\Omega_0 \setminus \partial\Omega_\varepsilon$. Then we extend the defeatured solution to F_ε^j by solving (3.6) with $\tilde{F} := F_\varepsilon^j$.

The results are presented in Figure 3.13b. As for the negative feature case, the error in Ω_0, the error in F_ε^j and the estimator converge with respect to the size of the feature as $\varepsilon^{\frac{3}{2}} \propto |\gamma_0|^{\frac{3}{4}}$ in the first geometry Ω_ε^3, and as $\varepsilon^{\frac{5}{2}} \propto |\gamma_0|^{\frac{5}{4}}$ in the second geometry Ω_ε^4. Moreover, the effectivity index is indeed almost independent of the size of the feature since it remains nearly equal to 3.10 and 3.22, respectively, for all values of ε. That is, again as predicted by the theory in Theorems 3.4.4 and 3.4.5, the estimator is both reliable and efficient, here in dimension three, and its effectivity index is independent of the size of the considered positive feature. Finally, and as in the two-dimensional case, we remark that the effectivity indices for the positive features are a little bit larger than the ones for the negative features.

3.5.2.3   Effect of the choice of the defeatured problem data

Let us study the effect of the choice of the defeatured problem data on the convergence of the defeaturing error and estimator. In particular, we will see that in the example of a geometry with one negative feature F, the convergence of the error and the estimator crucially depends on the value of the average $\overline{\left(g + \dfrac{\partial u_0}{\partial \mathbf{n}_F}\right)}^\gamma$. As seen in Remark 3.2.1, this average only depends on the Neumann boundary conditions g on γ and g_0 on γ_0,
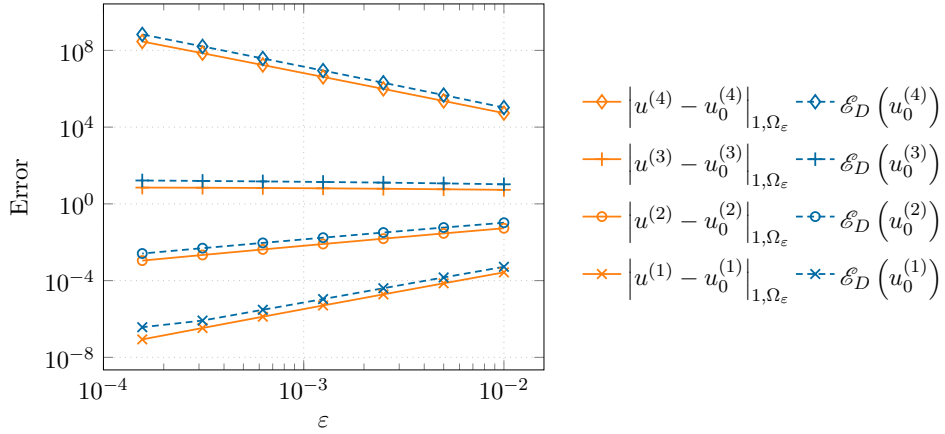
Figure 3.14 – Numerical test 3.5.2.3 – Convergence of the error and of the estimator with different Neumann boundary conditions.

and on the extension of the right hand side f in F. This means that one can obtain an optimal convergence rate of the defeaturing error by wisely choosing the defeatured data g_0 and f, considering the original data g. If possible, g_0 and f need to be chosen to satisfy the compatibility condition (3.12), or at least in such a way that the second term of the estimator in (3.11) converges faster than the first one. The same observation can be made in the positive feature case.

To show this, let $\varepsilon = \dfrac{10^{-2}}{2^k}$ for $k = 0, 1, \ldots, 6$. We consider a 2D geometry with one negative feature. More precisely, let Ω_0 be the disk centered at $(0,0)^T$ of radius 1, let F_ε be the disk centered at $(0,0)^T$ of radius ε, and let $\Omega_\varepsilon := \Omega_0 \setminus \overline{F_\varepsilon}$, as represented in Figure 3.7b. We solve Poisson problem (3.1) in Ω_ε with $f \equiv 1$ in Ω_ε, $g_D \equiv 0$ on $\Gamma_D := \partial \Omega_0$, and we choose different Neumann data $g = g_i$ on ∂F_ε for $i = 1, \ldots, 4$, where $g_1 \equiv 0$, $g_2 \equiv 1$, $g_3 \equiv \varepsilon^{-1}$, and $g_4 \equiv \varepsilon^{-3}$. Then, we solve the defeatured problem (3.3) in Ω_0, for which we need to choose an extension of f in F_ε, that we still call f. This extension should somehow mimic the behavior of the Neumann data g, as required by the compatibility condition, but instead of that, we choose the trivial extension $f \equiv 1$ in all four cases, and we will verify whether this is always a good choice or not. For $i = 1, \ldots, 4$, we call $u^{(i)}$ and $u_0^{(i)}$ the solutions of (3.1) and (3.3), respectively.

The results are presented in Figure 3.14. As we can see and as expected, the proposed estimator follows the convergence of the defeaturing error in all four cases. Moreover, the effectivity index always remains the same, as we were also expecting since the shape of the geometry never changes. However, we see that the trivial extension of f in F is not always a good choice since it slows down the convergence when $g = g_2$, it does not permit the error to decrease with ε when $g = g_3$, and it even implies the error to explode if ε decreases when $g = g_4$. The explanation is present in the expression of the estimator in (3.11): indeed, in the case $g = g_1$, the first term of (3.11) is dominant, while in the

(a) Geometry Ω_1 with the round feature F_1.

(b) Simplified geometry $\Omega_0 := \Omega_1 \cup F_1$.

(c) Geometry $\Omega_{\frac{1}{2}}$ with the round feature $F_{\frac{1}{2}}$.

(d) Simplified geometry $\Omega_0 := \Omega_{\frac{1}{2}} \cup F_{\frac{1}{2}}$.
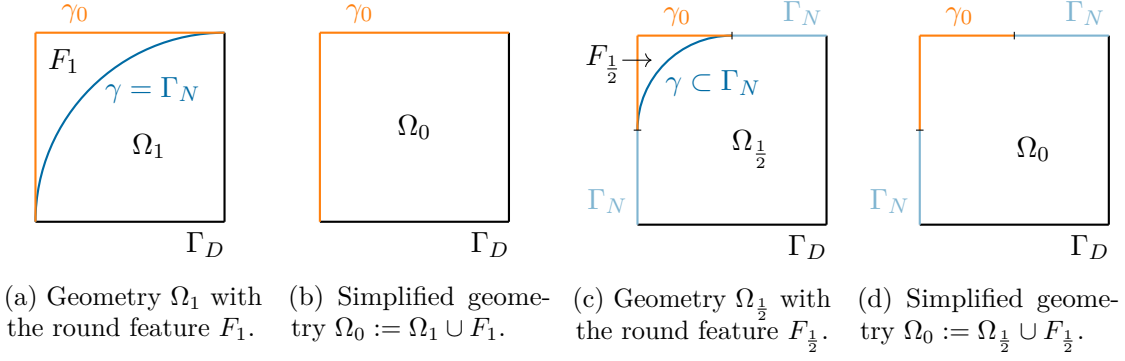
Figure 3.15 – Numerical test 3.5.3.1 – Geometries Ω_R with a round, for $R = 1$ and $R = \frac{1}{2}$.

other cases, the second term dominates because of the value of $\overline{\left(g + \dfrac{\partial u_0}{\partial \mathbf{n}_F}\right)}^{\gamma}$ due to the bad choice of f in F_ε. Consequently, the estimator not only tells us whether a feature is important for the given problem at hand, but it also tells us whether the choice of the defeaturing problem data is right, or if it should be reconsidered.

3.5.3 Non-Lipschitz features: fillets and rounds

Classical features one finds in design for manufacturing are fillets and rounds, that allow for example the use of round-tipped end mills to cut out some material. However, when considered as features isolated from the rest of the domain, fillets and rounds are non-Lipschitz feature domains. The *a posteriori* analysis of defeaturing in the presence of non-Lipschitz features is not covered by the presented theory. Nevertheless, thanks to the following numerical examples, we show that the proposed estimator still manages to capture the behavior of the defeaturing error when the features are non-Lipschitz fillets and rounds.

3.5.3.1 Round: a negative non-Lipschitz feature

Let us first consider the case of a round, that is, the rounding process creates a convex domain. For $R \in (0, 1]$, and as represented in Figure 3.15, let

$$\Omega_R := \left\{ \boldsymbol{x} = (x, y)^T \in \mathbb{R}^2 : \left\| \boldsymbol{x} - (R, 1 - R)^T \right\|_{\ell^2} < R, \ x < R, \ y > 1 - R \right\}$$
$$\cup \left((0, 1) \times (0, R] \right) \cup \left([R, 1) \times [1 - R, 1) \right),$$

$\Omega_0 := (0, 1)^2$, and $F_R := \Omega_0 \setminus \overline{\Omega_R}$. We remark that F_R is not a Lipschitz domain, that is, this case is not covered by the presented theory. We consider Poisson problem (3.1) with $f \equiv 0$ in Ω_R, $g_D(x, y) := x^2(1-x)^2 + y^2(1-y)^2$ on

$$\Gamma_D := \left((0, 1] \times \{0\} \right) \cup \left(\{1\} \times [0, 1) \right),$$

R	$\mathscr{E}_D(u_0)$	$\lvert u - u_0 \rvert_{1,\Omega_R}$	η_{eff}
1.00	$6.83 \cdot 10^{-3}$	$2.37 \cdot 10^{-3}$	2.88
0.99	$6.48 \cdot 10^{-3}$	$2.27 \cdot 10^{-3}$	2.85
0.50	$3.36 \cdot 10^{-4}$	$1.26 \cdot 10^{-4}$	2.67
0.25	$2.08 \cdot 10^{-5}$	$7.77 \cdot 10^{-6}$	2.67
0.125	$1.30 \cdot 10^{-6}$	$4.86 \cdot 10^{-7}$	2.67

Table 3.3 – Numerical test 3.5.3.1 – Results for the geometry with a round.

and $g \equiv 0$ on $\Gamma_N := \partial\Omega_R \setminus \overline{\Gamma_D}$. We solve the defeatured Poisson problem (3.3) with the same data and $g_0 \equiv 0$ on $\gamma_0 := \partial F_R \setminus \overline{\Gamma_N}$.

The results are presented in Table 3.3, and for all considered values of R, we indeed have $\lvert u - u_0 \rvert_{1,\Omega_R} \lesssim \mathscr{E}_D(u_0)$ with a low effectivity index. In particular, the effectivity index is almost the same for all considered values of R in $(0, 0.5)$ while it is slightly larger for $R \in (0.5, 1)$, since the geometries for $R \in (0, 0.5)$ are almost an homothety of one another, while it is not when $R > 0.5$ because of the closeness of the boundary Γ_D from the boundary γ. This example shows that our estimator estimates well the defeaturing error even if the feature is not a Lipschitz domain, and it confirms the fact that we can indeed have a feature that is attached to the Dirichlet boundary, $\overline{\gamma} \cap \overline{\Gamma_D} \neq \emptyset$, but $\gamma \cap \Gamma_D = \emptyset$ as in the case $R = 1$.

3.5.3.2 Fillet: a positive non-Lipschitz feature

Now, let us consider the case of a fillet, that is, the filleting process creates a non-convex domain. Since the fillet F is a complex positive feature we possibly do not want to mesh, we will consider two different feature extensions $\tilde{F}^1$ and $\tilde{F}^2$ containing F to solve the extension problem (3.6). We will compare them, and we will also compare the results with the one obtained without feature extension, that is, for $\tilde{F} = F$. In particular, we remark again that F is not a Lipschitz domain, that is, this example is not covered by the presented theory. As illustrated in Figure 3.16, let

$$\Omega_0 := (0,1)^2 \setminus \left[\frac{1}{2}, 1\right]^2, \qquad \tilde{F}^1 := \left(\frac{1}{2}, 1\right)^2,$$

$$\tilde{F}^2 := \tilde{F}^1 \setminus \left\{ \boldsymbol{x} = (x,y)^T \in \mathbb{R}^2 : \left\| \boldsymbol{x} - (1,1)^T \right\|_{\ell^2} \leq \frac{1}{4}, \ x \leq 1, \ y \leq 1 \right\},$$

$$F := \tilde{F}^1 \setminus \left\{ \boldsymbol{x} = (x,y)^T \in \mathbb{R}^2 : \left\| \boldsymbol{x} - (1,1)^T \right\|_{\ell^2} \leq \frac{1}{2}, \ x \leq 1, \ y \leq 1 \right\},$$

$$\Omega := \text{int}\left(\overline{\Omega_0} \cup \overline{F} \right).$$

The feature extension $\tilde{F}^1$ is the bounding box of F, it is therefore a very simple geometry but $\left| \tilde{F}^1 \right| \gg |F|$. At the contrary, $\tilde{F}^2$ is a little bit more complex, but $\left| \tilde{F}^2 \right| \approx |F|$.

(a) Exact original geometry $\Omega = \mathrm{int}\left(\overline{\Omega_0 \cup F}\right)$.

(b) Simplified geometry Ω_0 and feature extension $\tilde{F}^1$.

(c) Simplified geometry Ω_0 and feature extension $\tilde{F}^2$.
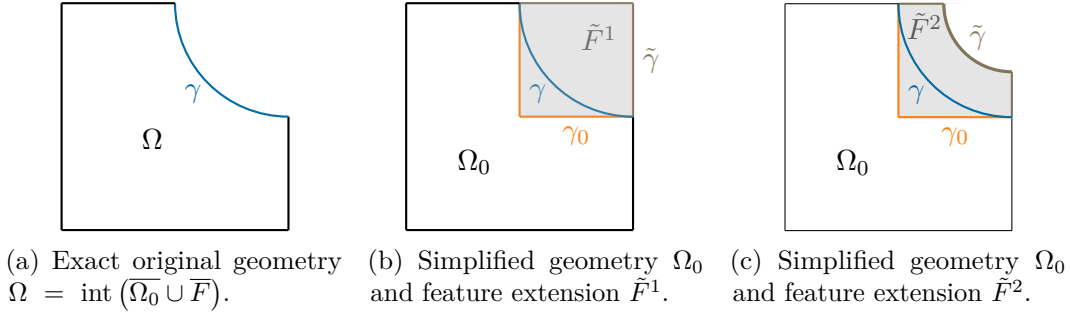
Figure 3.16 – Numerical test 3.5.3.2 – Geometry $\Omega = \mathrm{int}\left(\overline{\Omega_0 \cup F}\right)$ with a fillet F, and two possible extended features.

Extension	$\mathscr{E}_D(u_{\mathrm{d}})$	$|u - u_{\mathrm{d}}|_{1,\Omega}$	$|u - u_0|_{1,\Omega_0}$	$|u - \tilde{u}_0|_{1,F}$	η_{eff}
$\tilde{F}^1$	1.78	$2.92 \cdot 10^{-1}$	$1.69 \cdot 10^{-1}$	$2.39 \cdot 10^{-1}$	6.11
$\tilde{F}^2$	1.71	$2.89 \cdot 10^{-1}$	$1.69 \cdot 10^{-1}$	$2.34 \cdot 10^{-1}$	5.93
F	1.33	$2.69 \cdot 10^{-1}$	$1.69 \cdot 10^{-1}$	$2.01 \cdot 10^{-1}$	4.94

Table 3.4 – Numerical test 3.5.3.2 – Results for the geometry with a fillet.

We consider Poisson problem (3.1) with $f \equiv 0$ in Ω,

$$g_D(x, y) := \cos\left(\pi x\right) + 10\cos(5\pi x)$$

on $\Gamma_D := (0,1) \times \{0\}$, and $g \equiv 0$ on $\Gamma_N = \partial\Omega \setminus \overline{\Gamma_D}$. We solve the defeatured Poisson problem (3.3) with the same data and with $g_0 \equiv 0$ on $\gamma_0 := \partial\Omega_0 \cap \partial F$. Then, we solve the Dirichlet extension problem (3.6) firstly in $\tilde{F}^1$ and secondly in $\tilde{F}^2$, with $\tilde{g} \equiv 0$ on $\tilde{\gamma} := \partial\tilde{F}^1 \setminus \overline{\gamma_0}$ and $\tilde{\gamma} := \partial\tilde{F}^2 \setminus \overline{\gamma_0}$, respectively. Finally, we also solve (3.6) by taking $\tilde{F} := F$ itself.

The results are presented in Table 3.4, and we indeed have $|u - u_{\mathrm{d}}|_{1,\Omega} \lesssim \mathscr{E}_D(u_{\mathrm{d}})$ with a reasonably low effectivity index in all three cases. Note that the effectivity index is higher in this case than in the case of a round since not only the geometry Ω but also the feature F are simplified, respectively by Ω_0 and by $\tilde{F}^1$ or $\tilde{F}^2$. Moreover, F contains the extension $\tilde{F}^1$ that itself contains the extension $\tilde{F}^2$, and this is reflected both on the defeaturing error and on the estimator. Indeed, both the error and the estimator are larger when the considered extension is $\tilde{F}^1$ instead of $\tilde{F}^2$, and smaller when $\tilde{F} = F$. Based on the developed theory and on the experiments of Section 3.5.2, the effectivity index η_{eff} changes because the shapes of F, $\tilde{F}^1$ and $\tilde{F}^2$ are different, not because an extension is bigger than the other one. Furthermore, the effectivity index on the fillet is larger than the one on the round: as already remarked in Section 3.5.2, the effectivity index is in general larger for positive features than for negative ones. Finally, the effectivity indices for both the round and the fillet are larger than for the other negative and positive features, respectively, and this can come from the fact that rounds

and fillets are non-Lipschitz features.

Remark 3.5.1 (Effectivity indices)**.** Let us summarize the observations made on the behavior of the effectivity indices.

- The effectivity index of every test case is independent of the measure of the feature (see Sections 3.5.2.1 and 3.5.2.2), but it depends on their shape (see Section 3.5.1.1).

- The observed effectivity indices are small when Lipschitz features are considered: in both two and three dimensions, the value of the effectivity index ranges between 1 and 4 (see Sections 3.5.1 and 3.5.2), in general with smaller values for negative features than for positive ones. While we have no evidence of it, the difference possibly comes from the smoothness of the extended defeatured solution u_d. Indeed, in the positive feature case, a γ_0-Dirichlet extension of u_0 is necessary to define the error in the whole geometry Ω. This extension is in $H^1(\Omega)$ by definition, but its gradient jumps at the boundary γ_0, making it possibly less regular than the defeatured solution that one can have in the negative feature case.

- The observed effectivity indices are larger when non-Lipschitz features are considered, but such geometries are not considered in the presented theory. The special cases of rounds and fillets are analyzed in Section 3.5.3, and the observed effectivity indices in those cases are smaller than 3 and 5, respectively.

- The observed effectivity indices in the case of an extended positive feature, that is, a feature for which $\tilde{F} \supsetneq F$, are larger than in the case of a positive feature, while still remaining relatively small (see Section 3.5.3.2). Indeed, in the former case, not only the geometry Ω but also the feature F are simplified, respectively by Ω_0 and by $\tilde{F}$.

4 *A posteriori* error estimation: multi-feature geometries

When complex engineering designs are created, they may contain a large number of features. In this chapter, we generalize the analysis of Chapter 3 to a geometry containing N_f distinct complex features, for some $N_f \in \mathbb{N}$, $N_f \geq 1$. In particular, we generalize the *a posteriori* defeaturing error estimator introduced in Chapter 3 to multi-feature geometries. With the help of this *a posteriori* error estimator, we are then able to design an adaptive strategy which performs geometric adaptivity. More precisely, this algorithm is able to determine at each iteration step which features most affect the solution accuracy, in order to add them to the simplified geometrical model at the next iteration.

This chapter is therefore structured as follows. In Section 4.1, we first extend the analysis-aware defeaturing problem of Section 3.3 to multi-feature geometries. Subsequently, in Section 4.2, we generalize the *a posteriori* analysis of the defeaturing error presented in Section 3.4 to this framework. In particular, we introduce a defeaturing error estimator which has similar properties as in the single feature case, and whose effectivity index is independent of the number N_f of features. The analysis is extended to a linear elasticity problem in Section 4.3, and eventually to Stokes equations in Section 4.4. We then introduce in Section 4.5 a geometric adaptive strategy driven by the defeaturing error estimators previously defined. Finally, in Section 4.6, we present a validation of the previously presented results. As in Chapter 3, our validation is obtained by comparing errors and defeaturing estimators for numerical solutions on very fine meshes. This chapter closely follows [Antolín and Chanon, 2022], and the notation generalizes the one used in Chapter 3.

4.1 Defeaturing Poisson's problem: geometry with multiple features

In this section, let us consider Poisson problem (3.2) solved in an exact geometry Ω which contains $N_f \geq 1$ distinct complex geometrical features composing the set $\mathfrak{F} := \left\{ F^k \right\}_{k=1}^{N_f}$.

That is, for all $k = 1, \ldots, N_f$, feature F^k is an open Lipschitz domain which is composed of a (not necessarily connected) negative component F_n^k and a (not necessarily connected) positive component F_p^k that can have a non-empty intersection. More precisely,

$$F^k = \mathrm{int} \left(\overline{F_p^k} \cup \overline{F_n^k} \right),$$

where F_n^k and F_p^k are open Lipschitz domains such that if we let

$$F_p := \mathrm{int} \left(\bigcup_{k=1}^{N_f} \overline{F_p^k} \right), \quad F_n := \mathrm{int} \left(\bigcup_{k=1}^{N_f} \overline{F_n^k} \right), \quad \Omega_\star := \Omega \setminus \overline{F_p},$$

then

$$F_p \subset \Omega, \quad \left(\overline{F_n} \cap \overline{\Omega_\star} \right) \subset \partial\Omega_\star.$$

In this setting, the defeatured geometry is defined as in (3.24) by

$$\Omega_0 := \mathrm{int} \left(\overline{\Omega_\star} \cup \overline{F_n} \right) \subset \mathbb{R}^n, \tag{4.1}$$

and as before, we assume that $\Omega_\star$ and Ω_0 are open Lipschitz domains. Let us make the following assumption on the features.

Assumption 4.1.1. The features in $\mathfrak{F}$ are separated, that is, $\overline{F^k} \cap \overline{F^\ell} = \emptyset$ for every $k, \ell = 1, \ldots, N_f$, $k \neq \ell$.

Remark 4.1.2. In the currently considered setting in which features are discrete objects, it is always possible to satisfy Assumption 4.1.1 by changing the numbering of the features. Indeed, if there are $k, \ell = 1, \ldots, N_f$ such that $\overline{F^k} \cap \overline{F^\ell} \neq \emptyset$, then $F^{k,\ell} := \mathrm{int} \left(\overline{F^k} \cup \overline{F^\ell} \right)$ can be considered as a single feature that replaces the two features F^k and F^ℓ. However, the treatment of a geometry in which the boundary is complex everywhere is not treated here, see also Section 9.2.5.

As in the previous chapter, let $\mathbf{n}_0$ be the unitary outward normal to Ω_0, and for all $k = 1, \ldots, N_f$, let $\mathbf{n}^k \equiv \mathbf{n}_{F^k}$ be the unitary outward normal to F_n^k and to F_p^k. Note that we allow the same abuse of notation as in the single feature case whenever the outward normal to F_n^k has opposite sign from the one of F_p^k. Similarly to the single feature case, the analysis is performed under the following assumption on the exact problem (3.1):

Assumption 4.1.3. A Neumann boundary condition is imposed on the boundary of the features, that is, for all $k = 1, \ldots, N_f$,

$$\Gamma_D \cap \left(\partial F_n^k \cup \partial F_p^k \right) = \emptyset.$$

Then, for all $k = 1, \ldots, N_f$, let us introduce the notation $\gamma_{0,p}^k$, $\gamma_{0,n}^k$, γ_0^k, γ_p^k, γ_n^k and γ^k

analogous to the single feature case presented in Chapter 3, where an upper index k is added to the quantities referring to feature F^k. That is,

$$\gamma_0^k := \mathrm{int}\left(\overline{\gamma_{0,\mathrm{n}}^k} \cup \overline{\gamma_{0,\mathrm{p}}^k}\right) \subset \partial\Omega_0 \quad \text{with} \quad \gamma_{0,\mathrm{n}}^k := \partial F_{\mathrm{n}}^k \setminus \partial\Omega_\star, \quad \gamma_{0,\mathrm{p}}^k := \partial F_{\mathrm{p}}^k \setminus \partial\Omega,$$

$$\gamma^k := \mathrm{int}\left(\overline{\gamma_{\mathrm{n}}^k} \cup \overline{\gamma_{\mathrm{p}}^k}\right) \subset \partial\Omega \quad \text{with} \quad \gamma_{\mathrm{n}}^k := \partial F_{\mathrm{n}}^k \setminus \overline{\gamma_{0,\mathrm{n}}^k}, \quad \gamma_{\mathrm{p}}^k := \partial F_{\mathrm{p}}^k \setminus \overline{\gamma_{0,\mathrm{p}}^k},$$

so that $\partial F_{\mathrm{n}}^k = \overline{\gamma_{\mathrm{n}}^k} \cup \overline{\gamma_{0,\mathrm{n}}^k}$ with $\gamma_{\mathrm{n}}^k \cap \gamma_{0,\mathrm{n}}^k = \emptyset$, and $\partial F_{\mathrm{p}}^k = \overline{\gamma_{\mathrm{p}}^k} \cup \overline{\gamma_{0,\mathrm{p}}^k}$ with $\gamma_{\mathrm{p}}^k \cap \gamma_{0,\mathrm{p}}^k = \emptyset$. Moreover, let

$$\gamma_0 := \bigcup_{k=1}^{N_f} \gamma_0^k, \quad \gamma_{0,\mathrm{n}} := \bigcup_{k=1}^{N_f} \gamma_{0,\mathrm{n}}^k, \quad \gamma_{0,\mathrm{p}} := \bigcup_{k=1}^{N_f} \gamma_{0,\mathrm{p}}^k,$$

$$\gamma := \bigcup_{k=1}^{N_f} \gamma^k, \quad \gamma_{\mathrm{n}} := \bigcup_{k=1}^{N_f} \gamma_{\mathrm{n}}^k, \quad \gamma_{\mathrm{p}} := \bigcup_{k=1}^{N_f} \gamma_{\mathrm{p}}^k. \tag{4.2}$$

Similarly to the single negative feature case, consider any L^2-extension of the restriction $f|_{\Omega_\star}$ in all the negative components F_{n}^k, $k = 1, \ldots, N_f$, that we still write $f \in L^2(\Omega_0)$ by abuse of notation. Then instead of (3.1), we solve the defeatured problem (3.3) whose weak formulation is given in (3.4), and we obtain $u_0 \in H^1_{g_D, \Gamma_D}(\Omega_0)$.

As previously, since we are interested in the energy norm of the defeaturing error "$u - u_0$" in Ω, we need to extend the defeatured solution u_0 to the positive components F_{p}^k of the features. Therefore, for all $k = 1, \ldots, N_f$, we follow the same rationale for F_{p}^k as the one exposed in Chapter 3 for the positive component of a single positive or complex feature: let $\tilde{F}_{\mathrm{p}}^k \subset \mathbb{R}^n$ be a suitable (simple) domain extension of the positive component F_{p}^k of feature F^k, i.e., it is a Lipschitz domain that contains F_{p}^k and such that $\gamma_{0,\mathrm{p}}^k \subset \left(\partial\tilde{F}_{\mathrm{p}}^k \cap \partial F_{\mathrm{p}}^k\right)$. Furthermore, let

$$G_{\mathrm{p}}^k := \tilde{F}_{\mathrm{p}}^k \setminus \overline{F_{\mathrm{p}}^k}, \tag{4.3}$$

as in (3.25), and assume that G_{p}^k is Lipschitz for all $k = 1, \ldots, N_f$. As in the single feature case, note that G_{p}^k can be seen as a negative feature of F_{p}^k whose simplified geometry is $\tilde{F}_{\mathrm{p}}^k$.

To simplify the following exposition and even if this hypothesis could easily be removed, let us make the following assumption.

Assumption 4.1.4. Assume that

- $\tilde{F}_{\mathrm{p}}^k \cap \tilde{F}_{\mathrm{p}}^\ell = \emptyset$ for all $k, \ell = 1, \ldots, N_f$ such that $k \neq \ell$,

- if we let $\tilde{F}_{\mathrm{p}} := \bigcup_{k=1}^{N_f} \tilde{F}_{\mathrm{p}}^k$, then $\tilde{F}_{\mathrm{p}} \cap \Omega_\star = \emptyset$.

Then, and as illustrated in Figure 3.6 for the analogous single feature case, let us define

$$G_{\mathrm{p}} := \bigcup_{k=1}^{N_f} G_{\mathrm{p}}^k, \qquad \tilde{\Omega} := \mathrm{int}\left(\overline{\Omega_\star} \cup \overline{\tilde{F}_{\mathrm{p}}}\right) = \mathrm{int}\left(\overline{\Omega} \cup \overline{G_{\mathrm{p}}}\right),$$

Now, consider any L^2-extension of the restriction $f|_{F_{\mathrm{p}}^k}$ in each G_{p}^k, that we still write f by abuse of notation. For all $k = 1, \ldots, N_f$, let $\tilde{\mathbf{n}}^k$ be the unitary outward normal to $\tilde{F}_{\mathrm{p}}^k$, let $\tilde{\gamma}^k := \partial \tilde{F}_{\mathrm{p}}^k \setminus \partial F_{\mathrm{p}}^k$, and let γ_{p}^k be decomposed as $\gamma_{\mathrm{p}}^k = \mathrm{int}\left(\overline{\gamma_{\mathrm{s}}^k} \cup \overline{\gamma_{\mathrm{r}}^k}\right)$, where γ_{s}^k and γ_{r}^k are open, γ_{s}^k is the part of γ_{p}^k that is shared with $\partial \tilde{F}_{\mathrm{p}}^k$ while γ_{r}^k is the remaining part of γ_{p}^k, that is, the part that does not belong to $\partial \tilde{F}_{\mathrm{p}}^k$. This notation is also analogous to the single feature case illustrated in Figure 3.6, and as in (4.2), let

$$\tilde{\gamma} := \bigcup_{k=1}^{N_f} \tilde{\gamma}^k, \quad \gamma_{\mathrm{s}} := \bigcup_{k=1}^{N_f} \gamma_{\mathrm{s}}^k, \quad \gamma_{\mathrm{r}} := \bigcup_{k=1}^{N_f} \gamma_{\mathrm{r}}^k.$$

Now, for all $k = 1, \ldots, N_f$, let us extend the solution u_0 of (3.3) on $\tilde{F}_{\mathrm{p}}^k$ exactly as in (3.6), but to lighten the notation in the multi-feature context, we will write

$$u_k \equiv \tilde{u}_0^k, \qquad \text{for } k = 1, \ldots, N_f. \tag{4.4}$$

That is, the extension problem for $k = 1, \ldots, N_f$ reads: after choosing $\tilde{g}^k \in H^{\frac{1}{2}}(\tilde{\gamma}^k)$, find $u_k \equiv \tilde{u}_0^k \in H^1\left(\tilde{F}_{\mathrm{p}}^k\right)$, the weak solution of

$$\begin{cases} -\Delta u_k = f & \text{in } \tilde{F}_{\mathrm{p}}^k \\ u_k = u_0 & \text{on } \gamma_{0,\mathrm{p}}^k \\ \dfrac{\partial u_k}{\partial \tilde{\mathbf{n}}^k} = \tilde{g}^k & \text{on } \tilde{\gamma}^k \\ \dfrac{\partial u_k}{\partial \tilde{\mathbf{n}}^k} = g & \text{on } \gamma_{\mathrm{s}}^k, \end{cases} \tag{4.5}$$

that is, $u_k \in H^1_{u_0, \gamma_{0,\mathrm{p}}^k}\left(\tilde{F}_{\mathrm{p}}^k\right)$ satisfies for all $v^k \in H^1_{0, \gamma_{0,\mathrm{p}}^k}\left(\tilde{F}_{\mathrm{p}}^k\right)$,

$$\int_{\tilde{F}_{\mathrm{p}}^k} \nabla u_k \cdot \nabla v^k \, \mathrm{d}x = \int_{\tilde{F}_{\mathrm{p}}^k} f v^k \, \mathrm{d}x + \int_{\tilde{\gamma}^k} \tilde{g}^k v^k \, \mathrm{d}s + \int_{\gamma_{\mathrm{s}}^k} g v^k \, \mathrm{d}s. \tag{4.6}$$

Finally, let $u_{\mathrm{d}} \in H^1_{g_D, \Gamma_D}(\Omega)$ be the extended defeatured solution, that is,

$$u_{\mathrm{d}} \equiv \begin{cases} u_0|_{\Omega_\star} & \text{in } \Omega_\star = \Omega \setminus \overline{F_{\mathrm{p}}} \\ u_k|_{F_{\mathrm{p}}^k} = \tilde{u}_0^k|_{F_{\mathrm{p}}^k} & \text{in } F_{\mathrm{p}}^k, \text{ for all } k = 1, \ldots, N_f. \end{cases} \tag{4.7}$$
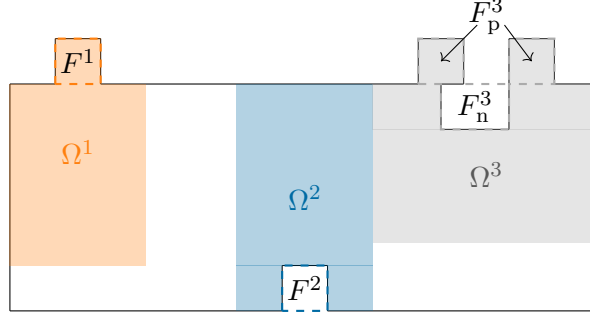
Figure 4.1 – Domain Ω with three separated features, and a possible choice of subdomains Ω^k, $k = 1, 2, 3$, satisfying Assumption 4.1.5.

Then, the energy error of the defeaturing error is defined by

$$\|\!|u - u_\mathrm{d}|\!\|_\Omega = \|\nabla(u - u_\mathrm{d})\|_{0,\Omega} = |u - u_\mathrm{d}|_{1,\Omega}.$$

For the *a posteriori* error analysis of the defeatured problem in multi-feature geometries (see Section 4.2 and Chapter 8), we will actually need a separability assumption on the features that is stronger than Assumption 4.1.1. The following assumption is illustrated in Figure 4.1:

Assumption 4.1.5. The features in $\mathfrak{F}$ are separated, that is,

- $\overline{F^k} \cap \overline{F^\ell} = \emptyset$ for every $k, \ell = 1, \ldots, N_f$, $k \neq \ell$,

- there exist sub-domains $\Omega^k \subset \Omega$, $k = 1, \ldots, N_f$ such that

  ○ $F_\mathrm{p}^k \subset \Omega^k$, $\quad \left(\gamma_\mathrm{n}^k \cup \gamma_\mathrm{r}^k\right) \subset \partial\Omega^k$, $\quad \gamma_{0,\mathrm{p}}^k \subset \partial(\Omega^k \cap \Omega_0)$,

  ○ $\left|\Omega^k\right| \simeq |\Omega|$ where the hidden constant is independent of the size of the features, i.e., the measure of Ω^k is comparable with the measure of Ω, not with the measure of the feature F^k,

  ○ $N_s := \max\limits_{J \subset \{1,\ldots,N_f\}} \left(\#J : \bigcap\limits_{k \in J} \Omega^k \neq \emptyset\right) \ll N_f$, that is, the maximum number N_s of superposed sub-domains Ω^k is limited and notably smaller than the total number of features N_f.

Remark 4.1.6. The second condition of Assumption 4.1.5 means that one cannot have an increasingly large number of features that are arbitrarily close to one another. Moreover, if $N_f = 1$, one can take $\Omega^1 := \Omega$.

To ease the notation in the following chapters and similarly to (3.27), let us respectively

denote the Neumann boundaries of Ω_0 and of $\tilde{F}_{\mathrm{p}}^k$ by

$$\Gamma_N^0 := (\Gamma_N \setminus \gamma) \cup \gamma_0 \quad \text{and} \quad \tilde{\Gamma}_N^k := \gamma_{\mathrm{s}}^k \cup \tilde{\gamma}^k, \quad k = 1, \ldots, N_f, \tag{4.8}$$

and let

$$\tilde{\Gamma}_N := \bigcup_{k=1}^{N_f} \tilde{\Gamma}_N^k = \gamma_{\mathrm{s}} \cup \tilde{\gamma}. \tag{4.9}$$

Finally, let us generalize the definitions of Γ and Σ from (3.28) as follows:

$$\Gamma^k := \gamma_{\mathrm{n}}^k \cup \gamma_{0,\mathrm{p}}^k \cup \gamma_{\mathrm{r}}^k, \quad \text{for } k = 1, \ldots, N_f, \tag{4.10}$$

$$\text{and} \quad \Sigma_{\mathrm{n}} := \left\{ \gamma_{\mathrm{n}}^k \right\}_{k=1}^{N_f}, \quad \Sigma_{0,\mathrm{p}} := \left\{ \gamma_{0,\mathrm{p}}^k \right\}_{k=1}^{N_f}, \quad \Sigma_{\mathrm{r}} := \left\{ \gamma_{\mathrm{r}}^k \right\}_{k=1}^{N_f},$$

$$\Sigma^k := \left\{ \gamma_{\mathrm{n}}^k, \gamma_{0,\mathrm{p}}^k, \gamma_{\mathrm{r}}^k \right\}, \quad \text{for } k = 1, \ldots, N_f,$$

$$\Sigma := \{ \sigma \in \Sigma^k : k = 1, \ldots, N_f \}. \tag{4.11}$$

The parts of boundary belonging to Σ will play an important role in the sequel, and we assume that Σ satisfies the isotropy Assumption 3.3.3.

In the remaining part of this chapter, the symbol $\lesssim$ will be used to mean any inequality which does not depend on the number N_f of features, on their size, or on the size of their positive extension $\tilde{F}_{\mathrm{p}}^k$, but which can depend on their shape. Moreover, we will write $A \simeq B$ whenever $A \lesssim B$ and $B \lesssim A$.

4.2 Multi-defeaturing error estimator for Poisson's problem

In this section, we generalize the defeaturing error estimator introduced in Chapter 3, in the case of a geometry that presents multiple features. As for the single feature case, we show that in this general setting, the derived estimator is an upper bound and a lower bound (up to oscillations) of the energy norm of the defeaturing error. The key issue in the subsequent analysis is to track the dependence of all constants from the sizes of the features and from their number.

Let us recall the definition of the defeatured solution u_{d} from (4.7), and the definitions of Σ, Σ^k, Σ_{n}, $\Sigma_{0,\mathrm{p}}$ and Σ_{r} from (4.11). Then for all $\sigma \in \Sigma$, let $k_\sigma \equiv k$ if $\sigma \in \Sigma^k$ for some $k = 1, \ldots, N_f$, and to mimic (3.29) in the multi-feature setting, let

$$d_\sigma \equiv \begin{cases} g - \dfrac{\partial u_{\mathrm{d}}}{\partial \mathbf{n}} & \text{if } \sigma \in \Sigma_{\mathrm{n}} \text{ or if } \sigma \in \Sigma_{\mathrm{r}}, \\[2ex] -\left(g_0 + \dfrac{\partial u_{\mathrm{d}}}{\partial \mathbf{n}^{k_\sigma}} \right) & \text{if } \sigma \in \Sigma_{0,\mathrm{p}}. \end{cases} \tag{4.12}$$

Then, we define the *a posteriori* defeaturing error estimator as:

$$\mathscr{E}_D(u_{\mathrm{d}}) := \left(\sum_{\sigma \in \Sigma} \mathscr{E}_D^\sigma(u_{\mathrm{d}})^2 \right)^{\frac{1}{2}}, \tag{4.13}$$

where for all $\sigma \in \Sigma$,

$$\mathscr{E}_D^\sigma(u_{\mathrm{d}}) := \left(|\sigma|^{\frac{1}{n-1}} \left\| d_\sigma - \overline{d_\sigma}^\sigma \right\|_{0,\sigma}^2 + c_\sigma^2 |\sigma|^{\frac{n}{n-1}} \left\| \overline{d_\sigma}^\sigma \right\|_{\ell^2}^2 \right)^{\frac{1}{2}},$$

with c_σ defined as in (3.10). Note that we can rewrite the estimator feature-wise, as follows:

$$\mathscr{E}_D(u_{\mathrm{d}}) = \left(\sum_{k=1}^{N_f} \sum_{\sigma \in \Sigma^k} \mathscr{E}_D^\sigma(u_{\mathrm{d}})^2 \right)^{\frac{1}{2}} = \left(\sum_{k=1}^{N_f} \mathscr{E}_D^k(u_{\mathrm{d}})^2 \right)^{\frac{1}{2}},$$

where for all $k = 1, \ldots, N_f$, we define $\mathscr{E}_D^k(u_k)$ as the defeaturing error estimator for feature F^k, that is,

$$\mathscr{E}_D^k(u_{\mathrm{d}}) := \left(\sum_{\sigma \in \Sigma^k} \mathscr{E}_D^\sigma(u_{\mathrm{d}})^2 \right)^{\frac{1}{2}}. \tag{4.14}$$

In this section, we first show that if the features satisfy the separability Assumption 4.1.5, the quantity $\mathscr{E}_D(u_{\mathrm{d}})$ is a reliable estimator for the defeaturing error, i.e., it is an upper bound for the defeaturing error with a hidden constant that is independent of the number of features N_f and of their size, see Theorem 4.2.3. Then, assuming that all $\sigma \in \Sigma$ are also regular according to Definition 2.1.3, and under mild assumptions for the two-dimensional case, we show that it is also efficient (up to oscillations), i.e., it is a lower bound for the defeaturing error up to oscillations, see Theorem 4.2.4. The proposed estimator indicates that the whole information on the error introduced by defeaturing multiple features, in the energy norm, is encoded in the boundary of the features, and can be accounted by suitably evaluating the error made on the normal derivative of the solution.

Remark 4.2.1. Note that in the estimator $\mathscr{E}_D(u_{\mathrm{d}})$, the terms involving the average values of d_σ only depend on the defeatured problem data (see the similar Remarks 3.2.1 and 3.4.2). As a consequence, if these terms dominate, this means that the defeatured problem data should be more accurately chosen. Moreover, under the following reasonable flux conservation assumptions for all $k = 1, \ldots, N_f$,

$$\int_{\tilde{\gamma}^k} \tilde{g}^k \, \mathrm{d}s = \int_{\gamma_{\mathrm{r}}^k} g \, \mathrm{d}s - \int_{\tilde{F}_{\mathrm{p}}^k \backslash F_{\mathrm{p}}^k} f \, \mathrm{d}x, \qquad \int_{\gamma_{0,\mathrm{p}}^k} g_0 \, \mathrm{d}s = \int_{\gamma_{\mathrm{p}}^k} g \, \mathrm{d}s + \int_{F_{\mathrm{p}}^k} f \, \mathrm{d}x,$$

$$\text{and} \qquad \int_{\gamma_{0,\mathrm{n}}^k} g_0 \, \mathrm{d}s = \int_{\gamma_{\mathrm{n}}^k} g \, \mathrm{d}s - \int_{F_{\mathrm{n}}^k} f \, \mathrm{d}x, \tag{4.15}$$

the defeaturing error estimator (4.13) rewrites $\mathscr{E}_D(u_{\mathrm{d}}) := \left(\sum_{\sigma \in \Sigma} |\sigma|^{\frac{1}{n-1}} \|d_\sigma\|_{0,\sigma}^2 \right)^{\frac{1}{2}}.$

Remark 4.2.2. In a similar fashion as Remarks 3.2.2 and 3.4.3, note that

$$\mathscr{E}_D(u_{\mathrm d}) \lesssim \left(\sum_{\sigma \in \Sigma} c_\sigma^2 \, |\sigma|^{\frac{1}{n-1}} \, \|d_\sigma\|_{0,\sigma}^2 \right)^{\frac{1}{2}} =: \tilde{\mathscr{E}}_D(u_{\mathrm d}).$$

However, when $n = 2$ and under the flux conservation conditions (4.15), $\tilde{\mathscr{E}}_D(u_{\mathrm d})$ is sub-optimal since in this case, $\tilde{\mathscr{E}}_D(u_{\mathrm d}) \lesssim \max_{\sigma \in \Sigma} (c_\sigma) \, \mathscr{E}_D(u_{\mathrm d})$.

4.2.1 Reliability

In this section, we state and prove that the error indicator defined in (4.13) is reliable, that is, it is an upper bound for the defeaturing error.

Theorem 4.2.3. *Let u be the solution of problem (3.2) defined in the exact domain Ω, and let $u_{\mathrm d}$ be the defeaturing solution defined in (4.7). If all $\sigma \in \Sigma$ are isotropic according to Definition 2.1.2, and if the features $\mathfrak{F}$ satisfy Assumption 4.1.5, then the defeaturing error in the energy norm is bounded in terms of the estimator $\mathscr{E}_D(u_{\mathrm d})$ introduced in (4.13) as follows:*

$$|u - u_{\mathrm d}|_{1,\Omega} \lesssim \mathscr{E}_D(u_{\mathrm d}),$$

where the hidden constant is independent of the number of features N_f and of their size.

Proof. This proof is an extension to the one of Theorem 3.4.4. Consider the exact problem (3.1) restricted to $\Omega_\star = \Omega \setminus \overline{F_{\mathrm p}}$ with the natural Neumann boundary condition on $\gamma_{0,\mathrm p}$. That is, since for all $k = 1, \ldots, N_f$, $\mathbf{n}^k = -\mathbf{n}$ on $\gamma_{\mathrm n}^k$, then $u|_{\Omega_\star} \in H^1_{g_D, \Gamma_D}(\Omega_\star)$ is the weak solution of

$$\begin{cases} -\Delta \left(u|_{\Omega_\star} \right) = f & \text{in } \Omega_\star \\ u|_{\Omega_\star} = g_D & \text{on } \Gamma_D \\ \dfrac{\partial \left(u|_{\Omega_\star} \right)}{\partial \mathbf{n}} = g & \text{on } \Gamma_N \setminus \gamma_{\mathrm p} \\ \dfrac{\partial \left(u|_{\Omega_\star} \right)}{\partial \mathbf{n}_0} = \dfrac{\partial u}{\partial \mathbf{n}_0} & \text{on } \gamma_{0,\mathrm p}. \end{cases} \qquad (4.16)$$

By abuse of notation, we omit the explicit restriction of u to $\Omega_\star$. Then for all test functions $v_0 \in H^1_{0,\Gamma_D}(\Omega_\star)$,

$$\int_{\Omega_\star} \nabla u \cdot \nabla v_0 \, \mathrm{d}x = \int_{\Omega_\star} f v_0 \, \mathrm{d}x + \int_{\Gamma_N \setminus \gamma_{\mathrm p}} g v_0 \, \mathrm{d}s + \int_{\gamma_{0,\mathrm p}} \frac{\partial u}{\partial \mathbf{n}_0} v_0 \, \mathrm{d}s. \qquad (4.17)$$

Then, let us consider the simplified problem (3.3) also restricted to $\Omega_\star$, with the natural Neumann boundary condition on $\gamma_{\mathrm n}$. Thus, since $u_{\mathrm d}|_{\Omega_\star} = u_0|_{\Omega_\star}$ by definition, if we omit

the explicit restriction of u_{d} to $\Omega_\star$, then for all $v_0 \in H^1_{0,\Gamma_D}(\Omega_\star)$,

$$\int_{\Omega_\star} \nabla u_{\mathrm{d}} \cdot \nabla v_0 \, \mathrm{d}x = \int_{\Omega_\star} f v_0 \, \mathrm{d}x + \int_{\Gamma_N \setminus \gamma} g v_0 \, \mathrm{d}s + \int_{\gamma_{\mathrm{n}}} \frac{\partial u_{\mathrm{d}}}{\partial \mathbf{n}} v_0 \, \mathrm{d}s + \int_{\gamma_{0,\mathrm{p}}} g_0 v_0 \, \mathrm{d}s. \quad (4.18)$$

Let $e := u - u_{\mathrm{d}} \in H^1_{0,\Gamma_D}(\Omega)$. So from (4.17) and (4.18), for all $v_0 \in H^1_{0,\Gamma_D}(\Omega_\star)$, we obtain

$$\int_{\Omega_\star} \nabla e \cdot \nabla v_0 \, \mathrm{d}x = \int_{\gamma_{\mathrm{n}}} \left(g - \frac{\partial u_{\mathrm{d}}}{\partial \mathbf{n}} \right) v_0 \, \mathrm{d}s + \int_{\gamma_{0,\mathrm{p}}} \left(\frac{\partial u}{\partial \mathbf{n}_0} - g_0 \right) v_0 \, \mathrm{d}s. \quad (4.19)$$

In a very similar fashion, we can deduce that for all $k = 1, \ldots, N_f$ and all $v^k \in H^1\!\left(F^k_{\mathrm{p}} \right)$,

$$\int_{F^k_{\mathrm{p}}} \nabla e \cdot \nabla v^k \, \mathrm{d}x = \int_{\gamma^k_{0,\mathrm{p}}} \frac{\partial (u - u_{\mathrm{d}})}{\partial \mathbf{n}^k} v^k \, \mathrm{d}s + \int_{\gamma^k_{\mathrm{r}}} \left(g - \frac{\partial u_{\mathrm{d}}}{\partial \mathbf{n}^k} \right) v^k \, \mathrm{d}s. \quad (4.20)$$

Let $v \in H^1_{0,\Gamma_D}(\Omega)$, then $v|_{\Omega_\star} \in H^1_{0,\Gamma_D}(\Omega_\star)$ and for all $k = 1, \ldots, N_f$, $v|_{F^k_{\mathrm{p}}} \in H^1(F^k_{\mathrm{p}})$. Therefore, from equations (4.19) and (4.20), since $\mathbf{n}_0 = -\mathbf{n}^{k_\sigma}$ on all $\sigma \in \Sigma_{0,\mathrm{p}}$, and since $\mathbf{n} = \mathbf{n}^{k_\sigma}$ on all $\sigma \in \Sigma_{\mathrm{r}}$, then recalling the definition of d_σ in (4.12), we obtain

$$\int_\Omega \nabla e \cdot \nabla v \, \mathrm{d}x = \sum_{\sigma \in \Sigma} \int_\sigma d_\sigma v \, \mathrm{d}s$$
$$= \sum_{\sigma \in \Sigma} \left[\int_\sigma \left(d_\sigma - \overline{d_\sigma}^\sigma \right) (v - \overline{v}^\sigma) \, \mathrm{d}s + \overline{d_\sigma}^\sigma \int_\sigma v \, \mathrm{d}s \right]. \quad (4.21)$$

For each $\sigma \in \Sigma$, the first terms of (4.21) can be estimated as in (3.17) thanks to Poincaré inequality of Lemma 2.3.8 and trace inequalities, using the domains Ω^k defined in Assumption 4.1.5 for $k = 1, \ldots, N_f$. That is,

$$\sum_{\sigma \in \Sigma} \int_\sigma \left(d_\sigma - \overline{d_\sigma}^\sigma \right) (v - \overline{v}^\sigma) \, \mathrm{d}s$$
$$\leq \sum_{\sigma \in \Sigma} \left\| d_\sigma - \overline{d_\sigma}^\sigma \right\|_{0,\sigma} \| v - \overline{v}^\sigma \|_{0,\sigma} \lesssim \sum_{\sigma \in \Sigma} |\sigma|^{\frac{1}{2(n-1)}} \left\| d_\sigma - \overline{d_\sigma}^\sigma \right\|_{0,\sigma} |v|_{\frac{1}{2},\sigma}$$
$$\lesssim \sum_{\sigma \in \Sigma_{\mathrm{n}} \cup \Sigma_{\mathrm{r}}} |\sigma|^{\frac{1}{2(n-1)}} \left\| d_\sigma - \overline{d_\sigma}^\sigma \right\|_{0,\sigma} \| v \|_{1,\Omega^{k_\sigma}} + \sum_{\sigma \in \Sigma_{0,\mathrm{p}}} |\sigma|^{\frac{1}{2(n-1)}} \left\| d_\sigma - \overline{d_\sigma}^\sigma \right\|_{0,\sigma} \| v \|_{1,\Omega^{k_\sigma} \cap \Omega_\star}.$$
$$(4.22)$$

Then, the last terms of (4.21) can be estimated thanks to Lemma 2.3.9 and trace inequalities, using again the domains Ω^k for $k = 1, \ldots, N_f$. That is,

$$\overline{d_\sigma}^\sigma \int_\sigma v \, \mathrm{d}s \lesssim |\sigma|^{\frac{1}{2}} \left| \overline{d_\sigma}^\sigma \right| \| v \|_{0,\sigma}$$
$$\lesssim \sum_{\sigma \in \Sigma_{\mathrm{n}} \cup \Sigma_{\mathrm{r}}} c_\sigma |\sigma|^{\frac{n}{2(n-1)}} \left| \overline{d_\sigma}^\sigma \right| \| v \|_{\frac{1}{2},\partial\Omega^{k_\sigma}} + \sum_{\sigma \in \Sigma_{0,\mathrm{p}}} c_\sigma |\sigma|^{\frac{n}{2(n-1)}} \left| \overline{d_\sigma}^\sigma \right| \| v \|_{\frac{1}{2},\partial\left(\Omega^{k_\sigma} \cap \Omega_\star\right)}$$
$$\lesssim \sum_{\sigma \in \Sigma_{\mathrm{n}} \cup \Sigma_{\mathrm{r}}} c_\sigma |\sigma|^{\frac{n}{2(n-1)}} \left| \overline{d_\sigma}^\sigma \right| \| v \|_{1,\Omega^{k_\sigma}} + \sum_{\sigma \in \Sigma_{0,\mathrm{p}}} c_\sigma |\sigma|^{\frac{n}{2(n-1)}} \left| \overline{d_\sigma}^\sigma \right| \| v \|_{1,\Omega^{k_\sigma} \cap \Omega_\star}.$$
$$(4.23)$$

81

Thus by choosing $v = e \in H^1_{0,\Gamma_D}(\Omega)$, if we combine (4.21), (4.22) and (4.23), and if we use the discrete Cauchy-Schwarz inequality, we get

$$
|e|^2_{1,\Omega} = \int_\Omega \nabla e \cdot \nabla e \, \mathrm{d}x
$$

$$
\lesssim \left[\sum_{\sigma \in \Sigma} \left(|\sigma|^{\frac{1}{n-1}} \left\| d_\sigma - \overline{d_\sigma}^\sigma \right\|^2_{0,\sigma} + c^2_\sigma |\sigma|^{\frac{n}{n-1}} \left| \overline{d_\sigma}^\sigma \right|^2 \right) \right]^{\frac{1}{2}} \left[\sum_{k=1}^{N_f} \left(\|e\|^2_{1,\Omega^k} + \|e\|^2_{1,\Omega^k \cap \Omega_\star} \right) \right]^{\frac{1}{2}}
$$

$$
\lesssim \mathscr{E}_D(u_\mathrm{d}) \left(\sum_{k=1}^{N_f} \|e\|^2_{1,\Omega^k} \right)^{\frac{1}{2}} \lesssim \mathscr{E}_D(u_\mathrm{d}) |e|_{1,\Omega}.
$$

We can conclude by simplifying on both sides. $\qquad\square$

4.2.2 Efficiency

In this section, we state and prove that the error indicator defined in (4.13) is efficient, that is, it is a lower bound for the defeaturing error, up to oscillations. In the case $n = 2$, the data compatibility conditions (4.15) are also required.

Theorem 4.2.4. *Consider the same notation and assumptions as in Theorem 4.2.3, and assume that all $\sigma \in \Sigma$ are also regular according to Definition 2.1.3. Then, assume that $\left| \gamma^k_\mathrm{n} \right| \simeq \left| \gamma^k_\mathrm{r} \right| \simeq \left| \gamma^k_{0,\mathrm{p}} \right|$ for all $k = 1, \ldots, N_f$. Moreover, for any $m \in \mathbb{N}$, let Π_m be such that $\Pi_m|_\sigma \equiv \Pi_{m,\sigma}$ for all $\sigma \in \Sigma$ where $\Pi_{m,\sigma}$ is the extension of the Clément operator defined in (3.8), and let d^k be such that $d^k|_\sigma \equiv d_\sigma$ on all $\sigma \in \Sigma^k$, for all $k = 1, \ldots, N_f$. Finally, suppose that either $n = 3$, or $n = 2$ and the flux conservation conditions (4.15) are satisfied. Then the defeaturing error, in the energy norm, bounds up to oscillations the estimator $\mathscr{E}_D(u_\mathrm{d})$ introduced in (4.13), that is,*

$$
\mathscr{E}_D(u_\mathrm{d}) \lesssim |u - u_\mathrm{d}|_{1,\Omega} + \mathrm{osc}(u_\mathrm{d}),
$$

where for any $m \in \mathbb{N}$, recalling definition (4.10) of Γ^k,

$$
\mathrm{osc}(u_\mathrm{d})^2 := \sum_{k=1}^{N_f} \left(\mathrm{osc}^k(u_\mathrm{d}) \right)^2, \tag{4.24}
$$

$$
\mathrm{osc}^k(u_\mathrm{d}) := \left| \Gamma^k \right|^{\frac{1}{2(n-1)}} \left\| d^k - \Pi_m \left(d^k \right) \right\|_{0,\Gamma^k} \qquad \text{for } k = 1, \ldots, N_f.
$$

Proof. This proof is an extension to the one of Theorem 3.4.5. Let $e := u - u_\mathrm{d} \in H^1_{0,\Gamma_D}(\Omega)$ and let $k \in \{1, \ldots, N_f\}$. First, recall the definition of Ω^k from Assumption 4.1.5, and let

$$
\Omega^k_\star := \Omega_\star \cap \Omega^k.
$$

Then, let us consider the exact problem (3.1) restricted to $\Omega^k_\star$, with the natural Neumann boundary condition on $\gamma^k_{0,\mathrm{p}}$, and the natural Dirichlet boundary condition on $\partial \Omega^k_\star \setminus \partial \Omega_\star$.

That is, similarly to (4.16), $u|_{\Omega_\star^k}$ is the weak solution of

$$
\begin{cases}
-\Delta\left(u|_{\Omega_\star^k}\right) = f & \text{in } \Omega_\star^k \\
u|_{\Omega_\star^k} = g_D & \text{on } \partial\Omega_\star^k \cap \Gamma_D \\
u|_{\Omega_\star^k} = \mathrm{tr}_{\partial\Omega_\star^k\setminus\partial\Omega_\star}(u) & \text{on } \partial\Omega_\star^k \setminus \partial\Omega_\star \\
\dfrac{\partial\left(u|_{\Omega_\star^k}\right)}{\partial\mathbf{n}} = g & \text{on } \partial\Omega_\star^k \cap \Gamma_N \\
\dfrac{\partial\left(u|_{\Omega_\star^k}\right)}{\partial\mathbf{n}_0} = \dfrac{\partial u}{\partial\mathbf{n}_0} & \text{on } \gamma_{0,\mathrm{p}}^k.
\end{cases}
\tag{4.25}
$$

By abuse of notation, we omit the explicit restriction of u to $\Omega_\star^k$. Then for all test functions $v_0 \in H^1_{0,\partial\Omega_\star^k\setminus[\Gamma_N\cup\gamma_{0,\mathrm{p}}^k]}(\Omega_\star^k)$,

$$
\int_{\Omega_\star^k} \nabla u \cdot \nabla v_0 \,\mathrm{d}x = \int_{\Omega_\star^k} f v_0 \,\mathrm{d}x + \int_{\partial\Omega_\star^k\cap\Gamma_N} g v_0 \,\mathrm{d}s + \int_{\gamma_{0,\mathrm{p}}^k} \frac{\partial u}{\partial\mathbf{n}_0} v_0 \,\mathrm{d}s.
\tag{4.26}
$$

Then, let us consider the simplified problem (3.3) also restricted to $\Omega_\star^k$, with the natural Neumann boundary condition on γ_{n}^k, and the natural Dirichlet boundary condition on $\partial\Omega_\star^k \setminus \partial\Omega_\star$. Thus, since $u_{\mathrm{d}}|_{\Omega_\star^k} = u_0|_{\Omega_\star^k}$ by definition, if we omit the explicit restriction of u_{d} to $\Omega_\star^k$, then for all $v_0 \in H^1_{0,\partial\Omega_\star^k\setminus[\Gamma_N\cup\gamma_{0,\mathrm{p}}^k]}(\Omega_\star^k)$,

$$
\int_{\Omega_\star^k} \nabla u_{\mathrm{d}} \cdot \nabla v_0 \,\mathrm{d}x = \int_{\Omega_\star^k} f v_0 \,\mathrm{d}x + \int_{(\partial\Omega_\star^k\cap\Gamma_N)\setminus\gamma_{\mathrm{n}}^k} g v_0 \,\mathrm{d}s + \int_{\gamma_{\mathrm{n}}^k} \frac{\partial u_{\mathrm{d}}}{\partial\mathbf{n}} v_0 \,\mathrm{d}s + \int_{\gamma_{0,\mathrm{p}}^k} g_0 v_0 \,\mathrm{d}s.
\tag{4.27}
$$

So from (4.26) and (4.27), for all $v_0 \in H^1_{0,\partial\Omega_\star^k\setminus[\Gamma_N\cup\gamma_{0,\mathrm{p}}^k]}(\Omega_\star^k)$,

$$
\int_{\Omega_\star^k} \nabla e \cdot \nabla v_0 \,\mathrm{d}x = \int_{\gamma_{\mathrm{n}}^k} \left(g - \frac{\partial u_{\mathrm{d}}}{\partial\mathbf{n}}\right) v_0 \,\mathrm{d}s + \int_{\gamma_{0,\mathrm{p}}^k} \left(\frac{\partial u}{\partial\mathbf{n}_0} - g_0\right) v_0 \,\mathrm{d}s.
\tag{4.28}
$$

Let $v \in H^1_{0,\partial\Omega^k\setminus\Gamma_N}(\Omega^k)$, so that $v|_{\Omega_\star^k} \in H^1_{0,\partial\Omega_\star^k\setminus[\Gamma_N\cup\gamma_{0,\mathrm{p}}^k]}(\Omega^k)$. Recall that $\Omega_\star = \Omega \setminus \overline{F}_{\mathrm{p}}$, so that $\Omega^k = \mathrm{int}\left(\overline{F_{\mathrm{p}}^k} \cup \overline{\Omega_\star^k}\right)$. Consequently, reusing equation (4.20), using (4.28), since $\mathbf{n}_0 = -\mathbf{n}^k$ on $\gamma_{0,\mathrm{p}}^k$, and since $\mathbf{n} = \mathbf{n}^k$ on γ_{r}^k, then if we recall definition (4.12) of d_σ,

$$
\int_{\Omega^k} \nabla e \cdot \nabla v \,\mathrm{d}x = \int_{\gamma_{\mathrm{n}}^k} \left(g - \frac{\partial u_{\mathrm{d}}}{\partial\mathbf{n}}\right) v \,\mathrm{d}s + \int_{\gamma_{0,\mathrm{p}}^k} \left(-g_0 - \frac{\partial u_{\mathrm{d}}}{\partial\mathbf{n}^k}\right) v \,\mathrm{d}s + \int_{\gamma_{\mathrm{r}}^k} \left(g - \frac{\partial u_{\mathrm{d}}}{\partial\mathbf{n}}\right) v \,\mathrm{d}s
$$

$$
= \sum_{\sigma\in\Sigma^k} \int_\sigma d_\sigma v \,\mathrm{d}s.
$$

Therefore, for all $v \in H^1_{0,\partial\Omega^k\setminus\Gamma_N}(\Omega^k)$,

$$
\sum_{\sigma\in\Sigma^k} \int_\sigma d_\sigma v \,\mathrm{d}s = \int_{\Omega^k} \nabla e \cdot \nabla v \,\mathrm{d}x \leq |e|_{1,\Omega^k} |v|_{1,\Omega^k}.
\tag{4.29}
$$

Now, let $H^{(k)} := \left\{ v \in H^{\frac{1}{2}}_{00}\left(\Gamma^k\right) : v|_\sigma \in H^{\frac{1}{2}}_{00}(\sigma), \text{ for all } \sigma \in \Sigma^k \right\}$ equipped with the norm

$$\|\cdot\|_{H^{(k)}} := \left(\sum_{\sigma \in \Sigma^k} \|\cdot\|^2_{H^{1/2}_{00}(\sigma)} \right)^{\frac{1}{2}},$$

and let $\left(H^{(k)}\right)^*$ be its dual space equipped with the dual norm $\|\cdot\|_{\left(H^{(k)}\right)^*}$. For all $w \in H^{(k)}$, let us define piecewise $u_w \in H^1_{0,\partial\Omega^k\setminus\left(\gamma^k_n \cup \gamma^k_r\right)}\left(\Omega^k\right) \subset H^1_{0,\partial\Omega^k\setminus\Gamma_N}\left(\Omega^k\right)$ as the unique solution of

$$\begin{cases} -\Delta\left(u_w|_{F^k_p}\right) = 0 & \text{in } F^k_p \\ u_w|_{F^k_p} = \left(w|_{\gamma^k_{0,p}\cup\gamma^k_r}\right)^\star & \text{on } \partial F^k_p, \end{cases} \qquad \begin{cases} -\Delta\left(u_w|_{\Omega^k_\star}\right) = 0 & \text{in } \Omega^k_\star \\ u_w|_{\Omega^k_\star} = \left(w|_{\gamma^k_{0,p}\cup\gamma^k_n}\right)^\star & \text{on } \partial\Omega^k_\star, \end{cases}$$

where $\left(w|_{\gamma^k_{0,p}\cup\gamma^k_r}\right)^\star$ and $\left(w|_{\gamma^k_{0,p}\cup\gamma^k_n}\right)^\star$ are the extensions by 0 of $w|_{\gamma^k_{0,p}\cup\gamma^k_r}$ on ∂F^k_p and of $w|_{\gamma^k_{0,p}\cup\gamma^k_n}$ on $\partial\Omega^k_\star$, respectively. Then by continuity of the solution on the data and from Lemma 2.3.11,

$$|u_w|_{1,\Omega^k} \lesssim \left(\|w\|^2_{H^{1/2}_{00}\left(\gamma^k_{0,p}\cup\gamma^k_r\right)} + \|w\|^2_{H^{1/2}_{00}\left(\gamma^k_{0,p}\cup\gamma^k_n\right)} \right)^{\frac{1}{2}} \lesssim \|w\|_{H^{(k)}}. \tag{4.30}$$

So thanks to (4.29) and (4.30), recalling that $d^k|_\sigma = d_\sigma$ on each $\sigma \in \Sigma^k$ by definition, then

$$\left\|d^k\right\|_{\left(H^{(k)}\right)^*} = \sup_{\substack{w \in H^{(k)} \\ w \neq 0}} \frac{\displaystyle\int_{\Gamma^k} d^k w \, ds}{\|w\|_{H^{(k)}}} \lesssim \sup_{\substack{w \in H^{(k)} \\ w \neq 0}} \frac{\displaystyle\sum_{\sigma \in \Sigma^k} \int_\sigma d_\sigma u_w \, ds}{|u_w|_{1,\Omega^k}}$$

$$\leq \sup_{\substack{v \in H^1_{0,\partial\Omega^k\setminus\Gamma_N}\left(\Omega^k\right) \\ v \neq 0}} \frac{\displaystyle\sum_{\sigma \in \Sigma^k} \int_\sigma d_\sigma v \, ds}{|v|_{1,\Omega^k}} \leq |e|_{1,\Omega^k}. \tag{4.31}$$

Moreover, using Remark 4.2.2 if $n = 3$, or Remark 4.2.1 if $n = 2$ and the flux conservation conditions (4.15) are verified, then

$$\mathscr{E}_D(u_d) \lesssim \left(\sum_{k=1}^{N_f} \sum_{\sigma \in \Sigma^k} |\sigma|^{\frac{1}{n-1}} \|d_\sigma\|^2_{0,\sigma} \right)^{\frac{1}{2}}.$$

Therefore, using the triangle inequality and since $\left|\gamma^k_n\right| \simeq \left|\gamma^k_r\right| \simeq \left|\gamma^k_{0,p}\right| \simeq \left|\Gamma^k\right|$ for all $k = 1, \ldots, N_f$, then

$$\sum_{\sigma \in \Sigma^k} |\sigma|^{\frac{1}{n-1}} \|d_\sigma\|^2_{0,\sigma} \lesssim \sum_{\sigma \in \Sigma^k} |\sigma|^{\frac{1}{n-1}} \left(\|\Pi_m\left(d_\sigma\right)\|^2_{0,\sigma} + \|d_\sigma - \Pi_m\left(d_\sigma\right)\|^2_{0,\sigma} \right)$$

$$\lesssim \left|\Gamma^k\right|^{\frac{1}{n-1}} \left\|\Pi_m\left(d^k\right)\right\|^2_{0,\Gamma^k} + \left|\Gamma^k\right|^{\frac{1}{n-1}} \left\|d^k - \Pi_m\left(d^k\right)\right\|^2_{0,\Gamma^k}.$$

Now, we use the definition of the broken norm in $H^{(k)}$ to apply the inverse inequality of Lemma 2.3.12. Recalling the definition of the oscillations in (4.24), and using again the triangle inequality, we thus obtain for all $k = 1, \ldots, N_f$,

$$
\sum_{\sigma \in \Sigma^k} |\sigma|^{\frac{1}{n-1}} \|d_\sigma\|_{0,\sigma}^2 \lesssim \left\| \Pi_m \left(d^k \right) \right\|_{\left(H^{(k)} \right)^*}^2 + \left(\operatorname{osc}^k(u_{\mathrm d}) \right)^2
$$
$$
\lesssim \left\| d^k \right\|_{\left(H^{(k)} \right)^*}^2 + \left\| \Pi_m \left(d^k \right) - d^k \right\|_{\left(H^{(k)} \right)^*}^2 + \left(\operatorname{osc}^k(u_{\mathrm d}) \right)^2.
$$

Finally, using (4.31), and applying Lemma 2.3.11 and Lemma 2.3.7, we obtain

$$
\mathscr{E}_D(u_{\mathrm d})^2 \lesssim \sum_{k=1}^{N_f} \left\| d^k \right\|_{\left(H^{(k)} \right)^*}^2 + \sum_{k=1}^{N_f} \left\| \Pi_m \left(d^k \right) - d^k \right\|_{\left(H^{(k)} \right)^*}^2 + \operatorname{osc}(u_{\mathrm d})^2
$$
$$
\lesssim \sum_{k=1}^{N_f} |e|_{1,\Omega^k}^2 + \sum_{k=1}^{N_f} \left\| \Pi_m \left(d^k \right) - d^k \right\|_{H_{00}^{-1/2}(\Gamma^k)}^2 + \operatorname{osc}(u_{\mathrm d})^2
$$
$$
\lesssim \left(|e|_{1,\Omega} + \operatorname{osc}(u_{\mathrm d}) \right)^2.
$$

This concludes the proof. $\qquad \square$

Remark 4.2.5. When the data is regular, it is always possible to choose m large enough so that the asymptotic behavior of the oscillations is $\mathcal{O} \left(\max\limits_{k=1,\ldots,N_f} \left| \Gamma^k \right|^{m + \frac{1}{2(n-1)}} \right)$. Therefore, we can make sure that the oscillations get small with respect to the defeaturing error, when the features get small.

4.3 Defeaturing in linear elasticity

In this section, we precisely state the defeaturing problem in a geometry on which a linear elasticity problem is defined. We keep the same notation and geometric assumptions as introduced in Section 4.1, as we directly treat the most general case of an exact geometry Ω containing multiple complex features. In this framework and with the help of Section 4.1, we derive an optimal *a posteriori* defeaturing error estimator, and we show its reliability and efficiency.

4.3.1 Defeaturing problem and *a posteriori* error estimator

Let $\Omega \subset \mathbb{R}^n$ be an open Lipschitz domain containing $N_f \geq 1$ complex features satisfying Assumptions 4.1.4 and 4.1.5, and let us first define the exact linear elasticity problem in the exact geometry Ω. To do so, considering a function $\boldsymbol{v} : \Omega \to \mathbb{R}^n$, let

$$
\mathbf{e}(\boldsymbol{v}) := \frac{1}{2} \left(\boldsymbol{\nabla} \boldsymbol{v} + \boldsymbol{\nabla} \boldsymbol{v}^T \right)
$$

be the linearized strain rate tensor, let $\mathbf{s}(\boldsymbol{v})$ be the Cauchy stress tensor in the medium, and let $\mathbb{C}$ denote the fourth-order material tensor. Then the linear elastic regime is governed by the constitutive relation called Hooke's law which is defined by

$$\mathbf{s}(\boldsymbol{v}) := \mathbb{C} : \mathbf{e}(\boldsymbol{v}), \quad \text{i.e.,} \quad \mathbf{s}(\boldsymbol{v})_{ij} = \sum_{k,\ell=1}^{n} \mathbb{C}_{ijk\ell}\,\mathbf{e}(\boldsymbol{v})_{k\ell}, \ \forall i,j=1,\ldots,n.$$

In particular in this work, we consider an isotropic linear elastic material. So if we denote δ the standard Kronecker delta, the components of $\mathbb{C}$ read

$$\mathbb{C}_{ijk\ell} = \lambda\delta_{ij}\delta_{k\ell} + \mu\left(\delta_{ik}\delta_{j\ell} + \delta_{i\ell}\delta_{jk}\right), \quad \forall i,j,k,\ell=1,\ldots,n,$$

where λ and μ denote the phenomenological first and second Lamé coefficients, respectively. That is, the constitutive relation can be rewritten as

$$\mathbf{s}(\boldsymbol{v}) = 2\mu\,\mathbf{e}(\boldsymbol{v}) + \lambda(\boldsymbol{\nabla} \cdot \boldsymbol{v})\mathbb{I}_n, \tag{4.32}$$

where $\mathbb{I}_n$ is the identity tensor in $\mathbb{R}^{n \times n}$. Owing to thermodynamic stability, we know that $\mu > 0$ and $\lambda + \dfrac{2}{3}\mu > 0$. Therefore, we assume that there exist $\mu_{\min}, \kappa_{\min} > 0$ such that

$$\mu, \lambda \in L^\infty(\Omega), \quad \mu(x) \geq \mu_{\min}, \quad \lambda(x) + \frac{2}{3}\mu(x) \geq \kappa_{\min}, \quad \text{a.e. in } \Omega. \tag{4.33}$$

Now, let $\partial\Omega = \overline{\Gamma_D} \cup \overline{\Gamma_N}$ with $\Gamma_D \cap \Gamma_N = \emptyset$, $|\Gamma_D| > 0$, let $\mathbf{n}$ be the unitary outward normal of Ω, and let $\boldsymbol{g}_D \in \boldsymbol{H}^{\frac{3}{2}}(\Gamma_D)$, $\boldsymbol{g} \in \boldsymbol{H}^{\frac{1}{2}}(\Gamma_N)$ and $\boldsymbol{f} \in \boldsymbol{L}^2(\Omega)$. The considered linear elasticity problem in the exact geometry Ω reads as follows:

$$\text{find } \boldsymbol{u} : \Omega \to \mathbb{R}^n, \text{ solution of}$$
$$\begin{cases} -\boldsymbol{\nabla} \cdot \mathbf{s}(\boldsymbol{u}) = \boldsymbol{f} & \text{in } \Omega \\ \boldsymbol{u} = \boldsymbol{g}_D & \text{on } \Gamma_D \\ \mathbf{s}(\boldsymbol{u})\mathbf{n} = \boldsymbol{g} & \text{on } \Gamma_N. \end{cases} \tag{4.34}$$

In the framework presented in Section 2.4, let us formally multiply the first equation of (4.34) by a test function $\boldsymbol{v}$, and let us integrate the resulting equation by parts using the boundary conditions given in (4.34). The weak formulation of the linear elasticity problem then reads:

$$\text{find } \boldsymbol{u} \in \boldsymbol{H}^1_{\boldsymbol{g}_D,\Gamma_D}(\Omega) \text{ such that for all } \boldsymbol{v} \in \boldsymbol{H}^1_{\boldsymbol{0},\Gamma_D}(\Omega),$$
$$\int_\Omega \mathbf{s}(\boldsymbol{u}) : \mathbf{e}(\boldsymbol{v})\,\mathrm{d}x = \int_\Omega \boldsymbol{f} \cdot \boldsymbol{v}\,\mathrm{d}x + \int_{\Gamma_N} \boldsymbol{g} \cdot \boldsymbol{v}\,\mathrm{d}s. \tag{4.35}$$

Let $\boldsymbol{z} := \boldsymbol{R}_{\Gamma_D}(\boldsymbol{g_D}) \in \boldsymbol{H}^1_{\boldsymbol{g}_D,\Gamma_D}(\Omega)$ be a lifting of the Dirichlet data $\boldsymbol{g}_D$ given by Theo-

rem 2.2.1, and for all $\boldsymbol{w}, \boldsymbol{v} \in V := \boldsymbol{H}^1_{\boldsymbol{0}, \Gamma_D}(\Omega)$, let

$$a_\Omega(\boldsymbol{w}, \boldsymbol{v}) := \int_\Omega \mathbf{s}(\boldsymbol{w}) : \mathbf{e}(\boldsymbol{v}) \, \mathrm{d}x, \tag{4.36}$$

$$\mathfrak{f}^{\boldsymbol{z}}_\Omega(\boldsymbol{v}) := \int_\Omega \boldsymbol{f} \cdot \boldsymbol{v} \, \mathrm{d}x + \int_{\Gamma_N} \boldsymbol{g} \cdot \boldsymbol{v} \, \mathrm{d}s - a_\Omega(\boldsymbol{z}, \boldsymbol{v}).$$

Then, finding $\mathring{\boldsymbol{u}} \in V$ such that $a_\Omega(\mathring{\boldsymbol{u}}, \boldsymbol{v}) = \mathfrak{f}^{\boldsymbol{z}}_\Omega(\boldsymbol{v})$ for all $\boldsymbol{v} \in V$ is equivalent to solving (4.35). If we equip V with the norm $\|\boldsymbol{\nabla} \cdot \|_{0,\Omega}$, it can be shown that under the assumptions written in (4.33) on the Lamé coefficients, $a_\Omega(\cdot, \cdot)$ is a continuous and coercive bilinear form on $V \times V$, and $\mathfrak{f}^{\boldsymbol{z}}_\Omega(\cdot)$ is a linear continuous functional, see [Ern and Guermond, 2021b]. Therefore, by Banach-Nečas-Babuška Theorem 2.4.2, problem (4.35) is well-posed.

Let Ω_0 be the defeatured domain as defined in (4.1). To introduce the corresponding defeatured problem, and as for Poisson's equation from Section 4.1, we need to choose an $\boldsymbol{L}^2$-extension of $\boldsymbol{f}$ in the negative components of the features, that we still write $\boldsymbol{f}$ by abuse of notation. Moreover, we assume that the constitutive relation (4.32) governing the linear elastic regime of the body deformation is also valid on functions defined everywhere in Ω_0, with the Lamé coefficients also satisfying (4.33) in the negative components of the features. Finally, recalling the notation from Section 4.1, the analysis is performed under Assumption 4.1.3 on the exact problem (4.34), that is, a Neumann boundary condition is imposed on the boundary of the features.

Then instead of the exact problem (4.34) and similarly to (3.3), the following defeatured problem is solved: after choosing $\boldsymbol{g}_0 \in \boldsymbol{H}^{\frac{1}{2}}(\gamma_0)$, find the weak solution $\boldsymbol{u}_0 \in \boldsymbol{H}^1(\Omega_0)$ of

$$\begin{cases} -\boldsymbol{\nabla} \cdot \mathbf{s}(\boldsymbol{u}_0) = \boldsymbol{f} & \text{in } \Omega_0 \\ \boldsymbol{u}_0 = \boldsymbol{g}_D & \text{on } \Gamma_D \\ \mathbf{s}(\boldsymbol{u}_0)\mathbf{n} = \boldsymbol{g} & \text{on } \Gamma_N \setminus \gamma \\ \mathbf{s}(\boldsymbol{u}_0)\mathbf{n}_0 = \boldsymbol{g}_0 & \text{on } \gamma_0, \end{cases} \tag{4.37}$$

that is, $\boldsymbol{u}_0 \in \boldsymbol{H}^1_{\boldsymbol{g}_D, \Gamma_D}(\Omega_0)$ satisfies for all $\boldsymbol{v}_0 \in \boldsymbol{H}^1_{\boldsymbol{0}, \Gamma_D}(\Omega_0)$,

$$\int_{\Omega_0} \mathbf{s}(\boldsymbol{u}_0) : \mathbf{e}(\boldsymbol{v}_0) \, \mathrm{d}x = \int_{\Omega_0} \boldsymbol{f} \cdot \boldsymbol{v}_0 \, \mathrm{d}x + \int_{\Gamma_N \setminus \gamma} \boldsymbol{g} \cdot \boldsymbol{v}_0 \, \mathrm{d}s + \int_{\gamma_0} \boldsymbol{g}_0 \cdot \boldsymbol{v}_0 \, \mathrm{d}s. \tag{4.38}$$

Using the same arguments as for problem (4.35), we can demonstrate that problem (4.38) is well-posed.

As previously, since we are interested in the energy norm of the defeaturing error "$\boldsymbol{u} - \boldsymbol{u}_0$" in Ω, we need to extend the defeatured solution $\boldsymbol{u}_0$ to the domain extension $\tilde{F}^k_{\mathrm{p}}$ of the positive component F^k_{p} of feature F^k, for all $k = 1, \ldots, N_f$. Thus, let us choose an

L^2-extension of $\boldsymbol{f}$ in $\tilde{F}_{\mathrm{p}}^k$, that we still write $\boldsymbol{f}$ by abuse of notation, and let us assume that the constitutive relation (4.32) governing the linear elastic regime of the body deformation is also valid for functions defined in $\tilde{F}_{\mathrm{p}}^k$, with the Lamé coefficients satisfying (4.33). Then similarly to (4.5), define for all $k = 1, \ldots, N_f$ the following extension of the solution $\boldsymbol{u}_0$ of (4.37) in $\tilde{F}_{\mathrm{p}}^k$: after choosing $\tilde{\boldsymbol{g}}^k \in \boldsymbol{H}^{\frac{1}{2}}(\tilde{\gamma}^k)$, find $\boldsymbol{u}_k \equiv \tilde{\boldsymbol{u}}_0^k \in \boldsymbol{H}^1\left(\tilde{F}_{\mathrm{p}}^k\right)$, the weak solution of

$$
\begin{cases}
-\boldsymbol{\nabla} \cdot \mathbf{s}(\boldsymbol{u}_k) = \boldsymbol{f} & \text{in } \tilde{F}_{\mathrm{p}}^k \\
\boldsymbol{u}_k = \boldsymbol{u}_0 & \text{on } \gamma_{0,\mathrm{p}}^k \\
\mathbf{s}(\boldsymbol{u}_k)\tilde{\mathbf{n}}^k = \tilde{\boldsymbol{g}}^k & \text{on } \tilde{\gamma}^k \\
\mathbf{s}(\boldsymbol{u}_k)\tilde{\mathbf{n}}^k = \boldsymbol{g} & \text{on } \gamma_{\mathrm{s}}^k,
\end{cases}
\tag{4.39}
$$

that is, $\boldsymbol{u}_k \in \boldsymbol{H}^1_{\boldsymbol{u}_0, \gamma_{0,\mathrm{p}}^k}\left(\tilde{F}_{\mathrm{p}}^k\right)$ satisfies for all $\boldsymbol{v}^k \in \boldsymbol{H}^1_{\boldsymbol{0}, \gamma_{0,\mathrm{p}}^k}\left(\tilde{F}_{\mathrm{p}}^k\right)$,

$$
\int_{\tilde{F}_{\mathrm{p}}^k} \mathbf{s}(\boldsymbol{u}_k) : \mathbf{e}(\boldsymbol{v}^k)\,\mathrm{d}x = \int_{\tilde{F}_{\mathrm{p}}^k} \boldsymbol{f} \cdot \boldsymbol{v}^k\,\mathrm{d}x + \int_{\tilde{\gamma}^k} \tilde{\boldsymbol{g}}^k \cdot \boldsymbol{v}^k\,\mathrm{d}s + \int_{\gamma_{\mathrm{s}}^k} \boldsymbol{g} \cdot \boldsymbol{v}^k\,\mathrm{d}s.
\tag{4.40}
$$

Using the same arguments as for problem (4.35), we can demonstrate that problem (4.40) is well-posed.

Finally, recalling that $\Omega_\star := \Omega \setminus \overline{F_{\mathrm{p}}}$, let $\boldsymbol{u}_{\mathrm{d}} \in \boldsymbol{H}^1_{\boldsymbol{g}_D, \Gamma_D}(\Omega)$ be the extended defeatured solution defined in a similar way as (4.7), that is,

$$
\boldsymbol{u}_{\mathrm{d}} \equiv \begin{cases}
\boldsymbol{u}_0|_{\Omega_\star} & \text{in } \Omega_\star \\
\boldsymbol{u}_k|_{F_{\mathrm{p}}^k} = \tilde{\boldsymbol{u}}_0^k|_{F_{\mathrm{p}}^k} & \text{in } F_{\mathrm{p}}^k, \text{ for all } k = 1, \ldots, N_f.
\end{cases}
\tag{4.41}
$$

Then, the defeaturing error is defined by $\|\|\boldsymbol{u} - \boldsymbol{u}_{\mathrm{d}}\|\|_\Omega$, where $\|\|\cdot\|\|_\Omega$ is the energy norm in Ω given by

$$
\|\|\boldsymbol{v}\|\|_\Omega := \left(a_\Omega(\boldsymbol{v}, \boldsymbol{v})\right)^{\frac{1}{2}} = \left(\int_\Omega \mathbf{s}(\boldsymbol{v}) : \mathbf{e}(\boldsymbol{v})\,\mathrm{d}x\right)^{\frac{1}{2}}, \quad \forall \boldsymbol{v} \in \boldsymbol{H}^1_{\boldsymbol{0}, \Gamma_D}(\Omega).
$$

As in Section 4.1, recalling definition (4.11) of Σ, the parts of boundary belonging to Σ will play an important role in the *a posteriori* defeaturing error analysis. In particular, we assume that Σ satisfies the isotropy Assumption 3.3.3.

For all $\sigma \in \Sigma$, recall that we let $k_\sigma \equiv k$ if $\sigma \in \Sigma^k$ for some $k = 1, \ldots, N_f$. Then, let

$$
\boldsymbol{d}_\sigma \equiv \begin{cases}
\boldsymbol{g} - \mathbf{s}(\boldsymbol{u}_{\mathrm{d}})\mathbf{n} & \text{if } \sigma \in \Sigma_{\mathrm{n}} \text{ or if } \sigma \in \Sigma_{\mathrm{r}}, \\
-\left(\boldsymbol{g}_0 + \mathbf{s}(\boldsymbol{u}_{\mathrm{d}})\mathbf{n}^{k_\sigma}\right) & \text{if } \sigma \in \Sigma_{0,\mathrm{p}}.
\end{cases}
\tag{4.42}
$$

We are now able to define the *a posteriori* defeaturing error estimator as

$$
\mathscr{E}_D(\boldsymbol{u}_{\mathrm{d}}) := \left(\sum_{\sigma \in \Sigma} \mathscr{E}_D^\sigma(\boldsymbol{u}_{\mathrm{d}})^2\right)^{\frac{1}{2}},
\tag{4.43}
$$

where for all $\sigma \in \Sigma$,

$$\mathscr{E}_D^\sigma(\boldsymbol{u}_{\mathrm{d}}) := \left(|\sigma|^{\frac{1}{n-1}} \left\| \boldsymbol{d}_\sigma - \overline{\boldsymbol{d}_\sigma}^\sigma \right\|_{0,\sigma}^2 + c_\sigma^2 |\sigma|^{\frac{n}{n-1}} \left\| \overline{\boldsymbol{d}_\sigma}^\sigma \right\|_{\ell^2}^2 \right)^{\frac{1}{2}},$$

with c_σ defined as in (3.10). Note that we can rewrite the estimator feature-wise, as follows:

$$\mathscr{E}_D(\boldsymbol{u}_{\mathrm{d}}) = \left(\sum_{k=1}^{N_f} \sum_{\sigma \in \Sigma^k} \mathscr{E}_D^\sigma(\boldsymbol{u}_{\mathrm{d}})^2 \right)^{\frac{1}{2}} = \left(\sum_{k=1}^{N_f} \mathscr{E}_D^k(\boldsymbol{u}_{\mathrm{d}})^2 \right)^{\frac{1}{2}},$$

where for all $k = 1, \ldots, N_f$, we define $\mathscr{E}_D^k(\boldsymbol{u}_k)$ as the defeaturing error estimator for feature F^k, that is,

$$\mathscr{E}_D^k(\boldsymbol{u}_{\mathrm{d}}) := \left(\sum_{\sigma \in \Sigma^k} \mathscr{E}_D^\sigma(\boldsymbol{u}_{\mathrm{d}})^2 \right)^{\frac{1}{2}}. \tag{4.44}$$

The proposed estimator indicates that all the information on the error introduced by defeaturing, in the energy norm, is encoded in the boundary of the features, and can be accounted by suitably evaluating the error made on the normal traction of the solution.

Remark 4.3.1. As in Remark 4.2.1, the terms involving the component-wise average values of $\boldsymbol{d}_\sigma$ in the estimator $\mathscr{E}_D(\boldsymbol{u}_{\mathrm{d}})$ only depend on the defeatured problem data. As a consequence, if these terms dominate, this means that the defeatured problem data should be more accurately chosen. Moreover, under the following reasonable vectorial data compatibility conditions for all $k = 1, \ldots, N_f$,

$$\int_{\tilde{\gamma}^k} \tilde{\boldsymbol{g}}^k \, \mathrm{d}s = \int_{\gamma_{\mathrm{r}}^k} \boldsymbol{g} \, \mathrm{d}s - \int_{\tilde{F}_{\mathrm{p}}^k \backslash F_{\mathrm{p}}^k} \boldsymbol{f} \, \mathrm{d}x, \qquad \int_{\gamma_{0,\mathrm{p}}^k} \boldsymbol{g}_0 \, \mathrm{d}s = \int_{\gamma_{\mathrm{p}}^k} \boldsymbol{g} \, \mathrm{d}s + \int_{F_{\mathrm{p}}^k} \boldsymbol{f} \, \mathrm{d}x,$$

$$\text{and} \qquad \int_{\gamma_{0,\mathrm{n}}^k} \boldsymbol{g}_0 \, \mathrm{d}s = \int_{\gamma_{\mathrm{n}}^k} \boldsymbol{g} \, \mathrm{d}s - \int_{F_{\mathrm{n}}^k} \boldsymbol{f} \, \mathrm{d}x, \tag{4.45}$$

the defeaturing error estimator (4.43) rewrites $\mathscr{E}_D(\boldsymbol{u}_{\mathrm{d}}) := \left(\sum_{\sigma \in \Sigma} |\sigma|^{\frac{1}{n-1}} \|\boldsymbol{d}_\sigma\|_{0,\sigma}^2 \right)^{\frac{1}{2}}$.

Remark 4.3.2. In a similar fashion as Remark 4.2.2, note that

$$\mathscr{E}_D(\boldsymbol{u}_{\mathrm{d}}) \lesssim \left(\sum_{\sigma \in \Sigma} c_\sigma^2 |\sigma|^{\frac{1}{n-1}} \|\boldsymbol{d}_\sigma\|_{0,\sigma}^2 \right)^{\frac{1}{2}} =: \tilde{\mathscr{E}}_D(\boldsymbol{u}_{\mathrm{d}}).$$

However, when $n = 2$ and under the data compatibility conditions (4.45), $\tilde{\mathscr{E}}_D(\boldsymbol{u}_{\mathrm{d}})$ is sub-optimal since in this case, $\tilde{\mathscr{E}}_D(\boldsymbol{u}_{\mathrm{d}}) \lesssim \max_{\sigma \in \Sigma} (c_\sigma) \, \mathscr{E}_D(\boldsymbol{u}_{\mathrm{d}})$. Indeed, no lower bound can be provided for $\tilde{\mathscr{E}}_D(\boldsymbol{u}_{\mathrm{d}})$.

In the remaining part of this section, we study the properties of the *a posteriori* defeaturing error estimator $\mathscr{E}_D(\boldsymbol{u}_{\mathrm{d}})$. We first show that if the features satisfy the separability

Assumption 4.1.5, the quantity $\mathscr{E}_D(\boldsymbol{u}_{\mathrm{d}})$ is a reliable estimator for the defeaturing error $\|\|\boldsymbol{u} - \boldsymbol{u}_{\mathrm{d}}\|\|_\Omega$, i.e., it is an upper bound for the defeaturing error with a hidden constant that is independent of the number of features N_f and of their size, see Theorem 4.3.3. Then, assuming that all $\sigma \in \Sigma$ are also regular according to Definition 2.1.3, and under mild assumptions for the two-dimensional case, we show that it is also efficient (up to oscillations), i.e., it is a lower bound for the defeaturing error up to oscillations, see Theorem 4.3.4. The key issue in the subsequent analysis is to track the dependence of all constants from the size of the features and from their number.

4.3.2   Reliability

In this section, we state and prove that the error indicator defined in (4.43) is reliable, that is, it is an upper bound for the defeaturing error.

Theorem 4.3.3. *Let $\boldsymbol{u}$ be the solution of problem (4.35), and let $\boldsymbol{u}_{\mathrm{d}}$ be the defeaturing solution defined in (4.41). If all $\sigma \in \Sigma$ are isotropic according to Definition 2.1.2, and if the features $\mathfrak{F}$ are separated as in Assumption 4.1.5, then the defeaturing error in the energy norm is bounded in terms of the estimator $\mathscr{E}_D(\boldsymbol{u}_{\mathrm{d}})$ introduced in (4.43) as follows:*

$$\|\|\boldsymbol{u} - \boldsymbol{u}_{\mathrm{d}}\|\|_\Omega \lesssim \mathscr{E}_D(\boldsymbol{u}_{\mathrm{d}}),$$

where the hidden constant is independent of the number of features N_f and of their size.

Proof. Let us follow similar steps as in the proof of Theorem 4.2.3. So to begin with, consider the exact problem (4.34) restricted to $\Omega_\star = \Omega \setminus \overline{F_{\mathrm{p}}}$ with the natural Neumann boundary condition on $\gamma_{0,\mathrm{p}}$. That is, since for all $k = 1, \ldots, N_f$, $\mathbf{n}^k = -\mathbf{n}$ on γ_{n}^k, then the restriction $\boldsymbol{u}|_{\Omega_\star} \in \boldsymbol{H}_{\boldsymbol{g}_D, \Gamma_D}^1(\Omega_\star)$ is the weak solution of

$$\begin{cases} -\boldsymbol{\nabla} \cdot \mathbf{s}\left(\boldsymbol{u}|_{\Omega_\star}\right) = \boldsymbol{f} & \text{in } \Omega_\star \\ \boldsymbol{u}|_{\Omega_\star} = \boldsymbol{g}_D & \text{on } \Gamma_D \\ \mathbf{s}(\boldsymbol{u}|_{\Omega_\star})\mathbf{n} = \boldsymbol{g} & \text{on } \Gamma_N \setminus \gamma_{\mathrm{p}} \\ \mathbf{s}(\boldsymbol{u}|_{\Omega_\star})\mathbf{n}_0 = \mathbf{s}(\boldsymbol{u})\mathbf{n}_0 & \text{on } \gamma_{0,\mathrm{p}}. \end{cases} \tag{4.46}$$

By abuse of notation, we omit the explicit restriction of $\boldsymbol{u}$ to $\Omega_\star$. Then for all test functions $\boldsymbol{v}_0 \in \boldsymbol{H}_{\boldsymbol{0}, \Gamma_D}^1(\Omega_\star)$,

$$\int_{\Omega_\star} \mathbf{s}(\boldsymbol{u}) : \mathbf{e}(\boldsymbol{v}_0)\,\mathrm{d}x = \int_{\Omega_\star} \boldsymbol{f} \cdot \boldsymbol{v}_0\,\mathrm{d}x + \int_{\Gamma_N \setminus \gamma_{\mathrm{p}}} \boldsymbol{g} \cdot \boldsymbol{v}_0\,\mathrm{d}s + \int_{\gamma_{0,\mathrm{p}}} \mathbf{s}(\boldsymbol{u})\mathbf{n}_0 \cdot \boldsymbol{v}_0\,\mathrm{d}s. \tag{4.47}$$

Then, let us consider the simplified problem (4.37) also restricted to $\Omega_\star$, with the natural Neumann boundary condition on γ_{n}. Thus, since $\boldsymbol{u}_{\mathrm{d}}|_{\Omega_\star} = \boldsymbol{u}_0|_{\Omega_\star}$ by definition, and if we

omit the explicit restriction of $\boldsymbol{u}_{\mathrm{d}}$ to $\Omega_{\star}$, then for all $\boldsymbol{v}_0 \in \boldsymbol{H}^1_{\boldsymbol{0},\Gamma_D}(\Omega_{\star})$,

$$\int_{\Omega_{\star}} \mathbf{s}(\boldsymbol{u}_{\mathrm{d}}) : \mathbf{e}(\boldsymbol{v}_0) \, \mathrm{d}x = \int_{\Omega_{\star}} \boldsymbol{f} \cdot \boldsymbol{v}_0 \, \mathrm{d}x + \int_{\Gamma_N \setminus \gamma} \boldsymbol{g} \cdot \boldsymbol{v}_0 \, \mathrm{d}s + \int_{\gamma_{\mathrm{n}}} \mathbf{s}(\boldsymbol{u}_{\mathrm{d}})\mathbf{n} \cdot \boldsymbol{v}_0 \, \mathrm{d}s + \int_{\gamma_{0,\mathrm{p}}} \boldsymbol{g}_0 \cdot \boldsymbol{v}_0 \, \mathrm{d}s.$$
$$(4.48)$$

Let $\boldsymbol{e} := \boldsymbol{u} - \boldsymbol{u}_{\mathrm{d}} \in \boldsymbol{H}^1_{\boldsymbol{0},\Gamma_D}(\Omega)$. So from (4.47) and (4.48), since $\mathbf{s}$ is linear by definition (see the constitutive relation (4.32)), for all $\boldsymbol{v}_0 \in \boldsymbol{H}^1_{\boldsymbol{0},\Gamma_D}(\Omega_{\star})$, we obtain

$$\int_{\Omega_{\star}} \mathbf{s}(\boldsymbol{e}) : \mathbf{e}(\boldsymbol{v}_0) \, \mathrm{d}x = \int_{\gamma_{\mathrm{n}}} \left(\boldsymbol{g} - \mathbf{s}(\boldsymbol{u}_{\mathrm{d}})\mathbf{n} \right) \cdot \boldsymbol{v}_0 \, \mathrm{d}s + \int_{\gamma_{0,\mathrm{p}}} \left(\mathbf{s}(\boldsymbol{u})\mathbf{n}_0 - \boldsymbol{g}_0 \right) \cdot \boldsymbol{v}_0 \, \mathrm{d}s, \quad (4.49)$$

In a very similar fashion, we can deduce that for all $k = 1, \ldots, N_f$ and all $\boldsymbol{v}^k \in \boldsymbol{H}^1\left(F_{\mathrm{p}}^k \right)$,

$$\int_{F_{\mathrm{p}}^k} \mathbf{s}(\boldsymbol{e}) : \mathbf{e}(\boldsymbol{v}^k) \, \mathrm{d}x = \int_{\gamma_{0,\mathrm{p}}^k} \left(\mathbf{s}(\boldsymbol{u}) - \mathbf{s}(\boldsymbol{u}_{\mathrm{d}}) \right)\mathbf{n}^k \cdot \boldsymbol{v}^k \, \mathrm{d}s + \int_{\gamma_{\mathrm{r}}^k} \left(\boldsymbol{g} - \mathbf{s}(\boldsymbol{u}_{\mathrm{d}})\mathbf{n}^k \right) \cdot \boldsymbol{v}^k \, \mathrm{d}s. \quad (4.50)$$

Therefore, let $\boldsymbol{v} \in \boldsymbol{H}^1_{\boldsymbol{0},\Gamma_D}(\Omega)$, then $\boldsymbol{v}|_{\Omega_{\star}} \in \boldsymbol{H}^1_{\boldsymbol{0},\Gamma_D}(\Omega_{\star})$ and $\boldsymbol{v}|_{F_{\mathrm{p}}^k} \in \boldsymbol{H}^1(F_{\mathrm{p}}^k)$ for all $k = 1, \ldots, N_f$. Therefore, from equations (4.49) and (4.50), since $\mathbf{n}_0 = -\mathbf{n}^{k_\sigma}$ on all $\sigma \in \Sigma_{0,\mathrm{p}}$, and since $\mathbf{n} = \mathbf{n}^{k_\sigma}$ on all $\sigma \in \Sigma_{\mathrm{r}}$, then recalling the definitions of $a_\Omega(\cdot,\cdot)$ in (4.36) and of $\boldsymbol{d}_\sigma$ in (4.42), we obtain

$$a_\Omega(\boldsymbol{e}, \boldsymbol{v}) = \int_\Omega \mathbf{s}(\boldsymbol{e}) : \mathbf{e}(\boldsymbol{v}) \, \mathrm{d}x = \sum_{\sigma \in \Sigma} \int_\sigma \boldsymbol{d}_\sigma \cdot \boldsymbol{v} \, \mathrm{d}s \qquad (4.51)$$

$$= \sum_{\sigma \in \Sigma} \left[\int_\sigma \left(\boldsymbol{d}_\sigma - \overline{\boldsymbol{d}_\sigma}^\sigma \right) \cdot (\boldsymbol{v} - \overline{\boldsymbol{v}}^\sigma) \, \mathrm{d}s + \overline{\boldsymbol{d}_\sigma}^\sigma \cdot \int_\sigma \boldsymbol{v} \, \mathrm{d}s \right]. \qquad (4.52)$$

For each $\sigma \in \Sigma$, the first terms of (4.52) can be estimated as in (3.17) thanks to the Poincaré inequality of Lemma 2.3.8 and trace inequalities, using the domains Ω^k defined in Assumption 4.1.5 for $k = 1, \ldots, N_f$. That is,

$$\sum_{\sigma \in \Sigma} \int_\sigma \left(\boldsymbol{d}_\sigma - \overline{\boldsymbol{d}_\sigma}^\sigma \right) \cdot (\boldsymbol{v} - \overline{\boldsymbol{v}}^\sigma) \, \mathrm{d}s$$

$$\lesssim \sum_{\sigma \in \Sigma} \left\| \boldsymbol{d}_\sigma - \overline{\boldsymbol{d}_\sigma}^\sigma \right\|_{0,\sigma} \| \boldsymbol{v} - \overline{\boldsymbol{v}}^\sigma \|_{0,\sigma} \lesssim \sum_{\sigma \in \Sigma} |\sigma|^{\frac{1}{2(n-1)}} \left\| \boldsymbol{d}_\sigma - \overline{\boldsymbol{d}_\sigma}^\sigma \right\|_{0,\sigma} |\boldsymbol{v}|_{\frac{1}{2},\sigma}$$

$$\lesssim \sum_{\sigma \in \Sigma_{\mathrm{n}} \cup \Sigma_{\mathrm{r}}} |\sigma|^{\frac{1}{2(n-1)}} \left\| \boldsymbol{d}_\sigma - \overline{\boldsymbol{d}_\sigma}^\sigma \right\|_{0,\sigma} \| \boldsymbol{v} \|_{1,\Omega^{k_\sigma}} + \sum_{\sigma \in \Sigma_{0,\mathrm{p}}} |\sigma|^{\frac{1}{2(n-1)}} \left\| \boldsymbol{d}_\sigma - \overline{\boldsymbol{d}_\sigma}^\sigma \right\|_{0,\sigma} \| \boldsymbol{v} \|_{1,\Omega^{k_\sigma} \cap \Omega_{\star}}.$$
$$(4.53)$$

Then, the last terms of (4.52) can be estimated thanks to Lemma 2.3.9 and trace

91

inequalities, using again the domains Ω^k for $k = 1, \ldots, N_f$. That is,

$$
\begin{aligned}
\overline{\boldsymbol{d}_\sigma}^\sigma \cdot \int_\sigma \boldsymbol{v} \, \mathrm{d}s &\lesssim |\sigma|^{\frac{1}{2}} \left\| \overline{\boldsymbol{d}_\sigma}^\sigma \right\|_{\ell^2} \|\boldsymbol{v}\|_{0,\sigma} \\
&\lesssim \sum_{\sigma \in \Sigma_\mathrm{n} \cup \Sigma_\mathrm{r}} c_\sigma |\sigma|^{\frac{n}{2(n-1)}} \left\| \overline{\boldsymbol{d}_\sigma}^\sigma \right\|_{\ell^2} \|\boldsymbol{v}\|_{\frac{1}{2}, \partial \Omega^{k_\sigma}} \\
&\quad + \sum_{\sigma \in \Sigma_{0,\mathrm{p}}} c_\sigma |\sigma|^{\frac{n}{2(n-1)}} \left\| \overline{\boldsymbol{d}_\sigma}^\sigma \right\|_{\ell^2} \|\boldsymbol{v}\|_{\frac{1}{2}, \partial(\Omega^{k_\sigma} \cap \Omega_\star)} \\
&\lesssim \sum_{\sigma \in \Sigma_\mathrm{n} \cup \Sigma_\mathrm{r}} c_\sigma |\sigma|^{\frac{n}{2(n-1)}} \left\| \overline{\boldsymbol{d}_\sigma}^\sigma \right\|_{\ell^2} \|\boldsymbol{v}\|_{1, \Omega^{k_\sigma}} \\
&\quad + \sum_{\sigma \in \Sigma_{0,\mathrm{p}}} c_\sigma |\sigma|^{\frac{n}{2(n-1)}} \left\| \overline{\boldsymbol{d}_\sigma}^\sigma \right\|_{\ell^2} \|\boldsymbol{v}\|_{1, \Omega^{k_\sigma} \cap \Omega_\star}.
\end{aligned}
\tag{4.54}
$$

Thus by choosing $\boldsymbol{v} = \boldsymbol{e} \in \boldsymbol{H}^1_{0,\Gamma_D}(\Omega)$, if we combine (4.52), (4.53) and (4.54), and if we use the discrete Cauchy-Schwarz inequality, we get

$$
\begin{aligned}
\|\|\boldsymbol{e}\|\|^2_\Omega = a_\Omega(\boldsymbol{e}, \boldsymbol{e}) &\lesssim \left[\sum_{\sigma \in \Sigma} \left(|\sigma|^{\frac{1}{n-1}} \left\| \boldsymbol{d}_\sigma - \overline{\boldsymbol{d}_\sigma}^\sigma \right\|^2_{0,\sigma} + c_\sigma^2 |\sigma|^{\frac{n}{n-1}} \left\| \overline{\boldsymbol{d}_\sigma}^\sigma \right\|^2_{\ell^2} \right) \right]^{\frac{1}{2}} \\
&\quad \left[\sum_{k=1}^{N_f} \left(\|\boldsymbol{e}\|^2_{1,\Omega^k} + \|\boldsymbol{e}\|^2_{1,\Omega^k \cap \Omega_\star} \right) \right]^{\frac{1}{2}} \\
&\lesssim \mathscr{E}_D(\boldsymbol{u}_\mathrm{d}) \left(\sum_{k=1}^{N_f} \|\boldsymbol{e}\|^2_{1,\Omega^k} \right)^{\frac{1}{2}} \lesssim \mathscr{E}_D(\boldsymbol{u}_\mathrm{d}) \|\boldsymbol{\nabla} \boldsymbol{e}\|_{0,\Omega}.
\end{aligned}
\tag{4.55}
$$

Finally, using the coercivity of $a_\Omega(\cdot, \cdot)$ in $\boldsymbol{H}^1_{0,\Gamma_D}(\Omega)$ equipped with the norm $\|\boldsymbol{\nabla} \cdot \|_{0,\Omega}$, then

$$
\|\|\boldsymbol{e}\|\|^2_\Omega \lesssim \mathscr{E}_D(\boldsymbol{u}_\mathrm{d}) \|\boldsymbol{\nabla} \boldsymbol{e}\|_{0,\Omega} \lesssim \mathscr{E}_D(\boldsymbol{u}_\mathrm{d}) \left(a_\Omega(\boldsymbol{e}, \boldsymbol{e}) \right)^{\frac{1}{2}} = \mathscr{E}_D(\boldsymbol{u}_\mathrm{d}) \|\|\boldsymbol{e}\|\|_\Omega,
\tag{4.56}
$$

and we can conclude by simplifying on both sides. $\qquad \square$

4.3.3 Efficiency

In this section, we state and prove that the error indicator defined in (4.43) is efficient, that is, it is a lower bound for the defeaturing error, up to oscillations. In the case $n = 2$, the data compatibility conditions (4.45) are also required.

Theorem 4.3.4. *Consider the same notation and assumptions as in Theorem 4.3.3, and assume that all $\sigma \in \Sigma$ are also regular according to Definition 2.1.3. Then, assume that $\left| \gamma_\mathrm{n}^k \right| \simeq \left| \gamma_\mathrm{r}^k \right| \simeq \left| \gamma_{0,\mathrm{p}}^k \right|$ for all $k = 1, \ldots, N_f$. Moreover, for any $m \in \mathbb{N}$, let $\boldsymbol{\Pi}_m$ be such that $\boldsymbol{\Pi}_m|_\sigma \equiv \boldsymbol{\Pi}_{m,\sigma}$ for all $\sigma \in \Sigma$, where $\boldsymbol{\Pi}_{m,\sigma}$ is the component-wise extension of the Clément operator defined in (3.8), and let $\boldsymbol{d}^k$ be such that $\boldsymbol{d}^k|_\sigma \equiv \boldsymbol{d}_\sigma$ on all $\sigma \in \Sigma^k$, for all $k = 1, \ldots, N_f$. Finally, suppose that either $n = 3$, or $n = 2$ and the data compatibility*

conditions (4.45) are satisfied. Then the defeaturing error, in the energy norm, bounds up to oscillations the estimator $\mathscr{E}_D(\boldsymbol{u}_{\mathrm{d}})$ introduced in (4.43), that is,

$$\mathscr{E}_D(\boldsymbol{u}_{\mathrm{d}}) \lesssim \|\!|\boldsymbol{u} - \boldsymbol{u}_{\mathrm{d}}|\!\|_\Omega + \mathrm{osc}(\boldsymbol{u}_{\mathrm{d}}),$$

where for any $m \in \mathbb{N}$, recalling definition (4.10) of Γ^k,

$$\mathrm{osc}(\boldsymbol{u}_{\mathrm{d}})^2 := \sum_{k=1}^{N_f} \left(\mathrm{osc}^k(\boldsymbol{u}_{\mathrm{d}}) \right)^2, \tag{4.57}$$

$$\mathrm{osc}^k(\boldsymbol{u}_{\mathrm{d}}) := \left| \Gamma^k \right|^{\frac{1}{2(n-1)}} \left\| \boldsymbol{d}^k - \boldsymbol{\Pi}_m \left(\boldsymbol{d}^k \right) \right\|_{0,\Gamma^k} \quad for\ k = 1, \ldots, N_f.$$

Proof. This proof follows similar steps as in the proof of Theorem 4.2.4. So let us define $\boldsymbol{e} := \boldsymbol{u} - \boldsymbol{u}_{\mathrm{d}} \in \boldsymbol{H}^1_{\boldsymbol{0},\Gamma_D}(\Omega)$ and let $k \in \{1, \ldots, N_f\}$. First, let us recall the definition of $\Omega_\star^k := \Omega_\star \cap \Omega^k$, where Ω^k is the domain associated to feature F^k defined in Assumption 4.1.5. Then, let us consider the exact problem (4.34) restricted to $\Omega_\star^k$, with the natural Neumann boundary condition on $\gamma_{0,\mathrm{p}}^k$, and the natural Dirichlet boundary condition on $\partial\Omega_\star^k \setminus \partial\Omega_\star$. That is, similarly to (4.46), $\boldsymbol{u}|_{\Omega_\star^k}$ is the weak solution of

$$\begin{cases} -\nabla \cdot \mathbf{s}\left(\boldsymbol{u}|_{\Omega_\star^k} \right) = \boldsymbol{f} & \text{in } \Omega_\star^k \\ \boldsymbol{u}|_{\Omega_\star^k} = \boldsymbol{g}_D & \text{on } \partial\Omega_\star^k \cap \Gamma_D \\ \boldsymbol{u}|_{\Omega_\star^k} = \mathrm{tr}_{\partial\Omega_\star^k \setminus \partial\Omega_\star}(\boldsymbol{u}) & \text{on } \partial\Omega_\star^k \setminus \partial\Omega_\star \\ \mathbf{s}\left(\boldsymbol{u}|_{\Omega_\star^k} \right) \mathbf{n} = \boldsymbol{g} & \text{on } \partial\Omega_\star^k \cap \Gamma_N \\ \mathbf{s}\left(\boldsymbol{u}|_{\Omega_\star^k} \right) \mathbf{n}_0 = \mathbf{s}(\boldsymbol{u})\mathbf{n}_0 & \text{on } \gamma_{0,\mathrm{p}}^k. \end{cases} \tag{4.58}$$

By abuse of notation, we omit the explicit restriction of $\boldsymbol{u}$ to $\Omega_\star^k$. Then for all test functions $\boldsymbol{v}_0 \in \boldsymbol{H}^1_{\boldsymbol{0},\partial\Omega_\star^k \setminus \left[\Gamma_N \cup \gamma_{0,\mathrm{p}}^k\right]}(\Omega_\star^k)$,

$$\int_{\Omega_\star^k} \mathbf{s}(\boldsymbol{u}) : \mathbf{e}(\boldsymbol{v}_0)\,\mathrm{d}x = \int_{\Omega_\star^k} \boldsymbol{f} \cdot \boldsymbol{v}_0\,\mathrm{d}x + \int_{\partial\Omega_\star^k \cap \Gamma_N} \boldsymbol{g} \cdot \boldsymbol{v}_0\,\mathrm{d}s + \int_{\gamma_{0,\mathrm{p}}^k} \mathbf{s}(\boldsymbol{u})\mathbf{n}_0 \cdot \boldsymbol{v}_0\,\mathrm{d}s. \tag{4.59}$$

Then, let us consider the simplified problem (4.37) also restricted to $\Omega_\star^k$, with the natural Neumann boundary condition on γ_{n}^k, and the natural Dirichlet boundary condition on $\partial\Omega_\star^k \setminus \partial\Omega_\star$. Thus, since $\boldsymbol{u}_{\mathrm{d}}|_{\Omega_\star^k} = \boldsymbol{u}_0|_{\Omega_\star^k}$ by definition, if we omit the explicit restriction of $\boldsymbol{u}_{\mathrm{d}}$ to $\Omega_\star^k$, then for all $\boldsymbol{v}_0 \in \boldsymbol{H}^1_{\boldsymbol{0},\partial\Omega_\star^k \setminus \left[\Gamma_N \cup \gamma_{0,\mathrm{p}}^k\right]}(\Omega_\star^k)$,

$$\int_{\Omega_\star^k} \mathbf{s}(\boldsymbol{u}_{\mathrm{d}}) : \mathbf{e}(\boldsymbol{v}_0)\,\mathrm{d}x = \int_{\Omega_\star^k} \boldsymbol{f} \cdot \boldsymbol{v}_0\,\mathrm{d}x + \int_{\left(\partial\Omega_\star^k \cap \Gamma_N\right) \setminus \gamma_{\mathrm{n}}^k} \boldsymbol{g} \cdot \boldsymbol{v}_0\,\mathrm{d}s$$

$$+ \int_{\gamma_{\mathrm{n}}^k} \mathbf{s}(\boldsymbol{u}_{\mathrm{d}})\mathbf{n} \cdot \boldsymbol{v}_0\,\mathrm{d}s + \int_{\gamma_{0,\mathrm{p}}^k} \boldsymbol{g}_0 \cdot \boldsymbol{v}_0\,\mathrm{d}s. \tag{4.60}$$

So from (4.59) and (4.60) and by linearity of $\mathbf{s}$, for all $\boldsymbol{v}_0 \in \boldsymbol{H}^1_{\mathbf{0},\partial\Omega_\star^k\backslash[\Gamma_N\cup\gamma_{0,\mathrm{p}}^k]}(\Omega_\star^k)$,

$$\int_{\Omega_\star^k} \mathbf{s}(\boldsymbol{e}) : \mathbf{e}(\boldsymbol{v}_0)\,\mathrm{d}x = \int_{\gamma_\mathrm{n}^k} \left(\boldsymbol{g} - \mathbf{s}(\boldsymbol{u}_\mathrm{d})\mathbf{n}\right)\cdot\boldsymbol{v}_0\,\mathrm{d}s + \int_{\gamma_{0,\mathrm{p}}^k}\left(\mathbf{s}(\boldsymbol{u})\mathbf{n}_0 - \boldsymbol{g}_0\right)\cdot\boldsymbol{v}_0\,\mathrm{d}s. \quad (4.61)$$

Let $\boldsymbol{v} \in \boldsymbol{H}^1_{\mathbf{0},\partial\Omega^k\backslash\Gamma_N}(\Omega^k)$, so that $\boldsymbol{v}|_{\Omega_\star^k} \in \boldsymbol{H}^1_{\mathbf{0},\partial\Omega_\star^k\backslash[\Gamma_N\cup\gamma_{0,\mathrm{p}}^k]}(\Omega_\star^k)$. Recall that $\Omega_\star = \Omega\setminus\overline{F_\mathrm{p}}$, so that $\Omega^k = \mathrm{int}\left(F_\mathrm{p}^k \cup \Omega_\star^k\right)$. Consequently, reusing equation (4.50), using (4.61), since $\mathbf{n}_0 = -\mathbf{n}^k$ on $\gamma_{0,\mathrm{p}}^k$, and since $\mathbf{n} = \mathbf{n}^k$ on γ_r^k, then if we recall definition (4.42) of $\boldsymbol{d}_\sigma$,

$$\begin{aligned}
\int_{\Omega^k} \mathbf{s}(\boldsymbol{e}) : \mathbf{e}(\boldsymbol{v})\,\mathrm{d}x &= \int_{\gamma_\mathrm{n}^k}\left(\boldsymbol{g} - \mathbf{s}(\boldsymbol{u}_\mathrm{d})\mathbf{n}\right)\cdot\boldsymbol{v}\,\mathrm{d}s + \int_{\gamma_{0,\mathrm{p}}^k}\left(-\boldsymbol{g}_0 - \mathbf{s}(\boldsymbol{u}_\mathrm{d})\mathbf{n}^k\right)\cdot\boldsymbol{v}\,\mathrm{d}s \\
&\quad + \int_{\gamma_\mathrm{r}^k}\left(\boldsymbol{g} - \mathbf{s}(\boldsymbol{u}_\mathrm{d})\mathbf{n}\right)\cdot\boldsymbol{v}\,\mathrm{d}s \\
&= \sum_{\sigma\in\Sigma^k}\int_\sigma \boldsymbol{d}_\sigma\cdot\boldsymbol{v}\,\mathrm{d}s.
\end{aligned} \quad (4.62)$$

Now, let $a_{\Omega^k}(\cdot,\cdot) : \boldsymbol{H}^1_{\mathbf{0},\partial\Omega^k\backslash\Gamma_N}(\Omega^k) \times \boldsymbol{H}^1_{\mathbf{0},\partial\Omega^k\backslash\Gamma_N}(\Omega^k) \to \mathbb{R}$ be defined by

$$a_{\Omega^k}(\boldsymbol{w},\boldsymbol{v}) = \int_{\Omega^k}\mathbf{s}(\boldsymbol{w}) : \mathbf{e}(\boldsymbol{v})\,\mathrm{d}x, \qquad \forall\boldsymbol{w},\boldsymbol{v}\in H^1_{\mathbf{0},\partial\Omega^k\backslash\Gamma_N}(\Omega^k).$$

Note that $a_{\Omega^k}(\cdot,\cdot)$ is continuous with respect to the norm $\|\boldsymbol{\nabla}\cdot\|_{0,\Omega^k}$. Thus using (4.62), for all $\boldsymbol{v}\in\boldsymbol{H}^1_{\mathbf{0},\partial\Omega^k\backslash\Gamma_N}(\Omega^k)$,

$$\sum_{\sigma\in\Sigma^k}\int_\sigma \boldsymbol{d}_\sigma\cdot\boldsymbol{v}\,\mathrm{d}s = \int_{\Omega^k}\mathbf{s}(\boldsymbol{e}):\mathbf{e}(\boldsymbol{v})\,\mathrm{d}x = a_{\Omega^k}(\boldsymbol{e},\boldsymbol{v}) \lesssim \|\boldsymbol{\nabla}e\|_{0,\Omega^k}\|\boldsymbol{\nabla}\boldsymbol{v}\|_{0,\Omega^k}. \quad (4.63)$$

Now, let $\boldsymbol{H}^{(k)} := \left\{\boldsymbol{v} \in \boldsymbol{H}^{\frac{1}{2}}_{00}\left(\Gamma^k\right) : \boldsymbol{v}|_\sigma \in \boldsymbol{H}^{\frac{1}{2}}_{00}(\sigma), \text{ for all } \sigma\in\Sigma^k\right\}$ equipped with the norm

$$\|\cdot\|_{\boldsymbol{H}^{(k)}} := \left(\sum_{\sigma\in\Sigma^k}\|\cdot\|^2_{\boldsymbol{H}^{1/2}_{00}(\sigma)}\right)^{\frac{1}{2}},$$

and let $\left(\boldsymbol{H}^{(k)}\right)^*$ be its dual space equipped with the dual norm $\|\cdot\|_{\left(\boldsymbol{H}^{(k)}\right)^*}$. For all $\boldsymbol{w}\in\boldsymbol{H}^{(k)}$, let us define piecewise $\boldsymbol{u}_{\boldsymbol{w}}\in\boldsymbol{H}^1_{\mathbf{0},\partial\Omega^k\backslash(\gamma_\mathrm{n}^k\cup\gamma_\mathrm{r}^k)}\left(\Omega^k\right) \subset \boldsymbol{H}^1_{\mathbf{0},\partial\Omega^k\backslash\Gamma_N}\left(\Omega^k\right)$ as the unique solution of

$$\begin{cases} -\boldsymbol{\nabla}\cdot\mathbf{s}\left(\boldsymbol{u}_{\boldsymbol{w}}|_{F_\mathrm{p}^k}\right) = \mathbf{0} & \text{in } F_\mathrm{p}^k \\ \boldsymbol{u}_{\boldsymbol{w}}|_{F_\mathrm{p}^k} = \left(\boldsymbol{w}|_{\gamma_{0,\mathrm{p}}^k\cup\gamma_\mathrm{r}^k}\right)^\star & \text{on } \partial F_\mathrm{p}^k, \end{cases} \qquad \begin{cases} -\boldsymbol{\nabla}\cdot\mathbf{s}\left(\boldsymbol{u}_{\boldsymbol{w}}|_{\Omega_\star^k}\right) = \mathbf{0} & \text{in } \Omega_\star^k \\ \boldsymbol{u}_{\boldsymbol{w}}|_{\Omega_\star^k} = \left(\boldsymbol{w}|_{\gamma_{0,\mathrm{p}}^k\cup\gamma_\mathrm{n}^k}\right)^\star & \text{on } \partial\Omega_\star^k, \end{cases}$$

where $\left(\boldsymbol{w}|_{\gamma_{0,\mathrm{p}}^k\cup\gamma_\mathrm{r}^k}\right)^\star$ and $\left(\boldsymbol{w}|_{\gamma_{0,\mathrm{p}}^k\cup\gamma_\mathrm{n}^k}\right)^\star$ are the extensions by $\mathbf{0}$ of $\boldsymbol{w}|_{\gamma_{0,\mathrm{p}}^k\cup\gamma_\mathrm{r}^k}$ on ∂F_p^k and of $\boldsymbol{w}|_{\gamma_{0,\mathrm{p}}^k\cup\gamma_\mathrm{n}^k}$ on $\partial\Omega_\star^k$, respectively. Then by continuity of the solution on the data and from

Lemma 2.3.11,

$$\|\boldsymbol{\nabla}\boldsymbol{u_w}\|_{0,\Omega^k} \lesssim \left(\|\boldsymbol{w}\|^2_{\boldsymbol{H}^{1/2}_{00}(\gamma^k_{0,\mathrm{p}}\cup\gamma^k_{\mathrm{r}})} + \|\boldsymbol{w}\|^2_{\boldsymbol{H}^{1/2}_{00}(\gamma^k_{0,\mathrm{p}}\cup\gamma^k_{\mathrm{n}})} \right)^{\frac{1}{2}} \lesssim \|\boldsymbol{w}\|_{\boldsymbol{H}^{(k)}}. \tag{4.64}$$

So thanks to (4.63) and (4.64), recalling that $\boldsymbol{d}^k|_\sigma = \boldsymbol{d}_\sigma$ on each $\sigma \in \Sigma^k$ by definition, then

$$\left\|\boldsymbol{d}^k\right\|_{(\boldsymbol{H}^{(k)})^*} = \sup_{\substack{\boldsymbol{w}\in\boldsymbol{H}^{(k)}\\\boldsymbol{w}\neq\boldsymbol{0}}} \frac{\int_{\Gamma^k} \boldsymbol{d}^k \cdot \boldsymbol{w}\,\mathrm{d}s}{\|\boldsymbol{w}\|_{\boldsymbol{H}^{(k)}}} \lesssim \sup_{\substack{\boldsymbol{w}\in\boldsymbol{H}^{(k)}\\\boldsymbol{w}\neq\boldsymbol{0}}} \frac{\displaystyle\sum_{\sigma\in\Sigma^k}\int_\sigma \boldsymbol{d}_\sigma \cdot \boldsymbol{u_w}\,\mathrm{d}s}{\|\boldsymbol{\nabla}\boldsymbol{u_w}\|_{0,\Omega^k}}$$

$$\leq \sup_{\substack{\boldsymbol{v}\in\boldsymbol{H}^1_{\boldsymbol{0},\partial\Omega^k\setminus\Gamma_N}(\Omega^k)\\\boldsymbol{v}\neq\boldsymbol{0}}} \frac{\displaystyle\sum_{\sigma\in\Sigma^k}\int_\sigma \boldsymbol{d}_\sigma \cdot \boldsymbol{v}\,\mathrm{d}s}{\|\boldsymbol{\nabla}\boldsymbol{v}\|_{0,\Omega^k}} \leq \|\boldsymbol{\nabla}\boldsymbol{e}\|_{0,\Omega^k}. \tag{4.65}$$

Moreover, using Remark 4.3.2 if $n = 3$, or Remark 4.3.1 if $n = 2$ and the data compatibility conditions (4.45) are satisfied, then

$$\mathscr{E}_D(\boldsymbol{u}_\mathrm{d}) \lesssim \left(\sum_{k=1}^{N_f} \sum_{\sigma\in\Sigma^k} |\sigma|^{\frac{1}{n-1}} \|\boldsymbol{d}_\sigma\|^2_{0,\sigma} \right)^{\frac{1}{2}}.$$

Therefore, using the triangle inequality and since $\left|\gamma^k_\mathrm{n}\right| \simeq \left|\gamma^k_\mathrm{r}\right| \simeq \left|\gamma^k_{0,\mathrm{p}}\right| \simeq \left|\Gamma^k\right|$ for all $k = 1, \dots, N_f$, then

$$\sum_{\sigma\in\Sigma^k} |\sigma|^{\frac{1}{n-1}} \|\boldsymbol{d}_\sigma\|^2_{0,\sigma} \lesssim \sum_{\sigma\in\Sigma^k} |\sigma|^{\frac{1}{n-1}} \left(\|\boldsymbol{\Pi}_m(\boldsymbol{d}_\sigma)\|^2_{0,\sigma} + \|\boldsymbol{d}_\sigma - \boldsymbol{\Pi}_m(\boldsymbol{d}_\sigma)\|^2_{0,\sigma} \right)$$

$$\lesssim \left|\Gamma^k\right|^{\frac{1}{n-1}} \left\|\boldsymbol{\Pi}_m\left(\boldsymbol{d}^k\right)\right\|^2_{0,\Gamma^k} + \left|\Gamma^k\right|^{\frac{1}{n-1}} \left\|\boldsymbol{d}^k - \boldsymbol{\Pi}_m\left(\boldsymbol{d}^k\right)\right\|^2_{0,\Gamma^k}.$$

Now, we use the definition of the broken norm in $\boldsymbol{H}^{(k)}$ to apply the inverse inequality of Lemma 2.3.12. Recalling the definition of the oscillations in (4.57), and using again the triangle inequality, we thus obtain for all $k = 1, \dots, N_f$,

$$\sum_{\sigma\in\Sigma^k} |\sigma|^{\frac{1}{n-1}} \|\boldsymbol{d}_\sigma\|^2_{0,\sigma} \lesssim \left\|\boldsymbol{\Pi}_m\left(\boldsymbol{d}^k\right)\right\|^2_{(\boldsymbol{H}^{(k)})^*} + \left(\mathrm{osc}^k(\boldsymbol{u}_\mathrm{d})\right)^2$$

$$\lesssim \left\|\boldsymbol{d}^k\right\|^2_{(\boldsymbol{H}^{(k)})^*} + \left\|\boldsymbol{\Pi}_m\left(\boldsymbol{d}^k\right) - \boldsymbol{d}^k\right\|^2_{(\boldsymbol{H}^{(k)})^*} + \left(\mathrm{osc}^k(\boldsymbol{u}_\mathrm{d})\right)^2.$$

Finally, using (4.65), applying Lemma 2.3.11 and then Lemma 2.3.7, we obtain

$$
\begin{aligned}
\mathscr{E}_D(\boldsymbol{u}_{\mathrm{d}})^2 &\lesssim \sum_{k=1}^{N_f} \left\| \boldsymbol{d}^k \right\|_{\left(\boldsymbol{H}^{(k)}\right)^*}^2 + \sum_{k=1}^{N_f} \left\| \boldsymbol{\Pi}_m \left(\boldsymbol{d}^k \right) - \boldsymbol{d}^k \right\|_{\left(\boldsymbol{H}^{(k)}\right)^*}^2 + \mathrm{osc}(\boldsymbol{u}_{\mathrm{d}})^2 \\
&\lesssim \sum_{k=1}^{N_f} \left\| \boldsymbol{\nabla} e \right\|_{0,\Omega^k}^2 + \sum_{k=1}^{N_f} \left\| \boldsymbol{\Pi}_m \left(\boldsymbol{d}^k \right) - \boldsymbol{d}^k \right\|_{\boldsymbol{H}_{00}^{-1/2}(\Gamma^k)}^2 + \mathrm{osc}(\boldsymbol{u}_{\mathrm{d}})^2 \\
&\lesssim \left(\left\| \boldsymbol{\nabla} e \right\|_{0,\Omega} + \mathrm{osc}(\boldsymbol{u}_{\mathrm{d}}) \right)^2.
\end{aligned}
$$

To conclude, we use the coercivity of the bilinear form $a_\Omega(\cdot,\cdot)$ in $\boldsymbol{H}_{0,\Gamma_D}^1(\Omega)$ to obtain

$$
\left\| \boldsymbol{\nabla} e \right\|_{0,\Omega} \lesssim \left\|\!\left\| e \right\|\!\right\|_\Omega,
$$

as in (4.56). $\qquad\square$

Remark 4.3.5. As in Remark 4.2.5, when the data is regular, it is always possible to choose m large enough so that the asymptotic behavior of the oscillations is $\mathcal{O}\left(\max\limits_{k=1,\ldots,N_f} \left| \Gamma^k \right|^{m+\frac{1}{2(n-1)}} \right)$. Therefore, we can make sure that the oscillations get small with respect to the defeaturing error, when the features get small.

4.4 Defeaturing in Stokes equations

In this section, we are interested in studying the defeaturing problem in the context of incompressible fluid flows, in the time-independent Stokes regime. So in this framework, we first precisely state the defeaturing problem in a multi-feature geometry, by keeping the same notation and geometric assumptions as introduced in Section 4.1. Then with the help of Sections 4.1 and 4.3, we derive an optimal *a posteriori* defeaturing error estimator, and we show its reliability and efficiency.

4.4.1 Defeaturing problem and *a posteriori* error estimator

Let $\Omega \subset \mathbb{R}^n$ be an open Lipschitz domain containing $N_f \geq 1$ complex features satisfying Assumptions 4.1.4 and 4.1.5, and let us first define the exact Stokes equations in Ω. To do so, considering a function $\boldsymbol{v} : \Omega \to \mathbb{R}^n$, let $\mathbf{e}(\boldsymbol{v})$ denote the linearized strain rate tensor in Ω, and let $\mathbf{s}(\boldsymbol{v})$ be the viscous stress tensor of the considered fluid. Assuming the fluid to be Newtonian, Galilean invariance implies that

$$
\mathbf{s}(\boldsymbol{v}) = 2\mu\, \mathbf{e}(\boldsymbol{v}) + \lambda(\boldsymbol{\nabla} \cdot \boldsymbol{v})\mathbb{I}_n, \tag{4.66}
$$

where $\mathbb{I}_n$ is the identity tensor in $\mathbb{R}^{n\times n}$, and the constants $\mu > 0$ and $\lambda \geq 0$ are now the dynamic and bulk viscosities, respectively. Note that in this section, $\mathbf{s}(\boldsymbol{v})$ is the viscous

stress tensor and not the total Cauchy stress tensor that would be defined by

$$\mathbb{r}(\boldsymbol{v}, q) := \mathbb{s}(\boldsymbol{v}) - q\,\mathbb{I}_n$$

for some function $q : \Omega \to \mathbb{R}$ in the space of pressures. Now, let $\partial\Omega = \overline{\Gamma_D} \cup \overline{\Gamma_N}$ with $\Gamma_D \cap \Gamma_N = \emptyset$, $|\Gamma_D| > 0$, let $\mathbf{n}$ be the unitary outward normal of Ω, and let $\boldsymbol{g}_D \in \boldsymbol{H}^{\frac{3}{2}}(\Gamma_D)$, $\boldsymbol{g} \in \boldsymbol{H}^{\frac{1}{2}}(\Gamma_N)$, $f_c \in L^2(\Omega)$ and $\boldsymbol{f} \in \boldsymbol{L}^2(\Omega)$. The considered Stokes equations in the exact geometry Ω read as follows:

$$\text{find } (\boldsymbol{u}, p) : \Omega \to \mathbb{R}^{n+1}, \text{ solution of}$$

$$\begin{cases} -\boldsymbol{\nabla} \cdot \mathbb{s}(\boldsymbol{u}) + \nabla p = \boldsymbol{f} & \text{in } \Omega \\ \boldsymbol{\nabla} \cdot \boldsymbol{u} = f_c & \text{in } \Omega \\ \boldsymbol{u} = \boldsymbol{g}_D & \text{on } \Gamma_D \\ \mathbb{s}(\boldsymbol{u})\mathbf{n} - p\mathbf{n} = \boldsymbol{g} & \text{on } \Gamma_N. \end{cases} \tag{4.67}$$

In the framework presented in Section 2.4, let us formally multiply the two first equations of (4.67) respectively by some test functions $\boldsymbol{v}$ and q, and let us integrate by parts the first resulting equation using the boundary conditions given in (4.67). The weak formulation of the Stokes equations then reads:

$$\text{find } (\boldsymbol{u}, p) \in \boldsymbol{H}^1_{\boldsymbol{g}_D, \Gamma_D}(\Omega) \times L^2(\Omega) \text{ such that for all } (\boldsymbol{v}, q) \in \boldsymbol{H}^1_{\boldsymbol{0}, \Gamma_D}(\Omega) \times L^2(\Omega),$$

$$\int_\Omega \mathbb{s}(\boldsymbol{u}) : \mathbb{e}(\boldsymbol{v})\,\mathrm{d}x - \int_\Omega p\boldsymbol{\nabla} \cdot \boldsymbol{v}\,\mathrm{d}x = \int_\Omega \boldsymbol{f} \cdot \boldsymbol{v}\,\mathrm{d}x + \int_{\Gamma_N} \boldsymbol{g} \cdot \boldsymbol{v}\,\mathrm{d}s,$$

$$-\int_\Omega q\boldsymbol{\nabla} \cdot \boldsymbol{u}\,\mathrm{d}x = -\int_\Omega qf_c\,\mathrm{d}x. \tag{4.68}$$

Note that if $f_c \equiv 0$, then (4.67) is also the system of equations describing the linear elastic problem of Section 4.3 in the incompressible limit $\lambda \to \infty$.

Let $\boldsymbol{z} := \boldsymbol{R}_{\Gamma_D}(\boldsymbol{g}_D) \in \boldsymbol{H}^1_{\boldsymbol{g}_D, \Gamma_D}(\Omega)$ be a lifting of the Dirichlet data $\boldsymbol{g}_D$ given by Theorem 2.2.1, and for all functions $\boldsymbol{w}, \boldsymbol{v} \in V := \boldsymbol{H}^1_{\boldsymbol{0}, \Gamma_D}(\Omega)$ and all $q \in L^2(\Omega)$, let

$$a_\Omega(\boldsymbol{w}, \boldsymbol{v}) := \int_\Omega \mathbb{s}(\boldsymbol{w}) : \mathbb{e}(\boldsymbol{v})\,\mathrm{d}x, \qquad \mathfrak{f}^{\boldsymbol{z}}_\Omega(\boldsymbol{v}) := \int_\Omega \boldsymbol{f} \cdot \boldsymbol{v}\,\mathrm{d}x + \int_{\Gamma_N} \boldsymbol{g} \cdot \boldsymbol{v}\,\mathrm{d}s - a_\Omega(\boldsymbol{z}, \boldsymbol{v}),$$

$$b_\Omega(\boldsymbol{v}, q) := -\int_\Omega q\boldsymbol{\nabla} \cdot \boldsymbol{v}\,\mathrm{d}x, \qquad \mathfrak{f}^{\boldsymbol{z}}_{c,\Omega}(q) := -\int_\Omega qf_c\,\mathrm{d}x - b_\Omega(\boldsymbol{z}, q). \tag{4.69}$$

Then, finding $\mathring{\boldsymbol{u}} \in V$ such that for all $\boldsymbol{v} \in V$ and all $q \in Q$,

$$a_\Omega(\mathring{\boldsymbol{u}}, \boldsymbol{v}) + b_\Omega(\boldsymbol{v}, p) = \mathfrak{f}^{\boldsymbol{z}}_\Omega(\boldsymbol{v}),$$

$$b_\Omega(\mathring{\boldsymbol{u}}, q) = \mathfrak{f}^{\boldsymbol{z}}_{c,\Omega}(q),$$

is equivalent to solving (4.68) since $\mathbb{s}$ is linear. If we equip V with the norm $\|\boldsymbol{\nabla} \cdot \|_{0,\Omega}$, it is possible to show that $a_\Omega(\cdot, \cdot)$ is a continuous and coercive bilinear form on $V \times V$,

$b_\Omega(\cdot,\cdot)$ is a continuous bilinear form on $V \times Q$ that satisfies the inf-sup condition (2.24), and the functionals $\mathfrak{f}_\Omega^z(\cdot)$ on V and $\mathfrak{f}_{c,\Omega}^z(\cdot)$ on Q are linear and continuous. We refer to [Ern and Guermond, 2021b] for the proof. Therefore, by Ladyzhenskaya-Babuška-Brezzi theorem, problem (4.68) is well-posed.

Let Ω_0 be the defeatured domain as defined in (4.1). To introduce the corresponding defeatured problem, and as for Poisson's equation from Section 4.1, we need to choose an $\boldsymbol{L}^2$-extension of $\boldsymbol{f}$ and an L^2-extension of f_c in the negative components of the features F_n, that we still write $\boldsymbol{f}$ and f_c by abuse of notation. Moreover, we assume that the viscous stress tensor $\mathbf{s}$ also satisfies (4.66) on functions defined everywhere in Ω_0. Finally, recalling the notation from Section 4.1, the analysis is performed under Assumption 4.1.3 on the exact problem (4.67), that is, a Neumann boundary condition is imposed on the boundary of the features.

Then, instead of the exact problem (4.67) and similarly to (3.3), the following defeatured problem is solved: after choosing $\boldsymbol{g}_0 \in \boldsymbol{H}^{\frac{1}{2}}(\gamma_0)$, find $(\boldsymbol{u}_0, p_0) \in \boldsymbol{H}^1(\Omega_0) \times L^2(\Omega_0)$, the weak solution of

$$
\begin{cases}
-\boldsymbol{\nabla} \cdot \mathbf{s}(\boldsymbol{u}_0) + \nabla p_0 = \boldsymbol{f} & \text{in } \Omega_0 \\
\boldsymbol{\nabla} \cdot \boldsymbol{u}_0 = f_c & \text{in } \Omega_0 \\
\boldsymbol{u}_0 = \boldsymbol{g}_D & \text{on } \Gamma_D \\
\mathbf{s}(\boldsymbol{u}_0)\mathbf{n} - p_0\mathbf{n} = \boldsymbol{g} & \text{on } \Gamma_N \setminus \gamma \\
\mathbf{s}(\boldsymbol{u}_0)\mathbf{n}_0 - p_0\mathbf{n} = \boldsymbol{g}_0 & \text{on } \gamma_0,
\end{cases}
\tag{4.70}
$$

that is, $(\boldsymbol{u}_0, p_0) \in \boldsymbol{H}_{\boldsymbol{g}_D,\Gamma_D}^1(\Omega_0) \times L^2(\Omega_0)$ satisfies for all $(\boldsymbol{v}_0, q_0) \in \boldsymbol{H}_{\mathbf{0},\Gamma_D}^1(\Omega_0) \times L^2(\Omega_0)$,

$$
\int_{\Omega_0} \mathbf{s}(\boldsymbol{u}_0) : \mathbf{e}(\boldsymbol{v}_0)\,\mathrm{d}x - \int_\Omega p_0 \boldsymbol{\nabla} \cdot \boldsymbol{v}_0\,\mathrm{d}x = \int_{\Omega_0} \boldsymbol{f} \cdot \boldsymbol{v}_0\,\mathrm{d}x + \int_{\Gamma_N \setminus \gamma} \boldsymbol{g} \cdot \boldsymbol{v}_0\,\mathrm{d}s + \int_{\gamma_0} \boldsymbol{g}_0 \cdot \boldsymbol{v}_0\,\mathrm{d}s,
$$

$$
- \int_\Omega q_0 \boldsymbol{\nabla} \cdot \boldsymbol{u}_0\,\mathrm{d}x = - \int_\Omega q_0 f_c\,\mathrm{d}x.
\tag{4.71}
$$

Using the same arguments as for problem (4.68), we can demonstrate that problem (4.71) is well-posed.

As previously, since we are interested in the global defeaturing error in Ω, we need to extend the defeatured solution $(\boldsymbol{u}_0, p_0)$ to the domain extension $\tilde{F}_\mathrm{p}^k$ of the positive component F_p^k of feature F^k, for all $k = 1, \ldots, N_f$. Thus, let us choose an $\boldsymbol{L}^2$-extension of $\boldsymbol{f}$ and an L^2-extension of f_c in $\tilde{F}_\mathrm{p}^k$, that we still write $\boldsymbol{f}$ and f_c by abuse of notation. Moreover, we assume that the viscous stress tensor $\mathbf{s}$ also satisfies (4.66) on functions defined in $\tilde{F}_\mathrm{p}^k$. Then, similarly to (4.5), define for all $k = 1, \ldots, N_f$ the following extension of the solution $(\boldsymbol{u}_0, p_0)$ of (4.70) in $\tilde{F}_\mathrm{p}^k$: after choosing $\tilde{\boldsymbol{g}}^k \in \boldsymbol{H}^{\frac{1}{2}}(\tilde{\gamma}^k)$, find

$(\boldsymbol{u}_k, p_k) \equiv \left(\tilde{\boldsymbol{u}}_0^k, \tilde{p}_0^k\right) \in \boldsymbol{H}^1\left(\tilde{F}_{\mathrm{p}}^k\right) \times L^2\left(\tilde{F}_{\mathrm{p}}^k\right)$, the weak solution of

$$
\begin{cases}
-\boldsymbol{\nabla} \cdot \mathbf{s}(\boldsymbol{u}_k) + \nabla p_k = \boldsymbol{f} & \text{in } \tilde{F}_{\mathrm{p}}^k \\
\boldsymbol{\nabla} \cdot \boldsymbol{u}_k = f_c & \text{in } \tilde{F}_{\mathrm{p}}^k \\
\boldsymbol{u}_k = \boldsymbol{u}_0 & \text{on } \gamma_{0,\mathrm{p}}^k \\
\mathbf{s}(\boldsymbol{u}_k)\tilde{\mathbf{n}}^k - p_k\tilde{\mathbf{n}}^k = \tilde{\boldsymbol{g}}^k & \text{on } \tilde{\gamma}^k \\
\mathbf{s}(\boldsymbol{u}_k)\tilde{\mathbf{n}}^k - p_k\tilde{\mathbf{n}}^k = \boldsymbol{g} & \text{on } \gamma_{\mathrm{s}}^k,
\end{cases}
\tag{4.72}
$$

that is,

$$
(\boldsymbol{u}_k, p_k) \in \boldsymbol{H}^1_{\boldsymbol{u}_0, \gamma_{0,\mathrm{p}}^k}\left(\tilde{F}_{\mathrm{p}}^k\right) \times L^2\left(\tilde{F}_{\mathrm{p}}^k\right)
$$

satisfies for all $(\boldsymbol{v}^k, q^k) \in \boldsymbol{H}^1_{\boldsymbol{0}, \gamma_{0,\mathrm{p}}^k}\left(\tilde{F}_{\mathrm{p}}^k\right) \times L^2\left(\tilde{F}_{\mathrm{p}}^k\right)$,

$$
\int_{\tilde{F}_{\mathrm{p}}^k} \mathbf{s}(\boldsymbol{u}_k) : \mathbf{e}(\boldsymbol{v}^k)\,\mathrm{d}x - \int_{\tilde{F}_{\mathrm{p}}^k} p_k \boldsymbol{\nabla} \cdot \boldsymbol{v}^k\,\mathrm{d}x = \int_{\tilde{F}_{\mathrm{p}}^k} \boldsymbol{f} \cdot \boldsymbol{v}^k\,\mathrm{d}x + \int_{\tilde{\gamma}^k} \tilde{\boldsymbol{g}}^k \cdot \boldsymbol{v}^k\,\mathrm{d}s + \int_{\gamma_{\mathrm{s}}^k} \boldsymbol{g} \cdot \boldsymbol{v}^k\,\mathrm{d}s,
$$

$$
-\int_{\tilde{F}_{\mathrm{p}}^k} q^k \boldsymbol{\nabla} \cdot \boldsymbol{u}_k\,\mathrm{d}x = -\int_{\tilde{F}_{\mathrm{p}}^k} q^k f_c\,\mathrm{d}x.
\tag{4.73}
$$

Using the same arguments as for problem (4.68), we can demonstrate that problem (4.73) is well-posed.

Finally, let $(\boldsymbol{u}_{\mathrm{d}}, p_{\mathrm{d}}) \in \boldsymbol{H}^1_{\boldsymbol{g}_D, \Gamma_D}(\Omega) \times L^2(\Omega)$ be the extended defeatured solution defined in a similar way as (4.7), that is,

$$
(\boldsymbol{u}_{\mathrm{d}}, p_{\mathrm{d}}) \equiv
\begin{cases}
(\boldsymbol{u}_0, p_0)|_{\Omega_\star} & \text{in } \Omega_\star = \Omega \setminus \overline{F_{\mathrm{p}}} \\
(\boldsymbol{u}_k, p_k)|_{F_{\mathrm{p}}^k} \equiv \left(\tilde{\boldsymbol{u}}_0^k, \tilde{p}_0^k\right)|_{F_{\mathrm{p}}^k} & \text{in } F_{\mathrm{p}}^k, \text{ for all } k = 1, \dots, N_f.
\end{cases}
\tag{4.74}
$$

Then, in the context of Stokes equations, we define the defeaturing error by

$$
\|\|\boldsymbol{u} - \boldsymbol{u}_{\mathrm{d}}\|\|_\Omega + \|p - p_{\mathrm{d}}\|_{0,\Omega},
$$

where $\|\|\cdot\|\|_\Omega := \left(a_\Omega(\cdot, \cdot)\right)^{\frac{1}{2}}$.

As in Sections 4.1 and 4.3, recalling definition (4.11) of Σ, the parts of boundary belonging to Σ will play an important role in the *a posteriori* defeaturing error analysis. In particular, we assume that Σ satisfies the isotropy Assumption 3.3.3.

Recall that $k_\sigma \equiv k$ if $\sigma \in \Sigma^k$ for some $k = 1, \dots, N_f$, and let us redefine $\boldsymbol{d}_\sigma$ for all $\sigma \in \Sigma$ in the context of Stokes equations. That is, let

$$
\boldsymbol{d}_\sigma \equiv
\begin{cases}
\boldsymbol{g} - \mathbf{s}(\boldsymbol{u}_{\mathrm{d}})\mathbf{n} + p_{\mathrm{d}}\mathbf{n} & \text{if } \sigma \in \Sigma_{\mathrm{n}} \text{ of if } \sigma \in \Sigma_{\mathrm{r}}, \\
-\left(\boldsymbol{g}_0 + \mathbf{s}(\boldsymbol{u}_{\mathrm{d}})\mathbf{n}^{k_\sigma} - p_{\mathrm{d}}\mathbf{n}^{k_\sigma}\right) & \text{if } \sigma \in \Sigma_{0,\mathrm{p}}.
\end{cases}
\tag{4.75}
$$

We are now able to define the *a posteriori* defeaturing error estimator as

$$\mathscr{E}_D(\boldsymbol{u}_{\mathrm{d}}, p_{\mathrm{d}}) := \left(\sum_{\sigma \in \Sigma} \mathscr{E}_D^{\sigma}(\boldsymbol{u}_{\mathrm{d}}, p_{\mathrm{d}})^2 \right)^{\frac{1}{2}}, \tag{4.76}$$

where for all $\sigma \in \Sigma$,

$$\mathscr{E}_D^{\sigma}(\boldsymbol{u}_{\mathrm{d}}, p_{\mathrm{d}}) := \left(|\sigma|^{\frac{1}{n-1}} \left\| \boldsymbol{d}_\sigma - \overline{\boldsymbol{d}}_\sigma^{\,\sigma} \right\|_{0,\sigma}^2 + c_\sigma^2 |\sigma|^{\frac{n}{n-1}} \left\| \overline{\boldsymbol{d}}_\sigma^{\,\sigma} \right\|_{\ell^2}^2 \right)^{\frac{1}{2}},$$

with c_σ is defined as in (3.10). Note that as previously, we can rewrite the estimator feature-wise, as follows:

$$\mathscr{E}_D(\boldsymbol{u}_{\mathrm{d}}, p_{\mathrm{d}}) = \left(\sum_{k=1}^{N_f} \sum_{\sigma \in \Sigma^k} \mathscr{E}_D^{\sigma}(\boldsymbol{u}_{\mathrm{d}}, p_{\mathrm{d}})^2 \right)^{\frac{1}{2}} = \left(\sum_{k=1}^{N_f} \mathscr{E}_D^k(\boldsymbol{u}_{\mathrm{d}}, p_{\mathrm{d}})^2 \right)^{\frac{1}{2}},$$

where for all $k = 1, \ldots, N_f$, we define $\mathscr{E}_D^k(\boldsymbol{u}_k, p_k)$ as the defeaturing error estimator for feature F^k, that is,

$$\mathscr{E}_D^k(\boldsymbol{u}_{\mathrm{d}}, p_{\mathrm{d}}) := \left(\sum_{\sigma \in \Sigma^k} \mathscr{E}_D^{\sigma}(\boldsymbol{u}_{\mathrm{d}}, p_{\mathrm{d}})^2 \right)^{\frac{1}{2}}.$$

The proposed estimator indicates that all the information on the error introduced by defeaturing is encoded in the boundary of the features, and can be accounted by suitably evaluating the error made on the normal viscous stress and pressure of the solution.

Remark 4.4.1. Similarly to Remarks 4.2.1 and 4.3.1, the terms involving the component-wise average values of $\boldsymbol{d}_\sigma$ in $\mathscr{E}_D(\boldsymbol{u}_{\mathrm{d}}, p_{\mathrm{d}})$ only depend on the defeatured problem data. As a consequence, if these terms dominate, this means that the defeatured problem data should be more accurately chosen. Moreover, under the reasonable data compatibility conditions (4.45) that represent flux conservation assumptions in this context, the defeaturing error estimator (4.76) rewrites $\mathscr{E}_D(\boldsymbol{u}_{\mathrm{d}}, p_{\mathrm{d}}) := \left(\sum_{\sigma \in \Sigma} |\sigma|^{\frac{1}{n-1}} \|\boldsymbol{d}_\sigma\|_{0,\sigma}^2 \right)^{\frac{1}{2}}.$

Remark 4.4.2. Similarly to Remark 4.2.2 and 4.3.2, note that

$$\mathscr{E}_D(\boldsymbol{u}_{\mathrm{d}}, p_{\mathrm{d}}) \lesssim \left(\sum_{\sigma \in \Sigma} c_\sigma^2 |\sigma|^{\frac{1}{n-1}} \|\boldsymbol{d}_\sigma\|_{0,\sigma}^2 \right)^{\frac{1}{2}} =: \tilde{\mathscr{E}}_D(\boldsymbol{u}_{\mathrm{d}}, p_{\mathrm{d}}).$$

However, when $n = 2$ and under the flux conservation conditions (4.45), $\tilde{\mathscr{E}}_D(\boldsymbol{u}_{\mathrm{d}}, p_{\mathrm{d}})$ is sub-optimal since in this case, $\tilde{\mathscr{E}}_D(\boldsymbol{u}_{\mathrm{d}}, p_{\mathrm{d}}) \lesssim \max_{\sigma \in \Sigma} (c_\sigma) \, \mathscr{E}_D(\boldsymbol{u}_{\mathrm{d}}, p_{\mathrm{d}}).$

In the remaining part of this section, we study the properties of the *a posteriori* defea-

turing error estimator $\mathscr{E}_D(\boldsymbol{u}_{\mathrm{d}}, p_{\mathrm{d}})$. We show that if the features satisfy the separability Assumption 4.1.5, the quantity $\mathscr{E}_D(\boldsymbol{u}_{\mathrm{d}}, p_{\mathrm{d}})$ is a reliable estimator for the defeaturing error $\|\!|\boldsymbol{u} - \boldsymbol{u}_{\mathrm{d}}|\!\|_\Omega + \|p - p_{\mathrm{d}}\|_{0,\Omega}$, i.e., it is an upper bound for the defeaturing error with a hidden constant that is independent of the number of features N_f and of their size, see Theorem 4.4.3. Then, assuming that all $\sigma \in \Sigma$ are also regular according to Definition 2.1.3 and under mild assumptions for the two-dimensional case, we show that it is also efficient (up to oscillations), i.e., it is a lower bound for the defeaturing error up to oscillations, see Theorem 4.4.4. As previously, the key issue in the subsequent analysis is to track the dependence of all constants from the size of the features and from their number.

4.4.2 Reliability

In this section, we state and prove that the error indicator defined in (4.76) is reliable, that is, it is an upper bound for the defeaturing error.

Theorem 4.4.3. *Let $(\boldsymbol{u}, p)$ be the weak solution of Stokes problem (4.68) in the exact geometry Ω, and let $(\boldsymbol{u}_{\mathrm{d}}, p_{\mathrm{d}})$ be the weak solutions of the Stokes problem in the defeatured geometry, as defined in (4.74). If all $\sigma \in \Sigma$ are isotropic according to Definition 2.1.2, and if the features $\mathfrak{F}$ are separated as in Assumption 4.1.5, then the defeaturing error is bounded in terms of the estimator $\mathscr{E}_D(\boldsymbol{u}_{\mathrm{d}}, p_{\mathrm{d}})$ introduced in (4.76) as follows:*

$$\|\!|\boldsymbol{u} - \boldsymbol{u}_{\mathrm{d}}|\!\|_\Omega + \|p - p_{\mathrm{d}}\|_{0,\Omega} \lesssim \mathscr{E}_D(\boldsymbol{u}_{\mathrm{d}}, p_{\mathrm{d}}),$$

where the hidden constant is independent of the number of features N_f and of their size.

Proof. Let us follow similar steps as in the proofs of Theorems 4.2.3 and 4.3.3. So to begin with, consider the exact problem (4.67) restricted to $\Omega_\star = \Omega \setminus \overline{F_{\mathrm{p}}}$ with the natural Neumann boundary condition on $\gamma_{0,\mathrm{p}}$, as in (4.46). By abuse of notation, we omit the explicit restriction of $\boldsymbol{u}$ and p to $\Omega_\star$. Then for all $(\boldsymbol{v}_0, q_0) \in \boldsymbol{H}^1_{\boldsymbol{0},\Gamma_D}(\Omega_\star) \times L^2(\Omega_\star)$,

$$\int_{\Omega_\star} \mathbf{s}(\boldsymbol{u}) : \mathbf{e}(\boldsymbol{v}_0)\,\mathrm{d}x - \int_{\Omega_\star} p\boldsymbol{\nabla} \cdot \boldsymbol{v}_0\,\mathrm{d}x = \int_{\Omega_\star} \boldsymbol{f} \cdot \boldsymbol{v}_0\,\mathrm{d}x + \int_{\Gamma_N \setminus \gamma_{\mathrm{p}}} \boldsymbol{g} \cdot \boldsymbol{v}_0\,\mathrm{d}s$$

$$+ \int_{\gamma_{0,\mathrm{p}}} \Big(\mathbf{s}(\boldsymbol{u})\mathbf{n}_0 - p\mathbf{n}_0\Big) \cdot \boldsymbol{v}_0\,\mathrm{d}s,$$

$$- \int_{\Omega_\star} q_0 \boldsymbol{\nabla} \cdot \boldsymbol{u}\,\mathrm{d}x = - \int_{\Omega_\star} q_0 f_c\,\mathrm{d}x. \tag{4.77}$$

Then, let us consider the simplified problem (4.70) also restricted to $\Omega_\star$, with the natural Neumann boundary condition on γ_{n}. Thus, since $\boldsymbol{u}_{\mathrm{d}}|_{\Omega_\star} = \boldsymbol{u}_0|_{\Omega_\star}$ by definition, and if we

omit the explicit restrictions of $\boldsymbol{u}_{\mathrm{d}}$ and p_{d} to $\Omega_\star$, for all $(\boldsymbol{v}_0, q_0) \in \boldsymbol{H}^1_{\mathbf{0},\Gamma_D}(\Omega_\star) \times L^2(\Omega_\star)$,

$$
\int_{\Omega_\star} \mathbf{s}(\boldsymbol{u}_{\mathrm{d}}) : \mathbf{e}(\boldsymbol{v}_0) \, \mathrm{d}x - \int_{\Omega_\star} p_{\mathrm{d}} \boldsymbol{\nabla} \cdot \boldsymbol{v}_0 \, \mathrm{d}x = \int_{\Omega_\star} \boldsymbol{f} \cdot \boldsymbol{v}_0 \, \mathrm{d}x + \int_{\Gamma_N \backslash \gamma} \boldsymbol{g} \cdot \boldsymbol{v}_0 \, \mathrm{d}s
$$

$$
+ \int_{\gamma_{\mathrm{n}}} \big(\mathbf{s}(\boldsymbol{u}_{\mathrm{d}})\mathbf{n} - p_{\mathrm{d}}\mathbf{n}\big) \cdot \boldsymbol{v}_0 \, \mathrm{d}s + \int_{\gamma_{0,\mathrm{p}}} \boldsymbol{g}_0 \cdot \boldsymbol{v}_0 \, \mathrm{d}s,
$$

$$
- \int_{\Omega_\star} q_0 \boldsymbol{\nabla} \cdot \boldsymbol{u}_{\mathrm{d}} \, \mathrm{d}x = - \int_{\Omega_\star} q_0 f_c \, \mathrm{d}x. \tag{4.78}
$$

Let $\boldsymbol{e_u} := \boldsymbol{u} - \boldsymbol{u}_{\mathrm{d}} \in \boldsymbol{H}^1_{\mathbf{0},\Gamma_D}(\Omega)$ and $e_p := p - p_{\mathrm{d}} \in L^2(\Omega)$. So from (4.77) and (4.78), since $\mathbf{s}$ is linear from its definition (4.66), then for all $(\boldsymbol{v}_0, q_0) \in \boldsymbol{H}^1_{\mathbf{0},\Gamma_D}(\Omega_\star) \times L^2(\Omega_\star)$, we obtain

$$
\int_{\Omega_\star} \mathbf{s}(\boldsymbol{e_u}) : \mathbf{e}(\boldsymbol{v}_0) \, \mathrm{d}x - \int_{\Omega_\star} e_p \boldsymbol{\nabla} \cdot \boldsymbol{v}_0 \, \mathrm{d}x = \int_{\gamma_{\mathrm{n}}} \big(\boldsymbol{g} - \mathbf{s}(\boldsymbol{u}_{\mathrm{d}})\mathbf{n} + p_{\mathrm{d}}\mathbf{n}\big) \cdot \boldsymbol{v}_0 \, \mathrm{d}s
$$

$$
+ \int_{\gamma_{0,\mathrm{p}}} \big(\mathbf{s}(\boldsymbol{u})\mathbf{n}_0 - p\mathbf{n}_0 - \boldsymbol{g}_0\big) \cdot \boldsymbol{v}_0 \, \mathrm{d}s,
$$

$$
- \int_{\Omega_\star} q_0 \boldsymbol{\nabla} \cdot \boldsymbol{e_u} \, \mathrm{d}x = 0. \tag{4.79}
$$

In a very similar fashion, we can deduce that for all $k = 1, \ldots, N_f$ and all test functions $(\boldsymbol{v}^k, q^k) \in \boldsymbol{H}^1\big(F_{\mathrm{p}}^k\big) \times L^2\big(F_{\mathrm{p}}^k\big)$,

$$
\int_{F_{\mathrm{p}}^k} \mathbf{s}(\boldsymbol{e_u}) : \mathbf{e}(\boldsymbol{v}^k) \, \mathrm{d}x - \int_{F_{\mathrm{p}}^k} e_p \boldsymbol{\nabla} \cdot \boldsymbol{v}^k \, \mathrm{d}x = \int_{\gamma_{0,\mathrm{p}}^k} \Big[\big(\mathbf{s}(\boldsymbol{u}) - \mathbf{s}(\boldsymbol{u}_{\mathrm{d}})\big)\mathbf{n}^k - (p - p_{\mathrm{d}})\mathbf{n}^k\Big] \cdot \boldsymbol{v}^k \, \mathrm{d}s
$$

$$
+ \int_{\gamma_{\mathrm{r}}^k} \big(\boldsymbol{g} - \mathbf{s}(\boldsymbol{u}_{\mathrm{d}})\mathbf{n}^k + p_{\mathrm{d}}\mathbf{n}^k\big) \cdot \boldsymbol{v}^k \, \mathrm{d}s,
$$

$$
- \int_{F_{\mathrm{p}}^k} q^k \boldsymbol{\nabla} \cdot \boldsymbol{e_u} \, \mathrm{d}x = 0. \tag{4.80}
$$

Therefore, let $(\boldsymbol{v}, q) \in \boldsymbol{H}^1_{\mathbf{0},\Gamma_D}(\Omega) \times L^2(\Omega)$, then $\boldsymbol{v}|_{\Omega_\star} \in \boldsymbol{H}^1_{\mathbf{0},\Gamma_D}(\Omega_\star)$ and $\boldsymbol{v}|_{F_{\mathrm{p}}^k} \in \boldsymbol{H}^1(F_{\mathrm{p}}^k)$ for all $k = 1, \ldots, N_f$. Therefore, from equations (4.79) and (4.80), since $\mathbf{n}_0 = -\mathbf{n}^{k_\sigma}$ on all $\sigma \in \Sigma_{0,\mathrm{p}}$, and since $\mathbf{n} = \mathbf{n}^{k_\sigma}$ on all $\sigma \in \Sigma_{\mathrm{r}}$, then recalling the definitions of $a_\Omega(\cdot, \cdot)$ and $b_\Omega(\cdot, \cdot)$ in (4.69) and of $\boldsymbol{d}_\sigma$ in (4.75), we obtain

$$
a_\Omega(\boldsymbol{e_u}, \boldsymbol{v}) + b_\Omega(\boldsymbol{v}, e_p) = \int_\Omega \mathbf{s}(\boldsymbol{e_u}) : \mathbf{e}(\boldsymbol{v}) \, \mathrm{d}x - \int_\Omega e_p \boldsymbol{\nabla} \cdot \boldsymbol{v} \, \mathrm{d}x = \sum_{\sigma \in \Sigma} \int_\sigma \boldsymbol{d}_\sigma \cdot \boldsymbol{v} \, \mathrm{d}s, \tag{4.81}
$$

$$
b_\Omega(\boldsymbol{e_u}, q) = - \int_\Omega q \boldsymbol{\nabla} \cdot \boldsymbol{e_u} \, \mathrm{d}x = 0. \tag{4.82}
$$

The right hand side of (4.81) can be estimated exactly as (4.51), and thus for all $\boldsymbol{v} \in \boldsymbol{H}^1_{\mathbf{0},\Gamma_D}(\Omega)$,

$$
\sum_{\sigma \in \Sigma} \int_\sigma \boldsymbol{d}_\sigma \cdot \boldsymbol{v} \, \mathrm{d}s \lesssim \mathscr{E}_D(\boldsymbol{u}_{\mathrm{d}}, p_{\mathrm{d}}) \|\boldsymbol{\nabla v}\|_{0,\Omega}. \tag{4.83}
$$

Now, remark that if we take $\boldsymbol{v} = \boldsymbol{e_u} \in \boldsymbol{H}^1_{\mathbf{0},\Gamma_D}(\Omega)$ and $q = e_p \in L^2(\Omega)$, then equation (4.82)

reads $b_\Omega(\boldsymbol{e_u}, e_p) = 0$, and thus using (4.83), equation (4.81) rewrites

$$a_\Omega(\boldsymbol{e_u}, \boldsymbol{e_u}) = \int_\Omega \boldsymbol{\mathfrak{s}}(\boldsymbol{e_u}) : \boldsymbol{\mathfrak{e}}(\boldsymbol{e_u}) \, \mathrm{d}x - \int_\Omega e_p \boldsymbol{\nabla} \cdot \boldsymbol{e_u} \, \mathrm{d}x$$

$$= \sum_{\sigma \in \Sigma} \int_\sigma \boldsymbol{d}_\sigma \cdot \boldsymbol{e_u} \, \mathrm{d}s$$

$$\lesssim \mathscr{E}_D(\boldsymbol{u}_\mathrm{d}, p_\mathrm{d}) \|\boldsymbol{\nabla} \boldsymbol{e_u}\|_{0,\Omega}.$$

Using the coercivity of $a_\Omega(\cdot, \cdot)$ in $\boldsymbol{H}^1_{\boldsymbol{0}, \Gamma_D}(\Omega)$ equipped with the norm $\|\boldsymbol{\nabla} \cdot \|_{0,\Omega}$, then

$$\|\!|\boldsymbol{e_u}|\!\|_\Omega^2 = a_\Omega(\boldsymbol{e_u}, \boldsymbol{e_u}) \lesssim \mathscr{E}_D(\boldsymbol{u}_\mathrm{d}, p_\mathrm{d}) \|\boldsymbol{\nabla} \boldsymbol{e_u}\|_{0,\Omega}$$

$$\lesssim \mathscr{E}_D(\boldsymbol{u}_\mathrm{d}, p_\mathrm{d}) \Big(a(\boldsymbol{e_u}, \boldsymbol{e_u}) \Big)^{\frac{1}{2}} = \mathscr{E}_D(\boldsymbol{u}_\mathrm{d}, p_\mathrm{d}) \|\!|\boldsymbol{e_u}|\!\|_\Omega, \qquad (4.84)$$

so that if we simplify on both sides,

$$\|\!|\boldsymbol{e_u}|\!\|_\Omega \lesssim \mathscr{E}_D(\boldsymbol{u}_\mathrm{d}, p_\mathrm{d}). \qquad (4.85)$$

Finally, since $b_\Omega(\cdot, \cdot)$ satisfies the inf-sup condition (2.24), using (4.81) and (4.83), using the continuity of $a_\Omega(\cdot, \cdot)$ in $\boldsymbol{H}^1_{\boldsymbol{0}, \Gamma_D}(\Omega)$, and then its coercivity as in (4.84), then

$$\|e_p\|_{0,\Omega} \lesssim \sup_{\substack{\boldsymbol{v} \in \boldsymbol{H}^1_{\boldsymbol{0}, \Gamma_D}(\Omega) \\ \boldsymbol{v} \neq \boldsymbol{0}}} \frac{b_\Omega(\boldsymbol{v}, e_p)}{\|\boldsymbol{\nabla} \boldsymbol{v}\|_{0,\Omega}} = \sup_{\substack{\boldsymbol{v} \in \boldsymbol{H}^1_{\boldsymbol{0}, \Gamma_D}(\Omega) \\ \boldsymbol{v} \neq \boldsymbol{0}}} \frac{\displaystyle\sum_{\sigma \in \Sigma} \int_\sigma \boldsymbol{d}_\sigma \cdot \boldsymbol{v} \, \mathrm{d}s - a_\Omega(\boldsymbol{e_u}, \boldsymbol{v})}{\|\boldsymbol{\nabla} \boldsymbol{v}\|_{0,\Omega}}$$

$$\leq \sup_{\substack{\boldsymbol{v} \in \boldsymbol{H}^1_{\boldsymbol{0}, \Gamma_D}(\Omega) \\ \boldsymbol{v} \neq \boldsymbol{0}}} \frac{\displaystyle\sum_{\sigma \in \Sigma} \int_\sigma \boldsymbol{d}_\sigma \cdot \boldsymbol{v} \, \mathrm{d}s}{\|\boldsymbol{\nabla} \boldsymbol{v}\|_{0,\Omega}} - \inf_{\substack{\boldsymbol{v} \in \boldsymbol{H}^1_{\boldsymbol{0}, \Gamma_D}(\Omega) \\ \boldsymbol{v} \neq \boldsymbol{0}}} \frac{a_\Omega(\boldsymbol{e_u}, \boldsymbol{v})}{\|\boldsymbol{\nabla} \boldsymbol{v}\|_{0,\Omega}}$$

$$\lesssim \mathscr{E}_D(\boldsymbol{u}_\mathrm{d}, p_\mathrm{d}) + \|\boldsymbol{\nabla} \boldsymbol{e_u}\|_{0,\Omega}$$

$$\lesssim \mathscr{E}_D(\boldsymbol{u}_\mathrm{d}, p_\mathrm{d}) + \|\!|\boldsymbol{e_u}|\!\|_\Omega. \qquad (4.86)$$

We can therefore conclude by combining (4.85) and (4.86). $\qquad \square$

4.4.3 Efficiency

In this section, we state and prove that the error indicator defined in (4.76) is efficient, that is, it is a lower bound for the defeaturing error, up to oscillations. In the case $n = 2$, the data compatibility conditions (4.45) are also required.

Theorem 4.4.4. *Consider the same notation and assumptions as in Theorem 4.4.3, and assume that all $\sigma \in \Sigma$ are also regular according to Definition 2.1.3. Then, assume that $\left|\gamma_\mathrm{n}^k\right| \simeq \left|\gamma_\mathrm{r}^k\right| \simeq \left|\gamma_{0,\mathrm{p}}^k\right|$ for all $k = 1, \ldots, N_f$. Moreover, for any $m \in \mathbb{N}$, let $\boldsymbol{\Pi}_m$ be*

such that $\mathbf{\Pi}_m|_\sigma \equiv \mathbf{\Pi}_{m,\sigma}$ *for all* $\sigma \in \Sigma$, *where* $\mathbf{\Pi}_{m,\sigma}$ *is the component-wise extensions of the Clément operator defined in (3.8), and let* $\boldsymbol{d}^k$ *be such that* $\boldsymbol{d}^k|_\sigma \equiv \boldsymbol{d}_\sigma$ *on all* $\sigma \in \Sigma^k$, *for all* $k = 1, \ldots, N_f$. *Finally, suppose that either* $n = 3$, *or* $n = 2$ *and the data compatibility conditions (4.45) are satisfied. Then the defeaturing error bounds the estimator* $\mathscr{E}_D(\boldsymbol{u}_{\mathrm{d}}, p_{\mathrm{d}})$ *introduced in (4.76) up to oscillations, that is*

$$\mathscr{E}_D(\boldsymbol{u}_{\mathrm{d}}, p_{\mathrm{d}}) \lesssim \|\|\boldsymbol{u} - \boldsymbol{u}_{\mathrm{d}}\|\|_\Omega + \|p - p_{\mathrm{d}}\|_{0,\Omega} + \mathrm{osc}(\boldsymbol{u}_{\mathrm{d}}, p_{\mathrm{d}}),$$

where for any $m \in \mathbb{N}$,

$$\mathrm{osc}(\boldsymbol{u}_{\mathrm{d}}, p_{\mathrm{d}})^2 := \sum_{k=1}^{N_f} \left(\mathrm{osc}^k(\boldsymbol{u}_{\mathrm{d}}, p_{\mathrm{d}}) \right)^2,$$

$$\mathrm{osc}^k(\boldsymbol{u}_{\mathrm{d}}, p_{\mathrm{d}}) := \left| \Gamma^k \right|^{\frac{1}{2(n-1)}} \left\| \boldsymbol{d}^k - \mathbf{\Pi}_m \left(\boldsymbol{d}^k \right) \right\|_{0,\Gamma^k} \qquad \text{for } k = 1, \ldots, N_f.$$

Proof. This proof follows similar steps as in the proof of Theorems 4.2.4 and 4.3.4. So let $\boldsymbol{e_u} := \boldsymbol{u} - \boldsymbol{u}_{\mathrm{d}} \in \boldsymbol{H}^1_{\boldsymbol{0},\Gamma_D}(\Omega)$, let $e_p := p - p_{\mathrm{d}} \in L^2(\Omega)$, and let $k \in \{1, \ldots, N_f\}$. First, let us recall the definition of $\Omega^k_\star := \Omega_\star \cap \Omega^k$, where Ω^k is the domain associated to feature F^k defined in Assumption 4.1.5. Then, let us consider the exact problem (4.67) restricted to $\Omega^k_\star$, with the natural Neumann boundary condition on $\gamma^k_{0,\mathrm{p}}$, and the natural Dirichlet boundary condition on $\partial\Omega^k_\star \setminus \partial\Omega_\star$. That is, similarly to (4.46), $\left(\boldsymbol{u}|_{\Omega^k_\star}, p|_{\Omega^k_\star} \right)$ is the weak solution of

$$\begin{cases} -\nabla \cdot \mathbf{s} \left(\boldsymbol{u}|_{\Omega^k_\star} \right) + \nabla \left(p|_{\Omega^k_\star} \right) = \boldsymbol{f} & \text{in } \Omega^k_\star \\ \boldsymbol{\nabla} \cdot \left(\boldsymbol{u}|_{\Omega^k_\star} \right) = f_c & \text{in } \Omega^k_\star \\ \boldsymbol{u}|_{\Omega^k_\star} = \boldsymbol{g}_D & \text{on } \partial\Omega^k_\star \cap \Gamma_D \\ \boldsymbol{u}|_{\Omega^k_\star} = \mathrm{tr}_{\partial\Omega^k_\star \setminus \partial\Omega_\star}(\boldsymbol{u}) & \text{on } \partial\Omega^k_\star \setminus \partial\Omega_\star \\ \mathbf{s} \left(\boldsymbol{u}|_{\Omega^k_\star} \right) \mathbf{n} - p|_{\Omega^k_\star} \mathbf{n} = \boldsymbol{g} & \text{on } \partial\Omega^k_\star \cap \Gamma_N \\ \mathbf{s} \left(\boldsymbol{u}|_{\Omega^k_\star} \right) \mathbf{n}_0 - p|_{\Omega^k_\star} \mathbf{n}_0 = \mathbf{s}(\boldsymbol{u})\mathbf{n}_0 - p\mathbf{n}_0 & \text{on } \gamma^k_{0,\mathrm{p}}. \end{cases} \tag{4.87}$$

By abuse of notation, we omit the explicit restriction of $\boldsymbol{u}$ and p to $\Omega^k_\star$. Then for all test functions $(\boldsymbol{v}_0, q_0) \in \boldsymbol{H}^1_{\boldsymbol{0},\partial\Omega^k_\star \setminus [\Gamma_N \cup \gamma^k_{0,\mathrm{p}}]}(\Omega^k_\star) \times L^2(\Omega^k_\star)$,

$$\int_{\Omega^k_\star} \mathbf{s}(\boldsymbol{u}) : \mathbf{e}(\boldsymbol{v}_0) \, \mathrm{d}x - \int_{\Omega^k_\star} p\boldsymbol{\nabla} \cdot \boldsymbol{v}_0 \, \mathrm{d}x = \int_{\Omega^k_\star} \boldsymbol{f} \cdot \boldsymbol{v}_0 \, \mathrm{d}x + \int_{\partial\Omega^k_\star \cap \Gamma_N} \boldsymbol{g} \cdot \boldsymbol{v}_0 \, \mathrm{d}s$$

$$+ \int_{\gamma^k_{0,\mathrm{p}}} \left(\mathbf{s}(u)\mathbf{n}_0 - p\mathbf{n}_0 \right) \cdot \boldsymbol{v}_0 \, \mathrm{d}s,$$

$$- \int_{\Omega^k_\star} q_0 \boldsymbol{\nabla} \cdot \boldsymbol{u} \, \mathrm{d}x = - \int_{\Omega^k_\star} q_0 f_c \, \mathrm{d}x. \tag{4.88}$$

Then, let us consider the simplified problem (4.70) also restricted to $\Omega^k_\star$, with the natural Neumann boundary condition on γ^k_{n}, and the natural Dirichlet boundary condition on

$\partial\Omega_\star^k \setminus \partial\Omega_\star$. Thus, since $\left(\boldsymbol{u}_{\mathrm{d}}|_{\Omega_\star^k}, p_{\mathrm{d}}|_{\Omega_\star^k}\right) = \left(\boldsymbol{u}_0|_{\Omega_\star^k}, p_0|_{\Omega_\star^k}\right)$ by definition, if we omit the explicit restrictions to $\Omega_\star^k$, then for all $(\boldsymbol{v}_0, q_0) \in \boldsymbol{H}^1_{\boldsymbol{0},\partial\Omega_\star^k \setminus [\Gamma_N \cup \gamma^k_{0,\mathrm{p}}]}(\Omega_\star^k) \times L^2(\Omega_\star^k)$,

$$\int_{\Omega_\star^k} \boldsymbol{s}(\boldsymbol{u}_{\mathrm{d}}) : \boldsymbol{\varepsilon}(\boldsymbol{v}_0) \, \mathrm{d}x - \int_{\Omega_\star^k} p_{\mathrm{d}} \boldsymbol{\nabla} \cdot \boldsymbol{v}_0 \, \mathrm{d}x = \int_{\Omega_\star^k} \boldsymbol{f} \cdot \boldsymbol{v}_0 \, \mathrm{d}x + \int_{(\partial\Omega_\star^k \cap \Gamma_N) \setminus \gamma^k_{\mathrm{n}}} \boldsymbol{g} \cdot \boldsymbol{v}_0 \, \mathrm{d}s$$

$$+ \int_{\gamma^k_{\mathrm{n}}} \left(\boldsymbol{s}(u_{\mathrm{d}})\mathbf{n} - p_{\mathrm{d}}\mathbf{n}\right) \cdot \boldsymbol{v}_0 \, \mathrm{d}s + \int_{\gamma^k_{0,\mathrm{p}}} \boldsymbol{g}_0 \cdot \boldsymbol{v}_0 \, \mathrm{d}s,$$

$$- \int_{\Omega_\star^k} q_0 \boldsymbol{\nabla} \cdot \boldsymbol{u}_{\mathrm{d}} \, \mathrm{d}x = - \int_{\Omega_\star^k} q_0 f_c \, \mathrm{d}x. \tag{4.89}$$

So for all $(\boldsymbol{v}_0, q_0) \in \boldsymbol{H}^1_{\boldsymbol{0},\partial\Omega_\star^k \setminus [\Gamma_N \cup \gamma^k_{0,\mathrm{p}}]}(\Omega_\star^k) \times L^2(\Omega_\star^k)$, using (4.88), (4.89), and the linearity of $\boldsymbol{s}$, we obtain

$$\int_{\Omega_\star^k} \boldsymbol{s}(\boldsymbol{e_u}) : \boldsymbol{\varepsilon}(\boldsymbol{v}_0) \, \mathrm{d}x - \int_{\Omega_\star^k} e_p \boldsymbol{\nabla} \cdot \boldsymbol{v}_0 \, \mathrm{d}x = \int_{\gamma^k_{\mathrm{n}}} \left(\boldsymbol{g} - \boldsymbol{s}(\boldsymbol{u}_{\mathrm{d}})\mathbf{n} + p_{\mathrm{d}}\mathbf{n}\right) \cdot \boldsymbol{v}_0 \, \mathrm{d}s$$

$$+ \int_{\gamma^k_{0,\mathrm{p}}} \left(\boldsymbol{s}(\boldsymbol{u})\mathbf{n}_0 - p\mathbf{n}_0 - \boldsymbol{g}_0\right) \cdot \boldsymbol{v}_0 \, \mathrm{d}s,$$

$$- \int_{\Omega_\star^k} q_0 \boldsymbol{\nabla} \cdot \boldsymbol{e_u} \, \mathrm{d}x = 0. \tag{4.90}$$

Let $(\boldsymbol{v}, q) \in \boldsymbol{H}^1_{\boldsymbol{0},\partial\Omega^k \setminus \Gamma_N}(\Omega^k) \times L^2(\Omega^k)$, so $\left(\boldsymbol{v}|_{\Omega_\star^k}, q|_{\Omega_\star^k}\right) \in \boldsymbol{H}^1_{\boldsymbol{0},\partial\Omega_\star^k \setminus [\Gamma_N \cup \gamma^k_{0,\mathrm{p}}]}(\Omega_\star^k) \times L^2(\Omega_\star^k)$. Recall that $\Omega_\star = \Omega \setminus \overline{F_{\mathrm{p}}}$, so that $\Omega^k = \mathrm{int}\left(F_{\mathrm{p}}^k \cup \Omega_\star^k\right)$. Consequently, reusing equation (4.80), using (4.90), since $\mathbf{n}_0 = -\mathbf{n}^k$ on $\gamma^k_{0,\mathrm{p}}$, and since $\mathbf{n} = \mathbf{n}^k$ on γ^k_{r}, then if we recall definition (4.75) of $\boldsymbol{d}_\sigma$,

$$\int_{\Omega^k} \boldsymbol{s}(\boldsymbol{e_u}) : \boldsymbol{\varepsilon}(\boldsymbol{v}) \, \mathrm{d}x - \int_{\Omega^k} e_p \boldsymbol{\nabla} \cdot \boldsymbol{v} \, \mathrm{d}x$$

$$= \int_{\gamma^k_{\mathrm{n}}} \left(\boldsymbol{g} - \boldsymbol{s}(\boldsymbol{u}_{\mathrm{d}})\mathbf{n} + p_{\mathrm{d}}\mathbf{n}\right) \cdot \boldsymbol{v} \, \mathrm{d}s + \int_{\gamma^k_{0,\mathrm{p}}} \left(-\boldsymbol{g}_0 - \boldsymbol{s}(\boldsymbol{u}_{\mathrm{d}})\mathbf{n}^k + p_{\mathrm{d}}\mathbf{n}^k\right) \cdot \boldsymbol{v} \, \mathrm{d}s$$

$$+ \int_{\gamma^k_{\mathrm{r}}} \left(\boldsymbol{g} - \boldsymbol{s}(\boldsymbol{u}_{\mathrm{d}})\mathbf{n}^k + p_{\mathrm{d}}\mathbf{n}^k\right) \cdot \boldsymbol{v} \, \mathrm{d}s$$

$$= \sum_{\sigma \in \Sigma^k} \int_\sigma \boldsymbol{d}_\sigma \cdot \boldsymbol{v} \, \mathrm{d}s,$$

$$\text{and } - \int_{\Omega^k} q \boldsymbol{\nabla} \cdot \boldsymbol{e_u} \, \mathrm{d}x = 0. \tag{4.91}$$

Now, let

$$a_{\Omega^k}(\cdot, \cdot) : \boldsymbol{H}^1_{\boldsymbol{0},\partial\Omega^k \setminus \Gamma_N}(\Omega^k) \times \boldsymbol{H}^1_{\boldsymbol{0},\partial\Omega^k \setminus \Gamma_N}(\Omega^k) \to \mathbb{R},$$

$$b_{\Omega^k}(\cdot, \cdot) : \boldsymbol{H}^1_{\boldsymbol{0},\partial\Omega^k \setminus \Gamma_N}(\Omega^k) \times L^2(\Omega^k) \to \mathbb{R},$$

be defined by

$$a_{\Omega^k}(\boldsymbol{w}, \boldsymbol{v}) = \int_{\Omega^k} \boldsymbol{s}(\boldsymbol{w}) : \boldsymbol{\varepsilon}(\boldsymbol{v}) \, \mathrm{d}x, \qquad \forall \boldsymbol{w}, \boldsymbol{v} \in \boldsymbol{H}^1_{\boldsymbol{0},\partial\Omega^k \setminus \Gamma_N}(\Omega^k),$$

$$b_{\Omega^k}(\boldsymbol{v}, q) = - \int_{\Omega^k} q \boldsymbol{\nabla} \cdot \boldsymbol{v} \, \mathrm{d}x, \qquad \forall \boldsymbol{v} \in \boldsymbol{H}^1_{\boldsymbol{0},\partial\Omega^k \setminus \Gamma_N}(\Omega^k), \forall q \in L^2(\Omega^k).$$
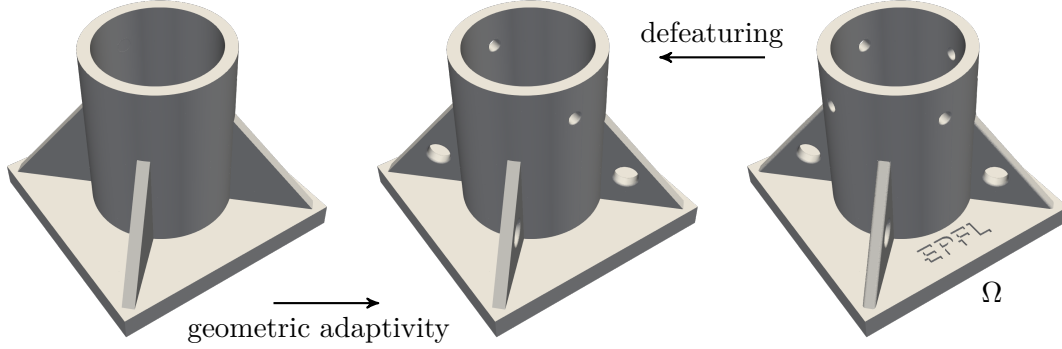
Figure 4.2 – Illustration of defeaturing and geometric adaptivity.

Note that $a_{\Omega^k}(\cdot,\cdot)$ and $b_{\Omega^k}(\cdot,\cdot)$ are continuous with respect to the norms $\|\boldsymbol{\nabla}\cdot\|_{0,\Omega^k}$ for $\boldsymbol{H}^1_{\boldsymbol{0},\partial\Omega^k\backslash\Gamma_N}(\Omega^k)$, and $\|\cdot\|_{0,\Omega^k}$ for $L^2(\Omega^k)$. Thus using (4.91), for all $\boldsymbol{v}\in\boldsymbol{H}^1_{\boldsymbol{0},\partial\Omega^k\backslash\Gamma_N}(\Omega^k)$,

$$\sum_{\sigma\in\Sigma^k}\int_\sigma \boldsymbol{d}_\sigma\cdot\boldsymbol{v}\,\mathrm{d}s = a_{\Omega^k}(\boldsymbol{e_u},\boldsymbol{v})+b_{\Omega^k}(\boldsymbol{v},e_p)\lesssim\left(\|\boldsymbol{\nabla}\boldsymbol{e_u}\|_{0,\Omega^k}+\|e_p\|_{0,\Omega^k}\right)\|\boldsymbol{\nabla}\boldsymbol{v}\|_{0,\Omega^k}. \quad (4.92)$$

The rest of the proof is identical to the one of Theorem 4.3.4, replacing (4.63) by (4.92). □

Remark 4.4.5. As in Remarks 4.2.5 and 4.3.5, when the data is regular, it is always possible to choose m large enough so that the asymptotic behavior of the oscillations is $\mathcal{O}\left(\max_{k=1,\dots,N_f}\left|\Gamma^k\right|^{m+\frac{1}{2(n-1)}}\right)$. Therefore, we can make sure that the oscillations get small with respect to the defeaturing error, when the features get small.

4.5   An adaptive geometric refinement strategy

In this section, we aim at defining an adaptive analysis-aware defeaturing strategy in a geometry Ω containing $N_f\geq 1$ distinct complex features. More precisely, starting from a fully defeatured geometry Ω_0, we want to precisely define a strategy that determines when and which geometrical features need to be reinserted in the geometrical model, among those that have been removed by defeaturing. Note that the word *defeaturing* may be misleading when thinking of an adaptive strategy: the geometry Ω_0 in which the problem is actually solved is (partially) defeatured, but the adaptive algorithm selects the features that need to be *added* to the geometrical model, in order to solve the differential problem up to a given accuracy. The concept of geometric adaptivity is illustrated in Figure 4.2.

In the sequel, we elaborate on each of the building blocks which compose one iteration of

an iterative process, as introduced in Section 2.5.3. To do so, let $i \in \mathbb{N}$ be the current iteration index of the adaptive geometric refinement strategy. For simplicity in this section, let us always write u_{d} the defeatured solution, even in the context of linear elasticity for which it should be $\boldsymbol{u}_{\mathrm{d}}$, or in the context of Stokes equations for which it should be $(\boldsymbol{u}_{\mathrm{d}}, p_{\mathrm{d}})$. To begin the process, let $\Omega_0^{(0)}$ be the fully defeatured geometry defined as in (4.1). That is, $\Omega_0^{(0)}$ is the domain in which all features of Ω are removed: their positive component is cut out, and their negative component is filled with material. Since some features will be reinserted during the adaptive process, we denote $\Omega_0^{(i)}$ the simplified geometry at the i-th iteration, and in general, we use the upper index (i) to refer to objects at the same iteration. However, to alleviate the notation, we will drop the index (i) when it is clear from the context. In particular, we will write $\Omega_0 \equiv \Omega_0^{(i)}$.

4.5.1 Solve and estimate

In the framework of Poisson's problem, we first solve the defeatured problem (3.4), respectively (4.38) in the framework of linear elasticity, and (4.71) in the framework of Stokes equations, defined in the (partially) defeatured geometry Ω_0. Then, we solve the local extension problem (4.6), respectively (4.40) and (4.73), for each feature having a non-empty positive component. We thus obtain the defeaturing solution $u_{\mathrm{d}} \equiv u_{\mathrm{d}}^{(i)}$ defined in (4.7), respectively (4.41) and (4.74), as an approximation of the exact solution u of (3.2), respectively (4.35) and (4.68), at iteration i. Then, the defeaturing error is estimated by $\mathscr{E}_D(u_{\mathrm{d}})$ defined in (4.13), respectively (4.43) and (4.76).

4.5.2 Mark

In this section, we drop the dependence of the defeaturing error estimator on the defeatured pressure p_{d} when Stokes equations are considered, without loss of clarity. Now, recalling that $N_f \equiv N_f^{(i)}$ at the current iteration i, we select and mark features

$$\left\{ F^{k_{\mathrm{m}}} \right\}_{k_{\mathrm{m}} \in I_{\mathrm{m}}} \subset \mathfrak{F} \quad \text{with } I_{\mathrm{m}} \subset \left\{ 1, \ldots, N_f^{(i)} \right\}$$

to be added to the (partially) defeatured geometry $\Omega_0 \equiv \Omega_0^{(i)}$. In the following, we use the maximum strategy presented in (2.36), but a Dörfler strategy as in (2.37) could also be used. That is, first recall definition (4.14) of the single feature contributions $\mathscr{E}_D^k(u_{\mathrm{d}})$ of the defeaturing error estimator $\mathscr{E}_D(u_{\mathrm{d}})$, for $k = 1, \ldots, N_f$. Then, after choosing a marking parameter $0 < \theta \leq 1$, a feature $F^{k_{\mathrm{m}}}$ is marked, i.e., $k_{\mathrm{m}} \in I_{\mathrm{m}}$, if it verifies

$$\mathscr{E}_D^{k_{\mathrm{m}}}(u_{\mathrm{d}}) \geq \theta \max_{k=1,\ldots,N_f} \left(\mathscr{E}_D^k(u_{\mathrm{d}}) \right). \tag{4.93}$$

In other words, the set of marked features are the ones giving the most substantial contribution to the defeaturing error estimator. The smallest is θ, the more features are selected, and inversely.

4.5.3 Refine

In this step, the defeatured geometry $\Omega_0^{(i)}$ is refined, meaning that the marked features $\left\{F^k\right\}_{k\in I_{\mathrm{m}}}$ are inserted in the geometrical model. That is, the new partially defeatured geometrical model $\Omega_0^{(i+1)}$ at the next iteration is built as follows:

$$\Omega_0^{\left(i+\frac{1}{2}\right)} = \Omega_0^{(i)} \setminus \overline{\bigcup_{k\in I_{\mathrm{m}}} F_{\mathrm{n}}^k}, \tag{4.94}$$

$$\Omega_0^{(i+1)} = \mathrm{int}\left(\overline{\Omega_0^{\left(i+\frac{1}{2}\right)} \cup \overline{\bigcup_{k\in I_{\mathrm{m}}} F_{\mathrm{p}}^k}}\right). \tag{4.95}$$

And thus in particular,

$$F_{\mathrm{n}}^{(i+1)} := F_{\mathrm{n}}^{(i)} \setminus \overline{\bigcup_{k\in I_{\mathrm{m}}} F_{\mathrm{n}}^k}, \quad F_{\mathrm{p}}^{(i+1)} := F_{\mathrm{p}}^{(i)} \setminus \overline{\bigcup_{k\in I_{\mathrm{m}}} F_{\mathrm{p}}^k},$$

$$\tilde{F}_{\mathrm{p}}^{(i+1)} := \tilde{F}_{\mathrm{p}}^{(i)} \setminus \overline{\bigcup_{k\in I_{\mathrm{m}}} \tilde{F}_{\mathrm{p}}^k}, \quad \Omega_\star^{(i+1)} := \Omega \setminus \overline{F_{\mathrm{p}}^{(i+1)}},$$

and as in definition (4.1),

$$\Omega_0^{(i+1)} = \mathrm{int}\left(\overline{\Omega_\star^{(i+1)} \cup \overline{F_{\mathrm{n}}^{(i+1)}}}\right).$$

Once the mesh and the defeatured geometry have been refined, the modules SOLVE and ESTIMATE presented in Section 4.5.1 can be called again. To do so, we update Ω_0 as $\Omega_0^{(i+1)}$, we define $N_f^{(i+1)} := N_f^{(i)} - \#I_{\mathrm{m}}$, we update the set of features $\mathfrak{F}$ as $\mathfrak{F} \setminus \left\{F^k\right\}_{k\in I_{\mathrm{m}}}$, and we renumber the features from 1 to $N_f^{(i+1)}$. The adaptive loop is continued until a certain given tolerance on the error estimator $\mathscr{E}_D(u_{\mathrm{d}})$ is reached, or until the set $\mathfrak{F}$ is empty, meaning that all the features have been added to the geometrical model.

Remark 4.5.1. Note that a more precise geometric refinement strategy could be performed since G_{p}^k can be seen as a negative feature of F_{p}^k whose simplified domain is $\tilde{F}_{\mathrm{p}}^k$, for all $k = 1, \ldots, N_f$. More precisely, for each $k = 1, \ldots, N_f$, one could consider separately the contributions to $\mathscr{E}_D^k(u_{\mathrm{d}})$ given by

- γ_{n}^k and $\gamma_{0,\mathrm{p}}^k$, which indicate whether feature F^k should be added to the defeatured geometrical model Ω_0;

- γ_{r}^k, which indicates whether the negative feature G_{p}^k of F_{p}^k should be removed from the simplified positive component $\tilde{F}_{\mathrm{p}}^k$ of F^k.

However, since this adds an extra complexity without introducing new conceptual ideas, this strategy is not further developed in the remaining part of this thesis.

4.6 Numerical considerations and experiments

In this section, we perform a few numerical experiments to illustrate the validity of the proposed *a posteriori* defeaturing error estimators. Thanks to the experiments, we also demonstrate that the adaptive procedure presented in Section 4.5 ensures the convergence of the defeaturing error.

To estimate the error introduced by defeaturing the problem geometry in practice, one needs to perform the same steps (i)–(iii) as presented in Section 3.5, where steps (ii) and (iii) are repeated for each feature. More precisely, in step (ii), one solves the extension problem (4.6) on the simplified positive component $\tilde{F}_{\mathrm{p}}^k$ of every feature F^k, $k = 1, \ldots, N_f$, while in step (iii), the boundary averages and integrals $\overline{d_\sigma}^\sigma$ and $\left\| d_\sigma - \overline{d_\sigma}^\sigma \right\|_{0,\sigma}$ are computed for each $\sigma \in \Sigma$ as defined in (4.12).

The numerical experiments of this section have been implemented as in Chapter 3. That is, we use IGA on very fine meshes for the numerical approximation of the PDEs, and multipatch and trimming techniques for the geometrical description of the features.

4.6.1 Impact of some feature properties on the defeaturing error

While validating the theory developed in Section 4.2 for Poisson's problem, we study in this section the impact of some properties of the geometrical features on the defeaturing error and estimator. In particular, we study the influence of the size and shape of the features, of the distance between them, and of their number.

4.6.1.1 Size and shape of the features

Let us consider again the numerical experiment of Chapter 3, Section 3.5.1.2, in which we have considered a geometry with a very small important feature, and a large feature whose presence or absence does not affect much the solution accuracy. The considered geometry is illustrated in Figure 4.3b. From (3.49), we see that the results provided in this numerical experiment have already used the multi-feature defeaturing error estimator presented in this chapter.

Let us then perform the same test, but with square holes instead of circular ones. That is, let us consider the same defeatured geometry $\Omega_0 = (0,1)^2$, and the same data to solve Poisson equation (3.1), but now $\Omega := \Omega_0 \setminus \left(\overline{F^1} \cup \overline{F^2} \right)$, where F^1 and F^2 are squares centered at $(1.1 \cdot 10^{-3}, 1.1 \cdot 10^{-3})^T$ and $(8.9 \cdot 10^{-1}, 8.9 \cdot 10^{-1})^T$, respectively, and whose sides have length $2 \cdot 10^{-3}$ and $2 \cdot 10^{-1}$, respectively. The geometry is illustrated in Figure 4.3b, and we recall that the solution has a high gradient close to the bottom left corner where F^1 is located, and is almost constantly equal to zero close to the top right corner where F^2 is located.

(a) Exact domain with two circular features.   (b) Exact domain with two square features.

Figure 4.3 – Numerical test 4.6.1.1 – Exact geometries used for the comparison between feature sizes and shapes (not at scale).

Features	$\mathscr{E}_D^1(u_0)$	$\mathscr{E}_D^2(u_0)$	$\mathscr{E}_D(u_0)$	$|u - u_0|_{1,\Omega}$	η_{eff}
Circular holes	$5.03 \cdot 10^{-2}$	$7.86 \cdot 10^{-6}$	$5.03 \cdot 10^{-2}$	$1.45 \cdot 10^{-2}$	3.47
Square holes	$6.29 \cdot 10^{-2}$	$7.73 \cdot 10^{-6}$	$6.29 \cdot 10^{-2}$	$1.64 \cdot 10^{-2}$	3.84

Table 4.1 – Numerical test 4.6.1.1 – Results of the comparison between feature sizes and shapes.

Results are presented in Table 4.1. In both geometries, independently of the shape of the features, F^1 is indeed more important than F^2 since the estimator for F^1 is four orders of magnitude larger than the estimator for F^2. In both cases, the proposed estimator well estimates the defeaturing error since the effectivity index η_{eff} is reasonably low, with values comparable to the single feature experiments of Chapter 3. This validates the theory developed in Section 4.2.

4.6.1.2   Distance between features

The following numerical example is used to show that Assumption 4.1.5 is very weak, as one can consider features that are arbitrarily close to one another, as soon as the number of close features is bounded. Indeed, consider a geometry with either two square features, one positive and one negative, or one complex feature, as follows. Let $\Omega_0 := (0,1)^2$, let $s \in (-0.1, 0.8)$, and let $\Omega_s := \text{int}\left(\overline{\Omega_0} \cup \overline{F_s^1} \setminus \overline{F_s^2}\right)$ with

$$F_s^1 := \left(0.4 - \frac{s}{2}, 0.5 - \frac{s}{2}\right) \times (1, 1.1),$$

$$F_s^2 := \left(0.5 + \frac{s}{2}, 0.6 + \frac{s}{2}\right) \times (0.9, 1),$$

as illustrated in Figure 4.4. That is,

- if $s \leq 0$, then $F_s^1 \cup F_s^2$ needs to be considered as the single feature of Ω_s because of Assumption 4.1.5, where F_s^1 is the positive component of that feature, and F_s^2 is its negative component. In this case, we let $\gamma_{0,s}^1 := \gamma_{0,\text{p}}$, $\gamma_{0,s}^2 := \gamma_{0,\text{n}}$, $\gamma_s^1 := \gamma_\text{p}$, and $\gamma_s^2 := \gamma_\text{n}$;

(a) Simplified domain Ω_0 for $s = 0.1$.

(b) Exact domain Ω_s for $s = 0.1$.

(c) Zoom on part of the upper boundary of Ω_0 (up) and Ω_s (down) for $s = 0$.

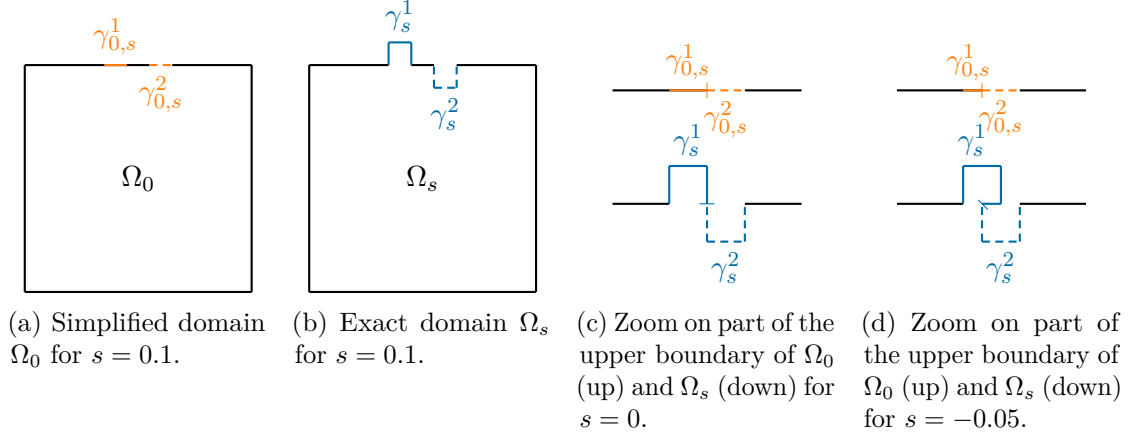(d) Zoom on part of the upper boundary of Ω_0 (up) and Ω_s (down) for $s = -0.05$.

Figure 4.4 – Numerical test 4.6.1.2 – Simplified domain Ω_0 and exact domains Ω_s for different values of s.

- if $s > 0$, then F_s^1 and F_s^2 are two distinct features satisfying Assumption 4.1.5 and separated by a distance s, where F_s^1 is positive, and F_s^2 is negative. In this case, we let $\gamma_{0,s}^1 := \gamma_{0,p}^1 = \gamma_0^1$, $\gamma_{0,s}^2 := \gamma_{0,n}^2 = \gamma_0^2$, $\gamma_s^1 := \gamma_p^1 = \gamma^1$, and $\gamma_s^2 := \gamma_n^2 = \gamma^2$, following the multi-feature notation presented in this chapter.

Let us consider Poisson problem (3.1) with $f \equiv 0$ in Ω, $g_D(x, y) := 40 \cos(\pi x) + 10 \cos(5\pi x)$ on

$$\Gamma_D := (0, 1) \times \{0\},$$

and $g \equiv 0$ on $\Gamma_N := \partial\Omega_s \setminus \overline{\Gamma_D}$. We solve the defeatured Poisson problem (3.3) with the same data, and we take $g_0 \equiv 0$ on

$$\gamma_{0,s}^1 = \left(0.4 - \frac{s}{2}, 0.5 - \frac{|s|}{2}\right) \times \{1\}$$

$$\text{and} \quad \gamma_{0,s}^2 = \left(0.5 + \frac{s}{2}, 0.6 + \frac{s}{2}\right) \times \{1\}.$$

Finally, we solve the Dirichlet extension problem (4.5) in $\tilde{F}_s^1 = F_s^1$.

We choose different values of s in order to consider different cases:

- with $s = 2 \cdot 10^{-1}$, the distance between the features and the distance between $\gamma_{0,s}^1$ and $\gamma_{0,s}^2$ are of the same order of magnitude as the measures of $\gamma_{0,s}^1$ and $\gamma_{0,s}^2$;

- with $s = 2 \cdot 10^{-4}$, the distance between $\gamma_{0,s}^1$ and $\gamma_{0,s}^2$ is several orders of magnitude smaller than the measures of $\gamma_{0,s}^1$ and $\gamma_{0,s}^2$;

- with $s = 0$, the boundaries of the feature components intersect in one single point;

- with $s = -1 \cdot 10^{-3}$, the measure of the intersection between the boundaries of the

s	$\mathscr{E}_D(u_\mathrm{d})$	$|u - u_\mathrm{d}|_{1,\Omega_s}$	η_eff
$2.0 \cdot 10^{-1}$	1.58	1.49	1.73
$2.0 \cdot 10^{-4}$	2.84	1.68	1.69
$0.0 \cdot 10^{0}$	2.84	1.68	1.69
$-1.0 \cdot 10^{-3}$	27.0	15.1	1.78
$-9.9 \cdot 10^{-2}$	24.5	14.3	1.71

Table 4.2 – Numerical test 4.6.1.2 – Results for the problem with two features; $s > 0$ corresponds to separate features, while $s < 0$ corresponds to features with overlapping boundaries.

feature components is several orders of magnitude smaller than the measures of the boundaries of the features;

- with $s = -9.9 \cdot 10^{-2}$, the measure of the intersection between the boundaries of the feature components is of the same order of magnitude as the measures of the boundaries of the features.

The results are presented in Table 4.2, and we indeed see that the defeaturing estimator approximates well the defeaturing error in all the different presented cases. In particular, we observe that the effectivity index η_eff is not influenced by the distance separating the positive and negative components of the feature(s). This confirms the fact that Assumption 4.1.5 in not very restrictive in practice.

4.6.1.3 Number of features

Under Assumption 4.1.5, the effectivity index of the defeaturing error estimator should not depend on the number of features present in the original geometry Ω. To verify this, let $\Omega_0 := (0,1)^2$ be the fully defeatured domain, and let $\Omega := \Omega_0 \setminus \bigcup_{k=1}^{N_f} \overline{F^k}$, where $N_f = 27$, and the features F^k are circular holes of random radii in the interval $(0, 0.01)$, which are randomly distributed in Ω_0 such that Assumption 4.1.5 is satisfied. For the sake of reproducibility, the values of the radii and centers of the features are entered in Table 4.3. The exact domain Ω with all the 27 features, is represented in Figure 4.5a.

Suppose that we want to find a good approximation of the solution of Poisson problem (3.1) in Ω, whose exact solution is shown in Figure 4.5c. That is, we consider the data $f(x,y) := -18e^{-3(x+y)}$ in Ω_0, $g_D(x,y) := e^{-3(x+y)}$ on

$$\Gamma_D := \Big([0,1) \times \{0\} \Big) \cup \Big(\{0\} \times [0,1) \Big),$$

$g(x,y) := -3e^{-3(x+y)}$ on $\partial \Omega_0 \setminus \overline{\Gamma_D}$ and $g \equiv 0$ on ∂F^k for $k = 1, \dots, N_f$. Thus we perform the adaptive algorithm introduced in Section 4.5 starting from the fully defeatured

Feature index k	1	2	3	4	5	6	7	8	9
Radius $[\cdot 10^{-2}]$	8.13	6.64	3.89	7.40	8.18	6.00	0.85	9.22	0.54
Center $[\cdot 10^{-2}]$	0.98	2.84	5.46	7.16	8.99	0.67	3.12	4.95	7.06
	0.93	1.24	0.57	0.93	1.04	3.40	3.03	3.08	2.48
Feature index k	10	11	12	13	14	15	16	17	18
Radius $[\cdot 10^{-2}]$	5.27	1.19	3.80	8.13	2.44	8.84	7.13	3.78	2.49
Center $[\cdot 10^{-2}]$	8.86	0.67	3.28	5.01	7.44	8.93	1.10	2.44	5.45
	2.90	5.35	4.46	5.09	4.88	5.07	6.93	6.78	7.73
Feature index k	19	20	21	22	23	24	25	26	27
Radius $[\cdot 10^{-2}]$	2.53	6.67	0.50	6.85	6.20	7.47	8.77	2.00	1.00
Center $[\cdot 10^{-2}]$	7.27	9.21	0.22	3.26	5.01	7.06	8.99	4.00	1.00
	7.33	6.96	8.24	9.15	9.10	8.78	8.98	7.00	9.00

Table 4.3 – Numerical test 4.6.1.3 – Data of the 27 circular features.
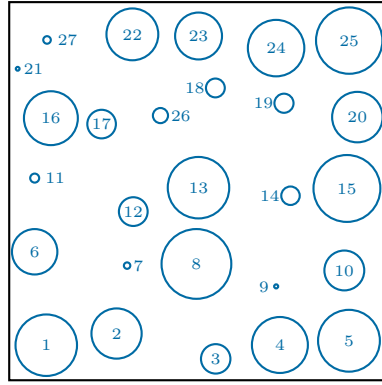
(a) Exact domain Ω with 27 features.
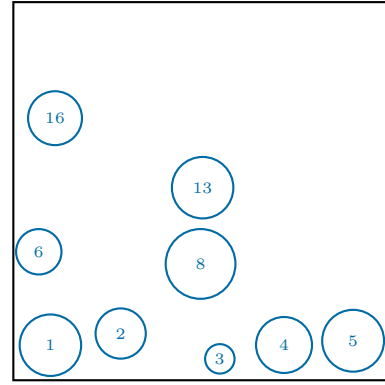
(b) Partially defeatured domain $\Omega^{(i)}$ at iteration $i = 7$.
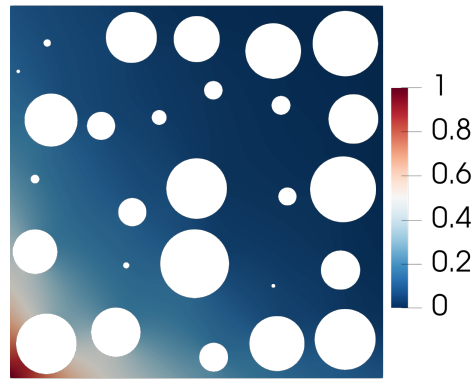
(c) Exact solution in Ω

Figure 4.5 – Numerical test 4.6.1.3 – Geometry with 27 features, considered exact solution, and corresponding partially defeatured geometrical model at iteration $i = 7$.
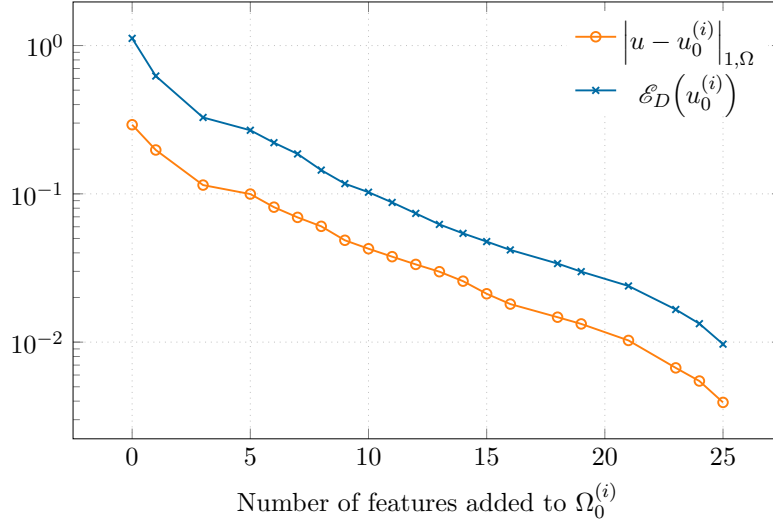
Figure 4.6 – Numerical test 4.6.1.3 – Behavior of the defeaturing error and estimator with respect to the number of features in the defeatured geometrical model $\Omega_0^{(i)}$ equal to $27 - N_f^{(i)}$. Each marker corresponds to the value at one iteration $i \geq 0$.

domain $\Omega_0^{(0)} := \Omega_0$, with marking parameter $\theta = 0.95$. We recursively solve the partially defeatured problem (3.3) in $\Omega_0^{(i)}$ at each iteration $i \geq 0$, and we call $u_0^{(i)}$ its solution.

The results are presented in Figure 4.6, and the sets of added features at each iteration are the following: $\{1\}$, $\{2, 6\}$, $\{4, 16\}$, $\{8\}$, $\{3\}$, $\{5\}$, $\{13\}$, $\{12\}$, $\{17\}$, $\{22\}$, $\{11\}$, $\{10\}$, $\{15\}$, $\{23\}$, $\{24, 16\}$, $\{7\}$, $\{20, 27\}$, $\{18, 25\}$, $\{21\}$, $\{14\}$, $\{19, 9\}$. For instance, the error is divided by 10 when 9 out of the 27 features are inserted in the partially defeatured geometrical model, i.e., a third of total number of features; this happens at iteration $i = 7$, and $\Omega_0^{(7)}$ is represented in Figure 4.5b. Remark that the iteration index is directly linked to the number $N_f^{(i)}$ at each iteration i, that is, to the number of features that are still missing in the simplified geometrical model $\Omega_0^{(i)}$ with respect to the 27 features in Ω. Moreover, we can see that the effectivity index is independent of the number of features that are not in the simplified geometrical model in which the problem is solved. Indeed, η_{eff} remains around the same value at each iteration, between 2.1 and 3.8. This confirms the theory developed in this chapter, in particular the reliability and efficiency results of Theorems 4.2.3 and 4.2.4.

4.6.2   Three dimensional elastic structure

For this next numerical experiment, let us consider the exact domain Ω and the corresponding defeatured domain Ω_0 represented in Figure 4.7. More precisely, the base has dimensions $200 \times 200 \times 20$ [mm], and the cylinder has a height of 150 [mm]. Moreover and in particular, the exact domain contains 20 features numbered as illustrated in
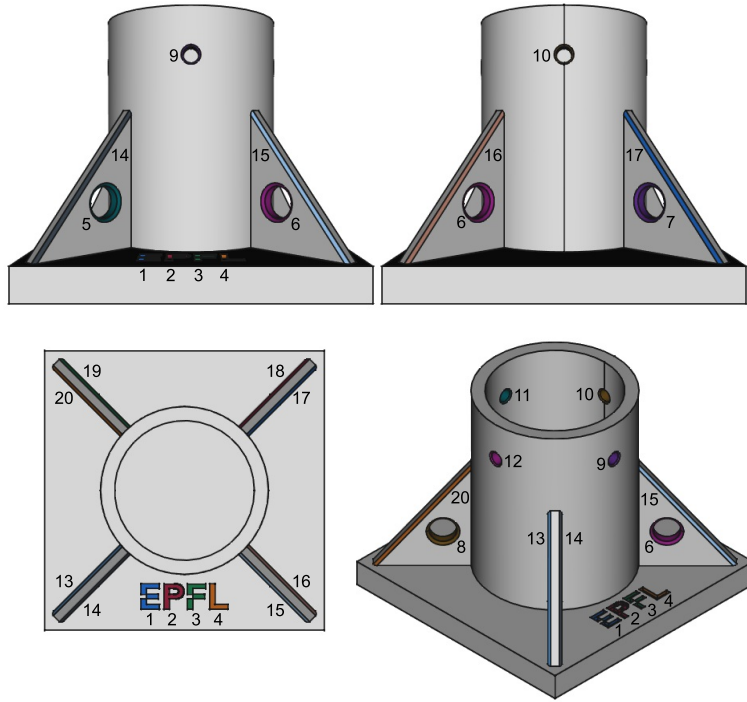
(a) Exact geometry Ω and numbering of the 20 features (in color).
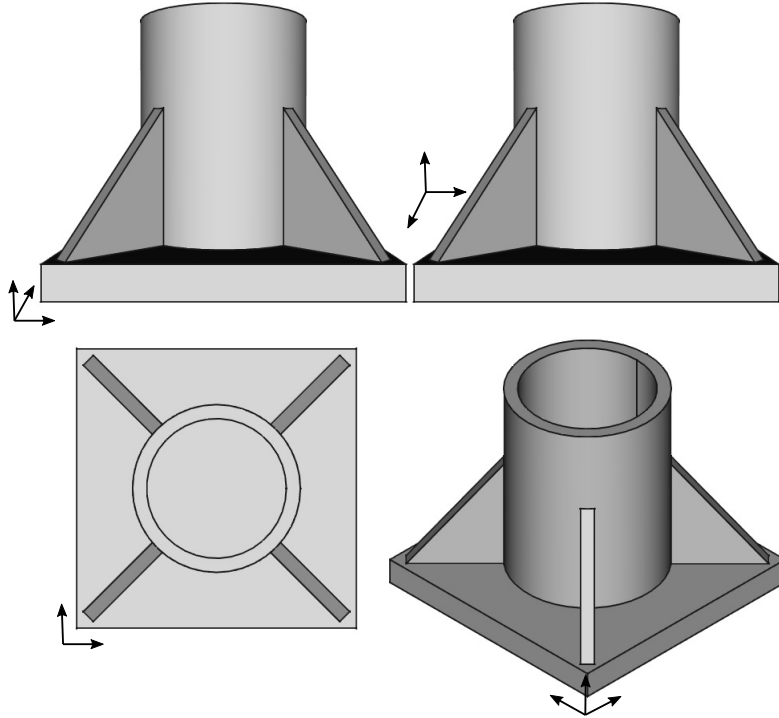
(b) Defeatured geometry Ω_0

Figure 4.7 – Numerical test 4.6.2 – Exact and defeatured 3D domains; the colored boundaries correspond to γ^k, for each feature $k = 1, \ldots, 20$ as numbered in (a)

Figure 4.7a:

- F^1 to F^4 are the four letters of the carved "EPFL" logo, in order (see also Figure 4.2 in which these features are more visible).

- F^5 to F^8 are the four holes in the stiffeners, counted counter-clockwise beginning from the one on the left of the "EPFL" logo.

- F^9 to F^{12} are the four holes in the vertical part of the structure, counted counter-clockwise beginning from the one above the "EPFL" logo.

- F^{13} to F^{20} are the eight rounds present on the left and right diagonal angles of the stiffeners, counted counter-clockwise beginning from the left round of the stiffener on the left of the "EPFL" logo.

Rounds, holes and carved logos are three of the most typical features that finite element analysis practitioners encounter in CAD designs. These features are interesting to analyze, since they are usual candidates to be removed before creating a finite element mesh.

Taking the origin at the bottom lower left corner of the structure, let Γ_D be the bottom of the structure and $\Gamma_N := \partial\Omega \setminus \overline{\Gamma_D}$, let $\boldsymbol{f} = \boldsymbol{0}$ [Pa], $\boldsymbol{g}_D = \boldsymbol{0}$ [mm], and

$$
\boldsymbol{g} \, [\mathrm{N} \cdot \mathrm{mm}^{-1}] = \begin{cases} \boldsymbol{0} & \text{on } \Gamma_N \setminus \overline{\Gamma_{\text{top}}} \\ \boldsymbol{e}_x = (1, 0, 0)^T & \text{on } \Gamma_{\text{top}}, \end{cases}
$$

where Γ_{top} is the top face of the cylinder. Then let $\boldsymbol{u} \in \boldsymbol{H}^1_{\boldsymbol{0},\Gamma_D}(\Omega)$ be the solution of the linear elasticity problem given by (4.35), where the material properties correspond to steel. That is, the Lamé parameters λ and μ are expressed in terms of the Young modulus $E = 210 \cdot 10^9$ [Pa] and Poisson's ration $\nu = 0.3$ [–] as

$$
\lambda = \frac{E\nu}{(1+\nu)(1-2\nu)} \quad \text{and} \quad \mu = \frac{E}{2(1+\nu)}.
$$

Now, let us extend $\boldsymbol{f}$ by $\boldsymbol{0}$ in all features so that $\boldsymbol{f} = \boldsymbol{0}$ [Pa] in Ω_0, and let $\boldsymbol{g}_0 = \boldsymbol{0}$ [N·mm^{-1}] on $\gamma_0 := \partial\Omega_0 \setminus \overline{\partial\Omega}$. Then we compute the defeatured solution $\boldsymbol{u}_{\mathrm{d}} \equiv \boldsymbol{u}_0 \in \boldsymbol{H}^1_{\boldsymbol{0},\Gamma_D}(\Omega_0)$ given by problem (4.38). Finally, we compute the estimator $\mathscr{E}_D(\boldsymbol{u}_{\mathrm{d}})$ defined in (4.43) by computing each feature contribution $\mathscr{E}_D^k(\boldsymbol{u}_{\mathrm{d}})$ for $k = 1, \ldots, 20$ as in (4.44).

To numerically solve the exact and defeatured problems, we discretize them using immersed isogeometric analysis thanks to the Igatools library, see [Pauletti et al., 2015]. For the geometric description of the structure and the features, and for the local meshing process required, trimming techniques have been used, see e.g., [Antolín et al., 2019, 2022]. The interested reader is referred to Chapter 6 and to [Cottrell et al., 2009] for a presentation of isogeometric analysis and advanced spline technologies. A rather fine

Feature index k	1	2	3	4	5	6	7	8	9	10
$\mathscr{E}_D^k(\boldsymbol{u}_{\mathrm{d}})$ [$\cdot 10^{-3}$J]	5.540	8.255	8.617	3.632	196.9	196.9	196.9	196.8	176.1	74.05
Feature index k	11	12	13	14	15	16	17	18	19	20
$\mathscr{E}_D^k(\boldsymbol{u}_{\mathrm{d}})$ [$\cdot 10^{-3}$J]	176.1	74.05	25.00	42.17	41.76	25.21	25.52	41.88	41.93	25.58

Table 4.4 – Numerical test 4.6.2 – Feature contributions $\mathscr{E}_D^k(\boldsymbol{u}_{\mathrm{d}})$ to the multi-feature estimator $\mathscr{E}_D(\boldsymbol{u}_{\mathrm{d}})$.

Iteration i	0	1	2	3	4
Marked features	$5, 6, 7, 8$	$9, 11$	$10, 12$	$14, 15, 18, 19$	$17, 20$
$\mathscr{E}_D\left(\boldsymbol{u}_{\mathrm{d}}^{(i)}\right)$ [$\cdot 10^{-3}$J]	487.7	283.5	139.8	91.16	47.29
Iteration i	5	6	7	8	9
Marked features	$13, 16$	3	2	1	4
$\mathscr{E}_D\left(\boldsymbol{u}_{\mathrm{d}}^{(i)}\right)$ [$\cdot 10^{-3}$J]	34.70	14.37	11.25	7.151	3.823

Table 4.5 – Numerical test 4.6.2 – Results of the adaptive defeaturing strategy for $n_{\mathrm{el}} = 128$ elements.

mesh is used in order to reduce the error coming from numerical approximation. More precisely, the bounding box of Ω_0 is meshed with $n_{\mathrm{el}} = 128$ elements per direction, and B-splines of degree 2 and regularity 1 are used. Results are presented in Table 4.4, where we report each feature contribution $\mathscr{E}_D^k(\boldsymbol{u}_{\mathrm{d}})$ for $k = 1, \ldots, 20$. The obtained error estimator is equal to $\mathscr{E}_D(\boldsymbol{u}_{\mathrm{d}}) = 4.877 \cdot 10^{-1}$ [J]. Moreover, the magnitude of the solution displacements $\boldsymbol{u}$ and $\boldsymbol{u}_{\mathrm{d}}$, and the corresponding von Mises stress distributions are shown in Figures 4.8 and 4.9, respectively.

We can first see that the absence of features F^5 to F^8 in the defeatured geometry significantly affects the solution in the stiffeners. This is indeed reflected in the estimator: the estimator contributions of those four features is very large, corresponding to around half of the total error estimator. On the other hand, the solution is basically constant around the "EPFL" logo, no deformation is observed around it. We can therefore expect that the absence of features F^1 to F^4 in the defeatured geometry is not affecting much the accuracy of the solution. This is indeed observed in the estimator contributions of those features, as $\mathscr{E}_D^1(\boldsymbol{u}_{\mathrm{d}})$ to $\mathscr{E}_D^4(\boldsymbol{u}_{\mathrm{d}})$ are the lowest contributions of the estimator, corresponding to around $1\% - 2\%$ of $\mathscr{E}_D(\boldsymbol{u}_{\mathrm{d}})$. This is a typical situation that simulation practitioners encounter daily: carved logos and trademarks are usually defeatured before creating a finite element mesh, since they complicate the meshing process and increase the number of elements, but they contribute little to the accuracy of the problem solution. The proposed estimator identifies them straightaway.

Let us now run the adaptive algorithm introduced in Section 4.5 with $\theta = 0.99$ as marking parameter, until all features are added to the geometrical model. We call $\boldsymbol{u}_{\mathrm{d}}^{(i)}$ the solution
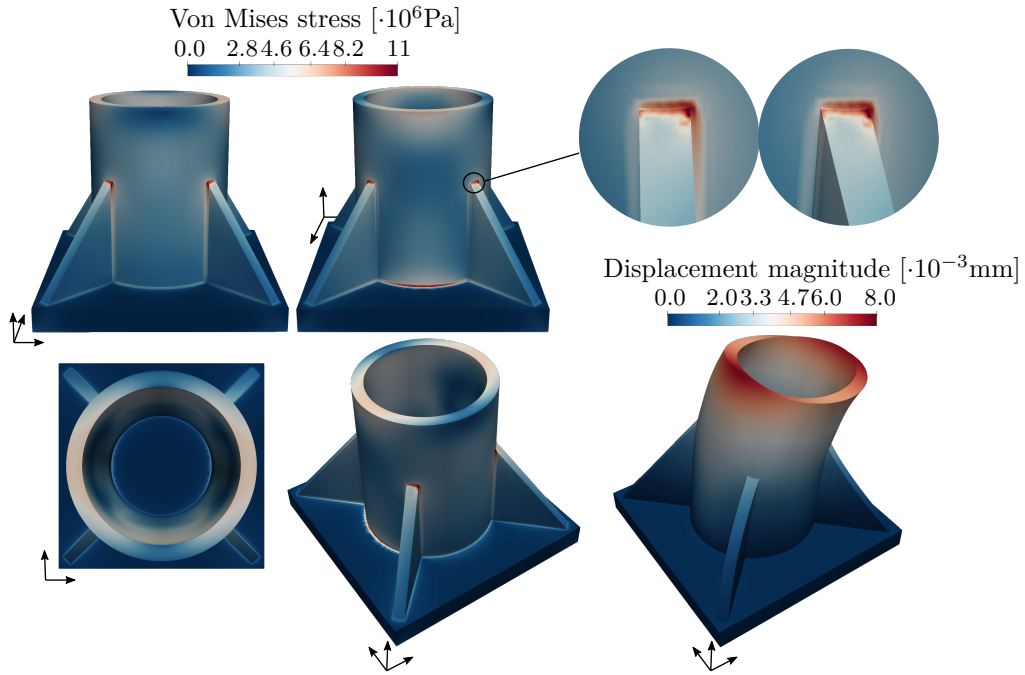
Figure 4.8 – Numerical test 4.6.2 – Defeatured solution in the defeatured geometry Ω_0. The views correspond to Figure 4.7, and the deformed configuration is magnified $[\times 5 \cdot 10^3]$ for visualization purposes.
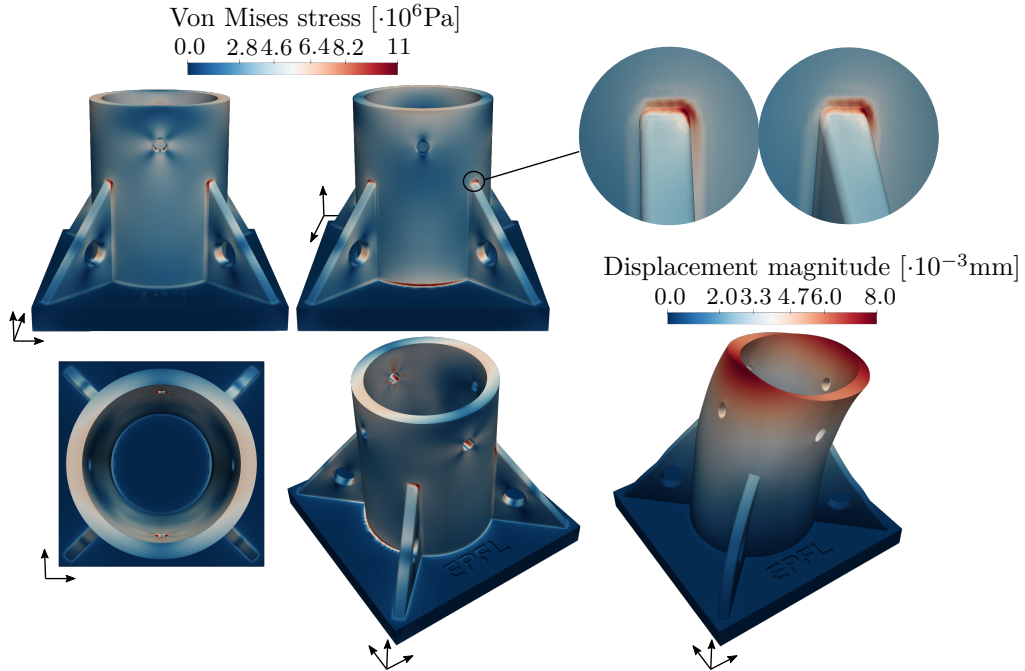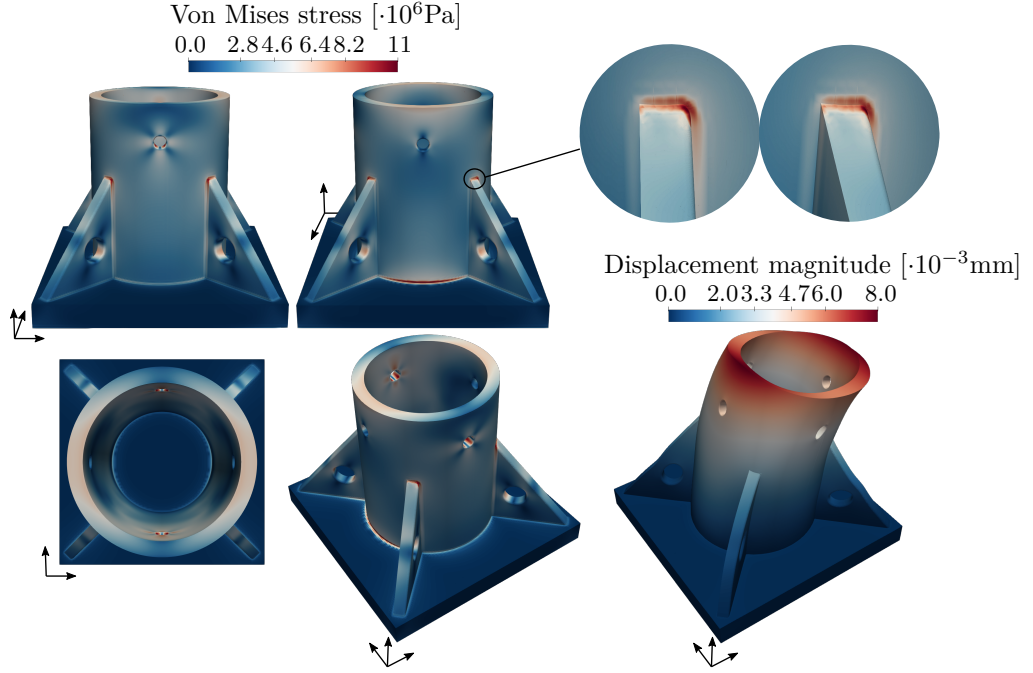

Figure 4.9 – Numerical test 4.6.2 – Exact solution in the exact geometry Ω. The views correspond to Figure 4.7, and the deformed configuration is magnified $[\times 5 \cdot 10^3]$ for visualization purposes.

Figure 4.10 – Numerical test 4.6.2 – Partially defeatured solution in the partially defeatured geometry obtained at iteration 4. The letters of the "EPFL" logo and the four rounds F^{13}, F^{16}, F^{17} and F^{20} are the missing features in this geometry. The views correspond to Figure 4.7, and the deformed configuration is magnified $[\times 5 \cdot 10^3]$ for visualization purposes.

of the defeatured problem (4.38) at iteration i. In Table 4.5, we report the indices of the features that are added to the defeatured geometrical model at each iteration, together with the value of the estimator $\mathscr{E}_D\left(\boldsymbol{u}_{\mathrm{d}}^{(i)}\right)$. The magnitude of the solution displacement and the corresponding von Mises stress distribution at iteration 4 are represented in Figure 4.10. Comparing the values of the estimator at each iteration and the von Mises stress distributions around each feature, we can see that the features that are added to the geometrical model at each iteration seem to be the ones that are affecting the most the solution accuracy, as one would expect. We can also see that to reduce the error estimator by 90%, it is enough to consider 12 features out of the total 20 features of Ω (see iteration 4, whose solution is represented in Figure 4.10).

For instance, the holes F^9 and F^{11} are added before the holes F^{10} and F^{12} during the adaptive process, because of the direction in which the structure is bending due to the Neumann traction in the x-direction; this is reflected by the variation of the von Mises stresses that are larger in F^9 and F^{11} than in F^{10} and F^{12}. By symmetry of the structure, we can see that larger stresses are present around the rounds F^{14}, F^{15}, F^{18} and F^{19} than around the other four rounds. This is again coming from the direction of the bending. And very interestingly, the estimator is able to capture this effect, as rounds F^{14}, F^{15}, F^{18} and F^{19} are introduced in the defeatured geometry after iteration 3, while the other
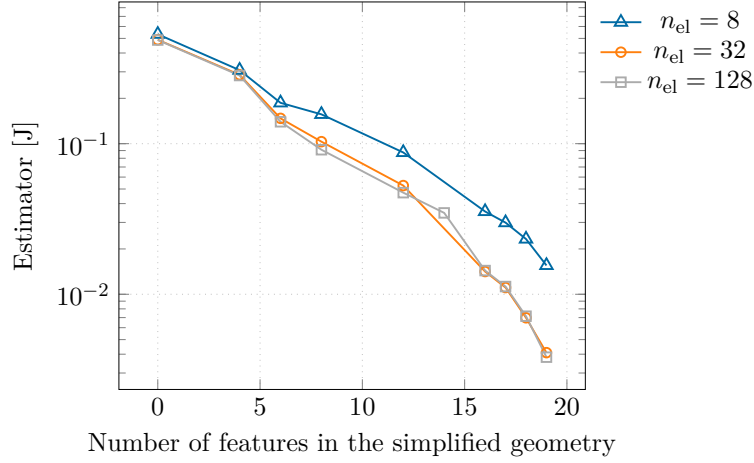
119

Figure 4.11 – Numerical test 4.6.2 – Results of the adaptive defeaturing strategy for different discretization parameters.

Iteration i	0	1	2	3	4	5	6	7	8	9
$n_{el} = 8$	5, 6, 7, 8	9, 11	10, 12	14, 15, 18, 19	13, 16, 17, 20	1	2	3	4	×
$n_{el} = 32$	5, 6, 7, 8	9, 11	10, 12	14, 15, 18, 19	13, 16, 17, 20	3	2	1	4	×
$n_{el} = 128$	5, 6, 7, 8	9, 11	10, 12	14, 15, 18, 19	17, 20	13, 16	3	2	1	4

Table 4.6 – Numerical test 4.6.2 – Marked features at each iteration on different mesh refinements.

rounds are introduced later, after iterations 4 and 5. Rounds are other typical examples of features that are candidates to be removed. However in this case, the situation is usually less clear. Indeed, from one hand, rounds complicate the meshing process and increase the number of elements in the model. But on the other hand, depending on the boundary conditions, removing rounds may lead to the creation of singularities in the solution. The proposed estimator is able to determine the impact of removing those rounds.

Finally, the numerical error has not been considered in this chapter. However, it is interesting to note that the estimator is still able to drive the proposed adaptive strategy on a coarser mesh. Indeed, this algorithm has been performed on multiple meshes containing a different number n_{el} of elements in each space direction of the bounding box of Ω_0. More precisely, we have considered $n_{el} = 8$, 32 and 128. In all three cases, the convergence of the estimator $\mathscr{E}_D\left(\boldsymbol{u}_d^{(i)}\right)$ is reported in Figure 4.11, and the features chosen at each iteration are reported in Table 4.6. We can observe that except for features whose error contributions are very close to one another, the adaptive algorithm is able to correctly choose the important features, even on the coarsest mesh.

A numerical framework for analysis-aware defeaturing

Part II

5 | An adaptive finite element defeaturing strategy

Finding the closed-form solution of a BVP can only be achieved in simplified scenarios, even when the BVP is defined in a relatively simple geometry and is expressed in variational form as in (2.12). As a consequence, an enormous amount of effort has been put into the development of numerical methods that suitably approximate the solution of BVPs. We concentrate in particular on Galerkin finite element methods, which are techniques based on a discretization of the variational problem, and which allow us to benefit from the computational power of modern computers. Moreover, the interoperability between the design of complex objects and the numerical resolution of PDEs on those objects has been a major challenge since the introduction of finite element methods. Advanced numerical techniques have been developed to tackle this issue, and IGA, introduced in Chapter 6, is one of the most successful methods advancing in this direction. However, dealing with very complex geometries remains challenging, and even the most recent and most efficient numerical methods may come at a prohibitive cost.

In this chapter, we therefore want to integrate the analysis-aware defeaturing framework introduced in Part I of this thesis, into an adaptive finite element framework. More precisely, in the context of Poisson's problem, we generalize the geometric refinement strategy of Chapter 4, Section 4.5, by introducing an adaptive algorithm which is twofold. On the one hand, starting from a fully defeatured geometry on which the solution can be computed, the adaptive strategy is able to perform some geometric refinement by introducing previously removed features. This reduces the error due to defeaturing, as in Chapter 4. On the other hand, the algorithm is also able to perform some standard mesh refinement on the underlying finite element mesh. This allows a reduction of the discretization error. To steer the adaptive strategy, we introduce an *a posteriori* estimator of the overall error between the exact solution of the PDE defined in the exact domain, and the numerical approximation of the solution of the corresponding PDE defined in the defeatured domain. The proposed estimator is able to control both the defeaturing error and the numerical error contributions to the overall error.

The chapter is structured as follows. We first define the Galerkin approximation of a Poisson problem in Section 5.1, and we shortly review the basics of finite element methods in Section 5.2. Subsequently, the numerical approximation of the defeatured problem is described in Section 5.3. Finally, in Section 5.4, we design a combined mesh and geometric adaptive strategy in the context of analysis-aware defeaturing. This strategy will be made more precise in the special case of THB-spline based IGA in the remaining chapters of Part II of this thesis. The two last sections of this chapter closely follow [Buffa et al., 2022a].

5.1 Galerkin approximation

One of the most successful numerical approaches to approximately solve BVPs is the so-called Galerkin approximation, that we summarize in this section. In the following derivation, we use Poisson problem (2.26) defined in an open Lipschitz domain $\mathfrak{D}$ as model problem, and we keep the same notation as in Example 2.4.4. However, the presented results of this section are not only valid for Poisson problem (2.26), but for a wider range of BVPs whose variational form writes as in (2.26) and verifies Lax-Milgram theorem. To recall the possible generalization of the following study, we denote $\|\cdot\|_V$ the norm on $V := H^1_{0,\Lambda_D}(\mathfrak{D})$ instead of $\|\nabla \cdot \|_{0,\mathfrak{D}}$.

Let us consider a family $\{V^h\}_{h>0}$ of finite-dimensional subspaces of tV on which problem (2.12) is defined, i.e., for all $h \in \mathbb{R}$, $h > 0$,

$$\{0\} \neq V^h \subset V.$$

In case of inhomogeneous Dirichlet boundary conditions, i.e., $u_D \not\equiv 0$, we need to address the unbalance of the spaces of test and admissible functions. So let us assume for simplicity that there exists a known function z_s^h satisfying the prescribed Dirichlet boundary conditions, such that there is $\mathring{u}_s^h \in V^h$ which verifies

$$u_s^h = \mathring{u}_s^h + z_s^h.$$

Moreover, we assume that for all $v \in V$,

$$\lim_{h \to 0} \inf_{v^h \in V^h} \|v - v^h\|_V = 0. \tag{5.1}$$

Then the Galerkin formulation of problem (2.26) reads:

$$\text{find } u_s^h = \mathring{u}_s^h + z_s^h, \text{ where } \mathring{u}_s^h \in V^h, \text{ such that}$$
$$a\left(\mathring{u}_s^h, v^h\right) = \mathfrak{f}(v^h) - a(z_s^h, v^h) =: \mathfrak{f}^{z_s^h}(v^h), \quad \forall v^h \in V^h. \tag{5.2}$$

Now, let us state the following important stability and convergence result.

Theorem 5.1.1 ([Ciarlet, 2002, Section 2.1])**.** *Under the assumptions of Lax-Milgram theorem stated in Section 2.4, there exists a unique solution u_s^h to (5.2), which furthermore is stable since*

$$\left\| u_s^h \right\|_V \leq \frac{1}{\mathfrak{a}} \left\| \mathfrak{f}^{z_s^h} \right\|_{V^*},$$

where $\mathfrak{a}$ is the coercivity constant of the bilinear form $a(\cdot, \cdot)$, as defined in (2.19). Moreover, if u_s is the solution of the exact variational problem (2.26), it follows that

$$\left\| u_s - u_s^h \right\|_V \leq \frac{\mathfrak{C}}{\mathfrak{a}} \inf_{v^h \in V^h} \left\| u_s - v^h \right\|_V, \tag{5.3}$$

where $\mathfrak{C}$ is the continuity constant of the bilinear form $a(\cdot, \cdot)$, as defined in (2.14). Hence u_s^h converges to u_s, owing to (5.1).

Inequality (5.3), stating that the approximated solution u_s^h is the best approximation of u_s in V^h, is commonly referred to as Céa's lemma.

Since V^h is a finite-dimensional space, let $N \in \mathbb{N}$ denote its dimension, also called number of degrees of freedom, and let $\Phi := [\varphi_1, \varphi_2, \dots, \varphi_N]$ denote one of its basis. This implies that for all $v^h \in V^h$, there exist coefficients $\{v_i\}_{i=1}^N$ such that

$$v^h = \sum_{i=1}^N v_i \varphi_i = \Phi \mathbf{v},$$

where $\mathbf{v} \in \mathbb{R}^N$ is the vector of coefficients $\{v_i\}_{i=1}^N$. In particular, let $\mathbf{z}_s := [z_1, z_2, \dots, z_N]$ be the vector of known coefficients of z_s^h in the basis Φ. Then accordingly, one can algebraically rewrite the Galerkin formulation (5.2) as:

find $\mathbf{u}_s = \mathring{\mathbf{u}}_s + \mathbf{z}_s$, $\mathring{\mathbf{u}}_s := [\mathring{u}_1, \mathring{u}_2, \dots, \mathring{u}_N]^T \in \mathbb{R}^N$ such that

$$\sum_{i,j=1}^N a(\mathring{u}_j \varphi_j, v_i \varphi_i) = \sum_{i=1}^N \mathfrak{f}(v_i \varphi_i) - \sum_{i,k=1}^N a(z_k \varphi_k, v_i \varphi_i), \quad \forall \mathbf{v} = [v_1, v_2, \dots, v_N]^T \in \mathbb{R}^N.$$
$$\tag{5.4}$$

By exploiting the linearity of $a(\cdot, \cdot)$ and $\mathfrak{f}(\cdot)$ and since $\mathbf{v}$ is arbitrary, then (5.4) is equivalent to the following problem:

find $\mathbf{u}_s = \mathring{\mathbf{u}}_s + \mathbf{z}_s$, $\mathring{\mathbf{u}}_s := [\mathring{u}_1, \mathring{u}_2, \dots, \mathring{u}_N]^T \in \mathbb{R}^N$ such that

$$A\mathring{\mathbf{u}}_s = \mathbf{f}^{\mathbf{z}_s}, \tag{5.5}$$

where $A \in \mathbb{R}^{N \times N}$ and $\mathbf{f}^{\mathbf{z}_s} := [\mathfrak{f}_1^{\mathbf{z}_s}, \mathfrak{f}_2^{\mathbf{z}_s}, \dots, \mathfrak{f}_N^{\mathbf{z}_s}] \in \mathbb{R}^N$, and for all $i, j = 1, \dots, N$,

$$A_{ij} := a(\varphi_j, \varphi_i), \qquad \mathfrak{f}_i^{\mathbf{z}_s} := \mathfrak{f}(\varphi_i) - A\mathbf{z}_s.$$

Matrix A is referred to as the stiffness matrix, $\mathbf{f}^{\mathbf{z}_s}$ is the right hand side vector, and $\mathbf{u}_s = \mathring{\mathbf{u}}_s + \mathbf{z}_s$ is the vector of solution coefficients.

5.2 Finite element methods

To correctly solve the Galerkin approximation (5.2) introduced in the previous section, the choice of finite-dimensional space V^h and basis Φ is crucial. To be able to develop a systematic routine which can tackle arbitrarily complex differential problems, we aim at defining Φ which:

- allows for geometrical flexibility,

- is suitable for a computer-based implementation,

- exhibits robust convergence properties, based on rigorous error bounds.

Let us also recall that Φ should be chosen so that V^h is consistent with V, meaning that V^h should verify (5.1).
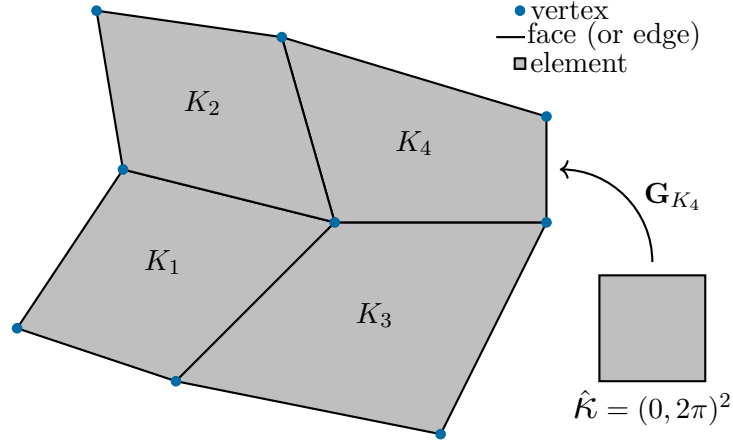
5.2.1 Finite element meshes

In a traditional finite element routine, the first step before defining a finite basis Φ consists in constructing a mesh that covers the computational domain $\mathfrak{D}$. Based on the definitions from [Ciarlet, 2002, Section 2.1], a mesh $\mathcal{Q}$ consists in a partition of (an approximation of) $\mathfrak{D}$ into a finite number of elements K. That is, if we assume that $\mathfrak{D}$ is a polyhedral domain,

$$\mathfrak{D} = \bigcup_{K \in \mathcal{Q}} \overline{K},$$

where

- each $K \in \mathcal{Q}$ is a non-empty bounded open Lipschitz polyhedron,

- $K_1 \cap K_2 = \emptyset$ for each distinct $K_1, K_2 \in \mathcal{Q}$,

- if $E = \overline{K_1} \cap \overline{K_2} \neq \emptyset$ for some distinct $K_1, K_2 \in \mathcal{Q}$, then E is a common entire face or entire edge, or a common vertex of K_1 and K_2,

- each $K \in \mathcal{Q}$ is obtained from a reference polyhedron $\hat{\mathcal{K}}$ via a bijective map $\mathbf{G}_K : \hat{\mathcal{K}} \to K$.

In this thesis, we restrict ourselves to quadrilateral and hexahedral elements, therefore justifying the notation $\mathcal{Q}$ denoting the mesh, and we consider $\hat{\mathcal{K}} := (0, 2\pi)^2$. The illustration of a finite element mesh is given in Figure 5.1. In the sequel, edges are called faces even when $n = 2$.

Figure 5.1 – Illustration of a finite element mesh $\mathcal{Q}$.

Moreover, we denote $n_{\mathrm{el}} := \#\mathcal{Q}$ the number of elements in $\mathcal{Q}$, and for all $K \in \mathcal{Q}$, we let h_K be the diameter of K, and ρ_K be the diameter of the largest ball inscribed in K. Then, we call mesh size the mesh parameter

$$h := \max_{K \in \mathcal{Q}} h_K. \tag{5.6}$$

Let us introduce a final definition that will be used in the sequel.

Definition 5.2.1. A mesh $\mathcal{Q}$ is *shape regular* if there exists a constant $\delta > 0$ such that for all $K \in \mathcal{Q}$,

$$\frac{h_K}{\rho_K} \leq \delta.$$

To finish this section, let us state two trace inequalities on mesh elements.

Lemma 5.2.2. *Let $\mathcal{Q}$ be a finite element mesh. Then for all $K \in \mathcal{Q}$ and for all $v \in H^1(K)$,*

$$\|v\|_{0,\partial K} \leq C_* \left(h_K^{-\frac{1}{2}} \|v\|_{0,K} + h_K^{\frac{1}{2}} \|\nabla v\|_{0,K} \right),$$

where C_* is a constant independent of h and h_K, but which can depend on the shape of K.

Proof. See [Di Pietro and Ern, 2011, Section 1.4.3]. $\qquad\square$

Lemma 5.2.3. *Let $\mathfrak{D} \subset \mathbb{R}^n$ be a Lipschitz domain, let $\Lambda \subset \mathbb{R}^{n-1}$ be an $(n-1)$-dimensional hyper-surface intersecting $\mathfrak{D}$, and let $\mathcal{Q}$ be a finite element mesh on $\mathfrak{D}$. If for all $K \in \mathcal{Q}$ such that $\Lambda_K := \Lambda \cap \overline{K} \neq \emptyset$, we have $h_K < h_0$ for some fixed $h_0 > 0$ (independent of K), then*

$$\|v\|_{0,\Lambda_K}^2 \leq C^* \left(h_K^{-1} \|v\|_{0,K}^2 + h_K \|\nabla v\|_{0,K}^2 \right), \quad \forall v \in H^1(K),$$

127

where C^* is a constant independent of v, K, h and of how Λ intersects K.

Proof. See [Guzmán and Olshanskii, 2018]. A proof under stronger assumptions can also be found in [Hansbo and Hansbo, 2002, 2004]. □

5.2.2   Finite element spaces

Having at hand a suitable description of the geometry from the previous section, we can now define the class of finite-dimensional subspaces $V^h \subset V$ called finite element spaces, on which the Galerkin approximation (5.2) is defined. These spaces V^h should result in a suitable approximation of functions in V, verifying in particular property (5.1). The fundamental aspect of FEM is to consider a piecewise polynomial space; more precisely, for all $K \in \mathcal{Q}$, the space

$$\mathcal{P}_K := \left\{ v^h|_K : v^h \in V^h \right\} \tag{5.7}$$

consists of algebraic polynomials, see [Ciarlet, 2002].

To precisely characterize a polynomial space on an element $K \in \mathcal{Q}$ following [Ainsworth and Oden, 1997], let us first denote $\hat{\varphi}^1, \hat{\varphi}^2, \ldots, \hat{\varphi}^{\hat{N}}$ the functions of a Lagrange basis spanning the polynomial space $\mathbb{Q}_P(\hat{\mathcal{K}})$ of degree $P \in \mathbb{N}$ on the reference element $\hat{\mathcal{K}}$. Note that $\hat{N} = \hat{N}(P)$ depends on the considered polynomial degree P. Given the bijective geometric mappings $\mathbf{G}_K : \hat{\mathcal{K}} \to K$ introduced in Section 5.2.1, the basis functions can be pushed forward to each element $K \in \mathcal{Q}$ of the physical space as follows:

$$\varphi_K^i := \hat{\varphi}^i \circ \mathbf{G}_K^{-1}, \qquad \text{for } i = 1, \ldots, \hat{N}.$$

Consequently, we can define the local (mapped) polynomial space in K for all $K \in \mathcal{Q}$ as

$$\mathbb{Q}_P(K) := \text{span} \left\{ \varphi_K^i : i = 1, \ldots, \hat{N} \right\}. \tag{5.8}$$

Let us now introduce the general definition of finite element, following [Ciarlet, 2002].

Definition 5.2.4. The triplet $(K, \mathcal{P}_K, \Psi_K)$ is called *finite element* if

- K is an open bounded polyhedron with nonempty interior and Lipschitz boundary,

- $\mathcal{P}_K$ is a finite-dimensional space of functions on K,

- $\Psi_K := \{ Z_i : \mathcal{P}_K \to \mathbb{R}, \ i = 1, \ldots, \hat{N} \}$ is a set of linear forms such that the map $\mathbf{Z}_\Psi : \mathcal{P}_K \to \mathbb{R}$ defined by $\mathbf{Z}_\Psi(\phi) = \left(Z_i(\phi) \right)_{i=1}^{\hat{N}}$ for all $\phi \in \mathcal{P}_K$ is an isomorphism. The linear forms Z_i are called degrees of freedom associated with element K, and the bijectivity of $\mathbf{Z}_\Psi$ is referred to as unisolvence.

Then, given a set of finite elements $\{(K, \mathcal{P}_K, \Psi_K) : K \in \mathcal{Q}\}$, a finite element space V^h corresponding to Galerkin problem (5.2) is a space verifying:

(i) for all $K \in \mathcal{Q}$, $\mathcal{P}_K$ is a finite-dimensional space such that

$$\mathbb{Q}_P(K) \subset \mathcal{P}_K = \left\{ v^h|_K : v^h \in V^h \right\},$$

(ii) $V^h \subset H^1_{0,\Lambda_D}(\mathfrak{D})$,

(iii) there exists a canonical basis Φ of V^h, whose functions have "small" supports and are easy to describe.

Let us state a result from [Ciarlet, 2002, Theorem 2.1.1] giving a sufficient condition for (ii) to hold.

Theorem 5.2.5. *Let W^h be a finite-dimensional space and suppose that for all $K \in \mathcal{Q}$,*

$$\left\{ w^h|_K : w^h \in W^h \right\} \subset H^1(K).$$

If $W^h \subset C^0(\overline{\mathfrak{D}})$, then

- *$W^h \subset H^1(\mathfrak{D})$,*

- *and if Λ_D is a union of faces of $\mathcal{Q}$,*

$$V^h := \{v^h \in W^h : v^h = 0 \text{ on } \Lambda_D\} \subset H^1_{0,\Lambda_D}(\mathfrak{D}).$$

In view of this theorem and to simplify the analysis, we make the following assumption for the remaining part of this thesis.

Assumption 5.2.6. When we consider the Galerkin approximation (5.2) of a Poisson problem (2.25),

- the Dirichlet boundary Λ_D is a union of faces of the considered mesh;
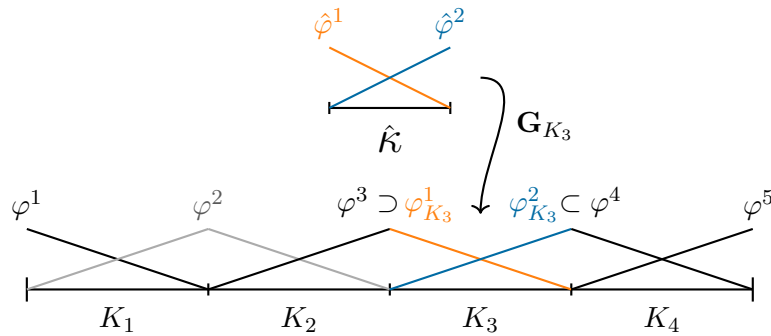

Figure 5.2 – Illustration of the one-dimensional basis functions $\hat{\varphi}^i$ on $\hat{\mathcal{K}}$ for a polynomial degree $P = 1$, and the corresponding one-dimensional finite element basis in a mesh with four elements.

- there exists a known and computable lifting $z_s^h := R_{\Lambda_D}(u_D)$ of the Dirichlet datum u_D given by Theorem 2.2.1.

If this assumption were not satisfied, we would need to build an approximation u_D^h of the Dirichlet datum u_D from which a lifting $z_s^h := R_{\Lambda_D}(u_D^h)$ can be obtained, and we would need to take into consideration the induced approximation error. For more details, the reader is referred for instance to [Brenner and Scott, 2008].

The definition of the classical finite element space of degree P, also called conforming finite element space, naturally follows from Definition 5.2.4 and from Theorem 5.2.5. It is defined by

$$V^h := \left\{ v^h \in C^0(\overline{\mathfrak{D}}) : v^h|_K \in \mathbb{Q}_P(K), \, \forall K \in \mathcal{Q} \right\}, \tag{5.9}$$

and its canonical basis $\Phi := [\varphi_1, \varphi_2, \ldots, \varphi_N]$ is obtained by associating the functions φ_K^i, $i = 1, \ldots, \hat{N}$, $K \in \mathcal{Q}$, which are equal to 1 at the same vertex of the mesh. This is illustrated in the one-dimensional example of Figure 5.2. For a detailed description and analysis of the classical FEM, the interested reader is referred for instance to [Ciarlet, 2002; Brenner and Scott, 2008; Quarteroni and Valli, 2008]. In a later chapter about IGA, we will build finite-dimensional spaces with larger global continuity, which allow for instance the treatment of a wider set of engineering problems.

5.2.3   Some convergence results

In this section, we provide some classical *a priori* estimates on the convergence behavior of FEM. For the sake of brevity, we only provide the most relevant results for this thesis, and we refer to [Ciarlet, 2002] for more details and the missing proofs.

Let us first verify that finite element spaces satisfy the required consistency condition (5.1). To do so, let us first provide a local result characterizing the approximation error on each element $K \in \mathcal{Q}$ with respect to the smoothness of the considered function and to the norm chosen to measure the error.

Theorem 5.2.7 ([Ciarlet, 2002, Theorem 3.1.6])**.** *Let* $\{(K, \mathcal{P}_K, \Psi_K) : K \in \mathcal{Q}\}$ *be a family of shape regular and affine finite elements whose reference element* $\left\{ \hat{\mathcal{K}}, \hat{\mathcal{P}}_{\hat{\mathcal{K}}}, \hat{\Psi}_{\hat{\mathcal{K}}} \right\}$ *satisfies the following inclusions: let the integer* $s \geq 0$ *denote the greatest order of partial derivatives occurring in the definition of* $\hat{\Psi}_{\hat{\mathcal{K}}}$, *and let* $m \geq 0$ *and* $k \geq 0$ *be two integers, such that*

$$H^{k+1}(\hat{\mathcal{K}}) \hookrightarrow C^s(\hat{\mathcal{K}})$$

$$H^{k+1}(\hat{\mathcal{K}}) \hookrightarrow H^m(\hat{\mathcal{K}})$$

$$\mathbb{Q}_k(\hat{\mathcal{K}}) \subset \hat{\mathcal{P}}_{\hat{\mathcal{K}}} \subset H^m(\hat{\mathcal{K}}).$$

Then there exists an operator $\Pi_K : H^{k+1}(K) \to \mathcal{P}_K$ *for all* $K \in \mathcal{Q}$ *and a constant* $C\left(\hat{\mathcal{K}}, \hat{\mathcal{P}}_{\hat{\mathcal{K}}}, \hat{\Psi}_{\hat{\mathcal{K}}}\right) > 0$ *such that, for all finite elements* K *in the family, and all functions* $v \in H^{k+1}(K)$,

$$\|v - \Pi_K v\|_{m,K} \le C\left(\hat{\mathcal{K}}, \hat{\mathcal{P}}_{\hat{\mathcal{K}}}, \hat{\Psi}_{\hat{\mathcal{K}}}\right) h_K^{k+1-m} |v|_{k+1,K}. \tag{5.10}$$

Building upon this result, it is possible to give a global approximation result for V^h defined in the entire domain $\mathfrak{D}$.

Theorem 5.2.8 ([Ciarlet, 2002, Theorem 3.2.1]). *Let* V^h *be a globally continuous finite element space defined from a family* $\{(K, \mathcal{P}_K, \Psi_K) : K \in \mathcal{Q}\}$ *of shape regular and affine finite elements whose reference element* $\left\{\hat{\mathcal{K}}, \hat{\mathcal{P}}_{\hat{\mathcal{K}}}, \hat{\Psi}_{\hat{\mathcal{K}}}\right\}$ *satisfies the following inclusions: let the integer* $s \ge 0$ *denote the greatest order of partial derivatives occurring in the definition of* $\hat{\Psi}_{\hat{\mathcal{K}}}$, *and let* $k \ge 0$ *and* $\ell \ge 0$ *be two integers with* $\ell \le k$, *such that*

$$H^{k+1}(\hat{\mathcal{K}}) \hookrightarrow C^s(\hat{\mathcal{K}})$$

$$\mathbb{Q}_k(\hat{\mathcal{K}}) \subset \hat{\mathcal{P}}_{\hat{\mathcal{K}}} \subset H^\ell(\hat{\mathcal{K}}).$$

Then there exists an operator $\Pi^h : H^{k+1}(\mathfrak{D}) \cap V \to V^h$ *and a constant* $C_\Pi > 0$ *independent of* h *such that for all functions* $v \in H^{k+1}(\mathfrak{D}) \cap V$,

$$\|v - \Pi^h v\|_{m,\mathfrak{D}} \le C_\Pi \, h^{k+1-m} |v|_{k+1,\mathfrak{D}}, \qquad 0 \le m \le \min\{1, \ell\}. \tag{5.11}$$

This results also shows the consistency condition (5.1) of V^h with respect to V when $m = k = 0$, in the context of Poisson problem (2.12). Finally, building upon the approximation results of Theorems 5.2.7 and 5.2.8, it is possible to obtain the following *a priori* estimate of the error coming from the Galerkin finite element approximation of the Poisson solution defined in (5.2).

Theorem 5.2.9 ([Ciarlet, 2002, Theorem 3.2.2]). *Let* $k + 1$ *be the regularity of the exact solution* u_s *of (2.12), and let* u_s^h *be its Galerkin finite element approximation (5.2). Then under the same hypothesis as Theorem 5.2.8, there exists a constant* $c > 0$ *independent of* h *such that*

$$\left\|u_s - u_s^h\right\|_{1,\mathfrak{D}} \le c \, h^k |u_s|_{k+1,\mathfrak{D}}. \tag{5.12}$$

Even if in the following, we concentrate instead on the *a posteriori* error analysis of the numerical error combined with defeaturing, this *a priori* result will allow us to verify the convergence of the numerical error in the numerical experiments presented in the remaining part of this work.

5.3 Finite element formulation of the defeaturing problem

In this section, we employ the Galerkin method introduced in Section 5.1 to solve and analyze the defeaturing problem defined in Part I. More precisely, let us consider Poisson equation (3.1) defined in a geometry Ω containing $N_f \geq 1$ features forming the set $\mathfrak{F}$, and let us use the same notation and assumptions introduced in Chapter 4.

Then, let $\mathcal{Q}_0$ be a finite element mesh on the defeatured geometry Ω_0 defined in (4.1), and let $V^h(\Omega_0) \subset H^1(\Omega_0)$ be a finite element space built from $\mathcal{Q}_0$, as introduced in Section 5.2. Moreover, let

$$V_0^h(\Omega_0) := V^h(\Omega_0) \cap H_{0,\Gamma_D}^1(\Omega_0),$$
$$\text{and} \quad V_{g_D}^h(\Omega_0) := V^h(\Omega_0) \cap H_{g_D,\Gamma_D}^1(\Omega_0).$$

Recall from Assumption 5.2.6 that for simplicity, the Dirichlet data $g_D \in \text{tr}_{\Gamma_D}\left(V^h(\Omega_0)\right)$, where $\text{tr}_{\Gamma_D}\left(V^h(\Omega_0)\right)$ is the trace space of the discrete functions of $V^h(\Omega_0)$ on Γ_D. Then, the Galerkin formulation of the defeaturing problem (3.4) can be written as follows:

$$\text{find } u_0^h \in V_{g_D}^h(\Omega_0) \text{ such that for all } v_0^h \in V_0^h(\Omega_0),$$
$$\int_{\Omega_0} \nabla u_0^h \cdot \nabla v_0^h \, dx = \int_{\Omega_0} f v_0^h \, dx + \int_{\Gamma_N \setminus \gamma} g v_0^h \, ds + \int_{\gamma_0} g_0 v_0^h \, ds. \tag{5.13}$$

When geometry Ω contains features F^k, $k = 1, \ldots, N_f$, with a non-empty positive component F_p^k, we need to extend the defeatured solution u_0^h to simplified domains $\tilde{F}_p^k$ containing F_p^k, in order to be able to suitably define the defeaturing error in Ω (see Chapter 3). To do so, we also employ the Galerkin method to discretize the weak extension problem (4.6) in $\tilde{F}_p^k \supset F_p^k$, as for Ω_0. More precisely, for all $k = 1, \ldots, N_f$, let $\tilde{\mathcal{Q}}^k$ be a finite element mesh defined on $\tilde{F}_p^k$, and let

$$\mathcal{Q} := \mathcal{Q}_0 \cup \tilde{\mathcal{Q}} \quad \text{with} \quad \tilde{\mathcal{Q}} := \bigcup_{k=1}^{N_f} \tilde{\mathcal{Q}}^k. \tag{5.14}$$

Furthermore, for all $k = 1, \ldots, N_f$, let $V^h\left(\tilde{F}_p^k\right) \subset H^1\left(\tilde{F}_p^k\right)$ be a finite element space built from $\tilde{\mathcal{Q}}^k$ that satisfies the following compatibility assumption.

Assumption 5.3.1. For all $k = 1, \ldots, N_f$, the finite-dimensional spaces $V^h(\Omega_0)$ and $V^h\left(\tilde{F}_p^k\right)$ satisfy

$$\text{tr}_{\gamma_{0,p}^k}\left(V^h(\Omega_0)\right) \subset \text{tr}_{\gamma_{0,p}^k}\left(V^h\left(\tilde{F}_p^k\right)\right),$$

so that $\text{tr}_{\gamma_{0,p}^k}\left(u_0^h\right) \in \text{tr}_{\gamma_{0,p}^k}\left(V^h\left(\tilde{F}_p^k\right)\right)$.

To take into account Dirichlet boundary conditions, let us introduce for all $k = 1, \ldots, N_f$

the finite dimensional spaces

$$V_0^h\left(\tilde{F}_{\mathrm{p}}^k\right) := V^h\left(\tilde{F}_{\mathrm{p}}^k\right) \cap H^1_{0,\gamma_{0,\mathrm{p}}^k}\left(\tilde{F}_{\mathrm{p}}^k\right)$$

$$\text{and} \quad V_{u_0^h}^h\left(\tilde{F}_{\mathrm{p}}^k\right) := V^h\left(\tilde{F}_{\mathrm{p}}^k\right) \cap H^1_{u_0^h,\gamma_{0,\mathrm{p}}^k}\left(\tilde{F}_{\mathrm{p}}^k\right).$$

Then, the Galerkin formulation of the extension problem (4.6) can be written as follows:

$$\text{find } u_k^h \equiv \tilde{u}_0^{h,k} \in V_{u_0^h}^h\left(\tilde{F}_{\mathrm{p}}^k\right) \text{ such that for all } v_k^h \in V_0^h\left(\tilde{F}_{\mathrm{p}}^k\right),$$

$$\int_{\tilde{F}_{\mathrm{p}}^k} \nabla u_k^h \cdot \nabla v_k^h \, \mathrm{d}x = \int_{\tilde{F}_{\mathrm{p}}^k} f v_k^h \, \mathrm{d}x + \int_{\tilde{\gamma}^k} \tilde{g}^k v_k^h \, \mathrm{d}s + \int_{\gamma_{\mathrm{s}}^k} g v_k^h \, \mathrm{d}s. \tag{5.15}$$

Note that to lighten the notation in the multi-feature context, we write

$$u_k^h \equiv \tilde{u}_0^{k,h}, \tag{5.16}$$

similarly to $u_k \equiv \tilde{u}_0^k$ defined in (4.4). If $N_f = 1$, we will drop the upper index $k = 1$ and write $\tilde{u}_0^h$ instead of $\tilde{u}_0^{1,h}$ or u_1^h. Furthermore, note that these extensions u_k^h can be computed separately (and in parallel) for each feature F^k, $k = 1, \ldots, N_f$.

Finally, let

$$u_{\mathrm{d}}^h \in W^h := V_{g_D}^h(\Omega_0)\Big|_{\Omega_\star} \oplus \left[\bigoplus_{k=1}^{N_f} V_{u_0^h}^h\left(\tilde{F}_{\mathrm{p}}^k\right)\Big|_{F_{\mathrm{p}}^k}\right] \subset H^1_{g_D,\Gamma_D}(\Omega) \tag{5.17}$$

be the discrete counterpart of u_{d} introduced in (4.7). That is, it is the discrete extended defeatured solution defined by

$$u_{\mathrm{d}}^h = u_0^h\Big|_{\Omega_\star} \text{ in } \Omega_\star = \Omega \setminus \overline{F_{\mathrm{p}}} \quad \text{and} \quad u_{\mathrm{d}}^h = u_k^h\Big|_{F_{\mathrm{p}}^k} \text{ in } F_{\mathrm{p}}^k \text{ for } k = 1, \ldots, N_f. \tag{5.18}$$

Then, we define the discrete defeaturing error (or overall error) as

$$\left\|\!\left\|u - u_{\mathrm{d}}^h\right\|\!\right\|_\Omega = \left\|\nabla\left(u - u_{\mathrm{d}}^h\right)\right\|_{0,\Omega} = \left|u - u_{\mathrm{d}}^h\right|_{1,\Omega}.$$

Remark 5.3.2. For each $k = 1, \ldots, N_f$, the only required compatibility between $V^h(\Omega_0)$ and $V^h\left(\tilde{F}_{\mathrm{p}}^k\right)$ is Assumption 5.3.1. Moreover, note that $\mathcal{Q}_0$ and $\tilde{\mathcal{Q}}^k$ are possibly overlapping meshes, but both should have $\gamma_{0,\mathrm{p}}^k$ as part of their boundary.

Remark 5.3.3. Note that the aim is to never solve the original problem (3.1) in the exact geometry Ω. Indeed, we assume that one needs to remove the features of Ω since solving a PDE in Ω is either too costly or even unfeasible (for instance, it could be impossible to mesh Ω). Therefore in principle, the original problem (3.1) is never solved in the discrete setting.

5.4 An adaptive analysis-aware defeaturing strategy

In this section, we aim at generalizing the adaptive analysis-aware defeaturing strategy presented in Chapter 4, Section 4.5, by considering the additional error coming from the numerical approximation of the defeatured solution u_{d}. In particular, starting from a very coarse mesh $\mathcal{Q}$ and from a fully defeatured geometry Ω_0, we want to precisely define a strategy that determines:

- when and where the mesh needs to be refined (standard h-refinement, or numerical adaptivity),

- when and which geometrical features that have been removed by defeaturing need to be reinserted in the geometrical model (geometric adaptivity, see Chapter 4).

We consider Poisson problem (3.1) defined in a geometry Ω containing $N_f \geq 1$ features, whose defeatured problem has been discretized via a Galerkin finite element method as described in Section 5.3.

Closely following the framework of adaptive finite elements from [Nochetto and Veeser, 2011] for elliptic PDEs, we extend and elaborate on the four building blocks composing one iteration of the adaptive process developed in Chapter 4. Let us recall them here:

$$\boxed{\text{SOLVE}} \longrightarrow \boxed{\text{ESTIMATE}} \longrightarrow \boxed{\text{MARK}} \longrightarrow \boxed{\text{REFINE}}$$

In particular, in Section 5.4.2, we propose an *a posteriori* estimator of the discrete defeaturing error $\left| u - u_{\mathrm{d}}^h \right|_{1,\Omega}$. Its reliability will be proven in Chapter 8 in the context of IGA with THB-splines under reasonable assumptions.

Let $i \in \mathbb{N}$ be the current iteration index, and as in Chapter 4, let us begin the adaptive process with $\Omega_0^{(0)}$ being the fully defeatured geometry defined as in (4.1). That is, $\Omega_0^{(0)}$ is the domain in which all features of Ω are removed: their positive component is cut out, and their negative component is filled with material. Since some features will be reinserted during the adaptive process, we denote $\Omega_0^{(i)}$ the simplified geometry at the i-th iteration, and in general, we use the upper index (i) to refer to objects at the same iteration. However, to alleviate the notation, we will drop the index (i) when it is clear from the context. In particular, we will write $\Omega_0 \equiv \Omega_0^{(i)}$.

5.4.1 Solve

Using suitable finite element spaces, we first solve Galerkin problem (5.13) defined in the (partially) defeatured geometry Ω_0. Then, we solve the local Galerkin extension problem (5.15) for each feature having a non-empty positive component. We thus obtain

the discrete defeaturing solution $u_{\mathrm{d}}^h \equiv u_{\mathrm{d}}^{h,(i)}$ defined in (5.18), as an approximation of the exact solution u of (3.1) at iteration i.

5.4.2 Estimate

In order to define the proposed *a posteriori* estimator $\mathscr{E}\left(u_{\mathrm{d}}^h\right)$ of the discrete defeaturing error $\left|u - u_{\mathrm{d}}^h\right|_{1,\Omega}$, let us first introduce some further notation. For each $\sigma \in \Sigma$, let d_σ be the continuous defeaturing error term defined in (4.12), and let d_σ^h be its discrete counterpart. That is, for all $k = 1, \ldots, N_f$ where $N_f \equiv N_f^{(i)}$, and for all $\sigma \in \Sigma^k$ where Σ^k is defined in (4.11),

$$
d_\sigma^h := \begin{cases} g - \dfrac{\partial u_{\mathrm{d}}^h}{\partial \mathbf{n}} & \text{if } \sigma = \gamma_{\mathrm{n}}^k \text{ or } \sigma = \gamma_{\mathrm{r}}^k \\[2mm] -\left(g_0 - \dfrac{\partial u_{\mathrm{d}}^h}{\partial \mathbf{n}^k} \right) & \text{if } \sigma = \gamma_{0,\mathrm{p}}^k. \end{cases}
\tag{5.19}
$$

Recall from Remark 4.2.1 that the average value of d_σ over any $\sigma \in \Sigma$ is a computable quantity, as it is independent of the unknown exact defeatured solution u_{d}.

If we define $\eta \in \mathbb{R}$ as the unique solution of $\eta = -\log(\eta)$, then recall from (3.10) that for all $\sigma \in \Sigma$, we let

$$
c_\sigma := \begin{cases} \max\left(-\log\left(|\sigma|\right), \eta \right)^{\frac{1}{2}} & \text{if } n = 2 \\[2mm] 1 & \text{if } n = 3. \end{cases}
\tag{5.20}
$$

We can now define the overall error estimator as follows:

$$
\mathscr{E}\left(u_{\mathrm{d}}^h\right) = \left[\alpha_D^2 \mathscr{E}_D\left(u_{\mathrm{d}}^h\right)^2 + \alpha_N^2 \mathscr{E}_N\left(u_{\mathrm{d}}^h\right)^2 \right]^{\frac{1}{2}},
\tag{5.21}
$$

where $\alpha_N > 0$ and $\alpha_D > 0$ are parameters to be tuned,

$$
\mathscr{E}_D\left(u_{\mathrm{d}}^h\right)^2 := \sum_{\sigma \in \Sigma} |\sigma|^{\frac{1}{n-1}} \left\| d_\sigma^h - \overline{d_\sigma^h}^\sigma \right\|_{0,\sigma}^2 + \mathscr{E}_C^2
\tag{5.22}
$$

accounts for the defeaturing error as in Part I, with

$$
\mathscr{E}_C^2 := \sum_{\sigma \in \Sigma} c_\sigma^2 |\sigma|^{\frac{n}{n-1}} \left| \overline{d_\sigma}^\sigma \right|^2
$$

that accounts for the data compatibility conditions (see Remark 4.2.1), and $\mathscr{E}_N\left(u_{\mathrm{d}}^h\right)$ accounts for the numerical error that depends on the chosen finite element method. More details are given below for the special case of IGA, see also Chapter 8 for an in-depth

study of this case. More precisely,

$$\mathscr{E}_N\left(u_{\mathrm{d}}^h\right)^2 := \mathscr{E}_N^0\left(u_0^h\right)^2 + \sum_{k=1}^{N_f} \mathscr{E}_N^k\left(u_k^h\right)^2,$$

where $\mathscr{E}_N^0\left(u_0^h\right)$ is the numerical error estimator of u_0^h in Ω_0 corresponding to the discretized problem (5.13), and for all $k = 1, \ldots, N_f$, $\mathscr{E}_N^k\left(u_k^h\right)$ is the numerical error estimator of u_k^h in $\tilde{F}_{\mathrm{p}}^k$ corresponding to the discretized extension problem (5.15).

Remark 5.4.1. Let us make some observations on the overall error estimator (5.21).

- The numerical error contribution $\mathscr{E}_N\left(u_0^h\right)$ to the estimator is computed on the same meshes used for the discretization, in Ω_0 and in $\tilde{F}_{\mathrm{p}}$. Instead, the defeaturing error contribution $\mathscr{E}_D\left(u_0^h\right)$ to the estimator considers boundary integrals which are not necessarily union of faces of the mesh, i.e., the pieces of boundaries $\sigma \in \Sigma$ are in general not fitted by the mesh.

- If $u_{\mathrm{d}} = u$ or in other words, without defeaturing error, the proposed estimator corresponds to the standard numerical residual error estimator between u_0 and u_0^h in Ω_0, and between u_k and u_k^h in $\tilde{F}_{\mathrm{p}}^k$ for all $k = 1, \ldots, N_f$, that is, $\mathscr{E}\left(u_{\mathrm{d}}^h\right) = \mathscr{E}_N\left(u_{\mathrm{d}}^h\right)$.

- If $u_0^h \equiv u_0$ in Ω_0 and $u_k \equiv u_k^h$ in $\tilde{F}_{\mathrm{p}}^k$ for all $k = 1, \ldots, N_f$, i.e., without numerical error, then $\mathscr{E}_N\left(u_{\mathrm{d}}^h\right) = 0$, and thus we recover the defeaturing error estimator introduced in Chapter 3 and generalized in Chapter 4.

- Under the exact data compatibility condition $\overline{d_\sigma}^\sigma = 0$ for all $\sigma \in \Sigma$ (see (4.15)), the term $\mathscr{E}_C$ vanishes. If $\mathscr{E}_C$ is large with respect to the other terms of $\mathscr{E}\left(u_{\mathrm{d}}^h\right)$, the defeaturing data should be chosen more carefully, i.e., the Neumann boundary data g_0 on γ_0, $\tilde{g}$ on $\tilde{\gamma}$, and the right hand side extension f in F_{n} and in each G_{p}^k, $k = 1, \ldots, N_f$.

The discrete defeaturing error estimator $\mathscr{E}\left(u_{\mathrm{d}}^h\right)$ introduced in (5.21) can easily be decomposed into local contributions. Indeed, $\mathscr{E}_D\left(u_{\mathrm{d}}^h\right)$ (and $\mathscr{E}_C$) can readily be decomposed into single feature contributions as follows:

$$\mathscr{E}_C^2 = \sum_{k=1}^{N_f} \left(\mathscr{E}_C^k\right)^2, \quad \mathscr{E}_D\left(u_{\mathrm{d}}^h\right)^2 = \sum_{k=1}^{N_f} \mathscr{E}_D^k\left(u_{\mathrm{d}}^h\right)^2, \tag{5.23}$$

$$\text{with} \quad \left(\mathscr{E}_C^k\right)^2 := \sum_{\sigma \in \Sigma^k} c_\sigma^2 |\sigma|^{\frac{n}{n-1}} \left|\overline{d_\sigma}^\sigma\right|^2$$

$$\text{and} \quad \mathscr{E}_D^k\left(u_{\mathrm{d}}^h\right)^2 := \sum_{\sigma \in \Sigma^k} |\sigma|^{\frac{1}{n-1}} \left\|d_\sigma^h - \overline{d_\sigma^h}^\sigma\right\|_{0,\sigma}^2 + \left(\mathscr{E}_C^k\right)^2, \quad \text{for } k = 1, \ldots, N_f.$$

Similarly, the numerical error estimator $\mathscr{E}_N\left(u_{\mathrm{d}}^h\right)$ can in general be decomposed into single mesh element contributions $\mathscr{E}_N^K\left(u_{\mathrm{d}}^h\right)$ for $K \in \mathcal{Q}$, in the form

$$\mathscr{E}_N\left(u_{\mathrm{d}}^h\right)^2 = \sum_{K \in \mathcal{Q}} \mathscr{E}_N^K\left(u_{\mathrm{d}}^h\right)^2.$$

These local decompositions are necessary to guide the adaptive refinement, both in terms of mesh and in terms of geometrical model.

In Chapter 8, we will analyze the particular case of IGA with C^1-continuous splines, and with a residual-based numerical error estimator. To define the numerical error estimator in this context, we first introduce the interior residuals r and the boundary residuals j as follows:

$$r := \begin{cases} f + \Delta u_0^h & \text{in } \Omega_0 \\ f + \Delta u_k^h & \text{in } \tilde{F}_{\mathrm{p}}^k, \quad \forall k = 1, \ldots, N_f, \end{cases} \tag{5.24}$$

and

$$j := \begin{cases} g - \dfrac{\partial u_{\mathrm{d}}^h}{\partial \mathbf{n}} & \text{on } \Gamma_N \setminus (\gamma_{\mathrm{n}} \cup \gamma_{\mathrm{r}}) \\[2mm] g_0 - \dfrac{\partial u_0^h}{\partial \mathbf{n}_0} & \text{on } \gamma_0 \\[2mm] \tilde{g} - \dfrac{\partial u_k^h}{\partial \tilde{\mathbf{n}}^k} & \text{on } \tilde{\gamma}^k, \ \forall k = 1, \ldots, N_f. \end{cases} \tag{5.25}$$

Furthermore, recalling definitions (4.8) and (4.9) of Γ_N^0 and $\tilde{\Gamma}_N$, let $\mathcal{E}_0$ be the set of faces of $\mathcal{Q}_0$ that are part of Γ_N^0, let $\tilde{\mathcal{E}}^k$ be the set of faces of $\tilde{\mathcal{Q}}^k$ that are part of $\tilde{\Gamma}_N^k$ for all $k = 1, \ldots, N_f$, and let

$$\mathcal{E} := \mathcal{E}_0 \cup \tilde{\mathcal{E}}, \quad \tilde{\mathcal{E}} := \bigcup_{k=1}^{N_f} \tilde{\mathcal{E}}^k. \tag{5.26}$$

For all $E \in \mathcal{E}$, we denote $h_E := \operatorname{diam}(E)$, similar to the notation h_K for all $K \in \mathcal{Q}$. Then, assuming that the mesh $\mathcal{Q}$ fits the boundary of the simplified domain Ω_0, the numerical error estimator is given by

$$\mathscr{E}_N\left(u_{\mathrm{d}}^h\right)^2 := \sum_{K \in \mathcal{Q}} h_K^2 \|r\|_{0,K}^2 + \sum_{E \in \mathcal{E}} h_E \|j\|_{0,E}^2. \tag{5.27}$$

Moreover, if we let $\mathcal{E}_K := \{E \in \mathcal{E} : E \subset \partial K\}$ for all $K \in \mathcal{Q}$, then the corresponding local contribution is

$$\mathscr{E}_N^K\left(u_{\mathrm{d}}^h\right)^2 := h_K^2 \|r\|_{0,K}^2 + \sum_{E \in \mathcal{E}_K} h_E \|j\|_{0,E}^2, \quad \forall K \in \mathcal{Q}. \tag{5.28}$$

Under reasonable assumptions, the reliability of $\mathscr{E}\left(u_{\mathrm{d}}^h\right)$ is demonstrated in Chapter 8 in

this framework. That is, it is proven that

$$\left| u - u_{\mathrm{d}}^h \right|_{1,\Omega} \lesssim \mathscr{E}\left(u_{\mathrm{d}}^h \right),$$

where the hidden constant is independent of the mesh size h, the number L of hierarchical levels of the mesh (see Chapter 6), the number N_f of features, and their size. The generalization to trimmed and multipatch geometries is also discussed in Chapters 7 and 8.

Remark 5.4.2. If a standard C^0-continuous finite element method is used, then the normal derivative jumps contributions of u_0^h and u_k^h should be added to $\mathscr{E}_N\left(u_{\mathrm{d}}^h \right)$. This is analogous to the jump contributions on the interfaces between patches appearing in the multipatch case that will be analyzed in Chapter 8.

5.4.3 Mark

We present here a maximum marking strategy derived from (2.36), but a Dörfler strategy as in (2.37) could also be easily derived in the same way. That is, recalling that $N_f \equiv N_f^{(i)}$ at the current iteration i, we select and mark elements $\mathcal{M} \subset \mathcal{Q}$ to be refined, and features

$$\left\{ F^{k_{\mathrm{m}}} \right\}_{k_{\mathrm{m}} \in I_{\mathrm{m}}} \subset \mathfrak{F} \quad \text{with } I_{\mathrm{m}} \subset \left\{ 1, \ldots, N_f^{(i)} \right\}$$

to be added to the (partially) defeatured geometry $\Omega_0 \equiv \Omega_0^{(i)}$. That is, after choosing a marking parameter $0 < \theta \leq 1$, the marked elements $K_{\mathrm{m}} \in \mathcal{M}$ and the marked features $F^{k_{\mathrm{m}}}$ for $k_{\mathrm{m}} \in I_{\mathrm{m}}$ verify

$$\alpha_N \, \mathscr{E}_N^{K_{\mathrm{m}}}\left(u_{\mathrm{d}}^h \right) \geq \theta \max \left(\alpha_N \max_{K \in \mathcal{Q}} \mathscr{E}_N^K\left(u_{\mathrm{d}}^h \right), \, \alpha_D \max_{k=1,\ldots,N_f} \mathscr{E}_D^k\left(u_{\mathrm{d}}^h \right) \right), \qquad (5.29)$$

$$\alpha_D \, \mathscr{E}_D^{k_{\mathrm{m}}}\left(u_{\mathrm{d}}^h \right) \geq \theta \max \left(\alpha_N \max_{K \in \mathcal{Q}} \mathscr{E}_N^K\left(u_{\mathrm{d}}^h \right), \, \alpha_D \max_{k=1,\ldots,N_f} \mathscr{E}_D^k\left(u_{\mathrm{d}}^h \right) \right). \qquad (5.30)$$

In other words, the set of marked elements and the set of selected features are the ones giving the most substantial contribution to the overall error estimator. The smallest is θ, the more elements and features are selected. Note also that the largest is α_N with respect to α_D in (5.21), the more importance is given to $\mathscr{E}_N\left(u_{\mathrm{d}}^h \right)$ with respect to $\mathscr{E}_D\left(u_{\mathrm{d}}^h \right)$, and vice-versa.

Remark 5.4.3. Note that without numerical error, or more precisely if $\mathscr{E}_N^K\left(u_{\mathrm{d}}^h \right) = 0$ for all $K \in \mathcal{Q}$, then the proposed marking strategy leads to the same marked features as the marking strategy introduced in Section 4.5.2. Similarly, without defeaturing error, or more precisely if $\mathscr{E}_D^k\left(u_{\mathrm{d}}^h \right) = 0$ for all $k = 1, \ldots, N_f$, then the proposed marking strategy leads to the same marked elements as the standard maximum marking strategy found in the adaptive finite element literature, see e.g. [Nochetto et al., 2009].

5.4.4 Refine

In the one hand, based on the set $\mathcal{M}$ of marked elements, the mesh $\mathcal{Q}$ is refined thanks to an h-refinement procedure corresponding to the chosen finite element method. During this refinement step, we need to make sure that Assumption 5.3.1 remains satisfied. In the other hand, the defeatured geometry $\Omega_0^{(i)}$ is refined, meaning that the marked features $\left\{F^k\right\}_{k \in I_{\mathrm{m}}}$ are inserted in the geometrical model. This is done exactly as in Section 4.5.3.

Once the mesh and the defeatured geometry have been refined, the modules SOLVE and ESTIMATE, respectively presented in Sections 5.4.1 and 5.4.2 can be called again. To do so, we update Ω_0 as $\Omega_0^{(i+1)}$, we define $N_f^{(i+1)} := N_f^{(i)} - \#I_{\mathrm{m}}$, we update the set of features $\mathfrak{F}$ as $\mathfrak{F} \setminus \left\{F^k\right\}_{k \in I_{\mathrm{m}}}$, and we renumber the features from 1 to $N_f^{(i+1)}$. The adaptive loop is continued until a certain given tolerance on the error estimator $\mathscr{E}\left(u_{\mathrm{d}}^h\right)$ is reached.

Remark 5.4.4. One does not want to remesh the geometrical model when features are added to it, as this would cancel the efforts made by standard h-refinement in the previous iterations. Therefore, in order to avoid remeshing when some features are added to the geometrical model, this adaptive strategy is designed to be used with mesh-preserving methods such as fictitious domain approaches or immersed methods, for which the computational domain is immersed in a background mesh, see e.g., [Hansbo and Hansbo, 2002; Haslinger and Renard, 2009; Rank et al., 2012; Burman et al., 2015]. This refinement step will be made clearer in the context of IGA in Chapter 8. We anticipate here that in general in IGA, the negative component of the added features can be introduced to the geometrical model by trimming, while their positive component can be introduced using multipatch geometry techniques. These advanced spline techniques are introduced in Chapter 6.

6 A review of isogeometric analysis and spline technologies

B-spline functions and their NURBS generalization are some of the main building blocks of CAD softwares, that have allowed the advent of isogeometric analysis. In this chapter, we first review in Section 6.1 the construction of B-splines and their main features for use in analysis. As the tensor-product structure of classical B-splines limit their use for the numerical approximation of PDEs, then in Section 6.2, we introduce and discuss two extensions that allow for local refinement, namely HB-splines and THB-splines. Subsequently in Section 6.3, we show the advantages of employing spline functions in a Galerkin discretization scheme by introducing IGA, first presented in the seminal work [Hughes et al., 2005]. Finally in Section 6.4, we extend the application of IGA to more general spline domains that are widely used in CAD, more specifically multipatch and trimmed domains.

6.1 An introduction to B-splines

B-splines are piecewise polynomial functions with possible high global regularity. The degree of the underlying polynomials is also called degree of the B-splines. In this section, we provide a precise definition of B-splines, and we state some of their important properties, following [Höllig, 2003]. The interested reader is referred to the seminal works [De Boor, 1972; Piegl and Tiller, 1997; Rogers, 2001]. To begin with, let us consider two strictly positive integers: let P denote the degree of the B-spline basis functions, and let N denote their number, which will correspond to the number of degrees of freedom of the corresponding B-spline space.

6.1.1 One-dimensional B-spline basis functions

Consider a non-decreasing sequence of $N + P + 1$ real values, called knot vector and denoted

$$\Xi := \{\xi_1, \xi_2, \ldots, \xi_{N+P+1}\}. \tag{6.1}$$

We call multiplicity the number of times a knot $\xi \in \Xi$ is repeated in the knot vector, and we call knot span each interval $[\xi_i, \xi_{i+1}]$, $i = 1, \ldots, N + P$. Note that if $\xi_i = \xi_{i+1}$, then the corresponding knot span is composed of a single point. As it is common practice in standard CAD, we assume in this thesis that knot vectors are always open, meaning that the first and last knots have multiplicity $P + 1$. This leads to an interpolatory B-spline basis at both ends of the parametric interval $[\xi_1, \xi_{N+P+1}]$. In the following, we will always assume for simplicity, and without constituting any limitation, that $\xi_1 = 0$ and $\xi_{N+P+1} = 1$. Therefore, the parametric interval will always be $[\xi_1, \xi_{N+P+1}] = [0, 1]$.

It is now possible to recursively define the univariate B-spline basis corresponding to the knot vector Ξ, using the following Cox-de Boor formula introduced in [De Boor, 1972]. The recursion starts for $P = 0$ with piecewise constant functions in $[0, 1]$: for all $i = 1, \ldots, N$, the i-th B-spline basis function of degree 0 is defined by

$$\hat{\beta}_{i,0}(\hat{x}) := \begin{cases} 1 & \text{if } \hat{x} \in [\xi_i, \xi_{i+1}), \\ 0 & \text{otherwise.} \end{cases} \tag{6.2}$$

Then, using the convention $\dfrac{0}{0} = 0$ and setting $\hat{\beta}_{N+1,P-1} \equiv 0$, B-spline basis functions of degree $P > 0$ are defined for all $i = 1, \ldots, N$ by

$$\hat{\beta}_{i,P}(\hat{x}) := \frac{\hat{x} - \xi_i}{\xi_{i+P} - \xi_i}\hat{\beta}_{i,P-1}(\hat{x}) + \frac{\xi_{i+P+1} - \hat{x}}{\xi_{i+P+1} - \xi_{i+1}}\hat{\beta}_{i+1,P-1}(\hat{x}), \quad \text{for } \hat{x} \in [0, 1], \tag{6.3}$$

where $\hat{\beta}_{i,P}$ denotes the i-th B-spline basis function of degree P. The corresponding B-spline basis is denoted

$$\hat{\mathcal{B}}_P := \left\{ \hat{\beta}_{i,P} : [0, 1] \to \mathbb{R}, \ i = 1, \ldots, N \right\}. \tag{6.4}$$

Note that for $P = 0$ and $P = 1$, the B-spline basis $\hat{\mathcal{B}}_P$ is identical to the classical finite element basis made of piecewise constant and piecewise linear polynomials, respectively. The most important properties of a B-spline basis are summarized in the following proposition.

Proposition 6.1.1. *Let $k_\xi \in \mathbb{N}$ denote the multiplicity of knot $\xi \in \Xi$. Then the B-spline basis functions satisfy the following properties:*

- *they are C^{P-k_ξ}-continuous in every $\xi \in \Xi$, and C^∞-continuous everywhere else;*

- *they have local support over at most $P + 1$ knot spans;*

- *they are pointwise non-negative, i.e., $\hat{\beta}(\hat{x}) \geq 0$ for all $\hat{\beta} \in \hat{\mathcal{B}}_P$ and all $\hat{x} \in [0, 1]$;*

- *they satisfy the partition of unity property, i.e.,*

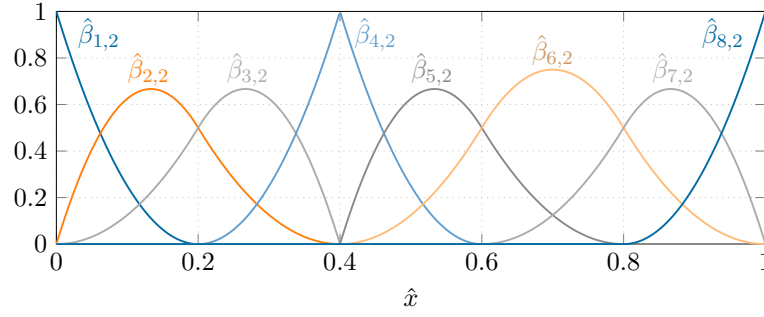$$\sum_{i=1}^{N+P+1} \hat{\beta}_{i,P}(\hat{x}) = 1, \qquad \forall \hat{x} \in [0, 1].$$

Figure 6.1 – One dimensional B-spline basis functions of degree $P = 2$ corresponding to the knot vector $\Xi = \{0, 0, 0, 0.2, 0.4, 0.4, 0.8, 1, 1, 1\}$. Note that the basis has a reduced continuity at the repeated knot 0.4.

To illustrate these properties, a quadratic B-spline basis is drawn in Figure 6.1.

6.1.2 One-dimensional non-uniform rational B-splines (NURBS)

Many free-form shapes can be easily described by the previously introduced B-spline functions. However, B-splines do not allow for the representation of a wide variety of important objects, mainly the ones which cannot be exactly represented by polynomials, such as conical sections. To remedy this issue, NURBS basis functions were introduced. Given a B-spline basis $\hat{\mathcal{B}}_P = \left\{ \hat{\beta}_{i,P} \right\}_{i=1}^N$ and some strictly positive reals $\{w_i\}_{i=1}^N$ called weights, the univariate NURBS basis functions are defined for all $i = 1, \ldots, N$ by

$$\hat{\chi}_{i,P}(\hat{x}) := \frac{\hat{\beta}_{i,P}(\hat{x}) w_i}{\sum_{j=1}^N \hat{\beta}_{j,P}(\hat{x}) w_j}, \quad \text{for } \hat{x} \in [0, 1]. \tag{6.5}$$

When all weights equal to 1, then thanks to the partition of unity property of B-spline bases, $\hat{\chi}_{i,P} \equiv \hat{\beta}_{i,P}$ for all $i = 1, \ldots, N$. Moreover, all properties of the underlying B-spline basis stated in Proposition 6.1.1 are inherited by the corresponding NURBS basis. For a geometric interpretation of NURBS functions as a projective transformation of B-splines with projection weights $\{w_i\}_{i=1}^N$, the interested reader is referred to [Piegl and Tiller, 1997] and [Cottrell et al., 2009].

6.1.3 Multivariate B-spline and NURBS basis functions

Multivariate B-spline basis functions are straight-forwardly defined as a tensor-product of univariate B-splines. More precisely, if $n = 2$ or $n = 3$ is the space dimension, then let $\boldsymbol{P} = (P_1, \ldots, P_n)$ be a vector of polynomial degrees, let $\boldsymbol{N} = (N_1, \ldots, N_n)$ be a vector of number of degrees of freedom in each space direction, let $\Xi^j := \left\{ \xi_i^j \right\}_{i=1}^{N_j + P_j + 1}$ be the knot vector corresponding to the parametric direction j, and let $\hat{\beta}_{i,P_j}^j$ be the i-th B-spline

(a) Interpolatory boundary basis function.

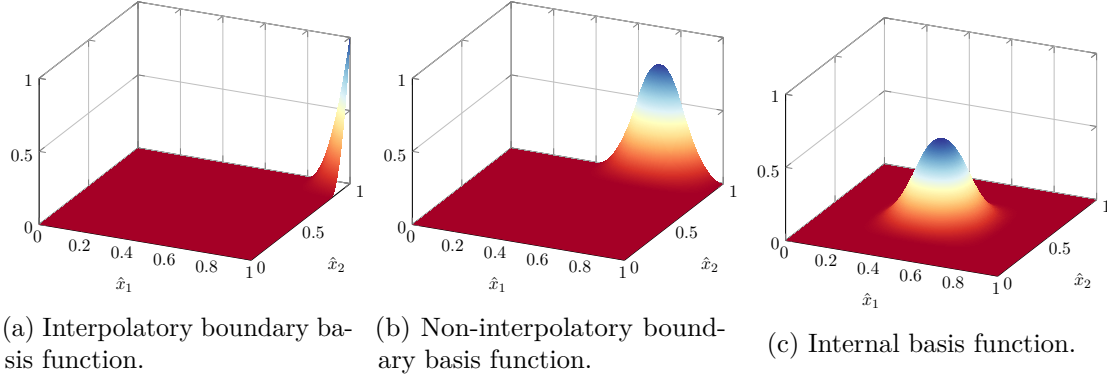(b) Non-interpolatory boundary basis function.

(c) Internal basis function.

Figure 6.2 – Example of bivariate quadratic B-spline basis functions.

basis function in the j-th direction, $j = 1, \ldots, n$. Then the multivariate B-spline basis of degree $\boldsymbol{P}$ is given by

$$\hat{\mathcal{B}}_{\boldsymbol{P}} := \left\{ \hat{\beta}_{\mathbf{i}, \boldsymbol{P}} : \mathbf{i} \in \mathbf{I} \text{ and } \hat{\beta}_{\mathbf{i}, \boldsymbol{P}} := \prod_{j=1}^{n} \hat{\beta}_{i_j, P_j}^{j} : [0, 1]^n \to \mathbb{R} \right\},$$

where $\mathbf{i} = (i_1, \ldots, i_n)$ is a multi-index denoting a position in the tensor-product structure, and $\mathbf{I} := \{1, \ldots, N\}^n$ is the set of such indices. Some examples of bivariate B-spline basis functions are drawn in Figure 6.2.

Moreover, multivariate NURBS basis functions are defined in a similar way as univariate NURBS basis functions in (6.5), from a multivariate B-spline basis $\hat{\mathcal{B}}_{\boldsymbol{P}} = \left\{ \hat{\beta}_{\mathbf{i}, \boldsymbol{P}} \right\}_{\mathbf{i} \in \mathbf{I}}$ and from strictly positive weights $\{w_{\mathbf{i}}\}_{\mathbf{i} \in \mathbf{I}}$. For the sake of simplicity, and without constituting any limitation, we assume in this thesis that the degrees P_j are identical in each parametric direction j, and therefore the vector $\boldsymbol{P}$ can be simplified to a single scalar value P. In the sequel, the dependence on P of the spline bases is omitted, unless explicitly needed in the exposition.

6.1.4 Parametric Bézier mesh

For $j = 1, \ldots, n$, let us consider the set $Z^j \subset \Xi^j$ of non-repeated knots in the j-th direction, written $Z^j := \left\{ \zeta_1^j, \ldots, \zeta_{M_j}^j \right\}$ with $M_j \in \mathbb{N} \setminus \{0, 1\}$. The values of Z^j are called breakpoints, and they naturally partition the parametric domain $(0, 1)^n$ into a Cartesian grid

$$\hat{\mathcal{Q}} := \left\{ \hat{K}_{\mathbf{m}} := \bigtimes_{j=1}^{n} \left(\zeta_{m_j}^j, \zeta_{m_j+1}^j \right) : \mathbf{m} = (m_1, \ldots, m_n), \right.$$

$$\left. 1 \leq m_j \leq M_j - 1 \text{ for } j = 1, \ldots, n \right\}.$$

The grid $\hat{\mathcal{Q}}$ is called parametric Bézier mesh, and each $\hat{K}_{\mathbf{m}}$ is referred to as parametric element, sometimes also called cell. Furthermore, let us define the support extension of a parametric element $\hat{K}_{\mathbf{m}}$. For all $j = 1, \ldots, n$, let i_j be the index verifying $P_j + 1 \leq i_j \leq N_j$ such that we can uniquely rewrite the interval $\left(\zeta_{m_j}^j, \zeta_{m_j+1}^j \right) = \left(\xi_{i_j}^j, \xi_{i_j+1}^j \right)$. Then the support extension of $\hat{K}_{\mathbf{m}}$ is given by

$$S_{\text{ext}} \left(\hat{K}_{\mathbf{m}} \right) := \bigtimes_{j=1}^{n} S_{\text{ext}} \left(\zeta_{m_j}^j, \zeta_{m_j+1}^j \right), \tag{6.6}$$

$$\text{where} \quad S_{\text{ext}} \left(\zeta_{m_j}^j, \zeta_{m_j+1}^j \right) := \left(\xi_{i-P_j}^j, \xi_{i+P_j+1}^j \right).$$

6.1.5 Refinement strategies

Splines are successfully used in computations thanks to their capability of enriching the approximation space without changing the underlying geometrical description. More precisely, the following three different space refinement strategies can be used:

- Knot insertion. This consists in adding new knots to a given knot vector Ξ, thereby creating a new augmented knot vector $\Xi_+ \supset \Xi$. In each space direction, an extra univariate basis function is introduced with every new knot. While one can see strong similarities with the h-refinement (also called mesh refinement) strategy of the classical C^0-continuous FEM, it is worth noting that knot insertion allows for a greater flexibility. Indeed, this procedure also allows to control the global continuity of the B-spline basis: if knot insertion increases the multiplicity of some original knots, then the resulting refined basis has lower global continuity than the original one.

- Degree elevation. Similarly to the p-refinement strategy of classical FEM, the underlying polynomial degree P is increased to $P_+ > P$. However, while the B-spline space is enriched, the global continuity of the functions is preserved. Therefore, the original multiplicity k_ξ of every knot $\xi \in \Xi$ is increased by $P_+ - P$ to preserve the original continuity of order $P - k_\xi = P_+ - (k_\xi + P_+ - P)$.

- k-refinement. This consists in elevating the degree P to $P_+ > P$, followed by the insertion of some knots. This produces a new B-spline basis which has maximal $C^{P_+ - 1}$-continuity at the newly inserted knots, and whose original continuity is preserved at the previously already existing knots.
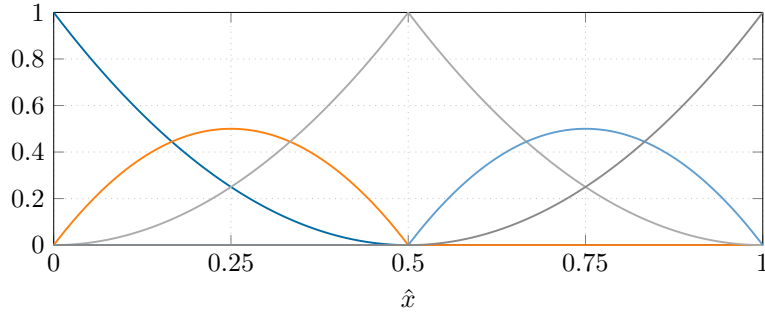
These different refinement strategies are illustrated in Figure 6.3. However in this thesis, we only concentrate on knot insertion in the case in which it is equivalent to standard mesh refinement, and we assume that both the B-spline degree and the global continuity of the basis are fixed.
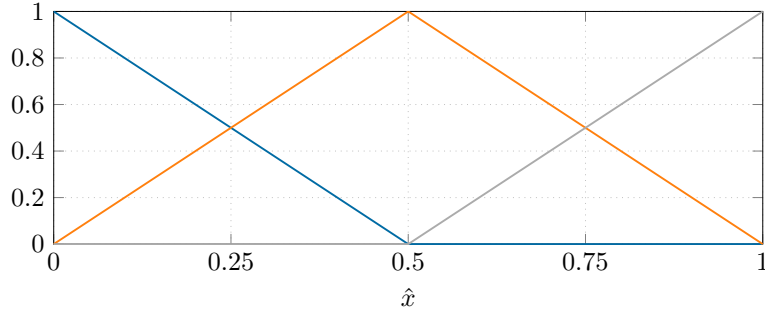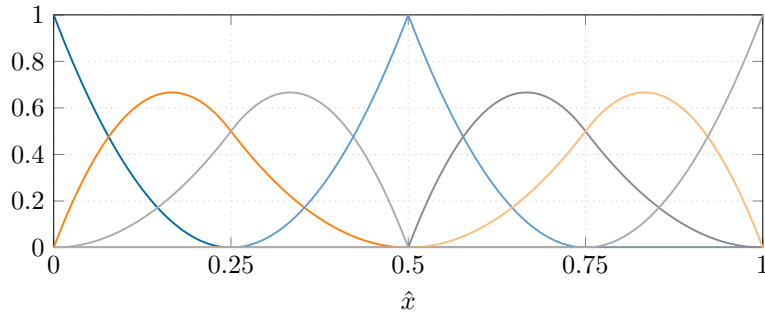
(a) Initial linear B-spline basis associated with $\Xi = \{0, 0, 0.5, 1, 1\}$.
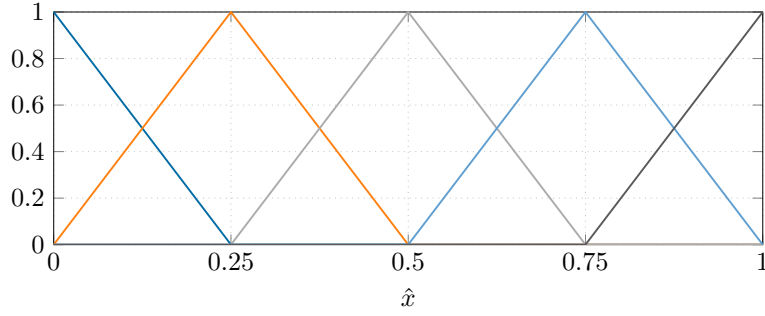
(b) Knot insertion: B-spline basis with new knots 0.25 and 0.75, i.e., $\Xi_+ = \{0, 0, 0.25, 0.5, 0.75, 1, 1\}$.

(c) Degree elevation: quadratic B-spline basis, i.e., $\Xi_+ = \{0, 0, 0, 0.5, 1, 1, 1\}$.

(d) k-refinement: quadratic B-spline basis with new knots 0.25 and 0.75, i.e., $\Xi_+ = \{0, 0, 0, 0.25, 0.5, 0.5, 0.75, 1, 1, 1\}$

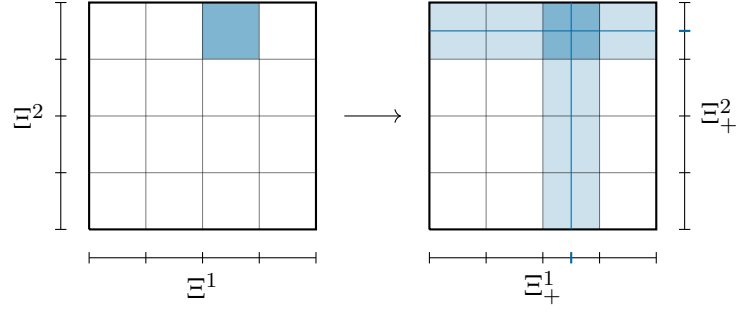Figure 6.3 – Illustration of the different refinement strategies.

Figure 6.4 – Illustration of the non-local refinement capability of multivariate B-splines due to their tensor-product structure: for the B-spline mesh element in dark blue, all the elements in light blue on the right also need to be refined.

6.2 Hierarchical B-splines and their truncated counterpart

The refinement strategies introduced in the previous section act globally on the whole domain, and the tensor-product structure of multivariate B-splines does not allow for local refinement, see Figure 6.4. To overcome this limitation, a vast variety of technologies have been developed, among which we find

- hierarchical B-splines (HB-splines) [Forsey and Bartels, 1988; Greiner and Hormann, 1996; Kraft, 1997],

- truncated hierarchical B-splines (THB-splines) [Giannelli et al., 2012, 2016],

- T-splines [Bazilevs et al., 2010; Scott et al., 2012; Beirão da Veiga et al., 2013],

- subdivision surfaces [Peters and Reif, 2008],

- polynomial splines over T-meshes (PHT-splines) [Deng et al., 2008],

- LR-splines [Dokken et al., 2013; Bressan, 2013],

- U-splines [Thomas et al., 2018].

In the remaining chapters of this thesis, we work with HB-splines and their truncated extension, since they are mathematically well-understood, conceptually simple, and easy to implement.

6.2.1 Hierarchical B-splines

In this section, we introduce and motivate the use of HB-splines, following [Vuong et al., 2011; Kraft, 1997]. Let $\hat{\mathfrak{D}} := (0,1)^n$ denote the parametric domain, and let $L \in \mathbb{N}$ be the number of hierarchical levels. Consider a sequence $\hat{\mathcal{B}}^0, \hat{\mathcal{B}}^1, \ldots, \hat{\mathcal{B}}^L$ of multivariate

B-spline bases defined on $\hat{\mathfrak{D}}$, determined by their corresponding degree and knot vectors, and such that

$$\text{span}\left\{\hat{\mathcal{B}}^0\right\} \subset \text{span}\left\{\hat{\mathcal{B}}^1\right\} \subset \ldots \subset \text{span}\left\{\hat{\mathcal{B}}^L\right\}. \tag{6.7}$$

Let N^ℓ denote the dimension of $\hat{\mathcal{B}}^\ell$, for all $\ell = 0, \ldots, L$. Moreover, let $\hat{\mathcal{Q}}^\ell$ be the Bézier mesh corresponding to the B-spline basis $\hat{\mathcal{B}}^\ell$ for all $\ell = 0, \ldots, L$. An element $\hat{K}$ is a cell of level ℓ if $\hat{K} \in \hat{\mathcal{Q}}^\ell$, and we write $\text{lev}\left(\hat{K}\right) = \ell$.

Then, let

$$\underline{\hat{\mathfrak{D}}}^L = \left\{\hat{\mathfrak{D}}^0, \hat{\mathfrak{D}}^1, \ldots, \hat{\mathfrak{D}}^L\right\} \tag{6.8}$$

be a hierarchy of nested sub-domains of $\hat{\mathfrak{D}}$ of depth L, that is, such that

$$\hat{\mathfrak{D}} =: \hat{\mathfrak{D}}^0 \supseteq \hat{\mathfrak{D}}^1 \supseteq \ldots \supseteq \hat{\mathfrak{D}}^L := \emptyset,$$

and such that $\hat{\mathfrak{D}}^\ell$ is a union of elements of level $\ell - 1$, i.e.,

$$\hat{\mathfrak{D}}^\ell = \text{int}\left(\bigcup_{\hat{K} \in \hat{\mathcal{Q}}^{\ell-1}_*} \overline{\hat{K}}\right), \quad \hat{\mathcal{Q}}^{\ell-1}_* \subset \hat{\mathcal{Q}}^{\ell-1}, \quad \forall \ell = 1, \ldots, L.$$

We are now able to recursively define the HB-spline basis $\hat{\mathcal{H}} = \hat{\mathcal{H}}\left(\underline{\hat{\mathfrak{D}}}^L\right)$ as follows:

$$\begin{cases} \hat{\mathcal{H}}^0 := \hat{\mathcal{B}}^0; \\ \hat{\mathcal{H}}^{\ell+1} := \hat{\mathcal{H}}^{\ell+1}_\ell \cup \hat{\mathcal{H}}^{\ell+1}_{\ell+1}, \ \ \ell = 0, \ldots, L - 2; \\ \hat{\mathcal{H}} := \hat{\mathcal{H}}^{L-1}, \end{cases} \tag{6.9}$$

where for all $\ell = 0, \ldots, L - 1$,

$$\begin{aligned} \hat{\mathcal{H}}^{\ell+1}_\ell &:= \left\{\hat{\beta} \in \hat{\mathcal{H}}^\ell : \ \text{supp}\left(\hat{\beta}\right) \not\subset \hat{\mathfrak{D}}^{\ell+1}\right\}, \\ \hat{\mathcal{H}}^{\ell+1}_{\ell+1} &:= \left\{\hat{\beta} \in \hat{\mathcal{B}}^{\ell+1} : \ \text{supp}\left(\hat{\beta}\right) \subset \hat{\mathfrak{D}}^{\ell+1}\right\}, \end{aligned} \tag{6.10}$$

and the supports are considered to be open. In other words, HB-spline basis functions of level ℓ are the B-splines of level ℓ whose support is only constituted of elements of level equal or higher than ℓ, and of at least one element of level ℓ. An example of HB-spline basis is illustrated in Figure 6.5. We refer to a function $\hat{\beta} \in \hat{\mathcal{H}}$ as an active function, and to a function $\hat{\beta} \in \hat{\mathcal{H}} \cap \hat{\mathcal{B}}^\ell$ as an active function of level ℓ, for $\ell = 0, \ldots, L$. For more details on HB-splines, the interested reader is referred to [Garau and Vázquez, 2018].

6.2.2   Truncated hierarchical B-splines

HB-splines are missing some desirable properties such as for instance the partition of unity property. In [Giannelli et al., 2012], the THB-spline basis has therefore been introduced as
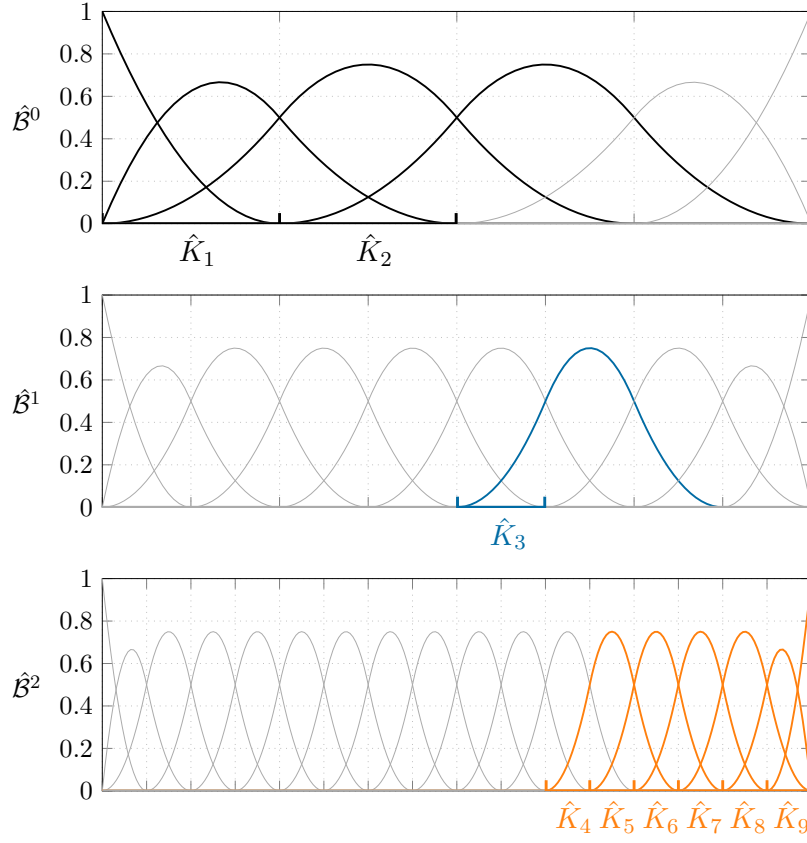
(a) Three levels of B-spline basis functions. Active elements and active functions of each level are highlighted in color.
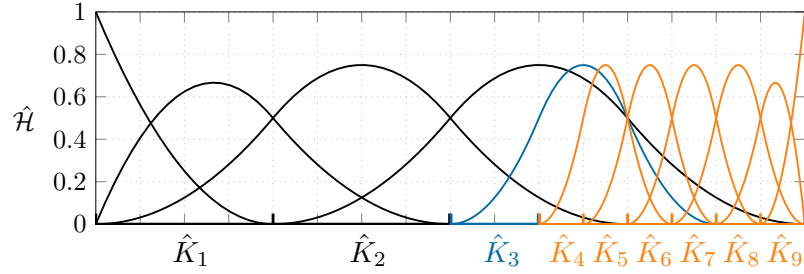
(b) HB-spline basis functions corresponding to the hierarchy in (a).
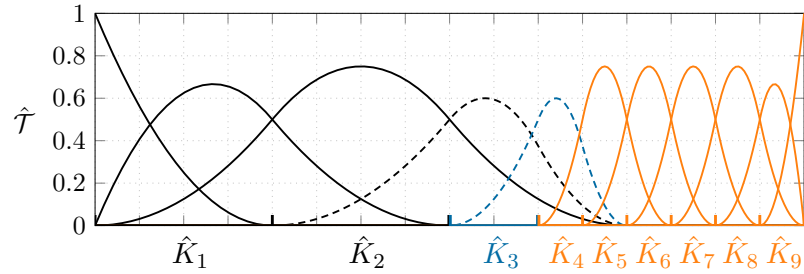
(c) THB-spline basis functions corresponding to the hierarchy in (a). Dashed functions are the ones that have been truncated.

Figure 6.5 – Example of a HB-spline basis on three levels, with its corresponding truncated counterpart.

a variant of HB-splines which spans the same space and which has better properties from a numerical standpoint. In particular, THB-spline basis functions satisfy the partition of unity property, they have a smaller support with respect to their corresponding HB-spline basis functions, and they possess strongly stable stability constants, see [Giannelli et al., 2014]. Let us now introduce their definition.

Thanks to the nested property (6.7) of B-spline spaces forming a hierarchical space, it is possible to write every $\hat{\beta} \in \hat{\mathcal{B}}^{\ell-1}$ for all $\ell = 1, \ldots, L$, with respect to the B-spline basis functions of level ℓ, that is, there exist some $c_i^\ell(\hat{\beta}) > 0$ for all $i = 1, \ldots, N^\ell$, such that

$$\hat{\beta} = \sum_{i=1}^{N^\ell} c_i^\ell(\hat{\beta}) \hat{\beta}_i^\ell.$$

Then, let us define the truncation operator trunc^ℓ with respect to level ℓ as

$$\mathrm{trunc}^\ell \hat{\beta} := \sum_{i=1}^{N^\ell} \hat{c}_i^\ell(\hat{\beta}) \hat{\beta}_i^\ell \qquad \text{for } \hat{\beta} \in \hat{\mathcal{B}}^{\ell-1},$$

where

$$\hat{c}_i^\ell(\hat{\beta}) = \begin{cases} 0 & \text{if } \hat{\beta}_i^\ell \in \hat{\mathcal{H}} \cap \hat{\mathcal{B}}^\ell, \\ c_i^\ell(\hat{\beta}) & \text{otherwise.} \end{cases}$$

Note that $\mathrm{trunc}^L \hat{\beta} = \hat{\beta}$ for all $\hat{\beta} \in \hat{\mathcal{B}}^{L-1}$. If we recursively apply this truncation operator to the HB-splines of $\hat{\mathcal{H}}$ from (6.9), we obtain a different basis spanning the same space as $\hat{\mathcal{H}}$, i.e., the THB-spline basis defined by

$$\hat{\mathcal{T}} := \left\{ \mathrm{trunc}^L \left(\ldots \left(\mathrm{trunc}^{\ell+1} \hat{\beta} \right) \cdots \right) : \hat{\beta} \in \hat{\mathcal{B}}^\ell \cap \hat{\mathcal{H}}, \ell = 0, \ldots, L-1 \right\}.$$

An example of THB-spline basis is illustrated in Figure 6.5.

6.2.3 Parametric hierarchical mesh

Consider a domain hierarchy $\hat{\mathfrak{D}}^L$ as defined in (6.8), on which a HB-spline basis and its corresponding THB-spline basis can be constructed. The parametric hierarchical mesh associated to the hierarchy $\hat{\mathfrak{D}}^L$ is defined as the union of the active elements of each level, that is,

$$\hat{\mathcal{Q}} := \bigcup_{\ell=0}^{L} \hat{\mathcal{Q}}_A^\ell, \quad \text{with} \quad \hat{\mathcal{Q}}_A^\ell := \left\{ \hat{K} \in \hat{\mathcal{Q}}^\ell : \hat{K} \subseteq \hat{\mathfrak{D}}^\ell, \hat{K} \not\subseteq \hat{\mathfrak{D}}^{\ell+1} \right\}. \tag{6.11}$$

We refer to a parametric element $\hat{K} \in \hat{\mathcal{Q}}$ as an active element (or active cell), and to an element $\hat{K} \in \hat{\mathcal{Q}}_A^\ell$ as an active element of level ℓ, for $\ell = 0, \ldots, L$.

Moreover, recall definition (6.6) of the support extension $S_{\text{ext}}\left(\hat{K}\right)$ of a parametric element $\hat{K}$, and let us extend it to the hierarchical context. The multilevel support extension of a parametric element $\hat{K} \in \hat{\mathcal{Q}}^\ell$ with respect to level k, with $0 \le k \le \ell \le L$, is defined by

$$S_{\text{ext}}\left(\hat{K}, k\right) := S_{\text{ext}}\left(\hat{K}'\right), \quad \text{with } \hat{K}' \in \hat{\mathcal{Q}}^k \text{ and } \hat{K} \subseteq \hat{K}'.$$

We are now able to define the notions of $\mathcal{H}$- and $\mathcal{T}$-admissibility of the hierarchical mesh $\hat{\mathcal{Q}}$, following [Buffa and Giannelli, 2016; Buffa et al., 2021b]. To do so, let us consider the auxiliary domains $\hat{\omega}_{\mathcal{H}}^0 = \hat{\omega}_{\mathcal{T}}^0 := \hat{\mathfrak{D}}^0 = \hat{\mathfrak{D}}$, and for $\ell = 1, \ldots, L$,

$$\hat{\omega}_{\mathcal{H}}^\ell := \bigcup \left\{ \overline{\hat{K}} : \hat{K} \in \hat{\mathcal{Q}}^\ell, S_{\text{ext}}\left(\hat{K}, \ell - 1\right) \subseteq \hat{\mathfrak{D}}^\ell \right\},$$
$$\hat{\omega}_{\mathcal{T}}^\ell := \bigcup \left\{ \overline{\hat{K}} : \hat{K} \in \hat{\mathcal{Q}}^\ell, S_{\text{ext}}\left(\hat{K}, \ell\right) \subseteq \hat{\mathfrak{D}}^\ell \right\}.$$

In other words, domains $\hat{\omega}_{\mathcal{H}}^\ell$, respectively $\hat{\omega}_{\mathcal{T}}^\ell$, are the regions of $\hat{\mathfrak{D}}^\ell$ where all the active basis functions of level $\ell - 1$, respectively of level $\ell - 1$ truncated with respect to level ℓ, are equal to zero. With these notions in hand, let us introduce the following definition.

Definition 6.2.1. The mesh $\hat{\mathcal{Q}}$ is said to be $\mathcal{H}$-*admissible* of class $\mathfrak{m} \in \{2, \ldots, L-1\}$, respectively $\mathcal{T}$-*admissible* of class $\mathfrak{m}$, if for all $\ell = \mathfrak{m}, \mathfrak{m}+1, \ldots, L-1$,

$$\hat{\mathfrak{D}}^\ell \subseteq \hat{\omega}_{\mathcal{H}}^{\ell-\mathfrak{m}+1}, \qquad \text{respectively} \quad \hat{\mathfrak{D}}^\ell \subseteq \hat{\omega}_{\mathcal{T}}^{\ell-\mathfrak{m}+1}.$$

From [Buffa and Giannelli, 2016, Proposition 9], this implies that the THB-spline basis functions in $\hat{\mathcal{T}}$ which take nonzero values over any element $\hat{K} \in \hat{\mathcal{Q}}$ belong to at most $\mathfrak{m}$ successive levels. If this property is preserved in a mesh refinement procedure, then the number of basis functions acting on any element of the mesh is guaranteed to remain bounded. More precisely, the number of non-zero splines acting on any mesh element is smaller than $\mathfrak{m}(P+1)^n$, where we recall that P is the degree of the splines.

Finally let us provide the following definition.

Definition 6.2.2 ([Bracco et al., 2018]). For all $\ell = 0, \ldots, L$ and all $\hat{K} \in \hat{\mathcal{Q}} \cap \hat{\mathcal{Q}}_A^\ell$, the $\mathcal{H}$-*neighborhood*, respectively $\mathcal{T}$-*neighborhood*, of $\hat{K}$ with respect to $\mathfrak{m} \in \{2, \ldots, L-1\}$ is the set

$$\mathcal{N}_{\mathcal{H}}\left(\hat{\mathcal{Q}}, \hat{K}, \mathfrak{m}\right) := \begin{cases} \left\{ \hat{K}' \in \hat{\mathcal{Q}}_A^{\ell-\mathfrak{m}+1} : \hat{K}' \cap S_{\text{ext}}\left(\hat{K}, \ell - \mathfrak{m} + 1\right) \ne \emptyset \right\} & \text{if } \ell - \mathfrak{m} + 1 \ge 0, \\ \emptyset & \text{otherwise,} \end{cases}$$

respectively

$$\mathcal{N}_{\mathcal{T}}\left(\hat{\mathcal{Q}}, \hat{K}, \mathfrak{m}\right) := \begin{cases} \left\{ \hat{K}' \in \hat{\mathcal{Q}}_A^{\ell-\mathfrak{m}+1} : \hat{K}' \cap S_{\text{ext}}\left(\hat{K}, \ell - \mathfrak{m} + 2\right) \ne \emptyset \right\} & \text{if } \ell - \mathfrak{m} + 1 \ge 0, \\ \emptyset & \text{otherwise.} \end{cases}$$

(a) B-spline curve in blue, control points and corresponding control polygon in orange.

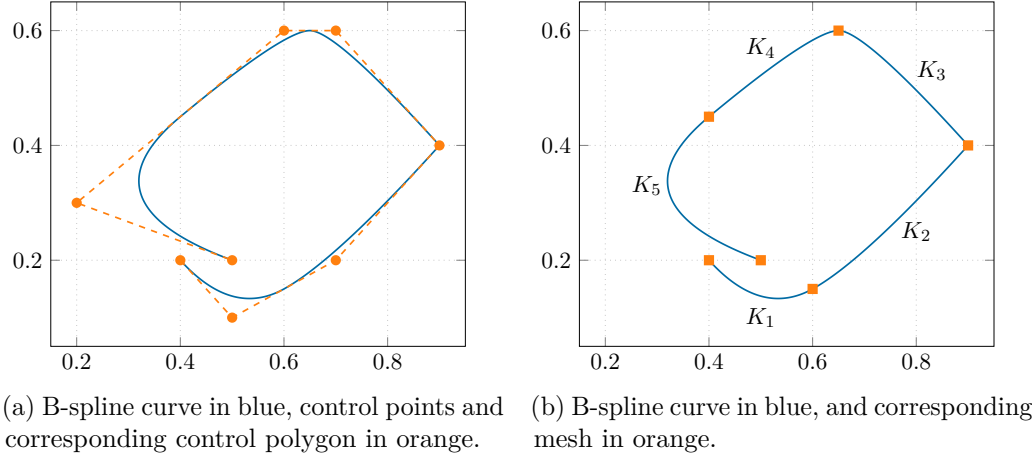(b) B-spline curve in blue, and corresponding mesh in orange.

Figure 6.6 – Example of quadratic B-spline curve in $\mathbb{R}^2$, associated with the knot vector $\Xi = \{0, 0, 0, 0.2, 0.4, 0.4, 0.8, 1, 1, 1\}$ whose basis in drawn in Figure 6.1.

We will see in a later chapter that this set is used to define a mesh refinement algorithm able to preserve the class of admissibility of the mesh, as in [Buffa and Giannelli, 2016].

6.3   Isogeometric analysis

In Sections 6.1 and 6.2, B-splines and their hierarchical extensions have only been introduced in the parametric domain $\hat{\mathfrak{D}} := (0,1)^n$. More general spline geometries $\mathfrak{D}$ can be defined as linear combination of the (truncated hierarchical) B-spline basis functions $\hat{\beta}_{\mathbf{i},\mathbf{p}}$ with some control points $\{\mathbf{C_i}\}_{\mathbf{i}\in\mathbf{I}} \subset \mathbb{R}^n$ of the physical domain, where the notation $\mathbf{i} \in \mathbf{I}$ is taken from Section 6.1.3. That is, $\mathfrak{D}$ is the image of a mapping $\mathbf{F} : \hat{\mathfrak{D}} \to \mathbb{R}^n$ defined by

$$\mathbf{F}(\hat{\boldsymbol{x}}) = \sum_{\mathbf{i}\in\mathbf{I}} \hat{\beta}_{\mathbf{i},\mathbf{p}}(\hat{\boldsymbol{x}})\mathbf{C_i} \quad \text{for all } \hat{\boldsymbol{x}} \in \hat{\mathfrak{D}}.$$

Note that in general, the control points are not interpolatory, which is a distinguishing feature with respect to standard FEM nodes. However, since we are using open knot vectors in each parametric direction, then the boundary vertices of the geometry are interpolated. The example of a B-spline curve is drawn in Figure 6.6 with its corresponding control points.

If $\mathfrak{D}$ is a (TH)B-spline geometry determined by (the refinement of) a mapping $\mathbf{F} : \hat{\mathfrak{D}} \to \mathfrak{D}$, we define the physical (hierarchical) mesh $\mathcal{Q}(\mathfrak{D})$ corresponding to $\hat{\mathcal{Q}}$ as

$$\mathcal{Q}(\mathfrak{D}) := \left\{ K := \mathbf{F}\left(\hat{K}\right) : \hat{K} \in \hat{\mathcal{Q}} \right\}, \tag{6.12}$$

on which the following classical assumption is made (see e.g., [Beirão da Veiga et al., 2014]).

Assumption 6.3.1. The isogeometric mapping $\mathbf{F} : \hat{\mathfrak{D}} \to \mathfrak{D}$ is bi-Lipschitz, its restriction $\mathbf{F}|_{\overline{\hat{K}}} \in C^\infty\left(\overline{\hat{K}}\right)$ for every $\hat{K} \in \hat{\mathcal{Q}}$, and $\mathbf{F}^{-1}|_{\overline{K}} \in C^\infty(\overline{K})$ for every $K \in \mathcal{Q}(\mathfrak{D})$.

All definitions that were previously introduced in the parametric domain $\hat{\mathfrak{D}}$ are readily transferred to the physical domain $\mathfrak{D}$, thanks to the isogeometric mapping $\mathbf{F}$. In particular, if (T)HB-splines are considered, Definition 6.2.1 is extended to the physical hierarchical mesh $\mathcal{Q}(\mathfrak{D})$ as follows.

Definition 6.3.2. The mesh $\mathcal{Q}(\mathfrak{D})$ defined by (6.12) is said to be $\mathcal{H}$-*admissible* of class $\mathfrak{m} \in \{2, \ldots, L-1\}$, respectively $\mathcal{T}$-*admissible* of class $\mathfrak{m}$, if the underlying parametric mesh $\hat{\mathcal{Q}}$ is $\mathcal{H}$-admissible of class $\mathfrak{m}$, respectively $\mathcal{T}$-admissible of class $\mathfrak{m}$.

Moreover, the notion of $\mathcal{H}$- and $\mathcal{T}$-neighborhood with respect to $\mathfrak{m} \in \{2, \ldots, L-1\}$ from Definition (6.2.2) can also be easily transferred to a physical element as follows:

Definition 6.3.3. The $\mathcal{H}$-*neighborhood* with respect to $\mathfrak{m} \in \{2, \ldots, L-1\}$, respectively $\mathcal{T}$-*neighborhood* with respect to $\mathfrak{m}$ of a physical element $K \in \mathcal{Q}(\mathfrak{D})$ is the set of push-forward elements of the $\mathcal{H}$-neighborhood, respectively $\mathcal{T}$-neighborhood, of the pull-back $\mathbf{F}^{-1}(K) \in \hat{\mathcal{Q}}$. That is,

$$\mathcal{N}_{\mathcal{H}}\Big(\mathcal{Q}(\mathfrak{D}), K, \mathfrak{m}\Big) := \left\{ K' := \mathbf{F}\Big(\hat{K}'\Big) : \hat{K}' \in \mathcal{N}_{\mathcal{H}}\Big(\hat{\mathcal{Q}}, \mathbf{F}^{-1}(K), \mathfrak{m}\Big) \right\},$$

$$\mathcal{N}_{\mathcal{T}}\Big(\mathcal{Q}(\mathfrak{D}), K, \mathfrak{m}\Big) := \left\{ K' := \mathbf{F}\Big(\hat{K}'\Big) : \hat{K}' \in \mathcal{N}_{\mathcal{T}}\Big(\hat{\mathcal{Q}}, \mathbf{F}^{-1}(K), \mathfrak{m}\Big) \right\}. \tag{6.13}$$

Furthermore, the isogeometric paradigm consists in using the same basis functions for the description of the computational domain and for the finite dimensional space on which one seeks the Galerkin solution of a PDE. That is, in IGA, the numerical solution of a PDE defined in the B-spline domain $\mathfrak{D}$, image of the isogeometric mapping $\mathbf{F}$, is sought in the finite dimensional space spanned by

$$\mathcal{B}(\mathfrak{D}) := \left\{ \beta := \hat{\beta} \circ \mathbf{F}^{-1} : \hat{\beta} \in \hat{\mathcal{B}} \right\}. \tag{6.14}$$

The space $\mathcal{H}(\mathfrak{D})$, resp. $\mathcal{T}(\mathfrak{D})$, can be similarly defined when $\mathfrak{D}$ is a HB-spline domain, resp. THB-spline domain, by replacing $\hat{\mathcal{B}}$ by $\hat{\mathcal{H}}$, resp. $\hat{\mathcal{T}}$, in (6.14). That is,

$$\mathcal{H}(\mathfrak{D}) := \left\{ \beta := \hat{\beta} \circ \mathbf{F}^{-1} : \hat{\beta} \in \hat{\mathcal{H}} \right\}, \tag{6.15}$$

$$\text{resp.} \quad \mathcal{T}(\mathfrak{D}) := \left\{ \beta := \hat{\beta} \circ \mathbf{F}^{-1} : \hat{\beta} \in \hat{\mathcal{T}} \right\}. \tag{6.16}$$

It can be shown that (T)HB-splines yield a linearly independent basis suitable for the analysis. In the context of HB-splines, we refer the interested reader to [Höllig, 2003, Section 4.5] for a proof, and we recall that

$$V^h(\mathfrak{D}) := \text{span}\left\{\mathcal{T}(\mathfrak{D})\right\} = \text{span}\left\{\mathcal{H}(\mathfrak{D})\right\}.$$

To finish this section, let us state the existence of a quasi-interpolant operator on the (T)HB-spline space $V^h(\mathfrak{D})$.

Theorem 6.3.4. *Let $\mathfrak{D}$ be a Lipschitz domain, and let $\mathcal{Q}(\mathfrak{D})$ be a $\mathcal{T}$-admissible hierarchical mesh on $\mathfrak{D}$. If $\Lambda \subset \partial\mathfrak{D}$ if a union of full faces of the mesh $\mathcal{Q}(\mathfrak{D})$, then there exists a Scott-Zhang-type operator on $\mathfrak{D}$, that is, an operator*

$$I^h : H^1_{0,\Lambda}(\mathfrak{D}) \to \left\{ v^h \in V^h(\mathfrak{D}) : v^h|_\Lambda = 0 \right\} \tag{6.17}$$

such that for all $v \in H^1_{0,\Lambda}(\mathfrak{D})$,

$$\sum_{K \in \mathcal{Q}(\mathfrak{D})} h_K^{-2} \|v - I^h(v)\|_{0,K}^2 \lesssim \|\nabla v\|_{0,\mathfrak{D}}^2 \quad and \quad \sum_{K \in \mathcal{Q}(\mathfrak{D})} \|\nabla I^h(v)\|_{0,K}^2 \lesssim \|\nabla v\|_{0,\mathfrak{D}}^2. \tag{6.18}$$

The latter implies that for all $v \in H^1_{0,\Lambda}(\mathfrak{D})$,

$$\sum_{K \in \mathcal{Q}(\mathfrak{D})} \left\| \nabla\left(v - I^h(v)\right) \right\|_{0,K}^2 \lesssim \|\nabla v\|_{0,\mathfrak{D}}^2. \tag{6.19}$$

The construction of such an operator can be found in [Buffa and Giannelli, 2021] and [Buffa et al., 2021b, Section 6.1.3] in the case in which $\Lambda = \partial\mathfrak{D}$, but it readily generalizes to the case in which $\Lambda \subset \partial\mathfrak{D}$ is a union of full faces. The reader is also referred to [Lee et al., 2000; Buffa et al., 2016] for more details on quasi-interpolants in spline spaces.

6.4   Advanced spline technologies: multipatch and trimmed domains

The image of a single isogeometric mapping $\mathbf{F}$ as defined in Section 6.3, called patch, limits the variety of domains one can define with splines: it only allows for geometries that are images of the unit square if $n = 2$ or the unit cube if $n = 3$. Therefore in this section, we extend the range of applications of IGA by considering more general B-spline domains. We first consider domains defined by $N_p \geq 1$ patches, glued together with C^0-continuity. Then, we consider trimmed domains, corresponding to the active part of a patch that is cut by some trimming curve or surface.

6.4.1   Multipatch isogeometric analysis

Multipatch domains are defined as

$$\mathfrak{D} := \text{int} \left(\bigcup_{j=1}^{N_p} \overline{\mathfrak{D}^j} \right), \tag{6.20}$$
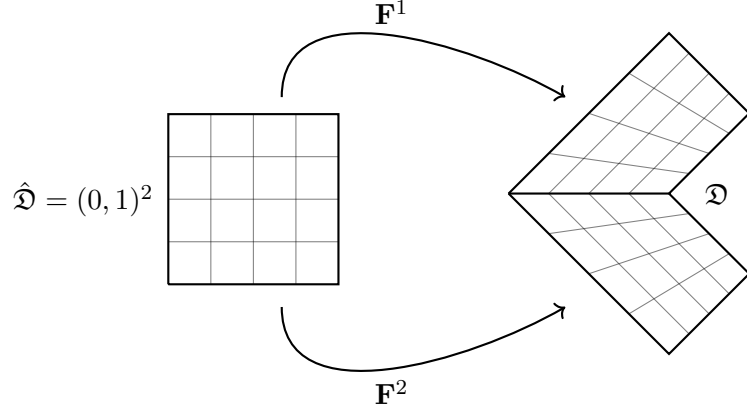
Figure 6.7 – Illustration of a multipatch isogeometric domain $\mathfrak{D}$ with $N_p = 2$ patches.

with $N_p \geq 1$, where each domain $\mathfrak{D}^j$ is the image of an isogeometric mapping

$$\mathbf{F}^j : (0,1)^n \to \mathfrak{D}^j$$

satisfying Assumption 6.3.1. An illustration of a multipatch domain is given in Figure 6.7. In this work, we assume that the patches do not overlap in the physical domain, that is, $\mathfrak{D}^i \cap \mathfrak{D}^j = \emptyset$ for all $i, j = 1, \ldots, N_p$ such that $i \neq j$. In the case of a multipatch isogeometric domain $\mathfrak{D}$, we define the corresponding multipatch mesh as

$$\mathcal{Q}(\mathfrak{D}) := \bigcup_{j=1}^{N_p} \mathcal{Q}(\mathfrak{D}^j), \tag{6.21}$$

where each $\mathcal{Q}(\mathfrak{D}^j)$ is defined as in (6.12). Moreover, we let $\hat{\mathcal{B}}^j$ denote the B-spline basis associated with each mesh $\mathcal{Q}(\mathfrak{D}^j)$, $j = 1, \ldots, N_p$.

To construct a suitable discrete space in a multipatch domain, we require the meshes to be conforming at the interfaces between patches, and we impose a C^0-continuity at those interfaces. More precisely, let

$$\Gamma^{i,j} := \partial \mathfrak{D}^i \cap \partial \mathfrak{D}^j, \quad \text{for } i, j = 1, \ldots, N_p, \, i \neq j$$

denote the interfaces between patches, and assume that they satisfy the following assumption.

Assumption 6.4.1. For all $i, j = 1, \ldots, N_p$ such that $i \neq j$,

- $\Gamma^{i,j}$ is either empty, or a vertex, or the image of a full edge or a full face of $(0,1)^n$ for both parametrizations $\mathbf{F}^i$ and $\mathbf{F}^j$;

- for every B-spline basis function $\hat{\beta}^i \in \hat{\mathcal{B}}^i$ such that $\hat{\beta}^i \circ (\mathbf{F}^i)^{-1} \neq 0$ on $\Gamma^{i,j}$, there exists a unique B-spline basis function $\hat{\beta}^j \in \hat{\mathcal{B}}^j$ such that $\hat{\beta}^i \circ (\mathbf{F}^i)^{-1} = \hat{\beta}^j \circ (\mathbf{F}^j)^{-1}$

on $\Gamma^{i,j}$;

- the control points associated to the interface functions of adjacent patches coincide.

This assumption allows us to ensure the C^0-continuity of the discrete functions at the patch interfaces, by associating the corresponding degrees of freedom on each side of the interface. For more details, the reader is referred to [Buffa et al., 2021b, Section 3.2.2].

In this case, the IGA numerical solution of a PDE defined in a multipatch domain $\mathfrak{D}$ is sought in the finite dimensional space

$$V^h(\mathfrak{D}) := \left\{ v^h \in C^0(\mathfrak{D}) : v^h|_{\mathfrak{D}^j} \in \text{span} \left\{ \mathcal{B}^j \right\}, \forall j = 1, \ldots, N_p \right\},$$

where for all $j = 1, \ldots, N_p$,

$$\mathcal{B}^j := \left\{ \beta := \hat{\beta} \circ \left(\mathbf{F}^j \right)^{-1} : \hat{\beta} \in \hat{\mathcal{B}}^j \right\}.$$

Note that C^0-continuity is imposed here between patches. The construction of spaces with higher continuity is currently a very active area of research, see [Toshniwal et al., 2017; Kapl et al., 2019; Bracco et al., 2020] for instance.

Finally, one can easily generalize the definition of (T)HB-splines basis functions of Section 6.2 to multipatch domains. The corresponding discrete isogeometric spaces defined in Section 6.3 can also easily be generalized to this setting, by considering on each hierarchical level a multi-patch space satisfying Assumption 6.4.1. For more details, we refer to [Buchegger et al., 2016] and [Garau and Vázquez, 2018, Section 3.4].

6.4.2   Isogeometric analysis in trimmed domains

Trimmed domains are obtained from a basic Boolean operation between standard (TH)B-spline domains, and they are nowadays a standard in most commercial CAD software. We consider the HB-spline basis functions in this section, but the same procedure can be performed with standard B-splines or with THB-splines.

Suppose that $\mathfrak{D}^{\mathrm{u}} \subset \mathbb{R}^n$ is a domain defined as the image of an isogeometric mapping $\mathbf{F} : (0,1)^n \to \mathfrak{D}^{\mathrm{u}}$, generated by a HB-spline basis $\hat{\mathcal{H}}$ and satisfying Assumption 6.3.1. Moreover, let $\{\omega_i\}_{i=1}^{N_t}$ be a set of bounded open Lipschitz domains in $\mathbb{R}^n$ that are trimmed away (i.e., cut) from $\mathfrak{D}^{\mathrm{u}}$ to obtain $\mathfrak{D}$, the computational domain. That is,

$$\mathfrak{D} := \mathfrak{D}^{\mathrm{u}} \setminus \overline{\omega}, \quad \text{with} \quad \omega := \text{int} \left(\bigcup_{i=1}^{N_t} \overline{\omega_i} \right). \tag{6.22}$$

The boundary of the trimmed geometry $\mathfrak{D}$ can then be decomposed into a part which coincides with the boundary of the non-trimmed domain, $\partial\mathfrak{D} \cap \partial\mathfrak{D}^{\mathrm{u}}$, and a trimmed part

(a) Non-trimmed rectangular domain $\mathfrak{D}^{\mathrm{u}}$ with a hierarchical mesh $\mathcal{Q}(\mathfrak{D}^{\mathrm{u}})$.

(b) Trimmed domain $\mathfrak{D}$, trimming curve Γ^{t}, and active hierarchical mesh in $\mathfrak{D}$.
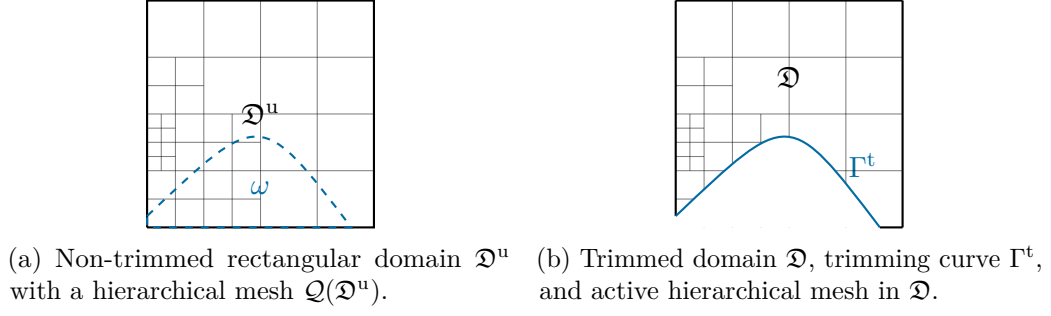
Figure 6.8 – Example of a trimmed domain $\mathfrak{D}$ obtained from trimming the blue domain ω from the original non-trimmed rectangular domain $\mathfrak{D}^{\mathrm{u}}$.

$\Gamma^{\mathrm{t}} := \partial\mathfrak{D} \setminus \overline{\partial\mathfrak{D}^{\mathrm{u}}}$, called trimming curve or surface. An example of trimmed geometry is illustrated in Figure 6.8.

Note that the underlying mathematical description of the original domain $\mathfrak{D}^{\mathrm{u}}$ is not altered by the trimming operation. Consequently, elements and basis functions are built with respect to the non-trimmed domain $\mathfrak{D}^{\mathrm{u}}$, and the correction needed because of trimming is handled at the integration level. In order to build suitable integration rules for the analysis, we need the description of the trimming curve or trimming surface $\mathbf{S}^{\mathrm{t}}$ in the parameter domain $(0,1)^n$. Since in general, the inverse mapping $\mathbf{F}^{-1}(\mathbf{S}^{\mathrm{t}})$ is not known analytically, integration is usually based on an approximation of the exact curve (or surface) determined by a given geometric tolerance, see e.g., [Hohmeyer, 1993; Farin et al., 2002]. Many techniques have been proposed in the literature to integrate trimmed elements, and we refer for instance to [Parvizian et al., 2007; Müller et al., 2013; Kudela et al., 2015]. In this thesis, the presented numerical examples use the re-parametrization tool presented in [Antolín et al., 2019, 2022]. The idea behind this tool is to create a high-order integration mesh on the cut elements, and to properly distribute integration points in the elements of this newly created mesh.

We can now generalize the isogeometric paradigm introduced in Section 6.3 to trimmed geometries. That is, let $\mathcal{H}(\mathfrak{D}^{\mathrm{u}})$ be defined as in (6.15), and let us consider the basis $\mathcal{H}(\mathfrak{D})$ of HB-spline basis functions whose support intersects $\mathfrak{D}$, i.e.,

$$\mathcal{H}(\mathfrak{D}) := \{\beta \in \mathcal{H}(\mathfrak{D}^{\mathrm{u}}) : \mathrm{supp}(\beta) \cap \mathfrak{D} \neq \emptyset\}.$$

In [Coradello et al., 2020], using the work of [Höllig, 2003, Section 4.5], it is shown that in the presence of trimming, (T)HB-splines yield a linearly independent basis suitable for the analysis.

Finally, the IGA numerical solution of a PDE defined in a trimmed domain $\mathfrak{D}$ is sought in the finite dimensional space spanned by the HB-spline basis functions restricted to $\mathfrak{D}$,

that is, in the finite dimensional space

$$V^h(\mathfrak{D}) := \operatorname{span}\left\{\beta|_{\mathfrak{D}} : \beta \in \mathcal{H}(\mathfrak{D})\right\}. \tag{6.23}$$

Remark 6.4.2. In an adaptive mesh refinement framework, we need to guarantee that a function $\beta \in \mathcal{H}(\mathfrak{D})$ is deactivated when all the elements in $\operatorname{supp}(\beta) \cap \mathfrak{D}$ are refined (see the recursive construction of HB-splines in (6.9)). To do so, we need to add the so-called ghost elements to the set of elements to refine, following [Coradello et al., 2020]. That is, when a trimmed element K is marked for refinement (see Section 5.4.3), all the elements in

$$\left\{K' \in \mathcal{Q}(\mathfrak{D}^{\mathrm{u}}) : K' \cap \mathfrak{D} = \emptyset,\ \operatorname{lev}(K) = \operatorname{lev}(K')\right.$$
$$\left. \text{and } \exists \beta \in \mathcal{H}(\mathfrak{D}^{\mathrm{u}}) \text{ such that } K \cup K' \subset \operatorname{supp}(\beta)\right\}$$

also need to be marked for refinement.

For more details about isogeometric methods in trimmed domains and some related open challenges, the reader is referred to [Marussig and Hughes, 2018] and references therein.

7 *A posteriori* error estimation: trimmed geometries

Many research papers, reviewed in [Buffa et al., 2021b], have tackled the important challenge of constructing locally refined splines, and using them within an adaptive paradigm. Research has now reached an advanced maturity on the subject. However, the use of locally refined splines on complex geometries defined by trimming operations is still at its first steps. In this chapter, we are interested in the study of an adaptive framework using (T)HB-splines in the context of trimmed geometries.

The use of THB-splines in the context of the Poisson problem and linear elasticity is studied in [Marussig et al., 2018] and in [de Prenter et al., 2020], where an emphasis is put on stability issues and bad conditioning of the system matrix caused by trimming, but no study of error indicators is given. To provide an approximation of the error, an implicit error estimator was introduced in [Coradello et al., 2020] in the context of (T)HB-spline isogeometric analysis on trimmed surfaces, extending their previous work [Antolín et al., 2020] on error estimation for linear fourth-order elliptic partial differential equations on non-trimmed geometries. The estimator relies on the solution of an additional residual-like system, but its reliability is not demonstrated. The contribution of this chapter differs from the aforementioned works as we introduce an explicit residual *a posteriori* estimator of the energy norm of the numerical error of the Poisson problem in trimmed geometries, and a mathematical proof of its reliability is given. Driven by the proposed estimator, and thanks to the local refinement capability given by HB-splines, we develop a fully adaptive error-driven numerical framework for the Poisson problem in trimmed geometries of arbitrary dimension. In this chapter, very general geometries are considered since the only hypothesis required on the trimming boundary is to be Lipschitz. Moreover, the reliability of the estimator is proven to be independent of the way the trimmed boundaries cut the underlying mesh, and thus in particular, it is independent of the size of the active part of the trimmed elements. Numerical examples are given to also show the efficiency of the proposed estimator.

When dealing with geometric domains defined by trimming, the main challenge faced

lies in the fact that the generated mesh is unfitted with the described physical domain. Therefore, this work is strongly related to the immersed or unfitted mesh methods. In particular, an implicit *a posteriori* estimator of the energy error due to numerical approximation is introduced in [Sun et al., 2020] for any polynomial degree, but its efficiency is only demonstrated numerically. In [He and Zhang, 2019], a reliable and efficient residual-based *a posteriori* error estimator is studied for a partially penalized linear immersed finite element method applied to elliptic interface problems. In the context of the cut finite element method, an estimator is proposed in [Burman et al., 2020] for an elliptic model problem with Dirichlet boundary conditions ensured by a ghost penalty stabilization (see [Burman, 2010]). In that paper, to avoid the dependence on the location of domain-mesh intersection, the efficiency for the term of ghost penalty is shown globally. In both [He and Zhang, 2019] and [Burman et al., 2020], a linear finite element basis is considered, while in the very recent work of [Chen et al., 2021], a reliable and efficient *hp*-residual type error estimator is given in the case of high-order unfitted finite element for interface problems in the framework of the local discontinuous Galerkin method. The reliable estimator we introduce in the present article for any polynomial degree is very similar to the one in [Chen et al., 2021] for two-dimensional domains, but our contribution deals with more general two- and three-dimensional computational domains. In particular, while the notion of "large element" is central in [Chen et al., 2021], we do not require any particular assumption on the way the trimming boundary intersects the underlying mesh. Thus in the proposed estimator, the scaling of the residuals with respect to the size of the trimmed mesh elements needs to be adapted.

While introducing the notation used in this chapter, we first state in Section 7.1 the considered model Poisson problem, and we precisely define the HB-spline based IGA numerical approximation of its solution. The computational domain of interest is a trimmed HB-spline domain. Subsequently, in Section 7.2, we introduce the *a posteriori* estimator of the error coming from this numerical approximation, in the energy norm, and its reliability is proven. In Section 7.3, we introduce the classical adaptive mesh refinement strategy adapted to the framework of trimmed domains, before presenting several numerical experiments in Section 7.4. This chapter closely follows [Buffa et al., 2021a].

In this chapter, the symbol $\lesssim$ indicates an inequality hiding a constant which does not depend on the mesh size h, on the size of the active part of the trimmed elements, nor on the number of hierarchical levels L (see Chapter 6). However, those inequalities may depend on the shape of the mesh elements. Moreover, we will write $A \simeq B$ whenever $A \lesssim B$ and $B \lesssim A$.

(a) Non-trimmed domain $\mathfrak{D}^{\mathrm{u}}$. (b) Trimmed domain $\mathfrak{D}$ and $\omega := \mathfrak{D}^{\mathrm{u}} \setminus \overline{\mathfrak{D}}$.
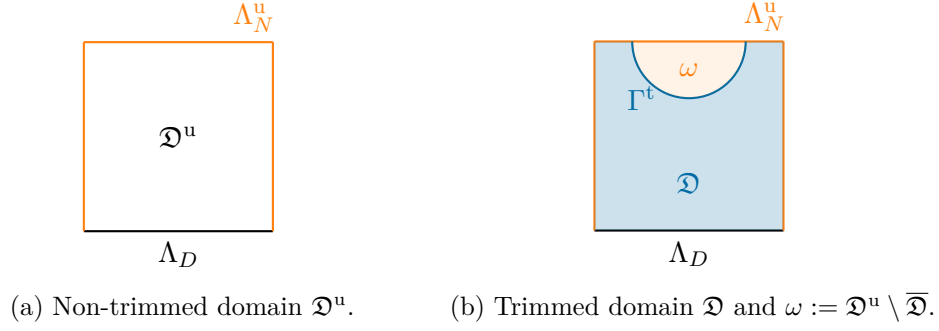
Figure 7.1 – Illustration of the notation used on the trimmed geometry $\mathfrak{D}$.

7.1 Trimming model problem

Let $\mathfrak{D}^{\mathrm{u}} \subset \mathbb{R}^n$ be a HB-spline domain as introduced in Chapter 6, i.e., it is the image of an isogeometric mapping $\mathbf{F} : (0,1)^n \to \mathfrak{D}^{\mathrm{u}}$, generated by a parametric HB-spline basis $\hat{\mathcal{H}}$ and satisfying Assumption 6.3.1. Then, let $\mathfrak{D} \subset \mathbb{R}^n$ be a Lipschitz domain trimmed from the HB-spline domain $\mathfrak{D}^{\mathrm{u}}$, as defined in (6.22). Moreover, let $\mathbf{n}$ be the unitary outward normal to $\partial\mathfrak{D}$, and let $\Lambda_N, \Lambda_D \subset \partial\mathfrak{D}$ be open such that $\Lambda_D \cap \Lambda_N = \emptyset$, $\overline{\Lambda_D} \cap \overline{\Lambda_N} = \partial\mathfrak{D}$ and $\Lambda_D \neq \emptyset$. Note that since $\mathfrak{D}$ is Lipschitz, then the trimming boundary

$$\Gamma^{\mathrm{t}} := \partial\mathfrak{D} \setminus \overline{\partial\mathfrak{D}^{\mathrm{u}}}$$

is also Lipschitz.

7.1.1 Continuous formulation

Let us consider Poisson's problem of Example 2.4.4 defined in $\mathfrak{D}$, where we recall that $u_D \in H^{\frac{1}{2}}(\Lambda_D)$ is the Dirichlet boundary condition imposed on Λ_D, $u_N \in L^2(\Lambda_N)$ is the Neumann boundary condition imposed on Λ_N, and $f \in L^2(\mathfrak{D})$ is the considered right hand side. That is, we want to find $u_s \in H^1_{u_D,\Lambda_D}(\mathfrak{D})$ which satisfies for all $v \in H^1_{0,\Lambda_D}(\mathfrak{D})$,

$$\int_{\mathfrak{D}} \nabla u_s \cdot \nabla v \, \mathrm{d}x = \int_{\mathfrak{D}} fv \, \mathrm{d}x + \int_{\Lambda_N} u_N v \, \mathrm{d}s. \tag{7.1}$$

Notation is illustrated in Figure 7.1. From Example 2.4.4, problem (7.1) admits a unique solution $u_s \in H^1_{u_D,\Lambda_D}(\mathfrak{D})$ according to Lax-Milgram theorem.

To simplify the subsequent analysis, we assume that $\overline{\Lambda_D} \cap \overline{\Gamma^{\mathrm{t}}} = \emptyset$, that is, we suppose that the Dirichlet boundary is not part of the trimming boundary Γ^{t}. If it were not the case, we would need to weakly impose the Dirichlet boundary conditions on $\overline{\Lambda_D} \cap \overline{\Gamma^{\mathrm{t}}}$ in the discrete setting, and make use of stabilization techniques, see, e.g., [Burman, 2010; Elfverson et al., 2019; Buffa et al., 2020].

7.1.2 Isogeometric analysis formulation with hierarchical B-splines

Let $\mathcal{Q}^{\mathrm{u}} := \mathcal{Q}(\mathfrak{D}^{\mathrm{u}})$ be (a refinement of) the physical hierarchical mesh on $\mathfrak{D}^{\mathrm{u}}$ as defined in (6.12), and let $\mathcal{E}^{\mathrm{u}}$ be the set of all faces of $\mathcal{Q}^{\mathrm{u}}$. Recall that here and in the sequel, edges are called faces even when $n = 2$, and assume that the Dirichlet boundary Λ_D is the union of full element faces. Moreover, let $h_K := \mathrm{diam}(K)$ for all $K \in \mathcal{Q}^{\mathrm{u}}$, let $h_E := \mathrm{diam}(E)$ for all $E \in \mathcal{E}^{\mathrm{u}}$, and let $h := \max_{K \in \mathcal{Q}^{\mathrm{u}}} h_K$.

Furthermore, let $\mathcal{Q} := \mathcal{Q}_{\mathrm{cut}} \cup \mathcal{Q}_{\mathrm{act}}$ be the active mesh intersecting the computational domain $\mathfrak{D}$, where

$$\mathcal{Q}_{\mathrm{cut}} := \{K \in \mathcal{Q}^{\mathrm{u}} : K \cap \mathfrak{D} \neq K, |K \cap \mathfrak{D}| > 0\}$$

is the set of cut (trimmed) elements, and

$$\mathcal{Q}_{\mathrm{act}} := \{K \in \mathcal{Q}^{\mathrm{u}} : K \subset \mathfrak{D}\}$$

is the set composed of the other active (non-trimmed) elements in $\mathfrak{D}$. Similarly, let $\mathcal{E}_N := \mathcal{E}_{\mathrm{cut}} \cup \mathcal{E}_{\mathrm{act}}$, where

$$\mathcal{E}_{\mathrm{cut}} := \{E \in \mathcal{E}^{\mathrm{u}} : E \cap \Lambda_N \neq E\} \qquad \text{and} \qquad \mathcal{E}_{\mathrm{act}} := \{E \in \mathcal{E}^{\mathrm{u}} : E \subset \Lambda_N\}.$$

Note that $\mathcal{E}_N$ is therefore the set of faces E of $\mathcal{E}^{\mathrm{u}}$ such that $|E \cap \Lambda_N| > 0$.

Remark 7.1.1. Note that the definition of $\mathcal{Q}_{\mathrm{cut}}$ (respectively $\mathcal{E}_{\mathrm{cut}}$) is numerically unstable and in practice, the condition $|K \cap \mathfrak{D}| > 0$ (resp. $|E \cap \Lambda_N| > 0$) is replaced by $|K \cap \mathfrak{D}| > \varepsilon_{\mathrm{cut}}$ (resp. $|E \cap \Lambda_N| > \varepsilon_{\mathrm{cut}}$) for some small $\varepsilon_{\mathrm{cut}} > 0$. The value of $\varepsilon_{\mathrm{cut}}$ is determined by the geometric modeling tool one uses to deal with trimmed elements, see [Antolín et al., 2019], and the induced error is a consistency error that is assumed to be negligible in the following analysis.

Recall that the trimming boundary is defined as $\Gamma^{\mathrm{t}} := \partial\mathfrak{D} \setminus \overline{\partial\mathfrak{D}^{\mathrm{u}}} \subset \Lambda_N$, and for all $K \in \mathcal{Q}$, let

$$\Gamma^{\mathrm{t}}_K := \Gamma^{\mathrm{t}} \cap \mathrm{int}(K).$$

Note that for all $K \in \mathcal{Q}_{\mathrm{act}}$, $\Gamma^{\mathrm{t}}_K = \emptyset$. Also note that for all internal faces $E \in \mathcal{E}_N$ such that $(E \cap \Lambda_N) \subset \Gamma^{\mathrm{t}}$ and $(E \cap \Lambda_N) \subset \partial(K \cap \mathfrak{D})$ for some $K \in \mathcal{Q}$, then $\Gamma^{\mathrm{t}}_K \cap (E \cap \Lambda_N) = \emptyset$, that is, this internal face is not included in Γ^{t}_K. Or in other words,

$$\Lambda_N = \mathrm{int}\left[\left(\bigcup_{E \in \mathcal{E}_N} \overline{E \cap \Lambda_N}\right) \cup \left(\bigcup_{K \in \mathcal{Q}_{\mathrm{cut}}} \overline{\Gamma^{\mathrm{t}}_K}\right)\right],$$

where the intersection of any two elements of the union is empty, and each contribution of the union only appears once.

Now, let us make the following assumptions on $\mathcal{Q}^{\mathrm{u}}$.

Assumption 7.1.2. The mesh $\mathcal{Q}^{\mathrm{u}}$ is shape regular according to Definition 5.2.1. As a consequence, $h_K \simeq h_E$ for all $K \in \mathcal{Q}^{\mathrm{u}}$ and all $E \in \mathcal{E}^{\mathrm{u}}$ with $E \subset \partial K$.

Assumption 7.1.3. The mesh $\mathcal{Q}^{\mathrm{u}}$ is $\mathcal{T}$-admissible of some fixed class $\mathfrak{m} \in \mathbb{N}$, $\mathfrak{m} \geq 2$, according to Definition 6.3.2.

Remark 7.1.4. Note that no further assumption on the trimming boundary Γ^{t} is required, other than Γ^{t} to be Lipschitz. In particular, and as already pointed out in [Guzmán and Olshanskii, 2018], the literature on unfitted finite elements commonly imposes an additional restriction on how Γ^{t} intersects the mesh $\mathcal{Q}^{\mathrm{u}}$. But we do not need here this assumption which, in 2D, requires that Γ^{t} does not intersect an edge of the mesh $\mathcal{Q}^{\mathrm{u}}$ more than once, and which is analogous in 3D, see, e.g., [Hansbo and Hansbo, 2002]. So for example, in this paper, Γ^{t}_K could be disconnected.

Following the isogeometric paradigm introduced and generalized to trimmed geometries in Chapter 6, let us define

$$\mathcal{H}^{\mathrm{u}} := \left\{ \beta := \hat{\beta} \circ \mathbf{F}^{-1} : \hat{\beta} \in \hat{\mathcal{H}} \right\},$$
$$\mathcal{H} := \left\{ \beta \in \mathcal{H}^{\mathrm{u}} : \mathrm{supp}\,(\beta) \cap \mathfrak{D} \neq \emptyset \right\}, \tag{7.2}$$

and let us also define the following approximation spaces:

$$V^h(\mathfrak{D}^{\mathrm{u}}) := \mathrm{span}\,\{\mathcal{H}^{\mathrm{u}}\}, \qquad\qquad V^h(\mathfrak{D}) := \mathrm{span}\,\{\beta|_{\mathfrak{D}} : \beta \in \mathcal{H}\},$$
$$V_0^h(\mathfrak{D}^{\mathrm{u}}) := V^h(\mathfrak{D}^{\mathrm{u}}) \cap H_{0,\Lambda_D}^1(\mathfrak{D}^{\mathrm{u}}), \qquad V_0^h(\mathfrak{D}) := V^h(\mathfrak{D}^{\mathrm{u}}) \cap H_{0,\Lambda_D}^1(\mathfrak{D}),$$
$$\text{and}\quad V_{u_D}^h(\mathfrak{D}^{\mathrm{u}}) := V^h(\mathfrak{D}^{\mathrm{u}}) \cap H_{u_D,\Lambda_D}^1(\mathfrak{D}^{\mathrm{u}}), \quad V_{u_D}^h(\mathfrak{D}) := V^h(\mathfrak{D}^{\mathrm{u}}) \cap H_{u_D,\Lambda_D}^1(\mathfrak{D}).$$

Note that a proof of the linear independence of the trimmed basis $\mathcal{H}$ in $\mathfrak{D}$ can be found in [Höllig, 2003, Section 4.5].

In the following, we assume that u_D is the trace of a discrete function in $V^h(\mathfrak{D})$, that we still write u_D by abuse of notation. Then, the Galerkin method with finite basis $\mathcal{H}$ is used to discretize the weak problem (7.1), which reads as follows: find $u_s^h \in V_{u_D}^h(\mathfrak{D})$ such that for all $v^h \in V_0^h(\mathfrak{D})$,

$$\int_{\mathfrak{D}} \nabla u_s^h \cdot \nabla v^h \, \mathrm{d}x = \int_{\mathfrak{D}} f v^h \, \mathrm{d}x + \int_{\Lambda_N} u_N v^h \, \mathrm{d}s. \tag{7.3}$$

In the following, we are interested in the *a posteriori* estimation of the energy error

$$\left\| \nabla \left(u_s - u_s^h \right) \right\|_{0,\mathfrak{D}} = \left| u_s - u_s^h \right|_{1,\mathfrak{D}} \tag{7.4}$$

in the trimmed geometry $\mathfrak{D}$.

Remark 7.1.5. The analysis is performed on this simple model Poisson problem for simplicity, but it can be readily extended to the estimation of the energy error for

a general steady elliptic diffusion-advection-reaction problem or to a linear elasticity problem, as soon as they verify the assumptions of the Lax-Milgram theorem.

7.2   An *a posteriori* error estimator on trimmed domains

In this section, we derive an *a posteriori* estimator of the energy error in the trimmed geometry $\mathfrak{D}$ between the exact solution u_s and the discrete solution u_s^h, and we prove its reliability. In the subsequent analysis, we assume for simplicity that the discrete functions are C^1-continuous. This assumption is not needed, but it allows us to simplify the analysis while underlining the specificity of IGA with higher order B-splines. The general case of C^0-continuous basis functions could be treated in a similar way through the introduction of appropriate jump terms, following the classical theory of the adaptive finite element method. However, the addition of face jumps does not add any relevant additional insight to the analysis.

So more precisely, let

$$
\delta_K := \begin{cases} h_K & \text{if } K \in \mathcal{Q}_{\text{act}} \\ c_{K \cap \mathfrak{D}} |K \cap \mathfrak{D}|^{\frac{1}{n}} & \text{if } K \in \mathcal{Q}_{\text{cut}}, \end{cases}
$$

$$
\text{and} \quad \delta_E := \begin{cases} h_E^{\frac{1}{2}} & \text{if } E \in \mathcal{E}_{\text{act}} \\ c_{E \cap \Lambda_N} |E \cap \Lambda_N|^{\frac{1}{2(n-1)}} & \text{if } E \in \mathcal{E}_{\text{cut}}, \end{cases} \tag{7.5}
$$

where the constants $c_{K \cap \mathfrak{D}}$ and $c_{E \cap \Lambda_N}$ are defined as in (3.10). Then in Theorem 7.2.3, we will show that

$$
\mathscr{E}_N\left(u_s^h\right) := \left[\sum_{K \in \mathcal{Q}} \delta_K^2 \left\| f + \Delta u_s^h \right\|_{0,K \cap \mathfrak{D}}^2 + \sum_{E \in \mathcal{E}_N} \delta_E^2 \left\| u_N - \frac{\partial u_s^h}{\partial \mathbf{n}} \right\|_{0,E \cap \Lambda_N}^2 \right.
$$

$$
\left. + \sum_{K \in \mathcal{Q}_{\text{cut}}} h_K \left\| u_N - \frac{\partial u_s^h}{\partial \mathbf{n}} \right\|_{0,\Gamma_K^t}^2 \right]^{\frac{1}{2}} \tag{7.6}
$$

is a reliable *a posteriori* error estimator of the energy error (7.4).

7.2.1   Preliminary results on trimmed meshes

Before stating and proving the main theorem, let us state two lemmas which will allow us to take care of the trimmed elements and faces.

Lemma 7.2.1. *Let $K \in \mathcal{Q}_{\text{cut}}$, and let $K_{\mathfrak{D}} := K \cap \mathfrak{D} \neq \emptyset$. Then for all $v \in H^1(K)$,*

$$
\|v\|_{0,K_{\mathfrak{D}}} \lesssim c_{K_{\mathfrak{D}}} |K_{\mathfrak{D}}|^{\frac{1}{n}} \left(h_K^{-2} \|v\|_{0,K}^2 + \|\nabla v\|_{0,K}^2 \right)^{\frac{1}{2}} = \delta_K \left(h_K^{-2} \|v\|_{0,K}^2 + \|\nabla v\|_{0,K}^2 \right)^{\frac{1}{2}},
$$

where $c_{K_{\mathfrak{D}}}$ is defined in (3.10). The hidden constant is independent of the measures of $K_{\mathfrak{D}}$ and of K.

Proof. Let $v \in H^1(K)$ and let $\mathbf{F}_K : \hat{\mathcal{K}} \to K$, where $\hat{\mathcal{K}} := (0, 2\pi)^n$. That is, $\mathbf{F}_K = \mathbf{F} \circ \mathbf{G}_K$, where $\mathbf{F}$ is the isogeometric map defined in Section 6.3, and $\mathbf{G}_K$ is a linear mapping defined as in Section 5.2.1. So the Jacobian matrix of $\mathbf{G}_K$ written $\nabla \mathbf{G}_K$ is diagonal, and thanks to the shape regularity Assumption 7.1.2, each of its components $(\nabla \mathbf{G}_K)_{ii} \lesssim h_K$, $i = 1, \ldots, n$. Thanks to Assumption 6.3.1 on $\mathbf{F}$, if $\nabla \mathbf{F}$ denotes the Jacobian matrix of $\mathbf{F}$, then $|\det(\nabla \mathbf{F})| \simeq 1$, $\|\nabla \mathbf{F}\|_{\boldsymbol{L}^\infty(\mathbf{F}^{-1}(K))} \lesssim 1$, and $\|\nabla \mathbf{F}^{-1}\|_{\boldsymbol{L}^\infty(K)} \lesssim 1$. So if we let $\hat{v} := v \circ \mathbf{F}_K$, then by the Hölder inequality, for all $p \geq 1$,

$$\|v\|^2_{0,K_{\mathfrak{D}}} \leq |K_{\mathfrak{D}}|^{1-\frac{1}{p}} \|v\|^2_{L^{2p}(K_{\mathfrak{D}})} \leq |K_{\mathfrak{D}}|^{1-\frac{1}{p}} \|v\|^2_{L^{2p}(K)} \lesssim |K_{\mathfrak{D}}|^{1-\frac{1}{p}} h_K^{\frac{n}{p}} \|\hat{v}\|^2_{L^{2p}(\hat{\mathcal{K}})}. \quad (7.7)$$

By Sobolev embedding (see Theorem 2.3.1), we know that $H^1(\hat{\mathcal{K}})$ can be continuously embedded in $L^{2p}(\hat{\mathcal{K}})$ for every $1 \leq p < \infty$ if $n = 2$, or for every $1 \leq p \leq 3$ if $n = 3$. So, if $n = 3$, by taking $p = 3$ in (7.7) and by Sobolev embedding,

$$\|v\|^2_{0,K_{\mathfrak{D}}} \lesssim |K_{\mathfrak{D}}|^{\frac{2}{3}} h_K \|\hat{v}\|^2_{1,\hat{\mathcal{K}}} \lesssim |K_{\mathfrak{D}}|^{\frac{2}{3}} h_K \left(h_K^{-3} \|v\|^2_{0,K} + h_K^{-1} \|\nabla v\|^2_{0,K} \right)$$
$$= c^2_{K_{\mathfrak{D}}} |K_{\mathfrak{D}}|^{\frac{2}{n}} \left(h_K^{-2} \|v\|^2_{0,K} + \|\nabla v\|^2_{0,K} \right).$$

Let us now consider the case $n = 2$. From Lemma 2.3.3,

$$\|\hat{v}\|_{L^{2p}(\hat{\mathcal{K}})} \leq c\sqrt{p} \|\hat{v}\|_{1,\hat{\mathcal{K}}},$$

where c is a constant independent of p and of the measure of K. So by taking

$$p = \max\left(-\log\left(|K_{\mathfrak{D}}|\right), \eta \right) = c^2_{K_{\mathfrak{D}}}$$

in (7.7), then $|K_{\mathfrak{D}}|^{-\frac{1}{p}} \lesssim 1$ and $h_K^{\frac{2}{p}} \simeq |K|^{\frac{1}{p}} = |K|^{c^{-2}_{K_{\mathfrak{D}}}} \leq |K|^{c^{-2}_K} \lesssim 1$, and thus

$$\|v\|^2_{0,K_{\mathfrak{D}}} \lesssim p |K_{\mathfrak{D}}|^{1-\frac{1}{p}} h_K^{\frac{2}{p}} \|\hat{v}\|^2_{1,\hat{\mathcal{K}}} \lesssim c^2_{K_{\mathfrak{D}}} |K_{\mathfrak{D}}| \left(h_K^{-2} \|v\|^2_{0,K} + \|\nabla v\|^2_{0,K} \right)$$
$$= c^2_{K_{\mathfrak{D}}} |K_{\mathfrak{D}}|^{\frac{2}{n}} \left(h_K^{-2} \|v\|^2_{0,K} + \|\nabla v\|^2_{0,K} \right). \qquad \square$$

Lemma 7.2.2. *Let $E \in \mathcal{E}_{\mathrm{cut}}$, and let $E_N := E \cap \Lambda_N \neq \emptyset$. Then for all $v \in H^{\frac{1}{2}}(E)$,*

$$\|v\|_{0,E_N} \lesssim c_{E_N} |E_N|^{\frac{1}{2(n-1)}} \left(h_E^{-1} \|v\|^2_{0,E} + |v|^2_{\frac{1}{2},E} \right)^{\frac{1}{2}} = \delta_E \left(h_E^{-1} \|v\|^2_{0,E} + |v|^2_{\frac{1}{2},E} \right)^{\frac{1}{2}},$$

where c_{E_N} is defined in (3.10). The hidden constant is independent of the measures of E_N and of E.

Proof. Note that this proof generalizes the one of Lemma 2.3.9, and it follows the same ideas as in the proof of Lemma 7.2.1. Let $v \in H^{\frac{1}{2}}(E)$ and let $\mathbf{F}_E : \hat{\mathcal{E}} \to E$, where $\hat{\mathcal{E}} := (0, 2\pi)^{n-1}$. That is, $\mathbf{F}_E = \mathbf{F} \circ \mathbf{G}_E$, where $\mathbf{F}$ is the isogeometric map defined in Section 6.3, and $\mathbf{G}_E$ is a linear mapping. So the Jacobian matrix of $\mathbf{G}_E$ written $\nabla \mathbf{G}_E$ is diagonal, and thanks to the shape regularity Assumption 7.1.2, each of its components $(\nabla \mathbf{G}_E)_{ii} \lesssim h_E$, $i = 1, \ldots, n-1$. Thanks to Assumption 6.3.1 on $\mathbf{F}$, if $\nabla \mathbf{F}$ denotes the

Jacobian matrix of $\mathbf{F}$, then $|\det(\nabla\mathbf{F})| \simeq 1$, $\|\nabla\mathbf{F}\|_{L^\infty(\mathbf{F}^{-1}(K))} \lesssim 1$, and $\|\nabla\mathbf{F}^{-1}\|_{L^\infty(K)} \lesssim 1$. So if we let $\hat{v} := v \circ \mathbf{F}_E$, then by the Hölder inequality, for all $p \geq 1$,

$$\|v\|_{0,E_N}^2 \leq |E_N|^{1-\frac{1}{p}} \|v\|_{L^{2p}(E_N)}^2 \leq |E_N|^{1-\frac{1}{p}} \|v\|_{L^{2p}(E)}^2 \lesssim |E_N|^{1-\frac{1}{p}} h_E^{\frac{n-1}{p}} \|\hat{v}\|_{L^{2p}(\hat{\mathcal{E}})}^2. \quad (7.8)$$

By Sobolev embedding (see Theorem 2.3.1), we know that $H^{\frac{1}{2}}(\hat{\mathcal{E}})$ can be continuously embedded in $L^{2p}(\hat{\mathcal{E}})$ for every $1 \leq p < \infty$ if $n = 2$, or for every $1 \leq p \leq 2$ if $n = 3$. So, if $n = 3$, by taking $p = 2$ in (7.8) and by Sobolev embedding,

$$\|v\|_{0,E_N}^2 \lesssim |E_N|^{\frac{1}{2}} h_E \|\hat{v}\|_{\frac{1}{2},\hat{\mathcal{E}}}^2 \lesssim |E_N|^{\frac{1}{2}} h_E \left(h_E^{-3} \|v\|_{0,E}^2 + h_E^{-1} |v|_{\frac{1}{2},E}^2 \right)$$

$$= c_{E_N}^2 |E_N|^{\frac{1}{n-1}} \left(h_E^{-2} \|v\|_{0,E}^2 + |v|_{\frac{1}{2},E}^2 \right).$$

Let us now consider the case $n = 2$. From Lemma 2.3.2,

$$\|\hat{v}\|_{L^{2p}(\hat{\mathcal{E}})} \leq c\sqrt{p} \|\hat{v}\|_{\frac{1}{2},\hat{\mathcal{E}}},$$

where c is a constant independent of p and of the measure of E. So by taking

$$p = \max\left(-\log(|E_N|), \eta \right) = c_{E_N}^2$$

in (7.8), then $|E_N|^{-\frac{1}{p}} \lesssim 1$ and $h_E^{\frac{1}{p}} = |E|^{c_{E_N}^{-2}} \leq |E|^{c_E^{-2}} \lesssim 1$, and thus

$$\|v\|_{0,E_N}^2 \lesssim p |E_N|^{1-\frac{1}{p}} h_E^{\frac{1}{p}} \|\hat{v}\|_{\frac{1}{2},\hat{\mathcal{E}}}^2 \lesssim c_{E_N}^2 |E_N| \left(h_E^{-2} \|v\|_{0,E}^2 + |v|_{\frac{1}{2},E}^2 \right)$$

$$= c_{E_N}^2 |E_N|^{\frac{1}{n-1}} \left(h_E^{-2} \|v\|_{0,E}^2 + |v|_{\frac{1}{2},E}^2 \right). \qquad \square$$

7.2.2 Reliability of the *a posteriori* error estimator

Let us now state and prove the main theorem, stating the efficiency of the proposed *a posteriori* error estimator.

Theorem 7.2.3. *Let u_s be the exact solution of problem (7.1) in the trimmed geometry $\mathfrak{D}$, and let u_s^h be its discretized counterpart that solves Galerkin problem (7.3). Moreover, assume that the mesh $\mathcal{Q}^{\mathrm{u}}$ satisfies Assumptions 7.1.2 and 7.1.3 of shape regularity and $\mathcal{T}$-admissibility, and $h < h_0$ for some fixed $h_0 > 0$. Then the numerical error, in the energy norm, is bounded in terms of the estimator $\mathscr{E}_N\left(u_s^h\right)$ introduced in (7.6) as follows:*

$$\left\|\nabla\left(u_s - u_s^h\right)\right\|_{0,\mathfrak{D}} \lesssim \mathscr{E}_N\left(u_s^h\right).$$

Proof. Let $e := u_s - u_s^h$. Then for all $v \in H_{0,\Lambda_D}^1(\mathfrak{D})$, from (7.1),

$$\int_{\mathfrak{D}} \nabla e \cdot \nabla v \, \mathrm{d}x = \sum_{K \in \mathcal{Q}} \left[\int_{K \cap \mathfrak{D}} \left(f + \Delta u_s^h \right) v \, \mathrm{d}x + \int_{\Lambda_N \cap \overline{K}} \left(u_N - \frac{\partial u_s^h}{\partial \mathbf{n}} \right) v \, \mathrm{d}s \right]. \quad (7.9)$$

Let us define the interior and boundary residuals as follows:

$$r_K := f + \Delta u_s^h \in L^2(K \cap \mathfrak{D}), \qquad\qquad \forall K \in \mathcal{Q},$$

$$j_E := u_N - \frac{\partial u_s^h}{\partial \mathbf{n}} \in L^2(E \cap \Lambda_N), \qquad\qquad \forall E \in \mathcal{E}_N,$$

$$j_K := u_N - \frac{\partial u_s^h}{\partial \mathbf{n}} \in L^2(\Gamma_K^{\mathrm{t}}), \qquad\qquad \forall K \in \mathcal{Q}_{\mathrm{cut}}. \qquad (7.10)$$

So with the particular choice $v = e$, we can rewrite (7.9) as

$$\|\nabla e\|_{0,\mathfrak{D}}^2 = \sum_{K \in \mathcal{Q}} \int_{K \cap \mathfrak{D}} r_K e \, \mathrm{d}x + \sum_{E \in \mathcal{E}_N} \int_{E \cap \Lambda_N} j_E \, e \, \mathrm{d}s + \sum_{K \in \mathcal{Q}_{\mathrm{cut}}} \int_{\Gamma_K^{\mathrm{t}}} j_K e \, \mathrm{d}s. \qquad (7.11)$$

Moreover, recall that $\omega := \mathfrak{D}^{\mathrm{u}} \setminus \overline{\mathfrak{D}}$ (see Figure 7.1). Then, let $e^{\mathrm{u}} \in H_{0,\Lambda_D}^1(\mathfrak{D}^{\mathrm{u}})$ be the extension of e to $\mathfrak{D}^{\mathrm{u}}$ such that $e^{\mathrm{u}}|_{\mathfrak{D}} = e$, and such that $e^{\mathrm{u}}|_\omega \in H_{e,\Gamma^{\mathrm{t}}}^1(\omega)$ is the weak solution of

$$\int_\omega \nabla e^{\mathrm{u}} \cdot \nabla w \, \mathrm{d}x = 0, \qquad \forall w \in H_{0,\Gamma^{\mathrm{t}}}^1(\omega).$$

Since the measures of both ω and Γ^{t} are independent of h, then by continuity of the elliptic solution on the data and by the trace inequality,

$$\|e^{\mathrm{u}}\|_{1,\omega} \lesssim \|e\|_{\frac{1}{2},\Gamma^{\mathrm{t}}} \lesssim \|e\|_{1,\mathfrak{D}},$$

and thus by the Poincaré inequality,

$$\|\nabla e^{\mathrm{u}}\|_{0,\mathfrak{D}^{\mathrm{u}}} \lesssim \left(\|e^{\mathrm{u}}\|_{1,\mathfrak{D}}^2 + \|e^{\mathrm{u}}\|_{1,\omega}^2 \right)^{\frac{1}{2}} \lesssim \|e\|_{1,\mathfrak{D}} \lesssim \|\nabla e\|_{0,\mathfrak{D}}. \qquad (7.12)$$

Furthermore, since the hierarchical mesh $\mathcal{Q}^{\mathrm{u}}$ is $\mathcal{T}$-admissible, from Theorem 6.3.4, it is possible to build a Scott-Zhang-type operator $I^h : H_{0,\Lambda_D}^1(\mathfrak{D}^{\mathrm{u}}) \to V_0^h(\mathfrak{D}^{\mathrm{u}})$ such that for all $v \in H_{0,\Lambda_D}^1(\mathfrak{D}^{\mathrm{u}})$,

$$\sum_{K \in \mathcal{Q}^{\mathrm{u}}} h_K^{-2} \|v - I^h(v)\|_{0,K}^2 \lesssim \|\nabla v\|_{0,\mathfrak{D}^{\mathrm{u}}}^2 \qquad (7.13)$$

$$\text{and} \;\; \sum_{K \in \mathcal{Q}^{\mathrm{u}}} \left\| \nabla \left(v - I^h(v) \right) \right\|_{0,K}^2 \lesssim \|\nabla v\|_{0,\mathfrak{D}^{\mathrm{u}}}^2. \qquad (7.14)$$

Therefore, let

$$e^{\mathrm{u},h} := I^h(e^{\mathrm{u}}) \in V_0^h(\mathfrak{D}^{\mathrm{u}}).$$

Since $e^{\mathrm{u},h} \in V^h(\mathfrak{D}^{\mathrm{u}})$, from (7.3) and by performing integration by parts,

$$\int_{\mathfrak{D}} f e^{\mathrm{u},h} \, \mathrm{d}x + \int_{\Lambda_N} u_N e^{\mathrm{u},h} \, \mathrm{d}s = \int_{\mathfrak{D}} \nabla u_s^h \cdot \nabla e^{\mathrm{u},h} \, \mathrm{d}x$$

$$= \sum_{K \in \mathcal{Q}} \int_{K \cap \mathfrak{D}} \left(-\Delta u_s^h \right) e^{\mathrm{u},h} \, \mathrm{d}x + \int_{\Lambda_N} \frac{\partial u_s^h}{\partial \mathbf{n}} e^{\mathrm{u},h} \, \mathrm{d}s,$$

and thus recalling the notation introduced in (7.10),

$$\sum_{K\in\mathcal{Q}}\int_{K\cap\mathfrak{D}} r_K e^{\mathrm{u},h}\,\mathrm{d}x + \sum_{E\in\mathcal{E}_N}\int_{E\cap\Lambda_N} j_E\,e^{\mathrm{u},h}\,\mathrm{d}s + \sum_{K\in\mathcal{Q}_{\mathrm{cut}}}\int_{\Gamma_K^{\mathrm{t}}} j_K e^{\mathrm{u},h}\,\mathrm{d}s = 0.$$

Consequently, we can rewrite (7.11) as

$$\|\nabla e\|_{0,\mathfrak{D}}^2 = \sum_{K\in\mathcal{Q}}\int_{K\cap\mathfrak{D}} r_K (e - e^{\mathrm{u},h})\,\mathrm{d}x + \sum_{E\in\mathcal{E}_N}\int_{E\cap\Lambda_N} j_E (e - e^{\mathrm{u},h})\,\mathrm{d}s$$
$$+ \sum_{K\in\mathcal{Q}_{\mathrm{cut}}}\int_{\Gamma_K^{\mathrm{t}}} j_K (e - e^{\mathrm{u},h})\,\mathrm{d}s. \tag{7.15}$$

To begin the estimation of (7.15), let us consider the first term. Using the Hölder inequality and the discrete Cauchy-Schwarz inequality,

$$\sum_{K\in\mathcal{Q}}\int_{K\cap\mathfrak{D}} r_K (e^{\mathrm{u}} - e^{\mathrm{u},h})\,\mathrm{d}x$$
$$\le \sum_{K\in\mathcal{Q}} \delta_K \|r_K\|_{0,K\cap\mathfrak{D}}\, \delta_K^{-1}\big\|e^{\mathrm{u}} - e^{\mathrm{u},h}\big\|_{0,K\cap\mathfrak{D}}$$
$$\lesssim \left(\sum_{K\in\mathcal{Q}} \delta_K^2 \|r_K\|_{0,K\cap\mathfrak{D}}^2\right)^{\frac{1}{2}} \left(\sum_{K\in\mathcal{Q}_{\mathrm{act}}} \delta_K^{-2}\big\|e^{\mathrm{u}} - e^{\mathrm{u},h}\big\|_{0,K}^2 + \sum_{K\in\mathcal{Q}_{\mathrm{cut}}} \delta_K^{-2}\big\|e^{\mathrm{u}} - e^{\mathrm{u},h}\big\|_{0,K\cap\mathfrak{D}}^2\right)^{\frac{1}{2}}.$$
$$\tag{7.16}$$

Moreover, from Lemma 7.2.1, for all $K\in\mathcal{Q}_{\mathrm{cut}}$,

$$\delta_K^{-2}\big\|e^{\mathrm{u}} - e^{\mathrm{u},h}\big\|_{0,K\cap\mathfrak{D}}^2 \lesssim h_K^{-2}\big\|e^{\mathrm{u}} - e^{\mathrm{u},h}\big\|_{0,K}^2 + \big\|\nabla\big(e^{\mathrm{u}} - e^{\mathrm{u},h}\big)\big\|_{0,K}^2. \tag{7.17}$$

Thus from (7.17), using property (7.13) of the Scott-Zhang-type operator I^h, and by the continuous extension property (7.12),

$$\sum_{K\in\mathcal{Q}_{\mathrm{act}}} \delta_K^{-2}\big\|e^{\mathrm{u}} - e^{\mathrm{u},h}\big\|_{0,K}^2 + \sum_{K\in\mathcal{Q}_{\mathrm{cut}}} \delta_K^{-2}\big\|e^{\mathrm{u}} - e^{\mathrm{u},h}\big\|_{0,K\cap\mathfrak{D}}^2$$
$$\lesssim \sum_{K\in\mathcal{Q}_{\mathrm{act}}} h_K^{-2}\big\|e^{\mathrm{u}} - e^{\mathrm{u},h}\big\|_{0,K}^2 + \sum_{K\in\mathcal{Q}_{\mathrm{cut}}} \big\|\nabla(e^{\mathrm{u}} - e^{\mathrm{u},h})\big\|_{0,K}^2 \lesssim \big\|\nabla e^{\mathrm{u}}\big\|_{0,\mathfrak{D}^{\mathrm{u}}}^2 \lesssim \|\nabla e\|_{0,\mathfrak{D}}^2.$$
$$\tag{7.18}$$

Therefore, combining (7.16) and (7.18),

$$\sum_{K\in\mathcal{Q}}\int_{K\cap\mathfrak{D}} r_K (e^{\mathrm{u}} - e^{\mathrm{u},h})\,\mathrm{d}x \lesssim \left(\sum_{K\in\mathcal{Q}} \delta_K^2 \|r_K\|_{0,K\cap\mathfrak{D}}^2\right)^{\frac{1}{2}} \|\nabla e\|_{0,\mathfrak{D}}^2. \tag{7.19}$$

Now, let us consider the second term of (7.15). Similarly as for the internal residuals,

$$
\sum_{E \in \mathcal{E}_N} \int_{E \cap \Lambda_N} j_E(e - e^{\mathrm{u},h}) \, \mathrm{d}s \leq \sum_{E \in \mathcal{E}_N} \delta_E \, \|j_E\|_{0, E \cap \Lambda_N} \, \delta_E^{-1} \Big\| e^{\mathrm{u}} - e^{\mathrm{u},h} \Big\|_{0, E \cap \Lambda_N}
$$

$$
\lesssim \left(\sum_{E \in \mathcal{E}_N} \delta_E^2 \|j_E\|_{0, E \cap \Lambda_N}^2 \right)^{\frac{1}{2}} \left(\sum_{E \in \mathcal{E}_{\mathrm{act}}} \delta_E^{-2} \Big\| e^{\mathrm{u}} - e^{\mathrm{u},h} \Big\|_{0, E}^2 + \sum_{E \in \mathcal{E}_{\mathrm{cut}}} \delta_E^{-2} \Big\| e^{\mathrm{u}} - e^{\mathrm{u},h} \Big\|_{0, E \cap \Lambda_N}^2 \right)^{\frac{1}{2}} .
\tag{7.20}
$$

Moreover, from Lemma 7.2.2, for all $E \in \mathcal{E}_{\mathrm{cut}}$,

$$
\delta_E^{-2} \Big\| e^{\mathrm{u}} - e^{\mathrm{u},h} \Big\|_{0, E \cap \Lambda_N}^2 \lesssim h_E^{-1} \Big\| e^{\mathrm{u}} - e^{\mathrm{u},h} \Big\|_{0, E}^2 + \Big| e^{\mathrm{u}} - e^{\mathrm{u},h} \Big|_{\frac{1}{2}, E}^2 ,
$$

and thus

$$
\sum_{E \in \mathcal{E}_{\mathrm{act}}} \delta_E^{-2} \Big\| e^{\mathrm{u}} - e^{\mathrm{u},h} \Big\|_{0, E}^2 + \sum_{E \in \mathcal{E}_{\mathrm{cut}}} \delta_E^{-2} \Big\| e^{\mathrm{u}} - e^{\mathrm{u},h} \Big\|_{0, E \cap \Lambda_N}^2
$$

$$
\lesssim \sum_{E \in \mathcal{E}_N} h_E^{-1} \Big\| e^{\mathrm{u}} - e^{\mathrm{u},h} \Big\|_{0, E}^2 + \sum_{E \in \mathcal{E}_{\mathrm{cut}}} \Big| e^{\mathrm{u}} - e^{\mathrm{u},h} \Big|_{\frac{1}{2}, E}^2 .
\tag{7.21}
$$

For all $E \in \mathcal{E}_N$, let K_E be the element of $\mathcal{Q}^{\mathrm{u}}$ such that $(E \cap \Lambda_N) \subset \partial(K_E \cap \mathfrak{D})$, and note that by the shape regularity of $\mathcal{Q}^{\mathrm{u}}$, $h_{K_E} \simeq h_E$. Then for the first term of (7.21), using the scaled trace inequality of Lemma 5.2.2, properties (7.13) and (7.14) of the Scott-Zhang-type operator, and by the continuous extension property (7.12),

$$
\sum_{E \in \mathcal{E}_N} h_E^{-1} \Big\| e^{\mathrm{u}} - e^{\mathrm{u},h} \Big\|_{0, E}^2 \lesssim \sum_{E \in \mathcal{E}_N} \left(h_{K_E}^{-2} \Big\| e^{\mathrm{u}} - e^{\mathrm{u},h} \Big\|_{0, K_E}^2 + \Big\| \nabla \big(e^{\mathrm{u}} - e^{\mathrm{u},h} \big) \Big\|_{0, K_E}^2 \right)
$$

$$
\lesssim \Big\| \nabla e^{\mathrm{u}} \Big\|_{0, \mathfrak{D}^{\mathrm{u}}}^2 \lesssim \|\nabla e\|_{0, \mathfrak{D}}^2 .
\tag{7.22}
$$

Furthermore, remarking that $e^{\mathrm{u}} - e^{\mathrm{u},h} \in H_{0, \Lambda_D}^1(\mathfrak{D}^{\mathrm{u}})$, then the second term of (7.21) can be estimated using trace inequalities, property (7.14) of the Scott-Zhang-type operator, and the continuous extension property (7.12) as follows:

$$
\sum_{E \in \mathcal{E}_{\mathrm{cut}}} \Big| e^{\mathrm{u}} - e^{\mathrm{u},h} \Big|_{\frac{1}{2}, E}^2 \lesssim \sum_{E \in \mathcal{E}_{\mathrm{cut}}} \Big\| e^{\mathrm{u}} - e^{\mathrm{u},h} \Big\|_{1, K_E}^2 \leq \Big\| e^{\mathrm{u}} - e^{\mathrm{u},h} \Big\|_{1, \mathfrak{D}^{\mathrm{u}}}^2
$$

$$
\lesssim \Big\| \nabla \big(e^{\mathrm{u}} - e^{\mathrm{u},h} \big) \Big\|_{0, \mathfrak{D}^{\mathrm{u}}}^2 \lesssim \Big\| \nabla e^{\mathrm{u}} \Big\|_{0, \mathfrak{D}^{\mathrm{u}}}^2 \lesssim \|\nabla e\|_{0, \mathfrak{D}}^2 .
\tag{7.23}
$$

Therefore, combining (7.20), (7.21), (7.22) and (7.23),

$$
\sum_{E \in \mathcal{E}_N} \int_{E \cap \Lambda_N} j_E(e - e^{\mathrm{u},h}) \, \mathrm{d}s \lesssim \left(\sum_{E \in \mathcal{E}_N} \delta_E^2 \|j_E\|_{0, E \cap \Lambda_N}^2 \right)^{\frac{1}{2}} \|\nabla e\|_{0, \mathfrak{D}} .
\tag{7.24}
$$

Finally, let us consider the last term of (7.15): using the Hölder inequality and the discrete Cauchy-Schwarz inequality, then

$$\sum_{K \in \mathcal{Q}_{\text{cut}}} \int_{\Gamma_K^{\text{t}}} j_K(e^{\text{u}} - e^{\text{u},h}) \, \text{d}s \le \sum_{K \in \mathcal{Q}_{\text{cut}}} \|j_K\|_{0,\Gamma_K^{\text{t}}} \|e^{\text{u}} - e^{\text{u},h}\|_{0,\Gamma_K^{\text{t}}}$$

$$\lesssim \left(\sum_{K \in \mathcal{Q}_{\text{cut}}} h_K \|j_K\|_{0,\Gamma_K^{\text{t}}}^2 \right)^{\frac{1}{2}} \left(\sum_{K \in \mathcal{Q}_{\text{cut}}} h_K^{-1} \|e^{\text{u}} - e^{\text{u},h}\|_{0,\Gamma_K^{\text{t}}}^2 \right)^{\frac{1}{2}}.$$

$$(7.25)$$

Moreover, by the local scaled trace inequality of Lemma 5.2.3, by properties (7.13) and (7.14) of the Scott-Zhang-type operator, and by the continuous extension property (7.12),

$$\sum_{K \in \mathcal{Q}_{\text{cut}}} h_K^{-1} \|e^{\text{u}} - e^{\text{u},h}\|_{0,\Gamma_K^{\text{t}}}^2 \lesssim \sum_{K \in \mathcal{Q}_{\text{cut}}} \left(h_K^{-2} \|e^{\text{u}} - e^{\text{u},h}\|_{0,K}^2 + \|\nabla(e^{\text{u}} - e^{\text{u},h})\|_{0,K}^2 \right)$$

$$\lesssim \|\nabla e^{\text{u}}\|_{0,\mathfrak{D}^{\text{u}}}^2 \lesssim \|\nabla e\|_{0,\mathfrak{D}}^2.$$

$$(7.26)$$

Therefore, inserting (7.26) in (7.25), we obtain

$$\sum_{K \in \mathcal{Q}_{\text{cut}}} \int_{\Gamma_K^{\text{t}}} j_K(e^{\text{u}} - e^{\text{u},h}) \, \text{d}s \lesssim \left(\sum_{K \in \mathcal{Q}_{\text{cut}}} h_K \|j_K\|_{0,\Gamma_K^{\text{t}}}^2 \right)^{\frac{1}{2}} \|\nabla e\|_{0,\mathfrak{D}}. \qquad (7.27)$$

To conclude, we combine (7.15), (7.19), (7.24) and (7.27) and we divide by $\|\nabla e\|_{0,\mathfrak{D}}$ on both sides. $\qquad \square$

Remark 7.2.4. If problem (7.1) is discretized using the THB-spline basis instead of the HB-spline basis, then Theorem 7.2.3 is still valid under the same hypothesis. In particular, whether HB-splines or THB-splines are used, the mesh $\mathcal{Q}^{\text{u}}$ only needs to be $\mathcal{T}$-admissible, which is a weaker assumption than $\mathcal{H}$-admissibility (see Definitions 6.2.1 and 6.3.2). Indeed, in the proof of Theorem 7.2.3, the $\mathcal{T}$-admissibility is only needed to ensure properties (7.13) and (7.14) of the Scott-Zhang-type operator $I^h : H^1_{0,\Lambda_D}(\mathfrak{D}^{\text{u}}) \to V^h_0(\mathfrak{D}^{\text{u}})$. The construction of such an operator depends on the discrete space $V^h_0(\mathfrak{D}^{\text{u}})$ but not on the choice of basis for $V^h_0(\mathfrak{D}^{\text{u}})$, so it does not depend on whether one considers a HB-spline basis or its truncated counterpart. However, the sparsity and the conditioning of the matrices involved in the computation depend on this choice.

Remark 7.2.5. The proof of Theorem 7.2.3 can be readily extended to the setting of C^0-continuous trimmed (T)HB-spline basis functions through the introduction of appropriate jump terms, as the proof only relies on discretization-independent trace inequalities and on the existence of a Scott-Zhang-type interpolation operator with properties (7.13) and (7.14).

Remark 7.2.6. Similar arguments could be used to extend the proof of Theorem 7.2.3 to the more general case in which Dirichlet boundary conditions are also applied along the trimming boundary Γ^{t}. Indeed, in this case, Dirichlet boundary conditions need to be enforced weakly, using for instance Nitsche's method, but then the discrete problem

needs to be stabilized, following for instance [Burman, 2010; Burman and Hansbo, 2012; Elfverson et al., 2019; Buffa et al., 2020]. However, some work remains to be done because special care must to be given to the extra terms coming from the stabilized Nitsche's method, as they contain integrals over the trimmed Dirichlet boundary.

Remark 7.2.7. Theorem 7.2.3 states the reliability of the proposed error estimator but it does not state its efficiency, as the efficiency proof presents some further challenges. For instance, classical efficiency proofs on non-trimmed domains (see, e.g., [Verfürth, 1994; Nochetto and Veeser, 2011; Buffa and Giannelli, 2016]) make use of cut-off polynomial functions to localize the error in one element or in a patch of elements. Then, inverse inequalities are used to bound each estimator's residual contribution by a local error term. However, polynomial cut-off functions, sometimes also called bubble functions, cannot be defined in the (non-necessarily polygonal) active part of a trimmed element. Another path one could take is to extend each trimmed element residual to the full non-trimmed element, by considering the natural polynomial extension of the discrete solution and an L^2-extension of the source and Neumann boundary functions. Then, one could perform the same standard steps of the efficiency proof by considering cut-off functions in the non-trimmed elements. But in this case, the wrong element scalings would be obtained if $|K \cap \mathfrak{D}| \ll |K|$ for an element $K \in \mathcal{Q}_{\mathrm{cut}}$.

7.3 An adaptive mesh refinement strategy on trimmed geometries

Let us follow the framework of adaptivity introduced in Chapter 2, Section 2.5.3, in the context of elliptic partial differential equations defined on trimmed hierarchical domains, as initiated in [Coradello et al., 2020]. To do so, let us recall the four main building blocks composing one iteration of an adaptive loop:

$$\boxed{\text{SOLVE}} \longrightarrow \boxed{\text{ESTIMATE}} \longrightarrow \boxed{\text{MARK}} \longrightarrow \boxed{\text{REFINE}}$$
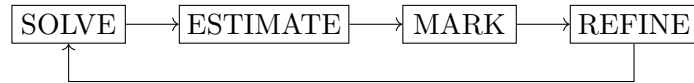
The first two modules of the iterative process, SOLVE and ESTIMATE, have been elaborated in Sections 7.1 and 7.2, respectively. That is, given an underlying $\mathcal{T}$-admissible mesh $\mathcal{Q}^{\mathrm{u}}$, we first approximate the exact solution u_s of problem (7.1) thanks to the Galerkin method based on the HB-spline basis $\mathcal{H}$ defined in (7.2). We thus obtain the IGA solution u_s^h solving problem (7.3). Then, we estimate the energy error $\left\| \nabla \left(u_s - u_s^h \right) \right\|_{0,\mathfrak{D}}$ thanks to the reliable estimator $\mathscr{E}_N \left(u_s^h \right)$ defined in (7.6).

We remark that $\mathscr{E}_N \left(u_s^h \right)$ can naturally be decomposed into local element contributions. More precisely, if we define the following local sets of faces

$$\mathcal{E}_K := \left\{ E \in \mathcal{E}_N : (E \cap \Lambda_N) \subset \partial(K \cap \mathfrak{D}) \right\},$$

then the estimator rewrites as

$$\mathscr{E}_N\left(u_s^h\right) := \left[\sum_{K \in \mathcal{Q}^{\mathrm{u}}} \mathscr{E}_N^K\left(u_s^h\right)^2 \right]^{\frac{1}{2}},$$

where for all $K \in \mathcal{Q}^{\mathrm{u}}$,

$$\mathscr{E}_N^K\left(u_s^h\right)^2 := \begin{cases} \delta_K^2 \left\| f + \Delta u_s^h \right\|_{0,K}^2 + \displaystyle\sum_{E \in \mathcal{E}_K} \delta_E^2 \left\| u_N - \frac{\partial u_s^h}{\partial \mathbf{n}} \right\|_{0,E \cap \Lambda_N}^2 & \text{if } K \in \mathcal{Q}_{\mathrm{act}} \\[2ex] \delta_K^2 \left\| f + \Delta u_s^h \right\|_{0,K \cap \mathfrak{D}}^2 + \displaystyle\sum_{E \in \mathcal{E}_K} \delta_E^2 \left\| u_N - \frac{\partial u_s^h}{\partial \mathbf{n}} \right\|_{0,E \cap \Lambda_N}^2 \\[2ex] \hspace{3cm} + h_K \left\| u_N - \frac{\partial u_s^h}{\partial \mathbf{n}} \right\|_{0,\Gamma_K^{\mathrm{t}}}^2 & \text{if } K \in \mathcal{Q}_{\mathrm{cut}} \\[2ex] 0 & \text{otherwise,} \end{cases}$$

and δ_K and δ_E are defined in (7.5).

Therefore, the MARK module selects a set of elements $\mathcal{M} \subset \mathcal{Q}$ according to some marking strategy. In the following, we use a Dörfler strategy as in (2.37), but a maximum strategy as in (2.36) could also be used. That is, given a fixed marking parameter $\theta \in (0,1]$, the set $\mathcal{M}$ of marked elements satisfies

$$\left[\sum_{K \in \mathcal{M}} \mathscr{E}_N^K\left(u_s^h\right)^2 \right]^{\frac{1}{2}} \geq \theta \mathscr{E}_N\left(u_s^h\right). \tag{7.28}$$

This strategy guarantees that the elements in $\mathcal{M}$ give a substantial contribution to the total error estimator $\mathscr{E}_N\left(u_s^h\right)$. Since for all $K \in \mathcal{Q}^{\mathrm{u}} \setminus \mathcal{Q}$, $\mathscr{E}_N^K\left(u_s^h\right) = 0$, then the elements outside of the trimmed domain $\mathfrak{D}$ will never be marked. But from the algorithmic point of view, to guarantee that a basis function $\beta \in \mathcal{H}$ is deactivated when all the elements in $\operatorname{supp}(\beta) \cap \mathfrak{D}$ are marked for refinement, we also need to enlarge $\mathcal{M}$ with the so-called ghost elements, see [Coradello et al., 2020]. That is, when a trimmed element $K \in \mathcal{Q}_{\mathrm{cut}}$ is marked for refinement, all the elements in

$$\{ K' \in \mathcal{Q}^{\mathrm{u}} : K' \cap \mathfrak{D} = \emptyset, \operatorname{lev}(K) = \operatorname{lev}(K')$$
$$\text{and } \exists \beta \in \mathcal{H}^{\mathrm{u}} \text{ such that } K \cup K' \subset \operatorname{supp}(\beta) \}$$

are also added to $\mathcal{M}$. Note that this is only needed for algorithmic reasons, while it does not change the active refined basis determined by the marking strategy.

Finally, based on the set $\mathcal{M}$ of marked elements, the hierarchical mesh $\mathcal{Q}^{\mathrm{u}}$ is refined so that its class of $\mathcal{T}$-admissibility and its properties are preserved. That is, we need to make sure that the refined mesh still satisfies Assumptions 7.1.2 and 7.1.3. Trimming influences the marking step, but it does not influence the admissibility property of the mesh $\mathcal{Q}^{\mathrm{u}}$. Therefore, the REFINE module corresponds to the non-trimmed case developed in [Buffa

and Giannelli, 2016] and summarized in Algorithms 1 and 2. The procedure is similar to what can be found in [Gantner and Praetorius, 2022, Algorithm 3.7]. Remark that this algorithm uses the notion of $\mathcal{T}$-neighborhood $\mathcal{N}_{\mathcal{T}}(\mathcal{Q}^{\mathrm{u}}, K, \mathfrak{m})$ of a hierarchical element K with respect to the admissibility class $\mathfrak{m}$, which has been defined in (6.13).

Algorithm 1

$\mathcal{Q}^{\mathrm{u}} = \mathrm{REFINE}(\mathcal{Q}^{\mathrm{u}}, \mathcal{M}, \mathfrak{m})$

1: $\mathcal{Q}^{\mathrm{u}} = \mathrm{MARK\_RECURSIVE}(\mathcal{Q}^{\mathrm{u}}, \mathcal{M}, \mathfrak{m})$
2: Subdivide all $K \in \mathcal{M}$ and update $\mathcal{Q}^{\mathrm{u}}$ by replacing K with its children.
3: **return** $\mathcal{Q}^{\mathrm{u}}$

Algorithm 2

$\mathcal{M} = \mathrm{MARK\_RECURSIVE}(\mathcal{Q}^{\mathrm{u}}, \mathcal{M}, \mathfrak{m})$

1: **repeat**
2: $\quad \mathcal{U} \leftarrow \bigcup_{K \in \mathcal{M}} \mathcal{N}_{\mathcal{T}}(\mathcal{Q}^{\mathrm{u}}, K, \mathfrak{m}) \setminus \mathcal{M}$
3: $\quad \mathcal{M} \leftarrow \mathcal{M} \cup \mathcal{U}$
4: **until** $\mathcal{U} = \emptyset$

7.4 Numerical experiments

In this last section, we present a few numerical examples that illustrate the validity of the proposed error estimator. Thanks to these experiments, we also demonstrate that the adaptive mesh refinement procedure from Section 7.3 ensures the optimal convergence of the numerical error $\left| u_s - u_s^h \right|_{1,\Omega}$. In particular, and as it is now classical in non-trimmed geometries, the adaptive strategy exhibits a substantial increase in accuracy with respect to the number of degrees of freedom compared to a uniform mesh refinement strategy.

All considered meshes are built and refined to be and remain $\mathcal{T}$-admissible of class $\mathfrak{m} = P$, where P is the degree of the B-splines considered in each experiment. Furthermore, we call N_{dof} the number of active degrees of freedom, that is, the number of HB-spline basis functions in $\mathcal{H}$ defined in (7.2).

7.4.1 Adaptive mesh refinement on a regular solution

As a first numerical experiment, we choose a regular problem defined in the unit square $\mathfrak{D}^{\mathrm{u}} = (0,1)^2$ trimmed by two disks ω_1 and ω_2 of radius 0.1 centered at $(0.25, 0.25)^T$ and $(0.75, 0.75)^T$, respectively. The trimmed geometry $\mathfrak{D} = (0,1)^2 \setminus (\overline{\omega_1} \cup \overline{\omega_2})$ is illustrated in Figure 7.2a. We choose the data f, u_D and u_N such that the exact solution of Poisson problem (7.1) is $u_s(x,y) = \sin(3\pi x) + \cos(5\pi y)$, with $\Lambda_D := (0,1) \times \{0\}$ and $\Lambda_N := \partial\mathfrak{D} \setminus \overline{\Lambda_D}$.

At the first iteration of the adaptive process presented in Section 7.3, the non-trimmed

geometry $\mathfrak{D}^{\mathrm{u}}$ is meshed with four elements in each direction, as represented in Figure 7.2a. At each iteration, the differential problem is discretized using Galerkin method with HB-splines of degree $P = 2$ on the trimmed mesh, as explained in Section 7.1.2, and the numerical solution u_s^h of (7.3) is obtained. Subsequently, we compute the energy error $\left\| \nabla \left(u_s - u_s^h \right) \right\|_{0,\mathfrak{D}}$ and the estimator $\mathscr{E}_N \left(u_s^h \right)$ defined in (7.6). The latter is then used to drive the mesh refinement strategy described in Algorithm 1, for which the elements to refine are determined using the Dörfler marking strategy (7.28) with parameter $\theta = 0.8$. The iterative process is stopped whenever the number of degrees of freedom of the HB-spline space exceeds 10^4.

The results are shown in Figure 7.2b, validating the theory presented in Section 7.2. Indeed, we can observe that the estimator follows the behavior of the energy error, as both of them have the same convergence rate of $\mathcal{O}\left(N_{\mathrm{dof}}^{-\frac{P}{2}} \right) = \mathcal{O}\left(N_{\mathrm{dof}}^{-1} \right)$. The effectivity index defined by

$$\eta_{\mathrm{eff}} := \frac{\mathscr{E}_N \left(u_s^h \right)}{\left\| \nabla \left(u_s - u_s^h \right) \right\|_{0,\mathfrak{D}}}$$

is nearly equal to 10, that is, it is very similar to the effectivity index observed in the case of a residual estimator on non-trimmed geometries, see e.g., [Buffa et al., 2021b].
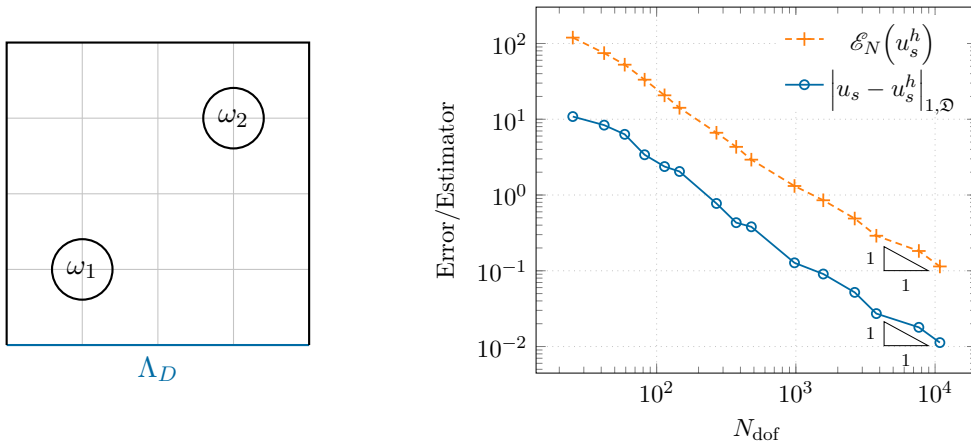
(a) Trimmed domain $\mathfrak{D}$ and original mesh (in gray).

(b) Convergence of the energy error and of the estimator with respect to the total number of degrees of freedom.

Figure 7.2 – Numerical test 7.4.1 – Trimmed geometry and convergence of the error and estimator on a regular problem.

(a) Trimmed domain $\mathfrak{D}$, original mesh (in gray), and highlighted cut elements with active part of measure $\simeq \varepsilon^2$.

(b) Final active mesh obtained with adaptive mesh refinement.

(c) Uniform mesh refinement.
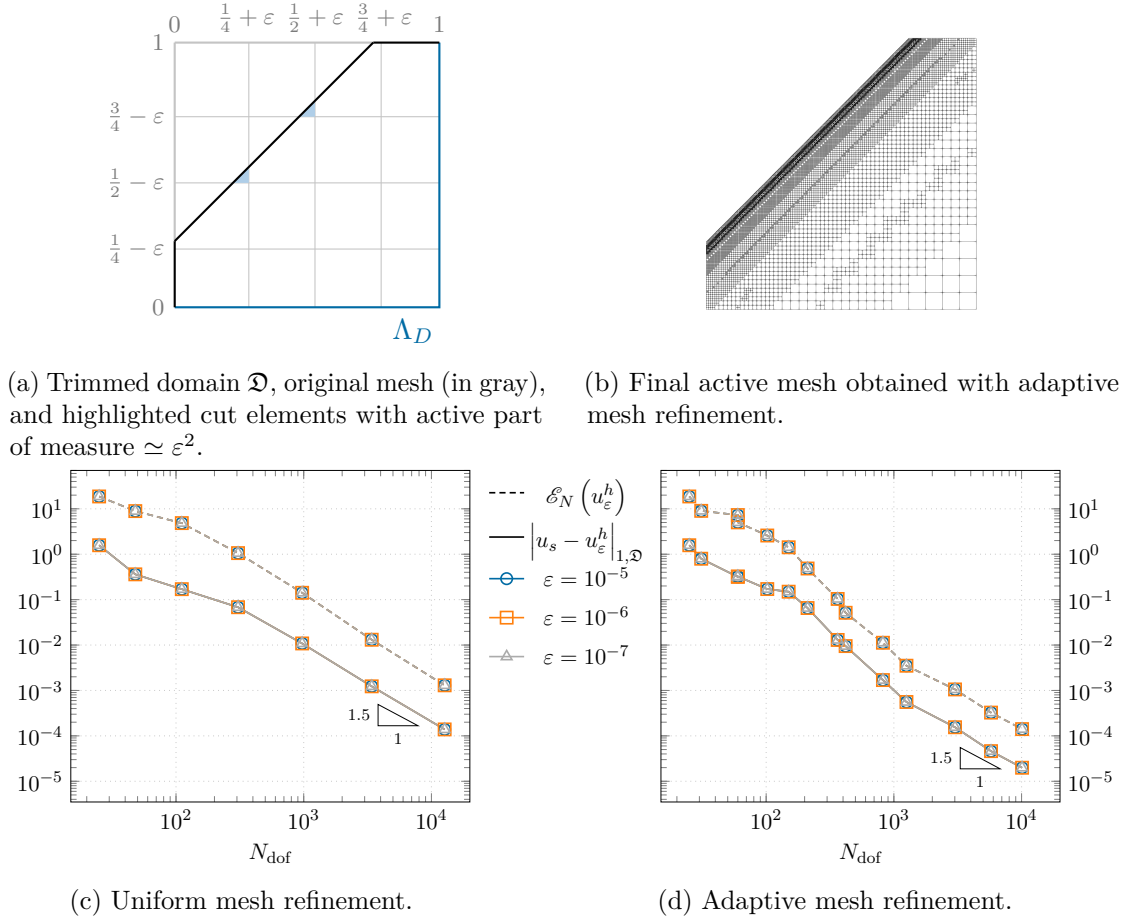
(d) Adaptive mesh refinement.

Figure 7.3 – Numerical test 7.4.2 – Trimmed pentagon geometry and convergence of the energy error and estimator with respect to the number of degrees of freedom.

7.4.2 Independence from the size of the active parts of the trimmed elements: regular solution

The aim of this second numerical experiment is to verify that the effectivity index η_{eff} is independent of the measure of the active part of the trimmed elements, that is of the measure of $K \cap \mathfrak{D}$ for every $K \in \mathcal{Q}$. To verify this, let $\mathfrak{D}$ be the pentagon obtained by trimming away a triangle from the unit square $\mathfrak{D}^{\mathrm{u}} := (0,1)^2$. More precisely, the trimming curve is the straight line passing through the points $(0, 0.25)$ and $(0.75, 1)$, as represented in Figure 7.3a. We choose the data f, u_D and u_N such that the exact solution of Poisson problem (7.1) is $u_s(x, y) = \arctan\left(15(x - y + 0.25)\right)$, where we define $\Lambda_D := \left((0,1) \times \{0\}\right) \cup \left(\{1\} \times (0,1)\right)$ and $\Lambda_N := \partial\mathfrak{D} \setminus \overline{\Lambda_D}$.

At the first iteration of the adaptive process of Section 7.3, the non-trimmed geometry $\mathfrak{D}^{\mathrm{u}}$ is meshed with four elements in each direction such that the internal knot lines are the lines defined by $x = \dfrac{k}{4} + \varepsilon$ and $y = \dfrac{k}{4} - \varepsilon$ for $k = 1, 2, 3$ and $\varepsilon > 0$ small. In this way,

175

the trimmed mesh has elements whose active triangular part have a measure proportional to ε^2, as shown in Figure 7.3a. We solve the Galerkin problem (7.3) with HB-splines of degree $P = 3$ in each direction and with $\varepsilon = 10^{-t}$ for $t = 5, 6, 7$, and we denote u_ε^h the obtained discretized solution. Note that the mesh depends on ε, but not the geometry $\mathfrak{D}$ itself. Both uniform refinement and the adaptive refinement described in Section 7.3 with $\theta = 0.9$ are performed. The algorithm stops when the number of degrees of freedom of the HB-spline space exceeds 10^4. The results are given in Figure 7.3c and 7.3d, respectively, and the final mesh obtained with adaptive refinement is represented in Figure 7.3b.

As in the first example, we can see that under both uniform and adaptive refinement, the estimator follows well the behavior of the energy error in the trimmed geometry, both of them having a convergence rate of $\mathcal{O}\left(N_{\text{dof}}^{-\frac{P}{2}}\right) = \mathcal{O}\left(N_{\text{dof}}^{-\frac{3}{2}}\right)$. Moreover, the presented results confirm the fact that the effectivity index η_{eff} is independent of ε, that is, it is independent of the measure of the active part of the trimmed elements. Indeed, for the different chosen values of ε, the curves representing the estimator are almost superposed, and this is also the case for the curves representing the numerical error. At the first iteration, where $\varepsilon \ll h$, the effectivity index is equal to 11.9 in all cases. Once the asymptotic regime is attained, and for every value of ε, the effectivity index is equal to 11.0 when uniform refinement is performed, while it is equal to 7.3 when the proposed adaptive refinement strategy is performed.

7.4.3 Independence from the size of the active parts of the trimmed elements: singular solution

To perform a more severe test with respect to the previous one, let us consider a problem whose solution presents a corner singularity, on a trimmed geometry with small active trimmed elements around that corner. To do so, let us consider the L-shaped domain $\mathfrak{D}$ obtained by trimming the square $(0.5, 1) \times (0, 0.5)$ from the unit square $(0, 1)^2$, as illustrated in Figure 7.4a. We choose the data f, u_D and u_N such that the exact solution of Poisson problem (7.1) is $u_s(r, \varphi) = r^{\frac{2}{3}} \sin\left(\frac{2\varphi}{3}\right)$ in the polar coordinate system $(\mathbf{e}_r, \mathbf{e}_\varphi)$ centered at $(0.5, 0.5)^T$, as represented in Figure 7.4a, with $\Lambda_D := \left((0, 1) \times \{1\}\right) \cup \left(\{0\} \times (0, 1)\right)$ and $\Lambda_N := \partial\mathfrak{D} \setminus \overline{\Lambda_D}$.

At the first iteration of the adaptive process, the non-trimmed geometry $\mathfrak{D}^{\mathrm{u}}$ is meshed with 4 elements in each direction such that the internal knot lines are the lines defined by $x = \frac{k}{4} - \varepsilon$ and $y = \frac{k}{4} + \varepsilon$ for $k = 1, 2, 3$ and $\varepsilon > 0$ small. In this way, the active part of the trimmed mesh elements are very thin, and their measure is proportional to εh, see Figure 7.4a. We solve the Galerkin problem (7.3) with HB-splines of degree $P = 2$ in each direction and with $\varepsilon = 10^{-t}$ for $t = 5, 6, 7$, and we denote u_ε^h the obtained discrete solution. As before, note that the mesh depends on ε, but not the geometry $\mathfrak{D}$ itself. As in the previous numerical experiment, both uniform refinement and the adaptive

(a) Trimmed parametric L-shaped domain $\mathfrak{D}$ and original mesh (in gray).

(b) Final active mesh on $\mathfrak{D}$ obtained with adaptive mesh refinement.

(c) Trimmed mapped L-shaped domain $\mathfrak{D}_{\mathbf{F}}$ and mapped original mesh (in gray).

(d) Final active mesh on $\mathfrak{D}_{\mathbf{F}}$ obtained with adaptive mesh refinement.
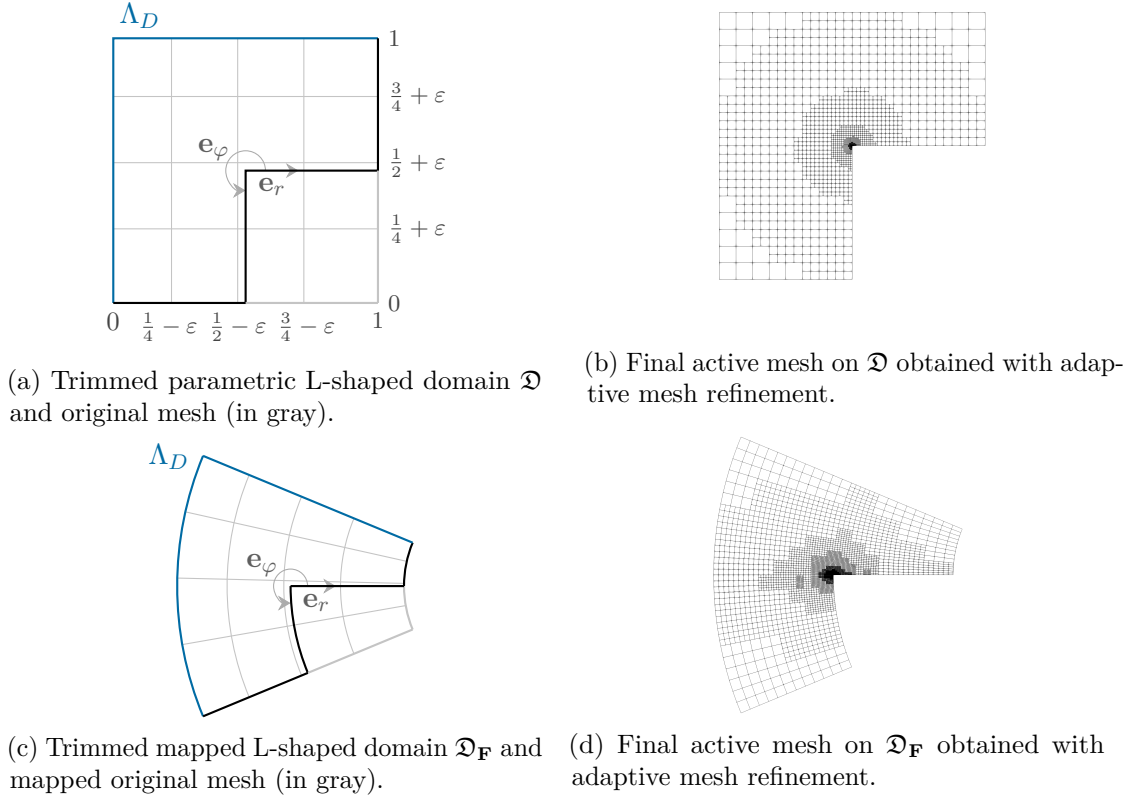
Figure 7.4 – Numerical tests 7.4.3 and 7.4.4 – Parametric and mapped L-shaped domains, with their corresponding final active meshes obtained with adaptive mesh refinement.

refinement described in Section 7.3 with $\theta = 0.9$ are performed. The algorithm stops either when the number of degrees of freedom of the HB-spline space exceeds 10^4, or when the number of hierarchical levels exceeds 12. The results are given in Figure 7.5a and 7.5b.

As in the previous example, under both uniform and adaptive refinement, the estimator follows well the behavior of the energy error in the trimmed geometry, and no dependence on ε is observed. Indeed, for the different values of ε, the corresponding curves are almost superposed. Moreover, the chosen differential problem presents a singularity at the corner $(0.5, 0.5)$. In particular, it can be shown that the exact solution $u_s \in H^{\beta - \delta}(\mathfrak{D})$ with $\beta = \dfrac{5}{3}$, for every $\delta > 0$. Therefore, one expects a convergence rate of $\mathcal{O}\left(h^{\frac{2}{3}}\right) = \mathcal{O}\left(N_{\text{dof}}^{-\frac{1}{3}}\right)$ under uniform h-refinement, see Theorem 5.2.9. This is indeed what is observed both for the estimator and for the error, with a small effectivity index nearly equal to 2.4 and independent of ε. As it is now standard in adaptivity, we can see in Figure 7.5b that the optimal asymptotic convergence rate of $\mathcal{O}\left(N_{\text{dof}}^{-\frac{P}{2}}\right) = \mathcal{O}\left(N_{\text{dof}}^{-1}\right)$ is recovered when the mesh is adaptively refined. In this case, the effectivity index is very small while still being independent of ε: it is nearly equal to 1.7 once the asymptotic regime is attained. The

(a) Uniform mesh refinement in the parametric L-shaped domain $\mathfrak{D}$.

(b) Adaptive mesh refinement in the parametric L-shaped domain $\mathfrak{D}$.

(c) Uniform mesh refinement in the mapped L-shaped domain $\mathfrak{D}_{\mathbf{F}}$.

(d) Adaptive mesh refinement in the mapped L-shaped domain $\mathfrak{D}_{\mathbf{F}}$.
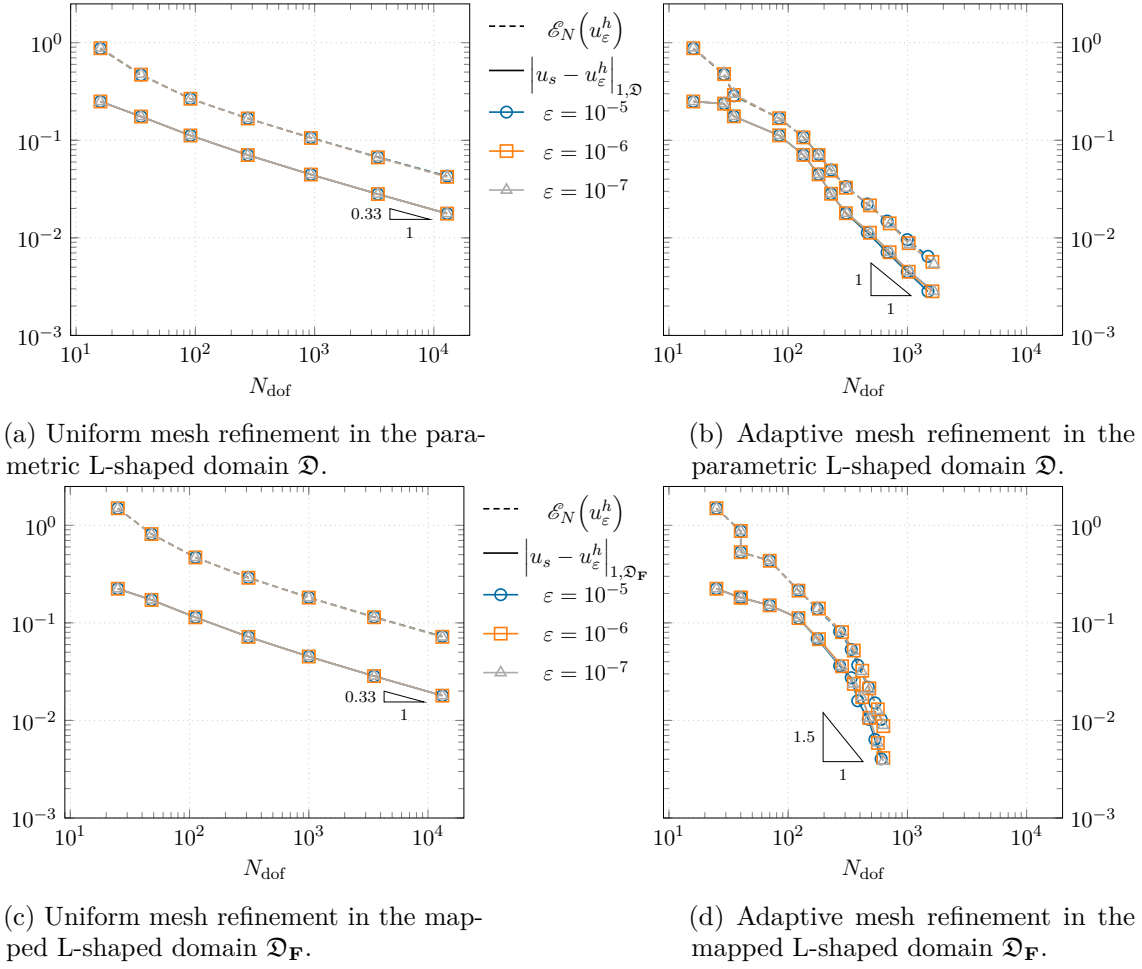
Figure 7.5 – Numerical tests 7.4.3 and 7.4.4 – Convergence of the energy error and estimator with respect to the number of degrees of freedom in the parametric and mapped L-shaped domains, under uniform and adaptive mesh refinements.

adaptive strategy exhibits a substantial increase in accuracy with respect to the number of degrees of freedom, in comparison with the uniform refinement strategy. Therefore, this test validates the theory presented in Section 7.2, and in particular, it validates the fact that the estimator is independent of the type of cut from which the trimmed geometry is obtained.

7.4.4 Singular solution in a mapped trimmed domain

In this last numerical experiment, we consider the geometry $\mathfrak{D}_{\mathbf{F}}$ obtained from the geometry $\mathfrak{D}$ of the previous example, mapped with an isogeometric mapping $\mathbf{F}$ (see Section 6.3). This numerical test was presented in [Bracco et al., 2018]. More precisely and as represented in Figure 7.4c, $\mathbf{F}(\mathfrak{D}^{\mathrm{u}})$ is the surface ruled between the arcs centered

at $(2,0)^T$ of radius 3 and 1, whose angle spans between $\frac{7\pi}{8}$ and $\frac{9\pi}{8}$. The curve that trims $\mathbf{F}(\mathfrak{D}^{\mathrm{u}})$ to obtain $\mathfrak{D}_{\mathbf{F}}$ is the image of the trimming curve defining $\mathfrak{D}$ in the parametric domain. That is, it is the line $\big((0,1) \times \{0\}\big) \cup \boldsymbol{A}$, where $\boldsymbol{A}$ is the arc centered at $(2,0)^T$ of radius 2, whose angle spans between π and $\frac{9\pi}{8}$. Therefore, $\mathfrak{D}_{\mathbf{F}}$ presents a re-entrant corner of angle $\frac{\pi}{2}$ in $(0,0)^T$. We choose the data f, u_D and u_N such that the exact solution of Poisson problem (7.1) is $u_s(r,\varphi) = r^{\frac{2}{3}} \sin\left(\frac{2\varphi}{3}\right)$ in the polar coordinate system $(\mathbf{e}_r, \mathbf{e}_\varphi)$ centered at $(0,0)^T$, and represented in Figure 7.4c. We consider $\Lambda_D := \mathbf{F}\big((0,1) \times \{1\}\big) \cup \mathbf{F}\big(\{0\} \times (0,1)\big)$ and $\Lambda_N := \partial\mathfrak{D} \setminus \overline{\Lambda_D}$.

At the first iteration of the adaptive process, the considered mesh is the same as in the previous parametric L-shaped domain example, so that the active part of the trimmed mesh elements are very thin, and their measure is proportional to εh. We solve the Galerkin problem (7.3) with HB-splines of degree $P = 3$ in each direction and with $\varepsilon = 10^{-t}$ for $t = 5, 6, 7$, and we denote u_ε^h the obtained discrete solution. As before, note that the mesh depends on ε, but not the geometry $\mathfrak{D}_{\mathbf{F}}$ itself. As in the previous numerical experiment, both uniform refinement and the adaptive refinement described in Section 7.3 with $\theta = 0.9$ are performed. The algorithm stops either when the number of degrees of freedom of the HB-spline space exceeds 10^4, or when the number of hierarchical levels exceeds 12. The results are given in Figure 7.5c and 7.5d.

As expected, the results are very similar to the ones of the previous experiment. Indeed, under both uniform and adaptive refinement, the estimator follows well the behavior of the energy error in the trimmed mapped geometry, and no dependence on ε is observed. Moreover, since the considered differential problem presents a corner singularity in $(0,0)$, then as previously, one expects a convergence rate of $\mathcal{O}\left(N_{\mathrm{dof}}^{-\frac{1}{3}}\right)$ under uniform refinement, while one expects to recover the optimal asymptotic convergence rate of $\mathcal{O}\left(N_{\mathrm{dof}}^{-\frac{P}{2}}\right) = \mathcal{O}\left(N_{\mathrm{dof}}^{-\frac{3}{2}}\right)$ under adaptive refinement. This is indeed the case for the uniform refinement strategy, and a small effectivity index nearly equal to 4.1 and independent of ε is obtained. However, a faster convergence is observed for the adaptive refinement strategy, both for the error and for the estimator: this is a common behavior when the asymptotic regime is not reached yet. Also in this case, a small effectivity index is obtained, being nearly equal to 2.3 and independent of ε.

8 A reliable adaptive isogeometric analysis defeaturing strategy

A combined mesh and geometric adaptive strategy has been introduced in Chapter 5, in the context of analysis-aware defeaturing. In principle, this algorithm could be used with any (mesh-preserving) finite element method which provides a Galerkin approximation of the defeaturing problem. The only required ingredient is a corresponding numerical error estimator, which can be decomposed into local mesh contributions. However, IGA naturally comes as an interesting numerical method of choice to treat defeaturing problems. Indeed, and as highlighted in Chapter 6, IGA was introduced to reduce the gap between the phase of designing complex objects, and the analysis phase in which one solves PDEs that are defined on these objects. Therefore in this chapter, we precise the adaptive strategy of Chapter 5 in the framework of (T)HB-spline based IGA.

To do so, we first introduce in Section 8.1 the IGA formulation of the considered defeaturing problem. In particular, we concentrate on Poisson's equation as model problem. Then, we introduce and prove in Section 8.2 the reliability of the *a posteriori* estimator of the IGA discrete defeaturing error, under some reasonable assumptions. This estimator is able to drive the adaptive strategy introduced in Chapter 5. But since this algorithm is designed to be used with mesh-preserving numerical methods, we subsequently discuss in Section 8.3 the extension of the adaptive procedure to trimmed and multipatch geometries in IGA. To finish, in Section 8.4, various numerical experiments are presented to illustrate the proposed adaptive strategy with IGA, and to validate and extend the presented theory. This chapter closely follows [Buffa et al., 2022a].

In this chapter, the symbol $\lesssim$ is used to mean any inequality which is independent of the size of the features, of their number, of the mesh size h, and of the number of hierarchical levels (see Chapter 6). However, those inequalities may depend on the shape of the features and of the mesh elements. Moreover, we will write $A \simeq B$ whenever $A \lesssim B$ and $B \lesssim A$.
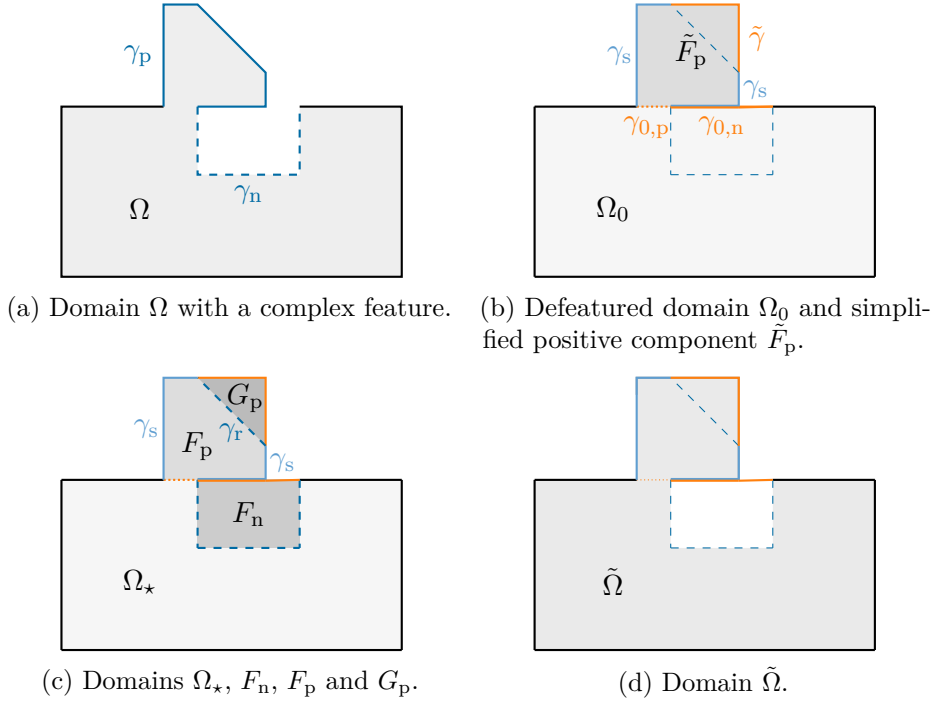
(a) Domain Ω with a complex feature.

(b) Defeatured domain Ω_0 and simplified positive component $\tilde{F}_{\mathrm{p}}$.

(c) Domains $\Omega_\star$, F_{n}, F_{p} and G_{p}.

(d) Domain $\tilde{\Omega}$.

Figure 8.1 – Illustration of the notation for a geometry with one complex feature.

8.1   Isogeometric analysis formulation of the defeaturing problem

Let us consider the defeaturing framework discussed in Chapter 4 in the context of Poisson's equation, and let us use the same notation. In particular, the notation corresponding to the considered geometric domains and boundaries is illustrated in Figure 8.1, which reproduces Figure 3.6. We assume that the defeatured geometry Ω_0 defined in (4.1) is a THB-spline domain generated by a THB-spline basis $\mathcal{T}(\Omega_0)$, see Section 6.2.2. Let $\mathcal{Q}_0 := \mathcal{Q}(\Omega_0)$ be the hierarchical mesh as defined in (6.12) on which the basis $\mathcal{T}(\Omega_0)$ is built, and let $V^h(\Omega_0)$ be the finite dimensional subspace of $H^1(\Omega_0)$ defined by

$$V^h(\Omega_0) := \mathrm{span}\left\{\mathcal{T}(\Omega_0)\right\}.$$

Recall that N_f denotes the number of features present in the exact geometry, and similarly, assume that for all $k = 1, \ldots, N_f$, the positive component extension $\tilde{F}_{\mathrm{p}}^k$ of feature F^k is a THB-spline domain generated by a THB-spline basis $\mathcal{T}\left(\tilde{F}_{\mathrm{p}}^k\right)$. Let $\tilde{\mathcal{Q}}^k := \mathcal{Q}\left(\tilde{F}_{\mathrm{p}}^k\right)$ be the hierarchical mesh as defined in (6.12) on which the basis $\mathcal{T}\left(\tilde{F}_{\mathrm{p}}^k\right)$ is built, and let $V^h\left(\tilde{F}_{\mathrm{p}}^k\right)$ be the finite dimensional subspace of $H^1\left(\tilde{F}_{\mathrm{p}}^k\right)$ defined by

$$V^h\left(\tilde{F}_{\mathrm{p}}^k\right) := \mathrm{span}\left\{\mathcal{T}\left(\tilde{F}_{\mathrm{p}}^k\right)\right\}.$$

Note that in this section, we assume that $\mathcal{Q}_0$ and $\tilde{\mathcal{Q}}^k$ are fitted to the simplified geometries Ω_0 and $\tilde{F}_p^k$, respectively, and recall the definition of the global mesh

$$\mathcal{Q} := \mathcal{Q}_0 \cup \tilde{\mathcal{Q}} \quad \text{with} \quad \tilde{\mathcal{Q}} := \bigcup_{k=1}^{N_f} \tilde{\mathcal{Q}}^k$$

from (5.14). Furthermore, let us make the following shape regularity assumption.

Assumption 8.1.1. For all $k = 1, \ldots, N_f$, the meshes $\mathcal{Q}_0$ and $\tilde{\mathcal{Q}}^k$ are shape regular, according to Definition 5.2.1.

Under Assumption 8.1.1, we say that $\mathcal{Q}$ is shape regular by abuse of terminology. As a consequence of Assumption 8.1.1, $|K|^{\frac{1}{n}} \simeq h_K \simeq h_E$ for all $K \in \mathcal{Q}$ and all $E \in \mathcal{E} \cap \partial K$, where $\mathcal{E}$ is the set of Neumann boundary faces as defined in (5.26). Moreover, specific to IGA with THB-splines, we also make the following assumption on $\mathcal{Q}$.

Assumption 8.1.2. $\mathcal{Q}$ is $\mathcal{T}$-admissible of class $\mathfrak{m}$ for some $\mathfrak{m} \in \mathbb{N}$, $\mathfrak{m} \geq 2$. That is, $\mathcal{Q}_0$ and $\tilde{\mathcal{Q}}^k$ are $\mathcal{T}$-admissible of class $\mathfrak{m}$ for all $k = 1, \ldots, N_f$, according to Definition 6.3.2.

Finally, we recall that for all $k = 1, \ldots, N_f$, the discrete spaces $V^h(\Omega_0)$ and $V^h\left(\tilde{F}_p^k\right)$ should have compatible traces on $\gamma_{0,p}^k$, following Assumption 5.3.1. Then, referring to Chapters 4 and 5 for the notation, we solve problem (5.13) in the simplified geometry Ω_0 to obtain the discrete defeatured solution $u_0^h \in V_{g_D}^h(\Omega_0)$, followed by problem (5.15) in $\tilde{F}_p^k$ for all $k = 1, \ldots, N_f$ to obtain the discrete defeatured solution extensions $u_k^h \in V_{u_0^h}^h\left(\tilde{F}_p^k\right)$. This allows us to define u_d^h, the discrete defeatured solution approximating the exact solution $u \in H_{g_D, \Gamma_D}^1(\Omega)$, as in (5.18). That is,

$$u_d^h = u_0^h\big|_{\Omega_\star} \text{ in } \Omega_\star = \Omega \setminus \overline{F_p} \quad \text{and} \quad u_d^h = u_k^h\big|_{F_p^k} \text{ in } F_p^k \text{ for } k = 1, \ldots, N_f. \tag{8.1}$$

In the subsequent analysis, we make the following assumption for simplicity.

Assumption 8.1.3. $V^h(\Omega_0) \subset C^1(\Omega_0)$ and $V^h\left(\tilde{F}_p^k\right) \subset C^1\left(\tilde{F}_p^k\right)$ for all $k = 1, \ldots, N_f$.

Remark 8.1.4. This assumption is not needed, but it allows us to simplify the analysis by avoiding normal derivative jump terms between elements. The general case could be treated in a similar way following the classical theory of the standard adaptive finite element method; it is also analogous to the multipatch case that will be analyzed in Section 8.3.

Furthermore, as a consequence of Assumption 8.1.2, it is possible to build Scott-Zhang-type operators

$$I_0^h : H_{0,\Gamma_D}^1(\Omega_0) \to V_0^h(\Omega_0)$$
$$\text{and} \quad \tilde{I}_k^h : H_{0,\gamma_{0,p}^k}^1\left(\tilde{F}_p^k\right) \to V_0^h\left(\tilde{F}_p^k\right), \quad \forall k = 1, \ldots, N_f,$$

having the following properties (see [Buffa and Giannelli, 2021], [Buffa et al., 2021b, Section 6.1.3]): for all $v \in H^1_{0,\Gamma_D}(\Omega_0)$, for all $k = 1, \ldots, N_f$ and all $w \in H^1_{0,\gamma^k_{0,\mathrm{p}}}\left(\tilde{F}^k_\mathrm{p}\right)$,

$$\sum_{K \in \mathcal{Q}_0} h_K^{-2} \left\| v - I_0^h(v) \right\|_{0,K}^2 \lesssim \|\nabla v\|_{0,\Omega_0}^2 \quad \text{and} \quad \sum_{K \in \mathcal{Q}_0} \left\| \nabla I_0^h(v) \right\|_{0,K}^2 \lesssim \|\nabla v\|_{0,\Omega_0}^2, \quad (8.2)$$

$$\sum_{K \in \tilde{\mathcal{Q}}^k} h_K^{-2} \left\| w - \tilde{I}_k^h(w) \right\|_{0,K}^2 \lesssim \|\nabla w\|_{0,\tilde{F}^k_\mathrm{p}}^2 \quad \text{and} \quad \sum_{K \in \tilde{\mathcal{Q}}^k} \left\| \nabla \tilde{I}_k^h(w) \right\|_{0,K}^2 \lesssim \|\nabla w\|_{0,\tilde{F}^k_\mathrm{p}}^2. \quad (8.3)$$

Note that the right equations imply that for all $v \in H^1_{0,\Gamma_D}(\Omega_0)$, for all $k = 1, \ldots, N_f$ and all $w \in H^1_{0,\gamma^k_{0,\mathrm{p}}}\left(\tilde{F}^k_\mathrm{p}\right)$,

$$\sum_{K \in \mathcal{Q}_0} \left\| \nabla\left(v - I_0^h(v) \right) \right\|_{0,K}^2 \lesssim \|\nabla v\|_{0,\Omega_0}^2, \quad (8.4)$$

$$\sum_{K \in \tilde{\mathcal{Q}}^k} \left\| \nabla\left(w - \tilde{I}_k^h(w) \right) \right\|_{0,K}^2 \lesssim \|\nabla w\|_{0,\tilde{F}^k_\mathrm{p}}^2. \quad (8.5)$$

Finally, we recall the isotropy Assumption 3.3.3 on all $\sigma \in \Sigma$, where Σ is defined in (4.11), and the definition of sub-domains Ω^k given by the separability Assumption 4.1.5. Let us now make the following technical assumption on the features.

Assumption 8.1.5. For all $k = 1, \ldots, N_f$, let $\Omega^k_\star$, Ω^k_0 and $\tilde{\Omega}^k$ be the sub-domains of, respectively, $\Omega_\star$, Ω_0 and $\tilde{\Omega}$, relative to Ω^k. More precisely,

$$\Omega^k_\star := \Omega^k \cap \Omega_\star, \quad \Omega^k_0 := \mathrm{int}\left(\overline{\Omega^k_\star} \cup \overline{F^k_\mathrm{n}} \right)$$
$$\text{and} \quad \tilde{\Omega}^k := \mathrm{int}\left(\overline{\Omega^k} \cup \overline{G^k_\mathrm{p}} \right) = \mathrm{int}\left(\overline{\Omega^k_\star} \cup \overline{\tilde{F}^k_\mathrm{p}} \right). \quad (8.6)$$

Then for all $k = 1, \ldots, N_f$, we assume that there exist generalized Stein extension operators

$$\mathsf{E}_{\Omega^k_\star \to \Omega^k_0} : H^1_{0,\Gamma_D \cap \partial\Omega^k}\left(\Omega^k_\star \right) \to H^1_{0,\Gamma_D \cap \partial\Omega^k}\left(\Omega^k_0 \right), \quad (8.7)$$

$$\mathsf{E}_{\Omega^k \to \tilde{\Omega}^k} : H^1_{0,\Gamma_D \cap \partial\Omega^k}\left(\Omega^k \right) \to H^1_{0,\Gamma_D \cap \partial\Omega^k}\left(\tilde{\Omega}^k \right), \quad (8.8)$$

$$\mathsf{E}_{\Omega^k_\star \to \tilde{\Omega}^k} : H^1_{0,\Gamma_D \cap \partial\Omega^k}(\Omega^k_\star) \to H^1_{0,\Gamma_D \cap \partial\Omega^k}\left(\tilde{\Omega}^k \right) \quad (8.9)$$

which are bounded, that is, they satisfy the following properties: for all $w \in H^1_{0,\Gamma_D \cap \partial\Omega^k}\left(\Omega^k_\star \right)$ and all $v \in H^1_{0,\Gamma_D \partial\Omega^k}\left(\Omega^k \right)$,

$$\left\| \nabla \mathsf{E}_{\Omega^k_\star \to \Omega^k_0}(w) \right\|_{0,\Omega^k_0} \lesssim \|\nabla w\|_{0,\Omega^k_\star}, \quad (8.10)$$

$$\left\| \nabla \mathsf{E}_{\Omega^k \to \tilde{\Omega}^k}(v) \right\|_{0,\tilde{\Omega}^k} \lesssim \|\nabla v\|_{0,\Omega^k}, \quad (8.11)$$

$$\left\| \nabla \mathsf{E}_{\Omega^k_\star \to \tilde{\Omega}^k}(w) \right\|_{0,\tilde{\Omega}^k} \lesssim \|\nabla w\|_{0,\Omega^k_\star}. \quad (8.12)$$

Note that such operators are built for a large class of domains in [Sauter and Warnke,

(a) Example of domain $\Theta\left(\tilde{F}_{\mathrm{p}}\right)$.

(b) Example of domains $\Theta(F_{\mathrm{n}})$ and $\Theta(G_{\mathrm{p}})$.
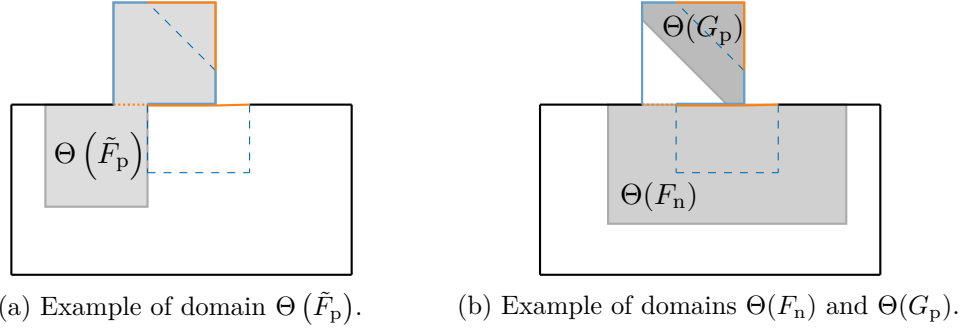
Figure 8.2 – Illustration of Assumption 8.1.5, where the different domains correspond to the ones of Figure 3.6.

1999], based on the Stein operator introduced in [Stein, 2016]. For example in [Sauter and Warnke, 1999], using the notation corresponding to $\mathsf{E}_{\Omega_\star^k\to\Omega_0^k}$, the construction is given for all domains such that there exists an open set $\Theta = \Theta\left(F_{\mathrm{n}}^k\right) \subset \Omega_0^k$ satisfying:

- $F_{\mathrm{n}}^k \subset \Theta$,

- $\Theta \setminus \overline{F_{\mathrm{n}}^k}$ is a simply connected Lipschitz domain,

- $\left|\partial F_{\mathrm{n}}^k \cap \Theta\right| \neq 0$,

- $\mathrm{dist}\left(\partial\Theta, \partial F_{\mathrm{n}}^k\right) \simeq \mathrm{diam}\left(F_{\mathrm{n}}^k\right)$,

as illustrated in Figure 8.2b. The domains Ω_0^k and F_{n}^k can be respectively replaced by $\tilde{\Omega}^k$ and $\tilde{F}_{\mathrm{p}}^k$, or by $\tilde{\Omega}^k$ and G_{p}^k (see definition (4.3) of the different domains), and the same statement remains valid. The corresponding open sets $\Theta\left(\tilde{F}_{\mathrm{p}}^k\right) \subset \tilde{\Omega}^k$ and $\Theta\left(G_{\mathrm{p}}^k\right) \subset \tilde{\Omega}^k$ are also illustrated in Figures 8.2a and 8.2b. In the same article, it is proven that a bounded generalized Stein extension operator exists for a wider class of domains such as domains containing long and thin holes as in Figure 8.3, but the construction of the extension operator has to be adapted to each considered situation. In Figure 8.4, it is represented a domain for which the required extension operator does not exist, in the sense that for all continuous extension operator, the hidden constant in (8.10) is not bounded.

8.2 Reliability of the discrete defeaturing error estimator

In this section, we use the special case of IGA with THB-splines to analyze the *a posteriori* discrete defeaturing error estimator $\mathscr{E}\left(u_{\mathrm{d}}^h\right)$ introduced in (5.21) on a given (fixed) defeatured geometrical model Ω_0, from which $N_f \geq 1$ features are missing. In particular, we show that the proposed estimator is reliable in the case in which the mesh is fitted to the simplified geometry, and under reasonable assumptions. That is, we show that it is an upper bound for the discrete defeaturing error between the analytic
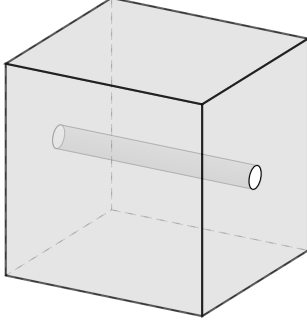
Figure 8.3 – Domain with a long and thin hole for which Assumption 8.1.5 is satisfied.
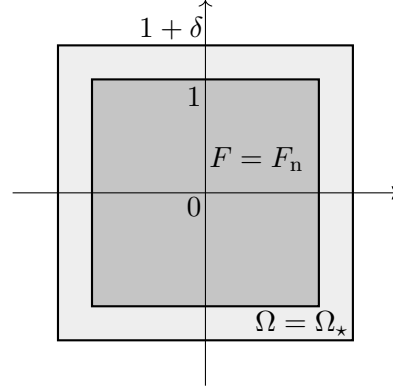

Figure 8.4 – Domain for which Assumption 8.1.5 is not satisfied since for all extension operator, the hidden constant C in (8.10) is such that $C \gtrsim \delta^{-\frac{1}{2}}$, with $\delta > 0$ (see [Sauter and Warnke, 1999]). Here, $\Omega_\star = \Omega := \Omega_0 \setminus \overline{F}$, $\Omega_0 := (-1 - \delta, 1 + \delta)^n$ and $F = F_n := (-1, 1)^d$.

solution u of the exact Poisson problem (3.2) and the discrete numerical solution u_d^h of the defeatured problem defined in (5.18), in the energy norm. We first demonstrate it in the simplest single feature case ($N_f = 1$) in which the only feature F is negative, and then we use this result to derive and prove the reliability of the estimator when F is a generic complex feature. Finally, we generalize the proof to multi-feature geometries for which $N_f \geq 1$.

8.2.1   Geometry with a negative feature

In this section, we analyze the proposed estimator in the case of a single negative feature F of Ω, meaning that the positive component $F_p = \emptyset$. Since we concentrate on the single feature case, we drop the upper index k everywhere, and since the feature is negative, then $\gamma = \gamma_n$, $\gamma_0 = \gamma_{0,n}$, $\Omega_\star = \Omega$, $\mathcal{Q} = \mathcal{Q}_0$, and $u_d^h = u_0^h\big|_\Omega$. Let us recall the definitions of the continuous and discrete defeaturing error terms $d_\gamma \in L^2(\gamma)$ and $d_\gamma^h \in L^2(\gamma)$ from (3.9) and (5.19), that is,

$$d_\gamma := g - \frac{\partial u_0}{\partial \mathbf{n}} \qquad \text{and} \qquad d_\gamma^h := g - \frac{\partial u_0^h}{\partial \mathbf{n}}, \tag{8.13}$$

and let us recall the definitions of the interior and boundary residuals $r \in L^2(\Omega_0)$ and $j \in L^2\left(\Gamma_N^0\right)$ from (5.24) and (5.25) with $\Gamma_N^0 := (\Gamma_N \setminus \gamma) \cup \gamma_0$, that is,

$$r := f + \Delta u_0^h \qquad \text{and} \qquad j := \begin{cases} g - \dfrac{\partial u_d^h}{\partial \mathbf{n}} & \text{on } \Gamma_N \setminus \gamma \\ g_0 - \dfrac{\partial u_0^h}{\partial \mathbf{n}_0} & \text{on } \gamma_0. \end{cases}$$

Then in this context, the discrete defeaturing error estimator defined in (5.21) writes as follows:

$$\mathscr{E}\left(u_0^h\right) := \left[\alpha_D^2 \mathscr{E}_D\left(u_0^h\right)^2 + \alpha_N^2 \mathscr{E}_N\left(u_0^h\right)^2\right]^{\frac{1}{2}}, \qquad (8.14)$$

where

$$\mathscr{E}_D\left(u_0^h\right)^2 := |\gamma|^{\frac{1}{n-1}} \left\|d_\gamma^h - \overline{d_\gamma^h}^\gamma\right\|_{0,\gamma}^2 + \mathscr{E}_C^2 \qquad \text{with} \quad \mathscr{E}_C^2 := c_\gamma^2 |\gamma|^{\frac{n}{n-1}} \left|\overline{d_\gamma}^\gamma\right|^2,$$

$$\mathscr{E}_N\left(u_0^h\right)^2 := \sum_{K \in \mathcal{Q}_0} h_K^2 \|r\|_{0,K}^2 + \sum_{E \in \mathcal{E}_0} h_E \|j\|_{0,E}^2,$$

and α_D and α_N are parameters to be tuned.

Let us now state and prove the main theorem of this section under the following technical hypothesis.

Assumption 8.2.1. Let $h_F := \mathrm{diam}(F)$ and

$$h_F^{\min} := \min\left\{h_K : K \in \mathcal{Q}_0,\, K \cap F \neq \emptyset\right\}.$$

Then we assume that $h_F \lesssim h_F^{\min}$, that is, F is either smaller or about the same size as the mesh that covers it.

This assumption means that asymptotically, the number of elements intersecting the feature cannot grow indefinitely. In the context of adaptivity with defeaturing, this hypothesis is quite natural. Indeed, if the number of feature elements grows, it means that the error is concentrated in the feature. More precisely, it either means that the defeaturing data f in F and g_0 in γ_0 are badly chosen, or that the feature is important to correctly approximate the exact solution u in Ω. In the first case, $\mathscr{E}_C$ will be large and the defeaturing data needs to be more accurately chosen. In the second case, feature F will be added by the adaptive algorithm defined in Chapter 5, and thus no refinement will be needed anymore in F. In Section 8.4, numerical experiments will show that this intuition is correct.

Theorem 8.2.2. *In the framework presented in Section 8.1, let u and u_0^h be the weak solutions of problems (3.2) and (5.13), respectively, where Ω is a geometry containing one negative feature F. Then under Assumption 8.2.1, the energy norm of the discrete defeaturing error is bounded in terms of the estimator $\mathscr{E}\left(u_0^h\right)$ introduced in (8.14) as follows:*

$$\left|u - u_0^h\right|_{1,\Omega} \lesssim \mathscr{E}\left(u_0^h\right).$$

Proof. For all $v \in H_{0,\Gamma_D}^1(\Omega)$, let us first use integration by parts on the exact domain Ω

to treat the discrete defeatured solution $u_0^h \in V_0^h(\Omega_0) \subset C^1(\Omega_0)$, i.e.,

$$\int_\Omega \nabla u_0^h \cdot \nabla v \, dx = -\int_\Omega \Delta u_0^h v \, dx + \int_{\Gamma_N} \frac{\partial u_0^h}{\partial \mathbf{n}} v \, ds. \tag{8.15}$$

Then, let $e := u - u_0^h$. Using (3.2), we obtain

$$\int_\Omega \nabla e \cdot \nabla v \, dx = \int_\Omega \left(f + \Delta u_0^h \right) v \, dx + \int_{\Gamma_N} \left(g - \frac{\partial u_0^h}{\partial \mathbf{n}} \right) v \, ds$$

$$= \int_\Omega r v \, dx + \int_{\Gamma_N \setminus \gamma} j v \, ds + \int_\gamma d_\gamma^h v \, ds. \tag{8.16}$$

The idea is to suitably extend v to Ω_0 to be able to correctly treat the elements and faces that are only partially in Ω. So by choosing $\Omega^1 := \Omega$ as we are considering the single feature case, and since $\Omega_\star = \Omega$ as we are considering the negative feature case, let $v_0 := \mathsf{E}_{\Omega \to \Omega_0}(v) \in H^1_{0,\Gamma_D}(\Omega_0)$ be the generalized Stein extension of v as defined in (8.7), and recall that $\Gamma_N^0 := (\Gamma_N \setminus \gamma) \cup \gamma_0$. Then, to deal with the elements and faces that are only partially in Ω, we add and subtract terms to (8.16) as follows:

$$\int_\Omega \nabla e \cdot \nabla v \, dx = \mathrm{I} + \mathrm{II}, \quad \text{with} \quad \mathrm{I} = \int_{\Omega_0} r v_0 \, dx + \int_{\Gamma_N^0} j v_0 \, ds,$$

$$\mathrm{II} = -\int_F r v_0 \, dx - \int_{\gamma_0} j v_0 \, ds + \int_\gamma d_\gamma^h v \, ds. \tag{8.17}$$

As term I is defined in Ω_0 and since $\mathcal{Q}_0$ is fitted to Ω_0, then term I, which accounts for the numerical error, is defined in a union of full elements. Term II accounts for the discrete defeaturing error and for the corresponding compatibility condition (see Remark 3.2.1), and its contributions come from the presence of feature F.

Let us first consider I and treat it using the Scott-Zhang-type operator I_0^h introduced in (8.2). To do so, let $v_0^h = I_0^h(v_0) \in V_0^h(\Omega_0)$, and by adding and substracting v_0^h, we can rewrite

$$\mathrm{I} = \int_{\Omega_0} r \left(v_0 - v_0^h \right) dx + \int_{\Gamma_N^0} j \left(v_0 - v_0^h \right) ds + \int_{\Omega_0} r v_0^h \, dx + \int_{\Gamma_N^0} j v_0^h \, ds. \tag{8.18}$$

Using (3.4) and (5.13), integrating by parts, and since $v_0^h \in V_0^h(\Omega_0)$, then by Galerkin orthogonality,

$$\int_{\Omega_0} r v_0^h \, dx + \int_{\Gamma_N^0} j v_0^h \, ds = \int_{\Omega_0} \nabla \left(u_0 - u_0^h \right) \cdot \nabla v_0^h = 0. \tag{8.19}$$

Thus from (8.19), using Hölder inequality and the discrete Cauchy-Schwarz inequality,

term (8.18) can be estimated as follows:

$$
\begin{aligned}
\mathrm{I} &= \sum_{K \in \mathcal{Q}_0} \int_K r\left(v_0 - v_0^h\right) \mathrm{d}x + \sum_{E \in \mathcal{E}_0} \int_E j\left(v_0 - v_0^h\right) \mathrm{d}s \\
&\leq \sum_{K \in \mathcal{Q}_0} h_K \|r\|_{0,K}\, h_K^{-1} \left\|v_0 - v_0^h\right\|_{0,K} + \sum_{E \in \mathcal{E}_0} h_E^{\frac{1}{2}} \|j\|_{0,E}\, h_E^{-\frac{1}{2}} \left\|v_0 - v_0^h\right\|_{0,E} \\
&\leq \left(\sum_{K \in \mathcal{Q}_0} h_K^2 \|r\|_{0,K}^2 \right)^{\frac{1}{2}} \left(\sum_{K \in \mathcal{Q}_0} h_K^{-2} \left\|v_0 - v_0^h\right\|_{0,K}^2 \right)^{\frac{1}{2}} \\
&\quad + \left(\sum_{E \in \mathcal{E}_0} h_E \|j\|_{0,E}^2 \right)^{\frac{1}{2}} \left(\sum_{E \in \mathcal{E}_0} h_E^{-1} \left\|v_0 - v_0^h\right\|_{0,E}^2 \right)^{\frac{1}{2}}.
\end{aligned}
$$

Then, using property (8.2) of the Scott-Zhang-type operator since $\mathcal{Q}_0$ is $\mathcal{T}$-admissible, and property (8.10) of the generalized Stein extension v_0 of v, we get

$$
\sum_{K \in \mathcal{Q}_0} h_K^{-2} \left\|v_0 - v_0^h\right\|_{0,K}^2 \lesssim \|\nabla v_0\|_{0,\Omega_0}^2 \lesssim \|\nabla v\|_{0,\Omega}^2.
$$

Moreover, for every $E \in \mathcal{E}_0$, let $K_E \in \mathcal{Q}_0$ be the element such that $E \subset \partial K_E$, and note that by the shape regularity of $\mathcal{Q}_0$, $h_{K_E} \simeq h_E$. Then using the scaled trace inequality of Lemma 5.2.2, properties (8.2) and (8.4) of the Scott-Zhang-type operator, and property (8.10) of the generalized Stein extension v_0 of v, we obtain

$$
\begin{aligned}
\sum_{E \in \mathcal{E}_0} h_E^{-1} \left\|v_0 - v_0^h\right\|_{0,E}^2 &\lesssim \sum_{E \in \mathcal{E}_0} \left(h_{K_E}^{-2} \left\|v_0 - v_0^h\right\|_{0,K_E}^2 + \left\|\nabla\left(v_0 - v_0^h\right)\right\|_{0,K_E}^2 \right) \\
&\lesssim \|\nabla v_0\|_{0,\Omega_0}^2 \lesssim \|\nabla v\|_{0,\Omega}^2.
\end{aligned}
$$

Therefore, from the last three inequalities,

$$
\mathrm{I} \lesssim \left(\sum_{K \in \mathcal{Q}_0} h_K^2 \|r\|_{0,K}^2 + \sum_{E \in \mathcal{E}_0} h_E \|j\|_{0,E}^2 \right)^{\frac{1}{2}} \|\nabla v\|_{0,\Omega} = \mathscr{E}_N\left(u_0^h\right) \|\nabla v\|_{0,\Omega}. \tag{8.20}
$$

Now, let us consider term II of (8.17). First, note that by integration by parts, for any constant $c \in \mathbb{R}$,

$$
\int_F r c\, \mathrm{d}x + \int_{\gamma_0} j c\, \mathrm{d}s + \int_\gamma \frac{\partial\left(u_0 - u_0^h\right)}{\partial \mathbf{n}_F} c\, \mathrm{d}s = \int_F \nabla\left(u_0 - u_0^h\right) \cdot \nabla c\, \mathrm{d}x = 0. \tag{8.21}
$$

Thus, adding (8.21) to II with the choice of constant $c := \overline{v}^\gamma$, we obtain

$$
\begin{aligned}
\text{II} &= -\int_F r v_0 \, \mathrm{d}x - \int_{\gamma_0} j v_0 \, \mathrm{d}s + \int_\gamma d_\gamma^h v \, \mathrm{d}s \\
&= -\int_F r \left(v_0 - \overline{v}^\gamma \right) \mathrm{d}x - \int_{\gamma_0} j \left(v_0 - \overline{v}^\gamma \right) \mathrm{d}s + \int_\gamma d_\gamma^h v \, \mathrm{d}s + \int_\gamma \frac{\partial \left(u_0 - u_0^h \right)}{\partial \mathbf{n}_F} \overline{v}^\gamma \, \mathrm{d}s \\
&= -\text{II}_1 + \text{II}_2,
\end{aligned}
\tag{8.22}
$$

with $\text{II}_1 := \displaystyle\int_F r \left(v_0 - \overline{v}^\gamma \right) \mathrm{d}x + \int_{\gamma_0} j \left(v_0 - \overline{v}^\gamma \right) \mathrm{d}s,$

$$
\text{II}_2 := \int_\gamma d_\gamma^h v \, \mathrm{d}s + \int_\gamma \frac{\partial \left(u_0 - u_0^h \right)}{\partial \mathbf{n}_F} \overline{v}^\gamma \, \mathrm{d}s.
$$

Moreover, recalling the definition of d_γ from (8.13), we note that

$$
d_\gamma^h + \frac{\partial \left(u_0 - u_0^h \right)}{\partial \mathbf{n}_F} = d_\gamma.
$$

Using this, we can rewrite II_2 of (8.22) as

$$
\begin{aligned}
\text{II}_2 &= \int_\gamma \left(d_\gamma^h - \overline{d_\gamma^h}^\gamma \right) v \, \mathrm{d}s + \overline{d_\gamma^h}^\gamma \int_\gamma v \, \mathrm{d}s + \frac{1}{|\gamma|} \int_\gamma \frac{\partial \left(u_0 - u_0^h \right)}{\partial \mathbf{n}_F} \, \mathrm{d}s \int_\gamma v \, \mathrm{d}s \\
&= \int_\gamma \left(d_\gamma^h - \overline{d_\gamma^h}^\gamma \right) \left(v - \overline{v}^\gamma \right) \mathrm{d}s + \frac{1}{|\gamma|} \int_\gamma \left(d_\gamma^h + \frac{\partial \left(u_0 - u_0^h \right)}{\partial \mathbf{n}_F} \right) \mathrm{d}s \int_\gamma v \, \mathrm{d}s \\
&= \int_\gamma \left(d_\gamma^h - \overline{d_\gamma^h}^\gamma \right) \left(v - \overline{v}^\gamma \right) \mathrm{d}s + \overline{d_\gamma}^\gamma \int_\gamma v \, \mathrm{d}s.
\end{aligned}
$$

These terms can be estimated exactly as in the proof of Theorem 3.2.3, that is,

$$
\text{II}_2 \lesssim \left(|\gamma|^{\frac{1}{n-1}} \left\| d_\gamma^h - \overline{d_\gamma^h}^\gamma \right\|_{0,\gamma}^2 + c_\gamma^2 |\gamma|^{\frac{n}{n-1}} \left| \overline{d_\gamma}^\gamma \right|^2 \right)^{\frac{1}{2}} \| \nabla v \|_{0,\Omega} = \mathscr{E}_D \left(u_0^h \right) \| \nabla v \|_{0,\Omega}. \tag{8.23}
$$

Finally, let us consider term II_1 of (8.22). Remark first that $\overline{v}^\gamma = \overline{v_0}^\gamma$ since $v_0 = v$ on γ by definition. Thus,

$$
\begin{aligned}
\text{II}_1 &= \int_F r \left(v_0 - \overline{v_0}^\gamma \right) \mathrm{d}x + \int_{\gamma_0} j \left(v_0 - \overline{v_0}^\gamma \right) \mathrm{d}s \\
&\leq \| r \|_{0,F} \left\| v_0 - \overline{v_0}^\gamma \right\|_{0,F} + \| j \|_{0,\gamma_0} \left\| v_0 - \overline{v_0}^\gamma \right\|_{0,\gamma_0}.
\end{aligned}
$$

Furthermore, by Friedrichs inequality of Lemma 2.3.5, since $\gamma \subset \partial F$,

$$
\left\| v_0 - \overline{v_0}^\gamma \right\|_{0,F} \lesssim h_F \| \nabla v_0 \|_{0,F},
$$

and thus by the trace inequality of Lemma 2.2.2,

$$
\left\| v_0 - \overline{v_0}^\gamma \right\|_{0,\gamma_0} \leq \left\| v_0 - \overline{v_0}^\gamma \right\|_{0,\partial F} \lesssim \left(h_F^{-1} \left\| v_0 - \overline{v_0}^\gamma \right\|_{0,F}^2 + h_F \| \nabla v_0 \|_{0,F}^2 \right)^{\frac{1}{2}} \lesssim h_F^{\frac{1}{2}} \| \nabla v_0 \|_{0,F}.
$$

Therefore, combining the last three inequalities and using property (8.10) of the generalized Stein extension v_0 of v, we obtain

$$\text{II}_1 \lesssim \left(h_F \|r\|_{0,F} + h_F^{\frac{1}{2}} \|j\|_{0,\gamma_0} \right) \|\nabla v_0\|_{0,F} \lesssim \left(h_F^2 \|r\|_{0,F}^2 + h_F \|j\|_{0,\gamma_0}^2 \right)^{\frac{1}{2}} \|\nabla v\|_{0,\Omega}. \quad (8.24)$$

From Assumption 8.2.1, $h_F \lesssim h_F^{\min}$, that is, for all $K \in \mathcal{Q}_0$ such that $K \cap F \neq \emptyset$, $h_F \lesssim h_K$. Consequently, inequality (8.24) can be rewritten as follows.

$$\begin{aligned}
\text{II}_1 &\leq \left(h_F^2 \sum_{\substack{K \in \mathcal{Q}_0 \\ K \cap F \neq \emptyset}} \|r\|_{0,K}^2 + h_F \sum_{\substack{E \in \mathcal{E}_0 \\ E \cap \gamma_0 \neq \emptyset}} \|j\|_{0,E}^2 \right)^{\frac{1}{2}} \|\nabla v\|_{0,\Omega} \\
&\lesssim \left(\sum_{\substack{K \in \mathcal{Q}_0 \\ K \cap F \neq \emptyset}} h_K^2 \|r\|_{0,K}^2 + \sum_{\substack{E \in \mathcal{E}_0 \\ E \cap \gamma_0 \neq \emptyset}} h_E \|j\|_{0,E}^2 \right)^{\frac{1}{2}} \|\nabla v\|_{0,\Omega} \\
&\leq \mathscr{E}_N\left(u_0^h \right) \|\nabla v\|_{0,\Omega}. \quad (8.25)
\end{aligned}$$

To conclude, we plug (8.20), (8.23) and (8.25) into (8.22) and (8.17), and thus for all test functions $v \in H_{0,\Gamma_D}^1(\Omega)$,

$$\int_\Omega \nabla e \cdot \nabla v \, \mathrm{d}x \lesssim \left[\mathscr{E}_D\left(u_0^h \right)^2 + \mathscr{E}_N\left(u_0^h \right)^2 \right]^{\frac{1}{2}} \|\nabla v\|_{0,\Omega} \simeq \mathscr{E}\left(u_0^h \right) \|\nabla v\|_{0,\Omega}. \quad (8.26)$$

We conclude by choosing $v = e \in H_{0,\Gamma_D}^1(\Omega)$ in (8.26), and by simplifying $\|\nabla e\|_{0,\Omega}$ on both sides. $\qquad \square$

Remark 8.2.3. Without Assumption 8.2.1, i.e., in the case in which the size of the feature is greater than the mesh size on it, $h_F \gg h_F^{\min}$, then term II_1 estimated by (8.24) is sub-optimal as the scaling of F is present in front of the residual terms instead of the mesh size.

Remark 8.2.4. Note that the estimation of term I in (8.18) gives an alternative proof to the one of [Buffa and Giannelli, 2016, Theorem 11] in the case of mixed boundary conditions.

8.2.2 Geometry with a complex feature

In this section, we extend the result of Section 8.2.1 by stating and proving the reliability of the proposed *a posteriori* estimator of the discrete defeaturing error in a geometry with one complex feature. So let F be the only complex feature of Ω, i.e., a feature containing both a negative component F_n and a positive component F_p, and let us recall the notation introduced in Chapter 5. In particular, recall that in the single feature

framework, $\tilde{u}_0^h$ is the numerical approximation of the Dirichlet extension of u_0^h in $\tilde{F}_{\mathrm{p}}$, where $\tilde{F}_{\mathrm{p}}$ is a simple extension of the feature's positive component, see (5.15). In this case, we recall the definition of the discrete defeatured solution u_{d}^h,

$$u_{\mathrm{d}}^h = u_0^h\Big|_{\Omega_\star} \text{ in } \Omega_\star = \Omega \setminus \overline{F_{\mathrm{p}}} \quad \text{and} \quad u_{\mathrm{d}}^h = \tilde{u}_0^h\Big|_{F_{\mathrm{p}}} \text{ in } F_{\mathrm{p}}. \tag{8.27}$$

Moreover, recall definitions (3.29) and (5.19) of the continuous and discrete defeaturing error terms $d_\sigma \in L^2(\sigma)$ and $d_\sigma^h \in L^2(\sigma)$ for all $\sigma \in \Sigma := \{\gamma_{\mathrm{n}}, \gamma_{0,\mathrm{p}}, \gamma_{\mathrm{r}}\}$, that is,

$$d_\sigma := \begin{cases} g - \dfrac{\partial u_{\mathrm{d}}}{\partial \mathbf{n}} & \text{if } \sigma = \gamma_{\mathrm{n}} \text{ or } \sigma = \gamma_{\mathrm{r}} \\[2mm] -\left(g_0 + \dfrac{\partial u_{\mathrm{d}}}{\partial \mathbf{n}_F}\right) & \text{if } \sigma = \gamma_{0,\mathrm{p}}, \end{cases}$$

$$\text{and} \quad d_\sigma^h := \begin{cases} g - \dfrac{\partial u_{\mathrm{d}}^h}{\partial \mathbf{n}} & \text{if } \sigma = \gamma_{\mathrm{n}} \text{ or } \sigma = \gamma_{\mathrm{r}} \\[2mm] -\left(g_0 - \dfrac{\partial u_{\mathrm{d}}^h}{\partial \mathbf{n}_F}\right) & \text{if } \sigma = \gamma_{0,\mathrm{p}}, \end{cases} \tag{8.28}$$

and recall definitions (5.24) and (5.25) of the interior and boundary residuals of u_0^h, denoted $r \in L^2(\Omega_0)$ and $j \in L^2\left(\Gamma_N^0\right)$ with $\Gamma_N^0 := (\Gamma_N \setminus \gamma) \cup \gamma_0$, and of the interior and boundary residuals of $\tilde{u}_0^h$, denoted $r \in L^2\left(\tilde{F}_{\mathrm{p}}\right)$ and $j \in L^2\left(\tilde{\Gamma}_N\right)$ with $\tilde{\Gamma}_N := \gamma_{\mathrm{s}} \cup \tilde{\gamma}$, that is,

$$r := \begin{cases} f + \Delta u_0^h & \text{in } \Omega_0 \\ f + \Delta \tilde{u}_0^h & \text{in } \tilde{F}_{\mathrm{p}}, \end{cases}$$

$$\text{and} \quad j := \begin{cases} g - \dfrac{\partial u_{\mathrm{d}}^h}{\partial \mathbf{n}} & \text{on } \Gamma_N \setminus (\gamma_{\mathrm{n}} \cup \gamma_{\mathrm{r}}) \\[2mm] g_0 - \dfrac{\partial u_0^h}{\partial \mathbf{n}_0} & \text{on } \gamma_0 \\[2mm] \tilde{g} - \dfrac{\partial \tilde{u}_0^h}{\partial \tilde{\mathbf{n}}} & \text{on } \tilde{\gamma}. \end{cases}$$

In this context, the discrete defeaturing error estimator defined in (5.21) writes as follows:

$$\mathscr{E}\left(u_{\mathrm{d}}^h\right) := \left[\alpha_D^2 \mathscr{E}_D\left(u_{\mathrm{d}}^h\right)^2 + \alpha_N^2 \mathscr{E}_N\left(u_{\mathrm{d}}^h\right)^2\right]^{\frac{1}{2}}, \tag{8.29}$$

where

$$\mathscr{E}_D\left(u_{\mathrm{d}}^h\right)^2 := \sum_{\sigma \in \Sigma} |\sigma|^{\frac{1}{n-1}} \left\|d_\sigma^h - \overline{d_\sigma^h}^\sigma\right\|_{0,\sigma}^2 + \mathscr{E}_C^2 \quad \text{with} \quad \mathscr{E}_C^2 := \sum_{\sigma \in \Sigma} c_\sigma^2 |\sigma|^{\frac{n}{n-1}} \left|\overline{d_\sigma}^\sigma\right|^2,$$

$$\mathscr{E}_N\left(u_{\mathrm{d}}^h\right)^2 := \sum_{K \in \mathcal{Q}} h_K^2 \|r\|_{0,K}^2 + \sum_{E \in \mathcal{E}} h_E \|j\|_{0,E}^2, \tag{8.30}$$

and α_D and α_N are parameters to be tuned.

Let us now state and prove the main theorem of this section under the following technical hypothesis, generalizing Assumption 8.2.1.

Assumption 8.2.5. For $S \in \left\{ F_{\mathrm{n}}, G_{\mathrm{p}}, \tilde{F}_{\mathrm{p}} \right\}$, let $h_S := \mathrm{diam}(S)$, let

$$
\mathcal{Q}_S = \begin{cases} \mathcal{Q}_0 & \text{if } S = F_{\mathrm{n}} \\ \tilde{\mathcal{Q}} & \text{otherwise,} \end{cases}
$$

and let

$$
h_S^{\mathrm{min}} := \min \left\{ h_K : K \in \mathcal{Q}_S,\, K \cap S \neq \emptyset \right\}.
$$

Assume that $h_S \lesssim h_S^{\mathrm{min}}$, that is, the feature is either smaller or about the same size as the mesh that covers it.

As already discussed in the negative feature case, and as suggested by some numerical experiments presented in Section 8.4, we will see that this assumption can be removed in practice.

Theorem 8.2.6. *In the framework presented in Section 8.1, let u be the weak solution of problem (3.2), and let u_{d}^h be the discrete defeaturing solution defined in (8.27), for which Ω is a geometry containing one complex feature F. Then under Assumption 8.2.5, the energy norm of the discrete defeaturing error is bounded in terms of the estimator $\mathscr{E}\left(u_{\mathrm{d}}^h \right)$ introduced in (8.29) as follows:*

$$
\left| u - u_{\mathrm{d}}^h \right|_{1,\Omega} \lesssim \mathscr{E}\left(u_{\mathrm{d}}^h \right).
$$

Proof. Let $e := u - u_{\mathrm{d}}^h$. We are looking for a characterization of the error similar to the one in (8.16). To do so, consider the exact problem (3.1) restricted to $\Omega_\star$ with the natural Neumann boundary condition on $\gamma_{0,\mathrm{p}}$, that is, the restriction $u|_{\Omega_\star} \in H^1_{g_D, \Gamma_D}(\Omega_\star)$ is the weak solution of

$$
\begin{cases} -\Delta \left(u|_{\Omega_\star} \right) = f & \text{in } \Omega_\star \\ u|_{\Omega_\star} = g_D & \text{on } \Gamma_D \\ \dfrac{\partial \left(u|_{\Omega_\star} \right)}{\partial \mathbf{n}} = g & \text{on } \Gamma_N \setminus \gamma_{\mathrm{p}} \\ \dfrac{\partial \left(u|_{\Omega_\star} \right)}{\partial \mathbf{n}_0} = \dfrac{\partial u}{\partial \mathbf{n}_0} & \text{on } \gamma_{0,\mathrm{p}}. \end{cases} \tag{8.31}
$$

By abuse of notation, we omit the explicit restriction of u to $\Omega_\star$. Then, for all test functions $v_{\mathrm{n}} \in H^1_{0,\Gamma_D}(\Omega_\star)$,

$$
\int_{\Omega_\star} \nabla u \cdot \nabla v_{\mathrm{n}} \, \mathrm{d}x = \int_{\Omega_\star} f v_{\mathrm{n}} \, \mathrm{d}x + \int_{\Gamma_N \setminus \gamma_{\mathrm{p}}} g v_{\mathrm{n}} \, \mathrm{d}s + \int_{\gamma_{0,\mathrm{p}}} \frac{\partial u}{\partial \mathbf{n}_0} v_{\mathrm{n}} \, \mathrm{d}s. \tag{8.32}
$$

Then from (8.32) for u and from integration by parts for u_0^h as in (8.15), for all functions $v_{\mathrm{n}} \in H_{0,\Gamma_D}^1(\Omega_\star)$,

$$
\int_{\Omega_\star} \nabla e \cdot \nabla v_{\mathrm{n}} \, \mathrm{d}x = \int_{\Omega_\star} (f + \Delta u_0^h) v_{\mathrm{n}} \, \mathrm{d}x + \int_{\Gamma_N \setminus \gamma_{\mathrm{p}}} \left(g - \frac{\partial u_0^h}{\partial \mathbf{n}} \right) v_{\mathrm{n}} \, \mathrm{d}s + \int_{\gamma_{0,\mathrm{p}}} \frac{\partial \left(u - u_0^h \right)}{\partial \mathbf{n}_0} v_{\mathrm{n}} \, \mathrm{d}s
$$

$$
= \int_{\Omega_\star} r v_{\mathrm{n}} \, \mathrm{d}x + \int_{\Gamma_N \setminus \gamma} j v_{\mathrm{n}} \, \mathrm{d}s + \int_{\gamma_{\mathrm{n}}} d_{\gamma_{\mathrm{n}}}^h v_{\mathrm{n}} \, \mathrm{d}s + \int_{\gamma_{0,\mathrm{p}}} \frac{\partial \left(u - u_0^h \right)}{\partial \mathbf{n}_0} v_{\mathrm{n}} \, \mathrm{d}s.
\tag{8.33}
$$

Moreover, in a similar fashion as in (8.31), consider the exact problem (3.1) restricted to F_{p} with the natural Neumann boundary condition on $\gamma_{0,\mathrm{p}}$. By abuse of notation and as previously, we omit the explicit restriction of u to F_{p}. So $u \in H^1(F_{\mathrm{p}})$ is one of the infinitely-many solutions (up to a constant) of

$$
\int_{F_{\mathrm{p}}} \nabla u \cdot \nabla v_{\mathrm{p}} \, \mathrm{d}x = \int_{F_{\mathrm{p}}} f v_{\mathrm{p}} \, \mathrm{d}x + \int_{\gamma_{\mathrm{p}}} g v_{\mathrm{p}} \, \mathrm{d}s + \int_{\gamma_{0,\mathrm{p}}} \frac{\partial u}{\partial \mathbf{n}_F} v_{\mathrm{p}} \, \mathrm{d}s, \quad \forall v_{\mathrm{p}} \in H^1(F_{\mathrm{p}}).
\tag{8.34}
$$

Recall that $\partial F_{\mathrm{p}} = \overline{\gamma_{\mathrm{p}}} \cup \overline{\gamma_{0,\mathrm{p}}}$ and $\gamma_{\mathrm{p}} = \mathrm{int}\left(\overline{\gamma_{\mathrm{s}}} \cup \overline{\gamma_{\mathrm{r}}} \right)$, where γ_{s} is the part of γ_{p} that is shared with $\partial \tilde{F}_{\mathrm{p}}$ while γ_{r} is the remaining part of γ_{p}, see Figure 8.1. Then for all $v_{\mathrm{p}} \in H^1(F_{\mathrm{p}})$, using (8.34) for u and by integration by parts for $\tilde{u}_0^h$,

$$
\int_{F_{\mathrm{p}}} \nabla e \cdot \nabla v_{\mathrm{p}} \, \mathrm{d}x = \int_{F_{\mathrm{p}}} \left(f + \Delta \tilde{u}_0^h \right) v_{\mathrm{p}} \, \mathrm{d}x + \int_{\gamma_{\mathrm{p}}} \left(g - \frac{\partial \tilde{u}_0^h}{\partial \mathbf{n}} \right) v_{\mathrm{p}} \, \mathrm{d}s + \int_{\gamma_{0,\mathrm{p}}} \frac{\partial \left(u - \tilde{u}_0^h \right)}{\partial \mathbf{n}_F} v_{\mathrm{p}} \, \mathrm{d}s
$$

$$
= \int_{F_{\mathrm{p}}} r v_{\mathrm{p}} \, \mathrm{d}x + \int_{\gamma_{\mathrm{s}}} j v_{\mathrm{p}} \, \mathrm{d}s + \int_{\gamma_{\mathrm{r}}} d_{\gamma_{\mathrm{r}}}^h v_{\mathrm{p}} \, \mathrm{d}s + \int_{\gamma_{0,\mathrm{p}}} \frac{\partial \left(u - \tilde{u}_0^h \right)}{\partial \mathbf{n}_F} v_{\mathrm{p}} \, \mathrm{d}s.
\tag{8.35}
$$

Moreover, before combining (8.33) and (8.35), let us consider the sum of some of their terms, or more precisely, the sum of the terms integrating over $\gamma_{0,\mathrm{p}}$. That is, since $\mathbf{n}_0 = -\mathbf{n}_F$ on $\gamma_{0,\mathrm{p}}$, then for all $v \in H^{\frac{1}{2}}(\gamma_{0,\mathrm{p}})$,

$$
\int_{\gamma_{0,\mathrm{p}}} \frac{\partial \left(u - u_0^h \right)}{\partial \mathbf{n}_0} v \, \mathrm{d}s + \int_{\gamma_{0,\mathrm{p}}} \frac{\partial \left(u - \tilde{u}_0^h \right)}{\partial \mathbf{n}_F} v \, \mathrm{d}s
$$

$$
= \int_{\gamma_{0,\mathrm{p}}} \left(g_0 - \frac{\partial u_0^h}{\partial \mathbf{n}_0} \right) v \, \mathrm{d}s + \int_{\gamma_{0,\mathrm{p}}} \left(-g_0 - \frac{\partial \tilde{u}_0^h}{\partial \mathbf{n}_F} \right) v \, \mathrm{d}s
$$

$$
= \int_{\gamma_{0,\mathrm{p}}} j v \, \mathrm{d}s + \int_{\gamma_{0,\mathrm{p}}} d_{\gamma_{0,\mathrm{p}}}^h v \, \mathrm{d}s.
\tag{8.36}
$$

Therefore, recalling the definition of $\Gamma_N^0 := (\Gamma_N \setminus \gamma) \cup \gamma_0$ where $\gamma_0 = \mathrm{int}\left(\overline{\gamma_{0,\mathrm{n}}} \cup \overline{\gamma_{0,\mathrm{p}}} \right)$ and the definition of $\Sigma := \{ \gamma_{\mathrm{n}}, \gamma_{\mathrm{r}}, \gamma_{0,\mathrm{p}} \}$, let us combine (8.33) and (8.35), using (8.36). That

is, for all $v \in H^1_{0,\Gamma_D}(\Omega)$, taking $v_{\mathrm{n}} := v|_{\Omega_\star}$ in (8.33) and $v_{\mathrm{p}} := v|_{F_{\mathrm{p}}}$ in (8.35), we obtain

$$\int_\Omega \nabla e \cdot \nabla v \,\mathrm{d}x = \int_{\Omega_\star} \nabla e \cdot \nabla v \,\mathrm{d}x + \int_{F_{\mathrm{p}}} \nabla e \cdot \nabla v \,\mathrm{d}x$$
$$= \int_{\Omega_\star} rv \,\mathrm{d}x + \int_{F_{\mathrm{p}}} rv \,\mathrm{d}x + \int_{\Gamma^0_N \setminus \gamma_{0,\mathrm{n}}} jv \,\mathrm{d}s + \int_{\gamma_{\mathrm{s}}} jv \,\mathrm{d}s + \sum_{\sigma \in \Sigma} \int_\sigma d^h_\sigma v \,\mathrm{d}s. \tag{8.37}$$

Let us now fix $v \in H^1_{0,\Gamma_D}(\Omega)$. As in the proof of Theorem 8.2.2, the idea is to suitably extend the function v to Ω_0 and to $\tilde{F}_{\mathrm{p}}$ in order to correctly treat the elements and faces that are only partially in Ω, and to be able to use Galerkin orthogonality in the simplified domains Ω_0 and $\tilde{F}_{\mathrm{p}}$. However, recalling (5.15), Galerkin orthogonality in $\tilde{F}_{\mathrm{p}}$ is only valid for discrete functions that vanish on $\gamma_{0,\mathrm{p}}$. Therefore, using the generalized Stein extensions of Assumption 8.1.5 with $\Omega^1 := \Omega$ as we are considering the single feature case, let

$$v_0 := \mathsf{E}_{\Omega_\star \to \Omega_0} (v|_{\Omega_\star}) \in H^1_{0,\Gamma_D}(\Omega_0),$$
$$\tilde{v} := \mathsf{E}_{\Omega \to \tilde{\Omega}}(v) \in H^1_{0,\Gamma_D}(\tilde{\Omega}),$$
$$\text{and} \quad \tilde{v}_\star := \mathsf{E}_{\Omega_\star \to \tilde{\Omega}} (v|_{\Omega_\star}) \in H^1_{0,\Gamma_D}(\tilde{\Omega}).$$

In particular, we note that

$$v_0 = v \text{ on } \gamma_{\mathrm{n}}, \quad \tilde{v} = v \text{ on } \gamma_{\mathrm{r}}, \quad \tilde{v} = \tilde{v}_\star = v \text{ on } \gamma_{0,\mathrm{p}}. \tag{8.38}$$

Thus if we define $w := \tilde{v}|_{\tilde{F}_{\mathrm{p}}} - \tilde{v}_\star|_{\tilde{F}_{\mathrm{p}}}$, then from (8.38), $w \in H^1_{0,\gamma_{0,\mathrm{p}}}(\tilde{F}_{\mathrm{p}})$. Moreover, using properties (8.10)–(8.12) of the extension operators, then

$$\|\nabla v_0\|_{0,\Omega_0} \lesssim \|\nabla v\|_{0,\Omega_\star}, \quad \|\nabla \tilde{v}\|_{0,\tilde{\Omega}} \lesssim \|\nabla v\|_{0,\Omega} \quad \text{and} \quad \|\nabla \tilde{v}_\star\|_{0,\tilde{\Omega}} \lesssim \|\nabla v\|_{0,\Omega_\star}. \tag{8.39}$$

And since $\tilde{F}_{\mathrm{p}} \subset \tilde{\Omega}$ and $\Omega_\star \subset \Omega$, then using (8.39),

$$\|\nabla w\|_{0,\tilde{F}_{\mathrm{p}}} \le \|\nabla \tilde{v}\|_{0,\tilde{F}_{\mathrm{p}}} + \|\nabla \tilde{v}_\star\|_{0,\tilde{F}_{\mathrm{p}}} \le \|\nabla \tilde{v}\|_{0,\tilde{\Omega}} + \|\nabla \tilde{v}_\star\|_{0,\tilde{\Omega}}$$
$$\lesssim \|\nabla v\|_{0,\Omega} + \|\nabla v\|_{0,\Omega_\star} \lesssim \|\nabla v\|_{0,\Omega}. \tag{8.40}$$

Consequently, since $v = v_0$ on $\Omega_\star$ and $v = \tilde{v}$ on F_{p}, then (8.37) can be rewritten as

$$\int_\Omega \nabla e \cdot \nabla v \,\mathrm{d}x = \int_{\Omega_\star} rv_0 \,\mathrm{d}x + \int_{\Gamma^0_N \setminus \gamma_{0,\mathrm{n}}} jv_0 \,\mathrm{d}s + \int_{F_{\mathrm{p}}} r\tilde{v} \,\mathrm{d}x + \int_{\gamma_{\mathrm{s}}} j\tilde{v} \,\mathrm{d}s + \sum_{\sigma \in \Sigma} \int_\sigma d^h_\sigma v \,\mathrm{d}s. \tag{8.41}$$

Then, similarly to (8.17) and since $\Omega_\star = \Omega_0 \setminus \overline{F_{\mathrm{n}}}$ and $F_{\mathrm{p}} = \tilde{F}_{\mathrm{p}} \setminus \overline{G_{\mathrm{p}}}$, we add and subtract

terms to (8.41), and then we rearrange them, as follows:

$$
\begin{aligned}
\int_\Omega \nabla e \cdot \nabla v \, \mathrm{d}x &= \left(\int_{\Omega_0} r v_0 \, \mathrm{d}x - \int_{F_\mathrm{n}} r v_0 \, \mathrm{d}x \right) + \left(\int_{\Gamma_N^0} j v_0 \, \mathrm{d}s - \int_{\gamma_{0,\mathrm{n}}} j v_0 \, \mathrm{d}s \right) \\
&\quad + \left(\int_{\tilde{F}_\mathrm{p}} r \tilde{v} \, \mathrm{d}x - \int_{G_\mathrm{p}} r \tilde{v} \, \mathrm{d}s \right) + \left(-\int_{\tilde{F}_\mathrm{p}} r \tilde{v}_\star \, \mathrm{d}x + \int_{\tilde{F}_\mathrm{p}} r \tilde{v}_\star \, \mathrm{d}s \right) \\
&\quad + \left(\int_{\gamma_\mathrm{s} \cup \tilde{\gamma}} j \tilde{v} \, \mathrm{d}s - \int_{\tilde{\gamma}} j \tilde{v} \, \mathrm{d}s \right) + \left(-\int_{\gamma_\mathrm{s} \cup \tilde{\gamma}} j \tilde{v}_\star \, \mathrm{d}s + \int_{\gamma_\mathrm{s} \cup \tilde{\gamma}} j \tilde{v}_\star \, \mathrm{d}s \right) \\
&\quad + \sum_{\sigma \in \Sigma} \int_\sigma d_\sigma^h v \, \mathrm{d}s \\
&= \int_{\Omega_0} r v_0 \, \mathrm{d}x + \int_{\Gamma_N^0} j v_0 \, \mathrm{d}s - \int_{F_\mathrm{n}} r v_0 \, \mathrm{d}x - \int_{\gamma_{0,\mathrm{n}}} j v_0 \, \mathrm{d}s \\
&\quad + \int_{\tilde{F}_\mathrm{p}} r \left(\tilde{v} - \tilde{v}_\star \right) \mathrm{d}x - \int_{G_\mathrm{p}} r \tilde{v} \, \mathrm{d}s + \int_{\tilde{F}_\mathrm{p}} r \tilde{v}_\star \, \mathrm{d}s \\
&\quad + \int_{\gamma_\mathrm{s} \cup \tilde{\gamma}} j \left(\tilde{v} - \tilde{v}_\star \right) \mathrm{d}s - \int_{\tilde{\gamma}} j \tilde{v} \, \mathrm{d}s + \int_{\gamma_\mathrm{s} \cup \tilde{\gamma}} j \tilde{v}_\star \, \mathrm{d}s + \sum_{\sigma \in \Sigma} \int_\sigma d_\sigma^h v \, \mathrm{d}s. \\
&= \mathrm{I}_0 + \tilde{\mathrm{I}} + \mathrm{II}_\mathrm{n} + \tilde{\mathrm{II}}_\mathrm{p} + \mathrm{II}_\mathrm{p}, \quad\quad\quad\quad\quad\quad\quad\quad\quad\quad\quad (8.42)
\end{aligned}
$$

where, recalling that $\tilde{\Gamma}_N := \gamma_\mathrm{s} \cup \tilde{\gamma}$ and $w := \tilde{v}|_{\tilde{F}_\mathrm{p}} - \tilde{v}_\star|_{\tilde{F}_\mathrm{p}}$, and by simple rearrangement of the terms,

$$
\begin{aligned}
\mathrm{I}_0 &= \int_{\Omega_0} r v_0 \, \mathrm{d}x + \int_{\Gamma_N^0} j v_0 \, \mathrm{d}s, \\
\tilde{\mathrm{I}} &= \int_{\tilde{F}_\mathrm{p}} r w \, \mathrm{d}x + \int_{\tilde{\Gamma}_N} j w \, \mathrm{d}s, \\
\mathrm{II}_\mathrm{n} &= -\int_{F_\mathrm{n}} r v_0 \, \mathrm{d}x - \int_{\gamma_{0,\mathrm{n}}} j v_0 \, \mathrm{d}s + \int_{\gamma_\mathrm{n}} d_{\gamma_\mathrm{n}}^h v \, \mathrm{d}s, \\
\tilde{\mathrm{II}}_\mathrm{p} &= -\int_{G_\mathrm{p}} r \tilde{v} \, \mathrm{d}x - \int_{\tilde{\gamma}} j \tilde{v} \, \mathrm{d}s + \int_{\gamma_\mathrm{r}} d_{\gamma_\mathrm{r}}^h v \, \mathrm{d}s, \\
\mathrm{II}_\mathrm{p} &= \int_{\tilde{F}_\mathrm{p}} r \tilde{v}_\star \, \mathrm{d}x + \int_{\tilde{\Gamma}_N} j \tilde{v}_\star \, \mathrm{d}s + \int_{\gamma_{0,\mathrm{p}}} d_{\gamma_{0,\mathrm{p}}}^h v \, \mathrm{d}s.
\end{aligned}
$$

As terms I_0 and $\tilde{\mathrm{I}}$ are defined in Ω_0 and $\tilde{F}_\mathrm{p}$, respectively, and since $\mathcal{Q}_0$ is fitted to Ω_0 and $\tilde{\mathcal{Q}}$ is fitted to $\tilde{F}_\mathrm{p}$, then terms I_0 and $\tilde{\mathrm{I}}$, which account for the numerical error, are defined in unions of full elements. Moreover, terms II_n, II_p and $\tilde{\mathrm{II}}_\mathrm{p}$ account for the discrete defeaturing error and for the corresponding compatibility conditions (see Remark 3.4.2), and their contributions come from the presence of feature F; more specifically, they come from the presence of the negative component F_n, the positive component F_p, and the extension $\tilde{F}_\mathrm{p}$ of the latter.

Term I_0 can be estimated exactly as term I of (8.17), using Galerkin orthogonality coming from (3.4) and (5.13), properties (8.2) and (8.4) of the Scott-Zhang-type operator I_0^h,

and property (8.39) of the generalized Stein extension v_0 of v, leading to

$$\mathrm{I}_0 \lesssim \left(\sum_{K \in \mathcal{Q}_0} h_K^2 \|r\|_{0,K}^2 + \sum_{E \in \mathcal{E}_0} h_E \|j\|_{0,E}^2 \right)^{\frac{1}{2}} \|\nabla v\|_{0,\Omega_\star}.$$

Since $w \in H_{0,\gamma_{0,\mathrm{p}}}^1\left(\tilde{F}_{\mathrm{p}} \right)$ from (8.38), then term $\tilde{\mathrm{I}}$ can be estimated in the same manner. That is, let us use Galerkin orthogonality coming from (3.7) and (5.15), properties (8.3) and (8.5) of the Scott-Zhang-type operator $\tilde{I}^h$, and the generalized Stein extension property (8.40) of w, to obtain the following estimate:

$$\tilde{\mathrm{I}} \lesssim \left(\sum_{K \in \tilde{\mathcal{Q}}} h_K^2 \|r\|_{0,K}^2 + \sum_{E \in \tilde{\mathcal{E}}} h_E \|j\|_{0,E}^2 \right)^{\frac{1}{2}} \|\nabla w\|_{0,\tilde{F}_{\mathrm{p}}}.$$

Now, let us consider term II_{n} of (8.42). It can be estimated exactly as term II of (8.17) using the decomposition given in (8.22), replacing F, Ω, γ and γ_0 by F_{n}, $\Omega_\star$, γ_{n} and $\gamma_{0,\mathrm{n}}$ respectively. Therefore, using integration by parts in F_{n}, using the proof of Theorem 3.4.4, Friedrichs inequality of Lemma 2.3.5, the trace inequality of Lemma 2.2.2, and since $v_0 = v$ on γ_{n}, we obtain

$$\mathrm{II}_{\mathrm{n}} \lesssim \left(|\gamma_{\mathrm{n}}|^{\frac{1}{n-1}} \left\| d_{\gamma_{\mathrm{n}}}^h - \overline{d_{\gamma_{\mathrm{n}}}^h}^{\gamma_{\mathrm{n}}} \right\|_{0,\gamma_{\mathrm{n}}}^2 + c_{\gamma_{\mathrm{n}}}^2 |\gamma_{\mathrm{n}}|^{\frac{n}{n-1}} \left| \overline{d_{\gamma_{\mathrm{n}}}}^{\gamma_{\mathrm{n}}} \right|^2 \right)^{\frac{1}{2}} \|\nabla v\|_{0,\Omega_\star}$$
$$+ \left(h_{F_{\mathrm{n}}}^2 \|r\|_{0,F_{\mathrm{n}}}^2 + h_{F_{\mathrm{n}}} \|j\|_{0,\gamma_{0,\mathrm{n}}}^2 \right)^{\frac{1}{2}} \|\nabla v\|_{0,\Omega_\star}.$$

After observing that $G_{\mathrm{p}} := \tilde{F}_{\mathrm{p}} \setminus \overline{F_{\mathrm{p}}}$ can be seen as a negative feature of the geometry F_{p} for which $\tilde{\gamma}$ is the simplified boundary replacing γ_{r}, and for which $\gamma_{0,\mathrm{p}}$ is the Dirichlet boundary, then term $\tilde{\mathrm{II}}_{\mathrm{p}}$ can be estimated in the same manner as term II_{n}. That is, using integration by parts in G_{p}, using the proof of Theorem 3.4.4, Friedrichs inequality of Lemma 2.3.5, the trace inequality of Lemma 2.2.2, and since $\tilde{v} = v$ on γ_{r}, we obtain

$$\tilde{\mathrm{II}}_{\mathrm{p}} \lesssim \left(|\gamma_{\mathrm{r}}|^{\frac{1}{n-1}} \left\| d_{\gamma_{\mathrm{r}}}^h - \overline{d_{\gamma_{\mathrm{r}}}^h}^{\gamma_{\mathrm{r}}} \right\|_{0,\gamma_{\mathrm{r}}}^2 + c_{\gamma_{\mathrm{r}}}^2 |\gamma_{\mathrm{r}}|^{\frac{n}{n-1}} \left| \overline{d_{\gamma_{\mathrm{r}}}}^{\gamma_{\mathrm{r}}} \right|^2 \right)^{\frac{1}{2}} \|\nabla v\|_{0,\Omega}$$
$$+ \left(h_{G_{\mathrm{p}}}^2 \|r\|_{0,G_{\mathrm{p}}}^2 + h_{G_{\mathrm{p}}} \|j\|_{0,\tilde{\gamma}}^2 \right)^{\frac{1}{2}} \|\nabla v\|_{0,\Omega}.$$

Finally, since

$$d_{\gamma_{0,\mathrm{p}}}^h - \frac{\partial \left(\tilde{u}_0 - \tilde{u}_0^h \right)}{\partial \mathbf{n}_F} = d_{\gamma_{0,\mathrm{p}}}$$

and since $\tilde{v}_\star = v$ on $\gamma_{0,\mathrm{p}}$ from (8.38), we can again apply the same steps to estimate II_{p}. To do so, we replace F, Ω, γ and γ_0 by $\tilde{F}_{\mathrm{p}}$, $\Omega_\star$, $\gamma_{0,\mathrm{p}}$ and $\tilde{\Gamma}_N$, respectively, in the estimation of II from (8.22). Therefore, using integration by parts in $\tilde{F}_{\mathrm{p}}$, using the proof of Theorem 3.4.4, Friedrichs inequality of Lemma 2.3.5 and the trace inequality of

Lemma 2.2.2, we obtain

$$
\begin{aligned}
\text{II}_{\text{p}} \lesssim & \left(|\gamma_{0,\text{p}}|^{\frac{1}{n-1}} \left\| d^h_{\gamma_{0,\text{p}}} - \overline{d^h_{\gamma_{0,\text{p}}}}^{\gamma_{0,\text{p}}} \right\|^2_{0,\gamma_{0,\text{p}}} + c^2_{\gamma_{0,\text{p}}} |\gamma_{0,\text{p}}|^{\frac{n}{n-1}} \left| \overline{d_{\gamma_{0,\text{p}}}}^{\gamma_{0,\text{p}}} \right|^2 \right)^{\frac{1}{2}} \|\nabla v\|_{0,\Omega_\star} \\
& + \left(h^2_{\tilde{F}_{\text{p}}} \|r\|^2_{0,\tilde{F}_{\text{p}}} + h_{\tilde{F}_{\text{p}}} \|j\|^2_{0,\gamma_{0,\text{p}}} \right)^{\frac{1}{2}} \|\nabla v\|_{0,\Omega_\star}.
\end{aligned}
$$

Consequently, plugging in the last five inequalities into (8.42), since $\Omega = \text{int}\left(\overline{\Omega_\star} \cup \overline{F_{\text{p}}}\right)$, using the discrete Cauchy-Schwarz inequality, and recalling the definition of $\mathscr{E}\left(u^h_{\text{d}}\right)$ in (8.29), we get

$$
\int_\Omega \nabla e \cdot \nabla v \, dx \lesssim \left[\mathscr{E}\left(u^h_{\text{d}}\right)^2 + \text{III}^2 \right]^{\frac{1}{2}} \|\nabla v\|_{0,\Omega}, \tag{8.43}
$$

where the terms of I_0 and $\tilde{\text{I}}$ contribute to the numerical error part $\mathscr{E}_N\left(u^h_{\text{d}}\right)$ of the estimator, the first terms in II_{n}, $\tilde{\text{II}}_{\text{p}}$ and II_{p} contribute to the defeaturing error part $\mathscr{E}_D\left(u^h_{\text{d}}\right)$ (and thus $\mathscr{E}_C$) of the estimator, while their last terms are collected in III, which is defined as

$$
\text{III}^2 := h^2_{F_{\text{n}}} \|r\|^2_{0,F_{\text{n}}} + h_{F_{\text{n}}} \|j\|^2_{0,\gamma_{0,\text{n}}} + h^2_{G_{\text{p}}} \|r\|^2_{0,G_{\text{p}}} + h_{G_{\text{p}}} \|j\|^2_{0,\tilde{\gamma}} + h^2_{\tilde{F}_{\text{p}}} \|r\|^2_{0,\tilde{F}_{\text{p}}} + h_{\tilde{F}_{\text{p}}} \|j\|^2_{0,\gamma_{0,\text{p}}}.
$$

From Assumption 8.2.5, $h_S \lesssim h^{\min}_S$ for all $S \in \left\{ F_{\text{n}}, G_{\text{p}}, \tilde{F}_{\text{p}} \right\}$. Thus for all $K \in \mathcal{Q}_0$ such that $K \cap F_{\text{n}} \neq \emptyset$, $h_{F_{\text{n}}} \lesssim h_K$, for all $K \in \tilde{\mathcal{Q}}$ such that $K \cap G_{\text{p}} \neq \emptyset$, $h_{G_{\text{p}}} \lesssim h_K$, and for all $K \in \tilde{\mathcal{Q}}$ such that $K \cap \tilde{F}_{\text{p}} \neq \emptyset$, $h_{\tilde{F}_{\text{p}}} \lesssim h_K$. Consequently, term III from (8.43) can be rewritten as (8.25) for the negative feature case, leading to

$$
\text{III} \lesssim \mathscr{E}_N\left(u^h_{\text{d}}\right). \tag{8.44}
$$

Therefore, combining (8.43) and (8.44),

$$
\int_\Omega \nabla e \cdot \nabla v \, dx \lesssim \left[\mathscr{E}\left(u^h_{\text{d}}\right)^2 + \mathscr{E}_N\left(u^h_{\text{d}}\right)^2 \right]^{\frac{1}{2}} \|\nabla v\|_{0,\Omega} \simeq \mathscr{E}\left(u^h_{\text{d}}\right) \|\nabla v\|_{0,\Omega}. \tag{8.45}
$$

To conclude, we choose $v = e \in H^1_{0,\Gamma_D}(\Omega)$ in (8.45), and we simplify $\|\nabla e\|_{0,\Omega}$ on both sides. $\qquad \square$

8.2.3   Geometry with multiple features

In this section, we further extend the result of Section 8.2.2 by stating and proving the reliability of the proposed *a posteriori* estimator of the discrete defeaturing error in a geometry with multiple complex features. So let

$$
\mathfrak{F} := \left\{ F^k \right\}^{N_f}_{k=1}
$$

be the set of $N_f \geq 1$ complex features of Ω, and let us use the notation of Section 8.1. In particular, we recall that the multi-feature notation is similar to the one used in the previous Section 8.2.2, but the upper index k is added to every quantity referring to feature F^k, for all $k = 1, \ldots, N_f$. We also recall that

$$\Sigma := \{\gamma_{\mathrm{n}}^k, \gamma_{0,\mathrm{p}}^k, \gamma_{\mathrm{r}}^k : k = 1, \ldots, N_f\}.$$

In this context, the discrete defeaturing error estimator has already been defined in (5.21), that is,

$$\mathscr{E}\left(u_{\mathrm{d}}^h\right) := \left[\alpha_D^2 \mathscr{E}_D\left(u_{\mathrm{d}}^h\right)^2 + \alpha_N^2 \mathscr{E}_N\left(u_{\mathrm{d}}^h\right)^2\right]^{\frac{1}{2}}, \tag{8.46}$$

where $\mathscr{E}_D\left(u_{\mathrm{d}}^h\right)$ and $\mathscr{E}_N\left(u_{\mathrm{d}}^h\right)$ are defined as in (8.30), and α_D and α_N are parameters to be tuned as in the single feature case.

Let us now state and prove the main theorem of this section, in the case in which every feature in $\mathfrak{F}$ verifies Assumption 8.2.5.

Theorem 8.2.7. *In the framework presented in Section 8.1, let u be the weak solution of problem (3.2), and let u_{d}^h be the discrete defeaturing solution defined in (8.1), where Ω is a geometry containing $N_f \geq 1$ complex features satisfying Assumptions 4.1.5 and 8.2.5. Then, the energy norm of the discrete defeaturing error is bounded in terms of the estimator $\mathscr{E}\left(u_{\mathrm{d}}^h\right)$ defined in (8.46) as follows:*

$$\left|u - u_{\mathrm{d}}^h\right|_{1,\Omega} \lesssim \mathscr{E}\left(u_{\mathrm{d}}^h\right). \tag{8.47}$$

Proof. The proof is very similar to the one of Theorem 8.2.6. That is, following the same steps and letting $e := u - u_{\mathrm{d}}^h$, we can write for all $v \in H_{0,\Gamma_D}^1(\Omega)$,

$$\int_\Omega \nabla e \cdot \nabla v \, \mathrm{d}x = \mathrm{I}_0 + \sum_{k=1}^{N_f} \left(\tilde{\mathrm{I}}^k + \mathrm{II}_{\mathrm{n}}^k + \tilde{\mathrm{II}}_{\mathrm{p}}^k + \mathrm{II}_{\mathrm{p}}^k\right), \tag{8.48}$$

where I_0 is defined as in (8.42), and for all $k = 1, \ldots, N_f$, $\tilde{\mathrm{I}}^k$, $\mathrm{II}_{\mathrm{n}}^k$, $\tilde{\mathrm{II}}_{\mathrm{p}}$ and $\mathrm{II}_{\mathrm{p}}^k$ are defined as $\tilde{\mathrm{I}}$, II_{n}, $\tilde{\mathrm{II}}_{\mathrm{p}}$ and II_{p} from (8.42), but for feature F^k. Then, these terms can be estimated as in the proof of Theorem 8.2.6. In particular, for the hidden constant in (8.47) to be independent of N_f, we use Assumptions 4.1.5 and 8.1.5 and the discrete Cauchy-Schwarz inequality. $\square$

8.3 The adaptive defeaturing strategy on complex spline geometries

In the previous section, we assumed that the considered mesh was fitting the boundary of the simplified domain Ω_0. In a geometric adaptive setting as presented in Chapter 5,

adding a new feature would require re-meshing the domain in order to satisfy this assumption. To avoid this, the REFINE step presented in Section 5.4.4 is designed to be used with a mesh-preserving method, which allows to take advantage of the efforts made by standard h-refinement in the previous iterations. In this section, we study how the adaptive analysis-aware defeaturing strategy presented in Chapter 5 can be performed in the special case of IGA with THB-splines. In particular, we use two mesh-preserving methods introduced in Chapter 6, which are trimming and multipatch geometry techniques.

To illustrate this section, let us take the example of an exact geometry Ω that contains at least two complex features (with both a positive and a negative component), and such that at some iteration of the adaptive strategy presented in Chapter 6, one feature is required to be added to the defeatured geometrical model Ω_0. Then, the negative component of this feature is added by trimming, while its positive component is added with an extra (possibly trimmed) patch. Therefore, Ω_0 is a trimmed multipatch domain at the next iteration, and the adaptive strategy needs to be precised in this case.

Considering trimmed multipatch domains also considerably extends the range of fully defeatured geometries that one can treat in the presented adaptive IGA defeaturing framework. Indeed, the image of a single isogeometric mapping $\mathbf{F}$ (see Chapter 6), called patch, limits the definition of Ω_0: it only allows for geometries that are images of the unit square if $n = 2$ or the unit cube if $n = 3$. However, the previously introduced setting can easily be generalized to open connected domains defined by $N_p \geq 1$ trimmed patches, glued together with C^0-continuity. Consequently, we explain in this section the required modifications of the SOLVE and ESTIMATE steps in the case of IGA in trimmed domains, and then we discuss its generalization to trimmed multipatch domains. To finish this section, we provide details of the REFINE step, in the most general context of trimmed multipatch defeatured geometries Ω_0 for which the exact geometry Ω contains multiple features.

8.3.1   Defeaturing trimmed multipatch domains

In this section, we first discuss the generalization of Section 8.2 and of the discrete defeaturing error estimator (8.46) to a single patch trimmed geometry Ω_0, relying on Chapter 7. The main differences come from the fact that the discrete spline space contains functions whose support are cut by the trimming boundary. In the numerical contribution of the error estimator $\mathscr{E}(u_{\mathrm{d}}^h)$, one therefore needs to adapt the mesh-dependent scaling factors in front of the residuals.

To do so, let us assume that Ω contains $N_f \geq 1$ complex features, and that its corresponding defeatured geometry Ω_0 is a domain trimmed from $\Omega_0^{\mathrm{u}} \subset \mathbb{R}^n$, as illustrated in

(a) Non-trimmed domain Ω_0^{u} with a hierarchical mesh $\mathcal{Q}_0^{\mathrm{u}}$.

(b) Trimmed defeatured domain Ω_0 with the hierarchical mesh $\mathcal{Q}_0^{\mathrm{u}}$ and the trimmed curve Γ_0^{t}.

(c) Exact domain Ω with a negative feature F, and the active mesh $\mathcal{Q}_0$ corresponding to Ω_0.
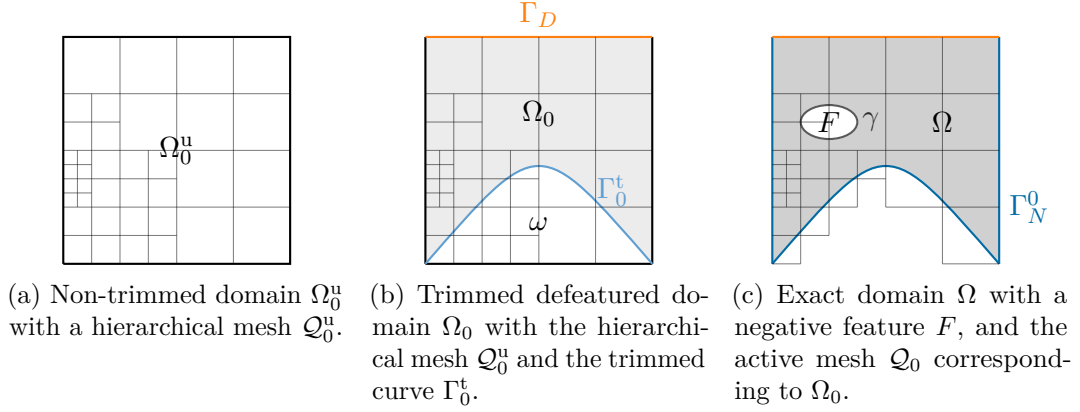
Figure 8.5 – Example of a trimmed defeatured geometry with the corresponding notation.

Figure 8.5. That is,

$$\Omega_0 := \Omega_0^{\mathrm{u}} \setminus \overline{\omega} \subset \mathbb{R}^n, \tag{8.49}$$

where ω is a union of bounded open domains in $\mathbb{R}^n$. For simplicity, assume that Neumann boundary conditions are imposed on the trimmed boundary, i.e.,

$$\Gamma_0^{\mathrm{t}} := \partial\Omega_0 \setminus \overline{\partial\Omega_0^{\mathrm{u}}} \subset \Gamma_N^0. \tag{8.50}$$

Otherwise, the imposition of Dirichlet boundary conditions on the trimmed boundary must be performed in a weak sense, and it would require stabilization techniques, see e.g., [Buffa et al., 2020].

Moreover, let $\mathcal{Q}_0^{\mathrm{u}} := \mathcal{Q}(\Omega_0^{\mathrm{u}})$ from (6.12) be (a refinement of) the hierarchical physical mesh on Ω_0^{u}, and let $\mathcal{E}_0^{\mathrm{u}}$ be the set of faces E of $\mathcal{Q}_0^{\mathrm{u}}$ such that $|E \cap \Gamma_N^0| > 0$. Furthermore, for all $k = 1, \ldots, N_f$, let the positive component extension $\tilde{F}_{\mathrm{p}}^k$ of feature F^k be a standard THB-spline domain as in Section 8.1, let $\tilde{\mathcal{Q}}^k := \mathcal{Q}\left(\tilde{F}_{\mathrm{p}}^k\right)$ be (a refinement of) the hierarchical mesh on $\tilde{F}_{\mathrm{p}}^k$, and let $\tilde{\mathcal{E}}^k$ be the set of faces of $\tilde{\mathcal{Q}}^k$ that are part of $\tilde{\Gamma}_N^k$ for all $k = 1, \ldots, N_f$, as in (5.26). We suppose that $\mathcal{Q}_0^{\mathrm{u}}$ and $\tilde{\mathcal{Q}}^k$, $k = 1, \ldots, N_f$, satisfy Assumptions 8.1.1 and 8.1.2. Then we redefine

$$\mathcal{Q} := \mathcal{Q}_{\mathrm{cut}} \cup \mathcal{Q}_{\mathrm{act}} \tag{8.51}$$

to be the union of the active mesh elements (i.e., the elements intersecting Ω_0 and all $\tilde{F}_{\mathrm{p}}^k$), where

$$\mathcal{Q}_{\mathrm{cut}} := \{K \in \mathcal{Q}_0^{\mathrm{u}} : K \cap \Omega_0 \neq K, |K \cap \Omega_0| > 0\}$$

is the set of cut (trimmed) elements, and

$$\mathcal{Q}_{\mathrm{act}} := \{K \in \mathcal{Q}_0^{\mathrm{u}} : K \subset \Omega_0\} \cup \tilde{\mathcal{Q}} \quad \text{with} \quad \tilde{\mathcal{Q}} := \bigcup_{k=1}^{N_f} \tilde{\mathcal{Q}}^k$$

is the set composed of the other active (non-trimmed) elements in Ω_0 and in all $\tilde{F}_{\mathrm{p}}^k$. Similarly, let

$$\mathcal{E} := \mathcal{E}_{\mathrm{cut}} \cup \mathcal{E}_{\mathrm{act}},$$

where

$$\mathcal{E}_{\mathrm{cut}} := \left\{ E \in \mathcal{E}_0^{\mathrm{u}} : E \cap \Gamma_N^0 \neq E \right\}$$

$$\text{and} \quad \mathcal{E}_{\mathrm{act}} := \left\{ E \in \mathcal{E}_0^{\mathrm{u}} : E \subset \Gamma_N^0 \right\} \cup \tilde{\mathcal{E}} \quad \text{with} \quad \tilde{\mathcal{E}} := \bigcup_{k=1}^{N_f} \tilde{\mathcal{E}}^k. \tag{8.52}$$

Finally, for all $K \in \mathcal{Q}$, let

$$\Gamma_K^{\mathrm{t}} := \Gamma_0^{\mathrm{t}} \cap \mathrm{int}(K) \qquad \text{and} \qquad \Omega_K := \begin{cases} \Omega_0 & \text{if } K \in \mathcal{Q}_0 \\ \tilde{F}_{\mathrm{p}} & \text{if } K \in \tilde{\mathcal{Q}}, \end{cases} \tag{8.53}$$

and for all $E \in \mathcal{E}$, let

$$\Gamma_N^E := \begin{cases} \Gamma_N^0 & \text{if } E \in \mathcal{E}_0 \\ \tilde{\Gamma}_N & \text{if } E \in \tilde{\mathcal{E}}. \end{cases} \tag{8.54}$$

In this framework, one can SOLVE the defeaturing problem as presented in Section 5.4.1. Then, to ESTIMATE the error, the numerical error contribution $\mathscr{E}_N\left(u_{\mathrm{d}}^h\right)$ of the discrete defeaturing error estimator $\mathscr{E}\left(u_{\mathrm{d}}^h\right)$ defined in (8.46) needs to be redefined as follows:

$$\mathscr{E}_N\left(u_{\mathrm{d}}^h\right)^2 := \sum_{K \in \mathcal{Q}} \delta_K^2 \|r\|_{0,K\cap\Omega_K}^2 + \sum_{E \in \mathcal{E}} \delta_E \|j\|_{0,E\cap\Gamma_N^E}^2 + \sum_{K \in \mathcal{Q}_{\mathrm{cut}}} h_K \|j\|_{0,\Gamma_K^{\mathrm{t}}}^2, \tag{8.55}$$

where

$$\delta_K := \begin{cases} h_K & \text{if } K \in \mathcal{Q}_{\mathrm{act}} \\ c_{K\cap\Omega_K} |K \cap \Omega_K|^{\frac{1}{n}} & \text{if } K \in \mathcal{Q}_{\mathrm{cut}}, \end{cases}$$

$$\text{and} \quad \delta_E := \begin{cases} h_E^{\frac{1}{2}} & \text{if } K \in \mathcal{E}_{\mathrm{act}} \\ c_{E\cap\Gamma_N^E} \left| E \cap \Gamma_N^E \right|^{\frac{1}{2(n-1)}} & \text{if } E \in \mathcal{E}_{\mathrm{cut}}, \end{cases} \tag{8.56}$$

and $c_{K\cap\Omega_K}$ and $c_{E\cap\Gamma_N^E}$ are defined as in (5.20). Term $\mathscr{E}_D\left(u_{\mathrm{d}}^h\right)$ of the estimator (8.46) remains unchanged.

Then with the help of Chapter 7, the proof of Theorem 8.2.7 can straightforwardly be generalized to this framework under the following technical assumption replacing Assumption 8.2.5:

Assumption 8.3.1. For $S \in \left\{F_{\mathrm{n}}^k, G_{\mathrm{p}}^k, \tilde{F}_{\mathrm{p}}^k\right\}_{k=1}^{N_f}$, let $h_S := \mathrm{diam}(S)$, let

$$
\mathcal{Q}_S = \begin{cases} \mathcal{Q}_0 & \text{if } S = F_{\mathrm{n}}^k \text{ for some } k = 1, \ldots, N_f \\ \tilde{\mathcal{Q}}^k & \text{if } S = G_{\mathrm{p}}^k \text{ or } S = \tilde{F}_{\mathrm{p}}^k \text{ for some } k = 1, \ldots, N_f, \end{cases}
$$

and let

$$
\delta_S^{\min} := \min \left\{\delta_K : K \in \mathcal{Q}_S, \, K \cap S \neq \emptyset\right\}.
$$

Assume that $h_S \lesssim \delta_S^{\min}$, that is, each feature is either smaller or about the same size as the trimmed mesh that covers it.

Unfortunately, in the trimmed case, this technical assumption affects the generality of the result since $\delta_S^{\min}$ depends on the trimming boundary. As in the non-trimmed case, and as suggested by some numerical experiments presented in Section 8.4, we will see that this assumption can be removed in practice.

Remark 8.3.2. The feature extension $\tilde{F}_{\mathrm{p}}^k$ could also be a trimmed domain for some (or all) $k = 1, \ldots, N_f$, and this section easily extends to this case. However, since $\tilde{F}_{\mathrm{p}}^k$ is chosen to be a simple domain containing F_{p}^k, then it is more naturally thought as a non-trimmed domain.

Now, assume that Ω_0 is a trimmed multipatch geometry, for which patches are glued together with C^0-continuity. Then we need to include the jumps between patches of the normal derivative of u_{d}^h, in the numerical contribution (8.55) of the discrete defeaturing error estimator (8.46). Under Assumption 8.3.1, and if we assume that the trimmed boundary does not intersect the interfaces between patches, the proof of Theorem 8.2.7 could easily be adapted to this framework. Indeed, its generalization to trimmed geometries has just been discussed. And if one is able to build a Scott-Zhang type operator as in Theorem 6.3.4 but on a multipatch domain, then it would be enough to add the normal derivative jump contributions to all terms in (8.48) (or equivalently in (8.42)), and the proof of Theorem 7.2.3 from Chapter 7 would readily be extended in the same way. Even if details are not given, the construction of such a Scott-Zhang type operator for (T)HB-splines on multipatch domains is discussed in [Buffa et al., 2021b, Section 6.1.5].

Remark 8.3.3. Not only Ω_0, but also the feature extension $\tilde{F}_{\mathrm{p}}^k$ could be a (possibly trimmed) multipatch domain for some $k = 1, \ldots, N_f$. In fact, since $\tilde{F}_{\mathrm{p}}^k$ is chosen to be a simple domain containing F_{p}^k, then it is more naturally thought as a single patch domain. But since its definition requires $\gamma_{0,\mathrm{p}} \subset \partial \tilde{F}_{\mathrm{p}}^k$ and $F_{\mathrm{p}}^k \subset \tilde{F}_{\mathrm{p}}^k$, then one sometimes has to build it as a multipatch geometry; an example is given in Figure 8.6.

(a) Domain with a general complex feature.

(b) Domain $\Omega_\star$ with the simplified extension $\tilde{F}_{\mathrm{p}}$ of the positive component F_{p}.

Figure 8.6 – Example of domain containing one feature whose simplified positive component $\tilde{F}_{\mathrm{p}}$ cannot be represented by a single patch.

8.3.2 Refine by preserving properties of meshes and discrete spaces

In this section, we make more precise the REFINE step of the adaptive analysis-aware defeaturing strategy presented in Chapter 5, in the context of IGA on multipatch trimmed geometries. First, we develop on the mesh refinement step; then, we develop on the update of the (partially) defeatured geometrical model. Note that one could equally choose to refine the geometrical model first, and then refine the mesh.

8.3.2.1 Mesh refinement step

To start the adaptive strategy, we always assume that the simplified domains Ω_0 and $\tilde{F}_{\mathrm{p}}^k$ for all $k = 1, \ldots, N_f$ are defined over the coarsest possible hierarchical mesh and not on a refinement of it, so that coarsening is not needed during the adaptive process. Then, we need to make sure that at each iteration, the refined meshes and corresponding discrete spaces satisfy Assumptions 5.3.1 and 8.1.2. That is, for all $k = 1, \ldots, N_f$, we need to enforce the compatibility of traces on $\gamma_{0,\mathrm{p}}^k$ between $V^h(\Omega_0)$ and $V^h\left(\tilde{F}_{\mathrm{p}}^k\right)$, and we need to preserve the class of $\mathcal{T}$-admissibility of all meshes, $\mathcal{Q}_0$ and $\tilde{\mathcal{Q}}^k$. To do so, we extend the mesh refinement strategy presented in [Buffa and Giannelli, 2016] and exposed in Chapter 7, that ensures the refined mesh to be of the same class of $\mathcal{T}$-admissibility $\mathfrak{m}$ as the original mesh. More precisely, if we decompose the set of marked elements as $\mathcal{M} = \mathcal{M}_0 \cup \tilde{\mathcal{M}}$, where $\mathcal{M}_0 \subset \mathcal{Q}_0$ and $\tilde{\mathcal{M}} := \bigcup_{k=1}^{N_f} \tilde{\mathcal{M}}^k$ with $\tilde{\mathcal{M}}^k \subset \tilde{\mathcal{Q}}^k$ for all $k = 1, \ldots, N_f$, and if we recall the definition (6.13) of $\mathcal{T}$-neighborhood of an element, then the refinement procedure that guarantees Assumptions 5.3.1 and 8.1.2 is given in Algorithm 3.

Algorithm 2 from Chapter 7 is called on lines 1 and 6 of Algorithm 3: it serves the scope of preserving the class of $\mathcal{T}$-admissibility of the given mesh, and it is called for all meshes $\mathcal{Q}_0$ and $\tilde{\mathcal{Q}}^k$, $k = 1, \ldots, N_f$. We recall that it finds the elements that are not originally marked, but which need to be refined in order to preserve the class of $\mathcal{T}$-admissibility. These elements are added to the original set of elements to be refined.

Algorithm 3

$\left[\mathcal{Q}_0, \tilde{\mathcal{Q}}\right] = \text{REFINE}(\mathcal{Q}_0, \tilde{\mathcal{Q}}, \mathcal{M}_0, \tilde{\mathcal{M}}, \mathfrak{m}, \gamma_{0,\mathrm{p}})$

1: $\mathcal{M}_0 \leftarrow \text{MARK\_RECURSIVE}(\mathcal{Q}_0, \mathcal{M}_0, \mathfrak{m})$

2: **for all** $k = 1, \ldots, N_f$ **do**
3:     **for each** $\tilde{K} \in \tilde{\mathcal{Q}}^k$ such that there exists $K \in \mathcal{M}_0$ with $\partial K \cap \gamma_{0,\mathrm{p}}^k = \partial \tilde{K} \cap \gamma_{0,\mathrm{p}}^k \neq \emptyset$
4:         $\tilde{\mathcal{M}}^k \leftarrow \tilde{\mathcal{M}}^k \cup \left\{\tilde{K}\right\}$
5:     **end for**

6:     $\tilde{\mathcal{M}}^k \leftarrow \text{MARK\_RECURSIVE}(\tilde{\mathcal{Q}}^k, \tilde{\mathcal{M}}^k, \mathfrak{m})$
7:     Subdivide all $K \in \tilde{\mathcal{M}}^k$ and update $\tilde{\mathcal{Q}}^k$ by replacing K with its children.
8: **end for**

9: Subdivide all $K \in \mathcal{M}_0$ and update $\mathcal{Q}_0$ by replacing K with its children.
    return $\left[\mathcal{Q}_0, \tilde{\mathcal{Q}}\right]$
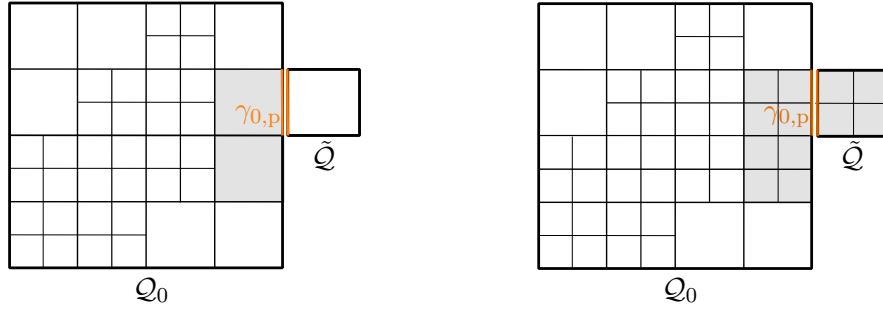
(a) Meshes $\mathcal{Q}_0$ and $\tilde{\mathcal{Q}}$ before refinement. Marked elements are in gray.

(b) Meshes $\mathcal{Q}_0$ and $\tilde{\mathcal{Q}}$ after refinement. Refined elements are in gray. The element of $\tilde{\mathcal{Q}}$ has been refined since the corresponding element of $\mathcal{Q}_0$ on the other side of $\gamma_{0,\mathrm{p}}$ is refined.

Figure 8.7 – Illustration of the refinement procedure.

Moreover, lines 3 to 5 of Algorithm 3 are added to the standard algorithm in order to take care of the positive component of feature F^k, for all $k = 1, \ldots, N_f$. More precisely, for each element of $\mathcal{Q}_0$ which has a face on $\gamma_{0,\mathrm{p}}^k$ and which is marked for refinement (either because it belongs to $\mathcal{M}_0$, or because it is used to preserve the class of $\mathcal{T}$-admissibility of $\mathcal{Q}_0$), we also mark for refinement the corresponding element of $\tilde{\mathcal{Q}}^k$ which is on the other side of the face, if any. This is illustrated in Figure 8.7. Note that it is not necessary to do this in the other direction, i.e., if we refine an element of $\tilde{\mathcal{Q}}^k$ which has a face on $\gamma_{0,\mathrm{p}}^k$, we do not need to refine the corresponding element of $\mathcal{Q}_0$ which is on the other side of the face, if any.

8.3.2.2   Geometric refinement step

Let $\Omega_0^{(i)}$ be the partially defeatured domain at iteration i of the adaptive procedure of Chapter 5, and from the set of marked features $\left\{F^k\right\}_{k\in I_{\mathrm{m}}}$, we follow (4.94) and (4.95) to build the partially defeatured domain $\Omega_0^{(i+1)}$ at iteration $i+1$. That is, in the first half step (4.94), domain $\Omega_0^{\left(i+\frac{1}{2}\right)}$ is built by trimming as in (6.22): the negative part of marked features $\bigcup_{k\in I_{\mathrm{m}}} F_{\mathrm{n}}^k$ is trimmed from $\Omega_0^{(i)}$ to obtain $\Omega_0^{\left(i+\frac{1}{2}\right)}$. Then from definition (4.3) of G_{p}^k, for all $k\in I_{\mathrm{m}}$,

$$F_{\mathrm{p}}^k = \tilde{F}_{\mathrm{p}}^k \setminus \overline{G_{\mathrm{p}}^k}.$$

So F_{p}^k is built by trimming as in (6.22), that is, G_{p}^k is trimmed from $\tilde{F}_{\mathrm{p}}^k$ to obtain F_{p}^k. Finally, in the second half step (4.95), we glue together the patches of $\Omega_0^{\left(i+\frac{1}{2}\right)}$ with the patches of F_{p}^k for all $k\in I_{\mathrm{m}}$ with C^0-continuity as in (6.20), and we obtain $\Omega_0^{(i+1)}$.

8.4   Numerical experiments

In this section, we perform numerical experiments to illustrate the validity of the proposed *a posteriori* discrete defeaturing error estimator (8.46), generalized to trimmed multipatch domains in Section 8.3. Thanks to these experiments, we also demonstrate that the adaptive procedure introduced in Chapter 5, and made more precise in the IGA framework in the present chapter, ensures the convergence of the discrete defeaturing error $\left|u-u_{\mathrm{d}}^h\right|_{1,\Omega}$. The proposed strategy combining mesh and geometric adaptivity has been implemented on top of the already-existing THB-spline based isogeometric mesh refinement strategy of *GeoPDEs* [Vázquez, 2016]. In particular, a specific module has been created for defeaturing, that takes care of the estimation of the contribution $\mathscr{E}_D\left(u_{\mathrm{d}}^h\right)$, and of the adaptive construction of partially defeatured geometries using multipatch and trimming techniques.

If not otherwise specified, THB-splines of degree $P=2$ are used in this section. Moreover, we call N_{dof} the total number of active degrees of freedom of the considered geometrical model Ω_0. More precisely, N_{dof} accounts for the number of active degrees of freedom in Ω_0, from which we add the number of active degrees of freedom in $\tilde{F}^k$ for all $k=1,\ldots,N_f$. If at some point, all features are added to the geometrical model, that is, if the geometrical model is the exact geometry Ω, then N_{dof} accounts for the total number of active degrees of freedom in Ω.

8.4.1   Convergence of the discrete defeaturing error and estimator

With the two numerical experiments presented in this section, we analyze the convergence of the proposed estimator with respect to the mesh size h and with respect to the size of a

(a) Exact domain Ω_ε.

(b) Patches (in black) and initial elements (in gray) used for the geometrical description of Ω_0.
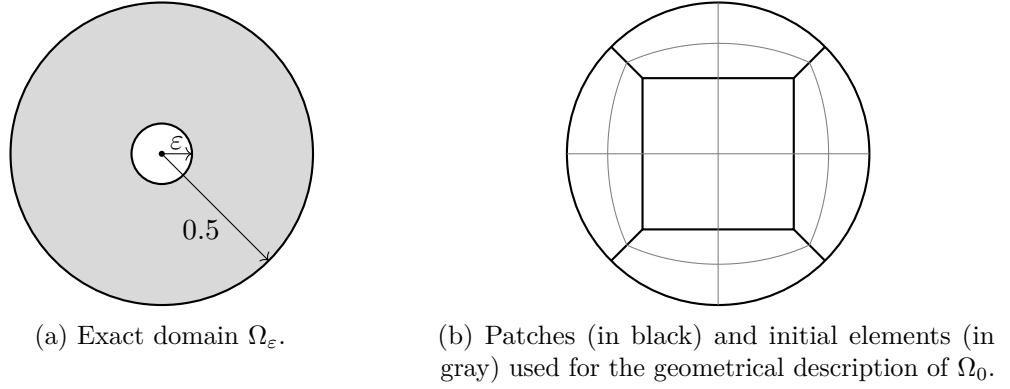
Figure 8.8 – Numerical test 8.4.1.1 – Exact and defeatured domains used for the convergence analysis.

given feature. We also compare the convergence of the estimator with the convergence of the discrete defeaturing error. The first experiment is performed in a geometry with one negative feature, while the second one is performed in a geometry containing one positive feature. In both experiments of this section, we only consider global mesh refinements without performing the proposed adaptive strategy yet, and we consider $\alpha_D = \alpha_N = 1$.

8.4.1.1 Negative feature

In this experiment, we consider a geometry with one negative feature. More precisely, for $k = -3, -2, \ldots, 6$, let $\varepsilon = \dfrac{10^{-2}}{2^k}$ and let $\Omega_\varepsilon := \Omega_0 \setminus \overline{F_\varepsilon}$, where Ω_0 is the disc centered at $(0,0)^T$ of radius 0.5, and F_ε is the disc centered at $(0,0)^T$ of radius $\varepsilon < 0.5$. The geometry is illustrated in Figure 8.8a. In other words, Ω_0 is the defeatured geometry obtained from Ω_ε by filling the negative feature F_ε.

We consider Poisson problem (3.1) solved in Ω_ε, we take $f \equiv -1$ in Ω_ε, $g_D \equiv 0$ on $\Gamma_D := \partial\Omega_0$, and $g \equiv 0$ on $\Gamma_N = \gamma := \partial F_\varepsilon = \partial\Omega_\varepsilon \setminus \partial\Omega_0$. The exact solution of problem (3.1) in Ω_ε is given by

$$u(x,y) = \frac{\varepsilon^2}{2} \left[\log\left(\frac{1}{2}\right) - \log\left(\sqrt{x^2 + y^2}\right) \right] + \frac{x^2 + y^2}{4} - \frac{1}{16}.$$

Then, we solve the defeatured Poisson problem (3.3) in Ω_0, where f is extended by -1 in $F_\varepsilon = \Omega_0 \setminus \overline{\Omega_\varepsilon}$. The exact defeaturing solution u_0 is given in Ω_0 by

$$u_0(x,y) = \frac{x^2 + y^2}{4} - \frac{1}{16}.$$

So in particular, the exact defeaturing error, i.e., without discretization error, is given by

$$\|\nabla(u - u_0)\|_{0,\Omega} = \sqrt{\frac{\pi}{2}} \, \varepsilon^2 \left[\log\left(\frac{1}{2}\right) - \log(\varepsilon) \right]^{\frac{1}{2}} \sim \varepsilon^2 \, |\log(\varepsilon)|^{\frac{1}{2}}. \tag{8.57}$$
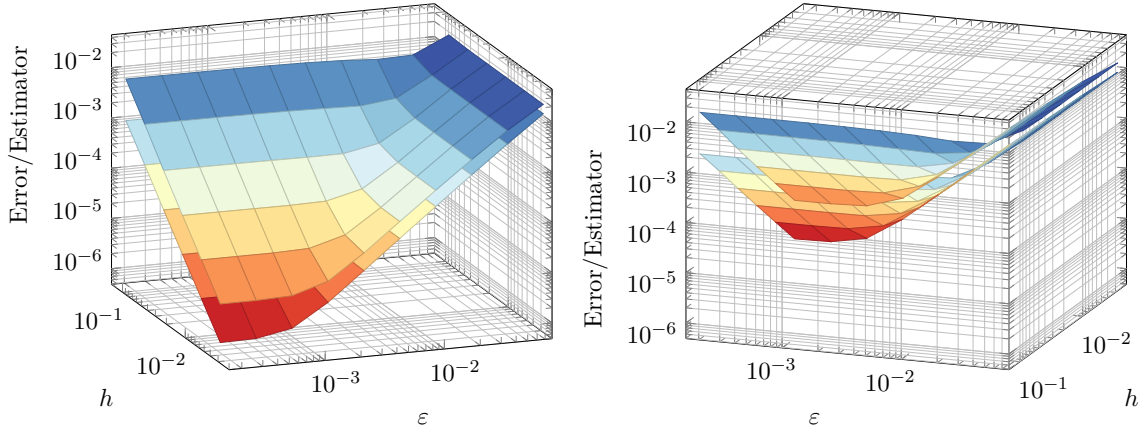
(a) A view on the error (lower surface) and estimator (upper surface).

(b) Another view on the error (lower surface) and estimator (upper surface).

$--- \; \mathcal{E}\left(u_{\mathrm{d}}^h\right) \quad \text{———} \; \left|u - u_{\mathrm{d}}^h\right|_{1,\Omega_\varepsilon} \quad \cdots\cdots \; h^2$
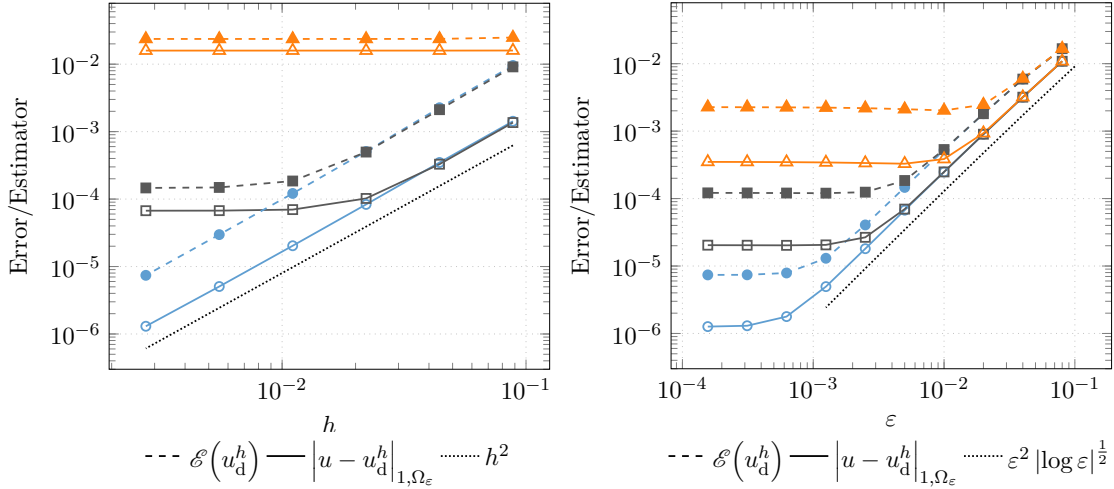
(c) In blue circles, $\varepsilon = 1.5625 \cdot 10^{-4}$; in gray squares, $\varepsilon = 2.5 \cdot 10^{-3}$; in orange triangles, $\varepsilon = 8 \cdot 10^{-2}$.

$--- \; \mathcal{E}\left(u_{\mathrm{d}}^h\right) \quad \text{———} \; \left|u - u_{\mathrm{d}}^h\right|_{1,\Omega_\varepsilon} \quad \cdots\cdots \; \varepsilon^2 \left|\log \varepsilon\right|^{\frac{1}{2}}$

(d) In blue circles, $h = 2.7621 \cdot 10^{-3}$; in gray squares, $h = 1.1049 \cdot 10^{-2}$; in orange triangles, $h = 4.4194 \cdot 10^{-2}$.

Figure 8.9 – Numerical test 8.4.1.1 – Convergence of the discrete defeaturing error and estimator with respect to the mesh size h under global h-refinement, and with respect to the feature size ε. In (a) and (b) are two different views on the surface error and on the surface estimator (the first one being below the second one). In (c), convergence with respect to h for three fixed values of ε. In (d), convergence with respect to ε for three fixed values of h.

Now, Ω_0 is divided into five conforming patches as illustrated in Figure 8.8b, and we consider 4^j elements in each patch, for $j = 0, \ldots, 5$. Thus in this experiment, $h = \dfrac{\sqrt{2}}{2^{j+1}}$, and we solve the defeatured Galerkin problem (5.13) using B-spline based IGA. Therefore, we look at the convergence of the discrete defeaturing error and estimator with respect

to the size of the mesh, subject to global dyadic refinement, and with respect to the size of the feature ε. Note that we never need to numerically create and mesh the exact geometry Ω_ε. Indeed, we do not perform adaptivity in this experiment, thus Ω_0 remains the geometrical model in which the PDE is solved, and for the computation of the error, the exact solution u is already known.
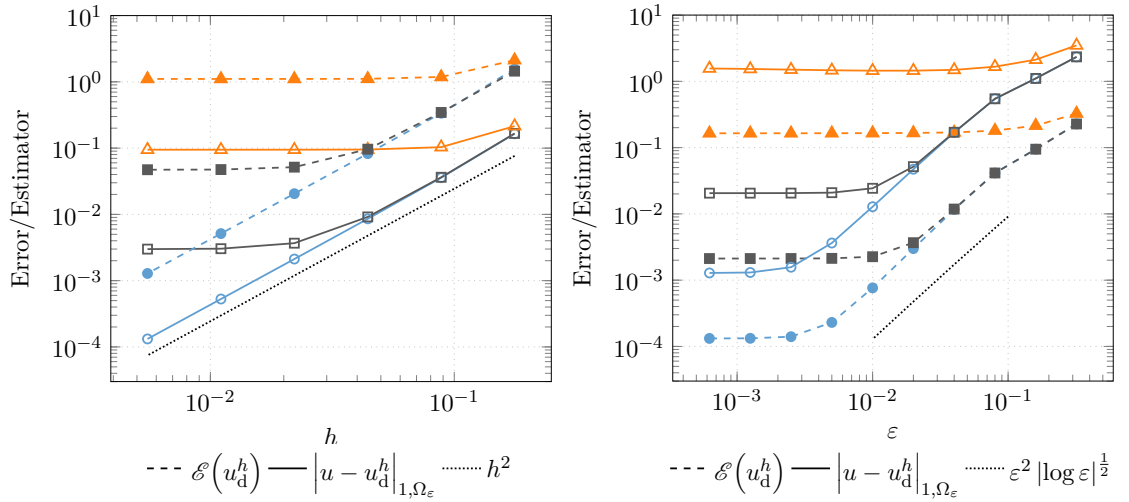
The results are presented in Figure 8.9. When ε is fixed and small, the numerical component of the error dominates over its defeaturing component, and thus the overall error converges as $h^P = h^2$, as expected. When ε is fixed and large, the defeaturing error dominates and thus the overall error does not converge with respect to h, and we observe a plateau. Similarly, when h is fixed and small, the numerical component of the error is negligible with respect to the defeaturing component, and thus the overall error converges as $\varepsilon^2 |\log(\varepsilon)|^{\frac{1}{2}}$, also as expected from (8.57). But when h is fixed and large, the numerical error dominates and thus the overall error does not converge with respect to ε, and we observe a plateau.

The exact same behavior and convergence rates are observed for the discrete defeaturing error estimator, confirming its reliability proven in Theorem 8.2.2, and showing also its efficiency. The effectivity index in the numerical-error-dominant regime is larger (around 5.8) than the one in the defeaturing-error-dominant regime (around 1.5), as expected from the literature (see e.g., [Buffa et al., 2021b] and Part I). Finally, the change of behavior between the two different regimes happen when $\varepsilon \approx h$, both for the overall error and for the proposed estimator.

8.4.1.2 Positive feature

In this experiment, we consider a geometry with one positive feature. That is, for $k = -5, -4, \ldots, 4$, let $\varepsilon = \dfrac{10^{-2}}{2^k}$ and let $\Omega_0 := \Omega_\varepsilon \setminus \overline{F_\varepsilon}$, where Ω_0 an L-shaped domain and F_ε is a fillet of radius ε rounding the corner of the L-shaped domain, as illustrated in Figure 8.10. Or in other words, Ω_0 is the defeatured geometry obtained from Ω_ε by removing the positive feature F_ε.

We consider Poisson problem (3.1) solved in Ω_ε with

$$\Gamma_D := \Big((0,1) \times \{0\} \Big) \cup \Big(\{0\} \times (0,1) \Big)$$

as illustrated in Figure 8.10, and $\Gamma_N := \partial\Omega_\varepsilon \setminus \overline{\Gamma_D}$. We choose the data f, g and g_D such that the exact solution is given by $u(x,y) = \sin(2\pi x)\sin(2\pi y)$ in Ω_ε. Then, we solve the defeatured Poisson problem (3.3) in Ω_0, where g_0 is chosen on γ_0 so that the exact defeatured solution is also given by $u_0(x,y) = \sin(2\pi x)\sin(2\pi y)$ in Ω_0. That is, we do not introduce any error coming from defeaturing in Ω_0. However, we solve the extension problem (3.6) in $\tilde{F}_\varepsilon$, the bounding box of F_ε, choosing $\tilde{g} \equiv 0$ on $\tilde{\gamma}$, and naturally extending f in $\tilde{F}_\varepsilon$. That is, we consider $f(x,y) = 8\pi^2 \sin(2\pi x)\sin(2\pi y)$ in Ω_0 and in $\tilde{F}_\varepsilon$.

(a) Exact domain Ω_ε.

(b) Simplified domain Ω_0, feature F_ε and feature extension G_ε.

(c) Four patches of Ω_0, and extended feature $\tilde{F}_\varepsilon$ as a single patch.
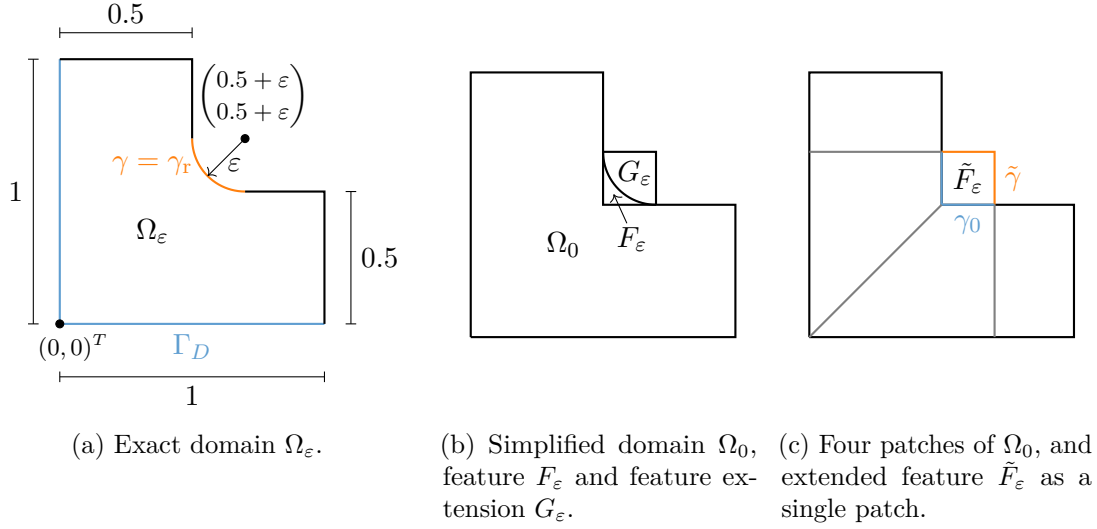
Figure 8.10 – Numerical test 8.4.1.2 – L-shaped domain with a positive fillet feature and its extension.

Therefore, the defeaturing component of the overall error comes from the bad choice of Neumann boundary condition $\tilde{g}$ in $\tilde{\gamma}$, which does not correspond to the exact solution u.

Then, Ω_0 is divided into four conforming patches as illustrated in Figure 8.10c, while $\tilde{F}_\mathrm{p}$ is a single patch. Moreover, we consider 4^j elements in each patch, for $j = 2, \ldots, 7$, so that in this experiment, $h = \dfrac{\sqrt{2}}{2^{j+1}}$. We solve the Galerkin problems (5.13) and (5.15), respectively corresponding to the defeatured and extension problems, using B-spline based IGA. Therefore, we look at the convergence of the discrete defeaturing error and estimator both under global dyadic refinement, and with respect to the size of the feature ε.

The results are presented in Figure 8.11. As for a negative feature, when ε is fixed and small, the numerical component of the error dominates over its defeaturing component, and thus the overall error converges as $h^P = h^2$, as expected. When ε is fixed and large, the defeaturing component of the error dominates and thus the overall error does not converge with respect to h, and we observe a plateau. Similarly, when h is fixed and small, the numerical error is negligible with respect to the defeaturing component of the error, and thus the overall error converges as $\varepsilon^2 \left| \log(\varepsilon) \right|^{\frac{1}{2}}$, also as expected from the previous numerical experiment and from Chapter 3. But again, when h is fixed and large, the numerical error dominates and thus the overall error does not converge with respect to ε, and we observe a plateau.

The overall estimator $\mathscr{E}\left(u_\mathrm{d}^h\right)$ follows the exact same behavior and convergence rates as the error. This numerical test shows that the reliability of the estimator proven in Theorem 8.2.6 can be extended to non-Lipschitz features such as F_ε, and it also shows
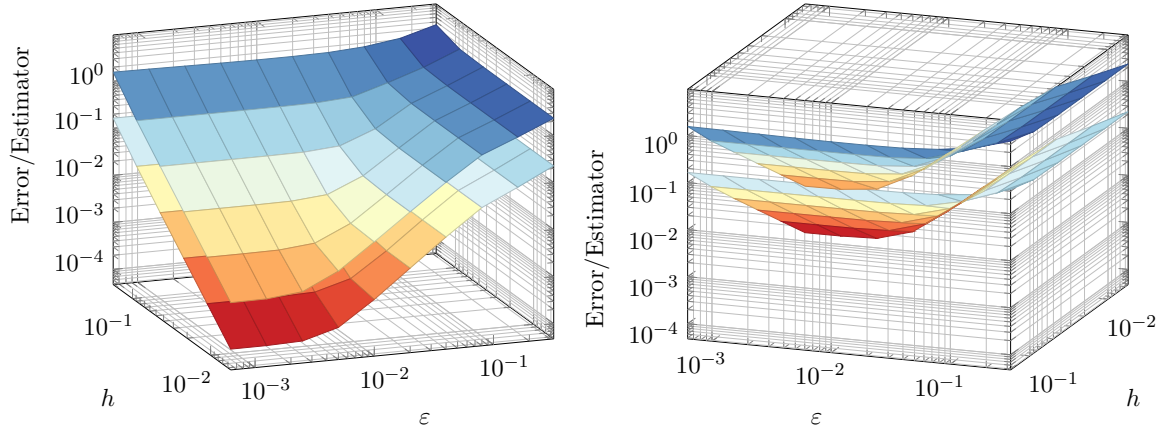
(a) A view on the error (lower surface) and estimator (upper surface).

(b) Another view on the error (lower surface) and estimator (upper surface).

$$--- \; \mathscr{E}\left(u_{\mathrm{d}}^{h}\right) \quad \underline{\quad\quad} \; \left|u - u_{\mathrm{d}}^{h}\right|_{1,\Omega_\varepsilon} \quad \cdots\cdots \; h^2$$

$$--- \; \mathscr{E}\left(u_{\mathrm{d}}^{h}\right) \quad \underline{\quad\quad} \; \left|u - u_{\mathrm{d}}^{h}\right|_{1,\Omega_\varepsilon} \quad \cdots\cdots \; \varepsilon^2 \left|\log \varepsilon\right|^{\frac{1}{2}}$$

(c) In blue circles, $\varepsilon = 6.25 \cdot 10^{-4}$; in gray squares, $\varepsilon = 2 \cdot 10^{-2}$; in orange triangles, $\varepsilon = 1.6 \cdot 10^{-1}$.

(d) In blue circles, $h = 5.5243 \cdot 10^{-3}$; in gray squares, $h = 2.2097 \cdot 10^{-2}$; in orange triangles, $h = 1.7678 \cdot 10^{-1}$.

Figure 8.11 – Numerical test 8.4.1.2 – Convergence of the discrete defeaturing error and estimator with respect to the mesh size h under global h-refinement, and with respect to the feature size ε. In (a) and (b) are two different views on the surface error and on the surface estimator (the first one being below the second one). In (c), convergence with respect to h for three fixed values of ε. In (d), convergence with respect to ε for three fixed values of h.

the efficiency of the estimator. In this case, the effectivity index in the numerical-error-dominant regime is slightly larger (around 10.7) than the one in the defeaturing-error-dominant regime (around 9.7), as expected from the literature. Indeed, in Chapter 3, we have seen that the effectivity index coming from the defeaturing component of the error estimator is larger in the case of an extended positive features, as the extension G_ε of F_ε can itself be seen as a negative feature whose simplified geometry is $\tilde{F}_\varepsilon$.

(a) Exact domain Ω (hole not at scale).

(b) Patches (in black) and initial elements (in gray) of Ω_0.
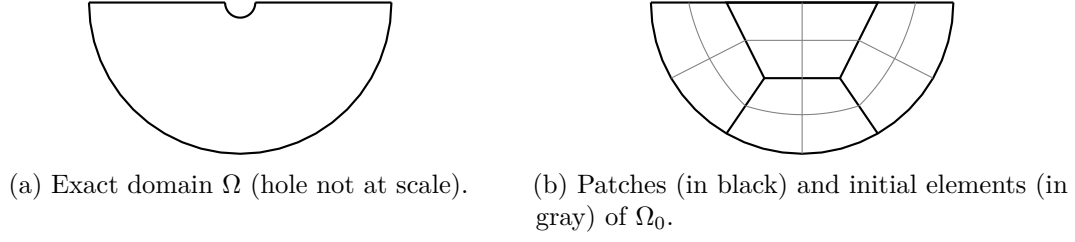
Figure 8.12 – Numerical test 8.4.2.1 – Exact and initial defeatured domains used for the adaptive strategy analysis.

8.4.2 Convergence of the adaptive strategy

In the following experiments, we analyze the convergence of the adaptive strategy proposed in Chapter 5 and specialized to the isogeometric framework in the present chapter. The analysis is first performed in a geometry containing a negative feature, then in a geometry containing a positive feature. Moreover, we compare the proposed strategy with the standard adaptive algorithm which only performs mesh refinement, and which does not consider the defeaturing error contribution. The latter algorithm is indeed widely used nowadays, because of the lack of a sound discrete defeaturing error estimator as the one proposed in this work.

8.4.2.1 Negative feature

Let us first consider a half disc with a circular hole, i.e., a geometry containing a negative feature. More precisely, and as illustrated in Figure 8.12, let

$$\Omega_0 := \left\{ \boldsymbol{x} = (x, y)^T \in \mathbb{R}^2 : \|\boldsymbol{x}\|_{\ell^2} < \frac{1}{2},\, y < 0 \right\},$$

$$F := \left\{ \boldsymbol{x} = (x, y)^T \in \mathbb{R}^2 : \|\boldsymbol{x}\|_{\ell^2} < 5 \cdot 10^{-3},\, y < 0 \right\},$$

$$\Omega := \Omega_0 \setminus \overline{F}.$$

We consider Poisson problem (3.1) in Ω, with $f \equiv -1$, $g_D \equiv 0$ on

$$\Gamma_D := \left\{ \boldsymbol{x} = (x, y)^T \in \mathbb{R}^2 : \|\boldsymbol{x}\|_{\ell^2} = \frac{1}{2},\, y < 0 \right\},$$

and $g \equiv 0$ on $\Gamma_N := \partial\Omega \setminus \overline{\Gamma_D}$. The exact solution of this problem is given by

$$u(x, y) = -\frac{5 \cdot 10^{-5}}{4} \log\left(2\sqrt{x^2 + y^2}\right) + \frac{x^2 + y^2}{4} - \frac{1}{16}, \quad \text{for all } (x, y) \in \Omega.$$

Then, we consider the defeatured problem (3.3) in Ω_0, where f is extended by -1 in F, and $g_0 \equiv 0$ on $\gamma_0 = \partial F \setminus \overline{\partial\Omega}$. We solve it using THB-spline based IGA, with Ω_0 being divided into 4 conforming patches, each of which is initially divided into 4 elements, as
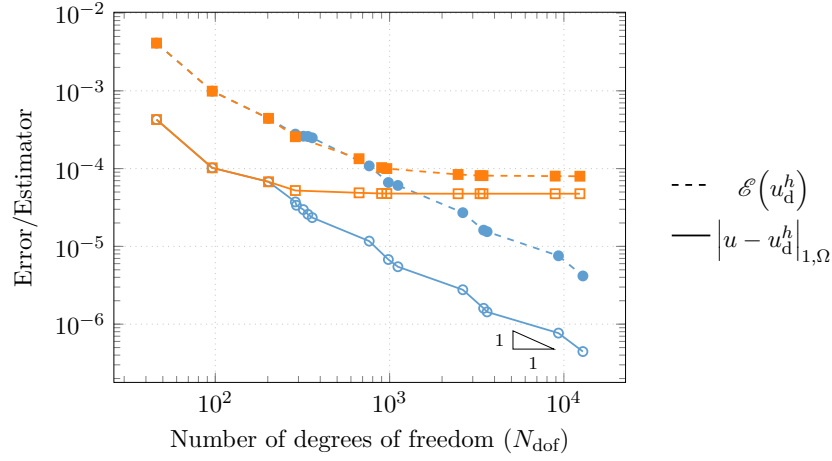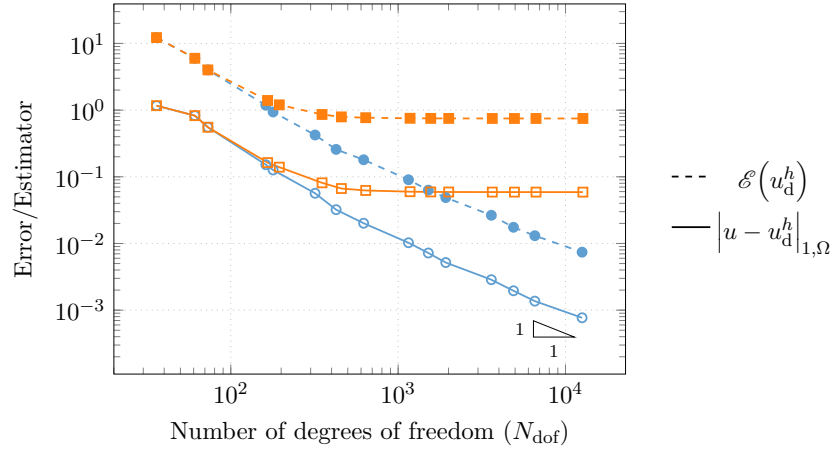
Figure 8.13 – Numerical test 8.4.2.1 – Convergence of the discrete defeaturing error and estimator with respect to the number of degrees of freedom. In blue circles, we consider the adaptive strategy presented in Chapter 5 and specialized to IGA in this chapter, for which the feature is added after iteration 4. In orange squares, we only consider mesh refinements, i.e., the feature is never added to the geometry.

illustrated in Figure 8.12b.

We first perform the adaptive strategy of Chapter 5. Then, we perform the same adaptive strategy but we never add the feature $F =: F^1$ to the geometrical model. This is done by not taking into account the contribution $\mathscr{E}_D\left(u_{\mathrm{d}}^h\right) = \mathscr{E}_D^1\left(u_{\mathrm{d}}^h\right)$ in the MARK module (see Section 5.4.3). That is, we only perform standard mesh refinement steps by neglecting the defeaturing error contribution, while still computing the overall error and the proposed estimator. In this experiment, we use $\alpha_N = \alpha_D = 1$, that is, we give the same weight to the contribution of the numerical part of the error estimate as to the one of the defeaturing part of the error estimate. Moreover, we choose the marking parameter $\theta = 0.5$. When performing the REFINE module presented in Section 5.4.4, we impose the mesh to be $\mathcal{T}$-admissible of class 2, and the mesh is dyadically refined. Moreover, when the feature F is marked for refinement, it is added to the geometrical model by trimming as explained in Section 8.3. Both adaptive strategies are stopped whenever the number of degrees of freedom exceeds 10^4.

The results are presented in Figure 8.13, and the final meshes obtained with each refinement strategy are drawn in Figure 8.14. Even if the exact solution is radial and the numerical solution is C^1-continuous in every patch, the obtained meshes are highly influenced by the interfaces between patches, on which the basis functions are only C^0-continuous. Let us first analyze the results obtained with the adaptive strategy of Chapter 5, represented as blue lines with circles in Figure 8.13. In particular, the feature is added after the third iteration, and the overall error converges as the inverse of the
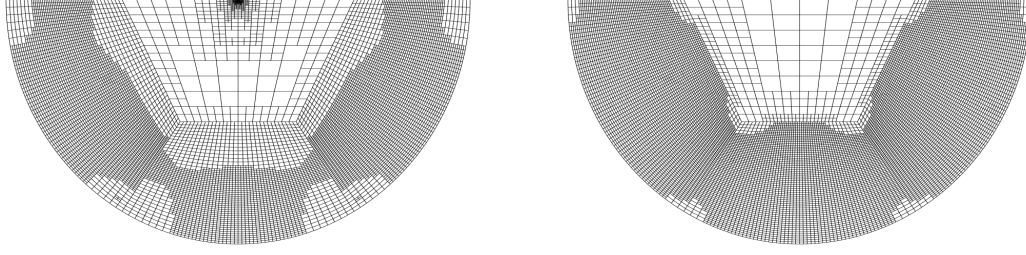
(a) Final mesh obtained with the adaptive defeaturing strategy presented in Chapter 5, where the feature has been added by trimming.

(b) Final mesh obtained with a standard IGA mesh refinement strategy, without geometric refinement.

Figure 8.14 – Numerical test 8.4.2.1 – Final meshes obtained with adaptive defeaturing, and with a standard mesh refinement strategy without geometric refinement.

number of degrees of freedom N_{dof}, that is, as $N_{\mathrm{dof}}^{-\frac{P}{2}}$, as expected. We verify that the geometrical feature is not added too late, otherwise we would first observe a plateau in the overall error followed by a large drop, followed again by a normal convergence. At the opposite, if the feature were added too early in the geometrical model, the convergence would not be affected, but it would be computationally more costly. Moreover, the discrete defeaturing error estimator follows very well the behavior of the error with a relatively low effectivity index of 9.41 on average, confirming once again its efficiency and reliability.

Then, we compare the results with the ones obtained with the adaptive strategy in which the feature is never added to the geometrical model, represented as orange lines with squares in Figure 8.13. We observe a plateau of the overall error with respect to the number of degrees of freedom beginning after the third iteration. This indicates that the feature should be added to the geometrical model after the third iteration, since the plateau would otherwise begin later. Thus the proposed combined adaptive strategy does not add the feature too early nor too late. Indeed, starting from iteration 4, the defeaturing component of the error dominates over the numerical component, and even if one continues to refine the mesh, the overall error cannot decrease any further if the geometrical model is not refined. Furthermore, the discrete defeaturing error estimator follows the behavior of the error, and in particular, the effectivity index in the last iterations is smaller than the one in the first iterations. This is coherent with what has been observed in the previous numerical experiments of Section 8.4.1, since the defeaturing contribution of the error dominates in the last iterations. We finally remark that the classical mesh adaptive strategy without geometric refinement does not see the feature, and therefore, it cannot be used to estimate the error in the presence of defeaturing.

Figure 8.15 – Numerical test 8.4.2.2 – Convergence of the discrete defeaturing error and estimator with respect to the number of degrees of freedom. In blue circles, we consider the adaptive strategy of Chapter 5 and specialized to IGA in this chapter, for which the feature is added after iteration 4. In orange squares, we only consider mesh refinements, i.e., the feature is never added to the geometry.

8.4.2.2 Positive feature

Let us now consider the same problem setting as in Section 8.4.1.2, i.e., a defeaturing problem on an L-shaped domain containing a positive fillet feature, and let us fix $\varepsilon = 0.1$. As in the previous Section 8.4.2.1, we first perform the adaptive strategy proposed in Chapter 5; then, we perform the classical mesh refinement adaptive strategy without geometric adaptivity, that is, the feature $F := F_\varepsilon$ is never added to the geometrical model. In both cases, we start with a mesh containing one element per direction and per patch (see Figure 8.10c for the patch decomposition of Ω_0), and the algorithm is stopped whenever the total number of degrees of freedom N_{dof} exceeds 10^4. If F is not in the geometrical model, recall that the total number of degrees of freedom N_{dof} accounts for the number of degrees of freedom of problem (5.13) in Ω_0, from which we add the number of degrees of freedom of problem (5.15) in $\tilde{F} := \tilde{F}_\varepsilon$. If the positive fillet F is marked for refinement, then it is added to the geometrical model as a trimmed patch, the considered patch being its bounding box $\tilde{F}$ as in Figure 8.10. In this case, we recall that N_{dof} accounts for the number of active degrees of freedom of the discrete problem in the exact (multipatch trimmed) domain $\Omega := \Omega_\varepsilon$. In this experiment, we use $\alpha_N = \alpha_D = 1$, and we choose the marking parameter $\theta = 0.5$. During the refining phase, we impose the mesh to be $\mathcal{T}$-admissible of class 2, and the marked elements are dyadically refined at each iteration.

The results are presented in Figure 8.15. The fillet is added after the third iteration of the adaptive strategy of Chapter 5, whose results are represented as blue lines with circles in Figure 8.15. As for the previous numerical experiment of Section 8.4.2.1, we can

see that the feature is not added too late, as there is no plateau nor a large drop in the convergence of the error and estimator. The overall error converges as the inverse of the number of degrees of freedom N_{dof}, that is, as $N_{\mathrm{dof}}^{-\frac{P}{2}}$, as expected. Moreover, the discrete defeaturing error estimator follows very well the behavior of the overall error with a relatively low effectivity index of 8.6 on average, confirming once again its efficiency and reliability.

Then, we compare the results with the ones obtained with the adaptive strategy in which the feature is never added to the geometrical model, represented as orange lines with squares in Figure 8.15. Beginning from iteration 4, we observe a plateau in the overall error with respect to the number of degrees of freedom, as the defeaturing component of the error starts to dominate over the numerical component. The overall error cannot decrease any further if the geometrical model is not refined, i.e., the fillet should be added. The discrete defeaturing error estimator follows the behavior of the error, and in particular, the effectivity index in the last eight iterations is equal to 12.6 in average. This is coherent with what has been observed in the numerical experiment of Section 8.4.1.2.

8.4.3 Impact of the feature size on the adaptive strategy

In this section, we consider the numerical approximation of the experiment presented in Chapter 3, Section 3.5.1.2. Thanks to this experiment, we study the impact of the size of the features on the discrete defeaturing error estimator, while validating the theory developed in Section 8.2. In particular, as the defeaturing error contribution of the estimator depends upon the size of the features and upon the size of the solution gradients "around" the feature, we show that the proposed adaptive strategy is able to tell when small features count more than big ones, also in the presence of numerical error. We also show that the numerical error estimator $\mathscr{E}_N\left(u_{\mathrm{d}}^h\right)$ is not a reliable estimator in the presence of defeaturing.

To do so, recall that the considered exact geometry Ω reproduced again in Figure 8.16a, contains two holes: a small one F^1 which is two orders of magnitude smaller than the

(a) Exact domain Ω with two features (not at scale).　　(b) Exact solution in Ω.
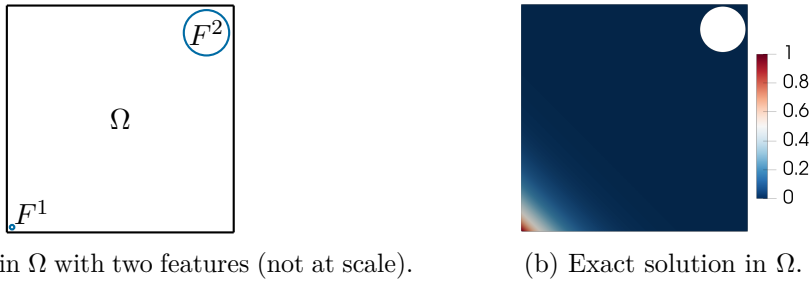
Figure 8.16 – Numerical test 8.4.3 – Geometry with two features of different size, and exact solution.
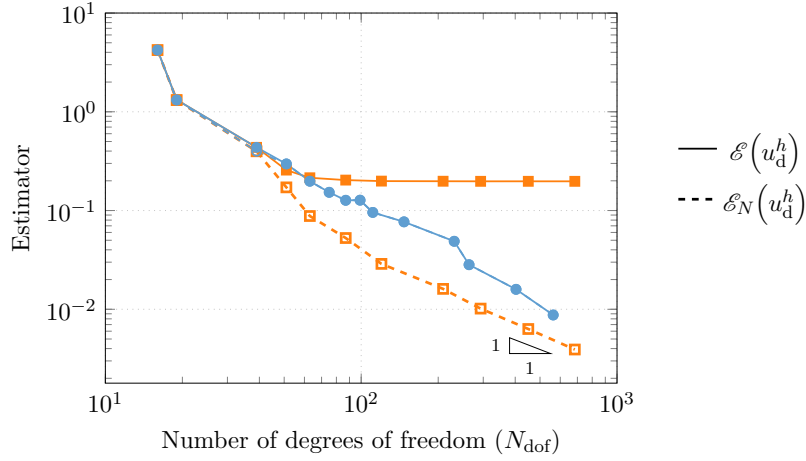
Figure 8.17 – Numerical test 8.4.3 – Convergence of the overall error estimator and of its numerical error component, with respect to the number of degrees of freedom. In blue circles, we consider the adaptive strategy of Chapter 5, specialized to IGA in this chapter. Feature F^1 is added after iteration 4 while F^2 is never added, and the overall error estimator and its numerical error component are basically superposed. In orange squares, we consider the standard adaptive mesh refinement strategy, that is, the adaptive process is only steered by the numerical contribution of the overall error estimator, and features are never added to the geometry.

other one F^2. Let $\Omega_0 := (0,1)^2$ be a single patch with 2 elements in each direction to start the adaptive algorithm, where Ω_0 is obtained by filling the holes of Ω. We also recall that the solution to the considered exact Poisson problem (3.1) solved in Ω has a very high gradient near F^1, and it is almost constantly zero near F^2, as it can be observed in Figure 8.16b. Therefore, one can expect:

- the mesh to be refined close to F^1,

- and the presence of F^1 to be more important than F^2 with respect to the solution accuracy, even if F^1 is notably smaller than F^2.

As for the numerical experiments of Section 8.4.2, we first perform the adaptive strategy described in Chapter 5. Then, we perform the same adaptive strategy but without geoemtric refinement, that is, we never add any of the two features F^1 and F^2 to the geometrical model. To do so, we do not take into account the defeaturing contributions $\mathscr{E}_D^1\left(u_{\mathrm{d}}^h\right)$ and $\mathscr{E}_D^2\left(u_{\mathrm{d}}^h\right)$ in the MARK module (see Section 5.4.3). In this experiment, we use $\alpha_N = 1$ and $\alpha_D = 4$ in both cases, and we choose $\theta = 0.5$ as marking parameter. For the REFINE module precised for IGA in Section 8.3.2, we impose the mesh to be $\mathcal{T}$-admissible of class 2, and the mesh is dyadically refined. Moreover, when a feature is marked for refinement, it is added to the geometrical model by trimming, as explained in Section 8.3.
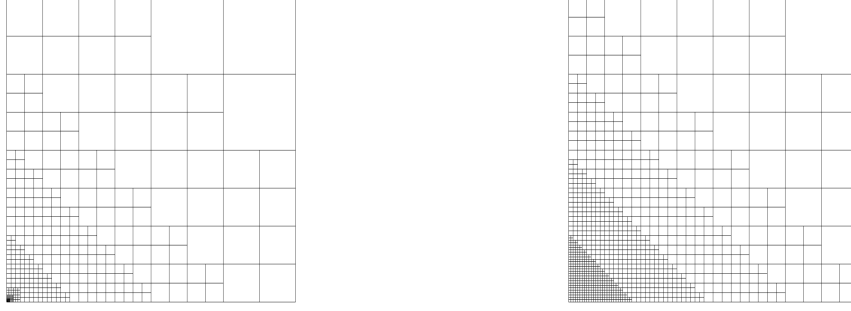
(a) Final mesh obtained with the adaptive defeaturing strategy of Chapter 5, where only F^1 has been added by trimming.

(b) Final mesh obtained with a standard IGA mesh refinement strategy, without geometric refinement.

Figure 8.18 – Numerical test 8.4.3 – Final meshes obtained with adaptive defeaturing and with a standard mesh refinement strategy.

Results are reported in Figure 8.17, and we reproduce in Figure 8.18 the meshes obtained when the total number of degrees of freedom exceeds 500. The blue line with circles corresponds to the adaptive strategy of Chapter 5. The small feature F^1 is added after the third iteration, while the large one, F^2, is never added to the geometry. This confirms our intuition on the problem and this is coherent with the results obtained in Section 3.5.1.2, even if F^1 is two orders of magnitude larger than F^2. Moreover, the final mesh is refined around F^1 as one would also observe when performing a standard mesh refinement algorithm. During of the fully adaptive strategy, the overall error converges as the inverse of the number of degrees of freedom N_{dof}, i.e., as $N_{\mathrm{dof}}^{-\frac{P}{2}}$, as expected. In Figure 8.17, the numerical error contribution $\mathscr{E}_N\left(u_{\mathrm{d}}^h\right)$ is basically superposed to the overall error estimator.

Furthermore, the orange lines with squares in Figure 8.17 correspond to the results of the standard mesh refinement adaptive strategy, in which the defeaturing component of the error is not considered. We can observe that the convergence of the overall error estimator is lost, because the defeaturing error contribution of the estimator remains high, even if the numerical error contribution $\mathscr{E}_N\left(u_{\mathrm{d}}^h\right)$ keeps converging as $N_{\mathrm{dof}}^{-\frac{P}{2}}$. The obtained final mesh is refined around the lower left corner, reflecting the high gradient of the solution in this area. However, if the feature is not added to the geometry, there is no hope to obtain a more accurate solution since the numerical error estimator does not see the feature. In particular, the numerical error contribution $\mathscr{E}_N\left(u_{\mathrm{d}}^h\right)$ goes almost two orders of magnitude below the overall error estimator, at the end of the adaptive loop. Therefore, the only numerical error estimator is not a reliable error estimator in the presence of defeaturing.

8.4.4 Fully adaptive strategy in a geometry with many features

In this last numerical experiment, we analyze the proposed fully adaptive strategy in a geometry with many features. More precisely, let $\Omega_0 := (0,1)^2$ be the fully defeatured domain, and let $\Omega := \Omega_0 \setminus \bigcup_{k=1}^{N_f} \overline{F^k}$, where $N_f = 27$ and the features F^k are some circular holes of radii in the interval $(0, 5 \cdot 10^{-3})$, distributed with some randomness in Ω_0, as illustrated in Figure 8.19a. For the sake of reproducibility, the values of the centers of the features are the same as in Table 4.3, and the radii are halved with respect to the ones reported in this table. Note in particular that this geometry satisfies Assumption 4.1.5.

We are interested in the solution of problem (3.1) defined in Ω, and we solve the Galerkin approximation (5.13) of the corresponding defeatured problem (3.3) in Ω_0. We consider a similar Poisson's problem as in the previous numerical experiment, that is, we let $f(x,y) := -128e^{-8(x+y)}$ in Ω_0, $g_D(x,y) := e^{-8(x+y)}$ on

$$\Gamma_D := \Big([0,1) \times \{0\}\Big) \cup \Big(\{0\} \times [0,1)\Big),$$

the bottom and left sides, $g(x,y) := -8e^{-8(x+y)}$ on $\partial\Omega_0 \setminus \overline{\Gamma_D}$, and finally $g \equiv 0$ on ∂F^k for all $k = 1, \ldots, N_f$. That is, as illustrated in Figure 8.19b, the exact solution u has a high gradient close to the bottom left corner, and it is almost constantly zero in the top right area of the domain.

As for the previous numerical experiments, we first perform the adaptive strategy described in Chapter 5, starting from the fully defeatured domain Ω_0 and from a uniform mesh of 16×16 elements in Ω_0, as illustrated in Figure 8.19c. Then, we perform the same adaptive strategy but without geometric refinement, that is, with this second strategy, holes are never added to the geometrical model. In this experiment, we use THB-splines of degree $P = 3$, we consider $\alpha_N = 1$ and $\alpha_D = 4$, and we choose $\theta = 0.3$ as marking parameter. For the REFINE module precised for IGA in Section 8.3.2, we impose the mesh to be $\mathcal{T}$-admissible of class 3, and the mesh is dyadically refined. Moreover, when a feature is marked for refinement, it is added to the geometrical model by trimming, as explained in Section 8.3.

The mesh and geometry obtained at iteration 9, and the final mesh and geometry obtained with both adaptive strategies when the total number of degrees of freedom exceeds 10^3 are represented in Figure 8.19. Results are reported in Figure 8.20. The blue lines with circles correspond to the adaptive strategy of Chapter 5, and the sets of marked features at each iteration are the following: $\{1\}$, $\{2, 6\}$, $\emptyset$, $\emptyset$, $\{3\}$, $\{4, 8, 11, 16\}$, $\{5\}$, $\emptyset$, $\{7, 12, 17\}$, $\{10, 13, 22\}$, $\{15\}$, $\{9, 14, 21, 23, 26, 27\}$. For instance, the error estimator is divided by 10 with the addition of only 4 out of the 27 features in the geometrical model, and with a number of degrees of freedom increased by slightly more than a third. Moreover, the overall estimator and its numerical and defeaturing contributions converge as $N_{\mathrm{dof}}^{-\frac{3}{2}} = N_{\mathrm{dof}}^{-\frac{P}{2}}$, as expected. Furthermore, the final mesh, represented in Figure 8.19f,
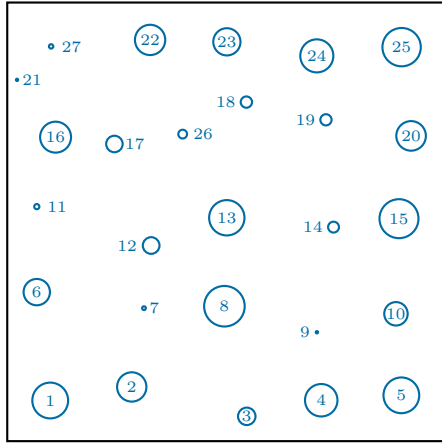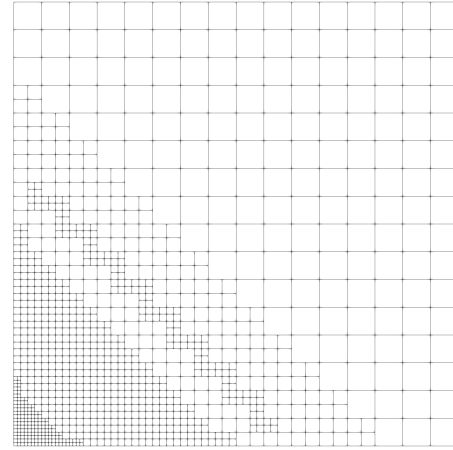
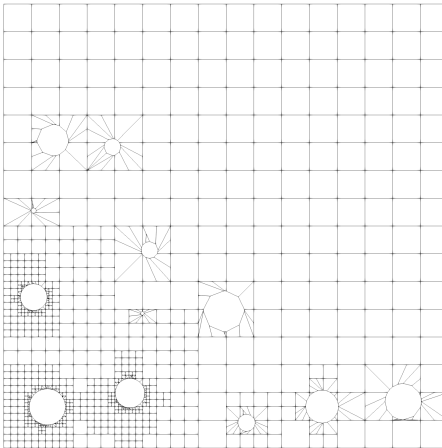(a) Exact domain Ω with 27 features.
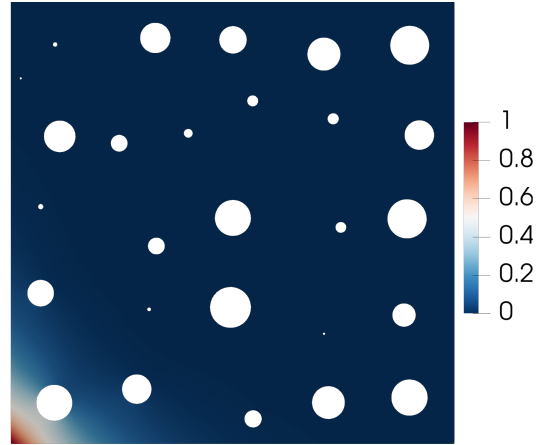
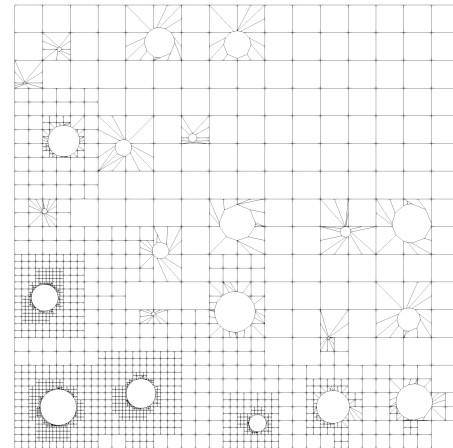(b) Exact solution in the exact domain.
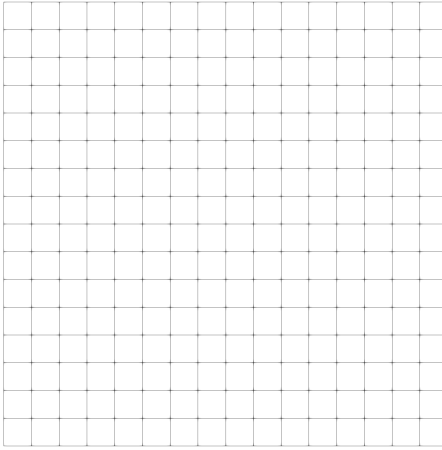
(c) Initial mesh.

(d) Final mesh obtained without geometric refinement.

(e) Mesh and geometry obtained with the combined refinement strategy at iteration 9.

(f) Final mesh and geometry obtained with the combined refinement strategy.

Figure 8.19 – Numerical test 8.4.4 – Considered geometry, initial mesh, and intermediate and final meshes and geometries obtained with adaptive strategies, with and without geometric refinement.
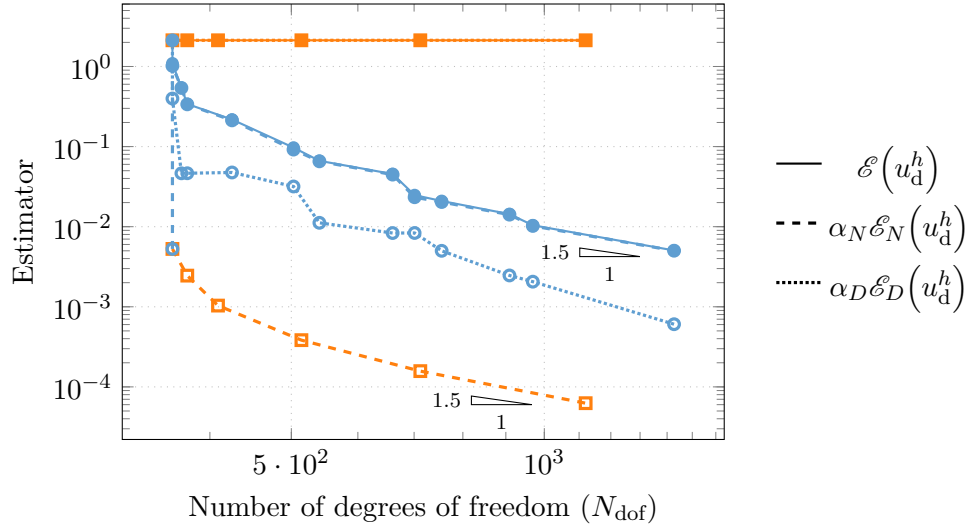
Figure 8.20 – Numerical test 8.4.4 – Convergence of the discrete defeaturing estimator with respect to the number of degrees of freedom. In blue circles, we consider the adaptive strategy of Chapter 5 in which features are iteratively added to the geometric model. Note that the dashed and solid blue curves are basically superposed. In orange squares, we only consider mesh refinements, i.e., the feature is never added to the geometry. In this case, note that the dotted and solid orange curves are basically superposed.

is refined towards the lower left angle of the domain, and the first selected features are also the ones closer to that angle. This is indeed expected as the exact solution has a high gradient around that corner.

The orange lines with squares in Figure 8.20 correspond to the results of the adaptive strategy without geometric refinement, i.e., when the defeaturing component of the error is not considered. We can observe that convergence is lost, because the defeaturing error contribution of the estimator is and remains very high, even if the numerical error contribution keeps converging as $N_{\text{dof}}^{-\frac{P}{2}}$. The obtained final mesh is refined around the lower left corner, reflecting the high gradient of the solution in this area, but if we do not add any feature to the geometry, one cannot obtain a more accurate solution. This is reflected by the proposed discrete defeaturing error estimator, validating the developed theory.

9 Concluding remarks and future outlook

This thesis provides a mathematical framework and some new understanding of analysis-aware defeaturing. The main findings leading towards this objective are summarized in the following, and further research directions are discussed.

9.1 Scientific contributions

The scientific contributions of this thesis are based on a published paper [Buffa et al., 2022b], a manuscript currently under review for publication [Buffa et al., 2021a], and two articles in preparation [Antolín and Chanon, 2022; Buffa et al., 2022a]. In the following, we systematically summarize the main findings of this work.

9.1.1 Contributions in Part I

In the context of Poisson, linear elasticity and Stokes equations, we have introduced a mathematical framework to study the accuracy impact of removing features in geometries in which the solution of a PDE is sought. In particular, we have defined a novel *a posteriori* energy error estimator for the analysis-aware geometric defeaturing of

- two- and three-dimensional geometries,

- containing an arbitrary number of negative, positive or generally complex features,

- on which Neumann boundary conditions are imposed.

The proposed defeaturing error estimator $\mathscr{E}_D$ has the following properties:

- it is not only driven by geometrical considerations, but also by the differential problem at hand;

- it is able to weight the impact of defeaturing in the energy norm, and its effectivity index is independent of the size of the geometrical features and of their number;

- it is able to determine whether the defeaturing error comes from the choice of defeaturing data (right hand side and Neumann boundary conditions), or if it comes from the importance of the presence of the feature itself;

- it is proven to be reliable and efficient up to oscillations;

- it is naturally decomposed into single feature contributions;

- it is simple, naturally parallelizable and computationally cheap;

- it has been tested on an extensive set of numerical experiments: in all of them, the estimator acts as an excellent approximation of the defeaturing error.

With the help of this error estimator, we have been able to design a geometric refinement strategy taking into account the defeaturing errors. More precisely, starting from a fully defeatured geometry, features are iteratively added to the geometrical model when their absence is responsible for most of the solution accuracy loss. That is, the strategy is able to build a (partially) defeatured geometric model containing few features, for which the defeaturing error is below a prescribed tolerance. Presented numerical experiments have demonstrated the convergence of the defeaturing error during the adaptive loop.

9.1.2   Contributions in Part II

Taking Poisson's equation as driving problem, we have considered a finite element approximation of the defeatured problem, and we have integrated the induced additional numerical error in the defeaturing framework of Part I. More precisely, we have first developed a fully adaptive scheme taking into account the discretization and the defeaturing errors, which performs both standard mesh refinements and geometric refinements. To steer this adaptive strategy, we have introduced a novel *a posteriori* estimator $\mathscr{E}$ of the energy norm of the discrete defeaturing error, i.e., the error between the exact solution computed in the exact domain and the numerical solution computed in the defeatured domain.

The adaptive process is designed to be performed with any mesh-preserving Galerkin FEM, as soon as the method provides a numerical error estimator which can be decomposed into local mesh element contributions. Since (T)HB-spline based IGA appears as a natural method to numerically solve PDEs in the context of adaptive analysis-aware defeaturing, the remaining part of this work consisted in making the proposed strategy more precise in the case in which IGA is the numerical method of choice.

Since the designed adaptive strategy requires a mesh-preserving numerical method with a reliable error estimator, we have first analyzed the numerical error in the absence of defeaturing error, in the following situation:

- (T)HB-spline based IGA is used to approximate Poisson's problem,

- in two- and three-dimensional trimmed domains,

- Neumann boundary conditions are imposed on the trimming curve or surface,

- the underlying hierarchical mesh is $\mathcal{T}$-admissible.

More precisely, we have introduced a novel *a posteriori* residual estimator of the numerical approximation error for (T)HB-spline based IGA in trimmed domains. The proposed numerical error estimator $\mathscr{E}_N$ has the following properties:

- it is proven to be reliable;

- its effectivity index is independent of the type of cut, and in particular, it is independent of the measure of the active part of the trimmed elements;

- it is naturally decomposed into local (trimmed and non-trimmed) element contributions;

- it has been tested on a wide range of numerical experiments, showing that it acts as an excellent approximation of the numerical error;

- it is able to drive an adaptive mesh refinement strategy on trimmed geometries.

The proposed mesh refinement strategy strongly relies on the adaptive strategies introduced for non-trimmed geometries, which also require an admissibility assumption of the underlying mesh. We have tested the adaptive process on different numerical experiments which exhibit both smooth and singular solutions. Optimal asymptotic rates of convergence are recovered with respect to the total number of degrees of freedom. Compared to uniform refinement, the adaptive strategy exhibits a substantial increase in accuracy with respect to the number of degrees of freedom, as it is now classical in non-trimmed geometries.

The previous findings have finally been combined in order to make more precise the fully adaptive strategy combining geometric and mesh refinements, in the context of (T)HB-spline based IGA. In particular, we have proven the reliability of the *a posteriori* estimator $\mathscr{E}$ of the overall error coming from the combination of defeaturing and numerical approximation. The proof is given for (T)HB-spline based IGA in mesh-fitted computational domains. Then, to perform the fully adaptive strategy, we have considered trimmed and multipatch domains as mesh-preserving methods, thanks to the numerical error estimator $\mathscr{E}_N$ defined for trimmed (T)HB-spline domains. Several numerical experiments have been performed to test the overall error estimator $\mathscr{E}$ and the related full adaptive strategy. In all of them, the overall error estimator provides an excellent approximation of the discrete defeaturing error, and it is able to correctly steer the adaptive process. In particular, it is able to correctly weight the impact of defeaturing with respect to the numerical approximation of the defeatured solution.

9.2 Future research directions

This thesis is only the tip of an iceberg of open problems in analysis-aware defeaturing. However, we believe that the presented results provide solid foundations for the upcoming research in the field. In the following, we propose several research directions which would be interesting extensions of this work, or whose findings would overcome some of its limitations.

9.2.1 Monotone error reduction of the combined adaptive strategy

In the proposed adaptive algorithm combining mesh and geometric refinements, monotone error reduction is not guaranteed. This comes in particular from the fact that the addition of a feature in the geometrical model introduces a discontinuity in the evaluation of the discretization error, first evaluated without the feature, and then with it. Finding strategies to alleviate this effect and obtain a monotone behavior would be interesting.

Moreover, and linked to the first point, the error estimation and the marking steps are controlled by some user-defined parameters α_N and α_D. These weights aim at balancing the respective numerical and defeaturing error contributions in the discrete defeaturing error estimator. More precisely, the two parameters α_N and α_D are necessary because of the different unknown constants linking both contributions with the overall error. Numerically, taking α_N and α_D such that $\dfrac{\alpha_D}{\alpha_N} = 4$ seems to be a good rule of thumb, since a classical effectivity index for the numerical error has a value around 10, while a standard effectivity index for the defeaturing error has a value around 2 or 3. However, the precise values of the effectivity indices are different for each problem at hand, and they may also change at each iteration of the adaptive loop as the geometric model gets refined. Therefore, it would be necessary to find a technique to approximate (the ratio between) these constants at each iteration. This task is closely related to [Gerasimov et al., 2015].

9.2.2 Generalization of the problem setting

In this thesis, we suppose that Neumann boundary conditions are imposed on the features' boundaries. For a complete study, it would be interesting to generalize the analysis to Dirichlet and mixed boundary conditions on the features. In this case, we still expect to obtain a representation of the defeaturing error solely involving (Dirichlet or mixed) error terms on the boundary of the features.

In the multifeature setting, we assumed that features are separated from one another. Therefore, the treatment of a geometry in which the boundary is complex everywhere is not treated, and its study in a defeaturing framework would be of great interest (see also Section 9.2.5).

Moreover, this work focuses on the global energy norm of the error, which is an important first step to understand the impact of defeaturing in analysis. Studying defeaturing using a local goal-oriented error measure would however be a further step attracting a broader industrial interest.

Finally, only linear elliptic PDEs are considered in this monograph. Based on this first step, an interesting extension would be the analysis of more complex problems, such as parabolic, hyperbolic, or non-linear PDEs.

9.2.3 A different defeaturing approach through coarsening

In our approach of defeaturing, we assume that one has decided *a priori* what to consider a feature and has access to a fully defeatured geometry Ω_0. However, we make the following three observations:

- in practice, defeaturing a (CAD) geometry may not be an easy task, see for instance [Thakur et al., 2009];

- the technical complexity of an immersed simulation is not mainly due to the number of features in the computational domain or to how complex they are, but rather on the possibility to construct a local reparametrization for integration purposes, see e.g. [Antolín et al., 2022] and references therein;

- the methodology developed in this work seems to be able to correctly select important features even on a coarse (immersed) mesh, see Section 4.6.2.

Therefore, one could try a different approach to hope for a better unified design-through-analysis workflow. More precisely, a first simulation could be ran on the exact geometry Ω, in which a very coarse immersed mesh is defined. Then, one could derive a geometric coarsening estimator which selects the features that can be removed while keeping the error below a prescribed tolerance. Finally, one could create a better (possibly boundary fitted) model of the partially defeatured geometry, in which mesh adaptivity is performed.

9.2.4 Geometric coarsening and time-dependent problems

Similar to strategies combining mesh refinement and coarsening [Carraturo et al., 2019], and linked to the previous section, it would be interesting to develop an adaptive algorithm that combines geometric refinement with geometric coarsening. This would be of particular interest when treating time-dependent problems. To illustrate this, let us consider for instance the wave equation in a domain containing a feature in its center. Before the wave approaches the feature, and some time after the wave has overcame it, the presence of the feature may not be needed to obtain an accurate solution; the computational domain could be defeatured. Instead, when the wave hits the feature, the
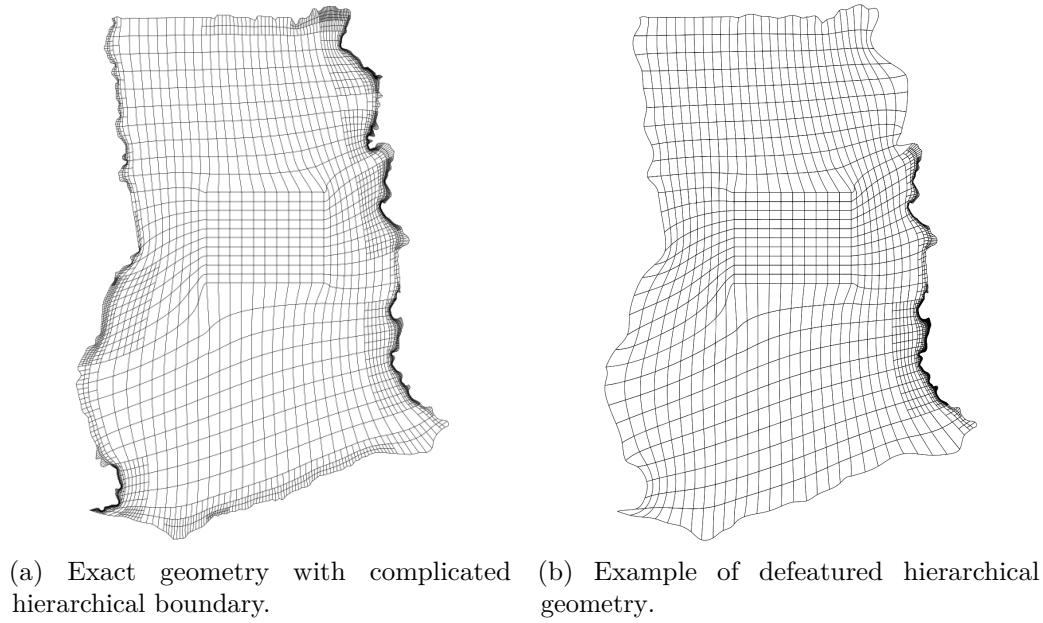
(a) Exact geometry with complicated hierarchical boundary.

(b) Example of defeatured hierarchical geometry.

Figure 9.1 – Illustration of hierarchical defeaturing.[11]

presence of the latter may be crucial to obtain an accurate solution, and thus it would not be advised to remove that feature. Therefore, we would need geometric refinement just before the wave hits the feature. Then, some computational time would be saved if geometric coarsening is performed some time after the wave overcomes the feature, in order to remove the latter from the geometric model.

9.2.5 Hierarchical analysis-aware defeaturing approach

In this thesis, features are assumed to be separated from one another, and defeaturing has been approached as an on/off switch: either the considered geometric model contains a certain feature, or it does not. However, another approach is possible, combined with the approximation properties of (T)HB-splines [Bracco et al., 2022]. More precisely, geometrical features may not only be seen as discrete holes and protrusions, but also as complicated continuous boundary patterns, such as oscillating or fractal-like boundaries. Therefore, given a hierarchical B-spline geometry Ω whose description requires a mesh on $L > 0$ hierarchical levels, a defeaturing method could consist in approximating Ω on a coarser mesh. A lower number $0 < L_0 \leq L$ of hierarchical levels would be used in the mesh regions in which a precise geometric model is not necessary to obtain an accurate solution, and vice versa. This idea is illustrated in Figure 9.1. An adaptive geometric refinement algorithm can be seen as a mesh refinement strategy in this case, and another mesh could be defined as a refinement of the geometric mesh for numerical approximation.

---

[11]Image courtesy to Alessandra Arrigoni and Jochen Hinz.

Bibliography

Acosta, G. and Borthagaray, J. P. (2017). A fractional Laplace equation: regularity of solutions and finite element approximations. *SIAM Journal on Numerical Analysis*, 55(2):472–495.

Adams, R. A. (1975). *Sobolev spaces*, volume 65 of *Pure and Applied Mathematics*. Academic Press.

Ainsworth, M. and Oden, J. T. (1997). *A posteriori* error estimation in finite element analysis. *Computer methods in applied mechanics and engineering*, 142(1-2):1–88.

Antolín, P., Buffa, A., and Coradello, L. (2020). A hierarchical approach to the *a posteriori* error estimation of isogeometric kirchhoff plates and kirchhoff–love shells. *Computer Methods in Applied Mechanics and Engineering*, 363:112919.

Antolín, P., Buffa, A., and Martinelli, M. (2019). Isogeometric analysis on V-reps: first results. *Computer Methods in Applied Mechanics and Engineering*, 355:976–1002.

Antolín, P., Buffa, A., Puppi, R., and Wei, X. (2021). Overlapping multipatch isogeometric method with minimal stabilization. *SIAM Journal on Scientific Computing*, 43(1):A330–A354.

Antolín, P. and Chanon, O. (2022). Analysis-aware defeaturing in multifeature geometries. *in preparation*.

Antolín, P. and Hirschler, T. (2022). Quadrature-free immersed isogeometric analysis. *Engineering with Computers*.

Antolín, P., Wei, X., and Buffa, A. (2022). Robust numerical integration on curved polyhedra based on folded decompositions. *Computer Methods in Applied Mechanics and Engineering*, 395:114948.

Babuška, I. and Rheinboldt, W. C. (1978). Error estimates for adaptive finite element computations. *SIAM Journal on Numerical Analysis*, 15(4):736–754.

Bazilevs, Y., Beirão da Veiga, L., Cottrell, J. A., Hughes, T. J. R., and Sangalli, G. (2006). Isogeometric analysis: approximation, stability and error estimates for h-refined meshes. *Mathematical Models and Methods in Applied Sciences*, 16(07):1031–1090.

Bibliography

Bazilevs, Y., Calo, V. M., Cottrell, J. A., Evans, J. A., Hughes, T. J. R., Lipton, S., Scott, M. A., and Sederberg, T. W. (2010). Isogeometric analysis using T-splines. *Computer Methods in Applied Mechanics and Engineering*, 199(5-8):229–263.

Becker, R. and Rannacher, R. (2001). An optimal control approach to *a posteriori* error estimation in finite element methods. *Acta numerica*, 10:1–102.

Beirão da Veiga, L., Buffa, A., Sangalli, G., and Vázquez, R. (2013). Analysis-suitable T-splines of arbitrary degree: definition, linear independence and approximation properties. *Mathematical Models and Methods in Applied Sciences*, 23(11):1979–2003.

Beirão da Veiga, L., Buffa, A., Sangalli, G., and Vázquez, R. (2014). Mathematical analysis of variational isogeometric methods. *Acta Numerica*, 23:157–287.

Ben Belgacem, F., Buffa, A., and Maday, Y. (2001). The mortar finite element method for 3D Maxwell equations: first results. *SIAM Journal on Numerical Analysis*, 39(3):880–901.

Bernardi, C. and Girault, V. (1998). A local regularization operator for triangular and quadrilateral finite elements. *SIAM Journal on Numerical Analysis*, 35(5):1893–1916.

Bracco, C., Giannelli, C., Großmann, D., Imperatore, S., Mokriš, D., and Sestini, A. (2022). THB-spline approximations for turbine blade design with local B-spline approximations. In Barrera, D., Remogna, S., and Sbibih, D., editors, *Mathematical and Computational Methods for Modelling, Approximation and Simulation*, volume 29, pages 63–82. Springer International Publishing, Cham.

Bracco, C., Giannelli, C., Kapl, M., and Vázquez, R. (2020). Isogeometric analysis with C^1-hierarchical functions on planar two-patch geometries. *Computers & Mathematics with Applications*, 80(11):2538–2562.

Bracco, C., Giannelli, C., and Vázquez, R. (2018). Refinement algorithms for adaptive isogeometric methods with hierarchical splines. *Axioms*, 7(3):43.

Brenner, S. C. and Scott, L. R. (2008). *The mathematical theory of finite element methods*, volume 3. Springer.

Bressan, A. (2013). Some properties of LR-splines. *Computer Aided Geometric Design*, 30(8):778–794.

Brezis, H. (2011). *Functional analysis, Sobolev spaces and partial differential equations*, volume 2. Springer.

Buchegger, F., Jüttler, B., and Mantzaflaris, A. (2016). Adaptively refined multi-patch B-splines with enhanced smoothness. *Applied Mathematics and Computation*, 272:159–172.

Buffa, A., Chanon, O., and Vázquez, R. (2021a). An *a posteriori* error estimator for isogeometric analysis on trimmed geometries. *arXiv:2112.14661*.

Buffa, A., Chanon, O., and Vázquez, R. (2022a). Adaptive analysis-aware defeaturing. *in preparation*.

Buffa, A., Chanon, O., and Vázquez, R. (2022b). Analysis-aware defeaturing: problem setting and *a posteriori* estimation. *Mathematical Models and Methods in Applied Sciences*, 32(02):359–402.

Buffa, A., Gantner, G., Giannelli, C., Praetorius, D., and Vázquez, R. (2021b). Mathematical foundations of adaptive isogeometric analysis. *arXiv preprint arXiv:2107.02023*.

Buffa, A. and Garau, E. M. (2017). Refinable spaces and local approximation estimates for hierarchical splines. *IMA Journal of Numerical Analysis*, 37:1125–1149.

Buffa, A., Garau, E. M., Giannelli, C., and Sangalli, G. (2016). *On quasi-interpolation operators in spline spaces*, pages 73–91. Springer International Publishing, Cham.

Buffa, A. and Giannelli, C. (2016). Adaptive isogeometric methods with hierarchical splines: error estimator and convergence. *Mathematical Models and Methods in Applied Sciences*, 26(01):1–25.

Buffa, A. and Giannelli, C. (2021). Remarks on Poincaré and interpolation estimates for truncated hierarchical B-splines. *Mathematical Models and Methods in Applied Sciences*, 31(03):525–535.

Buffa, A., Puppi, R., and Vázquez, R. (2020). A minimal stabilization procedure for isogeometric methods on trimmed geometries. *SIAM Journal of Numerical Analysis*, 58(5):2711–2735.

Buffa, A., Vázquez, R., Sangalli, G., and Beirão da Veiga, L. (2015). Approximation estimates for isogeometric spaces in multipatch geometries. *Numerical Methods for Partial Differential Equations*, 31(2):422–438.

Burman, E. (2010). Ghost penalty. *Comptes Rendus, Mathématique*, 348(21):1217–1220.

Burman, E., Claus, S., Hansbo, P., Larson, M. G., and Massing, A. (2015). CutFEM: discretizing geometry and partial differential equations. *International Journal for Numerical Methods in Engineering*, 104(7):472–501.

Burman, E. and Hansbo, P. (2012). Fictitious domain finite element methods using cut elements: II. A stabilized Nitsche method. *Applied Numerical Mathematics*, 62(4):328–341. Third Chilean Workshop on Numerical Analysis of Partial Differential Equations (WONAPDE 2010).

Bibliography

Burman, E., He, C., and Larson, M. G. (2020). *A posteriori* error estimates with boundary correction for a cut finite element method. *IMA Journal of Numerical Analysis*, 42(1):333–362.

Carraturo, M., Giannelli, C., Reali, A., and Vázquez, R. (2019). Suitably graded THB-spline refinement and coarsening: towards an adaptive isogeometric analysis of additive manufacturing processes. *Computer Methods in Applied Mechanics and Engineering*, 348:660–679.

Carstensen, C. and Sauter, S. (2004). *A posteriori* error analysis for elliptic PDEs on domains with complicated structures. *Numerische Mathematik*, 96(4):691–721.

Chen, Z., Li, K., and Xiang, X. (2021). An adaptive high-order unfitted finite element method for elliptic interface problems. *Numerische Mathematik*, 149:507–548.

Choi, K. K. and Kim, N.-H. (2005). *Structural Sensitivity Analysis and Optimization 1: Linear Systems*. Springer Science & Business Media.

Ciarlet, P. G. (2002). *The finite element method for elliptic problems*. Society for Industrial and Applied Mathematics.

Clément, P. (1975). Approximation by finite element functions using local regularization. *ESAIM: Mathematical Modelling and Numerical Analysis - Modélisation Mathématique et Analyse Numérique*, 9(R2):77–84.

Coradello, L., Antolín, P., Vázquez, R., and Buffa, A. (2020). Adaptive isogeometric analysis on two-dimensional trimmed domains based on a hierarchical approach. *Computer Methods in Applied Mechanics and Engineering*, 364:112925.

Cottrell, J. A., Hughes, T. J. R., and Bazilevs, Y. (2009). *Isogeometric analysis: towards integration of CAD and FEA*. Wiley.

Courant, R. (1943). Variational methods for the solution of problems of equilibrium and vibrations. *Bulletin of the American mathematical Society*, 49(1):1–23.

De Boor, C. (1972). On calculating with B-splines. *Journal of approximation theory*, 6:50–62.

de Prenter, F., Verhoosel, C. V., van Brummelen, E. H., Evans, J. A., Messe, C., Benzaken, J., and Maute, K. (2020). Multigrid solvers for immersed finite element methods and immersed isogeometric analysis. *Computational Mechanics*, 65(3):807–838.

Deng, J., Chen, F., Li, X., Hu, C., Tong, W., Yang, Z., and Feng, Y. (2008). Polynomial splines over hierarchical T-meshes. *Graphical models*, 70(4):76–86.

Destuynder, P. and Métivet, B. (1999). Explicit error bounds in a conforming finite element method. *Mathematics of Computation*, 68(228):1379–1396.

Di Pietro, D. A. and Ern, A. (2011). *Mathematical aspects of discontinuous Galerkin methods*, volume 69. Springer Science & Business Media.

Dokken, T., Lyche, T., and Pettersen, K. F. (2013). Polynomial splines over locally refined box-partitions. *Computer Aided Geometric Design*, 30(3):331–356.

Dörfler, W. (1996). A convergent adaptive algorithm for Poisson's equation. *SIAM Journal on Numerical Analysis*, 33(3):1106–1124.

Elfverson, D., Larson, M. G., and Larsson, K. (2019). A new least squares stabilized Nitsche method for cut isogeometric analysis. *Computer Methods in Applied Mechanics and Engineering*, 349:1–16.

Ern, A. and Guermond, J.-L. (2021a). *Finite Elements I: Approximation and Interpolation*, volume 72. Springer Nature.

Ern, A. and Guermond, J.-L. (2021b). *Finite Elements II: Galerkin approximation, elliptic and mixed PDEs*, volume 73. Springer Nature.

Farin, G., Hoschek, J., and Kim, M.-S. (2002). *Handbook of computer aided geometric design*. Elsevier.

Farouki, R. T. (1999). Closing the gap between CAD model and downstream application. *SIAM news*, 32(5):303–319.

Ferrandes, R., Marin, P., Léon, J.-C., and Giannini, F. (2009). *A posteriori* evaluation of simplification details for finite element model preparation. *Computers & Structures*, 87(1):73 – 80.

Fine, L., Remondini, L., and Leon, J.-C. (2000). Automated generation of FEA models through idealization operators. *International Journal for Numerical Methods in Engineering*, 49(1-2):83–108.

Forsey, D. R. and Bartels, R. H. (1988). Hierarchical B-spline refinement. In *Proceedings of the 15th annual conference on Computer graphics and interactive techniques*, pages 205–212.

Foucault, G., Marin, P., and Léon, J.-C. (2004). Mechanical criteria for the preparation of finite element models. In *IMR*, pages 413–426.

Gagliardo, E. (1957). Caratterizzazioni delle tracce sulla frontiera relative ad alcune classi di funzioni in n variabili. *Rendiconti del seminario matematico della università di Padova*, 27:284–305.

Gantner, G. and Praetorius, D. (2022). Adaptive BEM for elliptic PDE systems, part II: Isogeometric analysis with hierarchical B-splines for weakly-singular integral equations. *Computers & Mathematics with Applications*, 117:74–96.

Bibliography

Garau, E. M. and Vázquez, R. (2018). Algorithms for the implementation of adaptive isogeometric methods using hierarchical B-splines. *Applied Numerical Mathematics*, 123:58–87.

Gerasimov, T., Stein, E., and Wriggers, P. (2015). Constant-free explicit error estimator with sharp upper error bound property for adaptive FE analysis in elasticity and fracture. *International Journal for Numerical Methods in Engineering*, 101(2):79–126.

Giannelli, C., Jüttler, B., Kleiss, S. K., Mantzaflaris, A., Simeon, B., and Špeh, J. (2016). THB-splines: an effective mathematical technology for adaptive refinement in geometric design and isogeometric analysis. *Computer Methods in Applied Mechanics and Engineering*, 299:337–365.

Giannelli, C., Jüttler, B., and Speleers, H. (2012). THB-splines: the truncated basis for hierarchical splines. *Computer Aided Geometric Design*, 29(7):485–498.

Giannelli, C., Jüttler, B., and Speleers, H. (2014). Strongly stable bases for adaptively refined multilevel spline spaces. *Advances in Computational Mathematics*, 40(2):459–490.

Gopalakrishnan, S. H. and Suresh, K. (2007). A formal theory for estimating defeaturing-induced engineering analysis errors. *Computer-Aided Design*, 39(1):60–68.

Gopalakrishnan, S. H. and Suresh, K. (2008). Feature sensitivity: a generalization of topological sensitivity. *Finite Elements in Analysis and Design*, 44(11):696–704.

Grätsch, T. and Bathe, K.-J. (2005). *A posteriori* error estimation techniques in practical finite element analysis. *Computers & structures*, 83(4-5):235–265.

Grätsch, T. and Bathe, K.-J. (2006). Goal-oriented error estimation in the analysis of fluid flows with structural interactions. *Computer methods in applied mechanics and engineering*, 195(41-43):5673–5684.

Greiner, G. and Hormann, K. (1996). Interpolating and approximating scattered 3D-data with hierarchical tensor product B-splines. In *Proceedings of Chamonix*, volume 1. Citeseer.

Grisvard, P. (2011). *Elliptic Problems in Nonsmooth Domains*. Society for Industrial and Applied Mathematics.

Guzmán, J. and Olshanskii, M. (2018). Inf-sup stability of geometrically unfitted Stokes finite elements. *Mathematics of Computation*, 87(313):2091–2112.

Hackbusch, W. and Sauter, S. (1997a). Composite finite elements for problems containing small geometric details. *Computing and Visualization in Science*, 1(1):15–25.

Hackbusch, W. and Sauter, S. (1997b). Composite finite elements for the approximation of PDEs on domains with complicated micro-structures. *Numerische Mathematik*, 75(4):447–472.

Hadamard, J. (1932). *Le problème de Cauchy et les équations aux dérivées partielles linéaires hyperboliques.* Hermann, Paris.

Hannukainen, A., Stenberg, R., and Vohralík, M. (2012). A unified framework for *a posteriori* error estimation for the Stokes problem. *Numerische Mathematik*, 122(4):725–769.

Hansbo, A. and Hansbo, P. (2002). An unfitted finite element method, based on Nitsche's method, for elliptic interface problems. *Computer Methods in Applied Mechanics and Engineering*, 191(47-48):5537–5552.

Hansbo, A. and Hansbo, P. (2004). A finite element method for the simulation of strong and weak discontinuities in solid mechanics. *Computer Methods in Applied Mechanics and Engineering*, 193(33-35):3523–3540.

Haslinger, J. and Renard, Y. (2009). A new fictitious domain approach inspired by the extended finite element method. *SIAM Journal on Numerical Analysis*, 47(2):1474–1499.

He, C. and Zhang, X. (2019). Residual-based *a posteriori* error estimation for immersed finite element methods. *Journal of Scientific Computing*, 81(3):2051–2079.

Hohmeyer, M. E. (1993). Robust and efficient surface intersection for solid modeling.

Höllig, K. (2003). *Finite element methods with B-splines*, volume 26 of *Frontiers in Applied Mathematics.* Society for Industrial and Applied Mathematics, Philadelphia, PA.

Hrennikoff, A. (1941). Solution of problems of elasticity by the framework method. *Journal of Applied Mechanics*, 8:A169–A175.

Hughes, T. J. R. (2017). Isogeometric analysis: progress and challenges. *Computer Methods in Applied Mechanics and Engineering*, 316:1. Special Issue.

Hughes, T. J. R., Cottrell, J. A., and Bazilevs, Y. (2005). Isogeometric analysis: CAD, finite elements, NURBS, exact geometry, and mesh refinement. *Computer Methods in Applied Mechanics and Engineering*, 194:4135–4195.

Johnson, C. (1990). Adaptive finite element methods for diffusion and convection problems. *Computer Methods in Applied Mechanics and Engineering*, 82(1-3):301–322.

Johnson, C. and Hansbo, P. (1992). Adaptive finite element methods in computational mechanics. *Computer methods in applied mechanics and engineering*, 101(1-3):143–181.

Bibliography

Kapl, M., Sangalli, G., and Takacs, T. (2019). An isogeometric C^1-subspace on unstructured multi-patch planar domains. *Computer Aided Geometric Design*, 69:55–75.

Kargaran, S., Jüttler, B., Kleiss, S. K., Mantzaflaris, A., and Takacs, T. (2019). Overlapping multi-patch structures in isogeometric analysis. *Computer Methods in Applied Mechanics and Engineering*, 356:325–353.

Kraft, R. (1997). *Adaptive and linearly independent multilevel B-splines*. SFB 404, Geschäftsstelle.

Kudela, L., Zander, N., Bog, T., Kollmannsberger, S., and Rank, E. (2015). Efficient and accurate numerical quadrature for immersed boundary methods. *Advanced modeling and simulation in engineering sciences*, 2(1):1–22.

Lee, B.-G., Lyche, T., and Mørken, K. (2000). Some examples of quasi-interpolants constructed from local spline projectors. *Mathematical methods for curves and surfaces: Oslo*, pages 243–252.

Lee, K., Armstrong, C. G., Price, M. A., and Lamont, J. (2005). A small feature suppression/unsuppression system for preparing B-rep models for analysis. In *Proceedings of the 2005 ACM symposium on solid and physical modeling*, pages 113–124.

Li, M. and Gao, S. (2011). Estimating defeaturing-induced engineering analysis errors for arbitrary 3D features. *Computer-Aided Design*, 43(12):1587–1597.

Li, M., Gao, S., and Martin, R. R. (2011). Estimating the effects of removing negative features on engineering analysis. *Computer-Aided Design*, 43(11):1402–1412. Solid and Physical Modeling 2011.

Li, M., Gao, S., and Martin, R. R. (2013a). Engineering analysis error estimation when removing finite-sized features in nonlinear elliptic problems. *Computer-Aided Design*, 45(2):361–372.

Li, M., Gao, S., and Zhang, K. (2013b). A goal-oriented error estimator for the analysis of simplified designs. *Computer Methods in Applied Mechanics and Engineering*, 255:89–103.

Lions, J. L. and Magenes, E. (1973). *Non-Homogeneous Boundary Value Problems and Applications*, volume 1. Springer-Verlag.

Marussig, B., Hiemstra, R., and Hughes, T. J. R. (2018). Improved conditioning of isogeometric analysis matrices for trimmed geometries. *Computer Methods in Applied Mechanics and Engineering*, 334:79–110.

Marussig, B. and Hughes, T. J. R. (2018). A review of trimming in isogeometric analysis: challenges, data exchange and simulation aspects. *Archives of Computational Methods in Engineering*, 25(4):1059–1127.

Morin, P., Nochetto, R. H., and Siebert, K. G. (2002). Convergence of adaptive finite element methods. *SIAM review*, 44(4):631–658.

Müller, B., Kummer, F., and Oberlack, M. (2013). Highly accurate surface and volume integration on implicit domains by means of moment-fitting. *International Journal for Numerical Methods in Engineering*, 96(8):512–528.

Nguyen, V. P., Anitescu, C., Bordas, S. P., and Rabczuk, T. (2015). Isogeometric analysis: an overview and computer implementation aspects. *Mathematics and Computers in Simulation*, 117:89–116.

Nochetto, R. H., Siebert, K. G., and Veeser, A. (2009). Theory of adaptive finite element methods: an introduction. In *Multiscale, nonlinear and adaptive approximation*, pages 409–542. Springer.

Nochetto, R. H. and Veeser, A. (2011). Primer of adaptive finite element methods. In *Multiscale and adaptivity: modeling, numerics and applications*, pages 125–225. Springer.

Oden, J. T. and Prudhomme, S. (2002). Estimation of modeling error in computational mechanics. *Journal of Computational Physics*, 182(2):496–515.

Oden, J. T. and Vemaganti, K. (2000). Estimation of local modeling error and goal-oriented adaptive modeling of heterogeneous materials: I. Error estimates and adaptive algorithms. *Journal of Computational Physics*, 164(1):22–47.

OpenCASCADE (2018). Open CASCADE technology (version 7.3.0). http://www.opencascade.com.

Parvizian, J., Düster, A., and Rank, E. (2007). Finite cell method. *Computational Mechanics*, 41(1):121–133.

Pauletti, M. S., Martinelli, M., Cavallini, N., and Antolín, P. (2015). Igatools: An isogeometric analysis library. *SIAM Journal on Scientific Computing*, 37(4):C465–C496.

Peters, J. and Reif, U. (2008). *Subdivision surfaces*. Springer.

Piegl, L. and Tiller, W. (1997). *The NURBS book*. Springer-Verlag.

Quarteroni, A. and Valli, A. (2008). *Numerical approximation of partial differential equations*, volume 23. Springer Science & Business Media.

Rahimi, N., Kerfriden, P., Langbein, F. C., and Martin, R. R. (2018). CAD model simplification error estimation for electrostatics problems. *SIAM Journal on Scientific Computing*, 40(1):B196–B227.

Bibliography

Rank, E., Ruess, M., Kollmannsberger, S., Schillinger, D., and Düster, A. (2012). Geometric modeling, isogeometric analysis and the finite cell method. *Computer Methods in Applied Mechanics and Engineering*, 249:104–115.

Repin, S. and Sauter, S. (2020). *Accuracy of mathematical models: dimension reduction, homogenization, and simplification*, volume 33 of *EMS Tracts in Mathematics*. European Mathematical Society, Zürich.

Repin, S., Sauter, S., and Smolianski, A. (2003). *A posteriori* error estimation for the Dirichlet problem with account of the error in the approximation of boundary conditions. *Computing*, 70(3):205–233.

Riesenfeld, R. F., Haimes, R., and Cohen, E. (2015). Initiating a CAD renaissance: Multidisciplinary analysis driven design: Framework for a new generation of advanced computational design, engineering and manufacturing environments. *Computer Methods in Applied Mechanics and Engineering*, 284:1054–1072. Isogeometric analysis special issue.

Rogers, D. F. (2001). *An introduction to NURBS: with historical perspective*. Morgan Kaufmann.

Sauter, S. and Warnke, R. (1999). Extension operators and approximation on domains containing small geometric details. *East West Journal of Numerical Mathematics*, 7:61–77.

Schmidt, R., Wüchner, R., and Bletzinger, K.-U. (2012). Isogeometric analysis of trimmed NURBS geometries. *Computer Methods in Applied Mechanics and Engineering*, 241-244:93–111.

Scott, M. A., Li, X., Sederberg, T. W., and Hughes, T. J. R. (2012). Local refinement of analysis-suitable T-splines. *Computer Methods in Applied Mechanics and Engineering*, 213:206–222.

Sokolowski, J. and Zochowski, A. (1999). On the topological derivative in shape optimization. *SIAM journal on control and optimization*, 37(4):1251–1272.

Stein, E. M. (2016). *Singular Integrals and Differentiability Properties of Functions*. Princeton university press.

Sun, H., Schillinger, D., and Yuan, S. (2020). Implicit *a posteriori* error estimation in cut finite elements. *Computational Mechanics*, 65(4):967–988.

Tang, J., Gao, S., and Li, M. (2013). Evaluating defeaturing-induced impact on model analysis. *Mathematical and Computer Modelling*, 57(3):413–424.

Thakur, A., Banerjee, A. G., and Gupta, S. K. (2009). A survey of CAD model simplification techniques for physics-based simulation applications. *Computer-Aided Design*, 41(2):65–80.

Thomas, D., Engvall, L., Schmidt, S., Tew, K., and Scott, M. A. (2018). U-splines: splines over unstructured meshes. *Preprint, https://coreform.com/usplines.*

Toshniwal, D., Speleers, H., and Hughes, T. J. R. (2017). Smooth cubic spline spaces on unstructured quadrilateral meshes with particular emphasis on extraordinary points: geometric design and isogeometric analysis considerations. *Computer Methods in Applied Mechanics and Engineering*, 327:411–458.

Turevsky, I., Gopalakrishnan, S. H., and Suresh, K. (2008). Defeaturing: *A posteriori* error analysis via feature sensitivity. *International journal for numerical methods in engineering*, 76(9):1379–1401.

Turevsky, I., Gopalakrishnan, S. H., and Suresh, K. (2009). An efficient numerical method for computing the topological sensitivity of arbitrary-shaped features in plate bending. *International journal for numerical methods in engineering*, 79(13):1683–1702.

Vázquez, R. (2016). A new design for the implementation of isogeometric analysis in Octave and Matlab: GeoPDEs 3.0. *Computers & Mathematics with Applications*, 72(3):523–554.

Vemaganti, K. (2004). Modelling error estimation and adaptive modelling of perforated materials. *International Journal for Numerical Methods in Engineering*, 59(12):1587–1604.

Verfürth, R. (1994). *A posteriori* error estimation and adaptive mesh-refinement techniques. *Journal of Computational and Applied Mathematics*, 50(1-3):67–83.

Verfürth, R. (2013). *A posteriori error estimation techniques for finite element methods.* OUP Oxford.

Vohralík, M. (2011). Guaranteed and fully robust *a posteriori* error estimates for conforming discretizations of diffusion problems with discontinuous coefficients. *Journal of Scientific Computing*, 46(3):397–438.

Vuong, A. V., Giannelli, C., Jüttler, B., and Simeon, B. (2011). A hierarchical approach to adaptive local refinement in isogeometric analysis. *Computer Methods in Applied Mechanics and Engineering*, 200:3554–3576.

Wei, X., Marussig, B., Antolín, P., and Buffa, A. (2021). Immersed boundary-conformal isogeometric method for linear elliptic problems. *Computational Mechanics*, 68(6):1385–1405.

White, D. R., Saigal, S., and Owen, S. J. (2003). Meshing complexity of single part CAD models. In *IMR*, pages 121–134. Citeseer.

Yosida, K. (1974). *Functional analysis.* Springer Verlag, Berlin.

Zhang, K., Li, M., and Li, J. (2016). Estimation of impacts of removing arbitrarily con-
strained domain details to the analysis of incompressible fluid flows. *Communications
in Computational Physics*, 20(4):944–968.

Zienkiewicz, O. C. and Zhu, J. Z. (1987). A simple error estimator and adaptive procedure
for practical engineerng analysis. *International journal for numerical methods in
engineering*, 24(2):337–357.

Zuo, B.-Q., Huang, Z.-D., Wang, Y.-W., and Wu, Z.-J. (2015). Isogeometric analysis for
CSG models. *Computer Methods in Applied Mechanics and Engineering*, 285:102–124.

Ondine CHANON

Researcher in Mathematics

Swiss and French female citizen
Born on July 22nd, 1994
ondine.chanon@gmail.com

Education

2017–2022 **PhD in Mathematics**, *EPFL*, CH.
Thesis: *Adaptive analysis-aware defeaturing.*
Advisors: Prof. Annalisa Buffa and Dr. Pablo Antolín.

2014–2017 **M.Sc in Computational Science and Engineering**, *EPFL*, CH.

M.Sc in Mathematical Engineering, *Politecnico di Milano*, IT.
Thesis: *A numerical study of the isogeometric collocation method.*
Advisors: Prof. Alfio Quarteroni and Prof. Luca Dedè.

2011–2014 **B.Sc in Mathematics**, *EPFL*, Lausanne, CH.
Erasmus+ exchange year: *University of Waterloo,* Ontario, CA.

Publications and preprints

For all publications, authors appear in alphabetical order, except for publication 5 in which they are listed as per their contribution to the research.

1. Buffa A., **Chanon O.** and Vázquez R, "Adaptive analysis-aware defeaturing", *in preparation*, 2022.

2. Antolín P. and **Chanon O.**, "Analysis-aware defeaturing in multifeature geometries", *in preparation*, 2022.

3. Buffa A., **Chanon O.** and Vázquez R., "An *a posteriori* error estimator for isogeometric analysis on trimmed geometries", accepted in *IMA Journal of Numerical Analysis*, 2022.

4. Buffa A., **Chanon O.** and Vázquez R., "Analysis-aware defeaturing: problem setting and *a posteriori* estimation", *Mathematical Models and Methods in Applied Sciences*, 32(02):359–402, 2022.

5. Gervasio P., Dedè L., **Chanon O.** and Quarteroni A., "A computational comparison between isogeometric analysis and spectral element methods: accuracy and spectral properties", *Journal of Scientific Computing* 83(18), 2020.

6. **Chanon O.**, "Schottky signal analysis: tune and chromaticity computation". *CERN Technical Report ERN-STUDENTS-Note-2016-177*, 2016.

▬▬ Conferences, workshops and schools

Aug.2022 **15ᵗʰ WCCM & APCOM**, online.
Talk in mini-symposium: *An adaptive framework for analysis-aware defeaturing.*

Jul.2022 **WAND 2022**, Salzburg, AU.
Invited talk: *Adaptive analysis-aware geometric defeaturing.*

Jun.2022 **MATHICSE retreat**, Villars, CH.

Jun.2022 **RMMM conference**, Lausanne, CH.
Contributed talk: *An adaptive algorithm combining mesh and geometrical model refinement.*

Jun.2022 **ECCOMAS congress 2022**, Oslo, NO.
Talk in mini-symposium: *Adaptive analysis-aware defeaturing.*

Apr.2021 **Science communication class**, Lausanne, CH.
Short film about my PhD thesis: *Avions en papier [Paper planes].*

Sep.2021 **Swiss Numerics Day 2021**, Lausanne, CH.
Contributed talk: *An adaptive strategy for analysis-aware defeaturing.*

Jul.2021 **6ᵗʰ ECCOMAS Young Investigators Conference (YIC)**, online.
Talk in mini-symposium: *An a posteriori error estimator for analysis-aware defeaturing.*

Jun.2021 **10ᵗʰ ADMOS conference**, online.
Talk in mini-symposium: *An a posteriori error estimator for analysis-based defeaturing.*

Jan.2021 **14ᵗʰ WCCM & ECCOMAS congress 2020**, online.
Talk in mini-symposium: *An a posteriori error estimator for analysis-based defeaturing.*

Aug.2020 **Virtual Isogeometric Analysis conference (VIGA)**, online.
Talk in mini-symposium: *Analysis-aware defeaturing: first results.*

Nov.2019 **2ⁿᵈ ERC CHANGE workshop**, Sestri Levante, IT.
Talk: *An a posteriori error estimator for analysis-based defeaturing.*

Oct.2019 **Summer school on Mathematical and Computational Aspects of Machine Learning**, *Centro di Ricerca Matematica Ennio De Giorgi*, Pisa, IT.

May 2019 **Seminar for B.Sc students**, *EPFL*, Lausanne, CH.
Talk: *Un voyage dans le temps... mathématique [A mathematical time travel...].*

Oct.2018 **Computational engineering workshop**, *Mathematisches Forschungsinstitut Oberwolfach*, DE.
Participant with Oberwolfach Leibniz Graduate Students grant.

Jun.2018 **Isogeometric Analysis conference (IGA)**, Pavia, IT.

Jun.2018 **MATHICSE retreat**, Ste-Croix, CH..
Short talk.

Aug.2014 **Summer school on Scientific Visualization**, *Pierre and Marie Curie University*, Paris, FR.

Teaching and supervising

2017-2022   **Head teaching assistant**, *EPFL*, CH.
B.Sc/M.Sc courses (8 semesters): Numerical analysis and computational mathematics, Numerical analysis, Calculus, Linear algebra.

2012-2021   **Teaching assistant**, *EPFL*, CH/*University of Waterloo*, CA.
B.Sc courses (11 semesters): Numerical analysis, Calculus, Linear algebra, Geometry, Programming, General mathematics, French.

2019–2019   **Co-advisor**, M.Sc thesis, *EPFL*, CH/*Politecnico di Milano*, IT.
Thesis: *Innovative integration techniques on curvilinear elements*, S. Zaninelli. Co-advisors: Prof. Annalisa Buffa, Prof. Paola Antonietti, Dr. Pablo Antolín.

Employment and volunteering history

2018–2022   **First aid rescuer**, *EPFL*, CH.
Campus emergencies and events. Certifications: BLS-AED, IAS 1, IAS 2.

2020–2021   **Tutor**, *EPFL*, CH.
2012-2013   Student support during the Covid-19 crisis. Personal coaching of new students, organization of events.

2017–2020   **Volunteer at the Swiss Federation of Mathematical Games**, *EPFL*, CH.

2016–2019   **Master and PhD students representative**, *EPFL*, CH.

Jul.–Sep. 2016   **Signal processing research engineer intern**, *CERN*, Geneva, CH.
Internship: Development of data fitting algorithms in C++, Matlab and Root.

Jul.–Aug. 2015   **Software engineer intern**, *North Thin Ply Technology*, Penthalaz, CH.
Internship: Conception and simulation of textile structures in C++/C# with Cuda.

Personal skills

Tech tools   MATLAB, C++, Python, LaTeX, Git, ParaView.

Languages   French (native), English (fluent), Italian (fluent), German (elementary), Spanish (elementary).

Music   Certificate of musical studies in piano, *Conservatoire de Musique de Genève*, CH.